

Public reporting burden for this collection of information is estimated to average 1 hour per response, including the time for reviewing instructions, searching existing data sources, gathering and maintaining the data needed, and completing and reviewing the collection of information. Send comments regarding this burden estimate or any other aspect of this collection of information, including suggestions for reducing this burden to Washington Headquarters Services, Directorate for Information Operations and Reports, 1215 Jefferson Davis Highway, Suite 1204, Arlington, VA 22202-4302, and to the Office of Management and Budget, Paperwork Reduction Project (0704-0188), Washington, DC 20503.

1. AGENCY USE ONLY (Leave blank)		2. REPORT DATE 1 December 1998	3. REPORT TYPE AND DATES COVERED Conference Proceedings	
4. TITLE AND SUBTITLE XXIII International Conference on Phenomena in Ionized Gases, VOL 1			5. FUNDING NUMBERS F6170897W0048	
6. AUTHOR(S) Conference Committee				
7. PERFORMING ORGANIZATION NAME(S) AND ADDRESS(ES) Universite Paul Sabatier 118 Route de Narbonne Toulouse Cedex 31062 France			8. PERFORMING ORGANIZATION REPORT NUMBER N/A	
9. SPONSORING/MONITORING AGENCY NAME(S) AND ADDRESS(ES) EOARD PSC 802 BOX 14 FPO 09499-0200			10. SPONSORING/MONITORING AGENCY REPORT NUMBER CSP 97-1013	
11. SUPPLEMENTARY NOTES One book of Invited Papers and five volumes of Proceedings and Contributed Papers				
12a. DISTRIBUTION/AVAILABILITY STATEMENT Approved for public release; distribution is unlimited.			12b. DISTRIBUTION CODE A	
13. ABSTRACT (Maximum 200 words)  The Final Proceedings for XXIII International Conference on Phenomena in Ionized Gases, 17 July 1997 - 22 July 1997  kinetic, thermodynamics, and transport phenomena; elementary processes; low pressure glows; coronas, sparks, surface discharges, and high pressure glows; arcs; high frequency discharges; ionospheric magnetospheric, and astrophysical plasmas; plasma diagnostic methods; plasma surface effects; plasma processing; plasma flows; non ideal plasmas; waves and instabilities; non-linear phenomena; particle and laser beam interactions with plasmas; plasma sources of radiation; modeling; plasma for environmental issues; plasma thrusters; surface treatment; high pressure, non-thermal plasmas.				
14. SUBJECT TERMS  EOARD, Space Environment, Pulsed Power, Astrodynamics, Coatings, Fluids & Lubrication, Electromagnetics, High Power Generation, Lasers			15. NUMBER OF PAGES Too Many to Count	
			16. PRICE CODE N/A	
17. SECURITY CLASSIFICATION OF REPORT UNCLASSIFIED	18. SECURITY CLASSIFICATION OF THIS PAGE UNCLASSIFIED	19. SECURITY CLASSIFICATION OF ABSTRACT UNCLASSIFIED	20. LIMITATION OF ABSTRACT UL	

NSN 7540-01-280-5500

Standard Form 298 (Rev. 2-89)  
Prescribed by ANSI Std. Z39-18  
298-102

**X  
X  
I  
I  
I**

F61708-97-W 0048

CSP 97 - 1013

**I nternational  
C onference on  
P henomena in  
I onized  
G ases**

**Editors:** M.C. Bordage and A. Gleizes

19981216 001



**Proceedings**

**Contributed Papers**

**Vol. I**

**Thursday, July 17**

## **Organizers :**

Centre de Physique des Plasmas et leurs Applications de Toulouse (CPAT)  
Laboratoire de Génie Electrique de Toulouse (LGET)  
From the Université Paul Sabatier, Toulouse France.

## **International Scientific Committee**

R. d'Agostino	Italy
J. Allen	Great Britain
A. Bouchoule (Chairman)	France
E. Desoppere	Belgium
H. Kikuchi	Japan
E.E. Kunhardt	USA
J. Mentel	Germany
B. Milic	Yugoslavia
D. Morrow	Australia
A.H. Oien	Norway
A.A. Rukhadze	Russia
M. Sicha	Czech. Republic

## **Local Organizing Committee**

J.P. Bœuf	M.C. Bordage (Sec.)
H. Brunet (co-Chair.)	J.P. Couderc
B. Despax	M. Dziadowiec
A. Gleizes	B. Held
F. Massines	L.C. Pitchford (co-Chair.)
Y. Segui	S. Vacquie
M. Yousfi	G. Zissis

## **Sponsors**

Association pour le Développement de la Physique Atomique (ADPA)  
International Union of Pure and Applied Physics (IUPAP)  
Centre National de la Recherche Scientifique (CNRS)  
Université Paul Sabatier (UPS) of Toulouse  
Direction de la Recherche et Technologie (DRET)  
Commissariat à l'Energie Atomique (CEA), Cycle de Combustible  
Electricité de France through :  
    Club Arc Electrique, Club Chimie des Hautes Températures and Novelect  
Conseil Régional de la Région Midi-Pyrénées  
Conseil Général du Département de la Haute-Garonne  
Mairie de Toulouse  
CRT Plasma-Laser  
Union Radio Scientifique Internationale (URSI)  
US Department of Energy, US BMDO  
US Air Force through the EOARD

*The Local Organizing Committee wishes to express appreciation to the following corporations for their support :*

AGA S.A.	Thomson Tubes Electroniques
Motorola Semiconducteurs S.A.	Schneider Electric
Osram-Sylvania Inc.	Philips Lighting (for the Penning Award)

## FOREWORD

This volume is the first of five volumes which contain contributed papers that were accepted by the Local Organizing Committee of the XXIII ICPIG for presentation in poster sessions. These papers are to be listed in the INSPEC data base.

The contributions were submitted in camera-ready form by the authors. Therefore, the responsibility for the contents and the form of the papers rests entirely with the authors.

The first four volumes have been arranged by topics, the sequence of which corresponds to that of the respective poster sessions. The fifth volume is comprised of 'late' papers, those for which the authors registered after the deadline for printing of their papers.

The texts of the invited talks are to be published shortly after the conference in a special issue of *Journal de Physique*.

The editors would like to acknowledge the contributions of Mrs L. Fourmeaux, Mr J.M. Barachet and Mr J.P. Chaucheprat in the preparation of these volumes. The computer file of contributed papers and authors was prepared by C. de Peco, and her careful execution of this task is gratefully acknowledged.

April 1997

The Editors

For additional copies of this publication, please contact :

M.C. Bordage, CPAT, Université Paul Sabatier, 118 Route de Narbonne, 31062  
Toulouse cedex 4 France

Printed in France, in the Université Paul Sabatier of Toulouse , 1997



Topic number	SCHEDULE FOR POSTERS	
<b>VOLUME 1</b> THURSDAY, JULY 17		
MORNING		
1	Kinetics, thermodynamics and transport phenomena (Part A)	
2	Elementary processes (Part A)	
6	High frequency discharges (Part A)	
13	Waves and instabilities, including shock waves (Part A)	
AFTERNOON		
1	Kinetics, thermodynamics and transport phenomena (Part B)	
2	Elementary processes (Part B)	
6	High frequency discharges (Part B)	
12	Non-ideal plasmas. Clusters and dusty plasmas	
13	Waves and instabilities, including shock waves (Part B)	
18	Plasmas for environmental issues	
<b>VOLUME 2</b> FRIDAY, JULY 18		
MORNING		
3	Low pressure glows (Part A)	
5	Arcs (Part A)	
17	Numerical modeling (Part A)	
AFTERNOON		
3	Low pressure glows (Part B)	
5	Arcs (Part B)	
11	Generation and dynamics of plasma flows	
14	Non-linear phenomena and self-organization processes	
17	Numerical modeling (Part B)	
<b>VOLUME 3</b> SATURDAY, JULY 19		
7	Ionospheric, magnetospheric, and astrophysical plasmas	
16	Plasma sources of radiation	
19a	Highly ionized, low pressure plasmas	
19b	High pressure, non-thermal plasmas	
<b>VOLUME 4</b> MONDAY, JULY 21		
MORNING		
4	Coronas, sparks, surface discharges and high pressure glows (Part A)	
8	Plasma diagnostic methods (Part A)	
10	Physical aspects of plasma chemistry, plasma processing of surface and thin film technology (Part A)	
AFTERNOON		
4	Coronas, sparks, surface discharges and high pressure glows (Part B)	
8	Plasma diagnostic methods (Part B)	
9	Plasma wall interactions, electrode and surface effects	
10	Physical aspects of plasma chemistry, plasma processing of surface and thin film technology (Part B)	
15	Particle and laser beam interaction with plasmas	
<b>VOLUME 5</b> LATE PAPERS		

# CONTENTS

## Topic 1 : Kinetics, thermodynamics and transport phenomena

PLASMA-WALL INTERACTION IN AN OBLIQUE MAGNETIC FIELD Ahedo E.	I-2
CONCENTRATION AND TRANSPORT COEFFICIENTS IN PLASMA OUT OF THERMAL EQUILIBRIUM Andre P., Abbaoui M., Lefort A., Aubreton J., Elchinger M.F., Fauchais P.	I-4
THE EFFECT OF THE GEOMAGNETIC FIELD ON THE DEVELOPMENT OF THE UPWARD ATMOSPHERIC DISCHARGE Babich L.P., Kutsyk I.M., Kudryavtsev A.Yu., Mozgovoï A.L.	I-6
EVALUATION OF RUNAWAY ELECTRON AVALANCHING Babich L.P., Kutsyk I.M.	I-8
ON THE ELLIPSOIDAL MODEL OF STREAMER IN LONGITUDINAL MAGNETIC FIELD Babich L.P., Babich M. L., Kudryavtsev A.Yu.	I-10
CREATION OF A HIGH CONCENTRATION OF VIBRATIONALLY EXCITED H <sub>2</sub> MOLECULES IN A HYDROGEN FLUX PENETRATIVE THROUGH CESIUM-HYDROGEN DISCHARGE Bacal M., Baksht F.G., Ivanov V.G., Shkol'nik S.M.	I-12
THE NEAR WALL SHEATH-PRESHEATH TRANSITION IN AN OBLIQUE MAGNETIC FIELD Beilis I.I., Keidar M.	I-14
CARS SPECTROSCOPY AND NUMERICAL INVESTIGATIONS OF N <sub>2</sub> VIBRATIONAL KINETICS IN GLOW DISCHARGES Shakhatov V.A., Cenian A.	I-16
MEASUREMENT OF EFFECTIVE IONIZATION AND DRIFT OF POSITIVE IONS IN METHANE AND ITS MIXTURE WITH ARGON De Urquijo J., Arriaga C., Basurto E., Dominguez I., Alvarez I., Cisneros C.	I-18
EXPERIMENTAL AND THEORETICAL INVESTIGATION OF EXCIMER FORMATION IN ARGON IN THE LOW AND MIDDLE PRESSURE RANGE Fiermans V., Desoppere E., Wieme W.	I-20
QUANTUM EFFECTS ON THERMODYNAMIC PROPERTIES OF HOT AND DENSE HELIUM LIKE PLASMAS Rahal H., Gombert M.M.	I-22
ELECTRON ENERGY DISTRIBUTION FUNCTION IN DECAYING AR : NF <sub>3</sub> PLASMA : THE POSSIBILITY OF NEGATIVE ELECTRON MOBILITY Dyatko N.A., Capitelli M., Longo S., Napartovich A.P.	I-24
REVISITED COLLISION INTEGRALS AND TRANSPORT COEFFICIENTS OF HIGH TEMPERATURE AIR COMPONENTS Capitelli M., Gorse C., Longo S., Giordano D.	I-26

EVALUATION OF THE BASIC PARAMETERS IN PLASMAS IN THE MIXTURES OF ARGON AND CHLORINE Novakovic N.V., Milic B.S., Stojilkovic S.M.	I-28
EFFECTIVE SECONDARY EMISSION COEFFICIENT IN A HIGH PRESSURE NOBLE GAS Nagorny V.P., Drallos P.J.	I-30
SUB TO SUPERSONIC STREAMING OF IONS TOWARDS THE CATHODE IN A BEAM-GENERATED PLASMA MODEL Eldevik T., Oien A.H.	I-32
THE EFFECT OF REFLECTION OF FAST ELECTRONS FROM THE ANODE: MONTE CARLO SIMULATION OF LOW CURRENT DISCHARGES AT VERY HIGH E/N Stojanovic V.D., Petrovic Z.Lj.	I-34
TRAPPED ELECTRONS IN ANODE REGION OF STRATIFICATED INERT GAS DISCHARGE Golubovskii Y.B., Nekuchaev V.O., Ponomarev N.S.	I-36
THE MECHANISM OF LOSING FAST-MOVING ELECTRONS IN THE PENNING CELL Saenko V.A., Borisenko A.G., Rudnitsky V.A.	I-38
ONE-PARTICLE SPECTRAL FUNCTION IN DENSE PLASMAS Schepe R., Tamme D., Henneberger K.	I-40
THE INVESTIGATION VIBRATIONAL KINETICS AND HEATING OF N <sub>2</sub> IN THE PULSED DISCHARGE AND ITS AFTERGLOW BY CARS-SPECTROSCOPY AND OPTICAL INTERFEROMETRY Vereshchagin K.A., Smirnov V.V., Shakhmatov V.A.	I-42
PHYSICAL PROCESSES IN A NON-EQUILIBRIUM GAS DISCHARGE PLASMA IN MULTICOMPONENT MIXTURE Alexandrov A.F., Devyatov A.M., Shibkov V.M., Shibkova L.V., Singh D.P., Vaselli M.	I-44
INTEGRAL BOLTZMANN EQUATION WITH A SOURCE TERM Sukhinin G.I.	I-46
MODELING OF PHOTOLYTICALLY EXCITED LASER MEDIUMS PUMPED BY PLAN MULTI-CHANNEL SLIDING DISCHARGES Mikheev L.D., Tcheremiskine V.I., Sabonnadiere M.P., Sentis M.L., Malinowsky G.Y., Delaporte Ph.C.	I-48
INVESTIGATION OF THE P-1 MODEL FOR THE RADIATIVE TRANSFER IN SF <sub>6</sub> CIRCUIT-BREAKER ARCS Eby S.D., Trepanier J.Y.	I-50
REACTIVE CHARGED-PARTICLE TRANSPORT IN CROSSED ELECTRIC AND MAGNETIC FIELDS Li B., Robson R.E., White R.D.	I-52
TIME-DEPENDENT MULTITERM SOLUTION OF THE REACTIVE SPATIALLY-INHOMOGENEOUS BOLTZMANN EQUATION FOR CHARGED PARTICLE SWARMS IN A.C. ELECTRIC FIELDS White R.D., Robson R.E., Ness K.F.	I-54
INTERACTION OF AN ELECTRON BEAM WITH GASEOUS NITROGEN Vasenkov A.V.	I-56

## Topic 2 : Elementary processes

EXPERIMENTAL DETERMINATION OF THE SECONDARY TOWNSEND COEFFICIENT FOR RARE GASES. APPLICATION TO PLASMA DISPLAY PANEL Auday G., Guillot P., Galy J., Brunet H.	I-58
EXPERIMENTAL DETERMINATION AND R-MATRIX CALCULATION OF ELECTRON IMPACT EXCITATION RATE COEFFICIENTS OF NEUTRAL AND SINGLY IONIZED NITROGEN Frost R.M., Awakowicz P.	I-60
ELECTRON-IMPACT DISSOCIATION AND IONIZATION OF MOLECULES STUDIED BY LASER-INDUCED FLUORESCENCE TECHNIQUES Siegel R., Abramzon N., Becker K.	I-62
VUV EMISSIONS PRODUCED BY ELECTRON IMPACT ON SI-ORGANIC MOLECULES Kurunczi P., Martus K., Becker K.	I-64
NEGATIVE ELECTRON MOBILITY IN AR : F <sub>2</sub> MIXTURES. THE DEPENDENCE ON THE ARGON MOMENTUM TRANSFER CROSS SECTION Dyatko N.A., Capitelli M., Napartovich A.P.	I-66
ELECTRON INTERACTIONS WITH CCL <sub>2</sub> F <sub>2</sub> Christophorou L.G., Olthoff J.K., Wang Yicheng	I-68
STATIONARY ELECTRON DISTRIBUTION FUNCTIONS IN MULTIPLE DOUBLE LAYERS Conde L., Leon L.	I-70
NO (A <sup>2</sup> Σ <sup>+</sup> ) EXCITATION MECHANISM IN N <sub>2</sub> -O <sub>2</sub> PULSED RF DISCHARGE De Benedictis S., Dilecce G., Simek M.	I-72
TEMPERATURE DEPENDENCE OF DEEXCITATION RATE CONSTANTS OF NE( <sup>3</sup> P <sub>1</sub> ) AND NE( <sup>3</sup> P <sub>2</sub> ) BY AR, KR, XE AND N <sub>2</sub> Khadka D.B., Yamada K., Fukuchi Y., Odagiri T., Kameta K., Ukai M., Kouchi N., Hatano Y.	I-74
DIP STRUCTURE ON EEDF IN DIFFUSED N <sub>2</sub> PLASMAS Ohe K., Kimura T., Nakamura M.	I-76
IONIZATION COEFFICIENT IN ARGON-ISOBUTANE MIXTURES Krajcar-Bronic I., Grosswendt B.	I-78
ON THE INFLUENCE OF IONIZATION DEGREE ON ELECTRON MOBILITY IN PHOTOPLASMA OF SODIUM VAPOUR-INERT GAS MIXTURE Gorbunov N.A., Latyshev Ph.E., Melnikov A.S., Movtchan I.A., Smurov I.	I-80
OSCILLATING CHARACTER OF ELECTRON TEMPERATURE RELAXATION IN A RECOMBINING PLASMA Gorbunov N.A., Latyshev Ph.E., Stacewicz T., Chorazy J.	I-82
ISOMERIZATION OF HCN <sup>+</sup> TO CNH <sup>+</sup> VIA ION MOLECULE REACTIONS Hansel A., Glanschnig M., Scheiring Ch., Lindinger W., Freguson E.E.	I-84

EXPERIMENTAL AND THEORETICAL INVESTIGATIONS OF NEGATIVE IONS SPATIAL DISTRIBUTION IN OXYGEN DC DISCHARGE Ivanov V.V., Klopovskiy K.S., Lopaev D.V., Rakhimov A.T., Rakhimova T.V., Rulev G.B.	I-86
THE INFLUENCE OF THE LOW ENERGY VIBRATIONALLY EXCITATION ON THE ELECTRON DISSOCIATIVE ATTACHMENT COEFFICIENT IN PURE OZONE Lopaev D.V., Klopovskiy K.S., Popov N.A., Proshina O.V., Rakhimov A.T., Rakhimova T.V.	I-88
VIBRATIONAL AND ATOMIC KINETICS IN THE AFTERGLOW OF N <sub>2</sub> AND N <sub>2</sub> -AR MICROWAVE DISCHARGES Sa P.A., Loureiro J.	I-90
COMPARATIVE STUDIES ON Xe(1s <sub>4</sub> ) LASER LIGHT ABSORPTION AND ASSOCIATED OPTOGALVANIC SIGNAL IN A DC DISCHARGE IN NE-XE MIXTURES Sakai Y., Bratescu M.A., Musa G., Myamoto K.	I-92
INFLUENCE OF THE H <sub>2</sub> ON THE NEON NEGATIVE GLOW SPECTRA IN NE+1%Xe+H <sub>2</sub> MIXTURE Musa G., Baltog A., Lungu C.P.	I-94
MEASUREMENT OF EFFECTIVE DIFFUSION COEFFICIENT OF ELECTRONS IN LOW -DENSITY ARGON AFTERGLOWS Okada T., Sugawara M., Goto M.	I-96
EXCITATION OF 3P AND IONIC LEVELS IN ARGON TOWNSEND DISCHARGES Malovic G.N., Bozin J.V., Jelenkovic B.M., Petrovic Z.Lj.	I-98
NUMERICAL STUDY OF LOW PRESSURE ARGON DISCHARGES WITH RING-LIKE CATHODE GEOMETRY Belenguer Ph., Pitchford L.C.	I-100
INFLUENCE OF CH <sub>4</sub> ADDITION ON ACTIVE NITROGEN PRODUCED IN A LOW-PRESSURE DC DISCHARGE Pintassilgo C.D., Loureiro J., Cernogora G.	I-102
EXPERIMENTAL AND NUMERICAL STUDY OF TRAPPING AND BROADENING OF THE KR ( <sup>3</sup> P <sub>1</sub> → <sup>1</sup> S <sub>0</sub> ) RESONANCE LINE IN KR-AR MIXTURES Gardou J., Sewraj N., Marchal F., Millet P., Salamero Y.	I-104
DETERMINATION OF THE RADIATIVE LIFETIME OF THE <sup>1</sup> P <sub>1</sub> RESONANCE STATE IN KRYPTON BY MEANS OF THREE PHOTON EXCITATION Van Bever T., Desoppere E.	I-106

## Topic 6 : High frequency discharges

THE ASYMMETRICAL CAPACITIVE HF LOW PRESSURE DISCHARGE NEAR-ELECTRODE PLASMA ELECTRON ENERGY SPECTRUM Alexandrov A.F., Savinov V.P., Singaevsky I.F.	I-108
--	-------

INVESTIGATION ON THE AFTERGLOW OF PULSED MICROWAVE DISCHARGES IN AR, N <sub>2</sub> AND AIR Bhattacharjee S., Amemiya H.	I-110
INFLUENCE OF THE ASSUMPTIONS ON THE EEDF IN FLUID MODELS OF RF DISCHARGES Merad A., Bœuf J.P.	I-112
HEATING MODE TRANSITIONS IN A CAPACITIVELY COUPLED RADIO FREQUENCY DISCHARGE Deegan C.M., Hopkins M.B.	I-114
THE FORMATION OF RF SUSTAINED DOUBLE LAYER IN PLASMA RESONANCE Annaratone B.M., Allen J.E., Dyson A.E.	I-116
RF HYDROGEN PLASMA DISCHARGE USED FOR CHLORIDE REMOVAL FROM CORRODED COPPER SAMPLES El Shaer M., Mobasher M., Wuttman M.	I-118
BREAKDOWN IN A HYDROGEN PULSED DISCHARGE CREATED IN A RESONANT CAVITY Draghici-Lacoste A., Alves L., Ferreira C.M., Leprince P., Gousset G.	I-120
WAVE PROPAGATION CHARACTERISTICS IN A LOW PRESSURE NITROGEN SURFACE WAVE SUSTAINED DISCHARGE Dias F.M., Tatarova E., Ferreira C.M.	I-122
SELF-CONSISTENT MODEL FOR KINETIC PROCESSES IN MICROWAVE H <sub>2</sub> DISCHARGES Gordiets B.F., Pinheiro M.J., Ferreira C.M.	I-124
SOME RESULTS FROM HYDRODYNAMIC MODELLING OF DIFFUSION COOLED RADIOFREQUENCY SHEAT DISCHARGES Harendt A.	I-126
OPTICAL DIAGNOSTICS OF THE RF DISCHARGE BURNING AT ATMOSPHERIC PRESSURE AND INTERACTING WITH WATER SOLUTION Brablec A., Slavicek P., Klima M., Kapicka V.	I-128
STUDY OF A GAS FLOW IN A TWO-NOZZLE PLASMA REACTOR Kapoun K., Hubicka Z., Sery M., Sicha M.	I-130
THE STRUCTURE OF A CAPACITIVELY COUPLED PLASMA Kardneris S.N., Annaratone B.M., Allen J.E.	I-132
TEMPORAL EVOLUTION OF AN INDUCTIVELY-COUPLED RF DISCHARGE DURING MODE TRANSITION Matsuoka M., Kawaguchi M., Yoshida M.	I-134
ROLE OF ELECTROMAGNETIC WAVES IN ECR PLASMA UNIFORMITY Ueda Y., Kawai Y.	I-136
CHARACTERISTIC PROPERTIES OF THE MICROWAVE BREAKDOWN WAVE IN ELECTRICALLY NEGATIVE GASES Batanov G.M., Kossyi I.A., Malykh N.I., Matveev A.A., Sapozhnikov A.V., Silakov V.P.	I-138

LOW-FREQUENCY PERIODIC REGIME IN THE ECR ION SOURCES Lamoureux M., Girard A., Khodja H., Melin G.	I-140
RF HEATING OF PLASMA BETWEEN PARALLEL PLATES BY PLASMA-SHEATH RESONANCE Matsui T., Tsuda S., Yamada K.	I-142
MEASUREMENT OF INTERACTION BETWEEN PLASMA-LOADED SLOW WAVE STRUCTURE AND HIGH-POWER MICROWAVES Naito Y., Shiozaki A., Onose H., Hangai N., Minami K.	I-144
A NEW APPROACH TO RF DISCHARGE MODELLING AND THE EVALUATION OF RESULTING DISCHARGE PROPERTIES Praessler F., Hoffmann V., Suchaneck G., Wetzig K.	I-146
INFRARED ABSORPTION ANALYSIS OF ORGANOSILICON PLASMAS IN A MULTIPOLAR MICROWAVE PLASMA REACTOR Raynaud P., Marliere C., Berthomieu D., Segui Y., Durand J.	I-148
KINETICS OF F ATOMS AND $CF_x$ RADICALS IN A PULSED $CF_4$ MICROWAVE PLASMA Schwarzenbach W., Derouard J., Sadeghi N.	I-150
EXCITATION MECHANISMS AND ION KINETICS IN A 450 KHZ CAPACITIVELY COUPLED ARGON DISCHARGE Van de Grift M., Sadeghi N., Hbid T., Kroesen G.M.W., De Hoog F.J.	I-152
DYNAMICS OF THE FREELY LOCALIZED MICROWAVE DISCHARGE IN AIR Kuzovnikov A.A., Shibkov V.M., Shibkova L.V., Singh D.P., Vaselli M.	I-154
SURFACE WAVE SUSTAINED DISCHARGES IN PULSED REGIME OPERATION Grozev D., Kirov K., Makasheva K., Shivarova A.	I-156
GAS-DISCHARGE MAINTENANCE BY GUIDED MODE PROPAGATION IN STRONG MAGNETIC FIELD Shivarova A., Tarnev Kh.	I-158
EFFECTS OF NON-LOCAL ELECTRON KINETICS IN A RF CAPACITIVE DISCHARGE IN NITROGEN Stoykova E., Tatarova E., Bachev K., Zhelyazkov I.	I-160
TRANSITION FROM $\alpha$ - TO $\gamma$ -REGIME IN A RF CAPACITIVE DISCHARGE IN NITROGEN Stoykova E., Tatarova E., Bachev K., Zhelyazkov I.	I-162
DIAGNOSTIC STUDY OF RF PARALLEL PLATE REACTOR Kobayashi Y., Sando K., Sugawara M., Sato T.	I-164
A SURFACE WAVE BASED HIGH-DENSITY PLASMA SOURCE OPERATED NEAR 200 MHZ Tabbal M., Pauna O., Chaker M., Margot J.	I-166
A HIGH FLUX SOURCE OF N ATOMS BASED ON A $N_2$ HF DISCHARGE Merel P., Tabbal M., Chaker M., Moisan M., Ricard A.	I-168
ESTIMATION OF ELECTRON DENSITY DISTRIBUTION IN INDUCTIVELY COUPLED ELECTRODELESS DISCHARGE Watanabe Y., Yasuda M.	I-170

THEORETICAL STUDY OF ELECTROMAGNETIC PHENOMENA IN PLASMA LAYERS AND THIN FILMS	I-172
Yilmaz A., Bilikmen S., Rukhadze A.A.	

## Topic 12 : Non-ideal plasmas. Clusters and dusty plasmas

UNDERWATER LASER SPARKS SPECTROSCOPIC CHARACTERISATION USING HYDROGEN BALMER EMISSION LINES	I-174
Escarguel A., Lesage A., Richou J.	
OBSERVATION OF ORDERED STRUCTURE IN THERMAL DUSTY PLASMAS	I-176
Chernyshev A.V., Fortov V.E., Nefedov A.P., Petrov O.F.	
DUSTY PLASMA ORDERED STRUCTURES IN THE STRATIFIED DC GLOW DISCHARGE	I-178
Fortov V.E., Lipaev A.M., Molotkov V.I., Nefedov A.P., Petrov O.F., Torchinskii V.M.	
SHELL STRUCTURE OF PURE ION PLASMAS	I-180
Ignatov A.M.	
ELECTRON ENERGY DISTRIBUTION FUNCTION IN A DUSTY PLASMA	I-182
Ivanov V.V., Rakhimova T.V.	
SPECTRAL DIAGNOSTICS OF OPTICAL CONSTANTS OF PARTICLES IN DUSTY PLASMA	I-184
Kirillin A., Samarian A., Vaulina O.	
HIGH POWER DENSITY DUSTY MATTER COLLECTED AS A SOURCE OF HARD X-RAY	I-186
Kurilenkov Yu.K., Skowronek M., Louvet G., Romeas P.	
THE DENSITY EFFECT IN OPACITY OF PURE HYDROGEN PLASMA	I-188
Gavrilova T., Averyanov V.P., Vitel Y., Le Guen C., D'yachkov L., Kurilenkov Yu.K.	
RADIATION OF DENSE HELIUM PLASMA PRODUCED IN FLASHLAMPS	I-190
Vitel Y., El Bezzari M., D'yachkov L., Kurilenkov Yu.K.	
PROBE INDUCED INTERPENETRATION AND CIRCULATION IN PLASMA-DUST CRYSTALS	I-192
Law D.A., Steel W.H., Annaratone B.M., Allen J.E.	
LASER INDUCED MOTION OF MICROMETRE SIZE PARTICLES IN RF PLASMA SHEATHS	I-194
Steel W.H., Law D.A., Annaratone B.M., Allen J.E.	
NUMERICAL ANALYSIS ON FINE PARTICLE'S BEHAVIOUR IN AN ION-BEAM PLASMA SYSTEM	I-196
Ohno N., Nakamura M., Nunomura S., Takamura S.	
GENERATION OF CARBON CLUSTERS AND FULLERENES IN ARC JET	I-198
Sukhinin G.I., Nerushev O.A.	
SUBMICRONIC $Si_xC_{1-x}$ POWDER SYNTHESIS AND PALLADIUM COATING BY USING LOW PRESSURE DUSTY PLASMA PROPERTIES	I-200
Vivet F., Bouchoule A.	



OBSERVATION OF DUST LEVITATION IN A THERMOIONIC LOW PRESSURE DISCHARGE Arnas-Capeau C., Mikikian M., Doveil F.	I-202
---	-------

### **Topic 13 : Waves and instabilities, including shock waves.**

ION-ELECTRON INSTABILITY IN AN ELECTRON-COLLECTING CONTACTOR Lapuerta V., Ahedo E.	I-204
HALL EFFECT AS THE PRODUCER OF EFFECTIVE GRAVITY AND OF QUASI- ACOUSTIC- GRAVITY WAVES IN PLASMA FLOWS Alekseeva L.M.	I-206
ELECTRIC FIELD WAVES INSIDE THE POSITIVE COLUMN OF THE SELF- PULSED GAS DISCHARGE Alexandrov L.S., Chirkin M.V., Morozov D.A., Stepanov V.A.	I-208
NONLINEAR PLASMA WAVE PROPAGATION Lancellotti C., Dorning J.	I-210
EXPERIMENTAL STUDY OF AL LINE IN DENSE XENON PLASMA Kulish M., Gryaznov V., Mezhiba A., Mintsev V.B., Fortov V., Hoffmann D.H.H., Stockl C., Roth M., Sharkov B., Golubev A.	I-212
ELECTRON SHOCK WAVES : WAVE PROFILE FOR A RANGE OF SPEEDS Hemmati M.	I-214
ION SHEATH INSTABILITY IN MULTI-COMPONENT PLASMAS CONTAINING NEGATIVE IONS Koga K., Hayashi N., Kawai Y.	I-216
A 30 KHZ - 1 MHZ FAST SWEEPING METHOD FOR LANGMUIR PROBES APPLIED TO TURBULENT PLASMAS Leborgne L., Goulet J.C., Van Ootegem B., Vervisch P.	I-218
COMPUTER SIMULATION OF TWO-PLASMON DECAY INSTABILITY EXCITED BY A STRONG RUNNING PUMP WAVE IN TWO-SPECIES PLASMA Levchenko V.D., Sigov Y.S.	I-220
ON THE INFLUENCE OF RELATIVE ION CONCENTRATIONS ON QPESIC MODES IN WEAKLY IONIZED PLASMAS WITH SINGLY, DOUBLY AND TRIPLY CHARGED IONS Gajic D.Z., Milic B.S.	I-222
SOME PROPERTIES OF THE QPESIC INSTABILITIES IN WEAKLY IONIZED PLASMAS WITH IONS $A^+$ AND $A^{++}$ POSSESSING DIFFERENT TEMPERATURES Gajic D.Z., Milic B.S.	I-224
SPATIAL ATTENUATION OF LANGMUIR WAVES IN GAS-DISCHARGE NEON AND ARGON PLASMAS Zigman V.J., Milic B.S.	I-226

HIGH-POWER BACKWARD-WAVE OSCILLATOR OPERATING FAR FROM UPPER CUTOFF Tanaka K., Zheng X., Minami K., Nagahama T., Tokumasu H.	I-228
EXPERIMENTS ON NONNEUTRAL PLASMAS IN MULTI-RING-ELECTRODES TRAPS Mohri A., Michishita T., Yamazawa Y., Higaki H., Yuyama T., Tanaka H., Hirota A., Oishi H.	I-230
NONSTATIONARY PARAMETRIC PROCESSES IN A RELATIVISTIC SEMI-BOUNDED PLASMA Pavlenko V.N.	I-232
PROPAGATION OF WHISTLER WAVE PACKETS IN A COLLISIONAL PLASMA Sonnenschein E., Rutkevich I., Censor D.	I-234
ANALYSIS OF STABILITY OF STRONG SHOCK WAVES IN METALS Rutkevich I., Zaretsky E., Mond M.	I-236
RESTRICTED DENSITY PERTURBATIONS IN A MAGNETIZED ELECTRONEGATIVE GAS POSITIVE COLUMN Satoh H., Matsumoto M.	I-238
NEGATIVE CHARGE IN ANODE-SIDE REGION OF PLASMA ARC AS BASIS OF INITIATION MECHANISM OF HIGH-FREQUENCY INSTABILITY Smakhtin A.P., Rybakov V.V.	I-240
AMPLIFICATION OF SUBSONIC ION ACOUSTIC ENVELOPE IN A WEAKLY MAGNETIZED PLASMA Tsukabayashi I., Sato S., Nakamura Y.	I-242
EFFECTS OF NEGATIVE IONS ON DISPERSION RELATIONS OF ION WAVES Yoshimura S., Koga K., Nakamura Y., Watanabe T., Kawai Y.	I-244

## Topic 18 : Plasmas for environmental issues

SIMULTANEOUS TREATMENT OF IRON, ASH AND WOOD SIMULATING MISCELLANEOUS RADIOACTIVE SOLID WASTES BY THERMAL PLASMA Amakawa T., Yasui S., Adachi K.	I-246
COAXIAL UNDERWATER PULSED CORONA DISCHARGE AS A SOURCE OF NON-THERMAL PLASMA Clupek M., Sunka P., Babicky V., Cernak M.	I-248
KINETICS OF NITRIC OXIDE REMOVAL FROM $N_2 : O_2 : CO_2 : NO$ IN A POINT-TO-PLATE CORONA DISCHARGE Dors M., Nichipor G.V., Mizeraczyk J.	I-250
INFLUENCE OF NEUTRAL DYNAMICS ON CHEMICAL KINETICS FOR FLUE GAS DISCHARGE MODELING Eichwald O., Yousfi M., Bayle P., Benabdessadok M.D.	I-252

AN APPARATUS FOR ON-LINE MONITORING OF METAL TRACES IN ATMOSPHERIC AIR: THE INFLUENCE OF SOME PERTINENT PARAMETERS ON DETECTION Almi A., Sarrette J.P., Gomes A.M.	I-254
OXIDATION PROCESSES IN THE LIQUID SOLUTIONS BY MEANS OF GLIDING ARC AT ATMOSPHERIC PRESSURE Janca J., Maximov A.I.	I-256
PRODUCTION OF CHEMICALLY ACTIVE SPECIES BY POSITIVE STREAMER IN AIR Kulikovsky A.A.	I-258
ON-LINE MONITORING OF VOLATILE ORGANIC COMPOUNDS BY PROTON TRANSFER REACTION MASS SPECTROMETRY (PTR-MS) Lindinger W., Holzinger R., Prazeller P., Jordan A., Hansel A.	I-260
REMOVAL OF ETHYLACETATE USING CORONA DISCHARGE Machala Z., Morvova M.	I-262
THE INFLUENCE OF HYDROCARBONS ON THE REMOVAL OF NO <sub>x</sub> FROM EXHAUST GAS BY DIELECTRIC BARRIER DISCHARGES Niessen W., Schruft R., Wolf O., Neiger M.	I-264
ATMOSPHERIC PRESSURE ELECTRIC DISCHARGE IN FAST FLOWING AIR Pekarek S., Rosenkranz J., Hanitz F., Kriha V.	I-266
DEVELOPMENT OF A NEW REACTOR FOR THE REMOVING OF THE GASEOUS POLLUTANTS BY COLD PLASMAS Brethes S., Peyrous R., Held B., Coste C.	I-268
NO REMOVAL IN A PHOTO-TRIGGERED DISCHARGE REACTOR Rozoy M., Monin M.P., Postel C., Puech V.	I-270
THE MAIN CHANNELS OF FREON DESTRUCTION IN NANOSECOND CORONA DISCHARGE Akhmedzhanov R.A., Vikharev A.L., Gorbachev A.M., Ivanov O.A., Kolisko A.L.	I-272
ENERGY COST OF OZONE PRODUCTION IN NANOSECOND MICROWAVE DISCHARGES Akhmedzhanov R.A., Vikharev A.L., Gorbachev A.M., Ivanov O.A., Kolisko A.L.	I-274

***Topic 1***

**Kinetics, thermodynamics and  
transport phenomena.**

# Plasma-wall interaction in an oblique magnetic field

E. Ahedo

E.T.S.I. Aeronáuticos, Universidad Politécnica, Madrid, Spain

## 1. Formulation of the model

This contribution describes the steady state, 1-dimensional structure of a plasma immersed in a uniform magnetic field and interacting with an absorbing wall biased to a non-zero potential relative to the undisturbed plasma. Far from the wall it is assumed that some weak collisional process accelerates the plasma. This allows us not to include geometrical effects that would lead to 3-D models inevitably. Related works [1-3] will be discussed.

The wall is biased to a potential  $U_W$  relative to the potential of the plasma at a certain reference point far from the wall but still in the 1-D region, and the plasma is magnetized by an external, uniform magnetic field,  $\vec{B} = B_0(\vec{i}_x \cos \psi + \vec{i}_z \sin \psi)$ . The self-consistent electric field,  $\vec{E} = -\vec{i}_x dU/dx$  is part of the solution. The spatial structure of the plasma consists, basically, of an external quasineutral region or presheath and a space-charge sheath attached to the wall. The plasma dynamics are described by a set of macroscopic equations; it can be shown that there exists a conservation law related to the total momentum along  $B$  (and a second one in the collisionless regions). Some boundary conditions far from the wall cannot be properly fixed without matching the 1-D region with a most external 3-D region that would include the global geometry of the wall, but fortunately, the asymptotic behavior of the plasma in the 1-D region can be known just by assuming that the velocity of the attracted species,  $\vec{V}$ , goes to 0 at  $x \rightarrow -\infty$ .

Three length scales appear in the plasma response: the collision mean free path,  $\lambda_c$ , the magnetic gyro-radius,  $\lambda_m$ , and the Debye length,  $\lambda_d$ . Here, only weakly collisional plasmas,  $\lambda_d \ll \lambda_c$ , are considered, but we let  $\lambda_m \propto 1/B_0$  to take any value. The non-dimensional plasma response depends on five parameters:  $\Lambda_{cm} = \lambda_c/\lambda_m$ ,  $\Lambda_{dm} = \lambda_d/\lambda_m$ ,  $\psi$ ,  $\phi_W = |qU_W|/T$ , and  $T/T_r$ ;  $T$  and  $T_r$  are the temperatures of the attracted and repelled species, respectively.

i)  $\Lambda_{cm}$  and  $\Lambda_{dm}$  (with  $\Lambda_{cm} \gg \Lambda_{dm}$ ), both proportional to  $B_0$ , measure the strength of the B-field relative to the E-field in the quasineutral and non-neutral regions, respectively; therefore, these ratios indicate whether the plasma motion in the incidence plane,  $Oxz$ , tends to be along the B- or the E-lines.

ii) As the incidence angle,  $\psi$ , increases, the E and

B directions diverge and the competition between both fields to govern the direction of the plasma motion, is more dramatic; the ExB drift (along  $Oy$ ) increases with  $\psi$ , also.

iii) The wall potential,  $\phi_W = |qU_W|/T$ , appears in the equations as a boundary condition only; consequently, the structure of the external region is independent of  $\phi_W$ , and the solution to the plasma equations is universal for any  $\phi_W$ .

iv) The temperature ratio,  $T/T_r$ , affects the presence of repelled particles in the sheath, and the plasma velocity at the entrance of the sheath (that is related to the plasma sound velocity,  $C_s$ ).

## 2. Structure of the plasma region

Sketches of the plasma structure for different ranges of magnetic field strength and wall potential are drawn in Figures 1 and 2. The transition between two regions is defined by particular sonic conditions on the plasma motion. Except in one case, the equations corresponding to each case and each region can be integrated with simple and standard methods.

### 2.1. Case $\Lambda_{cm} \rightarrow \infty$ , $\Lambda_{dm} \rightarrow 0$

In this double limit the equations clearly define three different plasma regions. It corresponds to an intermediate magnetic field, very strong compared with the diffusion E-field, and very weak compared with the space-charge E-field. The plasma structure consists of

a) a B-aligned presheath: it extends from  $V_x = 0$  to  $V_x = C_s \cos \psi$  (point C), where  $\lambda_c dV_x/dx \rightarrow \infty$ ; due to the strong B-field, the plasma motion is along the B-lines and there is not ExB drift;

b) a Chodura layer[2], collisionless and quasineutral: it extends from point C to  $V_x = C_s$  (point S), where  $\lambda_m dV_x/dx \rightarrow \infty$ ; its typical thickness is  $\lambda_m$  here the stronger E-field is able to drift the plasma towards its direction and to produce an ExB drift.

c) a space-charge (Debye) sheath: it extends from point S till the wall; its typical thickness is  $\lambda_d$  magnetic effects are negligible in it, the plasma motion is dominated by the strong E-field.

Notice that the Chodura layer is a transition region to accommodate the external and near-to-the-wall plasma motions, channelled by  $\vec{B}$  and  $\vec{E}$ , respectively. This explains that there is no Chodura layer at normal incidence,  $\psi = 0$ , when points C and S coincide.

## 2.2 Case $\Lambda_{cm} = O(1)$

For weaker magnetic fields, when the limit  $\Lambda_{cm} \rightarrow 0$  is not a good approximation, the plasma structure consists of a presheath, that extends now until point S, and the Debye sheath. Point C is no more a singular point of the equations, and the Chodura layer disappears as a well-distinguished region. However, while  $\Lambda_{mc} \leq O(1)$ , the characteristics of the plasma motion do not change very much. The ratio  $V_z/V_x$  increases with both  $\Lambda_{mc}^{-1}$  and  $\psi$ , but the ExB drift is maximum for  $\Lambda_{mc} \sim 1$ . The presheath typical thickness is  $\lambda_c(\Lambda_{mc}^2 + \cos^2 \psi)/(\Lambda_{mc}^2 + 1)$ . For  $\Lambda_{mc} \gg 1$ , magnetic effects are negligible, of course, and the whole plasma field is along the E-lines.

For the particular case of grazing incidence,  $\psi \simeq \pi/2$ , the ExB drift is the main component of the plasma motion when  $\Lambda_{cm} \gg 1$ :  $V_y/V_x \sim \Lambda_{cm}$ . A consequence is that the limit  $\Lambda_{mc} = \infty$  does not make sense: there is not B-aligned presheath and there is no solution of the Chodura layer equations.

## 2.3 Case $\Lambda_{dm} = O(1)$

Here, point S is no longer a singular point, so the Chodura layer and the Debye sheath disappear as separate regions, and formed a single magnetized, non-neutral sheath, that matches with the presheath at point C. The plasma, that comes into the sheath aligned with  $B$ , is forced to drift in the E-field direction, but this drift is only significant while  $\Lambda_{dm}$  is small. There is also an ExB drift, that is maximum for  $\Lambda_{dm} \sim 1$ .

## 2.4 Case $\phi_W \gg 1$

In all the preceding cases we have implicitly assumed that  $\phi_W = O(1)$ . When  $\phi_W \gg 1$ , the structure of the space-charge sheath can be further explored. Except for a thin supersonic layer, where  $\phi \sim 1$ , thermal effects can be disregarded in the sheath. We have then a hypersonic (or cold-plasma) sheath, that admits an analytical solution, that is especially interesting for  $\Lambda_{dm} \ll 1$  due to the changing features of the plasma behavior within it, Figure 2(a).

## Acknowledgments

This work was supported by the Comisión Asesora de Investigación Científico Técnica of Spain, Project PB94-0417-C3-03.

## References

- [1] R. Chodura: Phys. Fluids **25** (1982) 1628.
- [2] K.U. Riemann: Phys. Plasmas **1** (1994) 552.
- [3] P.C. Stangeby: Phys. Plasmas **2** (1995) 702.

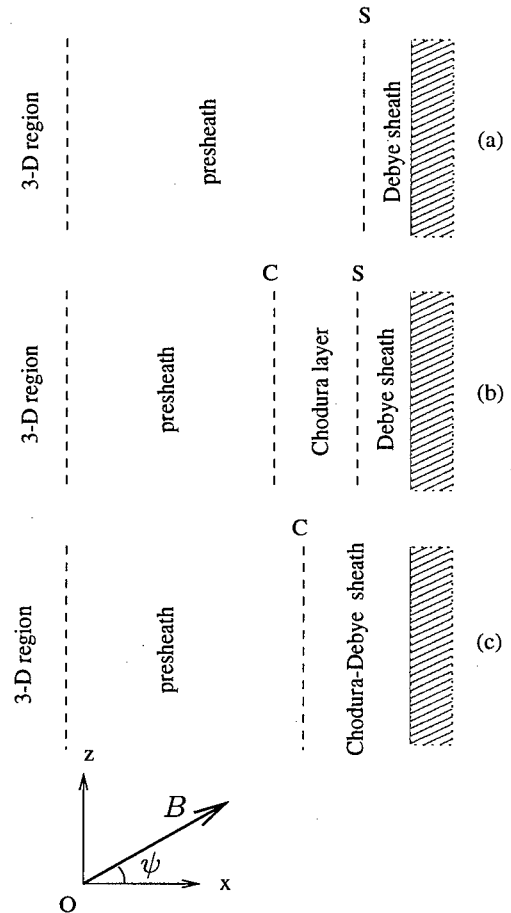


**Figure 1.-** Plasma regions for  $\phi_W = O(1)$  and (a)  $\Lambda_{dm} \rightarrow 0$ ,  $\Lambda_{cm} \leq O(1)$ ; (b)  $\Lambda_{dm} \rightarrow 0$ ,  $\Lambda_{cm} \rightarrow \infty$ ; (c)  $\Lambda_{dm} \geq O(1)$ ,  $\Lambda_{cm} \rightarrow \infty$ .

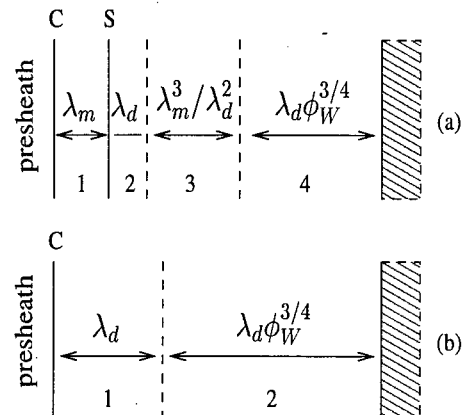


**Figure 2.-**  $\Lambda_{cm} \rightarrow \infty$ ,  $\phi_W \gg 1$ ,  $\Lambda_{dm}^{-4}$ . Collisionless plasma regions for (a)  $\Lambda_{dm} \ll 1$ : Chodura layer(1); supersonic(2) and hypersonic(3), unmagnetized sheath; magnetized sheath(4); (b)  $\Lambda_{dm} \sim 1$ : supersonic(1) and hypersonic(2), magnetized sheath.

# Concentration and transport coefficients in plasma out of thermal equilibrium

André P.<sup>1</sup>, Abbaoui M.<sup>1</sup>, Lefort A.<sup>1</sup>  
Aubreton J.<sup>2</sup>, Elchinger M.F.<sup>2</sup>, Fauchais P.<sup>2</sup>

1. LAEPT, CNRS URA 828, Université Blaise Pascal, 24, Avenue des Landais, F 63177 Aubière cedex, France.  
2. LMCTS, CNRS URA 320, Université de Limoges, 123, Av. Albet Thomas, 87060 Limoges cedex, France

## Introduction

The determination of the concentrations and transport coefficients are often needed in plasmas out of thermal equilibrium. In these plasmas, several temperatures can be defined: excitation (diatomic:  $T_{ex}^{diat}$  monoatomic:  $T_{ex}^{at}$ ), vibrational  $T_{vib}^{diat}$ , rotational  $T_{rot}^{diat}$ , translational (electrons  $T_{tr e-}$ ; heavy species  $T_{tr h}$ ). To determine the concentrations two methods are widely used: one is based on the Gibbs free energy minimisation [1] and the other on the chemical kinetic [2]. In this paper we compare the results of composition and transport properties obtained by using these two methods.

## Composition calculation

Concerning temperatures, the following assumptions have been made:

$$T_{ex}^{at} = T_{ex}^{diat} = T_{vib}^{diat} = \theta \cdot T_{tr h} \quad \text{and} \quad T_{rot} = T_{tr h}.$$

Therefore the plasma has two temperatures and the parameter  $\theta$  characterizes the thermal disequilibrium. If temperature and pressure are kept constant during irreversible transformations, the equilibrium is reached when the Gibbs free energy is minimum (GFEM). So with others equations (electrical neutrality and species conservation) the composition evolution with the heavy species temperature can be determined [1]. Figure 1 shows the composition of a pure nitrogen plasma at atmospheric pressure and for a thermal disequilibrium  $\theta = 1.5$ . In the case of the pseudo-kinetic method (PKM) the chemical equilibrium is reached when the following relationship is verified [2]

$$\ln\left(\frac{k_f^l}{k_r^l}\right) = \ln\left(\prod_i n_i^{\nu_i^l}\right) = \ln(K_l(T)) \quad \text{where } \nu_i^l \text{ are the}$$

stoichiometric coefficients difference of  $i$ th species for 1 reaction;  $n_i$  is the concentration of species  $i$ ;  $k_d^l$  and  $k_i^l$  are respectively forward and reverse reaction rate coefficients of chemical reaction  $l$  and  $K_l(T)$  is the equilibrium constant of chemical reaction  $l$ . This latter is calculated at thermal equilibrium. With the above relationships, the species concentration can be determined in a plasma out of thermal equilibrium. Each rate coefficient  $k_d^l$  or  $k_i^l$  was either dependent of  $T_{tr e}$  or  $T_{tr h}$  or of both temperatures [1]. The temperature range was chosen between 1,000 and 11,000 K to account for the presence of ionized species. Comparison of figures 1 and 3 shows that with the PKM method dissociation occurs at lower

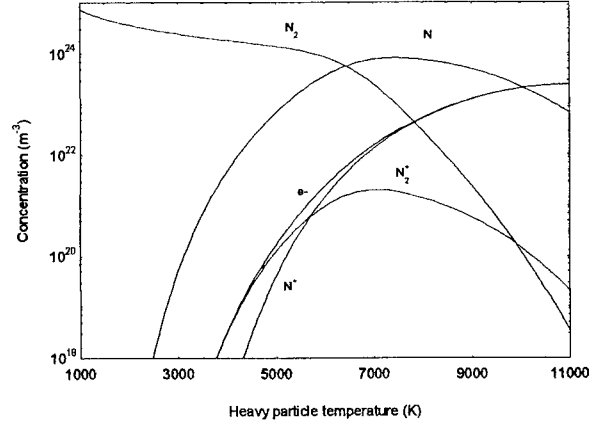


Fig. 1: Gibbs free energy minimisation ( $\theta = 1.5$ ).

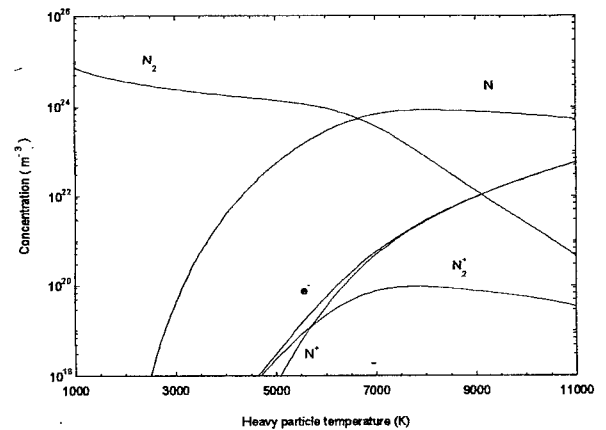


Fig. 2: PKM with each rate coefficients calculated at one temperature  $T_{tr e}$  or  $T_{tr h}$  ( $\theta = 1.5$ ).

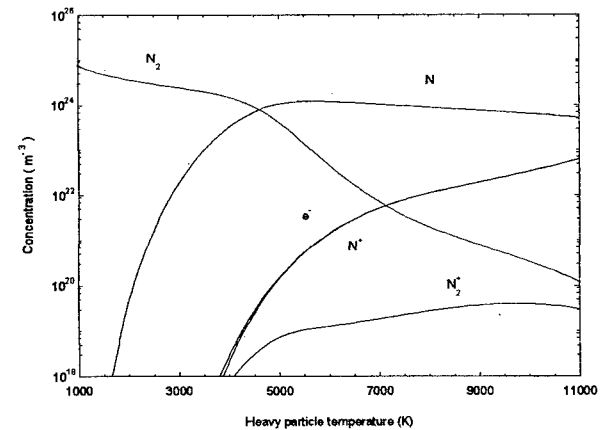


Fig. 3: Pseudo kinetic method with rate coefficients at two temperatures ( $\theta = 1.5$ ).

temperature 4,500 K against 6,500 K and ionizations of N and  $N_2$  are delayed to higher temperatures. When comparing both PKM curves dissociation occurs at lower temperature (in Fig.3) because the reaction rates are calculated at  $T_e$  against  $T_h$  for Fig.2.

## Transport properties

The transport properties have been then computed using the method of Sonine's polynomial expansion of the first order Chapman-Enskog approximation of Boltzmann's equation. Since electron mass is by far smaller than that of heavy species, the heavy-species Boltzmann equation was decoupled from that of the electrons. Therefore the electron and heavy-species transport properties were calculated independently following the method of Devoto [3,4].

Beside, for thermal conductivity were calculated the internal conductivity by using the method of Eucken [5] and the reactional conductivity by using a method similar to that of Butler and Brokaw but modified to account for two temperatures [6]. The requested derivatives of species composition were calculated by numerical derivation in case of pseudo kinetic method.

When looking at the viscosity  $\mu$  (Fig.4) as ionization starts at lower temperature with the GFEM the maximum of  $\mu$  occurs at 7,000 K against 10,000-11,000 K in the other cases. The slight differences are mainly due to the delay in dissociation with PKM at  $\theta=1.5$ . Fig.5 showing thermal conductivity exhibits the same tendencies. Dissociation peak at the same temperature for equilibrium, PKM corresponding to Fig.2 and GFEM at  $\theta=1.5$ , ionization peak at lower temperature (10,000 K) for GFEM at  $\theta=1.5$  (compared to equilibrium and PKM calculations. A similar behavior is seen for the electrical conductivity (see Fig.6) in good correlation with ionization behavior.

## Conclusion

We have calculated the composition of a multi-temperature nitrogen plasma by a Gibbs free energy minimisation and kinetic methods. Then, the transport properties were obtained. A few difference especially for dissociation and ionization can be seen between the results obtained with both methods.

## References

- [1] André P., Thèse DU n°771, Clermont Fd, 1995.
- [2] E. Richley and D.T. Tuma, J. Appl. Phys., 3 (12) (1982) 8537.
- [3] R.S. Devoto, Phys. Fluids, 29 (1966) 1230.
- [4] J. Aubreton, M.F. Elchinger and P. Fauchais, submitted to Plasma Chem. Plasma Proc.
- [5] A. Eucken, Physik Z., 14 (1913) 324.
- [6] J. Aubreton, Thèse d'Etat, Limoges, 1985.

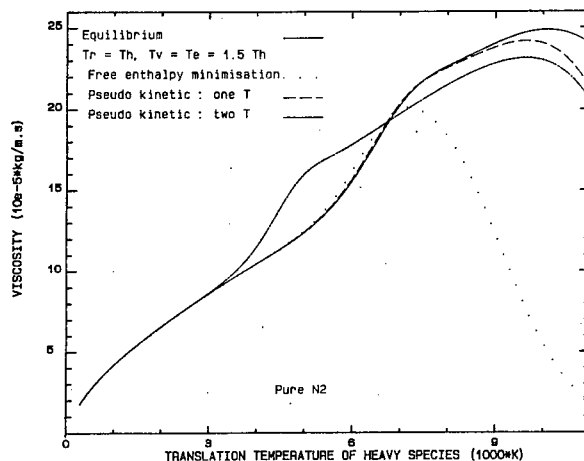


Fig. 4: The viscosity.

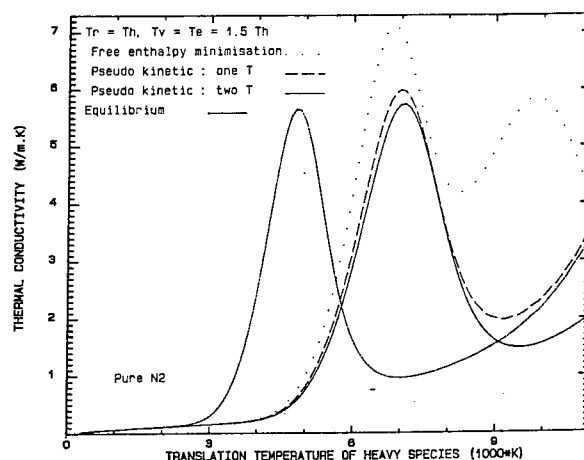


Fig. 5: The thermal conductivity.

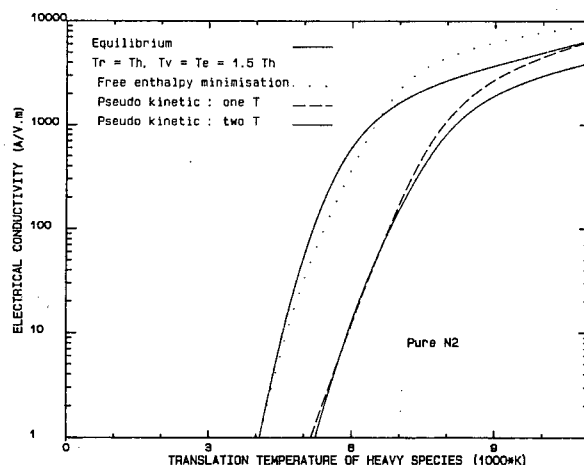


Fig. 6: The electrical conductivity.



# The effect of the geomagnetic field on the development of the upward atmospheric discharge.

L. P. Babich, I. M. Kutsyk, A. Yu. Kudryavtsev, A.L. Mozgovo

Russian Federal Nuclear Center-VNIIEF,

Mira st., 37, Sarov, 607190, Region of Nizhnii Novgorod, Russia.

Phone: 7-831-30-15041. E-mail: babich@expd.vniief.ru

## 1. Introduction.

Roussel-Dupre and Gurevich have developed a theory of gigantic atmospheric discharges directed upward from thundercloud tops into the Earth's stratosphere [1]. Formation of relativistic runaway electron avalanche initiated by cosmic-ray showers within the space domain of a thunderstorm electric field, is the heart of the theory. The theory allowed to treat the origin of wide columns of light radiance observed repeatedly above thunderclouds. These light phenomena are known as "blue jets" emitted blue light at altitudes below 35 km, and "red sprites" emitted red light at altitudes above 60 km. Roussel-Dupre and Gurevich have pointed out that geomagnetic field affected essentially the dynamics of gas discharge processes responsible for the light emission phenomena observed, especially at high altitudes above 40 km, where electron - neutral collision frequency is reduced to become lower than local value of the electron cyclotron frequency due to lower air density [1]. However the theory of the upward atmospheric discharges developed by now by Roussel-Dupre, Gurevich, Tunnel and Milikh, did not incorporated adequately the effect of geomagnetic field [1, 2]. So this problem remains to be solved. Results of the first calculations carried out with the aim to evaluate the effect of the geomagnetic field on the development of the relativistic runaway electron avalanche, are delivered in the present communication.

## 2. Model.

The approach adopted is to simulate a trajectory of a tested runaway electron moving under the joint action of three forces: accelerating electric force  $-eE$ , decelerating retarding force  $-F(\epsilon)p/p$  arising due to interactions of electrons with molecules of the background air, and the Lorentz magnetic force  $F_L = -e[v \times B]$  bending electron trajectory. Here  $p$  and  $v$  are the vectors of electron momentum and velocity,  $e$  is the elementary charge, the electric field intensity  $E$  is directed against to the direction of the electron motion  $p$ . The energy dependence of the absolute value of the retarding force  $F(\epsilon)$  was calculated from the relativistic Bethe formula for electron energy losses per unit path [3], available as well at [2]. Preliminary Monte - Carlo

calculations were carried out without magnetic field. The code used incorporated as well the elastic scattering of electrons by shielded coulomb potential of the atomic nucleus. These calculations were performed with the aim to estimate the minimal (threshold) energy  $\epsilon_{th}$  for secondary electrons to become runaways at a given electric field intensity and neutral particle number density of the air. It was convenient to introduce the "overvoltage" above the relativistic minimum of the retarding force  $F_{min}$  which exists in the vicinity of the electron energy  $\epsilon \approx 1 \text{ MeV}$ , as  $\delta = eE/(F_{min} \times P)$ . In the air  $F_{min}/P \approx 2.18 \text{ keV/cm/atm}$ .

## 3. Calculations and results.

The results of calculations obtained for three values of the "overvoltage"  $\delta$  are presented in Table 1.

Table 1

$\delta$	1.5	2.0	3.0
$\epsilon_{th}, \text{ MeV}$	1.3	0.6	0.2

This range of  $\delta$  was adopted due to exactly it corresponds to the electric field intensity at high altitudes above thunderstorm cloud arrays [1]. The calculated values of the threshold energy  $\epsilon_{th}$  were used as initial energies of electrons in the subsequent simulations of their trajectories in geomagnetic field. Calculations indicated that the process of relativistic avalanching at high altitudes is governed by relation between the vertical  $B_z$  and horizontal  $B_r$  components of the geomagnetic field inductance. The characteristic values of the ratio  $B_z/B_r$  realized at different latitudes in dense lower layers of the Earth's atmosphere where thunderstorms are raging, imply to consider two important cases.

The low latitude equatorial range was the first case. The approximate equality  $B_z \approx 0$  is valid there. In this domain a possibility for the avalanche of relativistic runaway electrons to develop at a given altitude  $h$  depends on the relation between local values of electric field intensity  $E$  and inductance of the geomagnetic field  $B$ . Either upward acceleration of electrons or strong bending of their trajectories with subsequent deceleration down to thermal energies are possible. Approximate value of the critical altitude  $h_{cr}$  at which electrons are thermalized, can be evaluated from the

obvious relation  $= eE/F_L \approx 1$ . Here the local electric force equals to  $eE = \delta \times F_{min} \times \exp(h/h_e)$  with  $F_{min} \approx 2.18 \text{ keV/cm}$  at the sea level ( $h = 0$ ,  $P = 1 \text{ atm}$ ) of the Earth atmosphere and a scaling value of the altitude  $h_e \approx 7 \text{ km}$ . The Lorentz force for relativistic electrons ( $v \approx c$ ) equals to  $F_L \approx ecB_r$ . The idea proved to be valid:  $\eta \approx 0.85 - 0.95$  were computed. In the considered range of "overvoltage"  $\delta$  from 1.5 to 3 and  $\eta \geq 1.5$  electrons appeared to travel upward along almost linear trajectories, with the average value of the cosine of the angle  $\theta$  between their velocity  $v$  and the upward directed axis  $z$  being calculated as large as  $\langle \cos \theta \rangle \approx 0.8$ . At  $\eta \leq 1$  electron trajectories stopped short. The length of the trajectory was calculated to be too small for the production of secondary electron with the energy above the threshold  $\varepsilon_{th}$ , sufficient for it to become runaway. As a result multiplication of runaway electrons terminated. The intermediate case  $1 < \eta < 1.5$  can not be described adequately in the framework of the approach adopted here. However it is worthy to note that the range of the altitudes  $\Delta h \approx 2.8 \text{ km}$  corresponding to these values of  $\eta$ , is essentially less than the values of the altitudes considered ( $\Delta h \ll h_{cr}$ ), thus indicating that the relative accuracy of the calculated altitudes  $h_{cr}$  to be rather high. Table 2 demonstrates the values of  $h_{cr}$  calculated for  $B_r = 35 \mu\text{T}$  and the above values of the "overvoltage".

Table 2.  $B_r = 35 \mu\text{T}$

$\delta$	1.5	2	3
$h_{cr}, \text{km}$	24	26.5	30

The effect of elastic scattering of electrons was studied. Adequate calculations showed that at  $\eta \geq 1.5$  the course of the atmospheric discharge is very much like that in the absence of the magnetic field. In the case of  $\eta \leq 1.5$  the small - angle elastic scattering, that constitute the largest portion of all scattering events, did not change the topology of the trajectories. On the other hand estimations performed show very low probability of those large - angle scattering events that lengthened electron trajectories and therefore were able to increase the probability of a secondary runaway electron production. The above approach did not take into account that threshold energies of secondary electrons  $\varepsilon_{th}$  were calculated without magnetic field. The effect of the geomagnetic field increases  $\varepsilon_{th}$  and as a result decreases the probability of a runaway electron to be produced. However the above consideration and results appeared to be valid even for threshold energies  $\varepsilon_{th}$  two times higher than the values presented in Table 1. Naturally in those regions of moderate latitudes where the vertical component of the geomagnetic field is so small as  $B_z \ll B_r$ , the runaway electron avalanche develops in the same way.

The regions of moderate latitudes (Alaska, Kanada, Russia) with  $B_z \approx 50 \mu\text{T}$  and  $B_r \approx 15 \mu\text{T}$  was considered as the second case incorporating efficiently both components of geomagnetic field. At these latitudes the effect of the geomagnetic field on the runaway electron avalanche differs very much from the first case on account of the vertical component  $B_z$  is essentially larger than horizontal one  $B_r$ . Calculations incorporated this field did not reveal any its influence on the development of the relativistic runaway avalanche in the range of the "overvoltage"  $\delta$  considered. The average value of the cosine was calculated to be  $\langle \cos \theta \rangle \geq 0.9$ . When the ratio  $B_z/B$  decreases the direction of the avalanche propagation deflects from the vertical line toward the vector of the geomagnetic field inductance ( $\langle \cos \theta \rangle \approx B_z/B$ ). The temp of the avalanche development slows down. It is reasonable to introduce the effective "overvoltage" as  $\delta_{ef} = \delta \times (B_z/B)$ . A special consideration is necessary for this case. It is beyond the framework of the present communication.

#### 4. Conclusion.

The effect of the geomagnetic field on the development of the relativistic runaway electron avalanche produced by thunderstorm electric field, appeared to be rather pronounced.

(1) The upper altitudes to which the avalanche of relativistic runaway electrons is able to propagate, are determined by the ratio of the thunderstorm electric field intensity to the local inductance of the geomagnetic field  $E/B$ . Roussel - Dupre and Gurevich supposed that the altitude is limited by the ratio of the electron elastic collision frequency to their local cyclotron frequency [1].

(2) The limit values of the altitudes allowing the propagation of relativistic runaway electron avalanche, were evaluated for different Earth's latitudes. The results allowed to predict the occurrence of a certain kind of light phenomena related to the gigantic discharges directed upward from the tops of thunderstorm cloud arrays.

(3) Most likely the "red sprites" are absent for thunderstorms occurred nearby to the Earth's equator. Both "blue jets" and "red sprites" are produced by thunderstorms occurred at moderate latitudes. Either types of phenomena can be observed at these latitudes.

#### 5. References.

- [1] R.A. Roussel-Dupre, A.V. Gurevich: J. Geophys. Res., **101** (1996) 2297.
- [2] R.A. Roussel-Dupre, A.V. Gurevich, T. Tunnel, and G.M. Milikh: Phys. Rev. E., **49**, No 3 (1994) 2257.
- [3] H.A. Bethe: Ann. Phys., **5**, (1930) 325.

## Evaluation of runaway electron avalanching.

L. P. Babich, I. M. Kutsyk.

Russian Federal Nuclear Center-VNIIEF,

Mira st., 37, Sarov, 607190, Region of Nizhnii Novgorod, Russia.

Phone: 7-831-30-15041. E-mail: babich@expd.vniief.ru

### 1. Introduction

To treat gigantic discharges directed upward from the top of thunderclouds, and possibly to explain the onset of the conventional contracted lightning, Gurevich, Roussel - Dupre, Milikh, and Tunnel [1, 2] have proposed and substantiated a hypothesis of relativistic runaway electron avalanches able to develop in a rather weak (in comparison with the conventional laboratory self-breakdown value) thunderstorm electric field. For the avalanches to develop the intensity of the electric force  $eE$  should be over the relativistic minimum of electron energy losses per unit path  $L_{min}$  that exists in the vicinity of electron energy  $\varepsilon \approx 1$  MeV. To describe the evolution of the runaway electron avalanche and calculate a rate of a runaway electron number increase, Roussel - Dupre et. al. have solved Boltzmann kinetic equation [2]. Results obtained infer the simplest approach assuming one-dimensional motion of electrons, is reasonable to evaluate rather accurately characteristic values of the avalanching process without solving the kinetic equation. Exactly such model underlies the present communication delivering results of computer simulations of the relativistic electron avalanche in the air of atmospheric density.

### 2. Model

We considered a beam of monoenergetic electrons with the energy  $\varepsilon_0$  propagating in the air of atmospheric density along the direction of the electric force  $-eE$  under the joint action of electric  $-eE$  and retarding forces  $F(\varepsilon) \propto p/p$ , with the absolute value of the last  $F(\varepsilon)$  being described by Bethe formula for inelastic electron energy losses  $L(\varepsilon)$  [3]. Here  $e > 0$  is the elementary charge and  $p$  is the runaway electron momentum. To characterize the intensity of the external electric field an "overvoltage"  $\delta = eE/F_{min}$  over the relativistic minimum of the retarding force  $F_{min} = 2.18$  keV/cm (normal conditions) was introduced [2]. Secondary electrons are produced with energies within the range  $[0, \varepsilon_0/2]$ . The less is the energy of a secondary electron  $\varepsilon$ , the larger is the angle  $\theta$  between momentum directions of primary and secondary electrons ( $\theta \approx \pi/2$  for  $\varepsilon \approx 0$ ). The angle is coupled with the energies  $\varepsilon_0$  and  $\varepsilon$  as follows  $\theta = [(\varepsilon/\varepsilon_0) \times (2mc^2 + \varepsilon_0)/(2mc^2 + \varepsilon)]^{1/2}$  [2]. For any given "overvoltage"  $\delta$  and the energy of the primary electron  $\varepsilon_0$  there is a minimum (threshold) energy of secondary electron  $\varepsilon_{min}$  and corresponding to it  $\theta_{min}$ , such, that secondary electrons with the

energy  $\varepsilon > \varepsilon_{min}$  are accelerated to be involved in the runaway electron avalanche. The others are decelerated down to the low-energy range to get an equilibrium with neutral particles of an ambient gas. The differential ionization cross section  $\sigma_{dif}(\varepsilon, \varepsilon_0)$  allows to calculate the cross section for the production of secondary runaway electrons

$$\sigma_i(\varepsilon_0, \varepsilon_{min}) = \int_{\varepsilon_{min}}^{\varepsilon_0/2} \sigma_{dif}(\varepsilon, \varepsilon_0) d\varepsilon.$$

The adequate free path of electrons  $l_i(\varepsilon_0, \varepsilon_{min}) = 1/(N\sigma_i)$  characterizes the length of  $e^-$  fold increase of runaway electron number for a given atomic number density of the air  $N = 2N_L$ , where  $N_L = 2.7 \times 10^{19} \text{ cm}^{-3}$  is Loshmidt number density. We used Moller formula for  $\sigma_{dif}$  [4] available as well at [2] or [5].

### 2. Results and discussion

Calculated values of  $\theta_{min}$ ,  $\varepsilon_{min}$ , and  $l_i(\varepsilon_0, \varepsilon_{min})$  for the "overvoltage"  $\delta = 2$  and a variety of  $\varepsilon_0$  are presented in Table 1 below. One can see that  $l_i \approx 16 - 24$  m for the energies ranging from 0.5 up to 10 MeV. At  $\delta = 2$  a runaway electron with the energy  $\varepsilon_{min}$  acquires along the distance 20 m the energy 4.4 MeV which is within the energy range considered.

The characteristic time for  $e^-$  fold increase of the number of runaway electrons in the runaway avalanche is defined as  $\tau_i = l_i/v \approx 1/N\sigma_i c$  provided that runaway electrons are of relativistic energy range ( $v \approx c$ ). For  $l_i = 16 - 24$  m the calculated time  $\tau_i \approx 55 - 66$  ns is more than four times larger than the value  $\tau_i \approx 14$  ns reported by Roussel - Dupre et. al. [2].

**Table 1** ( $\delta = 2$ )

$\varepsilon_0$	$\theta_{min}$	$\varepsilon_{min}$	$l_i$
MeV	rad	keV	m
0.50	0.920	149	28.07
0.75	0.994	156	22.60
1.00	1.035	160	20.82
2.00	1.104	167	18.76
4.00	1.150	171	18.00
10.00	1.170	175	17.60

Table 2 below demonstrates that calculations carried out for the "overvoltage" value equal to  $\delta = 5$ , gave the same discrepancy.

**Table 2** ( $\delta = 5$ )

$\varepsilon_0$	$\theta_{min}$	$\varepsilon_{min}$	$l_i$
MeV	rad	keV	m
0.10	0.890	39.0	6.14
0.20	1.070	42.0	4.23
0.40	1.175	46.5	4.66
1.00	1.260	49.5	5.03
5.00	1.330	51.0	4.80
10.00	1.340	52.0	3.92

We calculated that a deflection of the runaway electron momentum  $p$  into the angle range  $30^\circ$ - $50^\circ$  from the direction of  $-eE$  does not result in essential increase of the cross section for the production of secondary runaway electrons  $\sigma_i$ .

There is one more hypothetical reason, namely, the large angle elastic scattering of electrons, that possibly able to decrease  $\tau_i$ . There is a chance that electron with an energy below  $\varepsilon_{min}$  at the initial portion of its trajectory will suffer a large-angle scattering to be deflected in the direction of the electric force  $-eE$  and to become runaway. We emphasize that it is necessary for the scattering to be happened exactly at the beginning of the trajectory and the deflection to be occurred at the given angle and the direction wanted. The probability of such event is extremely low due to stochastic nature of the scattering process which tends to generate isotropic distribution of electron momentum and increase entropy of the electron

assembly in general. Even if such event is supposed to be happened and  $\sigma_i$  is calculated with the lower limit  $\varepsilon_{min} = 110 \text{ keV}$ , which at  $\delta = 2$  is the runaway energy threshold for  $\theta = 0$ , than for  $\varepsilon_0 = 1 \text{ MeV}$  one obtains only unessential decrease of  $l_i$  and  $\tau_i$  down to  $13 \text{ m}$  and  $43 \text{ ns}$  respectively.

The above arguments indicate that the large angle scattering only hampers for electrons with energies above  $\varepsilon_{min}$  to become runaways. Preliminary calculations support this conclusion. Elastic scattering in general only increases the value of  $\tau_i$ .

#### 4. Conclusion

Presently we are not able to explain the cause of so large discrepancy between results presented here and those reported by Roussel - Dupre et. al. [2]. We believe that it is not only due to more accurate approach adopted by Roussel - Dupre et al. Careful study of the discrepancy is urgent on account of laboratory experiments are being planned to study the avalanche of runaway electrons in the air.

#### 5. References

- [1] [A.V. Gurevich, G.M. Milikh, and R.A. Roussel-Dupre: Phys. Lett. A., **165** (1992) 463.
- [2] R.A. Roussel-Dupre, A.V. Gurevich, T. Tunnel, and G.M. Milikh: Phys. Rev. E., **49**, No 3 (1994) 2257.
- [3] H.A. Bethe: Ann. Phys., **5**, (1930) 325.
- [4] C. Moller: Ann. Physik, **14** (1932) 531.
- [5] H.A. Bethe and J. Ashkin: in *Experimental Nuclear Physics*, edited by E. Segre, 1, (John Wiley and Sons, New York, 1953), p. 277.

# On the ellipsoidal model of streamer in longitudinal magnetic field

L. P. Babich, M.L. Babich, A. Yu. Kudryavtsev

Russian Federal Nuclear Center-VNIIEF,

Mira st., 37, Sarov, 607190, Region of Nizhnii Novgorod, Russia.

Phone: 7-831-30-15041. E-mail: babich@expd.vniief.ru

Electrical breakdown in gases with external magnetic field is interesting due to arising possibility to control the discharge dynamics [1- 4]. The effect of the external longitudinal magnetic field with  $H_0 \parallel E_0$  on the electron avalanche evolution and the breakdown formation time  $t_f$  was studied by Mitani and Kubo [1] and Omarov, Rurhadze and Shikhaev [3]. Here  $H_0$  and  $E_0$  are vectors of external electric and magnetic field intensities. In the present communication an attempt is undertaken to consider a problem of the streamer propagation in longitudinal magnetic field. The consideration is carried out in the drift approximation in the framework of the mathematical model developed by Lozanskii and Firsov [5] for the case of  $H_0 = 0$ . The presence of the magnetic field leads to a necessity to take into account finite plasma conductivity at the streamer front. Therefore the Laplace equation for the scalar potential of the electric field  $\Phi(r, t)$ , adopted by Lozanskii and Firsov, is not sufficient. Adequate approach should proceed from the conductivity equation for the total current

$$\text{div}(j - \epsilon_0 \frac{\partial}{\partial t} \nabla \Phi) = 0, \quad (1)$$

where  $j$  is the conductivity current density. The streamer surface is defined as a some surface ( $\tilde{r}$ ), confining a plasma with a high conductivity and low electric field ( $E \ll E_0$ ). Lozanskii and Firsov adopted the following boundary conditions on this surface

$$\Phi(\tilde{r}) = 0, \quad (2)$$

$$d\Phi/dt|_{\tilde{r}} = 0 \quad (3)$$

Exactly nearby to ( $\tilde{r}$ ) a transient sheath exists, where the electric field intensity achieves its maximum value  $E_{\max}$ . It is permissible to neglect the bias current even at the nearest proximity of some surface ( $\tilde{r}_1$ ), where  $E(r) = E_{\max}(\tilde{r}_1)$ . Really, let at the vicinity of the streamer edge a small portion  $\delta^2 \ll 1$  of the maximal value of the electric field energy density in front of the streamer surface  $\epsilon_0(E_{\max})^2/2$ , was delivered to the gas. Here  $E_{\max} \approx E_a \approx E_0(a/r)^2/\Lambda$ , with  $\Lambda$  being a form-factor weakly depending on  $a/r$  ratio [5],  $2a$  is the length and  $2r$  is a diameter of the streamer,  $E_a$  is

the electric field intensity at the streamer edge. Then the following estimation seems to be reasonable

$$\begin{aligned} j/j_{dis} &= e n_e \mu_e E_a / \epsilon_0 (\partial E_a / \partial t) \approx \\ &\approx \delta^2 e \epsilon_0 E_a^2 \mu_e a / 2(\epsilon_{in} + T_e) \epsilon_0 2 E_a \dot{a} \approx \\ &\approx \delta^2 [e E_0 a / 4(\epsilon_{in} + T_e)] (a/r)^2. \end{aligned}$$

Here  $n_e$  and  $T_e$  are the electron number density and "temperature",  $\epsilon_{in}$  is the energy "price" of ionization event, and  $\mu_e$  is the coefficient of the electron mobility. On account of both  $eE_0 a / 4(\epsilon_{in} + T_e)$  and  $(a/r)^2 \gg 1$ , the inequality  $j/j_{dis} \gg 1$  is valid provided that  $\delta^2$  is sufficiently small to neglect the field variation, that is,  $\delta E_a \ll E_a$ . For instance, in the air at atmospheric pressure ( $E_0 > E_{st} \approx 30$  kV/cm,  $a \approx 1$  cm,  $\epsilon_{in} \approx 30$  eV,  $T_e \ll \epsilon_{in}$ ) the ratio  $eE_0 a / 4(\epsilon_{in} + T_e) > 100$  is realized. For instance, at  $\delta^2 = 10^{-2}$  the inequality  $j \gg j_{dis}$  is realized due to  $(a/r)^2 \gg 1$  in spite of the field intensity reduces only on 10% relative to its maximum value.

So the equation (1) is reduced to the equation for the potential between the surfaces  $\tilde{r}$  and  $\tilde{r}_1$  provided that  $j \gg j_{dis}$  and cylindrical symmetry of the problem are taken into account

$$\Delta_z \Phi + \frac{1}{1 + (\omega_{ce} / \nu_{en})^2} \Delta_p \Phi = 0. \quad (4)$$

The boundary condition (3) nearby to the streamer edge ( $\rho \rightarrow 0, z \rightarrow a$ ) is reduced to

$$\partial \Phi / \partial t + \mu_e [(\Delta_z \Phi)^2 + \frac{1}{1 + (\omega_{ce} / \nu_{en})^2} (\Delta_p \Phi)^2] = 0. \quad (5)$$

Here  $z \uparrow \downarrow E_0$ ,  $\rho \perp E_0$ , and  $\omega_{ce} = \mu_0 e H_0 / m$  is the electron cyclotron frequency, and  $\nu_{en}$  - is the frequency of electron collisions with neutral particles. Equations (4) and (5) written in coordinates  $z, y = \rho ((\omega_{ce} / \nu_{en})^2 + 1)^{0.5}$ , have the same presentation as at  $H_0 = 0$  (see [5]). As a result  $\Phi(\rho, z, t) = \phi(z, t) - \phi_{zz} \rho^2 / 4$ , where  $\phi(z, t) = \Phi(0, z, t)$ , is satisfied nearby to the streamer edge, so that the following relations deduced by Lozanskii and Firsov [5], still remain to

be valid even in the case when the external magnetic field is incorporated

$$\dot{a} = \mu_e \varphi_z(a, t), \quad (6)$$

$$[\dot{\varphi}_{zz}(a, t) \varphi_z(a, t) - \varphi_{zz}(a, t) \dot{\varphi}_z(a, t)] \varphi_{zz}^{-2}(a, t) = -\mu_e [\varphi_{zz}(a, t) \varphi_z^2(a, t) \varphi_{zz}^{-2}(a, t) - 2 \varphi_z(a, t)] = 0. \quad (7)$$

Following the procedure adopted by Lozanskii and Firsov [5] to calculate radius of the streamer edge  $R|_{\rho=0, z=a}$ , with  $H_0$  being taken into account, it is easy to deduce from (6) and (7) the following equation

$$\frac{dR}{da} = \frac{2}{1 + (\omega_{ce}/v_{en})^2} \left[ \frac{\varphi_z(a, t) \varphi_{zz}(a, t)}{\varphi_{zz}^2(a, t)} - 2 \right]. \quad (8)$$

The equation of the streamer surface follows from the condition (2)

$$\frac{\partial \rho}{\partial a} = \frac{E_\rho^2 / (1 + \omega_{ce}^2 / v_{en}^2) + E_z^2}{E_a E_\rho}, \quad (9)$$

At  $H_0 = 0$  this equation approximates with a sufficient accuracy the surface of the rotation ellipsoid with the exception of some domain nearby to  $z = 0$  [5]. For a streamer to develop, the form of its surface in the vicinity of its edges ( $\rho = 0, z = \pm a$ ) is of crucial importance. This was the reason why Lozanskii and Firsov adopted the ellipsoidal streamer model for which the right-hand side of equation (8) equals to zero. It is obvious, that inequality  $dR/da \geq 0$  is satisfied independently on the form of the streamer surface, that is the surface of the ellipsoid is the limit case. In the case of weak magnetic field, when in (9)  $(\omega_{ce}/v_{en})^2 \ll 1$ , the ellipsoid model is valid, and  $dR/da = 0$ . This case corresponds to experiments carried out by Omarov, Rukhadze, and Shikhaev [3], who obtained that in nitrogen the breakdown formation time  $t_f$  almost does not depend on  $H_0$  for the values lower than a certain  $H_l$  depending on  $(E_0, P)$ . In these experiments the cyclotron frequency  $\omega_{ce}(H_l)$  was almost equal to  $v_{en}$  in the molecular nitrogen of atmospheric density. As  $H_0$  increases, the surface described by (9), differs essentially from the surface of the ellipsoid. The equation (8) predicts that the radius of the streamer edge  $R$  is a decreasing function of the magnetic field intensity  $H_0$  increase. This corresponds to the decrease of the breakdown formation time  $t_f$  in nitrogen ( $dt_f/dH_0 < 0$ ) measured by Omarov, Rukhadze and Shikhaev [3] when the magnetic field intensity was increased at  $H_0 \geq H_l$ . This was due to the velocity of the streamer propagation is determined by

electric field intensity in the vicinity of its leading edges

$$\dot{a} = \mu_e \varphi_z(a, t) \approx a/R(H_0). \quad (10)$$

Therefore in strong external magnetic field, when the inequality  $\omega_{ce} \geq v_{en}$  is satisfied, the ellipsoid model of a plasma streamer with the ideal conductivity fails to be valid. The equations (8) and (9) predict the increase of the probability for narrow contracted channels to develop in longitudinal magnetic field.

Due to the action of the Lorentz force in magnetic field charged particles obtain a transverse component of the velocity [6]

$$u_\perp = e[E_\rho H_0]/m_{eq} \omega_{ce} H_0 (1 + m_{eq}^2 v^2/m^2 \omega_{ce}^2), \quad (11)$$

Here  $m_{eq}$  is the equivalent mass. In the result a circular current is generated, with its density being equal to zero at  $z = 0, \pm a$  and to maximum values on two circumferences, where  $E_\rho = E_\rho^{max}$ . The current direction does not depend on the carrier sign and is opposite for the anode and cathode halves of the streamer on account of opposite directions of  $E_\rho$ .

It was shown above, that in strong longitudinal magnetic field the streamer surface essentially differs from that of ellipsoid. A consequence is reduction of the curvature radius of the streamer head in a magnetic field and increase of its propagation speed. It is displayed in reduction of the breakdown formation time as the magnetic field intensity is increased.

## References

- [1]. K. Mitani, H. Kubo: J. Phys. Soc. Jap., **15** (1960) 678.
- [2]. M.-R. G. Kishov : Izvestiya Vuzov-Radiofizika, **23** (1980) 992 [in Russian].
- [3]. O.A. Omarov, A.A. Rukhadze, and A.Sh. Shikhaev: Zh. Tekhn. Fiz. **52** (1982) 255 [in Russian].
- [4]. A.T. Rakhimov, N.V. Suetin: Pis'ma Zh. Tekhn. Fiz. **10** (1984) 121.
- [5]. E.D. Lozanskii, O.B. Firsov: Spark Theory. Moscow. Atomizdat 1975 [in Russian].
6. V.E. Golant, A.P. Zgilevskii, and S.A. Sakharov: Fundamentals of Plasma Physics. Moscow. Atomizdat. 1977 [in Russian].

# Creation of a High Concentration of Vibrationally Excited H<sub>2</sub> Molecules in a Hydrogen Flux Penetrative through Cesium-Hydrogen Discharge

M.Bacal, F.G.Baksht, V.G.Ivanov, S.M.Shkolnik

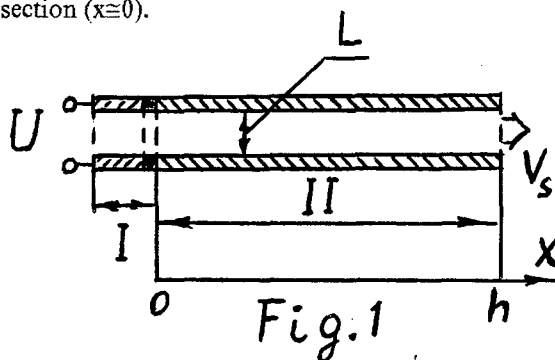
Laboratoire de Physique des Milieux Ionisés,  
Ecole Polytechnique, 91128, Palaiseau, France

A.F.Ioffe Physical-Technical Institute,  
26 Polytechnicheskaya, St. Petersburg, 194021, Russia

1. There is a considerable interest in the creation of vibrationally excited H<sub>2</sub> molecules because of their application to plasma chemistry, H<sup>-</sup> sources etc.. It was shown previously [1,2] that a low-voltage (LV) discharge in Cs-H<sub>2</sub> mixture might be used as an effective source of vibrationally excited H<sub>2</sub> molecules and H<sup>-</sup> ions, H<sup>-</sup> ions being created due to the dissociative attachment (DA) of heated thermal electrons to vibrationally excited H<sub>2</sub> molecules [3]. In the present communication, the new theoretical results, concerning the creation of excited H<sub>2</sub> molecules in this kind of the discharge, are reported. It will be shown that vibrational distribution function (VDF) of H<sub>2</sub> molecule may be significantly improved if vibrational excitation occurs in a moving flux of H<sub>2</sub> molecules penetrative through LV Cs-H<sub>2</sub> discharge.

2. The following theoretical model is considered (see Fig. 1). H<sub>2</sub> flux flows between two plates and passes through two sections one after another. The first section (I) is a discharge one, where LV Cs-H<sub>2</sub> discharge occurs and vibrationally excited H<sub>2</sub> molecules are created. In the next section (II) the excited hydrogen flows in a plane channel, which walls are unheated. The very significant intensification of H<sub>2</sub> high vibrational level population takes place at this section due to "Treanor diffusion" [4] of vibrational quanta up to high vibrational levels. At the exit of a channel (x=h) H<sub>2</sub> flux flows out with a sound velocity V<sub>s</sub>.

3. The system of balance equations [1] was solved for the determination of H<sub>2</sub> VDF f<sub>v</sub>(0) formed in LV Cs-H<sub>2</sub> discharge, i.e. in the first section (x=0).



The following processes were taken into account: e-v exchange, v-v exchange, v-t exchanges with hydrogen molecules and atoms, v-v' transitions due to the interaction between excited H<sub>2</sub> molecules and Cs atoms and due to the H<sup>-</sup> stripping, the destruction of H<sub>2</sub> molecules due to DA and reverse process - creation of excited H<sub>2</sub> molecules due to the associative detachment, the vibrational relaxation of H<sub>2</sub> molecules at the electrode surfaces. The Cs-H<sub>2</sub> plasma in LV discharge was considered as uniform one. The plasma parameters were determined by means of self-consistent solution of the system of the equations which describe the vibrational kinetics and the conservation of particles and energy in the discharge gap [5]. The calculated H<sub>2</sub> VDF f<sub>v</sub>(0) in the LV discharge is shown in Fig. 2. VDF is normalized to unity. The LV discharge parameters are as follows: H<sub>2</sub> concentration N<sub>H<sub>2</sub></sub><sup>(0)</sup> = 3·10<sup>16</sup> cm<sup>-3</sup>,

whole Cs concentration N<sub>Cs</sub><sup>(0)</sup> = 10<sup>14</sup> cm<sup>-3</sup>, interelectrode distance L=0.3 cm; cathode emission current j<sub>e</sub> = 10 A/cm<sup>2</sup>, discharge voltage U=6.9 V. The calculated electron temperature and concentration are: T<sub>e</sub> = 0.7 eV, n<sub>e</sub> = 6.4·10<sup>13</sup> cm<sup>-3</sup>.

4. The decrease of H<sub>2</sub> concentration in the channel of section II due to the diminution of pressure was taken into account. The relations, which describe the gas flow in section II, were obtained by means of the consideration of compressible viscous gas flow between two parallel plates. The length h of a channel was determined in such a way that a maximum possible value of the high vibrational level population took place at the end of a channel. In the example, which will be discussed here, this level will be chosen as v = 10.

VDF of H<sub>2</sub> molecules was calculated by means of the following set of equations:

$$\frac{d(N_v \cdot V)}{dx} = I_v^{(vv)} \{N_v\} + I_{vM}^{(vt)} \{N_v\} +$$

$$+\frac{1}{\tau}\left[\sum_{v'>v}N_{v'}w_{vv'}-N_v\sum_{v'<v}w_{vv'}\right], \quad (1)$$

( $v, v' = 0, 1, 2, \dots, 14$ ).

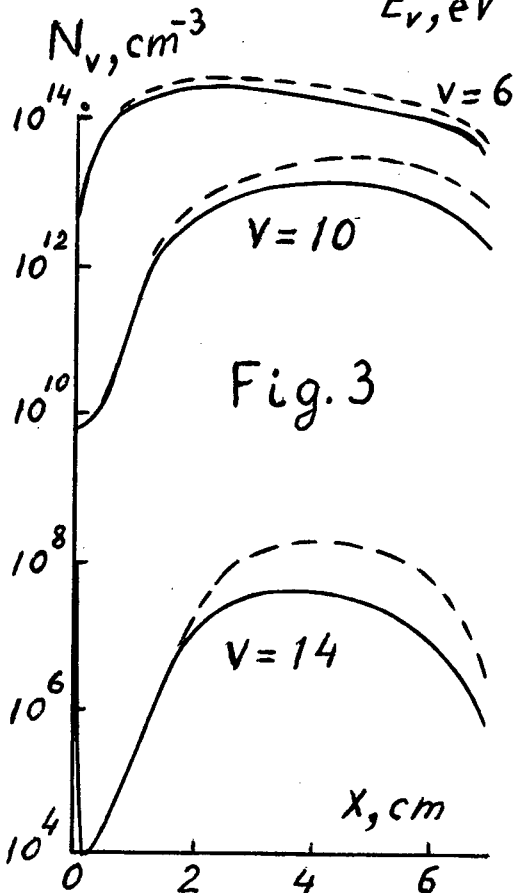
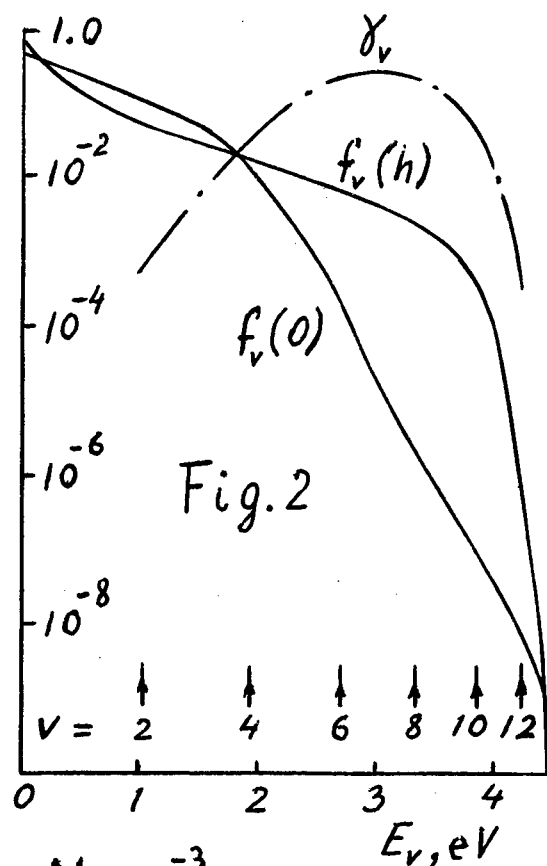
The right-hand terms in (1) describe v-v and v-t exchanges between  $H_2$  molecules and  $H_2$  vibrational relaxation at the wall surfaces [6].  $\tau \approx L^2/D_{sd}$ , where  $D_{sd}$  is  $H_2$  self-diffusion coefficient. The results of calculations are shown in Fig. 2, where VDF  $f_v(h)$  at the exit of a channel ( $x=h$ ) is depicted. In Fig. 2 the function

$$\gamma_v(T_e) = K_v(T_e)f_v(H)/\sum_v K_v(T_e)f_v(H), \quad (2)$$

which gives the probability of  $H^-$  generation due to the DA of electrons to  $H_2$  molecules excited at the level  $v$ , is also depicted. Here  $K_v(T_e)$  are the rate constants of  $H^-$  generation due to the DA of electrons to vibrationally excited  $v$  levels [7]. One can see that, indeed, very significant increase of VDF exists for  $v=6-10$  because of the vibrational quanta diffusion up to high  $v$  in a cold channel. It may be seen by means of the curve  $\gamma_v$  that the increase of VDF at the exit of a channel occurs just for such levels, which are the most essential ones in the process of DA. In Fig. 3 the distributions of the concentrations  $N_v(x)$  of vibrationally excited  $H_2$  molecules in the channel of section II are shown, the dotted lines being the results of calculations without surface deexcitation.

The proposed method of the creation of  $H_2$  VDF may be utilized, in particular, in two-camera  $H^-$  sources, where the processes of  $H_2$  vibrational excitation and  $H^-$  generation take place in the different gas volumes.

- [1] Baksht F.G., Ivanov V.G. J. Techn. Phys. (in Russian). 1992. V. 62, p. 195-200.
- [2] Baksht F.G., Djuzhev G.A., Elizarov L.I., Ivanov V.G., Kostin A.A., Nikitin A.G., Shkolnik S.M. Contributions to ICPIG XXI, 1993. p. 299-300, p. 301-302, p. 303-304.
- [3] Bacal M. and Hamilton G.W. Phys. Rev. Lett. 1979. V. 42, p. 1538-1540.
- [4] Treanor C.E., Rich J.W., Rehm R.G. J. Chem. Phys. 1968. V. 48. p. 1798-1807.
- [5] Baksht F.G., Djuzhev G.A., Elizarov L.I., Ivanov V.G., Kostin A.A., Nikitin A.G., Shkolnik S.M. Plasma Sources Sci. Technol. 1994. V. 3. No. 2, p. 88-98.
- [6] Hiskes J.R., Karo A.M. J. Appl. Phys. 1984. V. 56. No. 7, p. 1927-1938.
- [7] Wadehra J.M. Phys. Rev. A. 1984. V. 29. No. 1, p.106-110.





# THE NEAR WALL SHEATH-PRESHEATH TRANSITION IN AN OBLIQUE MAGNETIC FIELD

I. I. BEILIS and M. KEIDAR

Electrical Discharge and Plasma Laboratory  
Tel Aviv University, P. O. B. 39040, Tel Aviv 69978, ISRAEL

## 1. INTRODUCTION

The plasma-wall transition layer, generally, consists on two region: an electrostatic sheath and near sheath quasi-neutral plasma (presheath) [1]. In the presheath the conditions for the electrostatic sheath existence are formed. These conditions connect with ion velocity and electric field at the sheath-presheath interface. In the case without magnetic field the ion velocity can be smaller than the Bohm velocity [2,3]. The consistent solution of the sheath and presheath without magnetic field was also considered by Valentini [4]. The magnetic presheath was studied for floating wall case [5,6] and current carried wall case [7], and magnetized sheath was analysed by Holland *et al.* [8].

In the present work we develop a model of the plasma-wall transition layer which includes sheath and presheath in a magnetic field obliquely incident to the wall. In contrast to the works [5,6] the general current-carried presheath model without assumption about electron distribution function will be used.

## 2. MODEL.

**Presheath.** The magnetic field intersects the wall with angle  $\theta$  (Fig. 1). It is assumed that the presheath region is quasi-neutral i.e.  $Z_i N_i = N_e = N$ . In the present model the effect of ion collision with heavy particles is approximated by the effective collision frequency  $\nu_c$  of ions with neutral particles, assumed to be a background distributed uniformly in the presheath [6,7]. The plasma parameter distribution in the presheath may be described by the following two-fluid equation system:

$$\nabla \cdot (N_\alpha V_\alpha) = 0 \quad (1)$$

$$m_i V_i \cdot \nabla V_i = eN(E + V_i \times B) - \nabla P/N - \nu_c m_i V_i + \nu_{ie} m_e (V_e - V_i) \quad (2)$$

$$0 = -e(E + V_e \times B) - \nabla P/N - \nu_{ei} m_e (V_e - V_i) \quad (3)$$

where  $\alpha = e, i$ ;  $V_i, V_e$  are the ion and electron fluid velocity,  $E = -\nabla U$  is the electric field,  $U$  is the potential,  $B$  is the magnetic field,  $\nu_{ei}$  is the electron-ion collision frequency. It is assumed that the electrons and ions are ideal gases so that  $P_\alpha = NkT_\alpha$ , where  $k$  is the Boltzmann constant, and  $T_e, T_i$  are the electron and ion temperatures, which are assumed to be a constant.

The velocity components vary only along one direction  $x$ , normal to the wall. From the quasi-neutrality condition and Eq. (1) we have  $V_{ex} = \eta V_{ix}$ , where  $\eta = J_e/J_i$ ,  $J_e$  and  $J_i$  are the electron and ion currents normal to the wall. In the present model we used a constant electron to ion current ratio  $\eta$  as a parameter.

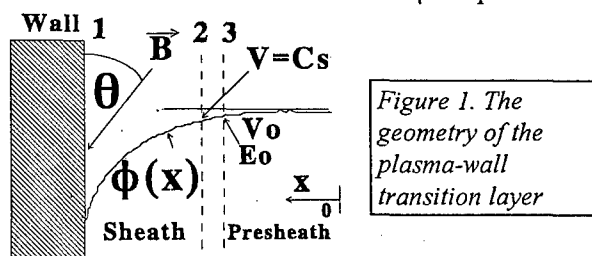


Figure 1. The geometry of the plasma-wall transition layer

The dimensionless variables are used:  $n_\alpha = N_\alpha/N_0$  ( $N_0$  is the plasma bulk density),  $\rho_i = C_s/\omega_i$ ,  $C_s^2 = k(T_i + Z_i T_e)/m_i$ ,  $\beta_e = \omega_e/\nu_{ei}$ ,  $\omega_e = eB/m_e$ ,  $\phi = eU/kT_e$ ,  $\varepsilon = T_e/T_i$ ,  $\psi = L_D/\rho_i$  and  $\mu = m_e/m_i$ . In additions the relation between  $\beta_e$  and  $\beta_i$  is used in the form of  $\beta_e = \beta_i \delta/\mu$ , where  $\delta = \nu_c/\nu_{ei}$ . The presheath edge (boundary 2) we defined as a boundary where ion velocity normal to the wall approaches to the  $C_s$ .

**Sheath.** The system of equations consists on the Poisson equation:  $\nabla^2 \phi = \psi^{-2} (n_e - n_i)$  (here coordinate was normalized by  $\rho_i$ ) and Boltzmann distribution for electrons:  $n_e = e^{-\phi}$ . In the first approximation ( $\psi \ll 1$ )

ion density varies as  $n_i = \frac{1}{\sqrt{1 - 2(\phi - \phi_0)(\frac{C_s}{V_0})^2 \frac{1}{1 + 1/\varepsilon}}}$  where

$V_0$  and  $\phi_0$  are ion velocity and potential at the sheath-presheath interface. At the sheath-presheath interface the conditions for the ion velocity  $V_0$  and electric field  $E_0$  are used and current continuity  $\eta = \text{const}$  in the presheath and sheath is employed. As it was pointed above at the boundary 2 (i.e.  $V_0 = C_s$ ) the electric field is infinite. Therefore the electric field must be taken before this boundary where  $V_0 < C_s$  i.e. ion velocity is smaller than the Bohm velocity (boundary 3). We will taken such the critical velocity  $V_0$  and electric field  $E_0$  (before boundary 2) which leads to the monotonic solution of the Poisson equation.

## 3. RESULTS

The electric potential distribution with respect to the plasma-presheath interface is plotted in Fig. 2 with angle  $\theta$  as a parameter. The potential distribution has a

maximum  $\phi_{\max}$ . In the case of an oblique magnetic field with  $\theta \geq 2^\circ$  and  $\eta = 1$  the value of  $\phi_{\max}$  decreases up to zero. As shown in Fig.2 the presheath potential drop in the case of  $\eta = 1$  increases with angle  $\theta$  while in the case of small  $\eta$  the presheath potential drop decreases with  $\theta$ .

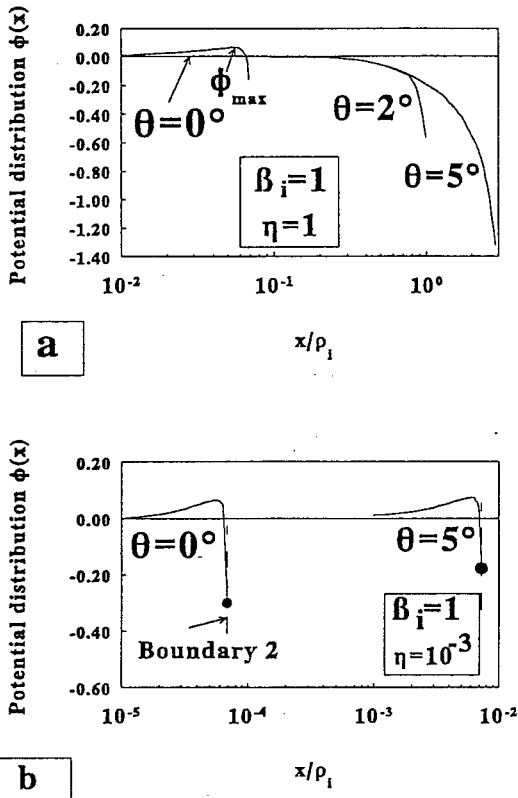


Figure 2. The potential distribution in the presheath

The potential distribution in the presheath-sheath structure is shown in Fig. 3. It can be seen that potential changes occur mainly in the sheath ( $\sim 6 kT_e/e$ ) while in the presheath the potential drop is less  $kT_e/e$ . The velocity  $V_0$  is about  $(0.6-0.88) \cdot C_s$  for  $\psi = 10^{-4}-10^{-2}$  and  $\eta = 1$  and increases with ion to the electron current ratio  $1/\eta$  as shown in Fig. 4 where  $\psi$  used as a parameter. In the case  $\psi > 10^{-3}$  the velocity  $V_0$  significant decreases. It should be noted that in this case the sheath is magnetized and more accurate solution should be used.

The current-voltage characteristic of the plasma-wall transition layer with incidence angle  $\theta$  as a parameter is shown in Fig. 5, where  $\Delta\phi$  is the total voltage of the transition layer. This characteristic does not depend on the incidence angle for  $\theta > 5^\circ$ . The change of  $\Delta\phi$  with incidence angle connects mainly with presheath voltage drop as can be seen in Fig.2.

#### REFERENCE

- [1] K. U. Reimann. J.Phys.D:Appl.Phys., 24(1991) 493.
- [2] I. Beilis. Proc. IX ISDEIV, Eindhoven, (1980) 65.

- [3] V. A. Godyak and N. Sternberg. IEEE Trans. Plasma Sci., 18, (1990) 159.
- [4] H. B. Valentini, E. Glauche, and D. Wolff. Plasma Source Sci., 4 (1995) 353.
- [5] R. Chodura. Phys. Fluids, 25(9) (1982) 1628.
- [6] K. U. Reimann, Phys. Plasmas, 1(3) (1994) 552.
- [7] M. Keidar, I. Beilis, R. L. Boxman, and S. Goldsmith, Proc. XXII ICPIG, 2 (1995) 157.
- [8] D. L. Holland, B. D. Fried, and G. J. Morales. Phys. Fluids B, 5 (6) (1993) 1723.

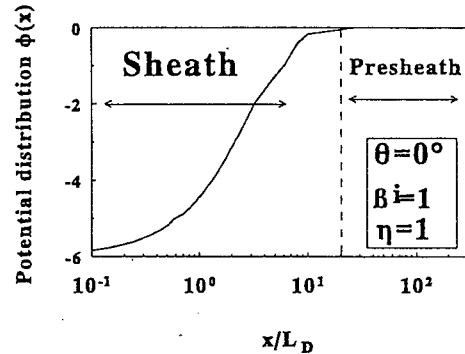


Figure 3. The potential distribution in the transition layer.

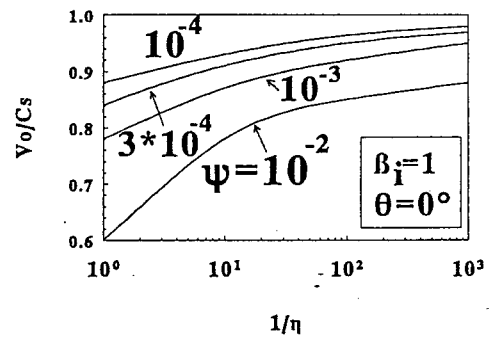


Figure 4. The critical ion velocity at the presheath-sheath interface.

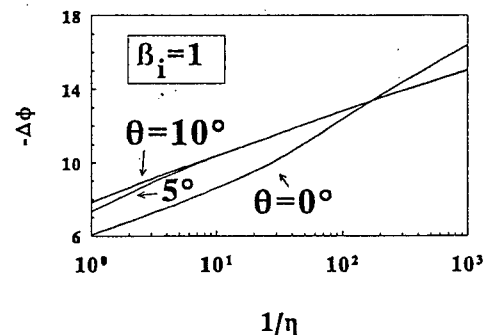


Figure 5. The current-voltage characteristic (ion branch).

# CARS-spectroscopy and numerical investigations of N<sub>2</sub> vibrational kinetics in glow discharges.

V.A.Shakhatov, A. Cénian

(a) Russian Academy of Sci., Moscow Radiotechnical Institute, Varshavskoye Shosse 132, Moscow

(b) Polish Academy of Sci., Institute of Fluid-Flow Machines, ul.Fiszera 14, Gdańsk

cenian@imppan.imp.pg.gda.pl

## 1. Introduction

Vibrational kinetics of the excited N<sub>2</sub> molecules in DC glow discharges was a subject of numerous studies previously, e.g. ref. 1-3, due to achieved high non-equilibrium between vibrational and translational degrees of freedom. This is crucial for laser techniques and significantly influences kinetics of plasma processes.

The  $T_v$  vibrational and  $T_g$  gas temperatures determined from vibrational and rotational distributions of the ground electronic state of N<sub>2</sub>, measured using CARS (Coherent Anti-Stoke Raman Spectroscopy) method, help to verify the rate constants for the VV exchange processes. Moreover, the probability of vibrational quenching in heterogeneous process (vibrational de-excitation on the wall) may be estimated.

## 2. Experiment

The discharge was realized in a slow flow of N<sub>2</sub> confined by water-cooled, quartz tube with the inner radius of 1.8 cm, at a pressure which was varied from 3.5 to 20 Torr. The distance between platinum electrodes was 58 cm. The reduced electric field  $E/N$  and the electric current were varied in the range 40 to 80 Td and 10 to 60 mA, respectively. The vibrational and rotational distributions were probed using CARS method. The time evolution of the gas temperature was measured at symmetry axis of the discharge tube using optical two-wave interferometer. The radial distributions of the gas temperature and electron density measured by optical interferometry and spectroscopic method discussed in ref. 3 and 4 allow a better comparison with the numerical calculations.

Figure 1 presents the optical scheme of the applied CARS spectrometer including: laser system (1), data-acquisition and processing set (2) automated on the basis of IBM PC (3). Its laser system consists of a narrow-band tuned dye laser pumped by the second harmonics of a single-mode Nd:YAG laser. The Nd:YAG-laser  $2\omega$  pulse (140 mJ) of 25

to 30 ns duration was directed collinearly with the dye-laser 6 mJ pulse along the symmetry axis of the discharge tube. The spatial resolutions of CARS achieved in this experiment were 100  $\mu$ m and 4 cm, in measurements perpendicular and along beam axis, respectively. The CARS signal was separated from the pump beams by the broadband filter (5), the monochromator (6) and sent to the optical multichannel analyzer (OMA III) (7) or through an optical fiber (8) to the photomultiplier tube (9).

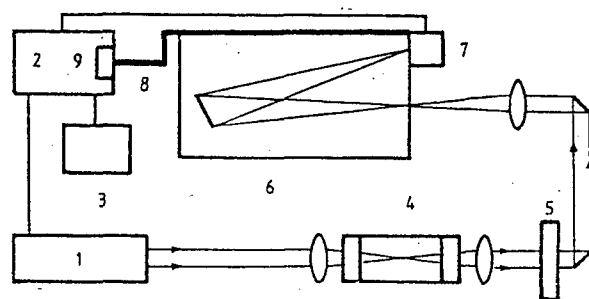


Fig. 1. The experimental set-up.

## 3. Model description.

The following elementary processes have been included in the model of a DC discharge in N<sub>2</sub>: the excitation and quenching of electronic states of N<sub>2</sub> ( $A^3\Sigma_u^+$ ,  $B^3\Pi_g$ ,  $C^3\Pi_u$ ,  $B'^3\Sigma_u^-$ ,  $a'^1\Sigma_u^-$ ,  $W^3\Delta_u$ ,  $a'^1\Pi_g$ ,  $w^1\Delta_u$ ), N( $^2P$ ,  $^2D$ ) and vibrational states of N<sub>2</sub> ( $X^1\Sigma_g^+$ ) in collision with electrons, molecules and atoms; the N<sub>2</sub> dissociation induced by electron collision (the cross section of the process includes contributions from electronic excitations with transition to predissociated states) and vibrational excitation with production of N( $^4S$ ); VV and VT relaxation processes. The heterogeneous quenching processes, diffusive and convective heat transfer from the volume were considered as well. The Boltzmann equation (discussed in ref. 5) has been solved to determine the rate constants for processes induced by electron collisions. The measured radial  $T_g$  and  $n_e$  profiles were used in the model to increase the accuracy of calculated vibrational levels populations  $N_v$  and the gas

temperature.

#### 4. Results and discussion.

The presented model was verified for various glow discharge conditions i.e. variable: gas pressure,  $p$ , and flow rate which determines the residence time of the  $N_2$  gas in the discharge ( $t_d$ ). The CARS measurements of vibrational and rotational distributions in the glow discharge were performed and the gas  $T_g$  and vibrational  $T_v = 3400/\ln(N_0/N_1)$  temperatures were determined. These temperatures are compared in Table I with those predicted by the model calculations, where two different values of heterogeneous quenching probabilities were assumed ( $\gamma = 10^{-4}$  and  $10^{-3}$ ). The last two sections correspond to CARS measurements done by Smirnov et al. [1], Massabieaux et al. [2] in discharge tubes with the inner radius of 0.7 and 1 cm,

Table I.  $T_g$  and  $T_v$  in DC discharges.

$T_g$ , K		$T_v$ , K		$p$ Torr	$t_d$ ms	$\gamma$
exp.	calc.	exp.	calc.			
$480 \pm 35$	512	$3790 \pm 350$	3700	3.5	30	$10^{-4}$
	470		3475			$10^{-3}$
$530 \pm 35$	545	$4320 \pm 360$	4255	7.0	15	$10^{-4}$
	530		4200			$10^{-3}$
$600 \pm 40$	610	$4270 \pm 370$	4240	9.5	15	$10^{-4}$
	605		4240			$10^{-3}$
$395 \pm 12$	400	$2850 \pm 100$	2790	12.0	30	$10^{-4}$
	[1] 360		2615			$10^{-3}$
$530 \pm 30$	470	$5300 \pm 350$	4960	2.0	11	$10^{-4}$
	[2] 420		4250			$10^{-3}$

respectively. Taking into account that the role of heterogeneous  $N_2$  vibrational quenching decreases with the pressure or tube diameter increase, the probability for the process can be deduced from Table I, i.e.  $\gamma = 10^{-4}$ . It is one of the very few experimental estimation of this probability. It has been reported in the work [6] – the same is true here – that the best agreement between theoretical and experimental values of  $T_v$  was achieved when the rates for the VV processes were taken from Billing et al. [7], at least for the five lowest vibrational levels  $v = 0, \dots, 5$  probed in our CARS experiment.

Table II.  $T_g$  in DC discharges.

$p$ Torr	$n_{e0}$ $cm^{-3}$	$E/N$ Td	$T_g$ , K	
			exp	calc.
15	$0.68 \cdot 10^{10}$	70	$760 \pm 50$	720
	$2.0 \cdot 10^{10}$	73	$1000 \pm 100$	1040
20	$1.1 \cdot 10^{10}$	52	$810 \pm 10$ [3]	860
	$3.9 \cdot 10^{10}$	59	$1175 \pm 25$ [3]	1170

Table II presents gas temperature  $T_g$  measured at the symmetry axis of the discharge

tube for various steady-state electron densities  $n_{e0}$ ; discharge tube radius was 1 cm. Theoretical results agree well with the values obtained here using CARS or published in ref. 3 (optical interferometry method).

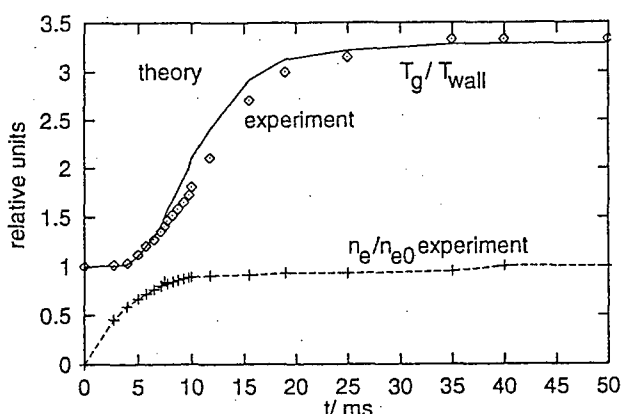


Fig. 2. Time evolution of  $T_g$  and  $n_e$ .

Figure 2 displays the time evolutions:  $T_g(t)$  and  $n_e(t)$  measured at the symmetry axis of the discharge tube using optical two-wave interferometer;  $p = 20$  Torr and  $n_{e0} = 2 \cdot 10^{10} cm^{-3}$ . Temperature  $T_g$  is normalized to the wall temperature  $T_w$  and  $n_e$  to  $n_{e0}$ , symbols represent experiment and solid line theory. The  $T_g(t)$  evolution for  $t < 10$  ms (influenced strongly by the VV exchange) is best fitted when rates for the VV processes ( $v > 9$ ) are calculated according to Zhuk et al. [8].

#### 5. Acknowledgement

The authors are grateful to O.A. Gordeev for providing us with his data base on the cross sections of electron excitation processes and for his helpful comments.

#### 6. References

1. V.V.Smirnov and V.I.Fabelinski: JETP Lett. 28 (1978) 28.
2. B.Massabieaux, G.Gousset et al.: J.Physique 48 (1987) 1939.
3. Yu.B.Golubovskii and V.M.Telenhko: Opt. & Spectr. 54 (1983) 60.
4. A.V.Bodronosov, K.A.Vereshchagin et al.: Sov.J.Tech. Phys. 64 (1994) 47 (in Russian).
5. A.V.Bodronosov, K.A.Vereshchagin et al.: High Temperature 34 (1996) 656.
6. O.A.Gordeev, V.A.Shahatov: Sov.J.Tech. Phys. 65 (1995) 40 (in Russian).
7. G.D.Billing and E.R.Fisher: Chem.Phys. 43 (1979) 395.
8. Yu.N.Zhuk and K.S.Klopovsky: Chem.Phys. Lett. 153 (1988) 181.

# Measurement of Effective Ionisation and Drift of Positive Ions in Methane and its mixture with Argon

J. de Urquijo, C. Arriaga, E. Basurto, I. Domínguez, I. Alvarez, and C. Cisneros

Instituto de Física, UNAM.

P.O. Box 48-3, 62251 Cuernavaca, Mor. México

## 1. Introduction

Low temperature plasma processes involving methane and methane-argon mixtures are nowadays widely used in important applied fields such as Plasma Chemical Vapour Deposition. Many basic studies regarding the optical emission of these discharges [1] have been carried out, as well as other diagnostic methods for the optimisation and simulation of these processes, which are in many instances strongly dependent on the gas mixture content and discharge parameters. In connection with the latter, knowledge of swarm and transport parameters over a wide range of the density-normalised electric field strength,  $E/N$ , is highly desirable, although not always available. For instance, studies on the drift velocity of electrons in  $\text{CH}_4$ -Ar mixtures have been done by Kleban et al [2], but only at low  $E/N$  values up to about 10 Td (1 Townsend =  $10^{-17}$  V cm<sup>2</sup>). The aim of this work was to measure the effective ionisation coefficients and the positive ion mobilities of pure methane and its mixture with 50% argon over a wide range of  $E/N$ .

## 2. Experimental method

The experimental apparatus was based on a previous design [3], but underwent some modifications and improvements. Briefly, it consists of a set of highly polished, parallel-plate metallic electrodes, 12 cm in diameter with rounded edges. A fixed 2 cm gap distance was used. Base pressures of 1  $\mu$ torr were achieved, while gas pressures varied over the range 0.1-50 torr. The avalanche was initiated by a 3 ns duration flash of photoelectrons released by the action of UV light from a nitrogen laser ( $\lambda=337$  nm) from the cathode. The ionic part of the avalanche was detected by the voltage drop across a resistor in series with the cathode, further amplified and recorded by a 100 MHz digitising oscilloscope. The value of this resistor and the stray capacitance associated in parallel to it gave a time constant between 10 and 20 ns, small enough to ensure the so called "differentiated pulse condition", where the voltage drop is proportional to the total displacement current due to all carriers drifting across the gap.

The resulting waveform was analysed by an expression for the positive ion current which considers

the processes of ionisation, attachment, and positive ion drift and longitudinal diffusion [4]. Small contributions at the beginning of the pulse from electron capture processes, and the remaining electron diffusion did not affect the evaluation of the pulse according to such equation, since the relevant swarm and transport parameters were derived from the middle and end portions of the pulse. The effective ionisation coefficient and the drift velocity were derived from a curve fitting procedure to the observed ionic pulses.

## 3. Results

The density-normalised effective ionisation coefficient,  $(\alpha-\eta)/N$ , where  $\alpha$  and  $\eta$  are the electron ionisation and attachment coefficients, respectively, are shown plotted in Fig. 1 as a function of  $E/N$ , for a 100%  $\text{CH}_4$ , and 50-50%  $\text{CH}_4$ -Ar mixture. Also, the effective ionisation coefficients for 100% Ar measured by Kruithof [5] are shown in the same figure for comparison. It is clearly seen that the effective ionisation coefficient increases smoothly as the Ar percentage in the mixture does up to about 400 Td. Above this value, the effective ionisation coefficients for the mixture are still slightly higher than those for pure methane, but those for argon become lower at the end of the range.

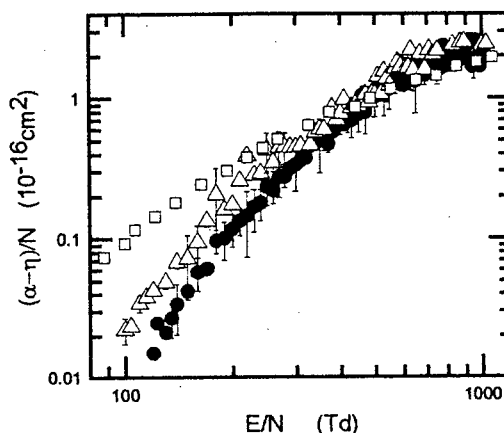


Fig. 1. The present effective ionisation coefficients for 100%  $\text{CH}_4$  (full circles), 50%  $\text{CH}_4$ -50% Ar mixture (open triangles), and 100% Ar (open squares, Reference 5)

Although there is clear evidence of electron capture processes taking place in methane under swarm conditions [6], the evaluation of  $\alpha$  and  $\eta$  was not performed because of the smallness of the negative ion contribution to the total current of the avalanche pulse.

The positive ion drift velocities,  $v_+$ , obtained from the same analysis, were converted into reduced mobilities by the well-known expression given by [7]

$$K_0 = (v_+ / N_0) / (E/N),$$

where  $N_0 = 2.69 \times 10^{19} \text{ cm}^{-3}$  is gas density at STP. These mobilities are shown plotted in Fig. 2 as a function of  $E/N$  for a pure  $\text{CH}_4$ , and for a 50-50%  $\text{CH}_4$ -Ar mixture. Qualitatively, there are two interesting features to discuss from these curves. The first of these relates to the earlier appearance of the wide maximum on the mobility curve of the methane-argon mixture. This is indicative of the strong influence of the argon neutrals on the scattering process. The second feature refers to the lowering of the mobility of the ions drifting in the mixture, which is also explainable by the presence of the argon neutrals. An inspection of the mobilities reported in the literature indicates that the mobility for  $\text{Ar}^+$  ions in pure Ar is much lower than the presently measured mobilities for pure methane and its mixture with Ar [9].

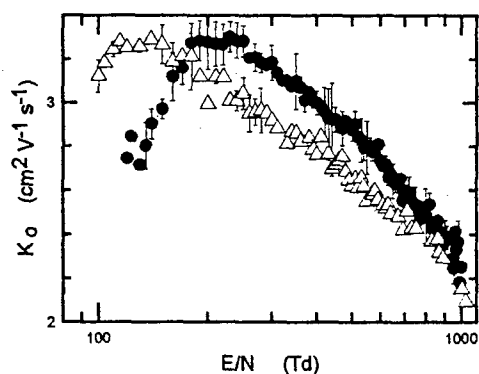


Fig. 2 Reduced mobility of positive ions in 100%  $\text{CH}_4$  (full circles), and 50-50%  $\text{CH}_4$ -Ar mixture (open triangles).

A comparison of the present 100%  $\text{CH}_4$  mobility data with mass-spectrometrically analysed ones up to  $E/N=500 \text{ Td}$  suggests that the ion under question may either be  $\text{CH}_5^+$  or  $\text{C}_2\text{H}_5^+$  [8]. As regards the identity of the ions drifting in the mixture, this must await a direct mass-spectroscopic assessment. However, since it is known that the mobility of  $\text{Ar}^+$  in Ar is about half that of the mixture [9], one might speculate that the observed curve may be the

unresolved mean of two or more of the most important positive daughter ions of methane.

To our knowledge, no previous measurements of either the effective ionisation coefficient or the positive ion mobilities have been published.

## References

- [1] Kokubo T, Tochikubo F and Makabe T, J. Phys. D, **22** 1281 (1987)
- [2] Kleban P, Foreman L and Davis H T, Phys. Rev. A, **23** 1546 (1981)
- [3] de Urquijo J, J. Phys. D, **16** 1603 (1983)
- [4] de Urquijo J, Alvarez I, and Cisneros C, J. Phys. D, **18** 29 (1985)
- [5] Kruithof A A, Physica, **7** 519 (1940)
- [6] Hunter S R, Carter J G, and Christophorou L G, J. Appl. Phys., **60** 24 (1986)
- [7] Mason E A and McDaniel E W, "Transport properties of Ions in Gases", Wiley, New York, 1988
- [8] de Urquijo J, Cisneros C, Alvarez I and Martinez H, in *Gaseous Dielectrics VII*, L.G. Christophorou, Ed., Plenum 1994, pp. 55-61.
- [9] Hornbeck J A, Phys. Rev., **84**, 615 (1951)

## Acknowledgements.

Thanks are due to C. Ruiz and A. Bustos for their assistance. This work was partially supported by DGAPA, Project IN104795.

# Experimental and theoretical investigation of excimer formation in argon in the low and middle pressure range

V. Fiermans, E. Desoppere and W. Wieme

Department of Applied Physics, University of Ghent, Rozier 44, B-9000 Ghent, Belgium

## Introduction

A kinetic model for the decay of excited species in an argon afterglow at "late times" is presented; it interconnects two atomic states and four excimer states in one consistent model. The excited states are subjected to elementary processes, each of which is characterised by a process rate; the sum of the process rates of all decay channels yields the loss rate of the excited state. Knowledge of all process rates allows the calculation of loss rates and decay rates, the latter being experimentally accessible. Measurements of the decay of the first and second continuum at pressures between 0.9 and 100 Torr are compared with theoretical estimates.

## Theory

The model describes the behaviour of all excited states which contribute significantly to the observed VUV continua: the  $\text{Ar}^*(^3\text{P}_1)$  and  $\text{Ar}^*(^3\text{P}_2)$  atomic states, and the higher and lower vibrational levels of the  $\text{Ar}_2^*(\text{o}_u^+)$  and  $\text{Ar}_2^*(\text{l}_u)$  excimer states (fig.1).

In the decay model the process rates  $\delta_{ij}$  represents the elementary process  $i \rightarrow j$ , the loss rate is

$$\nu_i = \sum_j \delta_{ij}, \quad j \quad i, \quad i = 1 \dots 6$$

The concentrations  $n_i(t)$  are described by a set of coupled linear differential equations

$$\frac{d}{dt} n_i(t) = -\nu_i(t) + \sum_j \delta_{ji} n_j(t)$$

The time dependence of the concentrations is represented by

$$n_i(t) = \sum_k a_{ik} e^{-\lambda_k t}$$

the decay rates  $\lambda_k$  are the roots of the eigenvalue equation. In the absence of reversible processes, decay rates equal loss rates and can be associated with the decay of a particular state.

## Decay of the atomic states

The metastable state  $^3\text{P}_2$  is annihilated after diffusion (D) to the wall, while the resonant  $^3\text{P}_1$  state decays by imprisoned resonance radiation (IRR). For the treatment of excimer formation (B3) and excitation transfer (ET) by three body collisions ( $\alpha_{M1}p^2, \alpha_{R1}p^2$ ) the concept of a quasimolecule was introduced [1]. The three body collision is treated microscopically as two successive two body collisions each linearly dependent on pressure with a fast redissociation process

reconnecting the quasimolecule to the atomic precursor. Collision induced radiation (CIR) ( $\alpha_{M1}p, \alpha_{R1}p$ ) occurs when radiative transitions from the quasimolecule are allowed.

Applied to argon, the sum of all relevant process rates results in calculated loss rates:

$$^3\text{P}_2 \quad \nu_1 = \frac{51}{\Lambda^2 p} + 16p + 35p^2$$

$$^3\text{P}_1 \quad \nu_2 = 5.710^4 + 2084p + 222p^2 \quad p \text{ in Torr.}$$

## Decay of the excimer states

$^{1,3}\Sigma_u^+$  excimers are formed in higher excited vibrational levels (symbol \*) by three body collision processes. In successive collisional steps the  $^{1,3}\Sigma_u^*$  states reach the vibrationally relaxed  $^{1,3}\Sigma_u^o$  states in thermal equilibrium with the gas. From each of the vibrational levels, radiative decay to the ground state is possible. However, the occurrence of two well separated VUV continua leads naturally to the assumption that only higher (\*) states contribute to the first continuum and only lower states (o) to the second continuum. The process rates of the 4 excimer states as taken from literature are given in what follows.

-Excimer radiation

in the second continuum (UV2)

$$^{1,3}\Sigma_u^o \quad \tau = 4.2 \text{ ns} \Rightarrow \beta_{Ru}^o = 2.4 \cdot 10^8 \text{ s}^{-1} \quad [2]$$

$$^{3,3}\Sigma_u^o \quad \Rightarrow \beta_{Mu}^* = 3.2 \cdot 10^5 \text{ s}^{-1} \quad [3]$$

in the first continuum (UV1)

$$^3\Sigma_u^* \quad \tau = 160 \text{ ns} \Rightarrow \beta_{Mu}^* = 6.12 \cdot 10^6 \text{ s}^{-1} \quad [4]$$

$$^1\Sigma_u^* \quad \Rightarrow \beta_{Ru}^* = 2.8 \cdot 10^8 \text{ s}^{-1} \quad [5]$$

-Collision induced radiation (CIR)

The p-term in the decay of the  $^{1,3}\Sigma_u^+$  states is interpreted here as collision induced radiation from a short-lived three body complex, analogous to collision induced radiation from a two body quasi-molecule.

$\alpha_{Mu}^o p = 3.22 \text{ p s}^{-1}$  [3],  $\alpha_{Ru}^o p = 547 \text{ p s}^{-1}$  derived using the principle of microscopic reversibility.

-Vibrational relaxation

Rare gas excimers change their vibrational state only in collisions with ground state atoms. Due to the depth of the  $^{1,3}\Sigma_u^+$  potential well (0.55 eV) one expects that the (\*)  $\rightarrow$  (o) relaxation requires a great number of steps to relax. A detailed study of the vibrational relaxation in argon can be found in [6], however, the assumption made in [1] remains valid: higher excited levels and

lower excited levels are connected by an equivalent relaxation rate  $\alpha_{Ru}^* p = 5.610^5 p \text{ s}^{-1}$  [7],  $\alpha_{Mu}^* p$  is unknown, but assumed equal to  $\alpha_{Mu}^* p$ .

### Process and loss frequencies

Based on the previous numbers, the loss rate for each excimer state is obtained by combining the relevant process rates:

$$^3\Sigma_u^*: \nu_3 = 6.12 \cdot 10^6 + 5.610^5 p$$

$$^1\Sigma_u^*: \nu_4 = 2.8 \cdot 10^8 + 5.610^5 p$$

$$^3\Sigma_u^0: \nu_5 = 3.2 \cdot 10^5 + 3.2 p$$

$$^1\Sigma_u^0: \nu_6 = 2.4 \cdot 10^8 + 547 p$$

The 6  $\nu_i$  values are shown as full lines in fig.2.

### Experiment

The decay of the first and second continuum in argon was measured in the "late afterglow" of a low current diffuse glow. The tube with a diameter of 36 mm and length 35 cm was provided with a  $\text{LiF}_2$  window; standard UHV techniques were used prior to filling. The detection system consisted of a 0.3 m Mc Person vacuum monochromator, followed by either a UV convertor and photomultiplier for the second continuum (120 to 140 nm) or a spiraltron electron multiplier for the first continuum (106 to 110 nm). Depending on intensity the signal was averaged on a Lecroy 9400 digital oscilloscope, or sent to a SRS multichannel scaler or to a photon counting chain. The intensity was recorded over at least two decades over the pressure range 0.9 to 100 Torr, and fitted to

$$I(t) = \sum_k I_k e^{-\lambda_{k,\text{exp}} t}$$

with  $\lambda_{k,\text{exp}}$  the experimental decay rate.

### Results

For the first continuum two components were found in the decay rate:

$$\lambda_{f,1} = (5.4 \pm 0.2) \cdot 10^4 + (1285 \pm 44)p + (145 \pm 5)p^2$$

$$\lambda_{f,2} = (68 \pm 11)p + (18.3 \pm 0.3)p^2$$

while the decay of the second continuum could always be fitted to a single exponential:

$$\lambda_{s,2} = \frac{82 \pm 20}{p} + (75 \pm 9)p + (18.5 \pm 0.3)p^2$$

Comparison of these results with the theoretical estimates (fig.2) leads to the attribution of the faster  $\lambda_{s,2}$  to the decay of the  $^3P_1$  atoms, while the

slower  $\lambda_{f,2}$  and  $\lambda_{s,2}$  are identified as the  $^3P_2$  decay

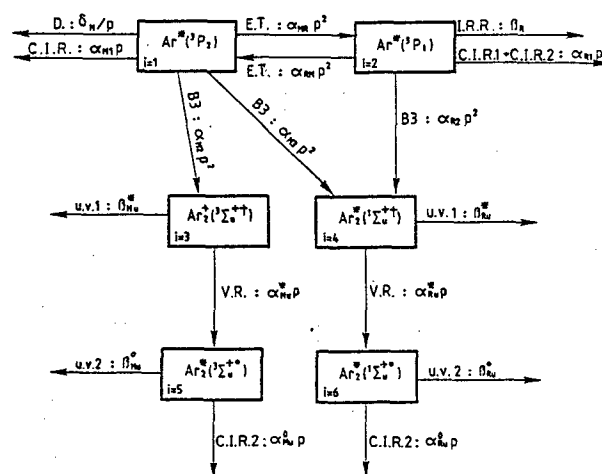


Fig.1. General model for the formation and decay of argon excimers

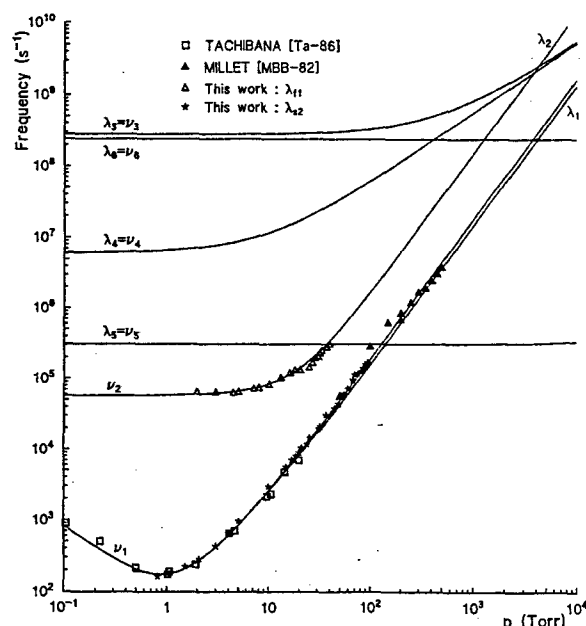


Fig.2. Measured and calculated loss-and decay rates  $\nu$  and  $\lambda$  as a function of pressure.

### References

- [1] H.Janssens et al., J.Chem.Phys.86(1987)4935
- [2] J.Keto et al., Chem.Phys.Lett.,33(1974)1365
- [3] P.Moutard et al., J.Chem.Phys.87(1987)4576
- [4] A.Madej et al., Phys.Rev.Lett.57(1986)1574
- [5] J.Cohen, B.Schneider, J.Chem.Phys.,88(1974)3230
- [6] L.Goubert et al., J.Phys.Chem.99(1995)15479
- [7] P.Millet et al., J.Phys.B,15(1982)2935



# Quantum Effects on Thermodynamic properties of Hot and Dense Helium like Plasmas

Hamid RAHAL and Marie-Madeleine GOMBERT

Laboratoire de Physique des Gaz et des Plasmas  
Bât. 212, Université de Paris-Sud, 91405 Orsay Cedex, France

## 1. Introduction

Earlier works on the determination of equation of state of fully ionized hydrogen plasmas show the importance of quantum description of  $e^-$  - ion and  $e^-$  -  $e^-$  interactions [1,2]. The approach used consists in calculating a pair distribution function on a complete basis set of Coulomb wave functions. With this temperature dependent pair distribution a density and temperature dependent plasma potential was evaluated. Thermodynamic functions were then deduced [2,3].

In this work we extend the study to helium like plasmas which contain (when not fully ionized) hydrogen like ions in addition to point like ions and electrons. The first step consists in obtaining a sufficiently accurate wave functions to describe the states of one electron in the field of hydrogen like ion. In contradistinction with the fully ionized plasma case, an efficient thermodynamic result is the ionization rate versus plasma temperature and density.

## 2. Pair correlation function

We have developed a semi-empirical model making use of a parametric  $e^-$  - ion potential [4,5] which is a sum of the coulombic potential and a  $1/r^2$  term. This model has permitted us to construct accurate bound and continuum wave functions for  $\ell \leq 2$  and for the helium isoelectronic sequence up to  $Z = 26$ .

The pair distribution function is a sum of bound and continuum state contributions :

$$g(r) = g_B(r) + g_C(r) \quad (1)$$

with :

$$g_B(r) = C \sum_{n=1}^{\infty} \sum_{\ell=0}^{n-1} (2\ell+1) \exp(-\beta E_{n\ell}) |R_{n\ell}(r)|^2 \quad (2)$$

and :

$$g_C(r) = C \sum_{\ell=0}^{\infty} (2\ell+1) \int_0^{\infty} dk \exp\left(-\frac{\beta \hbar^2 k^2}{2m}\right) \{R_{k\ell}(r)\}^2 \quad (3)$$

where  $C = (2\pi\beta\hbar^2/m)^{3/2}/4\pi$  is a normalization constant. For  $\ell > 2$ , the wave functions are the hydrogen like ones. For  $\ell \leq 2$ , they depend on a non integer effective angular momentum.

The corresponding pair distribution functions evaluated in the plasma differ from the classical ones at small separation. They are always finite at the origin. Therefore, they permit thermodynamic calculations pointing out the quantum effects.

## 3. Effective potential

The effective plasma potential is defined in terms of the pair correlation function as follows :

$$-\frac{\xi}{Z^2} u(x) = \frac{1}{\xi} \ln [g(x)] \quad (4)$$

where  $x = r/\lambda$  is a reduced distance and  $\lambda$  is the De Broglie wave length.  $\xi = L/\lambda$  is a quantum parameter,  $L$  being the Landau length.

This potential is calculated from pair distribution function calculations. We modeled numerical results with a functional form [6] and in the case of electron-hydrogen like ion interaction we write :

$$-\frac{\xi}{(Z-1)^2} u(x) = \frac{1}{x} [1 - \exp(-2x^2 - \alpha x^3)] + A [1 - \text{Erf}(Bx)] \quad (5)$$

in which  $A$  and  $B$  are Padé functions of the quantum parameter  $\xi$ , they depend on the temperature, the parameter  $\alpha$  ( $= 1/(Z-1)$ ) takes into account the nuclear charge effect (in relation to the spatial extent of the ion) on the optical electron state.

From Eq. (5) the high temperature ( $\xi \ll 1$ ) hydrogen like ( $\alpha=0$ ) plasma potential form is recovered [1]. Moreover, the limit  $\alpha=0$  and  $\xi=0$  (infinite temperature) of Eq. (5) gives the Kelbg potential [7].

## 4. Ionization rate of helium plasma

In the binary approximation the partition function of the system is written in terms of pair correlation functions. We show that the free energy of the system can be written in the form :

$$F = F_0 +$$

$$\frac{V}{2} \int d^3r \left[ \sum_{i=1}^n \sum_{j=1}^n \rho_i \rho_j (u_{ij}(r) - Z_i Z_j e^2 / r) \right] + \frac{V}{2} \frac{1}{\beta} \int \frac{d^3k}{(2\pi)^3} \left[ \ln \{D(k)\} + \sum_{i=1}^n C_{ii}(k) \right]. \quad (6)$$

where  $i$  and  $j$  stand for the various plasma components.  $u_{ij}(r)$  is the above defined effective potential,  $\rho_i$  is the  $i^{\text{th}}$  component density and  $C_{ij}(k)$  is related to the Fourier transform of the potential by the relation :  $C_{ij}(k) = -\beta(\rho_i \rho_j)^{1/2} C_{ij}(k)$ .  $D(k)$  is the determinant of the matrix made of the elements :  $I_{ij} - C_{ij}(k)$ . The free energy function can be written as a sum of an ideal term, a classical plasma term, an exchange term (ideal electron gas) and a quantum (diffraction) correction term :

$$F = F_0 + F_C + F_{ex} + F_Q. \quad (7)$$

The ionization rate of the plasma which is defined by :

$$x = \frac{\rho_{He^{++}}}{\rho_{He^+} + \rho_{He^{++}}} = \frac{\rho_{He^{++}}}{\rho_I} \quad (8)$$

is determined by solving the following equation :

$$\frac{dF}{dx} = 0. \quad (9)$$

In Fig. 1, we plot the ionization rate  $x$  versus total ionic density  $\rho_I$  for helium plasma at  $T=2 \cdot 10^5$  K. The interactions between the particles, when taken into account, give rise to a characteristic non monotonic behaviour in contradistinction to the ideal Saha result.

In Fig. 2, detailed contributions to the ionization rate are shown. The upper Coulomb curve is obtained when we consider classical Coulomb interaction between charged particles. The two lower curves are obtained when the electron-ion interaction is quantum described. The curve noted  $\alpha=0$  corresponds to the case where  $He^+$  ions are considered to be point like ones ; in this case electron-ion wave functions are the hydrogen like ones. The curve noted  $\alpha=1$  corresponds to a more accurate description of the electron- $He^+$  system ; the wave functions given by our atomic model take into account the spatial ion extent.

We note a difference of approximately 30% between the upper and the lower curves.

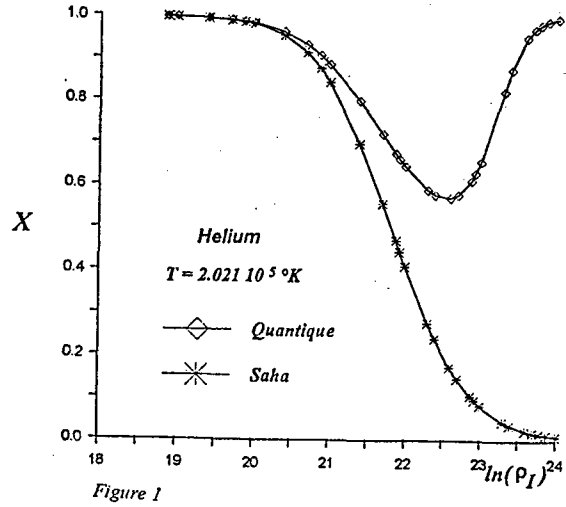


Figure 1

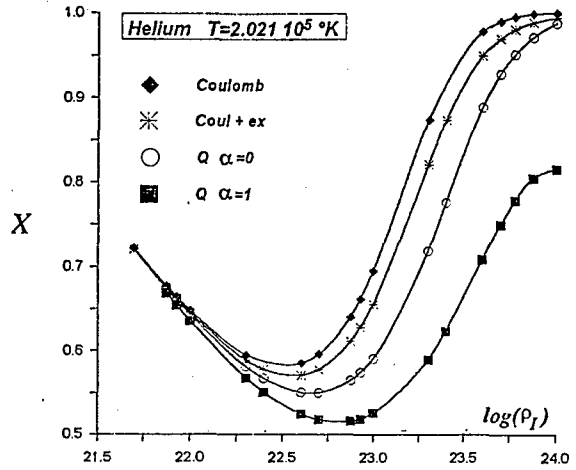


Figure 2

## 5. References

- [1] H. Minoo, M.-M. Gombert and C. Deutsch : Phys. Rev., **23A** (1981) 924
- [2] M.-M. Gombert and H. Minoo : Contr. Plasma Phys., **29** (1989) 4/5, 355
- [3] C. Deutsch, Y. Furutani and M.-M. Gombert : Physics Reports, **69** (1981) 85
- [4] H. Rahal, M.-M. Gombert and A. Valance : Physics Letters A **176** (1993) 443
- [5] H. Rahal and M.-M. Gombert : to be submitted to J. Phys. B
- [6] H. Rahal : Thesis, Université de Paris XI, 1995
- [7] G. Kelbg : Ann. Phys. (Leipzig) **12** (1963) 219

# Electron Energy Distribution Function in Decaying Ar : NF<sub>3</sub> Plasmas: the Possibility of Negative Electron Mobility.

<sup>1</sup>N A Dyatko, <sup>2</sup>M Capitelli, <sup>2</sup>S Longo and <sup>1</sup>A P Napartovich

<sup>1</sup> Troitsk Institute for Innovation and Fusion Research, 142092, Troitsk, Moscow region, Russia

<sup>2</sup> Centro di Studio per la Chimica dei Plasmi del Consiglio Nazionale delle Ricerche, Dipartimento di Chimica, Università di Bari, Italy

In the last years a number of papers has appeared on the negative mobility (drift velocity) of electrons in low temperature plasma (see references in [1]). Now it is known several different physical situations in which negative electron mobility was investigated: relaxing plasmas, beam sustained plasmas and decaying plasmas.

In present paper we have considered the Ar:NF<sub>3</sub> gas mixture under the following initial conditions: equal concentration of electrons and positive ions exists in the mixture and an external electric field is applied across the plasma. Such initial conditions can be created by short ionization pulse. For low electric field strengths the rate of removal of electrons by attachment processes exceeds the rate of ionization so that the considered plasma decays. During the decrease of the electron concentration the deformation of the shape of the electron energy distribution function with respect to the initial one occurs.

To calculate the electron concentration,  $n(t)$ , and the shape of the distribution function we solved a Boltzmann equation for  $F(u,t) = n(t) f(u,t)$  with the initial condition  $F(u,0) = n(0) f(u,0)$ ,  $t$  is the time and  $u$  is the electron energy. An appropriate Boltzmann equation can be written in the form

$$\sqrt{u} \frac{dF}{dt} = I_E + St(F).$$

$I_E$  describes the divergence of the flux of electrons along the energy axis driven by the electric field,  $St(F)$  is the rate of change of the distribution function  $F(u)$  due to elastic and inelastic collision processes,  $f(u,t)$  is the normalized electron energy distribution function (NEEDF):

$$\int_0^{\infty} \sqrt{u} f(u) = 1.$$

The following collision processes were taken into account: elastic scattering of electrons on Ar atoms, excitation of electronic levels of Ar and attachment of electrons to NF<sub>3</sub> molecules. Figure 1 shows the momentum transfer cross section of Ar [2] ( $Q_m$ ) and attachment cross section [3] ( $Q_a$ ). We have neglected electron-electron and electron-ion collisions as well as recombination processes i.e. we have considered initial ionization degrees less than  $10^{-7}$ .

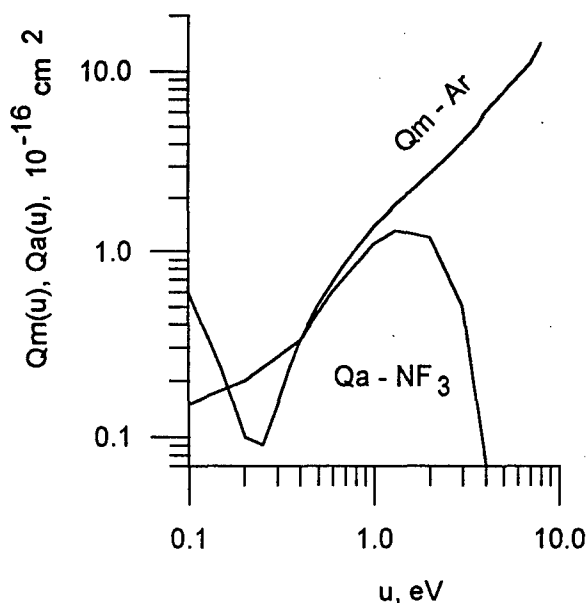


Fig. 1: Momentum transfer cross section of Ar and attachment cross section of NF<sub>3</sub>

All calculations were carried out for gas temperature  $T=300$  K and at atmospheric pressure. The initial function  $f(u,0)$  was considered as a Maxwellian one with the given temperature  $T_{e0}$ .

Calculations showed that during the decay of electron concentration the steady distribution function  $f(u)$  is formed and the decrease of electron concentration becomes exponential. In other words, after some time  $F(u,t)$  becomes a self-similar function in which the time and energy dependence are factorized:

$$F(u,t) = n(t)f(u), \text{ where } n(t) \sim \exp(-\nu t).$$

The decay frequency  $\nu$  corresponds to the attachment frequency. For a given  $E/N$  value  $f(u)$  and  $\nu$  does not depend on the initial conditions ( $T_{e0}$ ).

Figures 2 and 3 show the established NEEDF and drift velocity as a function of the electric field strength. We can note an increase of drift velocity in the range of  $E/N$  from  $1 \cdot 10^{-18}$  V cm<sup>2</sup> to  $3.2 \cdot 10^{-18}$  V cm<sup>2</sup>, followed by an abrupt transition from a positive value at  $3.2 \cdot 10^{-18}$  V cm<sup>2</sup> to a negative one at  $3.8 \cdot 10^{-18}$  V cm<sup>2</sup>. From  $3.8 \cdot 10^{-18}$  V cm<sup>2</sup> to  $3 \cdot 10^{-17}$  V cm<sup>2</sup> drift velocity is negative and equal to  $-3.0 \cdot 10^4$  cm s<sup>-1</sup>. Finally, the drift velocity increases again for  $E/N > 3 \cdot 10^{-17}$  V cm<sup>2</sup>.

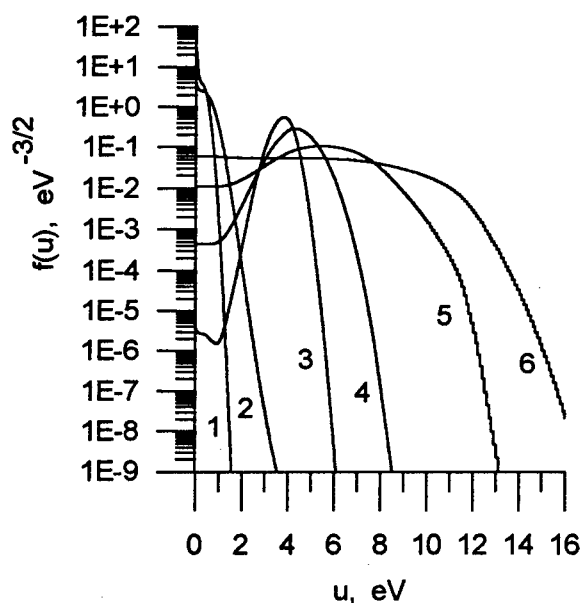


Fig. 2 Established NEEDF in decaying plasmas

Ar : NF<sub>3</sub> = 100 : 1.

1 -  $E/N = 10^{-18}$  V cm<sup>2</sup>, 2 -  $E/N = 3.2 \cdot 10^{-18}$  V cm<sup>2</sup>,  
3 -  $E/N = 3.8 \cdot 10^{-18}$  V cm<sup>2</sup>, 4 -  $E/N = 10^{-17}$  V cm<sup>2</sup>,  
5 -  $E/N = 3.10^{-17}$  V cm<sup>2</sup>, 6 -  $E/N = 10^{-16}$  V cm<sup>2</sup>.

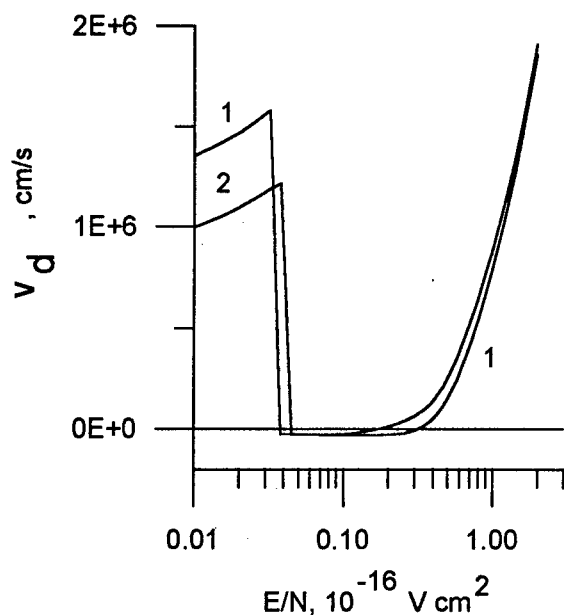


Fig. 3 Established electron drift velocity as a function of  $E/N$  in decaying Ar : NF<sub>3</sub> plasmas. 1- 1% NF<sub>3</sub>, 2- 0.5% NF<sub>3</sub>.

Before the explanation of these results let us point out that for the existence of negative electron mobility two conditions are necessary (but not sufficient) (see, for example, [1]): a) the first derivative of  $f(u)$  must be positive ( $df(u)/du > 0$ ) in some energy interval; b)  $d(\ln(Q_m))/du > 1$ , which means a fast growth of  $Q_m(u)$  with  $u$ . For Ar condition b) is satisfied between 0.5 and 10 eV (see fig. 1).

Unusual dependence of drift velocity on the electric field, presented in figure 3, is due to the shape

of attachment cross section. To understand better the problem, let us denote as  $u_m$  the energy at which the attachment cross section has a maximum. The momentum transfer cross section of Ar for  $u > u_m$  is greater than for  $u < u_m$ . The electrons in plasmas can be divided in two groups: the first group contains electrons with energies  $u < u_m$  and the second group contains electrons with energies  $u > u_m$ . The electron heating by the electric field can be considered as the driving force for the diffusion in the energy space. For moderate electric fields, the intensity of this diffusion is not sufficient to overcome the attachment cross section barrier. As a result, each group of electrons "has its own life". At the early time the concentrations of electrons of each group are defined by  $f(u, 0)$ . During plasma decay, the electron concentration is decreasing and the shape of steady state NEEDF depends on the ratio of the decay rates of each electron group. If the electric field is weak, the electrons with low energies disappear with relatively slow rate, since the attachment cross section is small at low energies. Electrons of the second group lose energy in elastic collisions and disappear quickly because of a large attachment cross section at energies lower than 3.5 eV. As a result, NEEDF presents a monotonic decrease as a function of energy. The corresponding NEEDF for  $E/N = 10^{-18}$  V cm<sup>2</sup> and  $E/N = 3.2 \cdot 10^{-18}$  V cm<sup>2</sup> are shown in figure 2 (curves 1 and 2). The increase of the electric field strength leads to an increase of the mean energy. Attachment rate of electrons of the first group increases, since the attachment cross section grows with energy. For values of  $E/N$  in the range  $3.2 \cdot 10^{-18}$  V cm<sup>2</sup> -  $3.8 \cdot 10^{-18}$  V cm<sup>2</sup> the decay rates of electrons of both groups are approximately equal. If the value of  $E/N$  parameter is greater than  $3.8 \cdot 10^{-18}$  V cm<sup>2</sup>, electrons of the first group disappear more quickly than the electrons of the second group. As a result, the NEEDF with a maximum at energies 4 eV - 5 eV is formed (see curves 3, 4, 5 in figure 2). The corresponding electron drift velocity becomes negative. With the further increase of the electric field, electrons of the first group get enough energy (during their lifetime) to overcome the attachment barrier in the energy space. In this case slightly inverted (or non-inverted) NEEDF is formed (curves 5, 6 in figure 2) and the corresponding drift velocity is positive.

This work was partially supported by Russian Basic Research Foundation 96-02-19265.

## References

- [1] A.I. Shchedrin, A.V. Ryabtsev, Dennis Lo: J.Phys. B: At. Mol. Opt.Phys., **29** (1996) 915
- [2] J.L. Pack, R.E. Voshall, A.V. Phelps, L.E. Kline: J. Appl. Phys., **71** (1992) 5363
- [3] S. Ushiroda, S. Kajita, Y. Kondo: J. Phys. D: Appl.Phys., **23** (1990) 47

# Revisited collision integrals and transport coefficients of high temperature air components

M. Capitelli\*, C. Gorse\*, S. Longo\*, D. Giordano\*\*

\* Centro Studio Chimica Plasmi del CNR and University Chemistry Department, Via Orabona 4, 70126 Bari, Italy

\*\* European Space Research and Technology Center, P.O. Box 299, 2200 AG Noordwijk, The Netherlands

## 1. Introduction

In a recent paper [1] we have reviewed the literature concerning the transport properties of high temperature gases. We present here collision integrals and transport coefficients of high temperature air species (in particular of nitrogen) including diffusion and viscosity collision integrals  $\Omega^{(l,s)}$ , translational ( $\lambda_{tr}$ ) and internal ( $\lambda_{int}$ ) thermal conductivity together with total thermal conductivity ( $\lambda_t$ ), viscosity ( $\eta$ ) and diffusion coefficients (D).

In this work we will also try to establish the accuracy of the calculated values comparing our results with the recent ones on the subject reported by the Ames group [2], by Murphy [3], by Ryabov [4] as well as with available experimental data.

## 2. Collision integrals

Accurate calculations of transport coefficients can be obtained once the collision integrals of the different interactions are known [5]. Performing three integrations we obtain the collision integrals as a function of temperature (T)

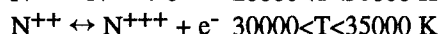
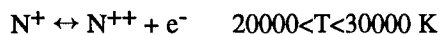
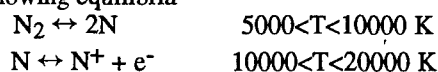
$$\Omega^{(l,s)}(T) = \left( (s+1)! (kT)^{s+2} \right)^{-1} \int_0^\infty e^{-E/kT} E^{s+1} Q^{(l)}(E) dE \quad (1)$$

The problem of calculating  $\Omega^{(l,s)}$  reduces to the knowledge of the interaction potential  $V(r)$ . For many interactions (Morse, exponential repulsive,  $Ar^{-n}$  forms) the collision integrals are tabulated so that the knowledge of relevant parameters is sufficient to obtain the collision integrals. For other important interactions (electron-atom, electron-molecule, resonant charge transfer) the diffusion cross section  $Q^{(l)}$  is introduced directly in the integral of eq. 1. From collision integrals the calculation of transport coefficients is straightforward [5].

A special treatment of the contribution of electronic energy to the transport of internal energy is being considered to take into account the dramatic increase of the transport cross-sections of high lying excited states with the principal quantum number.

## 3. Main interactions

In a high temperature environment different species can survive depending on the considered temperature range. As an example an atmospheric nitrogen plasma shows the following equilibria



This means that we pass from a low temperature system, where molecules and atoms coexist, to a high temperature one, where electrons, atoms and parent ions survive, ending to a temperature range in which only ions and electrons exist.

## 3.1 Dissociation range

### $N_2$ - $N_2$ , $N_2$ -N

For these interactions we use an exponential repulsive potential the parameters of which are taken from the experimental beam studies of Leonas [6]. The choice of repulsive potential for this interaction can be open to some question at low and intermediate temperature  $T < 2000$  K when attractive forces dominate the interaction. In this case a Lennard-Jones potential has been introduced to get a better agreement with experimental data.

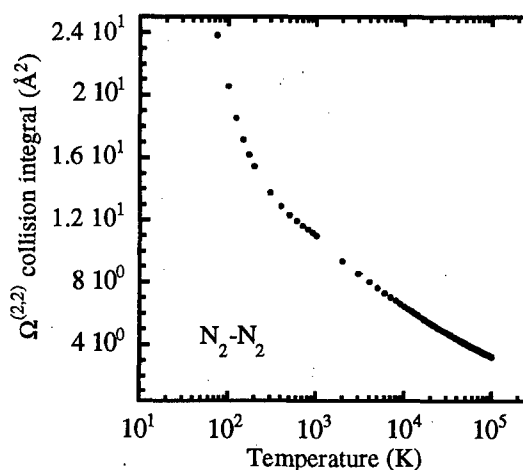


Fig.1  $\Omega^{(2,2)}$  collision integral for  $N_2$ - $N_2$  interaction as a function of temperature.

A sample of results for  $N_2$ - $N_2$  reported in fig. 1 shows an abrupt change in the slope due to the interplay of the different potentials. The present calculations are in satisfactory agreement with experimental results. A similar situation is found for  $N$ - $N_2$  also in relation with the experimental diffusion coefficient [7].

### N-N

The two  $N(^4S)$  atoms can interact over 4 potential curves, the collision integrals have been obtained by using a Morse potential for the  $1, 3, 5\Sigma$  interactions [8] and an exponential repulsive potential for  $7\Sigma$  [9]. The collision integrals of multi-potential interaction is an average of the different potentials. A comparison of the

present results with those of Ames'group shows a satisfactory agreement in the temperature range 2000-20000 K in which N atoms are the predominant species. At low temperature  $T < 1000$  K a Lennard-Jones potential is also used.

### 3.2 Partial ionization range

#### Ion-parent atom

##### N-N<sup>+</sup>

The diffusion type collision integral is dominated by charge exchange process while the viscosity type collision integral is dominated by valence forces, even though at low temperature polarizability forces should be taken into account. The interaction of ground state atoms  $N(^4S)/N(^3P)$  occurs through 12 potential curves. A comparison of our results with those calculated by Ames'group shows a satisfactory agreement (differences below 15%) in the temperature range 5000-20000K where the concentration of these species can be important. Larger differences (up to 35%) are observed outside this temperature range when N-N<sup>+</sup> species should not be important.

The diffusion collision integrals have been obtained by the usual approximation on the diffusion cross section ( $Q^l$ ) dominated by charge transfer (the experimental charge transfer measurements of Belyaev [10] are used). A comparison of the present calculations and the theoretical ones of Ames'group shows differences not exceeding 8%.

##### N<sub>2</sub>-N<sub>2</sub><sup>+</sup>, N<sub>2</sub>-N<sup>+</sup>

Diffusion type collision integrals for this interaction have been calculated by using the momentum transfer cross sections of Phelps [11] which include both resonant charge transfer cross sections and polarizability correction at low energy.

### 3.3 Electron neutral interaction

#### e-N<sub>2</sub>, e-N

The integrals calculated are given in this case by

$$Q^{l,s}(T) = \frac{4(l+1)}{(s+1)!(2l+1-(-1)^l)} \frac{1}{2KT} \int_0^\infty e^{-\varepsilon/KT} \left(\frac{\varepsilon}{KT}\right)^{s+1} \sigma^{(l)}(\varepsilon) d\varepsilon \quad 3)$$

Where  $\sigma^{(1)}$  and  $\sigma^{(2)}$  are the momentum transfer ( $l=1$ ) and transport ( $l=2$ ) cross sections respectively. As regards nitrogen molecules, we have used the momentum transfer cross section reported by Phelps and Pitchford [12]. To calculate  $\sigma^{(2)}$ , we have corrected for the ratio  $\sigma^{(2)}/\sigma^{(1)}$  expressed in terms of the coefficients of the differential cross section development into spherical harmonics. In the case of e-N, the momentum transfer cross section is the same used by Capitelli and Devoto [8]. In this case we have corrected for the ratio  $\sigma^{(2)}/\sigma^{(1)}$  by using phase shifts according to

$$\frac{\sigma^{(2)}(\varepsilon)}{\sigma^{(1)}(\varepsilon)} = \frac{\sum_l \frac{(l+1)(l+2)}{(2l+3)} \sin^2(\delta_l - \delta_{l+2})}{\sum_l (l+1) \sin^2(\delta_l - \delta_{l+1})} \quad 4)$$

where the phase shifts  $\delta_n$  as a function of  $\varepsilon$  are interpolated from the set calculated by Thompson [13].

### 3.4 Ion-ion and electron-electron

In this case we can use a screened Coulomb potential. Collision integrals for this interaction are known either in tabular [14] or in approximated closed forms [15].

### 4. Conclusions

We present results of calculations of collision integrals and transport coefficients of air components in the temperature range 50-100000K emphasising the degree of confidence of the results.

### 5. Acknowledgement

This work has been partially supported by "Progetto Strategico del CNR: Applicazioni Industriali dei Plasmi"

### 6. References

- [1] M. Capitelli, R. Celiberto, C. Gorse, D. Giordano, Plasma Chem. Plasma Process. 16, 267S (1996)
- [2] E. Levin, H. Partridge and J.R. Stallcop, AIAA 22nd Thermophys. Conf. Honolulu (1987) AIAA-87-1632; E. Levin, H. Partridge and J.R. Stallcop RIACS Techn. Report 89, 43 (1989)
- [3] A.B. Murphy and C.J. Arundell, Plasma Chem. Plasma Process. 14, 451 (1994)
- [4] V.V. Riabov JTHT 10, 209 (1996)
- [5] J.O. Hirschfelder, C.F. Curtiss and R.B. Bird, "Molecular theory of gases and liquids", J. Wiley and Sons, third printing (1966)
- [6] V.B. Leonas, Sov. Phys. Uspekhi 15, 266 (1973)
- [7] R.M. Fristrom and A.A. Westenberg, Flame Structure, Mc Graw-Hill New York (1965)
- [8] M. Capitelli and R. S. Devoto Phys. Fluids 16, 1835 (1967)
- [9] M. Capitelli, U.T. Lamanna, C. Guidotti and G.P. Arrighini, J.Chem.Phys., 79 (1983); C. Guidotti, G.P. Arrighini, M. Capitelli, U.T. Lamanna, Z. Naturforsch. A31, 1722 (1976)
- [10] Y.N. Belyaev and V.B. Leonas, Sov. Phys. Dokl. 11, 866 (1967)
- [11] A.V. Phelps, J. Phys. Chem. Ref. Data, 20, 557 (1991)
- [12] A.V. Phelps and L.C. Pitchford, JILA Report n°26, University of Colorado, Boulder, Colorado (1985)
- [13] D.G. Thomson, J. Phys. B: At. Mol. Phys. 4, 468 (1971)
- [14] H.S. Hahn, E.A. Mason, F.J. Smith, Phys. Fluids 14, 278 (1971)
- [15] R. L. Liboff, Phys. Fluids 2, 40 (1959)

## Evaluation of the basic parameters in plasmas in the mixtures of argon and chlorine

N.V. Novaković, B.S. Milić\* and S.M. Stojilković\*\*

Faculty of Philosophy, Dept. of Physics, P.O.B. 91, 18001 Niš, Yugoslavia

\*Faculty of Physics, P.O.B. 368, 11001 Belgrade, Yugoslavia

\*\*Faculty of Electronics, Niš, Yugoslavia

Low-temperature and low-pressure plasmas, virtually in local thermodynamical equilibrium, are of interest from the fundamental scientific point of view and from that of technical applications. The knowledge of basic parameters, such as the number densities of the constituents present or the transport coefficients, as functions of pressure and temperature of the system is of great interest in dealing with these plasmas.

The object studied in the present paper is the argon plasma contaminated by 20% of chlorine. It is taken that the plasma is kept under a constant pressure (0.1 kPa and 1.0 kPa), and at a constant temperature, varying between 500 K and 5000 K. The considerations are based on two essential items: (1) the assumption that the plasma is Maxwellian (temperatures of all the constituents are equal) [1] and that the thermal ionization is the most significant mechanism determining the final degree of ionization; (2) use is made (in conjunction) with Saha relations) of a modified expression for the effective Debye radius of plasma (and for the ensuing ionization energy lowering) as derived by the same authors previously [2,3].

The equilibrium plasma composition, i.e. the number densities of its various constituents, is determined in the present work by numerical methods, under the assumption that, in the temperature range considered, the species present are:  $e$ ,  $Cl_2$ ,  $Ar$ ,  $Cl$ ,  $Cl_2^+$ ,  $Ar^+$  and  $Cl^+$ . The standard procedure of using the Saha equations and equations of the law of mass action for the process dissociation, combined with the requirements of charge conservation and pressure constancy, is applied. The new detail in the evaluation of the plasma composition is that, in determining the modified Debye radius, the Landau length was used as the cut-off range rather than ionic radii. This alteration in the calculation procedure did not bring about any significant change in the final numerical results for transport coefficients, in spite of the fact that the Landau length was found to be about one order of magnitude larger.

Tables 1. and 2. show that dependence of the evaluated number densities of various constituents on temperature for pressures 0.1 kPa and 1.0 kPa, re-

spectively. It is seen that in the mixtures of argon and chlorine under the above conditions many different ionic and neutral particles can exist and the electron and ion number densities tend to increase with temperature, which is an easily comprehensible feature. The relation between the ionization energies and the relation between the dissociation energies of the species present is the factor of the primary significance in determining the above plasma properties. The energy of the first ionization of the chlorine (12.97 eV) is 1.21 times smaller than that of the argon (15.75 eV); the energy of the dissociation chlorine molecule (2.50 eV) is 1.61 times smaller than that of  $Cl_2^+$  (4.03 eV). On the other hand, the energy of the first ionization of chlorine is 1.13 times higher than that of the chlorine molecule.

Table 1.

	$T(K)$	$p = 100 Pa$	
$n(m^{-3})$	1000	3000	5000
$n_e$	$6.3 \cdot 10^{-6}$	$2.6 \cdot 10^{13}$	$8.8 \cdot 10^{17}$
$n_{Ar^+}$	$9.3 \cdot 10^{-16}$	$1.2 \cdot 10^{10}$	$3.0 \cdot 10^{16}$
$n_{Cl^+}$	$4.9 \cdot 10^{-14}$	$2.6 \cdot 10^{13}$	$8.5 \cdot 10^{17}$
$n_{Cl_2^+}$	$6.3 \cdot 10^{-6}$	$1.8 \cdot 10^{10}$	$2.2 \cdot 10^{12}$
$n_{Cl}$	$3.8 \cdot 10^{20}$	$4.9 \cdot 10^{21}$	$4.9 \cdot 10^{21}$
$n_{Cl_2}$	$4.6 \cdot 10^{21}$	$5.1 \cdot 10^{16}$	$2.1 \cdot 10^{15}$
$n_{Ar}$	$2.0 \cdot 10^{23}$	$2.0 \cdot 10^{23}$	$2.0 \cdot 10^{23}$

Table 2.

	$T(K)$	$p = 1000 Pa$	
$n(m^{-3})$	1000	3000	5000
$n_e$	$2.0 \cdot 10^{-5}$	$8.3 \cdot 10^{13}$	$2.8 \cdot 10^{18}$
$n_{Ar^+}$	$2.9 \cdot 10^{-15}$	$3.9 \cdot 10^{10}$	$9.6 \cdot 10^{16}$
$n_{Cl^+}$	$4.9 \cdot 10^{-14}$	$8.2 \cdot 10^{13}$	$2.7 \cdot 10^{18}$
$n_{Cl_2^+}$	$2.1 \cdot 10^{-5}$	$5.7 \cdot 10^{11}$	$7.1 \cdot 10^{13}$
$n_{Cl}$	$1.2 \cdot 10^{21}$	$4.9 \cdot 10^{22}$	$4.9 \cdot 10^{22}$
$n_{Cl_2}$	$4.8 \cdot 10^{22}$	$5.1 \cdot 10^{18}$	$2.1 \cdot 10^{17}$
$n_{Ar}$	$2.0 \cdot 10^{23}$	$2.0 \cdot 10^{23}$	$2.0 \cdot 10^{23}$

An inspection of Tables 1. and 2. further discloses that the increase of pressure raises the number densities of all the relevant constituents, the raise being obviously more noticeable in the neutrals. All these details are easily recognizable features of the Saha equation. It is very interesting the fact that the ratio of the electron number densities is about 3. The number density of chlorine ions is equal in the both cases (100 Pa and 1 kPa) for the temperature around 1000 K. At higher temperatures, if the pressure 10 times higher is, the ratio  $n_{Cl+}(p_2)/n_{Cl+}(p_1)$  is about 3. The ratio of the chlorine ions was found vary from 3.16 to 10. At lower temperatures the ionization of chlorine is not massive and practically argon is very small ionized. At relatively higher temperatures the electron number density values is similar to values of  $n_{Cl+}$ , confirming that all electrons arise in the first ionization of chlorine. The presence of chlorine brings enhancement in the values of the electron number density in this temperature range from 500 K to 5000 K. The overall degree of ionization is very small and this quantity is very little sensitive to pressure variations. All these details are easily recognizable features of the Saha equation.

species present (neutral atoms, singly charged ions and molecules) is by far the significant physical factor in determining the plasma composition and its transport coefficients.

## References

- [1] V.N. Kolesnikov: FIAN, **30** (1964) 66 (in Russ.)
- [2] B.S. Milić et al.: Czech. J. Phys., **B37** (1987) 1238
- [3] N.V. Novaković et al.: Phys. Scripta, **41** (1990) 265
- [4] L.G. Huxley, R.W. Crompton: The Diffusion and Drift on Electrons in Gases, John Wiley & Sons, New York, 1982, 43
- [5] N.V. Novaković et al.: Czech. J. Phys., **46** (1996) 973
- [6] N.V. Novaković: SFIN, **A1** (1996) 125

Table 3.

$T(K)$	$p=100Pa$		$p=1kPa$	
	$\mu_e \left(\frac{m^2}{Vs}\right)$	$\mu_i \left(\frac{m^2}{Vs}\right)$	$\mu_e \left(\frac{m^2}{Vs}\right)$	$\mu_i \left(\frac{m^2}{Vs}\right)$
500	$1.9 \cdot 10^3$	$5.6 \cdot 10^{-2}$	$1.9 \cdot 10^2$	$5.6 \cdot 10^{-3}$
1500	$5.9 \cdot 10^0$	$1.7 \cdot 10^{-4}$	$7.3 \cdot 10^{-1}$	$2.1 \cdot 10^{-5}$
2500	$4.8 \cdot 10^0$	$1.4 \cdot 10^{-4}$	$4.8 \cdot 10^{-1}$	$1.4 \cdot 10^{-5}$
3500	$4.5 \cdot 10^0$	$1.3 \cdot 10^{-4}$	$4.5 \cdot 10^{-1}$	$1.3 \cdot 10^{-5}$
4500	$4.4 \cdot 10^0$	$1.2 \cdot 10^{-4}$	$4.4 \cdot 10^{-1}$	$1.3 \cdot 10^{-5}$

The evaluation of the transport coefficients under the above conditions is based on the expression given by [4]. The same authors these quantities in plasmas of noble-gas with alkaline additives were evaluated previously [5,6] and in this case was used same procedure, but first time ion mobility was calculated. For example, the values of electron and ion mobilities in argon plasma with 20% chlorine as additive are given in Table 3. The electron mobility for the higher pressure is 10 times smaller, than the corresponding quantity at the same temperature for the pressure 0.1 kPa. It is seen that the ion mobility in argon plasma with chlorine as additive is than the electron mobility for four order of magnitude lower.

It is to be concluded from all that was said above that in the low-pressure and low-temperature thermal argon plasmas with chlorine as additive, the relations between the ionization energies of the atomic



# Effective Secondary Emission Coefficient in a High Pressure Noble Gas

V.P. Nagorny, P.J. Drallos

Plasma Dynamics Corp., 417 E.8 Mile Rd., Hazel Park, MI 48030, USA

The phenomenon of secondary electron emission from the surface under the action of a primary particle (photon, ion, excited atom, etc.) plays an important role in gas discharge physics. This role is reflected in the theory by the effective secondary emission coefficient (ESEC)  $\gamma$ : the number of electrons leaving the cathode surface per impinging primary particle [1,2]. In a high density gas  $\gamma$  grows with  $E/p$  at low  $E/p$  values (where  $E$  is the electric field and  $p$  is a gas pressure), and reaches a constant value at high  $E/p$  [2-5]. The mechanism responsible for this dependence is a reflection of a part of the secondary electrons from the gas atoms back to the cathode surface [1].

In this report we find an expression for ESEC based on a kinetic approach. We consider a typical case, when the voltage across the gap significantly exceeds the excitation/ionization potential of the gas atoms (compare with Ref. [6]). We limit our consideration to a weakly ionized noble gas under conditions when the electron mean free path  $\lambda_e$  is small compared to the scale-length  $l$  of the problem, and electric field  $E$  is uniform and directed normally to the surface, (compare with Refs. [6,7]). We assume, that the electric field is strong enough so that one can neglect the energy exchange between electrons and heavy particles in elastic collisions. Since the value of ESEC involves electron dynamics, its value will be different in the stationary and non-stationary cases. We will assume that the electric field is constant. Electron dynamics in a gas does not depend on the specific source of secondary electrons (ions, photons, etc.), and the resulting expressions can be applied to any of these sources. However, to be specific we will consider only one such a source - their liberation from the surface by the action of ions.

We consider a planar anode-cathode gap of width  $L$  and direct the  $Z$ -axis normally to the cathode, so that the electric field is anti-parallel to the axis, and we also choose  $z=0$  at the cathode. As was already mentioned we consider herein the case of a high density gas or weak electric field, so that the kinetic energy that the electron gains between two collisions is small compared to its kinetic energy,  $eE\lambda_e \ll W$ . In this case the electron distribution function (EVDF) is almost isotropic at distances from the electrode exceeding a few  $\lambda_e$  and can be represented as

$$f(\mathbf{r}, \mathbf{v}, t) = f_0(z, v, t) + \delta f(z, v, \theta, t), \quad (1)$$

with  $\delta f(z, v, \theta, t) \ll f_0(z, v, t)$ , and  $\theta$  is the angle between the velocity vector and the  $Z$ -axis..

The electron density  $n_e$  and electron current  $j_e$  are related to  $f_0$  and  $\delta f$ , respectively:

$$n_e = 4\pi \int_0^\infty v^2 f_0 dv, \quad j_e = -e \int v_z \delta f d^3v = \frac{4\pi e}{3} \int_0^\infty v^3 g dv$$

It is convenient to choose new independent variables  $(z, \varepsilon, \theta, t)$  instead of  $(z, v, \theta, t)$ , where

$$\varepsilon = mv^2/2 - eEz, \quad (2)$$

is the total electron energy,  $E = |E_z| = -E_z$ . In these variables functions  $f_0(\varepsilon, z, t)$  and  $\delta f(\varepsilon, z, \theta, t)$  satisfy the following equations [8]

$$\frac{\partial f_0}{\partial t} = \frac{1}{3v} \frac{\partial}{\partial z} \frac{v^3}{v_{tr}} \frac{\partial}{\partial z} f_0 + C_{il}(f_0) \quad (3)$$

$$\delta f = -g(z, \varepsilon, t) \cos \theta \quad (4)$$

$$g(\varepsilon, z, t) = \frac{v}{v_{tr}} \frac{\partial f_0}{\partial z}, \quad (5)$$

where  $v = v(z, \varepsilon)$  according to Eq. (2),  $v_{tr} = N\sigma_{tr}v$  is the electron collision frequency,  $\sigma_{tr}$  is the electron-atom momentum transfer cross-section, and  $C_{il}(f_0)$  is an inelastic collision term. According to Eq.(2)  $\varepsilon > 0$  at  $z=0$ , so that  $\varepsilon > 0$  is a necessary condition for electrons to return to the cathode, and for evaluating ESEC we need to know the electron distribution function only in the energy range  $\varepsilon > 0$ .

The inelastic collision term  $C_{il}(f_0)$  consists of two parts: the scattering-"out" of an element  $(d\mathbf{r}, d\mathbf{v})$  of a phase space ("sink" term) and scattering-"into" the element  $(d\mathbf{r}, d\mathbf{v})$ . Due to a large difference in masses of electrons and the background gas atoms, electrons do not change energy in elastic collisions. On the other hand, the energy change in inelastic collision is at least  $W_{ex}$ , where  $W_{ex}$  is the excitation threshold. According to a common situation in noble gases we assume that the excitation threshold is higher than the maximum energy of secondary electrons near the surface  $W_{max}$ , [9]. Thus after one inelastic collision the electron leaves the initial energy range  $0 < \varepsilon < W_{max}$  (energy becomes negative and electron leaves the region within which it could return to the cathode), so that the scattering-"into" term is absent in this energy range, and for  $C_{il}(f_0)$  we can write:

$$C_{il}(f_0) = -v_{il}(\nu) f_0 \quad (6)$$

where  $v_{il}(\nu) = N\nu \left( \sum_k \sigma_k(\nu) + \sigma_i(\nu) \right)$  is the energy dependent frequency of inelastic collisions;  $\sigma_k(\nu)$  is

an excitation cross-section, and  $\sigma_i(\nu)$  is the ionization cross-section.

The absence of the scattering-"in" term allows one to consider the EVDF and "differential ESEC"  $\gamma(W_0, E)$  independently for every energy layer  $(W_0, W_0 + dW_0)$ . Then, integrating  $\gamma(W_0, E)$  over the energy spectrum of emitted electrons we can find the ESEC.

To find  $\gamma(W_0, E)$  we assume that all electrons at the cathode have the energy  $\varepsilon = W_0$ . Then the stationary solution of Eq. (3) (with positive energy) differs from zero only at the energy equal to the initial energy of electrons,  $\varepsilon = W_0$ :

$f_0(z, \varepsilon) = F(z)\delta(\varepsilon - W_0) = F(z)\delta(W - eEz - W_0)$ , (7) where  $F(z)$  satisfies the following equation

$$\frac{1}{3\nu} \frac{\partial}{\partial z} \nu^3 \frac{\partial}{\partial z} F = \nu_{il}(\nu) F. \quad (8)$$

Here  $\nu$  is a function of  $z$  given by Eq. (2) with  $\varepsilon = W_0$ , and  $\nu_{il}(\nu) = \nu_{il}(W) = \nu_{il}(W_0 + eEz)$ . Since  $W_{\max} < W_{ex}$ , an inelastic collision can occur only beyond certain distances from the cathode  $z_I(W_0)$ :

$$z_I(W_0) \equiv (W_{ex} - W_0) / eE, \quad (9)$$

after the electron gains enough energy to excite atoms, so for  $z \leq z_I(W_0)$ ,  $\nu_{il}(\nu) = 0$ .

We assume that the electric field  $E/p$  is not very strong, so that after an electron reaches the excitation threshold it does not gain much energy before it undergoes an inelastic collision. In this case for  $\nu_{il}(\nu)$  above the threshold ( $z \geq z_I(W_0)$ ) we can use

$$\nu_{il}(\nu) = \nu'_{il}(W_{ex})(z - z_I)eE(z_I), \quad W > W_{ex} \quad (10)$$

where "prime" means the "energy derivative". Using Eq. (10) we obtain for  $F(z)$  in the region  $z \geq z_I(W_0)$

$$\frac{\partial^2 F}{\partial z^2} = (z - z_I) \frac{3\nu_{il}\nu'_{il}}{\nu_{ex}^2} eE(z_I) F \quad (11)$$

where we denoted  $\nu_{ex}^2 = 2W_{ex}/m$ .

For an isotropic distribution of secondary electrons and not very high electric fields,  $E/p \ll \tilde{X}$ , where  $\tilde{X} \equiv (W_{ex}/e)\sigma_{tr}(W_{ex}) \times 3.53 \times 10^{16}$  (V/cmTorr), we find for  $\gamma(W_0, E)$ :

$$\gamma(W_0, X) = G(W_0)\gamma_i \frac{1}{1 + w\alpha \left(\frac{\tilde{X}}{X}\right)^{1/3} + \psi(w) \frac{\tilde{X}}{X}}, \quad (12)$$

where  $G(W_0)\gamma_i$  is a vacuum differential secondary emission coefficient,  $w = W_0/W_{ex}$ , and  $X \equiv E/p$ . The function  $\psi(w)$  and coefficient  $\alpha$  are

$$\psi(w) = \frac{3}{4} w \int_w^1 \frac{\sigma_{tr}(W_{ex}y)dy}{\sigma_{tr}(W_{ex})y}, \quad \alpha = \frac{3}{4} \left( \frac{\sigma_{tr}(W_{ex})}{\sigma'_{il}(W_{ex})W_{ex}} \right)^{1/3},$$

and can be tabulated for every noble gas.

Integrating Eq.(12) over  $W_0$ , we find ESEC as a function of electric field.

$$\bar{\gamma}(X) = \int_0^{W_{\max}} \gamma(W_0, X) dW_0. \quad (13)$$

Equations (12) and (13) represent the main result of this report.

For specific examples we choose  $G(W_0) = 1/W_{\max}$  for  $W_0 < W_{\max}$ , and  $G(W_0) = 0$  for  $W_0 > W_{\max}$ . Then for a narrow distribution of emitted electrons (Xe-like case) Eqs.(12) and (13) give

$$\bar{\gamma}(E/p) = (\gamma_i / \beta w_{\max}) \ln(1 + \beta w_{\max}), \quad (14)$$

where

$$\beta w_{\max} \equiv \psi(w_{\max}) \frac{\tilde{X}}{X} + \alpha w_{\max} \left( \frac{\tilde{X}}{X} \right)^{1/3}. \quad (15)$$

For a wide distribution of emitted electrons (He-like case) we obtain

$$\bar{\gamma}(X) = \frac{\gamma_i}{\alpha w_{\max}} \left( \frac{X}{\tilde{X}} \right)^{1/3} \ln \left[ 1 + \frac{\alpha w_{\max}}{\psi} \left( \frac{X}{\tilde{X}} \right)^{2/3} \right] \approx \gamma_i \frac{1}{\psi} \frac{X}{\tilde{X}} \left[ 1 - \frac{\alpha w_{\max}}{2\psi} \left( \frac{X}{\tilde{X}} \right)^{2/3} \right]. \quad (16)$$

The plots of  $\bar{\gamma}(E/p)/\gamma_i$ , for different gases and experimental data of D.Felsh and P.Pech [3], are presented in the Figure below.

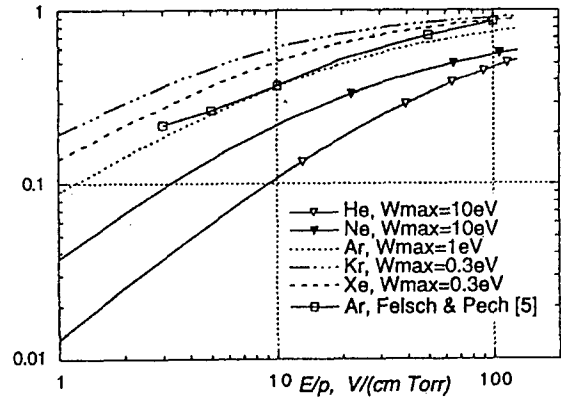


Fig.  $\bar{\gamma}(E/p)/\gamma_i$ , vs.  $E/p$  for different gases.

- [1] J.J.Thomson: *Conduction of Electricity Through Gases* 3rd Ed. Vol.1 (Cambridge: University Press) (1928).
- [2] L.B.Loeb: *Basic Processes of Gaseous Electronics* (Berkeley and Los Angeles: University of California Press) (1955).
- [3] R.N.Varney: *Phys. Rev.* **93** (1954) 1156
- [4] J.K.Theobald: *J.Appl. Phys.* **24** (1952) 123
- [5] D.Felsh, P.Pech: *Proc.ICPIG* 1 (1973) 3
- [6] V.P.Nagorny, et al.: *Proc.ICPIG* 2 (1995) 153
- [7] P.J.Drallos, et al.: *Comments on Plasma and Nuclear Fusion* **18** (1996) at press
- [8] A.V.Timofeev: *Sov. Phys.-Tech. Phys.* **15** (1970) 140.
- [9] H.D.Hagstrum: *Phys. Rev.* **104** (1956) 672

# Sub- to supersonic streaming of ions towards the cathode in a beam-generated plasma model

Tor Eldevik and Alf H. Øien

Department of Applied Mathematics, University of Bergen, Allégt. 55, 5007 Bergen, Norway

## 1. Introduction

The streaming of ions towards the cathode is studied for a steady state beam-generated plasma model. The flow model may have relevance to certain plasma devices. The ionizing beam electrons stream from the cathode towards the anode along a strong magnetic field on a background of neutral particles and bulk- electrons and ions. The plasma in the cathode-anode ionizing range consists of at least two regions that influence the ion-fluid motion: An outer region where the ions are accelerated under influence of a quasineutral electric field, pressure gradients and collisions, and a sheath region close to the cathode where the self-consistent electric field is dominating. A smooth transition between these regions assumes that a Bohm-criterium [1] is fulfilled: The ions have to be supersonic when entering the sheath region. In the model presented a pressure gradient due to temperature drop of ions towards the cathode is necessary for the sub- to supersonic transition of ion flow. Under such an assumption smooth solutions of the governing equations can be followed from the outer region and through the sheath region all the way to the cathode. The sub- to supersonic transition solution is found using a technique due to Bilicki et. al., [2].

## 2. Basic model and equations

### 2.1 Particle conservation equations, outer region

The model has been set up to describe in particular the ion flow in the 'ionizing' region where all charged particles predominately flow along magnetic field lines of constant length  $L$ , connecting the cathode and the anode. A one-dimensional model is therefore possible. We introduce characteristic scales and use non-dimensional variables for convenience:

$$x = \frac{x}{L}, \rho_\alpha = \frac{n_\alpha}{n_{pl}}, u_\alpha = \frac{v_\alpha}{v_{cs}}, \Phi = \frac{e}{kT_e} \phi,$$

$$\varepsilon = -\frac{eL}{kT_e} E, f_{\alpha\beta} = \frac{L}{v_{cs}} v_{\alpha\beta}, \tau_i = \frac{T_i}{T_e}.$$

Here  $v_{cs} = (\frac{kT_e}{m_i})^{1/2}$  is the ion-acoustic speed,  $v_{\alpha\beta}$  are collision frequencies and  $n_{pl}$  a characteristic plasma density. The beam-, the bulk-electron- and the ion-fluid, indexes 'b', 'e' and 'i' respectively, are assumed to obey the following particle conservation equations [3]:

$$\frac{d\rho_b u_b}{dx} = -n_0 \sigma_{b0} L \rho_b u_b$$

$$\frac{d\rho_e u_e}{dx} = 2n_0 \sigma_{b0} L \rho_b u_b$$

$$\frac{d\rho_i u_i}{dx} = n_0 \sigma_{b0} L \rho_b u_b$$

Subscript '0' refers to the neutral background. The model assumes that beam electrons experience only ionizing collision with the background. The result of one such collision is modeled as the loss of one electron from the beam and the gain of two electrons and one ion for the plasma.

### 2.2 Momentum and energy equations, outer region

In the outer region an overall charge neutrality is assumed, together with a negligible beam density  $\rho_b$  compared to the bulk densities so that  $\rho_i = \rho_e = \rho$ . Due to its high kinetic energy, the beam may be considered cold and the conservation of beam momentum reduces to

$$u_b \frac{du_b}{dx} - \frac{m_i}{m_e} \frac{d\Phi}{dx} = 0.$$

The timescale of the bulk electron motion is infinitesimal compared with the timescale of motion of the heavy ions. They instantly adjust to their environment of ions. We therefore neglect the acceleration term and set their temperature to be constant. The momentum conservation of bulk electrons then states that

$$\frac{d\rho}{dx} - \rho \frac{d\Phi}{dx} = \frac{m_e}{m_i} (\Gamma_b f_{b0} - \Gamma_e f_{e0} - (\Gamma_e - \Gamma_i) f_{ei}).$$

$\Gamma_\alpha = \rho_\alpha u_\alpha$ ,  $\alpha = 'b', 'e'$  and  $'i'$  are the particle fluxes from the particle conservation equations. The heavy ions are accelerated, and are generally assumed to have a temperature gradient,

$$\rho u_i \frac{du_i}{dx} + \tau_i \frac{d\rho}{dx} + \rho \frac{d\Phi}{dx} + \rho \frac{d\tau_i}{dx} = -u_i n_0 \sigma_{b0} L \Gamma_b - \Gamma_i f_{i0} - (\Gamma_i - \Gamma_e) f_{ie}.$$

Without an ion temperature gradient in this model it can be shown that the ion-streaming towards the cathode will not pass through the sonic point. To demonstrate the transition from sub-to supersonic streaming of ions we here for simplicity use the temperature gradient from classical heat conduction, and hence use

$$\tau_i^{5/2} \frac{d\tau_i}{dx} = c_T,$$

where  $c_T$  is a constant determined by the (ion) temperature difference between the cathode and the anode. With this equation we have a closed set of equations for  $u_i$ ,  $\rho$ ,  $\Phi$  and  $\tau_i$ . The set of equations may be put on the general form

$$A(y) \frac{dy}{dx} = b(x, y)$$

$$\text{where now } A(y) = \begin{pmatrix} \rho & u_i & 0 & 0 \\ 0 & 1 & -\rho & 0 \\ \rho u_i & \tau_i & \rho & \rho \\ 0 & 0 & 0 & \tau_i^{5/2} \end{pmatrix}, \quad y = \begin{pmatrix} u_i \\ \rho \\ \Phi \\ \tau_i \end{pmatrix}$$

and the components of  $\mathbf{b}$  are given by the right hand sides of the equations for particle conservation of ions, momentum conservation of bulk electrons and ions, and the ion temperature equation, respectively.

From Cramer's rule, the gradients are

$$\frac{dy_i}{dx} = \frac{N_i(x, y)}{\Delta(y)}, \quad i = 1, \dots, 4,$$

where  $\Delta(y)$  is the determinant of  $A$  and  $N_i(x, y)$  are similar determinants except that vector  $\mathbf{b}$  replaces the  $i$ 'th column. The system of equations is singular when  $\Delta(y) = -\rho^2(u_i^2 - u_{is}^2)\tau_i^{5/2}$ , where  $u_{is} = \sqrt{1 + \tau_i}$ , equals zero, i.e. at the sonic velocity. For solutions to pass through this velocity also all  $N_i$  must be zero there. The equations may be transformed into an autonomous form of 5 equations of 5 unknowns  $(x, y)$  by introducing a new independent variable  $t$ , setting

$$\frac{dx}{dt} = \Delta(y), \quad \frac{dy_i}{dt} = \frac{dy_i}{dx} \frac{dx}{dt} = N_i(x, y), \quad i = 1..4.$$

A closer study [2] of solutions of these 5 equations in the neighborhood of the above singularity, which is an equilibrium in the  $(x, y)$ -space, reveals the equilibrium is a saddle point in a two-dimensional subset of the 5 dimensional  $(x, y)$ -space. Two solutions pass exactly through the equilibrium, one from sub- to supersonic velocity, and one from super- to subsonic velocity.

### 2.3 Equations, inner region (cathode sheath)

The non-dimensional variables are the same, except that the characteristic lengthscale is changed from the length of the fieldlines  $L$  to the Debye-length  $\lambda_D$ , the lengthscale of the sheath. The mean free path of the particles in the model is much larger than  $\lambda_D$ . Hence one may assume that no collisions take place here. The particle flow is cold. In this regime all the unknowns are functions of the electrical potential  $\Phi$  only, and the problem reduces to solving one implicit integral equation in  $\Phi$  as a function of the new independent variable  $\xi = \frac{x}{\lambda_D}$ .

## 3. Solutions

In the cathode sheath the solutions should fulfill the boundary conditions  $u_b = u_{bc}$ ,  $\rho_b = \rho_{bc}$ ,  $\Phi = \Phi_c$  at  $\xi = 0$ . Subscript 'c' refers to cathode values, assumed known quantities. As  $\xi \rightarrow \infty$ , these solutions should match solutions at  $x=0$  from the outer region. Outer region solutions must be properly tuned and meet conditions also at the anode.

Background gas was assumed to be Hydrogen. Values in the numerical experiment were set to  $n_0 = 10^{18} m^{-3}$ ,  $n_{pl} = n_{bc} = 10^{17} m^{-3}$ ,  $v_{bc} = 3 \cdot 10^5 m/s$ ,  $L = 40m$ ,  $\Phi_A - \Phi_c = 100V$ ,  $T_e = 10eV$ ,  $T_A = 1eV$ . Subscript 'A' denotes anode. The collision cross sections used are  $\sigma_{b0} = 0.53 \cdot 10^{-20} m^2$ ,  $\sigma_{e0} = 9.5 \cdot 10^{-20} m^2$  and  $\sigma_{i0} = 20.0 \cdot 10^{-20} m^2$ , and a classical electron-ion collision frequency was assumed. Fig.1 shows the ion flow in the outer region, while Fig.2 shows the transition from sub- to supersonic flow. The transition takes place at  $s_s = 1.99cm \approx 267\lambda_D$  rather close to the cathode sheath in the outer region. The sheath extends approximately  $10\lambda_D$  from the cathode. The smooth curves are the physically acceptable ones. A non-physical (dashed) branch of flow is also shown.

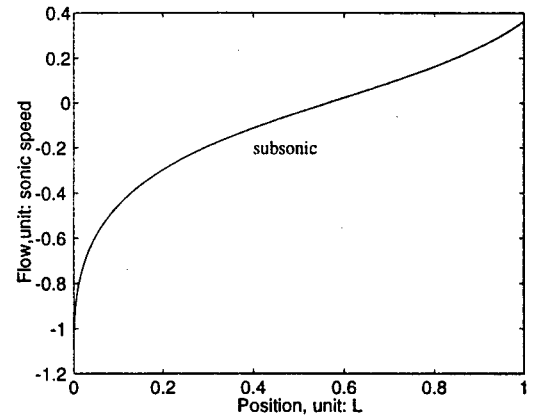


Fig.1. Ion flow in outer region. Cathode at left.

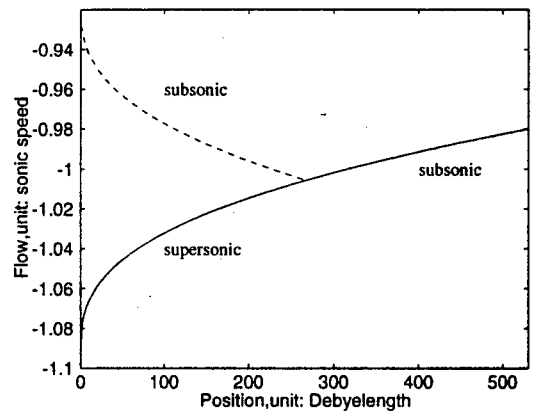


Fig.2. Ion flow close to the cathode sheath. Cathode at left.

## 4. References

- [1] D. Bohm: The Characteristics of Electrical Discharge in Magnetic Fields, ch. 3, (A. Guthrie, R.K. Wakerling, ed.) McGraw-Hill, New York (1949).
- [2] Z. Bilicki, C. Dafermos, J. Kestin, G. Majda, D.L. Zeng: Int. J. Multiphase Flow, **13** (1987) 511.
- [3] G. Evensen, A.H. Øien: Physica Scripta, **44** (1991) 587.

# The effect of reflection of fast electrons from the anode: Monte Carlo simulation of low current discharges at very high E/N

Vladimir D. Stojanović and Zoran Lj. Petrović

Institute of Physics, University of Belgrade, POB 57, 11001 Belgrade, Yugoslavia

## 1. Introduction

A Monte Carlo (MC) simulation code based on the null collision technique, suitable for following the electron motion in a steady state homogeneous electric field  $E$  in rarefied gases including the effect of the boundaries is developed and tested.

In this paper we study the effect of electron reflection and backscattering from the anode surface. This effect is represented by experimental data for reflection coefficient, secondary electron production, for energy distribution of reflected and secondary particles and for angular distribution.

## 2. Monte Carlo simulation code

MC code consists of a null collision procedure for determining the time of next collision. Moment of electron scattering is determined from the total cross section. Differential cross sections are used to determine the angle of scattering. In our procedure the differential cross section is therefore effectively normalized to the total cross section. Differential cross sections are taken from experimental and theoretical data in the literature and defined in up to 70 different energy segments for each process. Attention is paid to maintain the momentum transfer cross section in agreement with the standard swarm derived cross section sets.

Electrons hitting the anode may be either absorbed, or reflected with the loss of energy according to the available experimental data. In addition secondary electrons may be produced. The angular distribution of backscattered particles can be defined as well.

We sample excitation as well as ionization events in small spatial bins. Contributions of direct and back scattered electrons are separated. We also sample flux and energy of particles at fixed positions in the gap including the surface of the anode which we use to determine the electron energy distribution functions (EEDF). These energy distribution functions are relevant for experiments that sample the EEDF through a hole in the anode [1], but are not real EEDF of electrons in the discharge. Such

EEDF can be sampled by freezing the swarm of electrons at a fixed time and taking all the energies. We also sample directions of particles hitting the electrode.

The basic reason for developing the code was to model the experimental data of Phelps and coworkers [2-4] which are mainly the data for the spatial distribution of emission.

Data for the reflection coefficients were taken from [5] for graphite, [6] for stainless steel and [7] for gold. Energy distribution of backscattered particles was taken from the experiments of Gergely et al. [8] and the probability of secondary electron production from [9].

## 3. Results

### 3.1 Models of backscattering

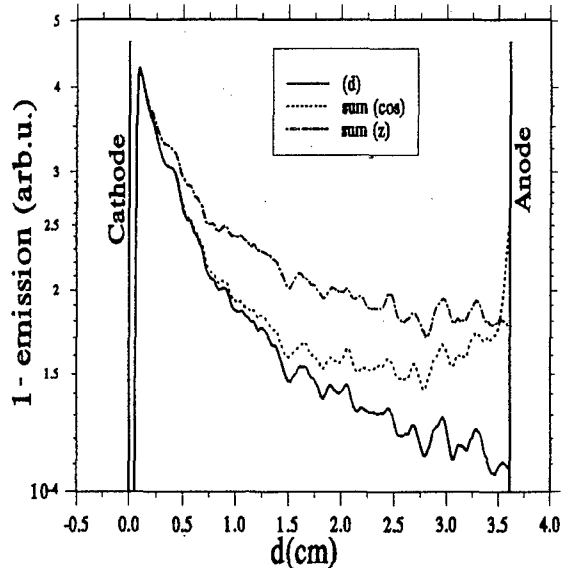


Fig. 1 Spatial profile of emission for  $E/N=69$  kTd ( $E=1398$  V/cm,  $p=58$  mTorr) with contribution of direct (d) electrons and the total emission including the effect of backscattered electrons with cosine (cos) and distribution along the field axis (z).

In Figure 1 we show the effect of selecting the cosine distribution of backscattered particles by showing the results for simulated spatial profiles of emission of the first negative band (1<sup>-</sup>) of nitrogen at 69 kTd. In those calculations we have assumed that the electrons are backscattered with triangular energy profile between 0.6 and 1 of the incoming energy, peaking at 0.95. There is small but observable difference between such distribution and triangular distribution from 0.8 to 1 peaking at 0.9 and a model where all electrons are backscattered with the all available energy.

### 3.2 Comparison with experimental data

In Fig. 2 we show the predicted and experimental data for absolute spatial emission profile for the second positive band (2<sup>+</sup>) of

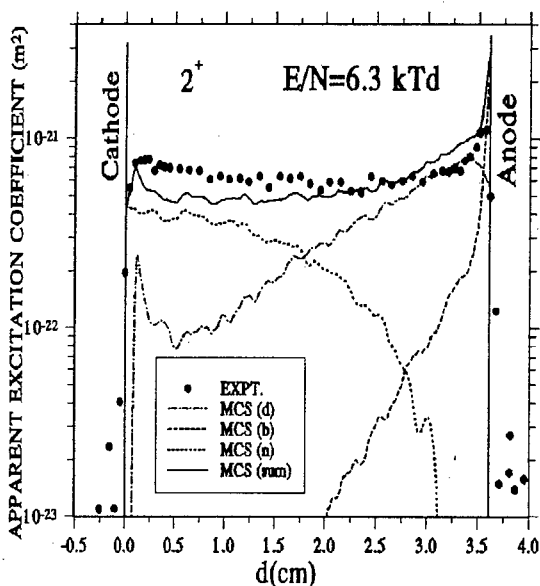


Fig. 2 Spatial profile of second positive band emission at 6.3 kTd ( $E=189$  V/cm,  $p=91$  mTorr). Experimental data are shown as points, contribution of direct electrons is denoted by (d), contribution of fast neutrals by (n), contribution of back scattered electrons with cosine distribution by (b). Total predicted emission is denoted by "sum" and shown as a solid line.

nitrogen obtained at 69 kTd. The Monte Carlo results are in excellent agreement with the experiment. Close to the anode back scattered electrons make a significant contribution to the profile. Monte Carlo simulation predicts the shape close to the anode very well and overall agreement is excellent.

### 4. References

- [1] S.B. Vrhovac, S.B. Radovanov, Z.Lj. Petrović and B.M. Jelenković: *J. Phys. D* **25** (1992) 217.
- [2] B.M. Jelenković and A.V. Phelps: *Phys. Rev. A* **36** (1987) 5310.
- [3] A.V. Phelps, B.M. Jelenković and L.C. Pitchford: *Phys. Rev. A* **36** (1987) 5327.
- [4] Z.Lj. Petrović, B.M. Jelenković and A. V. Phelps: *Phys. Rev. Lett.* **68** (1992) 325.
- [5] E.W. Thomas: "Atomic Data for Controlled Fusion Research vol. III Particle Interaction with Surfaces", Oak Ridge National Laboratory, Oak Ridge (1985).
- [6] E.W. Thomas: *Data Compendium for Plasma Surface Interactions, Nuclear Fusion*, special issue (1984).
- [7] S. Thomas and E.B. Pattinson: *J.Phys.D: Appl. Phys.* **3** (1970) 349.
- [8] G. Gergely, B. Gruzza and M. Menyhard: *Acta Phys. Academiae Sci. Hungaricae* **48** (1980) 337.
- [9] M. Rosler, W. Brauer, J. Devooght, J.C. Dehaes, A. Dubus, M. Cailler and J.P. Ganachaud: "Particle Induced Electron Emission I", *Springer Tracts in Modern Physics*, Springer Verlag-Berlin (1991) 67.

# Trapped electrons in anode region of stratified inert gas discharge

Y. B. Golubovskii\*, V. O. Nekuchaev, N. S. Ponomarev

\*Department of Optics, St. Petersburg University, Uljanovskaja 1, Peterhof, St. Petersburg, 198904, Russia  
Department of Physics, Ukhta Industrial Institute, Pervomajskaja 13, Ukhta, 169400, Russia

The problem of potential wells and reverse electric fields existence in striations has been discussed in a lot of works (see [1] and references to it). It was shown in [2] that a lot of reports about reverse fields in striations are the consequence of experimental errors connected with using of stationary probe for the measurements of plasma potential dependence along the discharge axis. The movement of kinetic striations through the anode region results in plasma potential oscillations as a whole with respect to anode with striations frequency. If one does not take into account these oscillations and defines the plasma potential axis dependence from its time dependence he will observe illusory potential wells. The electron distribution functions (EDF), measured in these "wells" don't reveal any features.

It was experimentally proved in present work that potential wells in striations in the positive column of rare gases don't exist, at

least under experimental conditions ( $p \approx 1 \div 5 \text{ torr}$ ,  $i \approx 5 \div 30 \text{ mA}$ ). But we have discovered that for certain time intervals there are potential axis profiles with wells of not large depth  $\varepsilon_0 \approx 1 \text{ eV}$  adjoining to the anode. The examples of such potential profiles for P- and S-striations in the neon DC discharge are shown in Fig.1. There is a strong correlation between the existence of potential wells and EDF measured. The distribution functions measured in the real wells differ sharply from the ones measured outside the wells by the existence of strongly expressed peak in the range of slow electrons with the energy less than the depth of a well. In Fig.2 the EDF measured in P-striations at the different distances from the anode for the curve 2 in Fig.1 are shown. It is clearly seen that EDF within the well is shrunk to the range of small energies and if one goes away from the anode the amplitude of slow electrons peak increases in a good

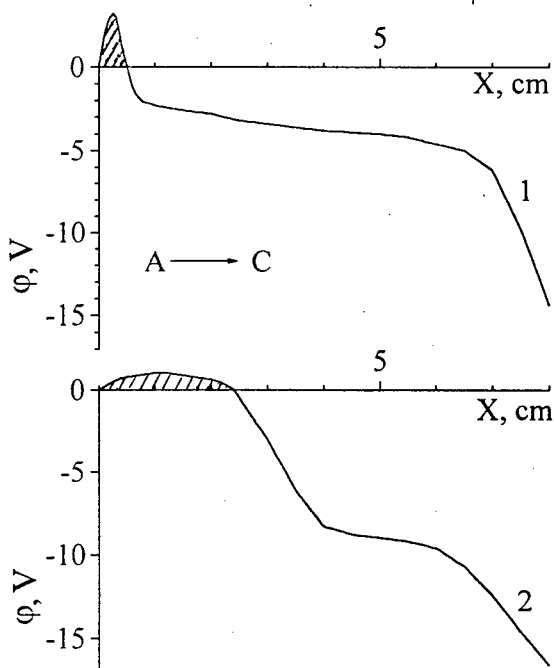


Fig.1. Potential profiles for S- (1) and P-striations (2). Wells are dashed.  $X=0$  - the coordinate of the anode.

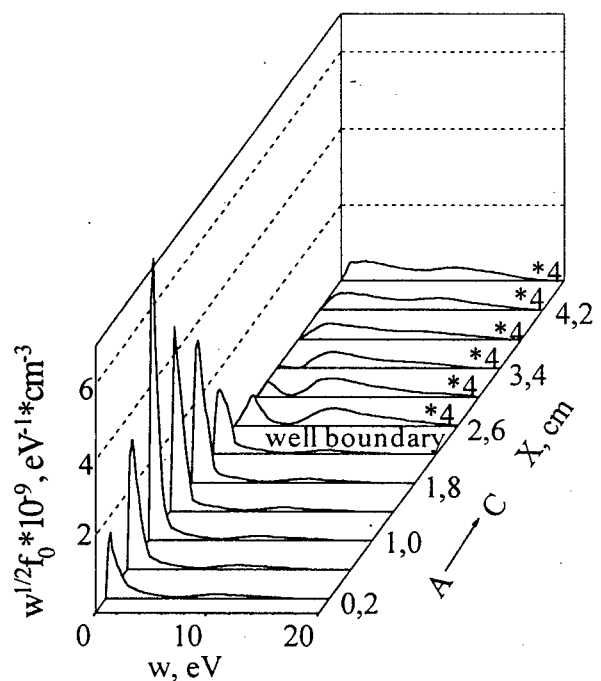


Fig.2. EDF measured in the near-anode region for P-striation.

firstly, reaches the maximum value in the middle of the well and then decreases. When we pass through the boundary of the well the EDF form changes strongly, the slow electrons peak disappears and EDF becomes typical for P-strata in the positive column.

The problem of EDF formation in the potential fields with wells has been solved by means of the division of electrons into two almost independent groups: trapped ( $\varepsilon < \varepsilon_0$ ) and free ( $\varepsilon > \varepsilon_0$ ) [3], where  $\varepsilon_0$  is the depth of the well. Note that fluid approach cannot explain the existence of these two groups of bulk electrons. The distribution function for trapped electrons was found on the base of one-dimensional kinetic equation in variables of  $\varepsilon$  - total energy (kinetic plus potential) and coordinate  $x$  [3]. If the energy relaxation length with respect to elastic and electron-electron collision is greater than well size one can assume that EDF for trapped electrons  $f_0^t(\varepsilon, x)$  depends on  $\varepsilon$  only. In this case it is possible to make an averaging of kinetic equation on coordinate  $x$  and find that maxwellian expression for EDF is valid

$$f_0^t(\varepsilon) \approx \frac{Q(\varepsilon_0)}{D(\varepsilon_0)} T_e \left[ \exp\left(\frac{\varepsilon_0 - \varepsilon}{T_e}\right) - 1 \right] \approx \text{const} \cdot \exp\left(-\frac{\varepsilon}{T_e}\right) \quad (2)$$

The value of  $T_e$  can be found from the integral energy balance for the trapped electrons

$$H_a^* + H_e^* - H_a^d - H_e^d - H_a^V = 0 \quad (3)$$

where  $H_a^*$  - describes the heating of trapped electron by means of inelastic collisions of free electrons with  $\varepsilon > \varepsilon_1$  and thus arising a slow electrons with energies  $\varepsilon - \varepsilon_1$ ,  $H_e^*$  - the heating due to cooling of free electrons in collisions with trapped ones,  $H_a^d$  - the flux of electron energy out of boundaries of the well due to collisions with atoms having non zero temperature  $T_a$ ;  $H_e^d$  - the diffusion cooling due to electron-electron collisions within the well,  $H_a^V$  - describes the energy exchange of trapped electrons in the elastic collisions with atoms in the well volume. The calculated value of  $T_e \approx 0.35$  eV

qualitative agreement with experimental one  $\sim 0.3$  eV.

The joint consideration of the equations of particle balance and energy balance for the trapped electrons has allowed to find the density  $n^t$  and temperature of trapped electrons by means of density  $n^i$  and mean energy of free electrons and therefore to calculate consistent EDF in the whole range of energies. The values of  $n^t/n^i \approx 2.6$  and  $T_e \approx 0.38$  eV obtained from two balance equations are in a good agreement with experimental data. In Fig.3 the comparison of EDF theoretically calculated for trapped and free electrons (solid) with the experimental function (dots) is shown.

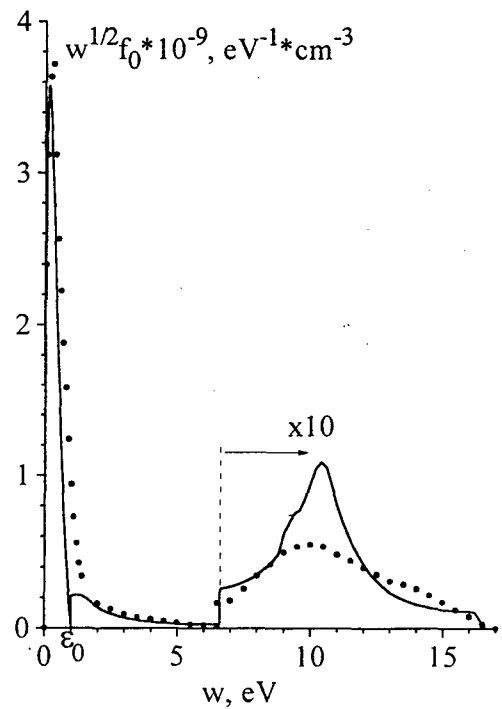


Fig.3. EDF measured (dots) and calculated (solid) for the potential profile with well.

#### References

- [1] V. I. Kolobov, V. A. Godyak: IEEE Trans. Plasma Sci., **23** (1995) 503
- [2] Y. B. Golubovskii, V. O. Nekuchaev, N. S. Ponomarev: XIII ESCAMPIG, Poprad (1996) Contr. Pap. 119
- [3] V. I. Kolobov, L. D. Tsandin: Phys. Rev., **46** (1992) 7837



## The mechanism of losing fast-moving electrons in the Penning cell

V.A.Saenko, A.G.Borisenko, V.A.Rudnitsky

Scientific Center "Institute for Nuclear Research"

47 Prospect Nauki, Kyiv 252028, Ukraine

Phone : (0-44) 265-38-39,

Fax : (0-44) 265-44-63

e-mail : kinn2@riskaudit.kiev.ua

The possibility of oscillating fast-moving electrons escaped from cathode-reflectors in the Penning cell was first mentioned in [1]. In [2] it is confirmed by the calculations of the mechanical properties of fast-moving electrons in the two-dimensional Penning cell, but the mechanism of losing oscillating electrons out of the cell and its dependence on the magnetic fields induction value  $B$  and the anode voltage  $V_a$  were not studied in [2]. But it is this mechanism that determines the main characteristic of the Penning discharge in a weak magnetic field, when the electron mean free path length exceeds the cell size and is comparable with the path length of oscillating fast-moving electrons [3]. Carrying out such investigations is the purpose of this work.

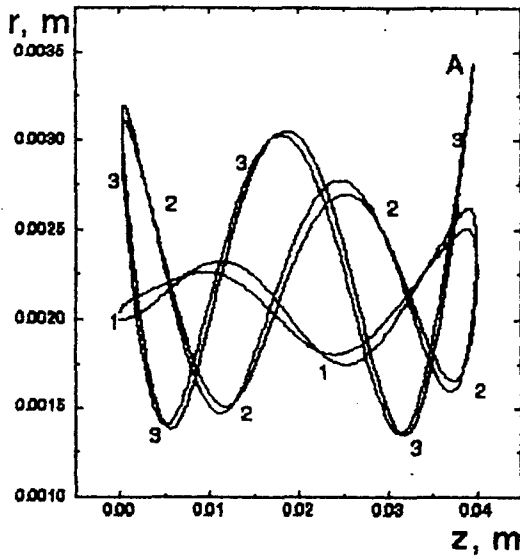
To do this, the electron motion in the three-dimensional Penning cell was calculated and the trajectories of  $r$ ,  $z$ , coordinates were studied. The beginning of the rectangular or cylindrical system of coordinates ( $x$ ,  $y$ ,  $z$  or  $r$ ,  $z$ ,  $\varphi$ ) was chosen in the center of the cathode-reflector. The anode was used in the form of the cylinder of the radius  $R_a$  and the length  $L$ , closed from the faces with cathode-reflectors at zero potential. The homogeneous magnetic field of the induction  $B$  is directed along the cell axis [4].

In very weak magnetic fields the electrons do not seem to oscillate and after escaping the cathode they fall on the anode. The increase in  $B$  changes the trajectory to a greater extent and the electron fallen within the opposite cathode can be reflected from it. This happens at some  $B_{cr} \approx 0.0075$  T. In the magnetic field  $B > B_{cr}$  at the same value of  $V_a$ , fast-moving electrons can already be reflected from any cathode and oscillate. The electrons escaped out of the cell move in the direction of cathodes. There are electrons which move to a definite moment (point A) along some curve (1 to 3) and after that they come back practically along the same curve (Fig.1). Fig.2 shows the trajectory of the electron which falls on the opposite cathode (1 to 5 regions). This curve is symmetrical relative to the cell symmetry axis. In changing from one curve to another with increasing  $B$ , the conditions of the electron motion change and electron performs different number of oscillations  $N$  at different values of  $B$ . This continues up to some maximal value of magnetic field induction (Fig.3,  $B = 0.035$  T). The dependence of the number  $N$  of electron oscillations on  $B$  is the result of studying a large number of electron trajectories under the same

initial conditions (the distance from the axis  $z$  to the point of escapign the cathode, the initial kinetic energy  $W_0$ ). An oscillation was determined as the reflection from one of the cathode. In this case the dependence  $N(B)$  can be constructed (Fig.3). The latter makes it possible to see the areas of magnetic field induction values  $B$ , where fast-moving electrons perform a large number of oscillations, which increases the probability of their ionizing the neutral particles of a discharge gap, and the intervals  $B$ , where fast-moving electrons are easily lost from a discharge ( $N \rightarrow 0$ ). Proceeding from this, in the places of minima a fast loss of electrons from a cell must cause the discharge extinction. To which this assumption the experiment was made and the curve of the Penning discharge ignition were taken. And indeed, in the area corresponding to deep minima in the dependence  $N(B)$ , the decrease in the discharge current up to zero is observed, i. e. the magnetic field  $B^*$  was found when the discharge doesn't burn, but it burns at  $B_1$  and  $B_2$  with  $B_1 < B^* < B_2$ .

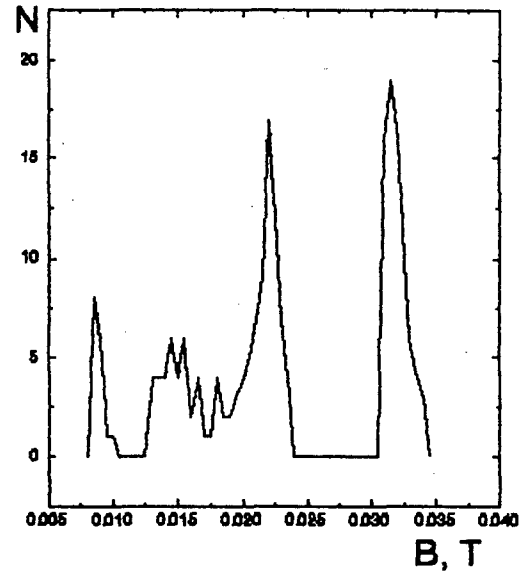
With further increasing the induction value of the magnetic field  $B$  and leaving the oscillation maximum region, from motion trajectories one can see that the fast-moving electrons formed on one of the cathodes, fall on another one without oscillations. It was experimentally observed that in large magnetic fields the discharge didn't ignite until another mechanism of upkeeping the discharge, a magnetronic one had started.

Thus, the oscillations of fast-moving electrons start at exceeding the magnetic induction  $B$  of some critical value  $B_{cr}$ . In large  $B > B_{cr}$  there are a number of maxima and minima in the dependence  $N(B)$ , and in this case the mechanism of losing fast-moving electrons resides in falling electrons on one of the cathodes according to the curves shown in Figs. 1 and 2. Further increase in magnetic field leads to cessation of oscillations so that an electron from one cathode, passing over a cell, falls on the opposite one. The main results following from the calculations are experimentally confirmed by the form of the curve of igniting the Penning discharge in the weak magnetic fields  $B \geq B_{cr}$ .

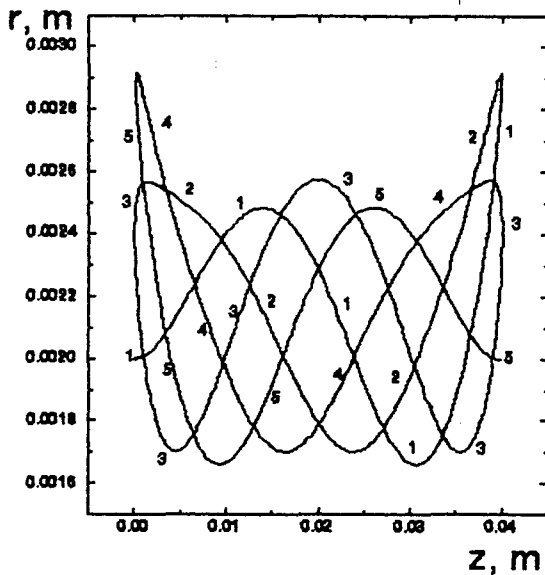


$V_a=700$  V;  $B=0.021$  T;  $W_0=2.15$  eV;  $R_a=0.009$  m;  
 $L=0.04$  m  
 1 to 3 is the sequence of trajectory lengths to the  
 return point A

Fig.1



$V_a=700$  V;  $W_0=2.15$  eV;  $R_a=0.009$  m;  $L=0.04$  m  
 Fig.3



$V_a=700$  V;  $B=0.016$  T;  $W_0=2.15$  eV;  $R_a=0.009$  m;  
 $L=0.04$  m  
 1 to 5 is the sequence of trajectory lengths portions  
 after each reflection.

Fig.2

### References.

1. E.T.Kucherenko, V.A. Saenko. Ukrainian Journal of Physics, 1964, V.9, N.8, P.194.
2. V.A. Saenko, B.V.Ivanisenko. Ukrainian Journal of Physics, 1971, V.15, N.6, P.1012.
3. E.T.Kucherenko, V.A. Saenko. Czechoslovak Journal of Physics, 1967, V.B17, N1, P.67.
4. V.A. Saenko, V.B.Taranov, A.G.Borisenko, V.A.Rudnitsky. The materials of the annual scientific conference of the Institute for Nuclear Research. 1995, P.256.

## One-particle spectral function in dense plasmas

R. Schepe, D. Tamm, K. Henneberger  
Department of Physics, Rostock University,  
D-18051 Rostock, Germany

### Abstract

Starting from a Green's function (GF) approach, the one-particle spectral function and the dynamical screening are calculated in a fully self-consistent RPA scheme. It is shown, that a quasi-particle approximation cannot adequately describe the corresponding features of a plasma.

### Introduction

Within the last years a microscopic description of many-particle systems under the influence of external fields has become more and more a challenging topic in physics[1]. Especially nonequilibrium phenomena play an important role nowadays. In the field of plasma physics it would be interesting to discuss pulse propagation in dense plasmas together with the interactions of photons and particles or particles with each other. Bound and scattering states are influenced by the field of the photons. A consistent description of all the resulting dynamic effects within an ionization kinetics is very difficult and – without knowing the equilibrium properties of a plasma in detail – surely not possible[4].

The goal of this article is to discuss the one-particle properties in RPA. Whereas self-energy determines the one-particle properties, the screening of the interaction is given by the polarization function. Both quantities can be expressed by vertex functions, and the lowest order approximation in this connection is the RPA. Strictly speaking vertex corrections had to be considered beyond RPA due to the Ward identity[2]. However, in the regarded parameter region our numerical studies show that such vertex corrections are very small and contribute less than one percent to the RPA expressions. It is important that both the damping of the one-particle states, which are determined by the dynamically screened Coulomb potential, and the polarization function, which governs the screening and itself is defined by the electronic properties, are calculated self-consistently.

Especially the one-particle damping is a crucial quantity for it and determines beside others e. g. the dephasing of a coherent polarization – the so-called  $T_2$  – time – in the plasma induced by an external laser field. Generally a wavevector ( $\vec{k}$ -) and frequency ( $\omega$ -) dependent one-particle damping has to be considered in this connection. In many publications a damping being  $\vec{k}$ -dependent only or even constant is discussed. E.

g., using the well known Lindhard dielectric function means to assume an infinitely weak damping. Attempts to generalize the Lindhard approach to finite and  $\vec{k}$ -dependent damping lead to series conceptual problems concerning sum-rules and the static long wavelength limit [3].

### The one-particle spectral function

We start from the one-particle Dyson equation of sort  $\alpha$  on the double time contour[1]:

$$G_{\alpha}^{-1}(1, 2) = G_{0,\alpha}^{-1}(1, 2) - \Sigma_{\alpha}(1, 2) \quad (1)$$

where  $G_{0,\alpha}^{-1}$  and  $\Sigma_{\alpha}$  denote the inverse GF of free particles and the self-energy, respectively. After Fourier transform one obtains for the retarded GF

$$G_{\alpha}^{ret}(\vec{k}, \omega) = \frac{1}{\omega - \frac{k^2}{2m_{\alpha}} - \Sigma_{\alpha}^{ret}(\vec{k}, \omega)}, \quad (2)$$

where

$$\Gamma_{\alpha}(\vec{k}, \omega) \equiv \Sigma_{\alpha}^{>}(\vec{k}, \omega) - \Sigma_{\alpha}^{<}(\vec{k}, \omega) = -2 \operatorname{Im} \Sigma_{\alpha}^{ret}(\vec{k}, \omega) \quad (3)$$

is the damping and

$$a_{\alpha}(\vec{k}, \omega) \equiv G_{\alpha}^{>}(\vec{k}, \omega) - G_{\alpha}^{<}(\vec{k}, \omega) = -2 \operatorname{Im} G_{\alpha}^{ret}(\vec{k}, \omega) \quad (4)$$

is the spectral function. The correlation functions are given as

$$G_{\alpha}^{<} = a_{\alpha}(\vec{k}, \omega) f_{\alpha}^{<}(\omega), \quad (5)$$

where  $f_{\alpha}^{<}$  correspond to the Fermi function  $f_{\alpha}$  according to  $f_{\alpha}^{>} = 1 - f_{\alpha}$  and  $f_{\alpha}^{<} = f_{\alpha}$ . The scattering rates are to be computed from

$$\Sigma_{\alpha}^{<}(\vec{k}, \omega) = \int \frac{d^3 q}{(2\pi)^3} f_{\alpha}^{<}(\vec{k} + \vec{q}) V_{\alpha\alpha}^{>}(\vec{q}, E_{\vec{k}+\vec{q}} - \omega), \quad (6)$$

where the screened potential propagators are given by

$$V_{\alpha\alpha}^{>}(\vec{k}, \omega) = n_B^{>}(\omega) \hat{V}_{\alpha\alpha}^s(\vec{k}, \omega), \quad (7)$$

and the following notations for the Bose function  $n_B^{>} = 1 + n_B$ ,  $n_B^{<} = n_B$  are used.

$\hat{V}_{\alpha\alpha}^s$  in (7) is the spectral part of the screened Coulomb potential. It can be expressed by the retarded quantity,

$$\begin{aligned} \hat{V}_{\alpha\alpha}^s(\vec{k}, \omega) &\equiv V_{\alpha\alpha}^{>}(\vec{k}, \omega) - V_{\alpha\alpha}^{<}(\vec{k}, \omega) \\ &= -2 \operatorname{Im} V_{\alpha\alpha}^{s,ret}(\vec{k}, \omega), \end{aligned} \quad (8)$$

from which the polarization function  $\Pi_{\alpha}$  comes into play using the "optical theorem"

$$\operatorname{Im} V_{\alpha\alpha}^{s,ret}(\vec{k}, \omega) = |V_{\alpha\alpha}^{s,ret}(\vec{k}, \omega)|^2 \operatorname{Im} \Pi_{\alpha}^{ret}(\vec{k}, \omega). \quad (9)$$

The RPA-polarization function on the Keldysh contour reads

$$\Pi_{\alpha}(1, 2) = 4\pi e_{\alpha}^2 G_{\alpha}(1, 2) G_{\alpha}(2, 1). \quad (10)$$

The spectral part of the polarization function  $\hat{\Pi}_\alpha$  is connected with the retarded polarization function  $\Pi_\alpha^{ret}$  via

$$\hat{\Pi}_\alpha(\vec{k}, \omega) \equiv \Pi_\alpha^>(\vec{k}, \omega) - \Pi_\alpha^<(\vec{k}, \omega) = -2 \text{Im} \Pi_\alpha^{ret}(\vec{k}, \omega), \quad (11)$$

and the dielectric function is defined from  $\Pi_\alpha^{ret}$  by

$$\epsilon(\vec{k}, \omega) = 1 - \sum_\alpha V_{\alpha\alpha}(\vec{k}, \omega) \Pi_\alpha^{ret}(\vec{k}, \omega), \quad (12)$$

where  $V_{\alpha\alpha}$  denotes the bare Coulomb potential.

We reformulate these equations by straightforward manipulations in order to solve them numerically by iteration. Using (6) – (9) and (12) we obtain the damping as

$$\Gamma_\alpha(\vec{k}, \omega) = -2 \int \frac{d^3 q}{(2\pi)^3} \int_{-\infty}^{\infty} \frac{d\Omega}{2\pi} \left[ n_B(\Omega) + f_\alpha(\omega + \Omega) \right] \times a_\alpha(\vec{k} + \vec{q}, \omega + \Omega) V_{\alpha\alpha}(\vec{q}) \text{Im}[\epsilon(\vec{q}, \Omega)]^{-1}. \quad (13)$$

Using the Kramers–Kronig relation the real part of the retarded one-particle self-energy  $\Sigma_\alpha^{ret}$  is given by

$$\text{Re} \Sigma_\alpha^{ret}(\vec{k}, \omega) = P \int_{-\infty}^{\infty} \frac{d\Omega}{2\pi} \frac{\Gamma_\alpha(\vec{k}, \Omega)}{\omega - \Omega}, \quad (14)$$

where  $P \int$  denotes a Cauchy-type principle value integral. After this the spectral function  $a_\alpha$  follows from eq. (4) as

$$a_\alpha(\vec{k}, \omega) = \frac{\Gamma_\alpha(\vec{k}, \omega)}{\left( \omega - \frac{k^2}{2m} - \text{Re} \Sigma_\alpha^{ret}(\vec{k}, \omega) \right)^2 + \frac{1}{4} \Gamma_\alpha^2(\vec{k}, \omega)}. \quad (15)$$

The retarded polarization function is obtained using eqs. (5) and (10) as the convolution of the spectral function

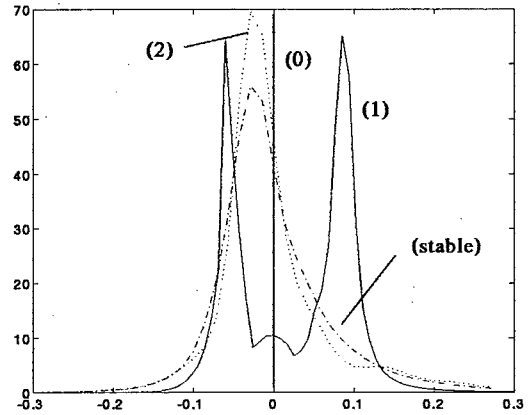
$$\Pi_\alpha^{ret}(\vec{k}, \omega) = - \int \frac{d^3 q}{(2\pi)^3} \int_{-\infty}^{\infty} \frac{d\omega_1}{2\pi} \int_{-\infty}^{\infty} \frac{d\omega_2}{2\pi} \times a_\alpha(\vec{q}, \omega_1) a_\alpha(\vec{q} + \vec{k}, \omega_2) \frac{f_\alpha(\omega_1) - f_\alpha(\omega_2)}{\omega - \omega_1 - \omega_2 + i\delta}. \quad (16)$$

We start with the free-particle approximation, i. e.  $\Sigma_\alpha^{ret} \rightarrow i\delta \rightarrow 0$ , for the spectral function (15) and the retarded polarization (16), leading in eq. (12) to the Lindhard dielectric function. Using these expressions in eqs. (13) – (16) we obtain in the next iteration step the retarded self-energy, spectral function, polarization function, and from (12) the dielectric function. Since the spectral function is modified in each iteration step, the chemical potential is to be corrected in the end of each cycle to reproduce the correct particle density via

$$n_\alpha(\mu_\alpha, \beta) = \int_{-\infty}^{\infty} \frac{d\omega}{2\pi} \int \frac{d^3 q}{(2\pi)^3} a_\alpha(\vec{q}, \omega) f_\alpha(\omega). \quad (17)$$

Moreover, after each iteration we checked the sum rules and the static long wavelength limit and found them fulfilled within the limit of numerical accuracy.

As result a  $\vec{k}$ - and  $\omega$ -dependent damping resulting in a broadened spectral function of the electrons is obtained. The  $\omega$ -dependence of the spectral function switches from a structure with three maxima after first iteration to a structure with



$\omega$ -dependence of the spectral function during several steps of iteration (zero of the frequency axis denotes the particle dispersion; electron density  $n = 10^{20} \text{ cm}^{-3}$ , temperature  $T = 2 \times 10^4 \text{ K}$ , non-ideality  $\gamma = 0.5$  [5]).

one maximum[6]. During the iteration procedure spectral weight is redistributed little by little, so that the spectral function in the end gets a shape which is neither a Gaussian nor a Lorentzian.

As a further consequence of this broadening the polarization function is smoothed in comparison with the Lindhard expressions, and the real part of the polarization function reproduces the static limit within the frame of numerical accuracy. Furthermore, sharp plasmon satellites seen in the first step, disappear in the course of iteration.

- [1] D. F. Dubois, in *Lectures in Theoretical Physics*, edited by W. E. Brittin and A. O. Barut (Gordon and Breach, New York, 1967), Vol. IX C, p. 469
- [2] J. C. Ward, *Phys. Rev.* **78** (1950) 182
- [3] N. D. Mermin, *Phys. Rev. B* **1**, 2362 (1970)
- [4] M. Schlages, Th. Bornath, *Physica A* **192** (1993), 262 – 279
- [5] W. D. Kraeft, D. Kremp, W. Ebeling and G. Roepke, *Quantum Statistics of Charged Particle Systems*, (Plenum Publishing Corp., New York, 1986)
- [6] R. Fehr and W. D. Kraeft, *Contrib. Plasma Phys.* **35** (1995), 463.

# The investigation vibrational kinetics and heating of N<sub>2</sub> in the pulsed discharge and its afterglow by CARS-spectroscopy and optical interferometry.

K.A. Vereshchagin, V.V. Smirnov and V.A. Shakhmatov.

Russian Academy of Sci., Moscow Radiotechnical Institute, Varshavskoe shosse 132, Moscow, Russia.

## Introduction

The pulsed discharges in molecular nitrogen are widely used in technological processes. For optimization of work of technological setup the problems on investigation vibrational kinetics and heating of N<sub>2</sub> are raised.

In present paper the measurements of the vibrational populations of the ground state of N<sub>2</sub> for levels  $v=0-5$  (VP) and growth of the gas temperature  $T_g$  as a function of time were carried out by coherent anti-Stokes Raman scattering spectroscopy (CARS) and optical interferometry in the pure molecular nitrogen in the pulsed discharge and its afterglow. From comparing of experimental and numerical data of the VP the summary cross section  $\sigma_{\Sigma} = \sum \sigma_v$  (the sum of first eight cross sections  $\sigma_v$  of the vibrational excitation of molecules by electrons) and the value of VV-exchange rate constant  $K_{01}^{10}$  was determined. Also the value of associative ionization rate constant of atoms in the metastable states N(<sup>2</sup>P) and N(<sup>2</sup>D) was appreciated. Using received value of  $\sigma_{\Sigma}$ , from existing models suggested for calculation VV-exchange rate constants the model was determined, which allows satisfactorily to fit results of calculation of the time variations of  $T_g$  to our experimental data.

## Experiment

In experiments two types of discharge were used. The first type of the pulsed discharge was created between metal plates positioned inside dielectric cell. The metal plates were spaced at distance 1 cm. The gas pressure was equal to 115 Torr. The value E/N (E is electrical field, N is the molecules concentration) during discharge early phase development varied between 180 and 200 Td. The duration of the discharge was 40 ns, which was calculated from half-height of the current pulse. The current reached 1.5 kA at maximum. Once pulse of current has been ended the value E/N became equal 10 Td at the stage of afterglow for a time 20  $\mu$ s. In the experiment the values of the VP and rotational temperature were measured by means of CARS spectroscopy. The pulsed CARS-spectrometer has been described in more detail in [1]. The rotational temperature obtained in the range delays from 50 ns to 20  $\mu$ s from the beginning of current pulse was equal to  $320 \pm 30$  K and for considered above pressure it was identified with that of gas. The second type of the pulsed discharge was created

inside a quartz tube with inner diameter 3.6 cm. The length of the discharge zone was about 35.5 cm. The gas pressure was equal to 6 Torr. The value E/N was about 20 - 30 Td. The current was 1 A at maximum. The time variations of  $T_g$  was measured using method of the optical interferometry based on photoelectric detection space displacement of the interferometric bands in the range delays from 100  $\mu$ s to 2 ms from the beginning of current pulse. The two - wave interferometer used in experiments has been described in more detail in [2]. Measured growth of  $T_g$  and concentration electrons  $N_e$  as a function of time are presented in Fig.1.

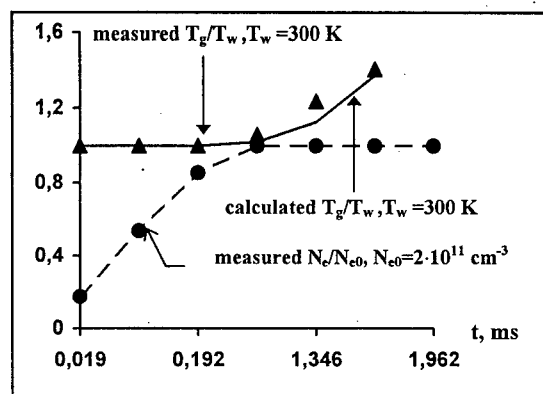


Fig.1

## Theory

The following kinds of the particles were included into the equations for the concentrations to describe the main elementary processes taking place in N<sub>2</sub> during discharge and its afterglow: nitrogen molecules in the ground state (the number of vibrational levels are 46; level  $v=47$  is proposed the level of dissociation by the vibrational excitation) and also in the electronically excited states  $A^3\Sigma_u^+$ ,  $B^3\Pi_g$ ,  $C^3\Pi_u$ ,  $B'^3\Sigma_u^-$ ,  $a'^1\Sigma_u^-$ ,  $W^3\Delta_u$ ,  $a^1\Pi_g$ ,  $w^1\Delta_u$ ; the atoms in the ground state  $^4S$  and in the excited states  $^2P$ ,  $^2D$ ; the ions  $N_2^+$ ,  $N^+$ ,  $N_3^+$ ,  $N_4^+$  and electrons. The list of the processes which were included into the equation describing time variations of  $T_g$  is given below: the elastic impacts of electrons on atoms and molecules; the rotational excitation molecules by electrons followed by rotationally - translational relaxation; vibrationally - vibrational (V-V) relaxation molecules on molecules; vibrationally - translational (V-T) relaxation molecules on molecules and atoms; the diffusion of the

vibrationally and electronically excited molecules to the walls with their following desactivation; quenching of electronically excited state  $A^3\Sigma_u^+$  [3]; heat removal from volume. The Boltzmann equation for the electron energy distribution function (EEDF) was solved to determine the values of rate constants for the dissociative electron-ion recombination and for collisions between electrons and molecules with consideration the main elementary processes which are following: the elastic impacts of electrons on atoms and molecules; the rotational, vibrational and electronic levels of molecules excitation by electrons; dissociation and ionization of molecules in the ground state in collisions with electrons; the unelastic and superelastic impacts of electrons on vibrationally and electronically excited molecules and atoms; electron - electron collisions.

## Results and discussion

Simulation of the time evolution of  $T_g$  shows, that in the case of the pulsed discharge created in tube, the vibration to translation energy exchange due to V-V collisions is dominant. As seen from Fig.1, the quantitative agreement between experimental and calculated values of  $T_g$  is achieved by using the VV-exchange rate constants reduced in model discussed in [4] for levels  $v>9$ . The experimental investigation and the numerical simulation of time evolution of the VP for above mentioned conditions of discharge created in dielectric cell has shown, that: the change of the VP for levels  $v=0-5$  is determined essentially as the result of the excitation of molecules by electrons in during discharge from 10 ns to 50 ns; the EEDF is markedly affected in owing to the production of atoms in the ground state  $N(^4S)$  and, in consequence of this, the VP for the five low levels are influenced indirectly. Fig.2 shows the VP deduced from CARS spectrum of  $N_2$  and the VP calculated for  $t=50$  ns.

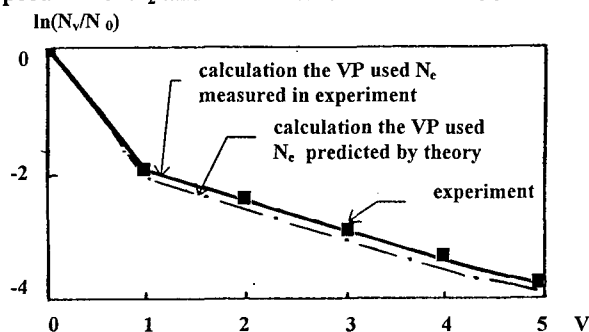


Fig.2

In early stage of afterglow discharge from 60 ns to 15  $\mu$ s the change of populations is caused primarily by unelastic and superelastic collisions between electrons and vibrationally excited molecules; in discharge afterglow later 16  $\mu$ s the prevailing elementary process of redistribution of the populations is VV-exchange. Fig.3 shows the VP deduced from CARS spectrum of  $N_2$  and the VP calculated for  $t=16$   $\mu$ s (a) and  $t=20$   $\mu$ s (b).

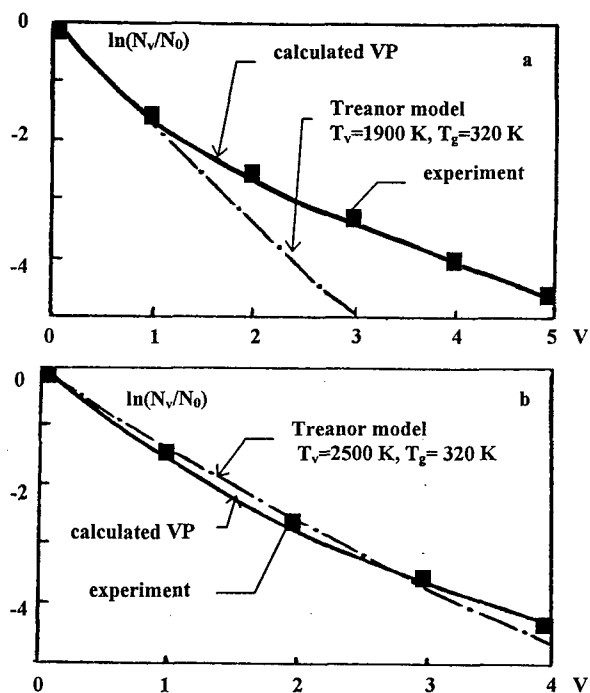


Fig.3

From comparing of experimental and numerical results were established, that: the value of  $\sigma_\Sigma$  is  $(10.5 \pm 1.2) \cdot 10^{-16}$  cm<sup>2</sup> which is in close agreement with result from [5]; the proposed refinement of rate constant for reaction of the associative ionization involving atoms of the metastable states  $N(^2P)$  and  $N(^2D)$  ( $10^{-13}$  cm<sup>3</sup>/s) improves the quantitative agreement between experiment and theory; the agreement between experimental and calculated values of the VP at 20  $\mu$ s is best accomplished at  $K_{01}^{10} = (9 \pm 1) \cdot 10^{-15}$  cm<sup>3</sup>/s which is equal to the value reduced in quantum-classical model suggested in [6]. Model presented in [4] for calculation VV-exchange rate constants for  $v>9$  satisfactorily fits results of calculation of the time variations of value  $T_g$  to our experimental data.

## References

1. S.I. Valyanskii, A.K. Vereshchagin and et. al.: Sov. J. Quantum Electron. 14 (1984) 1226.
2. A.V. Bodronosov, A.K. Vereshchagin and et. al.: Sov. J. Tech. Phys. 64 (1994) 47. (in Russian)
3. J.P. Boeuf, E.E. Kunhardt: J. Appl. Phys. 60 (1986) 915
4. Yu.N. Zhuk, K.S. Klopovsky: Chem. Phys. Letters 153 (1988) 181.
5. D. Levron, A.V. Phelps: Bull. Amer. Phys. Soc. 24 (1979) 129.
6. G.D. Billing, E.R. Fisher: Chem. Phys. 43 (1979) 395.

# PHYSICAL PROCESSES IN A NON-EQUILIBRIUM GAS DISCHARGE PLASMA IN MULTICOMPONENT MIXTURE

**A.F.Alexandrov, A.M.Devyatov, V.M.Shibkov, L.V.Shibkova**

Department of Physics, Moscow State University, 119899, Moscow, Russia

**D.P.Singh, M.Vaselli**

Istituto di Fisica Atomica e Molecolare. Via del Giardino, 7-56127, Pisa, Italy

The investigation of physical processes in non-equilibrium plasma of gas mixture is one of fundamental directions of low temperature weakly ionized plasma. Knowledge of redistribution degree of mixture components in dependence of discharge parameters and time of stationary establishment of mixture separation level allows to understand many physical and chemical processes and choose the optimal regime of work of apparatus in which the work substance is the gas mixture. At existence of electric current in gas there are the complicated interactions between both free charge particles between each other and with neutral gas atoms in ground and excitation states. In result of this interactions atoms acquire the additional energy and impulse. This fact can be cause of complex redistribution of gas density at electric current flowing. In gas mixture the phenomena are complicated because of the unequal effect of the same forces on atoms and ions of different components of mixture. The next mechanisms lead to space redistribution of gas components with strong different masses and ionization potentials: 1) transference the kinetic energy from ions to gas atoms; 2) "ionic wind"; 3) termodiffusion; 4) cataphoresis and some other mechanisms. The phenomenon radial and axial cathaphoresis is observed at passage of a electrical current to a mixture of gases and it is

connected with distinction of ionization potentials of a mixture components. Because of it the relative degree of ionization of weakly ionized component appears higher. It results in relatively greater transfer of this component in a kind of ions to cathode and walls discharged tube in longitudinal and radial electrical fields in comparison with ions hardly ionized component. At walls and cathode tube ions weakly ionized component are neutralized and create the area with increased density of atoms of this component. As the degree of ionization of a impurity exceeds a degree of ionization of a main gas up to the several orders, the space redistribution of the concentration of hardly ionized component can be neglected.

The theory of radial and axial redistribution of gas mixture at diffusion regime was elaborated. In it the problem about space distribution degree of mixture concentration in dependence on external parameters (discharge current, partial pressure, gas temperature) and influence this distribution on plasma characteristics were considered. At this point the base gas is considered as background, determined moving the particles and giving the inset to ionization; because of small degree of ionization the main gas radial redistribution can be neglected. The electron temperature is considered constant along section owing to high electron heat-

conductivity. In spite of these assumptions the analytic solution of total system of equations was not a success to decide. It is necessary to carry out the numerical calculations. This calculations give possibility to determine the degree of radial distribution in dependence on distance from cathode boundary of positive column, that is correlation the axial and radial distributions.

The space redistribution of components can be as useful, as harmful from the point of view of practical application of such discharges. Therefore it is necessary to know dependence of a degree of redistribution on conditions of existence of a ionized gas: the sort and structure of gases, partial pressure of components, density of a current, mass and energy of ionization of particles, sizes of a chamber, where plasma is created, and other. The degree of redistribution of components also depends on a kind of the discharge, on frequency of a enclosed electrical field (constant, HF, microwave categories).

On the basis of experimental and theoretical researches it is possible to do next conclusions.

1. Axial and radial redistribution of components at passage of electrical current through a tube occur simultaneously, mutually causing one another.
2. With growth of a discharge current and partial pressure of a main gas rate and degree of redistribution are increased.
3. Increase of partial pressure of a admixture gas results in decrease of a degree of redistribution.
4. The degree of redistribution under other constant conditions inversely proportional

depends on radius of tube and temperature of a gas.

5. The more difference of potentials of ionization and masses of a mixture components, the more radial and longitudinal redistribution.

6. The establishment time of stationary state of radial distribution was several time less than the reestablishment time of homogeneous radial distribution of mixture atoms after current pulse ending. The effective diffusion length diminished for mixture atoms.

7. Rate and degree of redistribution can be controlled by changing of an external magnetic field.

8. It is possible to control rate and degree of redistribution of one component by changing percentage of atoms of the other components in a multicomponent mixture.

9. The space redistribution of components of a mixture at passage of a electrical current can occur because of other physical reasons except of a cathaphoresis mechanism.

10. The redistribution of components of mixtures in the gas discharge can be used for thin clearing of gases from impurity. This method is echologically harmless, wasteless, high efficient, relatively cheap.

Reliability of experimental results are confirmed by independent optical and probe measurements of radial distributions of admixture ions and atoms in main and metastable states and also by comparison of experimental data with results of mathematical model of the investigated phenomenon.



# Integral Boltzmann Equation with a Source Term.

G.I. Sukhinin

Institute of Thermophysics, Novosibirsk, 630090, Russia

## 1. Introduction.

The Integral Boltzmann Equation (IBE) for spatial and energy distribution function  $f(r, e)$  of secondary electrons produced by a high energy electron beam with arbitrary density distribution is treated. With the help of Fourier-Bessel transformation, Green's function for IBE is found. Green's function is expressed through the "spectral" function  $\rho(v, e)$  which is a universal function for the given gas and is independent of gas density and electron beam profile. The correspondence between the distribution function  $f(r, e)$  and spectral function  $\rho(v, e)$  is equivalent to the correspondence of the wave function in quantum mechanics in coordinate and momentum representations. The developed theory permits one to find spatial dependences both of secondary electrons distribution function and their excitation rates in a plasma produced by electron beams in gases.

## 2. Integral Boltzmann Equation.

The electron beams with energy in keV- interval are widely used for gas diagnostics or activation [1,2]. In both cases, secondary electrons produced during gas ionization by primary beam electrons play a very important role because they have collisional cross sections of molecules excitation, ionization or dissociation greater than those for primary electrons. Some emissions in electron beam created plasma are caused mainly by secondary electrons. Intensity dependences on gas pressure become nonlinear due to the influence of secondary electrons. The energy and spatial distribution function of secondary electrons (EESDF) can be obtained from the Integral Boltzmann Equation with a source term describing the production of secondary electrons by the electron beam with energy  $E_b$ , density  $n_b$  and radial profile  $\chi(r)$  [1].

$$f(\vec{r}, e) = \alpha \iiint \frac{d^3 \vec{r}'}{4\pi} \frac{\exp[-\alpha \sigma_i(e) |\vec{r} - \vec{r}'|]}{|\vec{r} - \vec{r}'|^2} \left\{ q(E_b, e) \chi(\vec{r}') + \right. \\ \left. + \sum_j \sigma_j(e + \varepsilon_j) f(\vec{r}', e + \varepsilon_j) + \int_{e+I}^e d\varepsilon \sigma_i(\varepsilon) q(\varepsilon, \min(e, \varepsilon - e - I)) f(\vec{r}', \varepsilon) \right\} \quad (1)$$

where  $I$  is the ionization threshold of the molecule,  $\alpha = n_b \sigma_0 E_b$  - is dimensionless gas density,  $q(E_b, e)$  - the spectrum of secondary electrons produced during gas ionization by primary electrons. This equation describes the generation of secondary electron in point  $r'$ , elastic scattering and energy loss in non-elastic collisions (including ionization) with corresponding cross sections  $\sigma_j(e)$ . The EESDF here is normalized by the condition

$$\int de f(\vec{r}, e) (E_b/e)^{1/2} = \frac{n_s}{n_b}$$

The excitation rate,  $\Phi_j(r)$ , of  $j$ -state of molecule will be given by the expression

$$\frac{\Phi_j(\vec{r})}{n_b v_b \sigma_i(E_b)} = \int_{E_j} f(\vec{r}, e) \sigma_j(e) de$$

where  $\sigma_i(E_b)$  - is ionizing cross section for beam electrons.

## 3. Green's Function of IBE.

With the help of three-dimensional Fourier-Bessel transformation, we can introduce "spectral" function  $\rho(v, e)$ , and change the Integral Boltzmann Equation (1) into an equation with shifted arguments ( $v$  is the variable of transformation - the analog of wave number):

$$\sigma_i(e) \rho(v, e) = \frac{\sigma_i(e)}{v} \arctan \left[ \frac{v}{\sigma_i(e)} \right] \left\{ q(E_b, e) + \sum_j \sigma_j(e + \varepsilon_j) \rho(v, e + \varepsilon_j) + \right. \\ \left. + \int_{e+I}^{\infty} d\varepsilon \sigma_j(\varepsilon) q(\varepsilon, \min(e, \varepsilon - I)) \rho(v, \varepsilon) \right\} \quad (2)$$

The "spectral" function  $\rho(v, e)$  is connected with Green's function of the equation (1):

$$G(|\vec{r} - \vec{r}'|, e) = \quad (3)$$

$$= \frac{2}{\pi} \alpha^2 \int_0^{\infty} dv v \frac{\sin(\alpha v |\vec{r} - \vec{r}'|)}{|\vec{r} - \vec{r}'|} \rho(v, e)$$

Thus, the exact solution of the equation (1) can be presented in the form

$$f(\vec{r}, e) = \int \frac{d^3 \vec{r}'}{4\pi} \chi(\vec{r}') G(|\vec{r} - \vec{r}'|, e)$$

Spectral function  $\rho(v, e)$  is somewhat more general and universal than the distribution function  $f(r, e)$ . It does not depend on gas density and the structure of an electron beam profile and permits one to find a spatial distribution function for any gas density and any profile of an electron beam. It should be noted that the "spectral" function,  $\rho(v=0, e)$ , for "wave" number  $v=0$  corresponds to the EEDF of secondary electrons generated by an infinitely wide electron beam or to the space-averaged distribution function.

### 3. Diffusional Approximation.

Analyses and numerical calculations of Eq. (2) show that spectral function  $\rho(v, e)$  can be decomposed into two terms:

$$\rho(v, e) = \rho_1(v, e) + \rho_2(v, e)$$

The first term  $\rho_1(v, e)$  describes secondary electrons of the first generation which do not suffer any collisions, and the second term (which becomes the principal one for high gas densities) has specific Lorentz form:

$$\rho_2(v, e) = \frac{\rho_d(v, e)}{1 + (v/\sigma_d(e))^2} \quad (4)$$

It should be noted that the distribution function corresponding to this term satisfies a diffusion-like equation. The critical wave number,  $\sigma_d(e)$ , in Eq. (4) determines the coefficient of diffusion and is, in its turn, determined through the equation (2) by the whole set of collisional cross sections  $\sigma_j(e)$ . Thus, the "diffusion" of secondary electrons from the region of the electron beam is strongly connected with the energy dissipation.

### 4. Conclusions.

The theory of Integral Boltzmann Equation is established. Exact Green's function of IBEq is found. For the special case of cylindrical electron beams, this theory has been applied for the justification of electron beam diagnostics of rarefied gases. The calculations of radial profiles of emissions energy levels excitation rates evoked by an electron beam and secondary electrons in nitrogen and Ar-SiH<sub>4</sub> will be presented.

### References.

- [1] A.K.Rebrov, N.V.Karelov, S.I.Sukhinin, R.G.Sharafutdinov, J.C.Lengrand. Progress in Astronautics and Aeronautics, 74, part 2 (1981), 931.
- [2] R.G.Sharafutdinov et al. Appl. Phys. 79 (1996), 7274.

## Modeling of photolytically excited laser mediums pumped by plan multi-channel sliding discharges

L.D.Mikheev\*, V.I.Tcheremiskine, M.P.Sabonnadiere, M.L.Sentis, G.Y.Malinowsky\* and Ph.C.Delaporte

Institut de Recherche sur les Phénomènes Hors Equilibre, UMR 6594 CNRS, Aix-Marseille I and II Universities, Campus de Luminy, case 918, 13288 Marseille Cedex 09, France.

E-Mail : Sentis@mfncalcs.univ-mrs.fr

\*P.N.Lebedev Physical Institute, Quantum Radiophysics Department, Photochemical Processes Laboratory, Leninskiy prospekt 53, 117924 Moscow, Russia.

### 1. Introduction

High laser output and specific energetic characteristics have been obtained in recent years by sliding discharge VUV radiation pumping of photolytically excited laser mediums [1,2]. The inherent feature of those laser systems was the presence of refractive index and gain coefficient distribution inhomogeneities in their active medium which could limit their performance capabilities [1-4]. In the present work, we present a numerical investigation of photochemical lasers (XeF and HF) pumped by planar multi-channel sliding discharges [5] to demonstrate the possibility of advanced laser characteristic achievement using such pumping source.

### 2. Pumping source

The brightness temperature of a high-current sliding discharge plasma channel reaches the value of 30 k°K in UV and VUV spectral regions [1,4]. Multi channels placed in parallel and close to each other alone a plane dielectric substrate surface form a large area intensively radiating plan optical source [5]. In our pumping scheme we consider a gas laser medium pumped by two counterpropagating radiation fluxes issued from two such sources facing each other. Taking into account that the distance between two channels is much less than the active medium dimensions and that the ratio of this distance to a channel width is less than 5, the optical source is assumed, in our model, to be homogeneous, plane, and infinitely long with a surface brightness temperature up to 20 k°K in the VUV. This last assumption is justified by the fact that the surface radiation intensity for 20 and 30 k°K differs about five times in this spectral region.

### 3. Modeling and results

The model considers transport of pump radiation through a nonlinear dispersive medium coupled with chemical and kinetics describing the temporal and spatial evolution of particle species. The optical source is approximated as a quazimonochromatic pumping radiation source. Simulations are performed for the HF and XeF (C-A) lasers.

In the first simulation we consider  $\text{NF}_3$  as F atom donor to obtain an efficient optically excited HF laser based on nonchain chemical reactions. Figure 1 describes the reaction scheme of the main physical and chemical processes in a  $\text{NF}_3 / \text{H}_2 / \text{Ar}$  gas mixture. This model was constructed on the base of large bibliographic material analysis and particularly on Ref. [6] and [7].

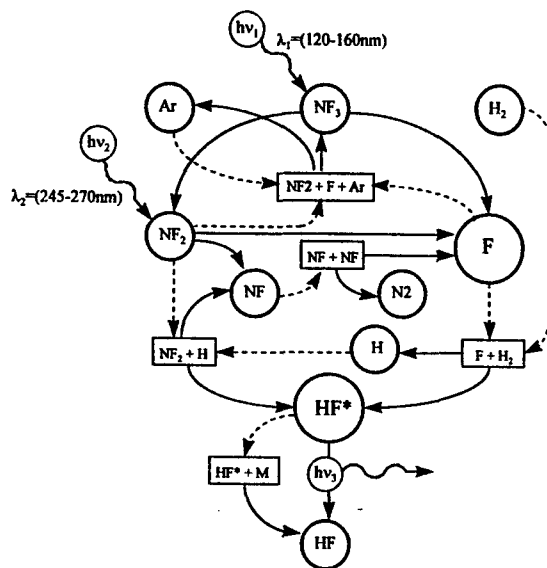
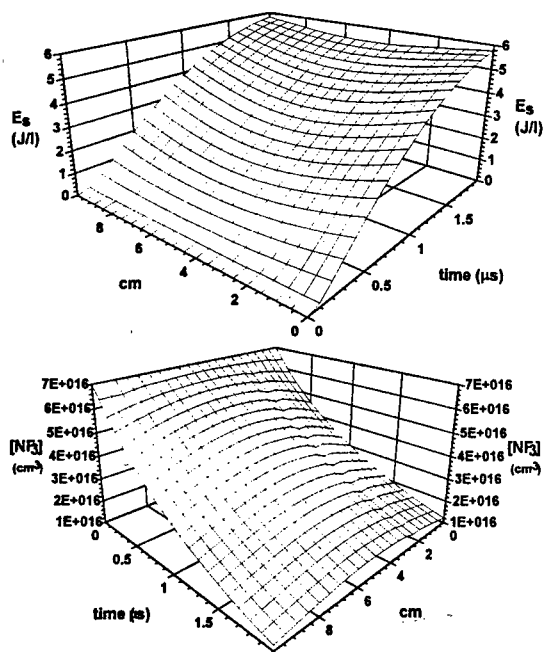


Fig. 1 : Schematic of the main processes of  $\text{HF}^*$  formation and desactivation in the  $\text{NF}_3 / \text{H}_2 / \text{Ar}$  gas mixture. Solid lines are reaction results and dashed lines show the involvement of different compounds in the reaction.

In the second simulation, we study the XeF laser system based on the  $\text{XeF}_2$  molecule photodissociation which produce  $\text{XeF}(\text{B-X})$  and  $\text{XeF}(\text{C-A})$  laser transitions excitation in the UV ( $\lambda = 353 \text{ nm}$ ) and visible ( $\lambda = 480 \text{ nm}$ ) spectral regions respectively [1-3]. The uniquely wide (70 nm FWHM)  $\text{XeF}(\text{C-A})$  transition is of particular interest due to the possibility of amplification of an ultrashort, down to 10 fs duration, laser pulse [8]. Part of computational results of the two photolytically excited lasers are introduced on Fig. 2 and 3.



**Fig. 2 :** Spatio-temporal active medium stored energy density  $E_s$  (a) and  $\text{NF}_3$  molecules concentration (b) distributions for  $\text{NF}_3 : \text{H}_2 : \text{Ar} = 7 \times 10^{16} : 1 \times 10^{17} : 1.2 \times 10^{19} \text{ cm}^{-3}$  initial gas mixture placed between two parallel 10 cm spaced planar optical sources with time-constant brightness temperature 20 k°K. The stored energy was defined by formula  $E_s = \sum v_i n_i^*$ , where  $v_i$  and  $n_i^*$  are the number of HF molecule vibrational levels and its population respectively.

The results show that high laser excitation characteristics and perfect gain distribution along the active laser medium can be obtained in both systems by application of the proposed multi-channel sliding discharge pumping scheme (Fig. 2a, 3). Fig. 2b demonstrates spatial homogeneity of  $\text{NF}_3$  molecules concentration along the laser medium that can be obtained in  $\text{NF}_3 / \text{H}_2$  system. It follows that the active medium will be optically homogeneous due to the fact, that the refractive index variation is mainly dependent on gas mixture chemical content [1,2].

#### 4. Conclusion

The results of our work show promising prospects of planar multi-channel sliding discharge application for the optical pumping of photolitically excited laser mediums. The proposed pumping configuration by two counterpropagating radiation fluxes from parallel oppositely situated multi-channel discharges makes it possible to obtain high energetic laser and homogeneous distribution of the active medium optical characteristics. We also expect to present an experimental results on the scope of the introduced material.

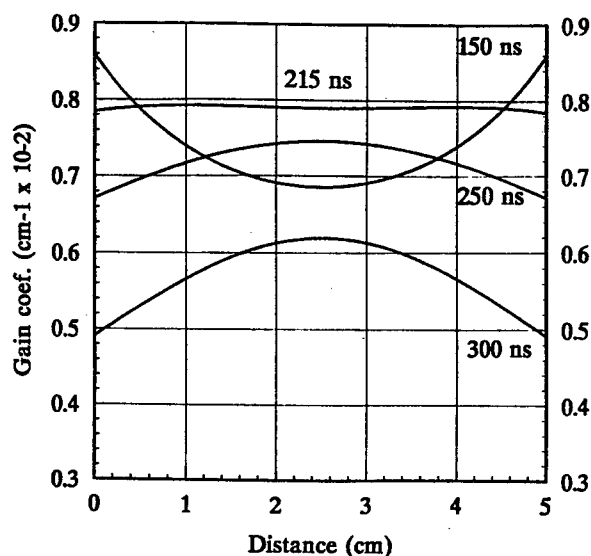


**Fig. 3 :**  $\text{XeF}(\text{C-A})$  transition gain coefficient distributions at various moments of time for the  $\text{XeF}_2 : \text{Kr} = 1 \times 10^{16} : 6.5 \times 10^{18} \text{ cm}^{-3}$  initial gas mixture placed between two parallel 5 cm spaced planar optical sources. Pumping radiation intensity temporal profile is defined by formula  $I = a \exp(-bt)$  with maximum at 300 ns correspondent to the surface brightness temperature 20 k°K.

We would like to acknowledge Prof. V.S.Zuev for helpful discussions.

This work was supported by the DRET (Direction des Recherches et des Etudes Techniques) of the french Defense Agency.

#### References

1. V.S.Zuev, N.G.Kashnikov and S.B.Mamaev, *Sov. J. Quantum Electron.* **22**, 973, 1992
2. V.S.Zuev and L.D.Mikheev, *Photochemical Lasers*, Harwood Academic Publishers, Chur etc., 1991
3. M.L.Sentis, V.I.Tcheremiskine, Ph.Delaporte, L.D.Mikheev and V.S.Zuev, *Appl. Phys. Lett.*, 1997 (accepted for publication).
4. R.E. Beverly III, *Appl. Phys. B*, **56**, 147-156, 1993
5. V.I.Tcheremiskine, M.L.Sentis, Ph.C.Delaporte, L.D.Mikheev and V.S.Zuev, report at the ICPIG, Toulouse, France, 1997.
6. T.Shirafuji and K.Tachibana, *Appl. Surf. Science*, **79/80**, 117-121, 1994.
7. J.B.Koffend, C.E.Gardner and R.F.Heidner, *J. Chem. Phys.* **83**, 2904-2912, 1985
8. L.D.Mikheev, *Laser and Particle Beames* **10**, 473, 1992

## Investigation of the P-1 Model for the Radiative Transfer in SF<sub>6</sub> Circuit-Breaker Arcs

S.D. Eby and J.-Y. Trépanier

Département de Génie Mécanique, École Polytechnique de Montréal

### Abstract

This paper presents another approach in the resolution of the radiative transfer in circuit-breaker arcs. A P-1 approximation is used to solve the radiative transfer equation (RTE). Results are compared to those obtained with the so-called "partial characteristics method".

### 1 Introduction

There is an increasing interest towards the development and use of computational tools for the prediction of circuit-breaker arc flow interaction. One of the most important issue in arc modelling is the prediction of the radiative transfer, which is a dominant mechanism for energy transfer in the arc.

Until recently, most of the authors working in the modelling aspects of circuit-breakers arcs were using the net emission coefficients, introduced by Lowke [1]. However, these coefficients only give an approximation of the net radiation leaving the hot part of the plasma and do not represent the strong self-absorption of an important part of the spectrum at the cold boundary of the arc.

A more recent method, the partial characteristics method, has been introduced by Sevast'yanenko and has been used by many workers in the field [2, 5]. Although the method greatly simplifies the radiation problem compared to the complete equation of radiative transfer, the method is still computer intensive since it requires the integration over the solid angle and this is usually carried out using many directions. It seems that for integration with a transient arc simulation, a cheaper model is still required and this is the objective of the present paper.

### 2 The P-1 Approximation

The RTE in an emitting-absorbing and scattering participating medium is

$$\hat{s} \cdot \nabla I_\lambda = \kappa_\lambda I_{b\lambda} - (\kappa_\lambda + \sigma_{s\lambda}) I_\lambda + \frac{\sigma_{s\lambda}}{4\pi} \int_{4\pi} I_\lambda(\hat{s}_i) \Phi_\lambda(\hat{s}_i, \hat{s}) d\Omega_i \quad (1)$$

where  $I_\lambda$  is the spectral radiation intensity in the direction  $\hat{s}$ ,  $\kappa_\lambda$ ,  $\sigma_{s\lambda}$  are respectively, the spectral absorption coefficient and scattering coefficient,  $I_{b\lambda}$  is spectral blackbody intensity,  $\Phi_\lambda$  is the spectral scattering phase function and  $\Omega_i$  denotes the solid angle.

The radiation intensity is then decomposed into directional-dependant coefficient  $Y_l^m(\hat{s})$ , the spherical harmonic and  $I_l^m(r)$  representing the spatial-dependance, by a Fourier series as

$$I_\lambda(r, \hat{s}) = \sum_{l=0}^{\infty} \sum_{m=-l}^l I_l^m(r) Y_l^m(\hat{s}) \quad (2)$$

Keeping the first term of the expansion, it can be shown [3] that the radiation intensity is related to the incident radiation  $G_\lambda$  and radiative flux  $q_\lambda$  by

$$I_\lambda(r, \hat{s}) = \frac{1}{4\pi} [G_\lambda(r) + 3q_\lambda \cdot \hat{s}] \quad (3)$$

For circuit-breaker arcs, as first approximation, the scattering term is negligible and has been dropped [6]. It is also assumed that the walls have negligible contribution due to the high temperature of the arc.

Then, substituting (3) in the RTE and integrating over all solid angles yields the governing equations for P-1 approximation:

$$\nabla G_\lambda = -3\kappa_\lambda q_\lambda \quad (4)$$

$$\nabla \cdot q_\lambda = \kappa_\lambda (4\pi I_{b\lambda} - G_\lambda) \quad (5)$$

Combining both equations leads to a Helmholtz equation for the incident radiation  $G$

$$\nabla \cdot \left( \frac{1}{\kappa_\lambda} \nabla G_\lambda \right) = 3\kappa_\lambda (G_\lambda - 4\pi I_{b\lambda}) \quad (6)$$

### 3 Bands model

Direct wavelength integration of equation (6) requires large computation times and there is a great difficulty due to the absorption spectrum which generally includes hundreds of spectral lines superposed on a continuum radiation. However, the SF<sub>6</sub> continuum spectrum presents natural bounds corresponding to ionization levels and transitions. The absorption coefficients have been taken from [4] where five bands have been used. The averaging has been performed in a special way to take into account the contribution of resonance lines. For these latter, an escape factor has been used to represent the self-absorption and this escape factor has been computed in function of the arc radius.

Defining mean values on band  $l = [\lambda_1, \lambda_2]$  by

$$q_l = \int_{\lambda_1}^{\lambda_2} q_\lambda d\lambda, \quad \nabla \cdot q_l = \int_{\lambda_1}^{\lambda_2} \nabla \cdot q_\lambda d\lambda \quad (7)$$

Then total fluxes can be deduced by performing a summation of results for each band

$$q = \sum_{l=1}^{N_{bands}} q_l, \quad \nabla \cdot q = \sum_{l=1}^{N_{bands}} \nabla \cdot q_l \quad (8)$$

## 4 Numerical solution

### 4.1 Discretization

A finite-volume technique has been used to discretize the Helmholtz equation (6) by band. For a given band  $l$  and a control volume  $V$ , we have

$$\int_V \nabla \cdot \left( \frac{\nabla G_l}{\kappa_l} \right) dV = \int_V 3\kappa_l (G_l - 4\pi I_{bl}) dV \quad (9)$$

The first integral can be transformed into a surface integral using the divergence theorem

$$\int_{\partial V} \frac{1}{\kappa_l} \nabla G_l \cdot n dS = \int_V 3\kappa_l (G_l - 4\pi I_{bl}) dV \quad (10)$$

### 4.2 Boundary conditions

One of the main concern in this approach is the boundary conditions. For an axisymmetric arc, a zero flux is imposed across the axis. We have tried classical boundary conditions found in the literature like Mark and Marshak for the nozzle wall. Finally, we simply set the incident radiation on the wall at zero.

### 4.3 Resolution

For a one-dimensional axisymmetric arc, we obtain a tridiagonal system which can be solved by a quick method such as the Thomas algorithm. After determining the incident radiation for each band, the radiation flux and the divergence of radiative flux can be computed using equations (8), the last one corresponding to the net emission.

## 5 Results and discussion

The first attempt was to validate the model with the net emission coefficients [1]. Figure 1 shows the results for an isothermal arc of radius 10 mm. We notice the same trend. The slight difference could be attributed to the difference of spectral absorptivities used in the two methods.

Comparison has also been made with the results of Raynal *et al.* [5]. Using the same temperature profile given for an arc of 5 mm, figure 2 compares the results obtained using a 3-D partial characteristics method and an axisymmetric P-1 approximation.

This results has been obtained using an equivalent arc radius of 2.5 mm for computing the averaged absorption coefficients.

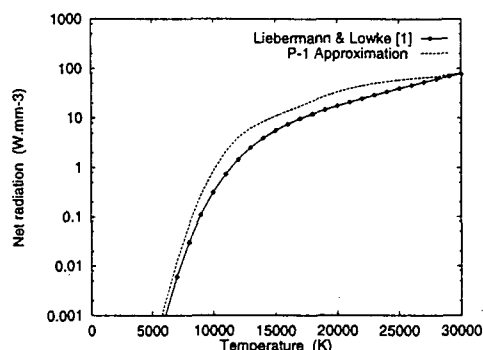


Figure 1: Net emission for a 10 mm radius arc

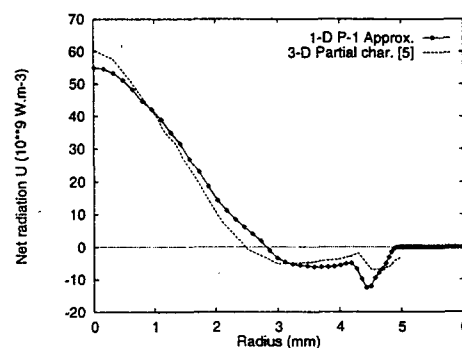


Figure 2: Net emission for Raynal's arc

## 6 Conclusion

The results indicates that this type of method produces results of sufficient accuracy to be used in a large variety of modelling studies. The results shown here present a great opportunity to solve the problem of radiation transfer in circuit-breakers with interesting costs. The model is currently being extended to two-dimensions.

## References

- [1] R.W. Liebermann and J.J. Lowke: J. Quant. Spectrosc. Radiat. transfer, vol. 16, 253-264, 1976
- [2] V. Aubrecht and J.J. Lowke, J. Phys. D: App. Phys. 2066, 2073-100, 1994
- [3] M. F. Modest, McGrawHill, 1993
- [4] Laboratoire Décharges dans les Gaz, Université Paul Sabatier, Toulouse, private communication
- [5] G. Raynal and A. Gleizes, High Temp. Chem. Processes, vol 3, 389-397, 1994
- [6] R.I. Souloukhin, Springer-Verlag, 1986

# Reactive Charged-particle Transport in Crossed Electric and Magnetic Fields

B. Li, R.E. Robson and R.D. White

Physics Department, James Cook University, Cairns QLD 4870 Australia

## Introduction

Theoretical studies of charged-particle transport in the presence of both electric and magnetic fields have advanced considerably in recent years [1-5]. However, not so many results have been reported for particle reactive (non-conservative) processes like ionisation, which can lead to interesting phenomena. For example, the gyration of electrons in a transverse magnetic field causes a much longer path in spanning a given straight line distance (between electrodes) compared with the case of no magnetic field. Therefore it is possible that they experience many more ionisation processes, thus resulting in a reduced breakdown voltage. It has been observed that the breakdown voltage at low gas pressures can be reduced from some tens of kilovolts to a few hundred volts by the application of a transverse magnetic field [6], an effect which lends itself to such applications as high current switches, cold cathode rectifiers and plasma preparation [1]. The multi-term method of Ness [2] can be used to calculate reactive electron transport properties for arbitrary field configurations, but, up to now, no work has been published in this respect, even for the simple crossed field situation. Vrhovac and Petrovic [7] have investigated reaction effects on transport coefficients of electrons in the framework of momentum-transfer-theory (MTT). In their model gas calculations, only average energy and drift velocity have been taken into consideration. In our work, all transport properties have been studied within MTT, and model calculations for electrons have been carried out to illustrate the magnitude of the reactive effects.

## Theory

For reactive swarms moving in crossed electric and magnetic fields, the momentum balance equation is,

$$-k\mathbf{T} \cdot \nabla n + nq(\mathbf{E} + \langle \mathbf{v} \rangle \times \mathbf{B}) = n\mu\bar{\nu}_m \langle \mathbf{v} \rangle, \quad (1)$$

while for the energy balance

$$-\frac{Q}{n\bar{\nu}_e} \cdot \nabla n = \langle \epsilon \rangle - r_1 \frac{3}{2} kT_0 - r_2 \frac{1}{2} m_0 \langle v \rangle^2 + \bar{\Omega}. \quad (2)$$

Here  $\mathbf{E}$  and  $\mathbf{B}$  stand for electric and magnetic fields respectively, and other quantities possess the same meaning as in [8,9]. In our coordinate system,  $q\mathbf{E}$  is in +z direction,  $\mathbf{B}$  in +y direction.

Proceeding in exactly the same way as in [8], we find that drift velocity and diffusion tensor are given by

$$\mathbf{W} = \mathbf{W}^* - \frac{k\mathbf{T}}{q} \cdot \frac{\partial \alpha}{\partial \mathbf{E}}, \quad (3)$$

$$\mathbf{D} = \frac{\partial \mathbf{W}}{\partial \mathbf{E}} \cdot \frac{k\mathbf{T}}{q} + \frac{1}{2} \frac{k\mathbf{T}}{q} \cdot \frac{\partial^2 \alpha}{\partial \mathbf{E} \partial \mathbf{E}} \cdot \frac{k\mathbf{T}}{q}, \quad (4)$$

respectively, where  $\alpha = \nu_a - \nu_I$ , with  $\nu_a$  and  $\nu_I$  are attachment and ionisation collision frequency separately.  $\mathbf{W}^*$  is the flux drift velocity [10], and  $\mathbf{T}$  is the temperature tensor. The balance equation for  $\mathbf{T}$  can be found as in [4]. The flux diffusion tensor [10] is defined as

$$\mathbf{D}^* = \frac{\partial \mathbf{W}^*}{\partial \mathbf{E}} \cdot \frac{k\mathbf{T}}{q}. \quad (5)$$

Note the structure of  $\mathbf{D}$ :

$$\mathbf{D} = \begin{pmatrix} D_x & \cdot & D_{xz} \\ \cdot & D_y & \cdot \\ D_{zx} & \cdot & D_z \end{pmatrix}. \quad (6)$$

The above expressions are applicable to arbitrary charged particle masses.

Generally speaking, reactions explicitly affect all the components of the drift velocity and diffusion tensor, for example, through the second term in (3) for the drift velocity.

## Results and Discussion

Although no restrictions on swarm masses have been placed in obtaining expressions (3) and (4), as a first step to our understanding of physical processes, it is convenient to consider electron swarms.

For electrons, as discussed by Robson [4],  $m \ll m_0$  and the near isotropic property of temperature tensor greatly simplifies calculation of transport properties. The isotropic nature of  $\mathbf{T}$  effectively removes any explicit effects of reaction on  $W_x$ ,  $D_{xz}$  and  $D_{zx}$ .

Figure 1 represents the drift velocity in the z direction, and the diffusion coefficients in the x and z directions for a simple ionisation model [9] with ionisation energy  $\epsilon_I = 10\text{eV}$ :

$$\sigma_m(\epsilon) = 10\epsilon^{-1/2},$$

$$\sigma_I(\epsilon) = \begin{cases} 0 & \epsilon < \epsilon_I, \\ 2 \times 10^{-3} \sigma_m & \epsilon > \epsilon_I. \end{cases}$$

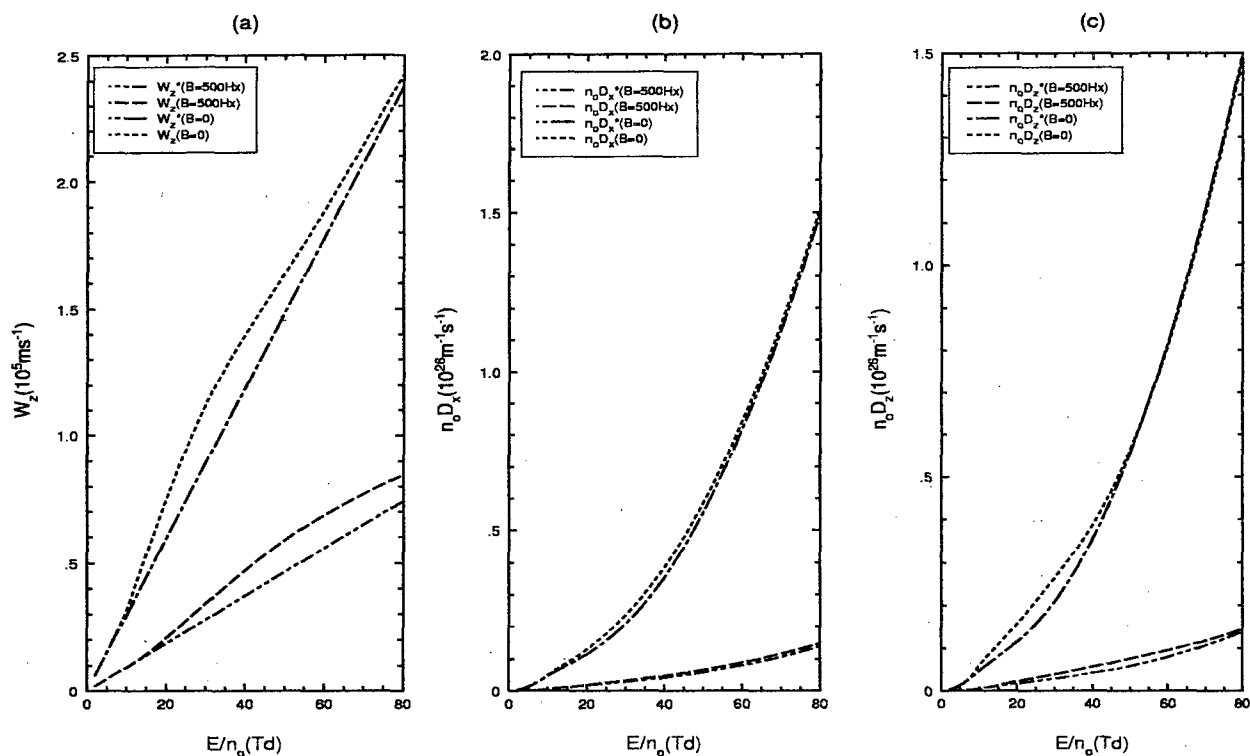


Figure 1: Transport properties for model gas [9]. (a) drift velocity in z direction, diffusion coefficients in (b) x direction and (c) z direction. Quantities with \* stand for flux properties.

Energies are in units of eV, and cross sections in  $\text{\AA}^2$ . Other parameters are:  $m/m_0 = 10^{-3}$ ,  $T_0 = 293\text{K}$ . A smoothing factor is used for the ionisation process in the vicinity of the threshold [11].

We observe that the explicit effect of ionisation is to enhance both  $W_z$  and  $D_x$  (The same applies to  $D_y$ , although this is not shown here). We can understand this change with the following picture of a traveling pulse. In the z-direction, particles at the leading edge of the swarm are more energetic than those at the trailing edge. Since  $dv_I/d\epsilon > 0$  for this model, particles are preferentially created at the leading edge, and there is an increase in the drift velocity in this direction. However for electrons, the spatial profiles of the average energy in both the x and y directions are approximately symmetric, with the average energy increasing with distance from the centroid. Consequently electrons are preferentially generated further from the centroid, and this reactive effect acts to enhance diffusion in these directions. By virtue of the symmetry however, there is no explicit reactive effect on these components of the drift velocity. As for the diffusion in the z direction, since the spatial profile of the average energy in this direction is not symmetric, the physical picture is not so clear cut. Figure 1 also shows that an applied magnetic field can change the relative magnitude of  $D_z$  and  $D_z^*$  from that of E field only, while  $D_x > D_x^*$  always.

With an increase in magnetic field, both the flux and bulk properties decrease, as we expected.

## Concluding Remarks

We have considered other models and plan also to present results for  $\mathbf{E}$  and  $\mathbf{B}$  arbitrarily oriented.

## References

- [1] M.J. Brennan, A.M. Garvie and L.J. Kelly, *Aust. J. Phys.* **43** (1990) 27
- [2] K.F. Ness, *Phys. Rev. E* **47** (1993) 327
- [3] K.F. Ness, *J. Phys. D* **27** (1994) 1848
- [4] R.E. Robson, *Aust. J. Phys.* **47** (1994) 279
- [5] R.D. White, M.J. Brennan and K.F. Ness, *J. Phys. D* (to be published)
- [6] D. Harcombe, R.T. Palmer and C.F. Gozna, *J. Sci. Instrum.* **40** (1963) 468
- [7] S.B. Vrhovac and Z.Lj. Petrovic, 1995 XXII International Conference on Phenomena in Ionized Gases Hoboken, USA; 1995 9<sup>th</sup> Swarm seminar Berkeley, USA
- [8] R.E. Robson, *J. Chem. Phys.* **85** (1986) 4486
- [9] R.E. Robson and K.F. Ness, *J. Chem. Phys.* **89** (1988) 4815
- [10] R.E. Robson, *Aust. J. Phys.* **44** (1991) 685
- [11] R.E. Robson, *Aust. J. Phys.* **37** (1984) 35



# Time-dependent multiterm solution of the reactive spatially-inhomogeneous Boltzmann equation for charged particle swarms in a.c. electric fields

R.D. White<sup>†</sup>, R.E. Robson<sup>†</sup> and K.F. Ness<sup>‡</sup>

<sup>†</sup>Physics Department, James Cook University, Cairns QLD 4870 Australia

<sup>‡</sup>Physics Department, James Cook University, Townsville QLD 4811 Australia

## Introduction

Recently a theoretical framework and associated time-dependent multi-term computer code has been developed for solving the reactive space-time dependent Boltzmann equation for the phase space distribution function (White 1996). The aim of the work was to overcome restrictions and approximations associated with many contemporary investigations (Ferreira *et al.* 1991, Kortshagen 1995). In particular, this study allows accurate calculation (typically to within 1%) of both the *full set* of transport coefficients and the distribution function  $f$ , with all of the following conditions satisfied:

- No restriction on the number of spherical harmonics in the velocity space decomposition of  $f$ ;
- No assumptions concerning the time-dependence of any of the components of the decomposition of  $f$  (i.e., avoiding restrictions associated with quasi-stationary approximations (Winkler *et al.* 1984); effective field theories (Ferreira *et al.* 1991); low-order Fourier-series truncations (Makabe and Goto 1988; Loureiro 1993));
- Valid for arbitrary charged particle masses, field amplitudes and applied frequencies;
- No assumption of spatial homogeneity (eg. local field approximation (Kortshagen 1995)); retention of the gradient term in the Boltzmann equation allowing for proper accounting of anisotropic diffusion effects;
- Rigorous treatment of reactions to ensure theoretical computation of *measurable* transport properties (Ness and Robson 1986).

We have found many interesting effects for a.c. fields, especially due to spatial gradients and reactions:

- The anomalous character of anisotropic diffusion (see also Maeda and Makabe (1994); Bzenic *et al.* (1994));
- Time-dependent negative differential conductivity (NDC) effects (see also Bzenic *et al.* (1995));
- The peculiar nature of reactive effects, eg, attachment may cause drift velocity to *lead* the field in phase.

Our approach also differs from contemporary authors to the extent that we have always attempted to first elucidate the *basic physics* through the use of simple model cross sections, before tackling real gases, and have drawn upon the extensive literature on the kinetic theory of d.c. swarms (Ness and Robson 1986) to help us explain the far more complicated a.c. phenomena. We have also found it helpful to consider transient processes and associated relaxation phenomena in coming to terms with the observed a.c. profiles.

## Theory

The velocity-dependence of  $f(\mathbf{r}, \mathbf{c}, t)$  is represented in terms of spherical harmonics:

$$f(\mathbf{r}, \mathbf{c}, t) = \sum_{l=0}^{\infty} \sum_{m=-l}^l f_m^{(l)}(\mathbf{r}, \mathbf{c}, t) Y_m^{(l)}(\hat{\mathbf{c}}). \quad (1)$$

No restrictions are placed on the number of spherical harmonics considered, nor is any particular form assumed for the time-dependence of the expansion coefficients. The speed dependence of the coefficients  $f_m^{(l)}(\mathbf{r}, \mathbf{c}, t)$  is represented by an expansion about a Maxwellian at a *time-dependent* basis temperature  $T_b(t)$  in terms of Sonine polynomials.  $T_b(t)$  is a parameter used to optimise convergence and is determined internally and automatically subject to specified accuracy requirements over the cycle.

It is assumed that the hydrodynamic stage has been reached and that the familiar density gradient expansion applies:

$$f(\mathbf{r}, \mathbf{c}, t) = \sum_{s=0}^{\infty} f^{(s)}(\mathbf{c}, t) \odot (-\nabla)^s n(\mathbf{r}, t). \quad (2)$$

This representation is justified by White (1996) and is in any case required for the determination of hydrodynamic (bulk) transport coefficients, viz, drift velocity  $\mathbf{W}(t)$ , diffusion tensor  $\mathbf{D}(t)$ , and attachment rate  $R_a(t)$ . These standard quantities are defined through the diffusion equation

$$\frac{\partial n}{\partial t} + \mathbf{W}(t) \cdot \nabla n - \mathbf{D}(t) : \nabla \nabla n = -R_a(t)n. \quad (3)$$

These measurable *bulk* transport coefficients differ from the *flux* coefficients defined in the density gradient expansion of the flux, through the inclusion of the explicit effects of reactions. The spatial variation in the average energy through the swarm results in a subsequent spatial variation of the source term in the continuity equation. A rigorous treatment of reactions then requires a density gradient expansion of this source term and subsequently the *bulk* transport coefficients appearing in the diffusion equation (3) *must* contain an explicit contribution from reactions:

$$R_a(t) = - \int J^R(f^{(0)}(\mathbf{c}, t)) d\mathbf{c}, \quad (4)$$

$$\begin{aligned} \mathbf{W}(t) &= \mathbf{W}^*(t) - S^{(1)}(t) \\ &= \int \mathbf{c} f^{(0)}(\mathbf{c}, t) d\mathbf{c} - \int J^R(f^{(1)}(\mathbf{c}, t)) d\mathbf{c}, \end{aligned} \quad (5)$$

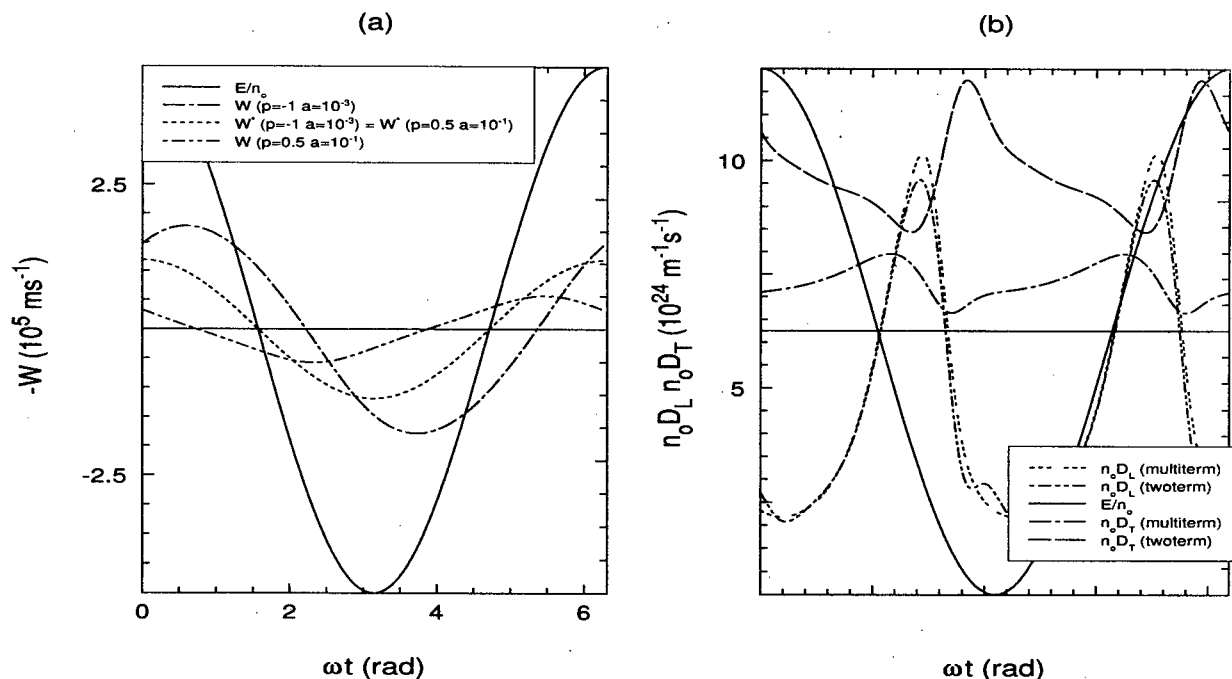


Figure 1: (a) Comparison of the twoterm and multiterm temporal profiles of  $n_o D_L$  and  $n_o D_T$  in methane ( $E/n_o = 10 \cos \omega t \text{ Td}$ ;  $\omega/n_o = 1 \times 10^{-15} \text{ rad m}^3 \text{ s}^{-1}$ ) (b) Comparison of the flux and bulk drift velocity for the attachment power law model ( $\sigma_A = a e^p \text{ \AA}^2$ ;  $E/n_o = 0.4 \cos \omega t \text{ Td}$ ;  $\omega/n_o = 1 \times 10^{-15} \text{ rad m}^3 \text{ s}^{-1}$ ).

$$\mathbf{D}(t) = \mathbf{D}^*(t) - S^{(2)}(t) \\ = \int c f^{(1)}(c, t) dc - \int J^R(f^{(2)}(c, t)) dc, \quad (6)$$

where  $J^R$  is the reactive component of the collision operator and  $\mathbf{W}^*$  and  $\mathbf{D}^*$  represent the flux drift and flux diffusion coefficients. *Previously, treatments of reactions in a.c electric fields have neglected the spatial variation in the source term.* The physical origin of transport brought about by energy selective creation or annihilation of swarm particles can be physically understood. The difference between the flux and bulk properties are highlighted in Figure 1(b).

To determine all the *bulk* transport coefficients defined in (3) in the presence of reactions, truncation of (2) at  $s = 2$  is necessary. Equation (2) together with (1), yields a hierarchy of *five* coupled kinetic equations. Much contemporary work however seems to revolve the spatially homogeneous member of this set, and is therefore totally inadequate for considering spatial effects of any sort, especially diffusion.

## Example results

Figure 1(a) represents the profiles associated with a two-term and multi-term truncation of (1) for the transverse and longitudinal diffusion coefficients for electrons in methane over a cycle of the electric field. The errors associated with the two-term approximation are obvious. One also observes the marked difference between the  $n_o D_L$  and  $n_o D_T$ . Figure 1(b) represents a comparison of the flux and bulk drift velocity for

a simple power law attachment model ( $\sigma_A = a e^p \text{ \AA}^2$ ). One should observe the errors associated with approximating the measurable bulk properties with the corresponding flux property. A particularly striking feature is the appearance of a negative phase lag in the  $p = 1/2$  profile (i.e., the drift preempts changes in the field). See White (1996) for a physical explanation. Calculations for other conservative and nonconservative model and real gases will be reported.

## Concluding remarks

The infrastructure exists in the present theory and code to study to the full plasma problem, ie, solving ion and electron Boltzmann equations coupled by Poisson's equation. The focus of present work is to address the full spatial problem, with no assumption of a hydrodynamic regime.

## References

- Bzenic S. *et al.* *Proc 17th SPIG*, 69 (1994)
- Ferreira C.M., *et al.* *IEEE Trans. Plasma Sci.* **19**, 229 (1991)
- Kortshagen U., *Plasma Sources Sci. Technol.* **4**, 172 (1995)
- Loureiro J., *Phys. Rev. E* **47**, 1262 (1993)
- Maeda K. and Makabe T., *Proc 17th SPIG*, 65 (1994)
- Makabe T. and Goto N., *J. Phys. D* **21**, 887 (1988)
- Ness K.F. and Robson R.E., *Phys. Rev. A* **34**, 2185 (1986)
- White R.D., *PhD Thesis, JCUNQ* (1996)
- Winkler R. *et al.* *Beitr. Plasma Phys.* **24**, 284 (1984).

# Interaction of an electron beam with gaseous nitrogen

A. V. Vasenkov

Institute of Thermophysics, Novosibirsk, 630090, Russia

Although many papers being devoted to the electron-gas interaction have been published, only a few [1,2] give information on the electron distribution function (EDF) as a function of electron energy and position. The main purpose of the paper is comprehend whether the available data on cross sections are sufficient to calculate very accurately the EDF in energies and space, and, in particular, to describe the measurements of Grun [3], Cohn and Caledonia[4], and Barrett and Hays [5].

To investigate the EDF in plasma, formed by a beam of electrons incident on gaseous nitrogen, the Monte Carlo (MC) electron degradation technique was used. The computer program follows electrons through a series of collisions. Elastic scattering, ionization, and excitation of electron states of molecules were considered. After the scattering event had been established, the anisotropic or isotropic scattering was performed. Elastic collisions are of first importance in scattering of electrons by molecules. Therefore, very accurate differential cross sections for the elastic scattering of electrons are needed in order to account properly for the behavior of electrons in gaseous media. In this study elastic scattering in  $N_2$  was treated using the form proposed by Porter and Jump[2] is represented by the following expression:

$$P_1(\theta, E) \sim 1/[1+2\gamma(E) - \cos(\theta)]^2 + \zeta(E)/[1 + 2\mu(E) + \cos(\theta)]^2$$

Parameters  $\gamma$ ,  $\zeta$ ,  $\mu$  were obtained by Porter and Jump [2] for the different energies at which data were available. The values of parameters at the intermediate energy points in this paper were found using the standard spline interpolative technique. Above 1 keV  $\gamma$  was obtained by extrapolating the empirically determined dependence to agree at energies above 20 keV with that from Moliere[6]:

$$\gamma = 1.70 \cdot 10^{-5} \gamma_e Z^{2/3} / (\tau(\tau+2))$$

where  $\tau = E/mc^2$  is the kinetic energy in units of the electron rest mass,  $Z$  is atomic number of the substance (for nitrogen,  $Z = 7$ ), and

$$\gamma_e = 1.13 + 3.76 (Z/[137(v/c)])^2$$

Data on inelastic differential cross sections in nitrogen published suggest that at electron energies from 10 eV to 60 eV inelastic collisions cause approximately the same amount of scatter as that resulting from elastic collisions. From the other side we have available the semiempirical generalized oscillator strengths of Porter et al [7] for angular inelastic scattering by the primary electrons at high energies which substantially forward peaked. Thus in the case of ionization or inelastic collisions with

excitation of optically allowed states, which are the most important inelastic events above 100 eV, the angular scattering was delta function forward. In the events with excitation of optically forbidden states it was assumed that electrons scattered according to the differential elastic cross section. Electron energy degradation was simulated using the formulas given in [7].

In order to test the accuracy of the present computational model, comparisons were made with laboratory measurements of emissions for electron beam injections in  $N_2$  [3-5]. The comparisons of the normalized energy deposition distribution, as defined by Grun [3], computed from the 3914 Å emission spatial profiles and measured by Barrett and Hays [5], Cohn and Caledonia[4], and Grun [3] over an energy range from 0.3 keV to 5 keV were performed. Table 1 compare practical range values determined using present scattering models with results of various authors [1-5]. The range results from current work are in rather good agreement with measurements at incident energies of 2 keV, 3 keV and 5 keV, but become systematically overestimating those from Barrett and Hays [5] at lower energies.

Table 1. Range data (in  $10^{-6}$  g/cm<sup>2</sup>) at selected incident energies ( $E_p$ ) (in keV). BH - Barrett and Hays [5], CC - Cohn and Caledonia [4], G - Grun [3], PVM - Porter et al [2], JG - Jackman and Green [1].

$E_p$	$P_1$	BH	CC	G	PVM	JG
0.1	0.31				0.33	0.37
0.3	1.19	1.06			1.13	1.25
0.5	2.24	2.13			2.16	
1.0	6.02	5.72			5.68	6.45
2.0	18.22	17.70	20.60		17.30	18.60
3.0	34.58	34.30	35.20			
5.0	80.88	83.00	77.20	76.40	83.40	91.50

Now let us concentrate on the shapes of deposition curves. At 0.3 keV (Fig. 1, a) calculated curve predict the peak on the larger distance from the point of injection than experimental data and also falloff in computations have more steep slope than that in measurements. At 5 keV (Fig. 1, b) the model gives practically the same value of the shoulder that seen from data of Grun[3] but position of maximum is in better agreement with data of Cohn and Caledonia[4].

To summarize briefly, it was shown that the MC method presented correctly predict the behavior of deposition curves measured but overestimate the position of peak from Barrett and Hays[5]. The dif-

ferences are the most significant at 0.3 keV and 3 keV.

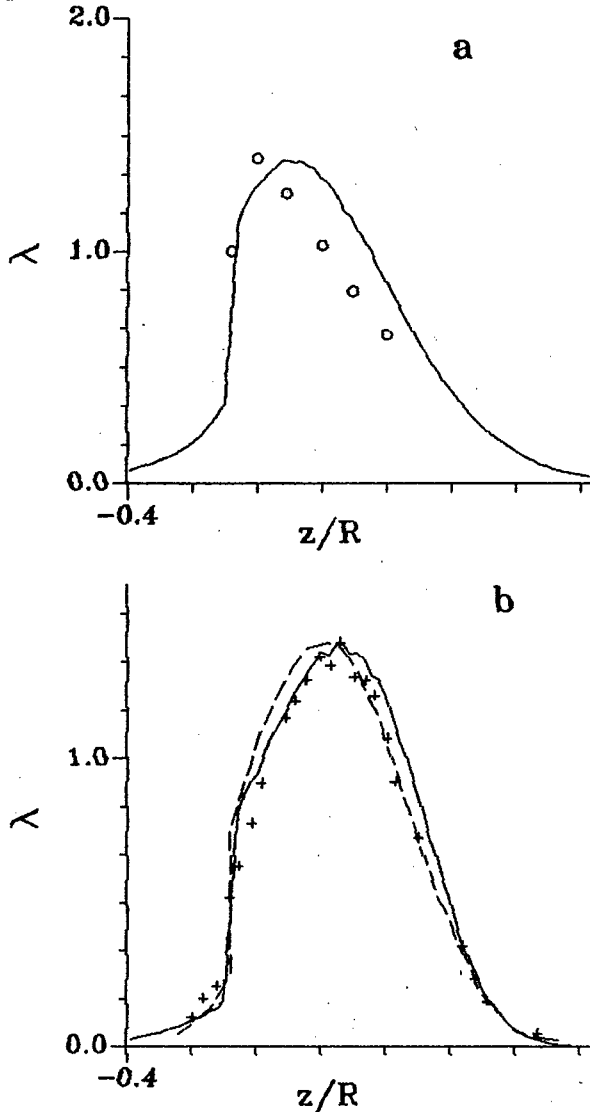


Fig. 1. The energy deposition curves at several energies: MC calculations -  $P_1$  (solid lines), Barrett and Hays[5](o), Cohn and Caledonia [4] (+), Grun [3] (dashed line); a)  $E_p = 0.3$  keV, b)  $E_p = 5.0$  keV.

The results given were obtained using the cross-section model ( $P_1$ ) which describes very accurately various experimental angular elastic cross sections. From the other side, the results obtained at low incident energies for depth of the peak and range values systematically overestimate those from Barrett and Hays[5]. If the latter experimental work is correct, then we can draw the conclusion that at low energies a very accurate consideration of anisotropy is needed both for elastic collisions and inelastic collisions.

To determine the distribution of electrons in energies formed after the incident electrons and all its secondaries and tertiaries had been completely degraded in energy, electron flux densities normalized to the total ionization rates were computed (Fig. 2).

It is seen from the Figure that in low-energy range distribution of electrons is practically independent of energy of incident electrons. The distinctions between the results from these calculations and those of Suhre and Verdeyen[9], Konovalov and Son[10] could be due to several reasons (two of them are mentioned here): (1) the cross sections are not the same; (2) the computation methods are not the same.

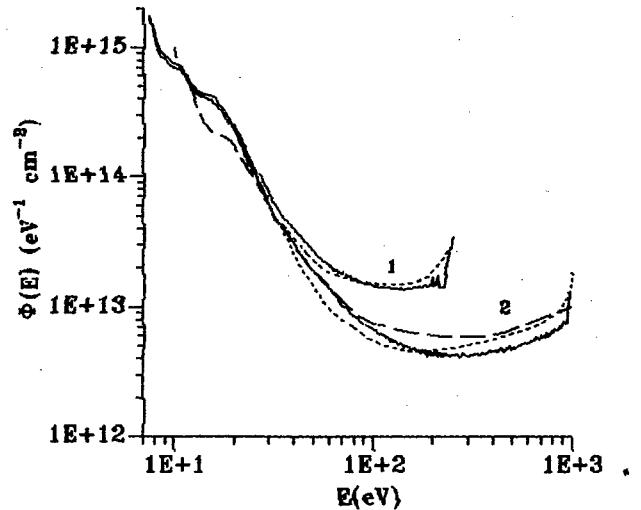


Fig. 2. Comparison of electron flux densities from Ref. 8 (short dashed lines), Ref. 9 (dashed line) with present calculations (solid lines): (1) -  $E_p = 250$  eV; (2) -  $E_p = 1$  keV.

The electron flux densities were obtained at different energies of incident electrons and distances to the point of injection. It was shown that while at low energies of incident electrons flux densities computed are different, at higher incident energies flux densities in low energy range are coming to be independent of incident energy and distance to the point of injection. Practical result from it is that spatial dependencies of excitation rates of forbidden states are similar to those of ionization at high incident energies and different at lower incident energies.

- [1] C. H. Jackman and A. E. S. Green: *J. Geophys. Res.*, **84** (1979) 2715.
- [2] H. S. Porter, F. Varosi, and H. G. Mayr: *J. Geophys. Res. A*, **92** (1987) 5933.
- [3] A. E. Grun: *Z. Naturf. A*, **12** (1957) 89.
- [4] A. Cohn and G. Caledonia: *J. Appl. Phys.*, **41** (1970) 3767.
- [5] J. L. Barrett and P. B. Hays: *J. Chem. Phys.*, **64** (1976), 743.
- [6] G. Moliere: *Z. Naturf.*, **3a** (1948) 78.
- [7] H. S. Porter, C. H. Jackman, and A. E. S. Green: *J. Chem. Phys.*, **65** (1976) 154.
- [8] D. R. Suhre and J. T. Verdeyen: *J. Appl. Phys.*, **47** (1976) 4484.
- [9] V. P. Konovalov, E. E. Son: *Zh. Teekh. Fiz.*, **50** (1980) 300 [*Sov. Phys. Tech. Phys.*, **25** (1980) 178].

## ***Topic 2***

# **Elementary processes.**

# Experimental determination of the secondary Townsend coefficient for rare gases. Application to plasma display panel.

G.Auday, Ph.Guillot, J.Galy, H.Brunet  
Centre de Physique des plasmas et de leurs Applications de Toulouse  
Université Paul Sabatier- 118, route de Narbonne, 31062 Toulouse Cedex  
Tel.: 05.61.55.84.91 - Email: guillot@cpa22.ups-tlse.fr

## Abstract

Experiments have been investigated in order to determine variations of the secondary electron emission coefficient vs. reduced field. Results are given as a function of the electrodes spacing for different electrodes materials and for different rare-gases. This research is supported by the company Thomson Tubes Electroniques.

## 1. Plasma display panel

### 1.1 Presentation

Thanks to significant progress made over recent years [1], plasma display panel (PDP) is the most promising candidate for large size flat screens. To replace cathode ray tube displays, PDPs offer many advantageous characteristics as robustness, low operating voltages, absence of geometrical distortion, uniform luminance, high contrast and extremely wide viewing angle.

### 1.2 Principles

The panel consists of two glass plates enclosing a gap filled with rare-gas mixture (neon-xenon) at 560 torr. Each plate carries a parallel array of electrodes and a dielectric layer with magnesium oxide (MgO) layer. The role of this layer is to protect the electrodes. At the intersection of two electrodes, representing an elementary PDP's cell or pixel, occurs an electric discharge emitting UV photons (147-173 nm). This emission is next used to excite phosphors which product one of the three fundamental colors (red, green or blue).

## 2. Secondary Townsend coefficient

One of the most important parameters in a discharge occurring between plane-parallel electrodes is the secondary electron emission coefficient or secondary Townsend coefficient called  $\gamma$ . It represents the number of secondary electrons knocked out by one positive ion hitting the cathode surface. This number depends on the kind of the electrodes material and the gas used for the discharge. Its knowledge is essential so as to simulate PDP's behavior and understand its

functioning. For modeling, the dependence of  $\gamma$  on  $E/p$  is useful ( $E$  is the electric field between the electrodes and  $p$  is the pressure of the gas).

## 3. Experiments

An experimental method allowing a systematic determination of this coefficient whatever the electrodes materials (metals, metals with dielectric, metals with phosphors...) and whatever the gas (rare gases, mixtures...) has been developed.

The electrodes (5 cm of diameter), were placed in the experimental chamber (see figure1). Their flat faces were pointing towards each other. The spacing  $d$  between them was adjustable from 0.2 cm to 1 cm. The chamber was connected to a gas system and vacuum pumps.

In the experiments, the pressure  $p$  was altered from 0.5 torr to 60 torr, which means  $0.1 \text{ torr.cm} \leq pxd \leq 12 \text{ torr.cm}$ .

The chamber was also connected to a circuit which caused breakdown between the electrodes. This electrical circuit allowed volt-ampere characteristics to be determined. Electrodes were sustained with dc voltage varying between 0V and 1000V. The external resistance could take values included between about 2000M $\Omega$  and 10k $\Omega$ . In this way, it was possible to have a current from  $10^{-10}$  A to  $10^{-2}$  A.

Visual observation of the discharge was possible thanks to a quartz window.

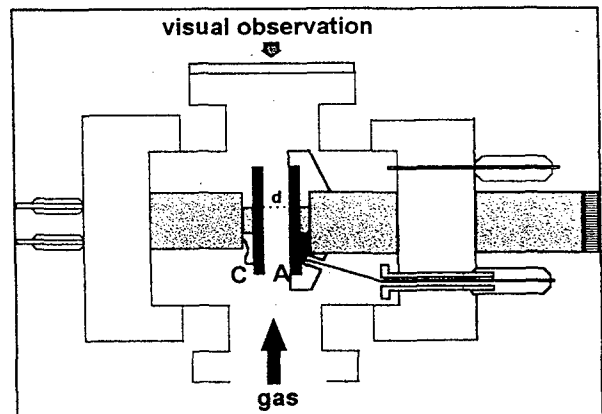


figure1 : Experimental chamber  
(C is the cathode and A is the anode).

### 3.1 Experimental technique

The different steps used to characterize the dependence of  $\gamma$  on  $E/p$  are the following:

(i) the different regions of the discharge could be observed: the Townsend discharge and the three regimes of the glow discharge (subnormal, normal and abnormal). Thus, the current-voltage characteristics of a dc-discharge could be plotted (see figure2) and the breakdown voltage  $V_{cl}$  for many values of product  $pxd$  was determined.

(ii) the next step was to represent the variations of this voltage  $V_{cl}$  vs.  $pxd$ , which is called the Paschen's curve (see figure3).

(iii) an examination of this curve finally gave the dependence of  $\gamma$  on  $E/p$ . In this view, one assumed  $E/p \approx V_{cl}/(pxd)$  and as the values of the first Townsend coefficient  $\alpha$  are known as a function of  $E/p$  thanks to Monte-Carlo simulation,  $\gamma(E/p)$  was next deduced from the formula :

$$1 + \frac{1}{\gamma} = e^{\alpha d}$$

$$\Leftrightarrow \gamma = \frac{1}{e^{\alpha d} - 1}$$

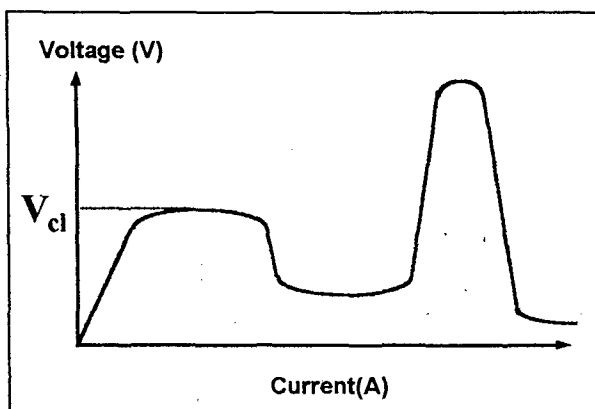


figure2 : Current-voltage characteristic for parallel-plane electrodes at one  $pxd$  value.

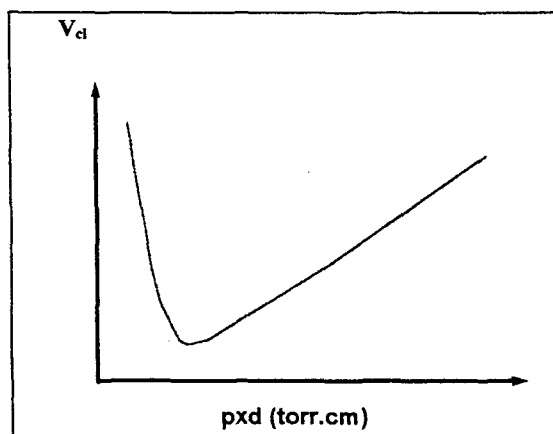


figure3 : Paschen's curve.

### 3.2 Experimental results

Experiments have been investigated for different electrode materials (stainless steel, copper, copper with MgO) and many gases (argon, krypton, xenon and neon).

Experimental results (current-voltage characteristics, Paschen's curves and variations of  $\gamma$  with  $E/p$ ) were found as a function of the electrode spacing ( $d=2\text{mm}$ ,  $4\text{mm}$ ,  $6\text{mm}$  and  $10\text{mm}$ ). In some cases, they were compared with results from literature.

The curves in figure4 are examples of variations of  $\gamma$  obtained for  $d=2\text{mm}$ .

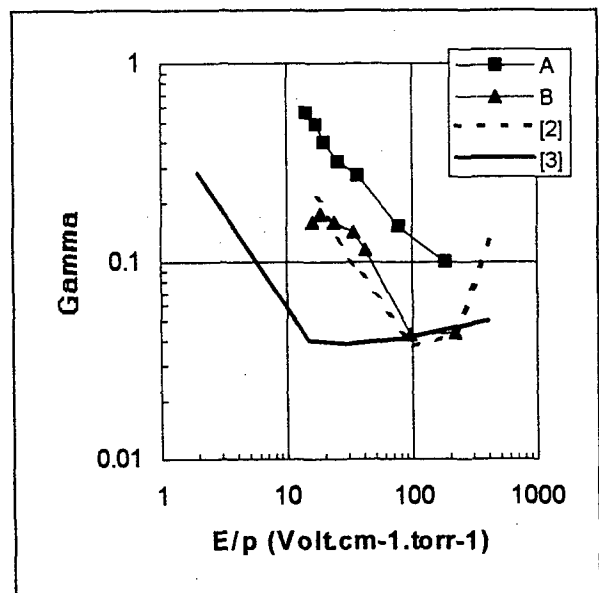


figure4 : Experimental variations of  $\gamma$  with  $E/p$  for neon. Symbols represent our results for steel (A) and copper (B) electrodes, respectively. The other curves are variations found for copper electrodes by [2] ( - - - ) and by [3] ( — ).

### References :

- [1] J.P.Bœuf, H.Doyeux. Europhysics News. 27, 1996, p.46-49
- [2] B.N. Klyarfel'd, L.G. Guseva. A.S. Pokrovskaya-Soboleva, Soviet Physics-Technical Physics, vol. 11, 4, October 1966, p.520-527
- [3] O. Sahni, C. Lanza, Journal of Applied Physics, vol. 47, 4, April 1976, p.1337-1340

# Experimental determination and R-Matrix calculation of electron impact excitation rate coefficients of neutral and singly ionized nitrogen

Robert M. Frost, Peter Awakowicz

Lehrstuhl für Technische Elektrophysik, Technische Universität München, Arcisstr. 21, D-80290 München, Germany

## Abstract

Collision strengths for neutral and singly ionized nitrogen have been calculated with the R-matrix method. The results were compared with measured coefficients obtained by means of a low pressure cascade arc plasma. The investigations were performed in an intensity calibrated spectroscopic system operated in the visible and VUV spectral range down to 53 nm.

## R-Matrix calculations

The codes for the collisional calculations were deduced from the *OPACITY PROJECT* [1]. The target modelling was performed by using *AUTOSTRUCTURE* [2], a code primarily corresponding to the well known *SUPERSTRUCTURE* [3] but dealing with Hartree potentials evaluated by Slater type orbitals. These potentials offer one optimization parameter  $\lambda_{nl}$  for each orbital  $nl$ . The close-coupling calculation includes the  $2s2p^4$ ,  $2s2p^33s$ ,  $2s^22p^23s$ ,  $2s^22p^23p$ ,  $2s^22p^23d$ ,  $2s^22p^3$  and the  $2p^5$  configurations for the nitrogen atom and the  $2s2p^3$ ,  $2s^22p3s$ ,  $2s^22p3p$ ,  $2s^22p3d$ ,  $2s^22p^2$  and the  $2p^4$  configurations for the ion. Since the application of pseudo orbitals did not improve the accuracy significantly, they have not been used.

## Experiment and calibration

For the purpose of the present investigations a stationary low pressure plasma was generated in a Maecker-type cascade arc [4]. The cascade consists of a stack of axially insulated, water-cooled copper plates with aligned center bores (7 mm $\varnothing$ ) forming the discharge channel. Silicon rubber rings between the plates are being used as vacuum seals. Two tungsten electrodes on the anode side and one external heated electrode on the cathode side share the current load. The discharge was operated at 8 A current and at pressure values between 30 and 1 hPa. The stack of cascade plates was isolated by a vacuum-tight acrylic glass cylinder which was pumped to prevent the influx of atmospheric oxygen. The plasma consisted mainly of helium with small admixtures of nitrogen. The gas composition was adjusted by calibrated mass flow controllers.

For the VUV intensity calibration in the range of 53 to 125 nm, the low pressure cascade arc was replaced by a 2 mm $\varnothing$  pure He discharge which was operated at normal pressure (952 hPa) and 100 A current. The comparison of the calculated continuum emission coefficient of the He plasma and the measured signal at 27 wavelength points yields the system response in the VUV. In order to examine the continuous intensity calibration at several

wavelength points, the normal pressure arc was replaced by a hollow cathode (8 mm $\varnothing$ , 60 mm length). A detailed description is given in Ref. [5].

The aforementioned discharges were investigated simultaneously by two optical systems, observing end-on nearly the same central region of the plasma columns from both directions. A 2-m monochromator at the cathode side served for diagnostic purposes in the visible (vis) region (250-550nm). For precise wavelength scans, especially of small line profiles, a photomultiplier (R928/1P28) was moved by a piezo shift system mounted on a precision mechanical drive. The response was obtained by a calibrated tungsten strip lamp. From the anode side, the VUV system was used for intensity measurements. A platinum coated spherical mirror focused the cross section of the plasma columns on the entrance slit of a 1-m McPherson monochromator (model 225) with a platinum-coated concave grating. A channeltron multiplier was operated in the photon counting mode. The discharge chambers and the VUV system were connected by a three-stage differential pumping system. For more information see Ref. [5]

## Plasma diagnostics

Due to the low electron density and the energetically high lying first excited state of the helium atom, the state of the plasma is strongly non-LTE. Therefore the Boltzmann and Saha equilibrium relations cannot serve for diagnostic purposes. The temperature of the heavy particles was derived by means of the Doppler broadening of the HeI 471.32 nm triplet measured in the minus fifth spectral order of the vis system, which results in a profile of 2.6 pm of the 2-m monochromator. The full halfwidth of the Doppler profile amounts at least to 5.0 pm and leads to temperatures between 2600 and 930 K for the different pressure values from 30 to 1 hPa.

The electron density was measured by the Stark broadening of the hydrogen Balmer  $\beta$ -line. Deuterium was filled in to keep the Doppler contribution small. A  $\chi^2$ -fitting procedure was performed with theoretical profiles from Ref. [6]. The electron densities cover the range from 7.3 to  $1.8 \times 10^{13} \text{ cm}^{-3}$ .

The electron temperature was determined by applying the corona balance to the level  $n=4$  of the helium ion. The measurement of the theoretically well known rate coefficient  $X_{14}(T_e)$  of this hydrogen-like system via the absolute line emission coefficient leads to accurate values of  $T_e$ . The resulting electron temperatures range



from 5.4 to 8.8 eV for the pressure values given above. For more details see Ref. [7].

### Measurements

The following collisional-radiative model was used for describing the on-axis plasma state:

$$n_e \left( \sum_{n \neq m}^N \eta_n X_{nm} + \frac{\eta_l^{z+1}}{\eta_l^z} a_{l,m} \right) + \sum_{n > m} \eta_n A_{nm} = \eta_m \left( n_e \left[ \sum_{n \neq m} X_{mn} + S_m \right] + \sum_{n < m} \Theta_{mn} A_{mn} \right).$$

Further on, the ground state population densities  $n_l$  of NI and NII have been determined by  $n_l = n_m / \eta_m$  via absolutely measured level population densities  $n_m$ . The calculated and Maxwellian-averaged collision strengths have been inserted. Reabsorption was taken into account by multiplying the Einstein coefficients  $A_{mn}$  by the corresponding escape factors  $\Theta_{mn}$ . The radial diffusion of the metastable particles was considered by assigning „diffusion-  $A_{mn}$ ’s“ to the meta-state to ground-state transitions. The rate coefficients were obtained by applying the corona balance under consideration of the cascade processes and the population contributions originating from the metastable states.

### Results

The rate coefficients  $X_{lm}$  for the NI transitions from the ground state  $2p^3 4S^0$  to the  $3s^4 P$  and the  $2p^4 P$  state have been found to be significantly smaller than earlier measured coefficients by Stone and Zipf [8], as frequently supposed in the literature. The second is plotted in Fig. 1 together with an older R-matrix calculation from [9]: The open circles, designated by *uncorrected*, show the rate coefficient without correction for the cascade and meta contributions.

In the figures 2 and 3 coefficients for an optical forbidden transition and an exchange transition in NII can be seen. The additional curve in Fig. 2 belongs to fine structure collision strengths published by [10].

### References

- [1] K.A. Berrington, P.G. Burke, K. Butler, M.J. Seaton, P.J. Storey, K.T. Taylor, Y. Yan, J. Phys. B: At. Mol. Phys. **20**, 6379 (1987)
- [2] N.R. Badnell, J. Phys. B: At. Mol. Phys. **19**, 3827 (1986)
- [3] W. Eissner, M. Jones, H. Nussbaumer, Comput. Phys. Commun. **8**, 270 (1974)
- [4] H. Maecker, Z. Naturforsch. **11a**, 457 (1956)
- [5] R. Frost, P. Awakowicz, Appl. Opt. **36** (1997)
- [6] C.R. Vidal, J. Cooper, E.W. Smith, Astrophys. J. Suppl. S. **214**, 37 (1973)
- [7] P. Awakowicz, K. Behringer, Plasma Phys. Control. Fusion **37**, 551 (1995)

- [8] E.J. Stone, E.C. Zipf, J. Chem. Phys. **58**, 10, 4278 (1973)
- [9] K.A. Berrington, P.G. Burke, W.D. Robb, J. Phys. B: At. Mol. Phys. **8**, 15, 2500 (1975)
- [10] R.P. Stafford, K.L. Bell, A. Hibbert, W.P. Wijesundera, Mon. Not. R. Astron. Soc. **268**, 816 (1994)

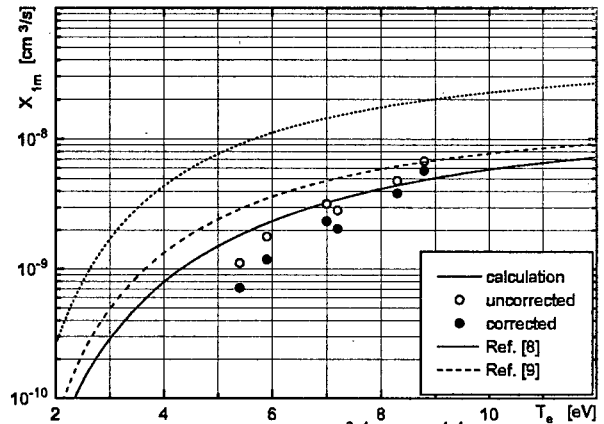


Fig. 1. Transition  $2p^3 4S^0 - 2p^4 4P$

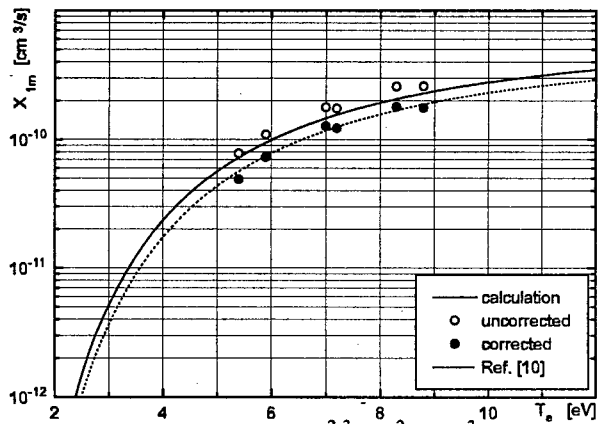


Fig. 2. Transition  $2p^2 3P - (2P) 3p^3 D$

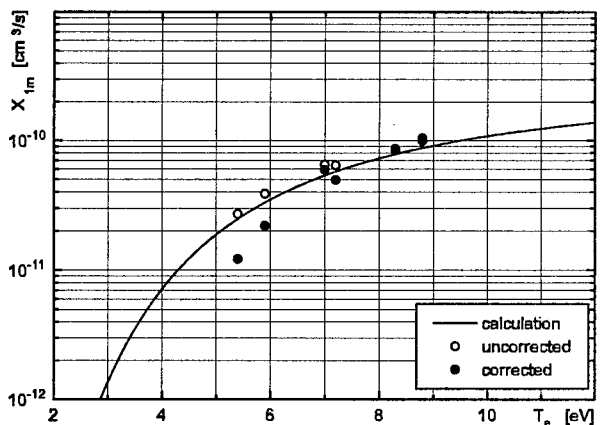


Fig. 3. Transition  $2p^2 3P - (2P) 3p^1 D$

### Acknowledgement

The authors thank the Dr. Johannes Heidenhain-Stiftung for its financial support of the experimental investigations

## Electron-Impact Dissociation and Ionization of Molecules Studied by Laser-Induced Fluorescence Techniques

R. Siegel<sup>1,3</sup>, N. Abramzon<sup>2</sup>, and K. Becker<sup>3</sup>

<sup>1</sup>National Institute of Standards and Technology, Gaithersburg, MD 20899 USA

<sup>2</sup>Physics Department, City College of C.U.N.Y., New York, NY 10031 USA

<sup>3</sup>Department of Physics and Engineering Physics, Stevens Institute of Technology, Hoboken, NJ 07030 USA

Electron-impact ionization and dissociation of molecules are very important processes in many applications including gas discharges and plasmas. While there is a reasonably broad database on total and partial molecular ionization cross sections and on cross sections for dissociative excitation of molecules (i.e. for the formation of electronically excited fragments), there is essentially no quantitative information available on cross sections for the formation of state-selected ions and there is only very limited information on cross sections for the formation of neutral ground-state dissociation fragments. This lack of data is largely due to experimental difficulties in the detection of the reaction products (state-selected ions and neutral ground-state dissociation products).

We have completed the construction and testing of a triple beam apparatus (crossed electron beam, gas beam, and laser beam) for the measurement of absolute electron-impact cross sections for the formation of neutral ground-state dissociation fragments. We use laser-induced fluorescence (LIF) techniques to pump the dissociation fragments from the ground state to an excited state and observe the subsequent spontaneous emission. The apparatus is also suitable to measure absolute cross sections for the formation of various state-selected ions, e.g.  $N_2^+$  ions in the  $X^1\Sigma_g^+$  ground state. For most molecules, the total ionization cross section (which is comparatively easy to measure) is virtually identical to the cross section for the formation of the molecular ion in its electronic ground state, since the cross sections for forming ions in electronically excited states are typically 2 orders of magnitude smaller than cross sections for the formation of ground-state ions [1]. However, this is not the case for  $N_2$ , where excited molecular ions are formed with appreciable cross sections [1]. Therefore, it is no longer justified to equate the total  $N_2$  ionization cross section with the cross section for the formation of  $N_2^+(X^1\Sigma_g^+)$  ions.

Our triple-beam apparatus consists of an electron beam with the following characteristics: beam energy 5 - 400 eV, energy spread 0.5 eV (FWHM), beam diameter in the interaction region 1-2 mm, beam current up to 10  $\mu$ A at 50 eV for

continuous operation (we also have the option to pulse the electron beam with beam rise and fall times of about 10 ns). The target gas beam (which intersects the electron beam at right angles) is an effusive beam emanating from a multi-capillary nozzle with an estimated number density in the interaction region of  $1 - 5 \times 10^{12}$  molecules/cm<sup>3</sup>. The laser beam (which counterpropagates the electron beam) is produced by an excimer-pumped dye laser. The XeCl Excimer laser generates 8-10 n pulses of 80-100 mJ at a repetition rate of 20-100 Hz. The dye laser (when operated with Excalite 392) produces pulses of about 4 mJ with a line width of 0.0015 nm in the range 373 - 397 nm. Optical detection is made in a direction perpendicular to both the electron beam and the gas beam. The entire triple-beam set-up is housed in a stainless-steel vacuum chamber pumped by a turbo-molecular pump station which achieves a typical background pressure of  $1 \times 10^{-7}$  Torr which rises to about  $4 \times 10^{-5}$  Torr under operating conditions. We employ gated photon detection techniques to record the LIF signal. The experiment is under complete computer control.

The first series of measurements were carried out investigating the ionization of  $N_2$  and the formation of  $N_2^+(X^1\Sigma_g^+)$  ground-state ions. This was done to avoid initially the added complications arising from dissociative processes, e.g. fragments formed with excess kinetic energy. In the  $N_2$  measurements the laser beam was tuned to pump the 0-0 vibrational band of the X - B transition of the  $N_2^+$  ions produced by electron-impact ionization of  $N_2$  at 391 nm and we detected the 0-1 vibrational band at 427 nm. By scanning the laser across the rotational lines of the 391 nm band, we obtained a rotationally resolved LIF spectrum of the 0-0 band. Fig. 1 shows a portion of this spectrum near the head of the P-branch. We note that this LIF spectrum was obtained in the presence of the continuous background emission produced by the continuous electron beam (beam energy 80 eV). Preliminary studies involving a pulsed electron beam showed that the signal-to-noise ratio of the spectrum in Fig. 1 can be improved significantly by recording the LIF signal only during periods in which the continuous

electron beam is turned off (pulsed electron beam mode).

The LIF spectrum serves as the basis to extract absolute cross sections for the formation of  $N_2^+(X^1\Sigma_g^+)$  ground-state ions as a function of the electron energy. This requires an absolute calibration of the relative signal which can be accomplished by e.g. Raleigh scattering from  $N_2$ , LIF measurements with a gas whose photo-absorption cross section is well-known, or by studying a process whose electron-impact cross section is well-known and can serve as a benchmark, or by carefully characterizing all quantities involved in the present experiment in absolute terms (which is perhaps the most difficult way to normalize the relative signal).

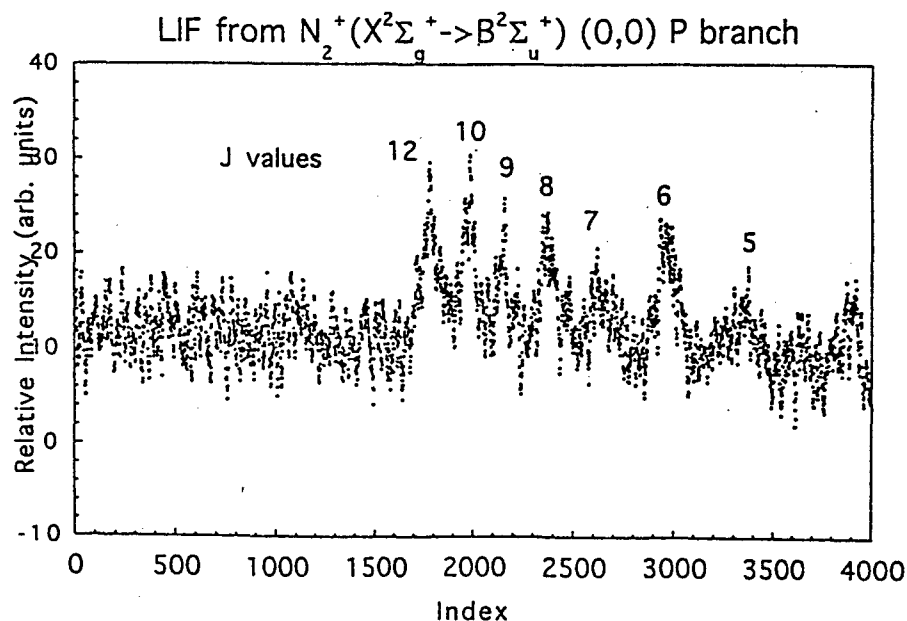
A detailed discussion of all aspects of the present experiment will be presented at the Conference. Preliminary values of the cross section for the formation of  $N_2^+(X^1\Sigma_g^+)$  ground-state ions will also be presented and future directions and potential applications for this experimental technique will be discussed.

This work was supported by the U.S. National Science Foundation.

### References

- [1] T.D. Mark and G.H. Dunn (editors), "Electron Impact Ionization", Springer Verlag, Vienna, 1985

Fig. 1: Rotationally Resolved LIF Spectrum near the Band Head of the  $N_2^+$  P Branch.



# VUV Emissions Produced by Electron Impact on Si-Organic Molecules

P. Kurunczi<sup>1</sup>, K. Martus<sup>2</sup>, and K. Becker<sup>3</sup>

<sup>1</sup>Physics Department, City College of C.U.N.Y., New York, NY 10031 USA

<sup>2</sup>Chemistry and Physics Department, William Paterson College, Wayne, NJ 07470 USA

<sup>3</sup>Department of Physics and Engineering Physics, Stevens Institute of Technology, Hoboken, NJ 07030 USA

Silicon-organic compounds are widely used in a variety of plasma-assisted thin film deposition, polymerization, and surface modification processes. Among the most commonly employed Si-organics are tetraethoxysilane (TEOS),  $\text{Si}(\text{O}-\text{CH}_2-\text{CH}_3)_4$ , tetramethylsilane (TMS),  $\text{Si}(\text{CH}_3)_4$ , and hexamethyldisiloxane (HMDSO),  $(\text{CH}_3)_3-\text{Si}-\text{O}-\text{Si}-(\text{CH}_3)_3$ . Collisional and spectroscopic data for these molecules are scarce despite the need for such data in efforts to understand and model the properties of these plasmas and to identify the important plasma-chemical reaction pathways. Previous work includes the measurement of absolute cross sections for the electron-impact ionization of TMS and TEOS [1,2] and the analysis of optical emissions in the near ultraviolet and visible (200 - 800 nm) produced by controlled electron impact on TMS, HMDSO, and TEOS [3,4]. No information is available on the production of energetic photons in the vacuum ultraviolet (VUV) regime (50 - 130 nm) by electron impact on these Si-organics. Energetic VUV photons with photon energies of 10 - 20 eV can affect plasma-assisted deposition, polymerization and surface modification either adversely or favorably (depending on the particular application).

We present a complete account of absolute photoemission cross sections and appearance energies for VUV emissions in the 50 - 130 nm range produced by electron impact on TEOS, TMS, and HMDSO under single collision conditions. The experiments were carried out using a conventional crossed electron-beam - (effusive) gas beam apparatus in conjunction with an optical detection system consisting of a VUV monochromator and a channel electron multiplier. The relative calibration of the wavelength-dependent sensitivity of the optical detection system was made using a comparison of measured and calculated  $\text{H}_2$  emission spectra in the wavelength region from 80 - 130 nm [5]. Absolute calibration of the measured cross sections utilizes the well-known cross section for H Lyman- $\alpha$  emission following electron impact on  $\text{H}_2$  [6]. Further details of the procedure and a detailed description of the entire apparatus have been given previously [3,4,7].

The present experiments revealed that the only electron-impact produced emissions in the VUV

from TEOS, TMS, and HMDSO of appreciable intensity are the Lyman series of atomic hydrogen in the wavelength region from about 90 nm to 122 nm. Atomic hydrogen emissions from these targets were also found previously in the visible (the H Balmer series), but they were not the only emissions in that region. In the VUV, no other emissions with photoemission cross sections larger than about  $1 \times 10^{-21} \text{ cm}^2$  at 100 eV were found. The VUV emission spectra of all three Si-organics were found to be very similar. As an example, the VUV emission spectrum produced by 100 eV electrons on TMS is shown in fig. 1. The emission spectrum has been corrected for the wavelength-dependent detection sensitivity of our detection system. The Lyman- $\alpha$ ,  $\beta$ , and  $\gamma$  lines are clearly resolved in the spectra, whereas the higher members of the Lyman series could not be resolved with the given spectral resolution.

Subsequently, we measured relative cross sections of the strongest emissions from threshold to about 200 eV which were then put on an absolute scale. Fig. 2 shows the relative Lyman- $\alpha$  photoemission cross sections from TMS as a function of electron energy. Similar curves were obtained for the other two target gases. While the absolute cross section values for TMS and HMDSO were found to be quite similar, the cross sections for TEOS were much smaller, similar to what was observed earlier for the UV/visible photoemission cross sections from TEOS, in particular for the Balmer cross sections. Detailed studies of the VUV cross section shapes in the near-threshold regions revealed prominent structures in the cross section curves (again similar to the Balmer cross section curves). This indicates that more than one break-up mechanism of the parent molecule contributes to a particular emission feature (which is not surprising in view of the complex molecular structure of the target species). Furthermore, we found evidence that the Lyman- $\alpha$  cross sections in all cases contained significant cascade contributions from the Balmer emissions. An attempt is underway to separate the direct contribution from the cascade contribution for the Lyman- $\alpha$  lines.

Similar to what was observed earlier for the UV/visible photoemission cross sections, the

measured appearance energies for the Lyman lines indicate that in all cases partial fragmentation of the parent molecule is the most likely mechanism by which the excited  $H(n=2)$  fragments are formed.

This work was supported by the U.S. National Science Foundation.

### References

- [1] R. Basner et al., *Int. J. Mass Spectrom. Ion Proc.* 153 (1996) 65
- [2] R. Basner et al., *Int. J. Mass Spectrom. Ion Proc.* (1997), in press
- [3] M. Ducrepin et al., *J. Appl. Phys.* 73 (1993) 7203
- [4] P. Kurunczi et al., *Contr. Plasma Phys.* 36 (1996) 723
- [5] J.M. Ajello et al., *Appl. Optics* 27 (1988) 890
- [6] J.M. Woolsey et al., *J. Phys. B* 19 (1986) L493 and references therein to other work
- [7] M.B. Roque et al., *J. Chem. Phys.* 94 (1991) 341

Fig. 1: TMS Emission Spectrum

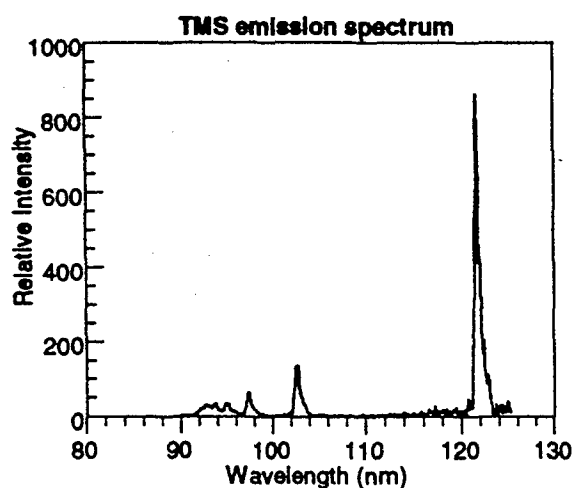
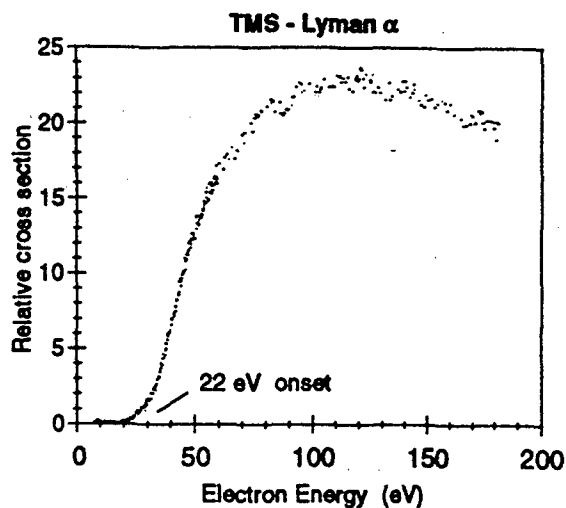


Fig. 2: Lyman- $\alpha$  Cross Section from TMS.



# NEGATIVE ELECTRON MOBILITY IN Ar:F<sub>2</sub> MIXTURES. THE DEPENDENCE ON THE ARGON MOMENTUM TRANSFER CROSS SECTION.

<sup>1</sup>N A Dyatko, <sup>2</sup>M Capitelli and <sup>1</sup>A P Napartovich

<sup>1</sup> Troitsk Institute for Innovation and Fusion Research, 142092, Troitsk, Moscow region, Russia

<sup>2</sup> Centro di Studio per la Chimica dei Plasmi del Consiglio Nazionale delle Ricerche, Dipartimento di Chimica, Università di Bari, Italy

In the last years a number of papers have appeared on the negative mobility (drift velocity) of electrons in low temperature plasmas, in particular in Ar:Cl<sub>4</sub> [1], Ar:F<sub>2</sub> [2] and Ar:NF<sub>3</sub> [2] mixtures. The purpose of present work is to investigate the influence of the form of the momentum transfer cross section of Ar on the calculated negative electron mobility in Ar:F<sub>2</sub> mixtures.

The investigation was made by solving of an appropriate Boltzman equation for the electron energy distribution function. Two situations were considered: a) steady state negative electron mobility in beam sustained plasmas (the corresponding Boltzmann equation and method of numerical solution are described in [1] ); b) quasi steady state negative electron mobility in decaying plasmas ( Boltzmann equation and solution method are described in [3]).

All calculations were carried out for gas mixture Ar:F<sub>2</sub> = 1:0.005 at room temperature (T=300 K) and at atmospheric pressure. In the case a) the electron beam current  $J_b=0.05 \text{ A cm}^{-2}$  and electron beam energy  $U_b=350$  were chosen. For the sake of completeness we also calculate electron drift velocity in pure Ar.

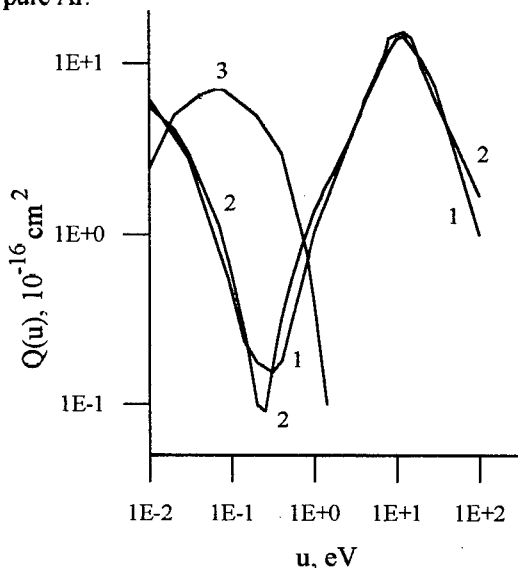


Fig. 1 Momentum transfer cross section of Ar and attachment cross section of F<sub>2</sub>. 1 - QmI, 2 - QmII, 3 - attachment cross section.

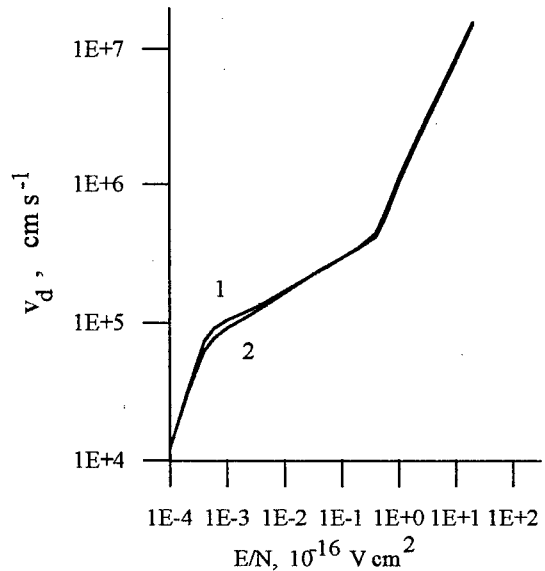


Fig. 2 Electron drift velocity as a function of E/N in pure Ar calculated with different momentum transfer cross sections. 1 - QmI, 2 - QmII

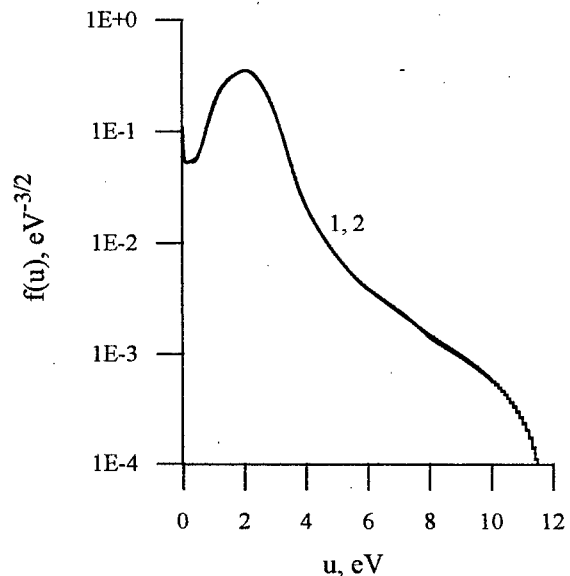


Fig. 3 Electron energy distribution function in electron beam sustained Ar:F<sub>2</sub> plasmas calculated with different momentum transfer cross sections.  $E/N = 2 \cdot 10^{-18} \text{ V cm}^{-2}$ , 1 - QmI, 2 - QmII

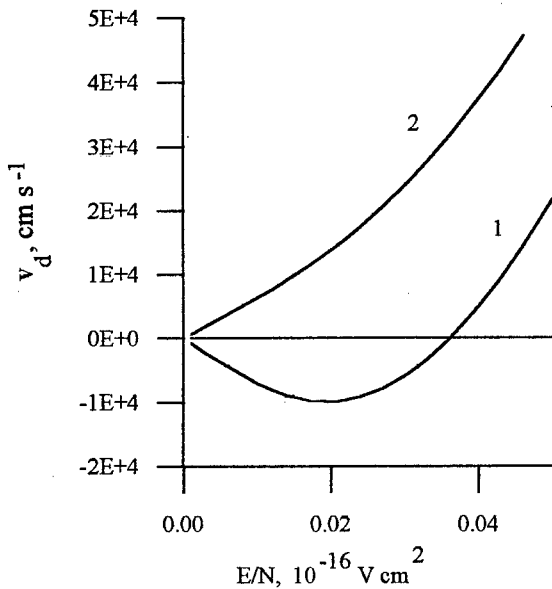


Fig. 4 Electron drift velocity in electron beam sustained Ar:F<sub>2</sub> plasmas calculated with different momentum transfer cross sections. 1 - Q<sub>mI</sub>, 2 - Q<sub>mII</sub>

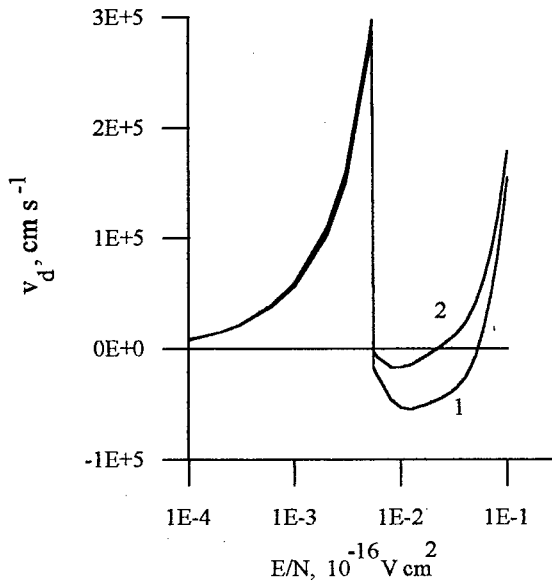


Fig. 5 Electron drift velocity as a function of E/N in decaying Ar:F<sub>2</sub> plasmas calculated with different momentum transfer cross sections. 1 - Q<sub>mI</sub>, 2 - Q<sub>mII</sub>.

Two momentum transfer cross sections of Ar were used in calculations: Q<sub>mI</sub> - [4] and Q<sub>mII</sub> - [5] (see figure 1). Cross sections for F<sub>2</sub> were taken from [6].

Electron drift velocity,  $v_d$ , was calculated by formula:

$$v_d = -\frac{1}{3} \frac{E}{N} \sqrt{\frac{2e}{m}} \int_0^\infty \frac{u}{Q_m(u)} \frac{df(u)}{du} du, \quad (1)$$

where  $f(u)$  is the isotropic part of the distribution function,  $e$  and  $m$  are the electron charge and mass respectively,  $u$  is the electron energy (eV),  $N$  is the

density of gas atoms and  $E$  is the electric field strength. Results of calculations are presented in figures 2-5.

As it follows from figure 2, in the case of pure Ar calculated  $v_d$  is practically independent of the choice of Q<sub>m</sub>.

In the case of the beam sustained plasmas situation is completely different (see figure 4). The drift velocity changes dramatically when the cross section Q<sub>mII</sub> instead Q<sub>mI</sub> is used in calculations. To clarify the reason of such significant changes let us consider graphs of electron energy distribution functions presented in figure 3. As it follows from this figure, distribution functions calculated with Q<sub>mII</sub> and Q<sub>mI</sub> are graphically indistinguishable and have a maximum at energies about 2 eV. The reduction in the value of  $f(u)$  at low energies is caused by the removal of slow electrons due to attachment to fluorine (see figure 1). From equation (1) it is clear that electrons at energies where the distribution function has a positive derivative ( $u < 2$  eV) contribute to negative mobility and electrons at energies where the distribution function has a negative derivative ( $u > 2$  eV) contribute to positive mobility. The resulting value of electron mobility depends on the correlation between these two parts of integral (1). In such a case mobility may be very sensitive to small variations of each part. According to figure 1 graphs of Q<sub>mI</sub> and Q<sub>mII</sub> have an intersection at energy about 2 eV, Q<sub>mII</sub>( $u$ ) > Q<sub>mI</sub>( $u$ ) between 0.3 and 2 eV and Q<sub>mII</sub>( $u$ ) < Q<sub>mI</sub>( $u$ ) between 2 and 10 eV. Since  $f(u)$  is practically the same in both cases substitution of Q<sub>mI</sub> by Q<sub>mII</sub> in the integral (1) leads to decreasing (by absolute value) of the negative part of integral and to increasing of the positive part. As a result, electron mobility becomes positive.

As it follows from figure 5, in the case of decaying plasmas calculated  $v_d$  is also sensitive to the form of the momentum transfer cross section.

This work was supported by Russian Basic Research Foundation 96-02-19265.

## References

- [1] N.A. Dyatko, A.P. Napartovich: Pis'ma Zh. Tekh. Fiz. 13 (1987) 1457 (Sov. Tech. Phys. Lett. 13 872)
- [2] Z. Rozenberg, M. Lando, M. Rokni: J. Phys. D: Appl. Phys., 21 (1988) 1593
- [3] N.A. Dyatko, A.P. Napartovich: Proc. XIth Europ. Sect. Conf. on Atom and Molecule Physics in Ionized Gases (St Petersburg, Russia, 1992) p.127
- [4] L.S. Frost, A.V. Phelps: Phys. Rev., 136 A (1964) 1538
- [5] J.L. Pack, R.E. Voshall, A.V. Phelps, L.E. Kline: J. Appl. Phys., 71 (1992) 5363
- [6] H.R. Scullerud: Austr. J. Phys., 36 (1983) 845

# ELECTRON INTERACTIONS WITH $\text{CCl}_2\text{F}_2$

L. G. Christophorou\*, J. K. Olthoff, and Yicheng Wang\*

National Institute of Standards and Technology, Gaithersburg, MD 20899-0001

We have completed a critically evaluated synthesis of the available information on cross sections and rate coefficients for collisional interactions of low energy electrons with dichlorodifluoromethane ( $\text{CCl}_2\text{F}_2$ ) [1]. This gas has many industrial uses and is of significant atmospheric and environmental interest. While the available data are limited, particularly for electron collision cross sections, a reasonably complete set of cross sections and transport data are assembled.

The work presented here includes a review, an assessment, and a discussion of the following processes related to electron interactions with  $\text{CCl}_2\text{F}_2$ : (1) *electron scattering*, including cross sections for total electron scattering, momentum transfer, differential elastic electron scattering, integral elastic electron scattering, and inelastic electron scattering for rotational and vibrational (direct and indirect) excitation; (2) *electron impact ionization*, including cross sections for total, partial, and double ionization, and coefficients for electron impact ionization; (3) *electron attachment*, including cross sections, rate

constants, and coefficients, and their energy and temperature dependencies, dissociative attachment fragment anions, and negative ion states; (4) *optical emission under electron impact*; and (5) *electron transport*, including electron drift velocity and ratio of transverse electron diffusion coefficient to electron mobility.

Figure 1 shows the cross sections (as a function of electron energy,  $\epsilon$ ) for total electron scattering, total direct vibrational excitation, integral elastic electron scattering, total ionization, and total electron attachment. These data are based primarily upon available experimental data. Stated uncertainties of the data from which these cross sections were derived vary from  $\pm 5\%$  to  $\pm 25\%$ . Other cross sections, not presented here, due to space limitations or uncertain reliability, are discussed in Ref. [1].

The structure in the total electron scattering and total electron attachment cross sections is due to negative ion resonances. The average positions of these resonances

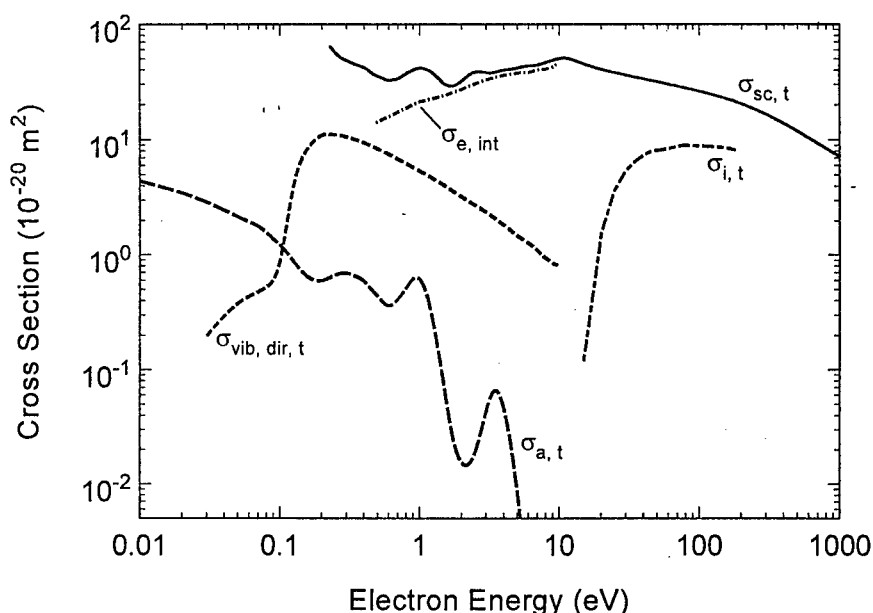


Fig. 1 Recommended cross sections for: total electron scattering,  $\sigma_{sc,t}(\epsilon)$ ; integral elastic electron scattering,  $\sigma_{e,int}(\epsilon)$ ; Bohr dipole approximation of total direct vibrational excitation,  $\sigma_{vib,dir,t}(\epsilon)$ ; total ionization,  $\sigma_{i,t}(\epsilon)$ ; and total electron attachment,  $\sigma_{a,t}(\epsilon)$ . Values for  $\sigma_{e,int}(\epsilon)$  and  $\sigma_{vib,dir,t}(\epsilon)$  are from Ref. [3], and the values for  $\sigma_{i,t}(\epsilon)$  are from Ref. [4]. Values for  $\sigma_{sc,t}$  and  $\sigma_{a,t}$  are synthesized from several independent measurements.



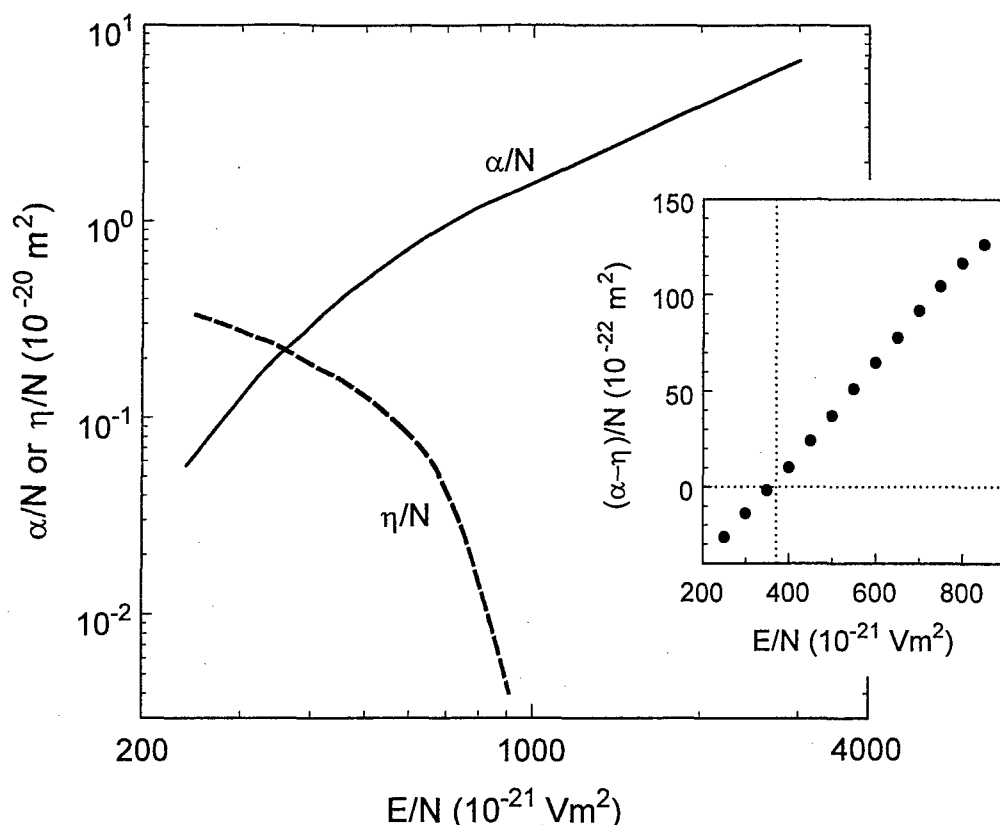


Fig. 2 Recommended density-reduced coefficients, based upon several experimental measurements, for electron impact ionization,  $\alpha/N$ ; attachment,  $\eta/N$ ; and effective ionization  $(\alpha-\eta)/N$ .

(below 10 eV), determined from the results of a number of experimental methods, are: 0.9 eV, 2.5 eV, 3.5 eV, 6.2 eV, and 8.9 eV. The 8.9 eV resonance lies in the region of electronic excitation and most likely is associated with excited electronic states. The 0.9 eV resonance is likely to be due to the lowest negative ion state which has a shallow minimum about 0.4 eV below the zero-level, as is indicated by the positive value of the adiabatic electron affinity of  $\text{CCl}_2\text{F}_2$  reported by Dispert and Lacmann [2].

The  $\text{CCl}_2\text{F}_2$  molecule fragments rather extensively under electron impact, principally via dissociative ionization and dissociative attachment; the latter process is temperature dependent. No measurements have been made to investigate dissociation into neutral fragments.

Figure 2 shows a plot of our recommended values for the coefficients of electron attachment, ionization, and effective ionization. Stated uncertainties for the coefficient data from which these values are derived range from  $\pm 3\%$  to  $\pm 15\%$ . Analysis of experimental measurements indicates that the effective ionization is zero when  $E/N = (371 \pm 5) \times 10^{-21} \text{ Vm}^2$  (one standard deviation).

The data in Figs. 1 and 2 can form the basis of Boltzmann and/or Monte Carlo calculations to determine model-dependent collision cross section sets for this molecule.

Such information is required along with additional experimental measurements on a wide range of electron collision processes for this molecule, foremost electron-impact cross sections for momentum transfer and dissociation of  $\text{CCl}_2\text{F}_2$  into neutral species.

The recommended data for this molecule, and for  $\text{CF}_4$  (Ref. [5]) and  $\text{CHF}_3$  (Ref. [6]), can be found on the WWW at <http://www.eeel.nist.gov/811/refdata>.

- [1] L. G. Christophorou, J. K. Olthoff, and Y. Wang, *J. Phys. Chem. Ref. Data* (submitted).
- [2] H. Dispert and K. Lacmann, *Intern. J. Mass Spectrom. Ion Phys.* **28**, 49 (1978).
- [3] A. Mann and F. Linder, *J. Phys. B* **25**, 1633 (1992).
- [4] K. Leiter, P. Scheier, G. Walder, and T. D. Märk, *Intern. J. Mass Spectrom. Ion Processes* **87**, 209 (1989).
- [5] L. G. Christophorou, J. K. Olthoff, and M. V. V. S. Rao, *J. Phys. Chem. Ref. Data* **25**, 1341 (1996).
- [6] L. G. Christophorou, J. K. Olthoff, and M. V. V. S. Rao, *J. Phys. Chem. Ref. Data* **26**(1), in press (1997).

\* Also at the Department of Physics, The University of Tennessee, Knoxville, TN 37996.

# Stationary electron distribution functions in multiple double layers

L. Conde and L. León  
Departamento de Física Aplicada.  
ETSI Aeronáuticos. UPM.  
28040 Madrid, (Spain).

## 1 Introduction.

In recent experiments with glow discharges with hemispherical symmetry, the radial plasma potential profile presents successive double layers joined in series [1]. These staircase electrostatic structures, are currently termed as *multiple double layers*. The plasma potential jumps separate concentric plasma sheaths with different properties and the outermost double layer limits with the positive column of the discharge. The electrons collected over this external boundary of the structure are later focused over a cavity formed anode which leaks neutral gas. The number of double layers, or equivalently, the quantity of plasma shells in the structure could be controlled by both, the discharge current and mass flow rate [1].

In this paper we discuss the structure and properties of the electron energy distribution functions along the axis of symmetry of structures composed by two or three successive double layers which constitute the boundary between different plasmas. The properties of the electric discharge and the details of the equipment and techniques employed are described in Ref. 1.

## 2 Experimental results.

In Figure 1 we represent the measured plasma potential profile along the axis of symmetry of the structure. The thickness of the plasma potential jump of the double layer is below the spatial resolution of our measurements. Then, the detailed structure of the double layer voltage drop could not be resolved.

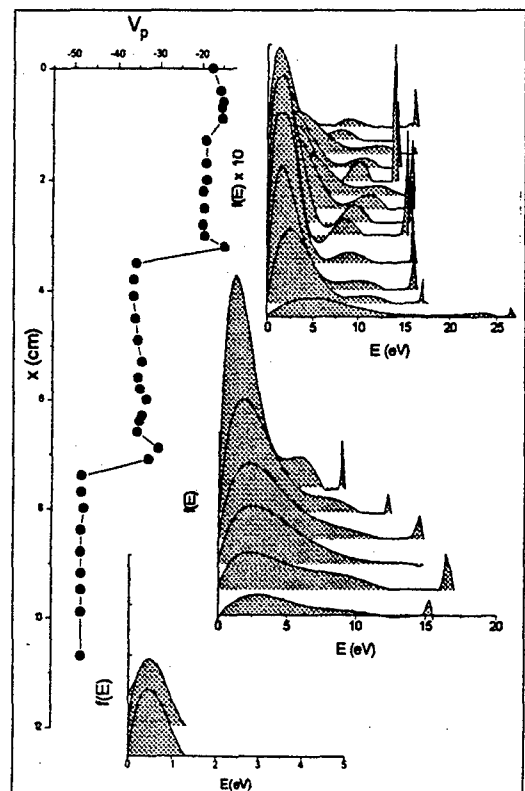


Figure 1: Radial plasma potential profile and electron energy distribution functions for different points along the radial coordinate  $X$ . The electron density  $f(E)$  is in arbitrary units.

In consequence, the electron distribution functions were obtained from the voltage current characteristic curves of collecting Langmuir probes at points where the plasma potential could be clearly determined [1 - 5].

The distribution functions corresponding to the positive column corresponds to the low potential values of Figure 1, which are roughly Maxwellian. The discharge current in this case was  $I_d = 40$  mA and the neutral gas mass flow rate 0.83 sccm (standard cubic centimeters). The electrons are accelerated towards the anode crossing the first plasma potential jump. Then, inside the new plasma shell, the electron distribution function spreads and later splits in two different peaks as the electron progress towards the anode. The low energy thermal population grows and a high energy group of electrons appear. The presence of this peculiar group of electrons was evidenced by the linear growth of the current collected with the bias voltage in the characteristic curves of the Langmuir probes [4]. The energy of the beam and peak height corresponding to this electron beam component was estimated by the corresponding knee in the characteristic curve in logarithmic scale [4].

This monoenergetic population becomes more important after the second plasma potential jump where three different populations coexist. In the plasma shell closer to the anode, the low energy thermal population grows. This is in accordance with the increment in the measured number electron density  $n_e$ . In addition, two different populations appear, a high energy monoenergetic population and a small intermediate energy peak.

### 3 Discussion and conclusions.

We conclude that electron populations at the high voltage side of the double layer presents contains different groups of electrons. First, a thermal Maxwellian component and groups of electrons accelerated by the double layer plasma potential drop. Secondly, a growing monoenergetic population which becomes more important as the density of the plasma shell is increased. On the

basis of our experimental data, we are not in position to determine the origin of this beam component. These monoenergetic group of electrons is not present in the positive column of our discharge and are originated by the multiple double layer structure. We conjecture that such monoenergetic electrons would be generated by a mechanism similar to the so called *hollow cathode effect* [6, 7]. The double layers presented in the structure are tridimensional and electrons could execute a pendulum motion between both sides of the plasma potential drop. Several models predict that the final result of this process would be the narrowing of the electron distribution corresponding to a particular group of electrons [6, 7].

### 4 References

1. L. Conde and L. León, *Phys. Plasmas*, 1, (8), (1994), 2441.
2. L. Conde, L. León and L.F. Ibañez. Accepted for publication in *IEEE Transactions of Plasma Science*.
3. Y.P. Raizer, *Gas Discharge Physics*, Berlin, Springer Verlag, (1991), Ch. VIII.
4. Hershkowitz, N. How Langmuir probes work, in *Plasma diagnostics. Discharge parameters and Chemistry*, O. Auciello and D.L. Flamm, Editors. London, (1989), Academic Press.
5. Vannaroni, G. et al. *J. Appl. Phys.* 71, (10), (1992), 4709.
6. V.I. Kobolov and L.D. Tsendin, *Plasma Sources Sci. Technol.* 4, (1995), 551.
7. V.I. Kobolov and L.D. Tsendin, *Phys. Rev. A.*, 46, (1992) 7837.

# NO(A<sup>2</sup>Σ<sup>+</sup>) EXCITATION MECHANISM IN N<sub>2</sub>-O<sub>2</sub> PULSED RF DISCHARGE

S. De Benedictis, G. Dilecce and M. Simek<sup>#</sup>

Centro di studio per la Chimica dei Plasmi - CNR

c/o Dipartimento di Chimica Università di Bari, via Orabona, 4 - 70126 Bari - ITALY

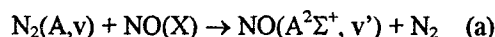
<sup>#</sup> Institute of Plasma Physics ASCR, Za Slovankou 3, 18200 Prague 8, Czech Republic

## 1. Introduction

The study of N<sub>2</sub>-O<sub>2</sub> mixture discharges is currently receiving renewed attention, both theoretical and experimental, because of its implications for environmental issues, chemical synthesis, material treatment and testing, as for spacecraft surface protective materials. Recent research work on this topic is devoted to DC, microwave and rf discharge investigation, under subsonic and supersonic flow regimes, both experimental and theoretical [1].

The kinetics in N<sub>2</sub>-O<sub>2</sub> plasma discharges is rather complex since, together with N<sub>2</sub>, O<sub>2</sub>, N, O, NO, N<sub>2</sub>O, NO<sub>2</sub> ground state species, numerous excited states are produced [1]. Because of this complexity most of the elementary kinetics have been studied in afterglow conditions selecting as much as possible single reaction channels.

One such process among the many is the excitation of NO(A<sup>2</sup>Σ<sup>+</sup>) by collision with the nitrogen triplet metastable:

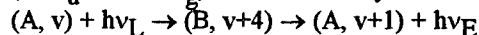


whose observable product is p+12Xthe strong NO-γ band emission. Levels v = 0, 1 and 2 of the metastable contribute to this process, and excitation of levels v' = 0, 1 of NO(A) has been observed [2]. We have studied process (a) in a rf pulsed discharge in order to identify the source of NO-γ band emission in our system. In this contribution we present the evidence that process (a) is by far the main NO(A) excitation mechanism. To this end we have used a Time-Resolved Laser Induced Fluorescence (TRLIF) technique to monitor the temporal behaviour of N<sub>2</sub>(A, v = 0, 1, 2) and of NO in the post-discharge, and a time-resolved detection of NO-γ band emission. Proper correlation of the experimental outcomes provides the mentioned result. A practical consequence of this knowledge is that the strong γ band emission can be used as a monitor of the nitrogen triplet metastable.

## 2. Experimental

The discharge is a typical parallel plates, capacitively coupled configuration, with 10 cm id. electrodes spaced by 5.5 cm. The 27 MHz rf excitation is fully modulated by a 100 Hz square pulse. We have used for

the nitrogen metastable a LIF excitation-detection scheme involving the Δv=4 and Δv=3 sequences of the (A<sup>3</sup>Σ<sub>u</sub><sup>+</sup> ← B<sup>2</sup>Π<sub>g</sub>) First Positive System transitions:



The laser, a Nd-YAG pumped dye laser with Rhodamine 640 and 610/640 delivers 30-40 mJ at λ<sub>L</sub> with a 10 Hz repetition rate. LIF detection of NO(X, v=0) level has been achieved by the excitation of (0,0) band at 226.28 nm and detection of (0,1) band at 236.33 nm of NO(A<sup>2</sup>Σ<sup>+</sup> - X<sup>2</sup>Π) γ System. The proper laser wavelength is obtained by a non linear mixing technique, in which R590 dye is pumped by the second harmonic of the Nd-YAG, and the doubled dye beam is mixed with the Nd-YAG fundamental beam at 1.06 μm. BBO crystals have been used for second harmonic generation and mixing. About 800 μJ per pulse are obtained at the required wavelength.

The laser operation is synchronised to the discharge pulse, and the laser shot is fired at a computer controlled variable delay with respect to the discharge switch-off. The fluorescence light passes through a 1 m fl monochromator, is revealed by a fast side-on photomultiplier, and measured by a 500 Msamples/s, 300 MHz Bw digitizing O-scope. The phototube supply is pulsed, so that its operation is restricted to a 25 μs window synchronised to the laser pulse. This allows to avoid the saturation of the last dynodes voltage partitioners due to the discharge induced continuous emission, and to raise the saturation level close to the space charge limit. This is very useful in this case since the discharge emission at λ<sub>E</sub> is comparable to the fluorescence intensity. Further details about the discharge and LIF apparatus can be found in [3].

The NO γ band emission measurement is achieved by the O-scope triggered by the discharge pulse. The monochromator is tuned to one of the two heads of the (0,3) band, at 259.57 nm of the (A<sup>2</sup>Σ<sup>+</sup> ← X<sup>2</sup>Π) γ-system.

## 3. Results

The decay of N<sub>2</sub>(A, v=0,1,2) and of the (0,3) band of NO γ-system in the post-discharge has been measured at O<sub>2</sub> percentages in the mixture in the range 0 - 23 % and at 0.1 Torr total pressure. All the decays are single exponential, so a first order quenching rate can be fitted for each of them. It is important to underline that

also NO(A) decay is single exponential with a quite large time constant ( $>100 \mu\text{s}$ ), with complete absence of a fast component (i.e. with a time constant  $<1 \mu\text{s}$ ) that clearly indicates the minor role of electron impact excitation with respect to collisional excitation by long living species. In order to compare  $\text{N}_2(\text{A})$  and  $\text{NO}(\text{A})$  decays, the decays of  $v=0, 1$  and  $2$  levels are combined by a weighted sum and a resultant decay rate is then extracted. The weights are calculated as the product of the branching ratios for  $\text{NO}(\text{A}, v=0)$  excitation by levels  $v=0, 1, 2$  of the metastable [2] and the population ratios of these three vibrational levels, calculated from the LIF measurements by a proper scaling [4]. This resultant decay rate is reported in fig. 1, and represents the decay rate of the excitation source of  $\text{NO}(\text{A}, v=0)$  by process (a). The  $\gamma$ -band decay must be also corrected according the time evolution of  $\text{NO}(\text{X})$  in the post-discharge in order to correlate it to the decay of its excitation sources. We have infact observed by LIF that  $\text{NO}$  density slightly increases in the post-discharge, as shown in fig. 2. The decay rate of  $\text{NO} \gamma$ -band after such correction is reported in fig. 1.

A clear correlation of the two rates in fig. 1 for all the mixture composition indicates process (a) as the most important  $\gamma$ -band excitation source. Another indication comes from verification of the following relation that holds in case of process (a) for each  $\text{N}_2\text{-O}_2$  mixture:

$$\frac{I_\gamma}{[\text{NO}] \sum_v W_v [\text{N}_2(\text{A}, v)]} = \text{const}$$

where  $I_\gamma$  is the  $\gamma$ -band emission intensity and  $W_v$  are the same weight described above.

A final note concerns the rotational excitation of  $\text{NO}(\text{A})$  that, as it comes out from fitting partially resolved rotational structure of (0,2) and (0,3) bands, cannot be characterised by a single Boltzmann temperature. Population of high  $J$ -levels can be characterised by significantly higher rotational temperature than low  $J$ -levels. Due to the short radiative time (200 ns) this could be related to the excitation mechanism and offers interesting matter for further investigation.

#### 4. Acknowledgements

This work has been partially supported by the Italian Space Agency (ASI). M. Simek undertook this work with the support of the "ITCP Programme for Training and Research in Italian Laboratories, Trieste, Italy".

#### 5. References

- [1] "Molecular Physics and Hypersonic flows", M. Capitelli Ed. NATO-ASI, Vol. C-482, Kluwer Ac. Publishers, 1996.
- [2] L.G. Piper, L.M. Cowles and W.T. Rawlins, *J. Chem. Phys.* **85** (1986) 3369.

[3] S. De Benedictis, G. Dilecce, *J. De Physique*, **6** (1996) 1189

[4] S. De Benedictis and G. Dilecce, submitted for publication.

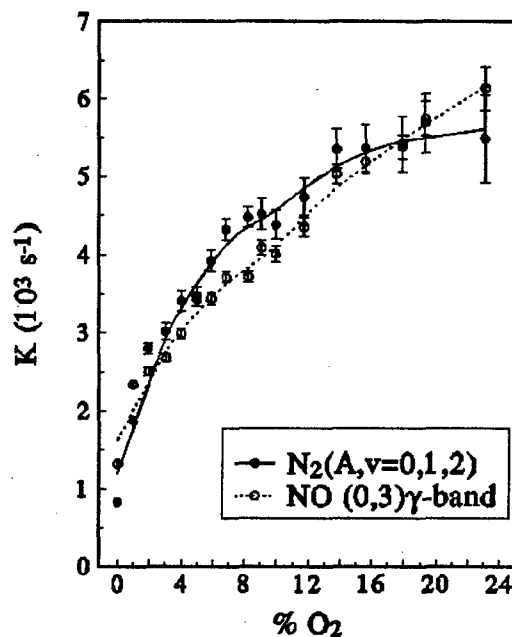


Fig.1 Decay rates of the combined  $\text{N}_2(\text{A}, v=0,1,2)$  levels and of  $\text{NO} \gamma$ -band corrected by  $\text{NO}(\text{X})$  time evolution.

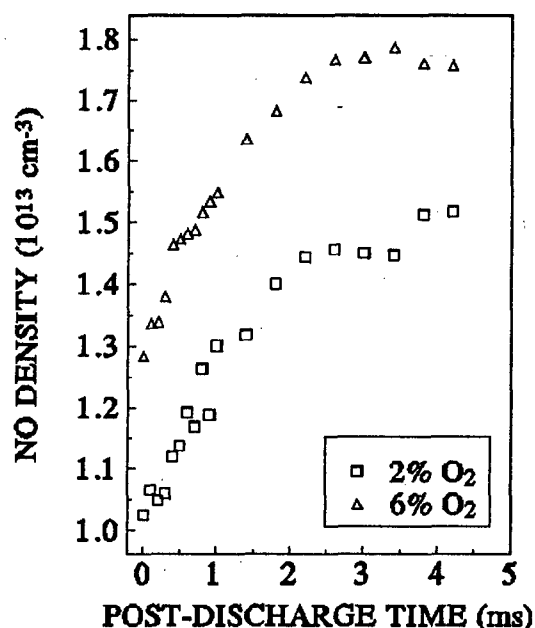


Fig.2 Examples of  $\text{NO}$  density behaviour in the post-discharge

**TEMPERATURE DEPENDENCE OF DEEXCITATION RATE CONSTANTS  
OF  $\text{Ne}(^3\text{P}_1)$  AND  $\text{Ne}(^3\text{P}_2)$  BY Ar, Kr, Xe, AND  $\text{N}_2$ .**

D. B. Khadka,\* K. Yamada,\* Y. Fukuchi,\* T. Odagiri,\* K. Kameta,\* M. Ukai<sup>†</sup>,  
N. Kouchi\* and Y. Hatano\*

\* Department of Chemistry, Tokyo Institute of Technology, Meguro-ku, Tokyo 152 Japan

<sup>†</sup> Department of Applied Physics, Tokyo University of Agriculture and Technology, Koganei-shi, Tokyo 184, Japan.

Collisional deexcitation of excited rare gas atoms by atoms and molecules is of great importance in both fundamental and applied sciences, which provides the information on essential features of chemical reactions, in particular, those including electronic energy transfer [1-4]. The collisional deexcitation is a key also to understand fundamental processes in the interaction of ionizing radiation with matter and the phenomena in ionized gases [3-5]. A major part of the deexcitation of the lowest excited neon and helium atoms by atoms and molecules, M, is ascribed to the collisional ionization of M [1-5].

Collisional deexcitation processes of excited neon atoms have not been extensively studied in comparison with those of excited helium atoms [1-5]. Our previous studies of the collisional deexcitation of excited rare gas atoms have shown that a pulse radiolysis method has a clear advantage over the other methods such as flowing afterglow and beam methods to obtain absolute rate constants or cross sections for the deexcitation of excited rare gas atoms not only in metastable states but also in resonant states, [1,3-5] the collisional deexcitation of  $\text{Ne}(^3\text{P}_1)$  and  $\text{Ne}(^3\text{P}_2)$  by M (M = Ar, Kr, Xe, and  $\text{N}_2$ ) has been studied in detail in this experiment. The temperature dependence of the rate constants for the deexcitation has been measured in the temperature range from 133 to 295K using a pulse radiolysis method and thus the collisional energy dependence of the deexcitation cross sections is obtained.

The apparatus and procedure in the present pulse radiolysis experiment have been described in detail previously [3-5]. Briefly, after an irradiation by an intense electron beam pulse onto a mixture of Ne with a trace amount of  $\text{SF}_6$  and M in a gas cell, the time-resolved optical absorption of  $[\text{Ne}(^3\text{P}_1): 1s_4 \rightarrow 2p_3]$  at 607.43 nm was measured, thereby, the time dependent variation of the density of  $\text{Ne}(^3\text{P}_1)$  was obtained by means of newly developed absorption law. The time-resolved optical absorption of  $[\text{Ne}(^3\text{P}_2): 1s_5 \rightarrow 2p_8]$  at 633.44 nm was also measured. A trace amount of  $\text{SF}_6$  was added to remove thermal electrons produced in irradiated sample gases. The cell is kept within the error limit of  $\pm 2$  degree at temperatures ranging from room temperature to 133K.

The total deexcitation rate of  $\text{Ne}^*$ ,  $\tau^{-1}$ , is written as

$$\tau^{-1} = \tau_0^{-1} + k_{\text{SF}_6} [\text{SF}_6] + k_{\text{M}} [\text{M}],$$

where  $[\text{SF}_6]$  and  $[\text{M}]$  are the densities of  $\text{SF}_6$  and M in Ne- $\text{SF}_6$ -M system, respectively. The slope of  $\tau^{-1}$  vs.  $[\text{M}]$  plots as one of the results is shown in Fig. 1 gives the deexcitation rate constants,  $k_{\text{M}}$ , under constant  $[\text{SF}_6]$ . The velocity averaged or thermally averaged cross section is given as  $\sigma_{\text{M}} = k_{\text{M}}(\pi\mu/8k_{\text{B}}T)^{1/2}$  at a mean collisional energy,  $E = (3/2)k_{\text{B}}T$ , where  $\mu$ ,  $k_{\text{B}}$ , and T are the reduced mass of Ne-M, Boltzmann constant, and absolute temperature, respectively.

The obtained experimental cross sections for the deexcitation of  $\text{Ne}(^3\text{P}_1)$  by Ar, Kr, Xe and  $\text{N}_2$  and  $\text{Ne}(^3\text{P}_2)$  by Ar, Kr, and Xe are shown in Fig. 2 as a function of mean collisional energy. The cross sections for Xe are clearly larger than Ar but slightly larger than Kr for both  $\text{Ne}(^3\text{P}_1)$  and  $\text{Ne}(^3\text{P}_2)$ . On the other hand, the cross sections for Xe and Kr are larger than  $\text{N}_2$  but slightly smaller than Ar for  $\text{Ne}(^3\text{P}_1)$ . Since the deexcitation of a resonant  $\text{Ne}(^3\text{P}_1)$  atom both contributions from an electron exchange interaction and a dipole-dipole interaction are involved, whereas that for a metastable  $\text{Ne}(^3\text{P}_2)$  atom is mainly ascribed to an electron exchange interaction. However, the optical oscillator strength for a  $\text{Ne}:^3\text{P}_1 \rightarrow ^1\text{S}_0$  transition is very small (0.010) in comparison with that for the  $\text{He}:2^1\text{P} \rightarrow 1^1\text{S}$  (0.276) [6]. Thus it is not likely that the deexcitation of  $\text{Ne}(^3\text{P}_1)$  is mainly ascribed to a dipole-dipole interaction. That is why the cross sections for  $\text{Ne}(^3\text{P}_1)$  are generally a little larger than those of  $\text{Ne}(^3\text{P}_2)$ . Moreover, we have performed the optical model calculation, which shows that an electron exchange interaction plays an important role in the deexcitation of  $\text{Ne}(^3\text{P}_1)$  in collisions with Ar, Kr, Xe, and  $\text{N}_2$  as one of the results is shown in Fig. 3 [7]. The calculation and comparison of the present experimental results indicates that although the deexcitation cross sections for  $\text{Ne}(^3\text{P}_1)$  are enhanced by a weakly allowed dipole-dipole interaction, the deexcitation processes for  $\text{Ne}(^3\text{P}_1)$  and  $\text{Ne}(^3\text{P}_2)$  are dominated by collisional ionization induced by an electron-exchange interaction.

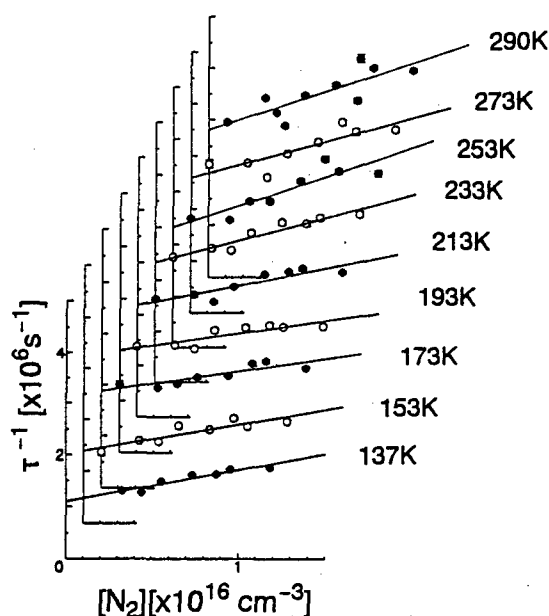


Fig. 1. Kinetic plots of the total deexcitation rate of  $\text{Ne}(^3\text{P}_1)$  vs. the number density of  $\text{N}_2$

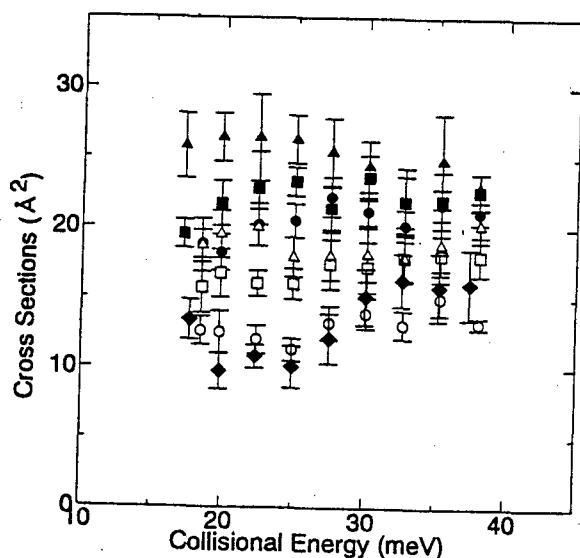


Fig. 2. The experimental cross sections for the deexcitation of  $\text{Ne}(^3\text{P}_1)$  by  $\bullet$ :Ar,  $\blacksquare$ :Kr,  $\blacktriangle$ :Xe, and  $\blacklozenge$ : $\text{N}_2$  and  $\text{N}(^3\text{P}_2)$  by  $\circ$ :Ar,  $\square$ :Kr and  $\triangle$ :Xe.

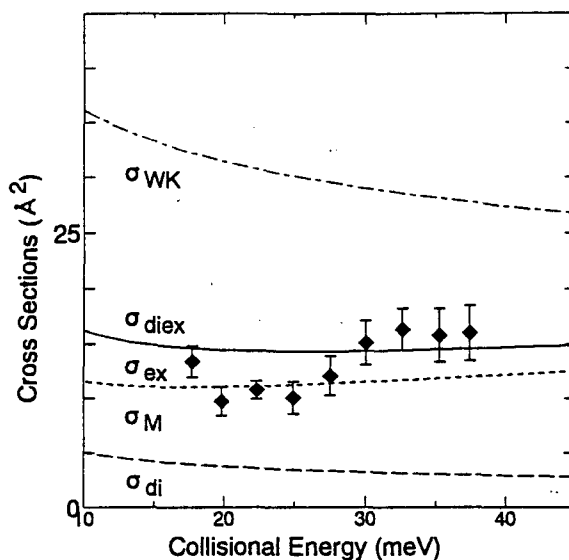


Fig. 3. The experimental cross sections for the deexcitation of  $\text{Ne}(^3\text{P}_1)$  by  $\bullet$ : $\text{N}_2$ . The total Penning ionization cross sections by an optical-model calculation of  $---$   $\sigma_{\text{di}}$ ,  $---$   $\sigma_{\text{ex}}$ ,  $---$  and  $\sigma_{\text{diex}}$  considering the dipole-dipole interaction, the electron exchange interaction, and both, respectively, and semi-classical cross sections,  $---$   $\sigma_{\text{WK}}$ .

#### References

- [1] A. J. Yencha, *Electron Spectroscopy—Theory, Techniques and Applications*, vol. 5, edited by C. R. Brundle and A. D. Baker, (Academic, New York, 1984), p.197.
- [2] A. Niehaus: *Adv. Chem. Phys.*, 45, (1981) 399, *Physics of Electronic and Atomic Collisions*, edited by S. Datz (North-Holland, Amsterdam, 1982), p.237.
- [3] Y. Hatano, "Pulse Radiolysis in the Gas Phase", in "Pulse Radiolysis", edited by Y. Tabata, (CRC Press, Boca Raton, 1991), p.199.
- [4] M. Ukai and Y. Hatano, "Gaseous Electronics and Its Applications", ed. R.W. Crompton, M. Hayashi, D. E. Boyd and T. Makabe, KTS Publ., Tokyo, (1991), p.51.
- [5] D. B. Khadka, Y. Fukuchi, K. Kameta, M. Ukai, N. Kouchi and Y. Hatano, *Proceedings of the 7<sup>th</sup> China-Japan Bilateral Symposium on Radiation Chemistry*, 1996.
- [6] A. A. Radzig and B. M. Smirnov, "Reference Data on Atoms, Molecules and Ions", *springer series in chemical physics*, 31 (Springer-Verlag Berlin Heidelberg, New York, Tokyo, 1985).
- [7] D. B. Khadka, Y. Fukuchi, M. Kitajima, K. Hidaka, M. Ukai, N. Kouchi and Y. Hatano, *J. Chem. Phys.*, to be published.

# Dip structure on EEDF in diffused N<sub>2</sub> plasmas

K.Ohe, T.Kimura and M.Nakamura,

*Department of Systems Engineering, Nagoya Institute of Technology,  
Showa - ku, Nagoya, 466, Japan*

## 1 Introduction

Electron energy loss process due to the vibrational collision produces a peculiar shape in electron energy distribution (EEDF) in low pressure N<sub>2</sub> discharges [1,2]. The effect of the collision process is strong for the low energy range, reducing a large amount of low energy electrons, so that even a dip structure appears about at 3 eV in EEPF (electron energy probability). Such a dip structure has been experimentally observed in a kind of dc glow N<sub>2</sub> discharges as well as in ECR N<sub>2</sub> plasmas [3]. Since the effect of vibrational collision process depends on the parameters, for instance, the gas pressure and the electron density, the EEPF detection over a wide range of parameters may stimulate the investigations of N<sub>2</sub> discharge plasmas.

In the present paper, we describe the observations of EEPF in a diffused N<sub>2</sub> plasma of low pressure dc glow discharges.

## 2 Experiment

N<sub>2</sub> plasmas generated by a dc discharge between a mesh anode and hot cathode made of tungsten wire of 0.3mm $\phi$  was diffused in a cylindrical glass chamber with 85cm length and 11cm $\phi$ . The plasma density exponentially decreased toward the chamber end. A movable cylindrical Langmuir probe with 12mm length and 0.1mm $\phi$  was installed in the plasma. The probe current detected as a function of a rampwise bias voltage was digitized by a two - channel A/D converter with 12 bits resolution. The second derivative of the current with respect to the bias voltage was obtained by digital filtering technique [4]. Experiment was performed over the range of gas pressure  $p$  from  $2.0 \times 10^{-3}$  Torr to  $2.2 \times 10^{-2}$  Torr and discharge current  $I_d$  from 50mA to 200mA, the electron density  $n_e$  being about  $10^{15} [m^{-3}]$ .

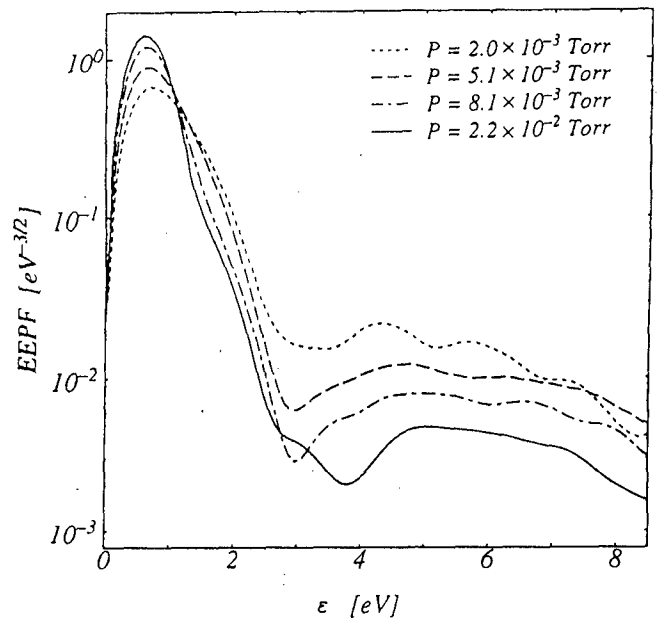


Figure 1: Dependence of EEPF on  $P$ , where the EEPF is normalized by unity.

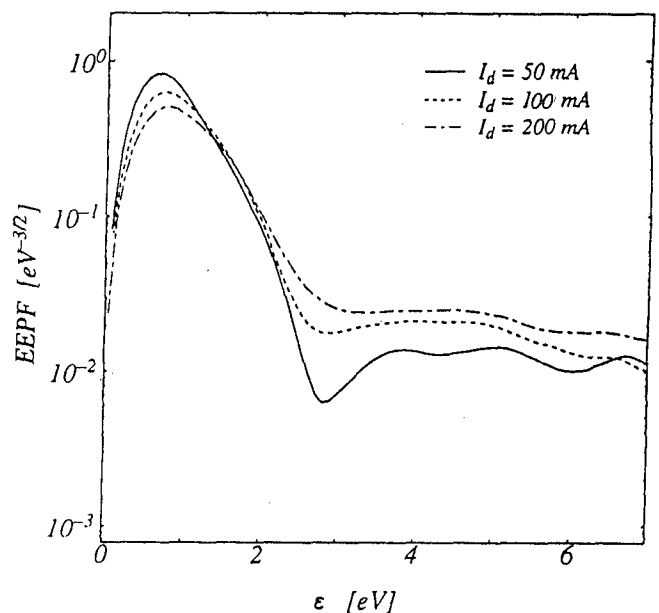


Figure 2: Dependence of EEPF on  $I_d$ .



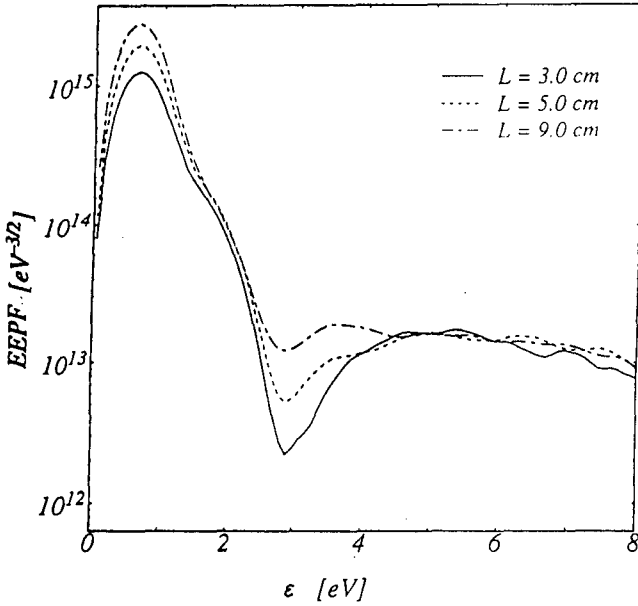


Figure 3: Variation of EPPF along the axial direction, where EPPF at  $L = 9.0\text{cm}$  is normalized by unity.

### 3 Results and Discussion

Some EPPFs depending on  $p$  are shown in Fig 1, where the position  $L$  of probe was  $7.0\text{cm}$  from the wall end of chamber, and  $I_d = 100\text{mA}$ . The dip on EPPF became deep with  $p$ . Such a variation of dip may be caused by the increase of electron energy loss due to the vibrational collision dependent of the increase in  $\text{N}_2$  molecules. A typical dependence of EPPF on  $I_d$  is illustrated in Fig 2, where  $L = 2.0\text{cm}$  and  $p = 2.0 \times 10^{-3}\text{Torr}$ . This figure shows that the dip became shallow with  $I_d$ . The increase in  $n_e$  with increasing  $I_d$  is related with the increase of superelastic collisions between electrons and neutrals with lower vibrational levels, eventually leading to filling the dip. An axial variation of EPPF is shown in Fig 3, where  $p = 8.1 \times 10^{-3}\text{Torr}$  and  $I_d = 50\text{mA}$ . The dip became deep with  $L$ . The density  $n_e$  produced by the dc discharge ( $L \simeq 9.0\text{cm}$ ) decreased toward the wall end due to the particle diffusion as shown by the decrease in the total area of EPPF. The axial decrease in  $n_e$  may contribute to reducing the superelastic collisions, thus enhancing the dip.

Assuming that  $\text{N}_2$  density is the Boltzmann distribution and the V-V and V-T reactions can be neglected, we can obtain simple rate equations for  $v = 0$  and  $v = 1$ . Then we can estimate the vibrational temperature  $T_v$  from the equations in a roughly approximate manner. The value  $T_v$  estimated was about  $2 \times 10^3 \text{ }^\circ\text{K}$ .

### 4 Conclusion

The EPPF was observed in a diffused  $\text{N}_2$  plasma produced by a dc discharge over a pressure range from  $2.0 \times 10^{-3}$  to  $2.2 \times 10^{-2}\text{Torr}$ . A dip in EPPF detected became deep with the increase of pressure and the decrease of the electron density as well as the increase of axial distance from the discharge.

### References

- [1] W.L.Nighan, Phys. Rev. **A2** (1970) 1989.
- [2] D.R.Suhre and J.T.Verdyen, J. Appl. phys. **47** (1976) 4485.
- [3] H.Amemiya, S.Ono and S.Tei, J. phys. Soc. Jpn. **56** (1987) 4312. J. Phys. Soc. Jpn. **63** (1994) 3295.
- [4] T.Kimura, A.yoneya and K.Ohe, Jpn. J. Appl. Phys. **30** (1991) 1877.

# IONIZATION COEFFICIENT IN ARGON-ISOBUTANE MIXTURES

Ines Krajcar Brionić<sup>1,2</sup> and Bernd Grosswendt<sup>2</sup>

<sup>1</sup>Rudjer Bošković Institute, P.O.Box 1016, HR-10001 Zagreb, CROATIA

<sup>2</sup>Physikalisch-Technische Bundesanstalt, D-38116 Braunschweig, GERMANY

## 1. Introduction

Electron multiplication in strong electric fields is the process which enables detection of low-energy ionizing radiation by a proportional counter. It is characterized by the mean gas amplification factor  $M$ , and depends on the type of the gas or gas mixture and its pressure, on the counter geometry and the applied high voltage. The physical quantity which determines the gas amplification is the ionization coefficient  $\alpha$ , defined as the number of secondary electrons formed by an electron per unit pathlength. Usually, the reduced ionization coefficient,  $\alpha/P$ , is referred to as a function of the reduced electric field strength  $S=E/P$ , where  $P$  is the (total) gas pressure.

In uniform electric fields (or slowly-varying non-uniform fields) the  $\alpha/P$  for a gas is a single valued function of  $S$ . The reduced gas gain,  $\ln M/K$ , where  $K=V/\ln(b/a)$  ( $V$  is the applied high voltage,  $b$  and  $a$  are cathode and anode diameters, respectively) is then also a single valued function of  $S$  for different  $K$  (or different pressures  $P$ ). However, in strong electric fields or when the electric field over an electron mean free path varies significantly, the electron cannot reach the equilibrium with the field [1]. Under such *non-equilibrium* conditions the electron transport parameters including  $\alpha/P$ , and therefore the reduced gas gain, are lower than expected.

A large number of UV photons created in the avalanche in a proportional counter filled with pure rare gases makes such counter practically unusable. A certain amount of a quenching admixture has to be added to the rare gas to assure a good proportional counter operation. If the amount of the quenching admixture is not high enough, then the non-quenched photons may cause additional avalanches and the gas gain increases faster than exponentially with the applied high voltage. The deviations from the straight line in a semi-log plot (*non-linear effect*) in gas mixtures limit the highest available gas gain. The purpose of this work is to find the composition of argon-isobutane mixture which assures complete quenching, and to determine the ionization coefficient of isobutane and mixtures in non-uniform electric fields.

## 2. Experiment

A cylindrical stainless steel proportional counter specially designed for low-energy X-ray measurements was used [2-4]. The anode radius was 12.5  $\mu\text{m}$ , and that of the cathode 25 mm. The  $^{55}\text{Fe}$  was used as a source of photons having 5.89 keV. Pure isobutane (>99.95%) and argon-isobutane mixtures of various concentrations (between 2.2 and 50%) at total pressures

10, 20, 30, 60 and 90 kPa were used as counting gases. The range of the reduced electric field strength at the anode surface ( $S_a$ ) covered by the experiment was  $5 \times 10^4 - 1.4 \times 10^6 \text{ Vm}^{-1}\text{kPa}^{-1}$ .

## 3. Results

### 3.1. Gas amplification

An example of gas gain curves for argon-isobutane mixtures at  $P = 30 \text{ kPa}$  is shown in Fig. 1. In pure isobutane at all pressures the gas amplification is an exponential function of the applied voltage in the whole range of gas gains,  $10 < M < 3 \times 10^4$ . In mixtures, gas gain obtained with the same applied high voltage decreases with the increase of isobutane concentration. The slopes of the gas gain curves decrease with the increase of isobutane concentration for constant total pressure. The slopes also decrease with the increase of total pressure for constant concentration fraction.

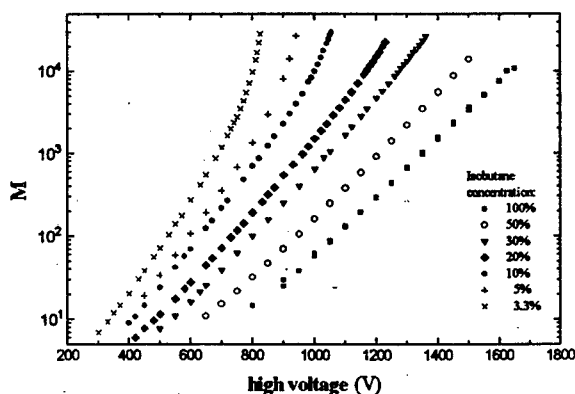


Fig. 1. Gas gain curves for isobutane and argon-isobutane mixtures at total pressure of 30 kPa.

In mixtures with low isobutane concentration a fast increase of the gas gain with the high voltage is observed. The range of the linearity of the gas gain in a semi-log plot narrows with the decrease of isobutane partial pressure. The highest gas gain still in the range of linear dependence,  $M_0$ , is shown in Fig. 2. as a function of the isobutane partial pressure  $p$ . No deviation of the gas gain from the straight line is observed for isobutane partial pressure larger than approximately 10 kPa, and  $M_0 \sim 2 \times 10^4$  for these relatively large partial pressures. The data for lower partial pressures (1-10 kPa) can be fitted by a function

$$M_0 = D (p/\text{kPa})^C \quad (1)$$

where  $C$  and  $D$  are fitting coefficients ( $C = 1.56 \pm 0.09$ ,  $D = 760$ ).

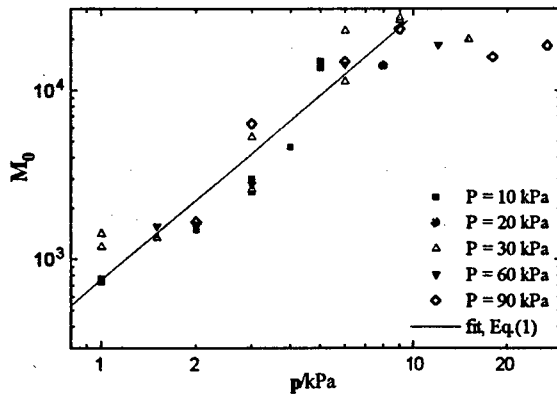


Fig. 2. Maximum gas gain that allows for exponential dependence of the gas gain on the applied high voltage,  $M_0$ , vs. isobutane partial pressure.

The plot of the reduced gas gain,  $\ln M/K$ , obtained under various pressures vs.  $S_a$  does not result in a single curve neither for pure isobutane nor for any mixture. For a constant  $S_a$  value, the reduced gas gain is lower for smaller gas pressures than for larger ones. This is typical of non-equilibrium effect. In pure isobutane the non-equilibrium effect is observed at  $S_a > 3 \times 10^5 \text{ Vm}^{-1} \text{ kPa}^{-1}$ , while in mixtures the corresponding electric field strengths are lower and decrease with the decreasing isobutane concentration.

### 3.2. Ionization coefficient

Gas gain can be calculated if the ionization coefficient  $\alpha/P$  is modeled as a function of  $S$ . Various such models can be found in the literature, but they have all been developed for conditions which result in the equilibrium of electrons with the electric field [1,5]. Recently, Segur *et al.* [1] have modified the gas gain models by taking into account the non-equilibrium effects. The obtained ionization coefficient has a form

$$\alpha/P = A(K) \exp[-B(K)/S] \quad (2)$$

where both  $A$  and  $B$  coefficients are explicit functions of the electric field gradient  $K$ . The mean gas amplification factor is then

$$\ln M/K = A(K)/B(K) \exp[-B(K)/S_a]. \quad (3)$$

The coefficients can be obtained from the measured gas gain data if  $\ln(\ln M/K)$  is plotted vs.  $S_a^{-1}$ . The present data result in linear plots for all studied gases (for mixtures only gas gains smaller than  $M_0$  were considered in the analysis), confirming the relation (2). The slope of the lines changed with the gas pressure. The coefficients  $A$  and  $B$  were determined for each pressure separately. It is found that both coefficients decrease with the increase of the total gas pressure, and for a constant total pressure both increase with the increase of isobutane concentration. The effective ionization potential  $V_i = B/A$  increases with the increase of total pressure, and for low isobutane concentrations it reaches the ionization potential of isobutane.

The ionization coefficient  $\alpha/P$  obtained for pure isobutane is shown in Fig. 3. For comparison, experimental values obtained in uniform electric fields

[6-8] and values calculated under equilibrium conditions [1] are also shown. No significant differences among various data sets are observed for  $S_a < 4 \times 10^5 \text{ Vm}^{-1} \text{ kPa}^{-1}$ . In higher fields, the highest  $\alpha/P$  values are the calculated ones [1], while the measured data in uniform fields [6] are lower, indicating onset of the non-equilibrium effects. Our  $\alpha/P$  curves follow generally the equilibrium curve only for low gains at the same pressure, while at higher gains they increase more slowly and are below the equilibrium curve. A similar behavior of  $\alpha/P$  is observed also in mixtures of the same isobutane concentration at different pressures.

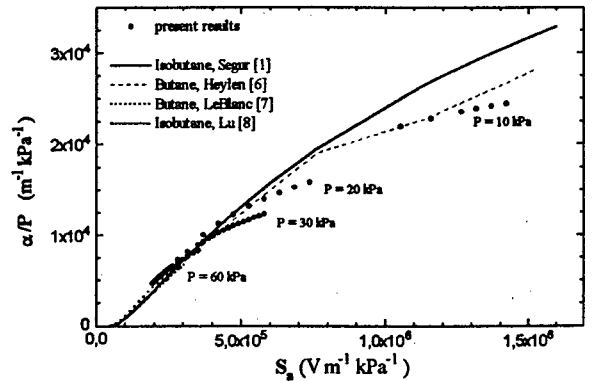


Fig. 3. Reduced ionization coefficient  $\alpha/P$  in isobutane compared to other experimental and theoretical results.

An interesting behavior of  $\alpha/P$  in argon-isobutane mixtures is observed. For a constant  $S_a$  value,  $\alpha/P$  increases with the decrease of isobutane concentration only at relatively low  $S_a$ , and at some value of the field  $\alpha/P$  starts to increase with the increase of isobutane concentration. The crossing point of  $\alpha/P$  curves is observed at about 1, 1.5, 2.5 and  $4 \times 10^5 \text{ Vm}^{-1} \text{ kPa}^{-1}$  for total pressures 90, 60, 30 and 10 kPa, respectively.

### 4. Conclusion

The isobutane partial pressure of 10 kPa regardless of the total pressure is necessary to assure a complete quenching of UV photons in argon-isobutane mixtures and to enable gas gains above  $10^4$ . The ionization coefficient  $\alpha/P$  under non-equilibrium conditions is obtained for pure isobutane and various argon-isobutane mixtures.

Work supported by the Alexander-von-Humboldt Stiftung.

### References

- [1] P. Segur, P. Olko, P. Colautti, Radiat. Prot. Dosim. 61/4 (1995) 323
- [2] D. Srdoč, B. Clark, Nucl. Instr. Meth. 78 (1970) 305
- [3] I. Krajcar Bronić, Radiat. Prot. Dosim. 61 (1995) 263
- [4] I. Krajcar Bronić, B. Grosswendt, Nucl. Instr. Meth. B 117 (1996) 5
- [5] T. Aoyama, Nucl. Instr. Meth. A 234 (1985) 125
- [6] A.E.D. Heylen, Int. J. Electr. 39 (1975) 653
- [7] O.H. LeBlanc, Jun., J.C. Devins, Nature, London, 188 (1960) 219
- [8] C. Lu, K.T. McDonald, Y. Zhu, Nucl. Instr. Meth. A 334 (1993) 328

## On the influence of ionization degree on electron mobility in photoplasma of sodium vapour - inert gas mixture

N.A. Gorbunov, Ph.E. Latyshev, A.S. Melnikov, I.A. Movtchan and I. Smurov\*

Physics Institute, St.-Petersburg University, Ulianovskaya 1, 198904, St. Petersburg, Russia

\* Ecole Nationale d'Ingénieurs de Saint-Etienne, 58, rue Jean Parot, 42023 St.-Etienne Cedex, France

The role of electron-electron collisions in electron energy distribution function (EEDF) formation in gas-discharge plasma, when electron average energy differs from gas temperature because of external electric field, was thoroughly analyzed in [1,2]. It was proved that plasma ionization degree considerably influences on electrons mobility in case when cross section of elastic electron-atom collisions non-monotonously depends on energy (heavy inert gases).

In resonant laser-induced plasma the main mechanism of electrons heating are superelastic collisions with excited atoms. In most experiments resonant transition during laser pulse is brought to saturation ( $\beta = g_0 N_i / g_i N_0 = 1$ , where  $N_i$  and  $g_i$  - concentration and statistical weight of the ground state ( $i=0$ ) and resonant excited state ( $i=1$ )). Relatively high density of resonant excited states ( $\eta \sim 10\text{-}20\%$ ) may be conserved until  $\sim 1 \mu\text{s}$  because of radiation trapping. A problem of electron mobility in laser afterglow plasma through the time range of excited atoms relaxation was not previously studied in details.

This work reports a parametric simulation of electron mobility in (Na + He) and (Na + Ar) mixtures by various ionization degree  $\gamma$ , components concentrations and resonant excited sodium atoms density (correlating with experimental conditions of [3]). Numerical simulation of kinetic equation was performed taking into account electron-electron and elastic electron-atom collisions, excitation and de-excitation by electron impact of resonant Na (3P) states. Electron mobility  $\mu$  versus buffer gas (He and Ar) pressure is presented in Fig.1, Fig.2.

The obtained results show that for Maxwellian distribution (dominant role of Coulomb collisions in EEDF formation) electron mobility in (Na + Ar) mixture exceeds for several times the one in (Na + He) mixture (curves 5,6 Fig.1, 7,8 Fig.2). This effect is sufficiently explained by the fact that the cross-section of elastic collisions in Ar is smaller than the one in He through the considered electron energy range (0.1-1 eV).

When the ionization degree is lower than  $10^{-7}$  the elastic collisions with buffer gas atoms and inelastic collisions with excited

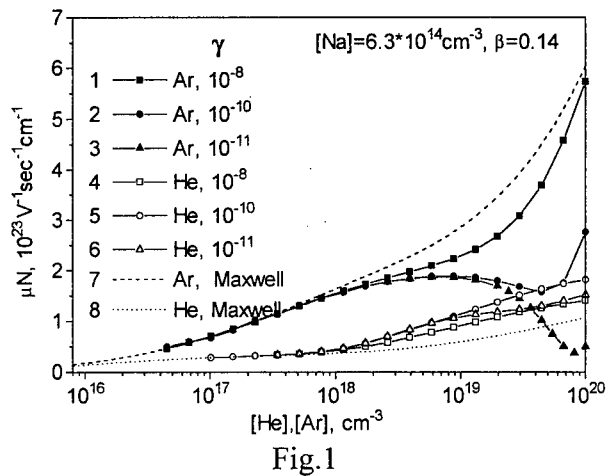


Fig.1

Na atoms notably affects EEDF shape leading to non-equilibrium distribution. In this case electron mobility in (Na + Ar) mixture becomes non-monotonous and reveals a drop for an order of magnitude (curve 3 Fig.1, curve 2 Fig.2), while in (Na + He) mixture the mobility continuously increases and may exceed the mobility in Ar. This obvious contrast in electron behaviour may be explained by different shape of elastic electron-atom collision cross-section in Ar and He. In Ar the cross section increases over (0.3-9) eV. Due to superelastic collisions with excited Na atoms a considerable part of electrons got into this energy range; consequently, the mobility drops. On the contrary, in mixture with He, where elastic collision cross-section reveals a very weak energy dependence, the electron mobility practically remains the same (curves 5,6 Fig.1, curves 3,4 Fig.2).

In [3] the measurements of photoionization current in Na mixture with He, Ne, Ar at (1-300) Torr inert gas pressure

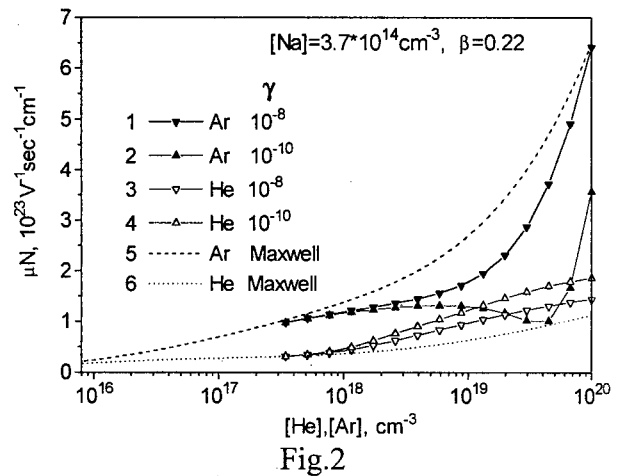


Fig.2

were performed. It was established that by similar experimental conditions the electron current in (Na+He) and (Na + Ne) mixtures is always higher than the one in (Na + Ar). Supposing Maxwellian distribution function the authors explained that effect by some complicated plasma-chemical reactions.

The present simulation clearly demonstrates that the observed decrease of photoplasma electron current may be caused by a drop of electron mobility in (Na + Ar) mixture caused by non-equilibrium EEDF shape. This effect may be rather significant and should be taken into account when plasma conductivity is considered.

The authors gratefully acknowledge Dr. T.Stasewicz for useful discussions.

- [1] Yu.B. Golubovsky, Yu.M. Kagan, R.I. Lyagustchenko, *Zh.Eksp.Teor.Fiz.*, **57**, 1969, p.2222.
- [2] M. Jousfi, A. Himoudi, A. Gaouar, *Phys.Rev. A*, **46**, 1992, p.7889.
- [3] T. Stasewicz, J.Krasinski, *Opt. communications*, **39**, 1981, p.35.

## Oscillating Character of Electron Temperature Relaxation in a Recombining Plasma

N. Gorbunov\*, Ph.Latyshev\*, T.Stacewicz\*\*, J. Chorazy\*\*

\* Physics Institute, St.-Petersburg University, Ulianovskaya 1, 198904, St. Petersburg, Russia

\*\* Institute of Experimental Physics, Warsaw University, Hoza 69,00-681 Warsaw, Poland.

Low temperature recombining plasma arises in many practically interesting cases like laser ablation plume, active media of powerful gas lasers, flash lamps etc. Such a plasma presents numerous intriguing phenomena. Among the most important ones are oscillations of electron temperature  $T_e$  and concentration  $N_e$  during recombination. These oscillations were registered experimentally in Ar afterglow discharge [1]. Similar unmonotonous  $T_e$  relaxation was obtained by numeric modeling of helium afterglow plasma [2].

In the reported experiments the  $T_e$  oscillations were observed in plasma generated optically in dense rubidium vapour ( $10^{13}$ - $10^{15}$  cm<sup>-3</sup>) with several Torr of He as buffer gas. The vapour was ionized by nanosecond laser pulses tuned to the Rb 5S→6P transition. The electron temperature was measured by Langmuir probe. The oscillations were usually observed for certain vapour densities and certain laser power corresponding to initial electron density of the order  $10^{11}$ - $10^{12}$  cm<sup>-3</sup>. Fig.1 presents a typical experimental result.

In order to find the criteria of the oscillations arise and to evaluate their damping factor a self-consistent system of differential equations for the electron temperature  $T_e$  as well as population of resonance atomic level  $N_1$  and higher excited level  $N_2$  was considered:

$$\begin{aligned} \partial T_e / \partial t = & -\nu_{ea}(T_e)(T_e - T_a) - \\ & -\varepsilon_{01}\beta_{01}(T_e)N_0 + \xi_1\beta_{10}(T_e)N_1 \end{aligned}$$

$$\partial N_1 / \partial t = -\beta_{10}(T_e)N_1N_e + \beta_{01}(T_e)N_0N_e + A_{21}N_2$$

$$\partial N_2 / \partial t = -A_{21}N_2 + \alpha_{rec}T_e^{-9/2}N_e^2N^+$$

Here  $\nu_{ea}$  describes rate of energy losses for elastic atomic collisions,  $T_a$  - atomic temperature,  $\xi_1$  - effective energy (depending on the ionization degree) transferred to the electron gas due to the excited level depopulation,  $\varepsilon_{01}$  - resonance level excitation threshold.  $\beta_{01}$  and  $\beta_{10}$  are excitation and deexcitation rate constants respectively and  $\alpha_{rec}$  denotes rate of three body electron recombination with positive atomic ions  $N^+$ .

The effective relaxation rate  $A_{21}$  of the  $N_2$  excited level is determined by multiple radiative processes. The  $A_{21}$  value is calculated as a total probability of the  $N_2$

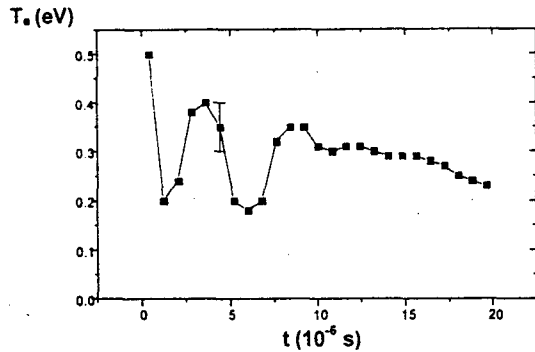


Fig.1

radiative decay via numerous intermediate states between  $N_1$  and  $N_2$ . Two groups of the higher excited  $N_2$  levels were considered, depending on the collisional or the radiative character of kinetics governing their population [3].

We started out the modeling with a simpler case for a pure Ar plasma, where  $\beta_{10}$  is a constant and the direct excitation from the ground state can be neglected ( $T_e \ll \epsilon_{01}$ ). Phase plane portrait ( $T_e, N_2$ ) of the equations system is shown in Fig. 2. Simulations were performed for three different effective rates ( $A_{21}$ ) of the radiative relaxation of the  $N_2$  excited level, but for the same initial conditions (point A in Fig.2).

The following results are reported:

1. The relaxation character strongly depends on the  $A_{21}$  value. The oscillating character is observed only for the  $A_{21}$  about  $10^5 \text{ s}^{-1}$ , while for the other  $A_{21}$  values the  $T_e$  evaluates without oscillations.

2. The oscillations mainly arise due to

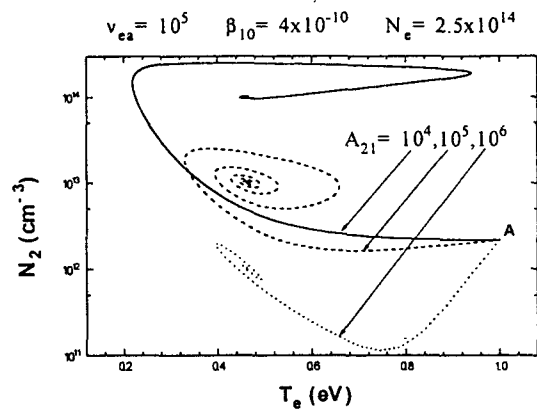


Fig.2

a strong nonlinear dependence of the three-particles recombination from the  $T_e$ . The decline of the  $T_e$  causes the increase of the excited level population. Consequently, it may lead to free electrons heating by inelastic collisions of II kind.

1. Oscillations occur only when certain phase conditions between the higher excited  $N_2$  level and the resonance  $N_1$  level populations (which play the main role in  $T_e$  balance) are fulfilled. Fig.2 demonstrates that the minimal damping of the oscillations occurs when the electron energy losses coefficient and the  $A_{21}$  value are approximately equal.

[1] Poljanskij M.N., Skrebov V.N., Shuhtin, Opt. Spectrosc. v.34, n.1, (28) 1973.

[2] Sits'ko Yu.I., Yacovlenko S.I., J. Tech. Phys, v.56, n.5 (1006), 1976.

[3] Biberman L.M., Vorobiev V.S., Jakubov I.T., *Kinetics of Nonequilibrium Low-temperature Plasma*, Moscow: Science, 1982.

# Isomerization of $\text{HCN}^+$ to $\text{CNH}^+$ via ion molecule reactions

A. Hansel, M. Glanschnig, Ch. Scheiring, W. Lindinger  
 Institut für Ionenphysik, Technikerstr. 25, 6020 Innsbruck, Austria  
 E.E. Ferguson  
 NOAA, Boulder, Colorado, USA

While thermodynamic data on the  $\text{HCN}^+ / \text{HCN}$  system are known with good accuracy  $\Delta H(\text{HCN}) = 31.5 \pm 1$  kcal/mol [1],  $\text{IP}(\text{HCN}) = 13.60 \pm 0.01$  eV [2], the values of the  $\text{CNH}^+ / \text{CNH}$  isomers are still in question. In the present selected ion flow drift tube study the two isomeric ions  $\text{HCN}^+$  and  $\text{CNH}^+$  were distinguished by the use of monitor gases,  $\text{SF}_6$ ,  $\text{CF}_4$ ,  $\text{O}_2$  and  $\text{Xe}$  which react differently with the two isomers [4]. The first part of the present study involved two reactions for which it was only necessary to assure that the mass  $27^+$

ions were the lowest energy isomer,  $\text{CNH}^+(v=0)$ . This was easily accomplished by reactions with  $\text{CO}$  or  $\text{CO}_2$  which efficiently isomerize  $\text{HCN}^+$  to  $\text{CNH}^+$  (see below). From the energy dependence of the endothermic reactions of  $\text{CNH}^+(v=0)$  with  $\text{C}$  and  $\text{Xe}$  we could establish the heat of formation  $\Delta H(\text{CNH}^+) = 327 \pm 1$  kcal/mol, the ionization potential  $\text{IP}(\text{CNH}) = 12.04 \pm 0.01$  eV and the heat of formation of the neutral  $\Delta H(\text{CNH}) = 49 \pm$  kcal/mol. The energy levels are summarized in Fig. 1.

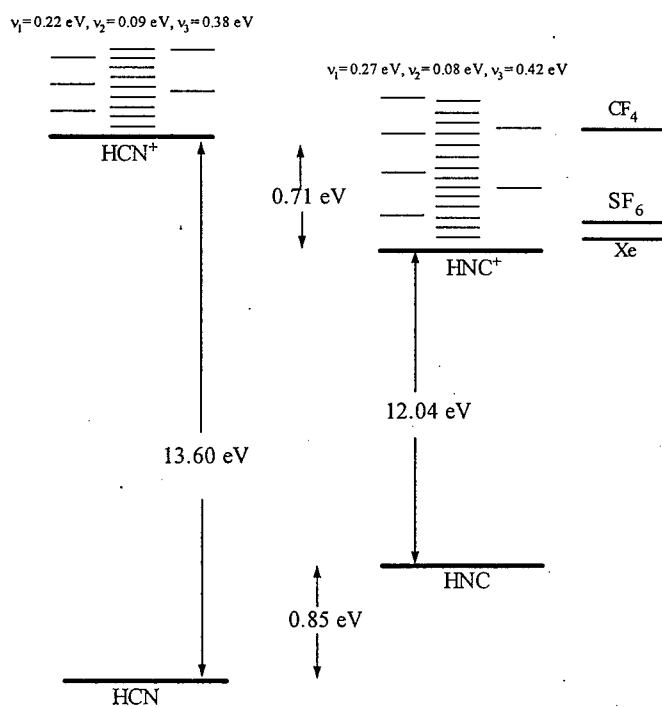
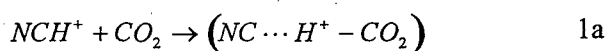


Fig. 1 Energy level diagram of  $\text{HCN}^+$  and  $\text{CNH}^+$ . The energy spacing of the three vibrational modes ( $v_1, v_2, v_3$ ) (values taken from Forney et al. [3] and references therein) is given for both isomeric structures together with the energy thresholds of the monitors  $\text{CF}_4$ ,  $\text{Xe}$ , and  $\text{SF}_6$ .



The second part of the present investigation is a continuation of a study of  $\text{HCN}^+/\text{CNH}^+$  ion chemistry carried out earlier in Christchurch [4]. In that study, carried out only at thermal ( $\sim 300$  K) energy, it was found that  $\text{HCN}^+$  is efficiently isomerized to the more stable isomer  $\text{CNH}^+$  by reactions with both CO and  $\text{CO}_2$ . It was speculated that the reaction mechanism was a "forth and back" proton transfer; first (step 1a) exothermic proton transfer from the C atom of  $\text{HCN}^+$  to CO (or  $\text{CO}_2$ ), followed by another exothermic proton transfer back (step 1b) to the N atom to produce  $\text{CNH}^+$  in the collision complex of the reaction.



It was suggested that a test of the model could be obtained by studying the kinetic energy dependence of the reaction, the idea being that as

the collision energy is increased the lifetime of the collision complex will be decreased leading to a lower probability of the reverse proton transfer and hence a decrease in  $\text{HNC}^+$  product and an increase in  $\text{HCO}^+$  (or  $\text{HCO}_2^+$ ) product.

The present investigation reports measurements providing this test which support the proposed model. A similar isomerization mechanism is expected to occur for any molecule M having a proton affinity such that both forward and reverse proton transfers are exothermic, i.e.  $\text{PA}(\text{CN at C}) < \text{PA}(\text{M}) < \text{PA}(\text{CN at N})$  if  $\text{HCN}^+$  does not otherwise react with M.

### Acknowledgments

Financial support by the "Fonds zur Förderung der wissenschaftlichen Forschung" Project No. P10014 is gratefully acknowledged.

### References

- [1] J. Berkowitz, G.B. Ellison, D. Gutman, *J. Phys. Chem.* **98** 2744 (1994)
- [2] J. Kreile, A. Schweig and W. Thiel *Chem. Phys. Lett.* **87** 473 (1982)
- [3] D. Forney, W.E. Thompson, and M.E. Jacox, *J. Chem. Phys.* **97**, 1664 (1992).
- [4] S. Petrie, C.G. Freeman, M. Meot-Ner(Mautner), M. J. McEwan and E.E. Ferguson, *J. Am. Chem. Soc.* **112**, 7121 (1990).

## Experimental and theoretical investigations of negative ions spatial distribution in oxygen DC discharge.

V.V. Ivanov, K.S. Klopovskiy, D.V. Lopaev, A.T. Rakhimov, T.V. Rakhimova, G.B. Rulev  
119899, Nuclear Physics Institute, Moscow State University, Moscow, Russia

### Introduction

The electronegative gas plasma are widely used in many applications in microtechnology. The complicated processes in the plasma volume and on wall surface make its understanding more difficult. The difficulties in the study of mechanisms of various processes in the low pressure electronegative plasma are due to insufficient information about the spatial profiles of charged particles (electrons, positive and negative ions) and about the electron distribution function (EDF), which can be spatially nonlocal at low pressure. In strong electronegative gases, e.g.  $\text{CF}_4$ , the spatial profiles of negative ions produced at electron attachment, are determined by the ion diffusion. The ion heating in high electric field increases the ion diffusion and significantly changed the charge particle profiles [1]. Oxygen is the weakly electronegative gas. The unique characteristics of oxygen discharge is connected with the electron production at associative detachment in the reactions between negative ions and active particles (atomic oxygen and excited metastable molecules of  $\text{O}_2(a^1\Delta_g)$ ). It has been shown in [2] that the  $\text{O}_2(a^1\Delta_g)$  molecules determine the RF discharge structure. This report is devoted to an investigation of the effect of ion diffusion and detachment processes on the spatial distribution of negative ions in positive column of oxygen DC glow discharge.

### Experiment

The experiments were carried out in a glass tube of 12 mm diameter at pressures of 0.15-1.5 Torr and at discharge current densities of 5-30  $\text{mA}/\text{cm}^2$ . Both the concentrations of the singlet and atomic oxygen, and the radial and axial electric field were measured [3,4]. The negative ions were detected by a laser photodetachment method. We used the emission of a Cu-vapor pulse laser on the wavelength of  $\lambda=510.8$  nm with the repetition rate of 8 kHz and one pulse energy of 0.4 mJ. The photoelectrons were collected by a moveable probe of 0.3 mm diameter and 1.2 mm length. The laser emission was collected by collimator in a 1.5 mm diameter parallel beam and then was entered into discharge tube along the tube diameter line. The trajectory of probe movement coincided with the axis of a laser beam. The laser beam was modulated by the chopper at frequency of 240 Hz. The charge collected by probe was detected using the charge-sensitive amplifier and lock-in amplifier.

The probe potential was scanned with a 130 mV step by using the lock-in amplifier internal DAC

channel, the scan time step being always more a time constant of

lock-in amplifier. The J-V (current-voltage) probe characteristics of photodetached electrons depended on probe position. All J-V characteristics for the different spatial points were correlated with the appropriate plasma potential. The plasma potential taken on respect to the one of anode for each probe position was determined by the maximum of the first derivative from the probe characteristics. An integral on J-V probe characteristics from  $U_s(R)$  up to  $U_s(R) + 5$  V was used as a useful signal where  $U_s(R)$  is voltage corresponding to plasma potential at the probe position R. The absolute calibration of the system has been carried out using our experimental data on EEDF and electron concentration [5] and measuring the EEDF and photocurrent saturation characteristics under the slight discharge modulation at the reference frequency. It was assumed that EEDF of photodetached electrons accessing the probe is the same as of discharge electrons. It should be noted that as our measurements have shown if  $U_p - U_s = \text{const}$

condition (where  $U_p$  is collecting probe potential,  $U_s$  is plasma potential) does not fulfills at ion spatial

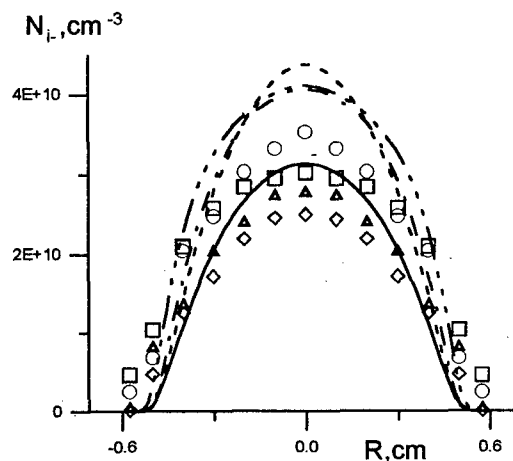


Fig.1

The radial distributions of negative ion concentration in positive column of DC discharge in pure oxygen. The tube walls position is shown by grey vertical columns. The discharge current density is of 5  $\text{mA}/\text{cm}^2$ .

—○— P=0.15 Torr  
—□— P=0.30 Torr  
—△— P=0.50 Torr  
—◇— P=1.00 Torr

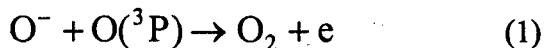
The experiment data and the calculation results are represented by symbols and lines respectively.

measurements by a probe method the discrepancy in experimental data can reach tens of percents in

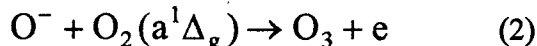
dependence on a space point even when the collecting probe potential is large.

## Results and Discussion

The radial distributions of negative ions are shown in Fig.1. The experimental results were analyzed on base of self - consistent PIC MC model of DC glow discharge [1]. The effect of the non-equilibrium ion diffusion on radial profiles of negative ions has been studied. The main detachment processes under our experiment conditions are:

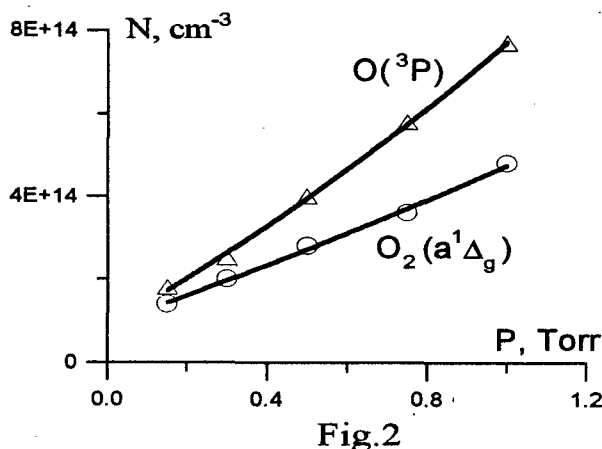


$$k_1 = 1.9 \cdot 10^{-10} \text{ cm}^3 \text{ s}^{-1} [2]$$



$$k_2 = 3 \cdot 10^{-11} \text{ cm}^3 \text{ s}^{-1} [6]$$

The atomic oxygen and  $\text{O}_2(a^1\Delta_g)$  concentration were



Concentrations of singlet oxygen and oxygen atoms versus the pressure in  $\text{O}_2$  DC discharge at current density of 5 mA/cm<sup>2</sup>.

taken from experimental measurements (Fig.2). It is supposed that  $\text{O}_2^+$  are the main positive ions and  $\text{O}^-$  are the main negative ions. The value of  $k_2$  is varied in scientific literature from  $3 \cdot 10^{-11}$  to  $3 \cdot 10^{-10} \text{ cm}^3 \text{ s}^{-1}$ . We choosed  $3 \cdot 10^{-11}$  value for the best agreement between the experimental and numerical values of the axial electric field at low pressures. The calculated radial distribution of  $\text{O}^-$  ions under the same experimental conditions are also shown in Fig.1. It is well seen in Fig.1 that the profiles of calculated and experimental radial distributions agree sufficiently well. However the calculated values of negative ions exceed the experimentally measured ones in  $\sim 1.5$  times. It can be explained by dependence of (1) and (2) reaction rate constants on plasma parameters. At present time these dependences are unknown. So according to mutual arrangement of  $\text{O}_2$  and  $\text{O}_2^-$  potential curves the rate constant of (1) process is assumed to be lowered with decreasing the pressure (i.e. with increasing the reduced field) owing to more high kinetic energy of  $\text{O}^-$  ions. However as one can presume from the potential

surface arrangement of  $\text{O}_3$  molecule and  $\text{O}_3^-$  anion [7,8] the (2) process can have got a noticeable activation energy up to  $\sim 0.5 \text{ eV}$  so that the ion heating can strongly influence on the reaction rate constant. At the present moment it is undoubtedly required the detailed information both about the detachment processes themselves including the charge transfer reactions and about the ion energy distribution function.

In order to understand how the nonequilibrium ion diffusion effects on the radial distribution we have carried out our calculations without taking into account the ion heating. Fig.3 represents the results of these calculations at pressure of 0.15 Torr, where an axial electric field is highest and therefore ion heating is most notable. As it is well seen the correct description of spatial distributions of negative ions can be achieved only taking into consideration the effects of ion nonequilibrium diffusion.

This work was supported by grant No. 95-02-05461 of Russian Fond of Fundamental Investigations (RFFI).  $N_i, \text{cm}^{-3}$

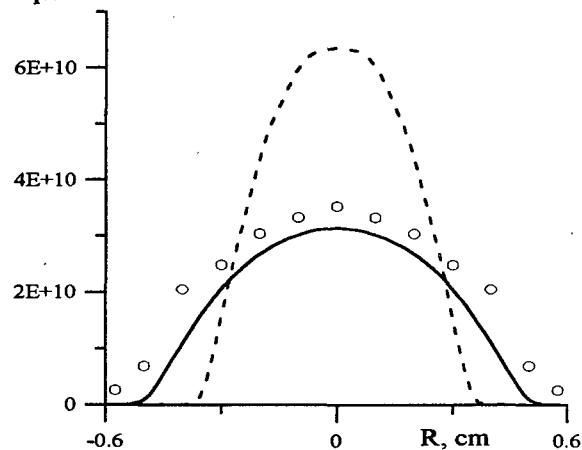


Fig. 3

All is the same as in Fig. 1 only at pressure of 0.15 Torr. The dashed line is radial distribution of negative ions without the nonequilibrium diffusion.

## References

- [1]. V.A.Feoktistov, V.V.Ivanov, A.M. Popov et al : J.Phys.D, 30 (1997) (to be published)
- [2]. V.A.Feoktistov, D.V.Lopaev, K.S.Klopovsky et al : J.Nucl.Mater. , 200 (1993) 309.
- [3]. V.V.Ivanov, D.V.Lopaev, A.T. Rakhimov et al ; Abstracts of invited lectures and contributed papers , ESCAMPIG 96, 20E (1996) 169.
- [4]. V.V.Ivanov, D.V.Lopaev, K.S.Klopovsky et al: (ibid) 20E (1996) 77
- [5]. V.V.Ivanov, D.V.Lopaev, K.S.Klopovsky et al: JETP Lett., 63(7) (1996) 537
- [6]. B.L.Upschulte, W.J.Marinelli, B.D.Green: J.Phys.Chem., 98 (1994) 837
- [7]. R.K. Curran, J.Chem.Phys., 35(5) (1961) 1849
- [8]. P.K.Walhout, C.Silva, P.F.Barbara, J.Phys.Chem., 100 (1996) 5188

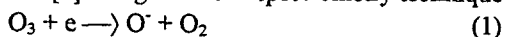
## The influence of the low energy vibrationally excitation on the electron dissociative attachment coefficient in pure ozone.

D.V.Lopaev, K.S.Klopovskiy, N.A.Popov, O.V.Proshina, A.T.Rakhimov, T.V.Rakhimova  
119899, Nuclear Physics Institute, Moscow State University, Moscow, Russia

Electronegative species (i.e., molecules of ozone,  $O_3$ ), which are produced in a gas discharge plasma, can effect on the gas breakdown dynamics and on the electrical characteristics of the discharge. Interpretation of the experimental data concerning the plasma with an ozone admixture is a rather complicated task because of the absence of the electron drift characteristics in ozone.

The work presented contains a cross section set of electron scattering on  $O_3$ -molecules (Fig. 1), as well as the results of calculation of the electron drift velocity  $V_{dr}$  (Fig.2a), the electron temperature  $T_e$  (Fig.2b), and the electron dissociative attachment coefficient  $\beta/[O_3]$  to  $O_3$  (Fig.3). The cross section set is normalized with respect to the experimental dissociative attachment coefficient [1], which has been measured in the reduced electric field range  $E/N = 1-20$  Td. The set allows one to calculate the EEDF for low  $E/N$  values. Moreover, the vibration excitation by electron impact (as well as dissociative attachment) rate constants of  $O_3$ -molecules in pure ozone are presented (Fig. 4).

The electron transport cross section on  $O_3$ -molecules (curve (1) on Fig.1) and the ozone rotational excitation by electron impact (curve (2)) in the range of low electron energies  $u = 0.001-0.1$  eV was determined using the data [2-4]. The electron impact vibrational excitation of  $O_3$ -molecules was experimentally studied in [5], in which the electron loss spectra were presented. The model integral cross section of this process was determined analogously to the case of known data concerning the vibrational cross sections of  $H_2O$  [6]. As the  $O_3$  and  $H_2O$ -molecules have similar parameters (the symmetry type, the angle, etc.), we can assume that these molecules should also have similar mechanism of the resonance excitation. The value of introduced by us vibrational cross section in maximum was normalized by the differential cross section value for ozone [5] at scattering angle  $80^\circ$ . Note that obtained by us cross section of vibrational excitation of  $O_3$  (curve (3)) is a model one and actually is a total cross section of excitation of all the vibrational modes of ozone. The ionization cross section of  $O_3$  (curve (5)-(7)) is taken from [7]. The dissociative attachment to  $O_3$ -molecules was studied in [1,8,9]. The currents of negative ions ( $O^-$  and  $O_2^-$ ) as a function of the electron energy were measured in [8] using the mass-spectrometry technique:



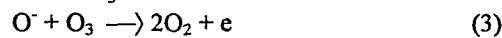
From these results we can conclude that reaction (1) dominates in dissociative attachment of low-energy electrons to  $O_3$ , as well as can determine

positions of the maxima of dissociative attachment cross sections with generation of the ions  $O^-$  and  $O_2^-$ . However, the absolute values of these cross sections have not been obtained in [8].

The results of [1] concerning the drift tube measurements of the attachment coefficient  $\beta/[O_3]$  in pure ozone in the range of the reduced electric fields from 3 to 10 Td produce a good experimental foundation, which allowed us to carry out the normalization of the cross section set (Fig. 1) for low values of  $E/N$ , as well as to calculate the drift velocity, the electron temperature, and to determine the dissociative attachment rate constant in pure ozone.

The near-threshold behaviour of attachment cross section (4) was taken from [1]. The value of maximum of this cross section was estimated from experimental results [10].

In order to use the data [1], one should take into account the role of reactions with participation of negative ions in charged particle balance in the drift tube. The reason for this is the fact that  $O^-$  concentration is controlled by the processes with participation of  $O_3$ -molecules:



$$k_3 = 3 \cdot 10^{-10} \text{ cm}^3/\text{s} \quad [9]$$



$$k_4 = 2 \cdot 10^{-10} \text{ cm}^3/\text{s} \quad [9].$$

Assuming that the  $O^-$  concentration is quasi-stationary for the electron drift times corresponding to the experiment [1], we can obtain the relation between the real value of the attachment coefficient  $\beta/[O_3]$  and the measured one  $(\beta/[O_3])_{eff}$

$$(\beta/[O_3])_{eff} = \beta/[O_3] \cdot k_3 / (k_3 + k_4) = \Gamma \beta/[O_3]$$

In conditions of the experiment [1], we have  $\Gamma = 0.4$ . Thus we can conclude that in pure ozone the processes of attachment play a significant role in forming the relation between the measured and real attachment coefficients. The EEDF calculations were carried out using the Boatsman equation solution in the two-term approximation.

We used the experimental data concerning attachment coefficients in pure ozone [1] to normalize the mentioned cross section set. Taking into account that these data have been obtained for small reduced electric fields, this normalization is correct only for low electron energies. The normalization was carried out as follows: the drift velocity  $V_{dr}$ , the rate constant  $K_a$  and the attachment coefficient  $\beta/[O_3] = K_a / V_{dr}$  as a function of  $E/N$  were calculated, and this was followed by comparison with the experimental data.

Returning to Fig. 1 we can note that the first sharp maximum (at energy about 0.3 eV) in the

vibrational cross section (3) corresponds to unknown before process of near-threshold resonance vibrational excitation of the  $O_3$ -molecules. The necessity to take into account such a resonance cross section follows from the comparison of the experimental data with the results of the numerical calculation of the attachment coefficient in pure ozone. Note that the possibility of  $O_3$  vibrational excitation of such a type in this energy range was mentioned by the authors of [1]. Fig. 3 shows the experimental values  $\beta/[O_3]$  as a function of  $E/N$ , as well as two variants of calculation of this coefficient: with (solid line) and without (dashed line) accounting for the near-threshold vibrational resonance. By varying the half-width of this resonance excitation in  $O_3$ , position of the maximum and its amplitude, we have managed to obtain a good accordance between the results of calculation and the experimental attachment coefficient in pure ozone in the range of  $E/N$  discussed. Fig.2a,b shows the calculated values of the drift velocity and the electron temperature  $T_e = 3/2 \langle u \rangle$  ( $u$  is the mean electron energy). It follows from the dependencies of these parameters on  $E/N$  that taking into account the resonance cross section leads to the decrease of the electron temperature and to the increase of the electron drift velocity in the range of  $E/N$  studied. This follows from the fact that the existence of a new inelastic process with a low energy threshold leads to a significant decrease of the EEDF in the energy range 0.2-0.6 eV. As the transport cross section is constant in the energy range studied, the decrease of the transport frequency leads to the increase of the drift velocity.

Using the normalized cross section set, we have calculated the rate constants of  $O_3$  vibrational excitation (curve 1 on Fig. 4) and of dissociative attachment (curve 2 on Fig. 4) in pure ozone.

The physical reason of this resonance is not quite clear yet; however, a similar behavior of the cross section near the threshold is typical for polar and 3-atomic molecules with a high polarisability. Another possibility to obtain such a resonance near the excitation threshold of  $O_3$  can be due to low-lying term of the negative ion  $O_3^-$  [6].

The work is supported by the Russian Foundation of Fundamental Research (grants 95-02-06326 and 96-02-18747).

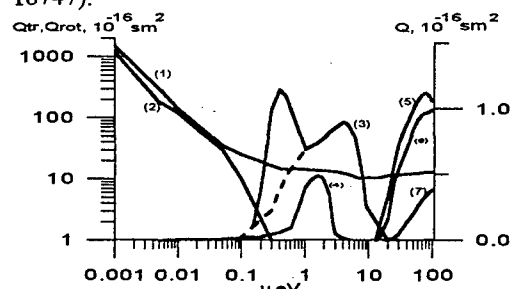


Fig.1

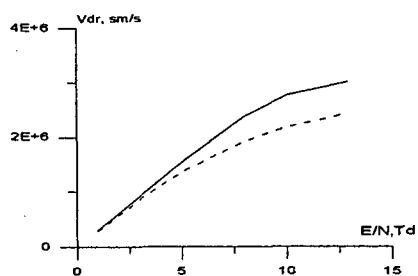


Fig.2a

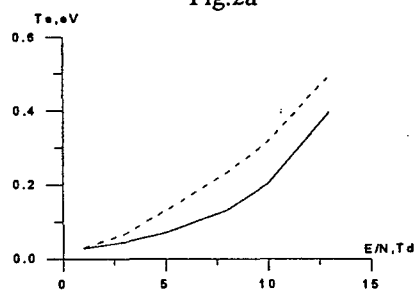


Fig.2b

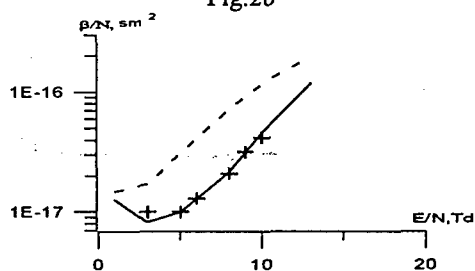


Fig.3

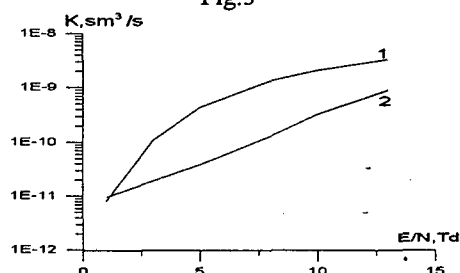


Fig.4

## References

- [1]. Stelman D., Moruzzi J.L., Phelps A.V.: J.Chem.Phys., 56 (1972) 4183.
- [2]. Joshipura K. N.: Ind. J. Pure Appl. Phys., 23 (1985) 525.
- [3]. Shyn T. W., Sweeney C. J.: Phys. Rev. A., 47 (1993) 2919
- [4]. Rudge M. R. H.: J. Phys. B., 7 (1974) 1323.
- [5]. Davies J. A., Johnstone W. M., Mason N. J. et al.: J. Phys. B., 26 (1993) L767.
- [6]. Seng G., Linder F.: J. Phys. B., 9 (1976) 2539
- [7]. Siegel M. W.: Int. J. Mass. Spectrom., 44 (1982) 19.
- [8]. R.K. Curran: J.Chem.Phys., 35 (1961) 1849.
- [9]. Lifshitz C., Wu R.L.C., Haartz J.C., Tiernan T.O.: J.Chem.Phys. 5 (1977) 2381
- [10]. Kajeta S., Ushiroda S., Kondo Y.: XIX ICPIG 1989, v.4, p.662-663.

# Vibrational and Atomic Kinetics in the Afterglow of N<sub>2</sub> and N<sub>2</sub>-Ar Microwave Discharges

P.A. Sá\* and J. Loureiro†

\*Faculty of Engineering, University of Oporto, 4099 Porto Codex, Portugal

†Centro de Electrodinâmica, Instituto Superior Técnico, 1096 Lisboa Codex, Portugal

## 1. Introduction

In a recent paper [1], we have investigated the conditions for appearing of the so-called pink afterglow, that is the emission of the first negative system bands  $N_2^+(B\ ^2\Sigma_u^+ - X\ ^2\Sigma_g^+)$ , downstream from a flowing microwave discharge in N<sub>2</sub> and N<sub>2</sub>-Ar. It was shown that this emission occurs as a result of the mechanisms leading to the formation of the ground ionic state  $N_2^+(X\ ^2\Sigma_g^+)$  by collisions between the electronic metastables  $N_2(A\ ^3\Sigma_u^+)$  and  $N_2(a'\ ^1\Sigma_u^-)$  and  $N_2(a') + N_2(a')$ , followed by a reaction for populating the upper ionic state  $N_2^+(B)$  involving collisions of  $N_2^+(X)$  with vibrationally excited molecules  $N_2(X, v, v \geq 12)$ . In this analysis the relaxation of the vibrational distribution of  $N_2(X, v)$  molecules was shown to play a central role in the emission of the 1<sup>-</sup> system bands in the short-lived afterglow region. Here, our purpose is to study the coupling of  $N_2(X, v)$  molecules with the other active species present in the afterglow and in particular to investigate if there is additional dissociation in the post-discharge due to a vibrational mechanism, since in certain conditions the  $N_2(X, v)$  distributions can present populated tails for times as long as 10<sup>-2</sup> s.

## 2. Discharge model

A stationary kinetic model for a microwave discharge in cylindrical geometry is developed by coupling the homogeneous electron Boltzmann equation, under the effective field approximation, to a system of rate balance equations for the vibrational levels  $N_2(X, v)$ , the most important electronic states of N<sub>2</sub>, and the ground state atoms N(<sup>4</sup>S). The continuity equations for the electrons and the main positive ions ( $N_2^+, N_4^+, Ar^+, Ar_2^+$ ) are still coupled to the former system in order to determine self-consistently the maintenance reduced electric field. The Boltzmann equation takes into account both inelastic and superelastic electron collisions, while the rate balance equations for the neutral heavy species include the vibration-vibration (V-V) energy exchange processes, the vibration-translation (V-T) energy exchanges in N<sub>2</sub>-N<sub>2</sub>, N<sub>2</sub>-N and N<sub>2</sub>-Ar collisions, and a large number of other processes taking into account the interplay of the species  $N_2(X, v)$ ,  $N_2(A\ ^3\Sigma_u^+, B\ ^3\Pi_g, C\ ^3\Pi_u, a'\ ^1\Sigma_u^-, a\ ^1\Pi_g, w$

$^1\Delta_u)$  and N(<sup>4</sup>S), in N<sub>2</sub>-N<sub>2</sub> and N<sub>2</sub>-Ar collisions. This system of equations still includes the processes of vibrational deactivation on the wall, dissociation by the V-V and V-T exchanges, wall atomic re-association, and diffusion and radiative losses. The total rate of ionization includes both ionization by direct and stepwise electron impact, as well as reactions for associative ionization in N<sub>2</sub> involving collisions between electronically excited molecules.

Fig.1 shows the mean power per length unit absorbed by the electrons calculated using this model, in a microwave N<sub>2</sub>-Ar discharge at  $\omega/2\pi = 2.45$  GHz in a 16 mm inner diameter pyrex tube, as a function of the fractional Ar concentration, for  $n_e = 2 \times 10^{11} \text{ cm}^{-3}$  (A) and  $5 \times 10^{11} \text{ cm}^{-3}$  (B), and  $p = 2$  Torr (full curves) and 10 Torr (broken). As the fractional Ar concentration increases the power per length unit for sustaining the discharge rapidly decreases because the total electron cross section for excitation is considerably smaller in Ar than in N<sub>2</sub>. We note that an increase in  $[Ar]/([N_2] + [Ar])$  produces a reduction of the maintenance electric field, which, in turn, leads to a decrease in  $dP_{abs}/dz$ .

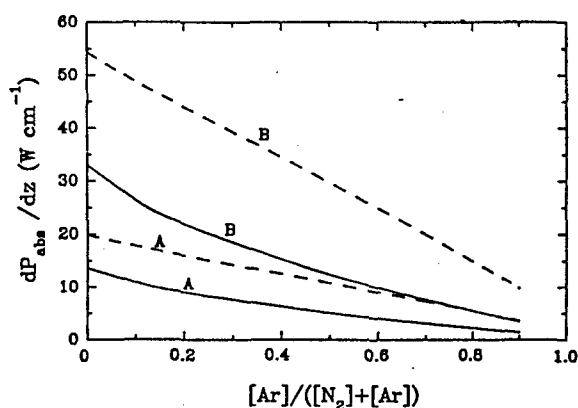


Fig.1 - Power per length unit for  $n_e = 2 \times 10^{11} \text{ cm}^{-3}$  (A),  $5 \times 10^{11} \text{ cm}^{-3}$  (B), and  $p = 2$  Torr (full), 10 Torr (broken).

## 3. Post-discharge relaxation

The concentrations for the different species in the discharge are used at the time  $t = 0$  in the post-discharge, where the relaxation of the above system of equations is investigated. As it was shown (see, e.g., Ref.[2]) the high-energy tail of the electron energy distribution function rapidly decreases in a time of 10<sup>-8</sup>–10<sup>-7</sup> s, so that the electron collisions

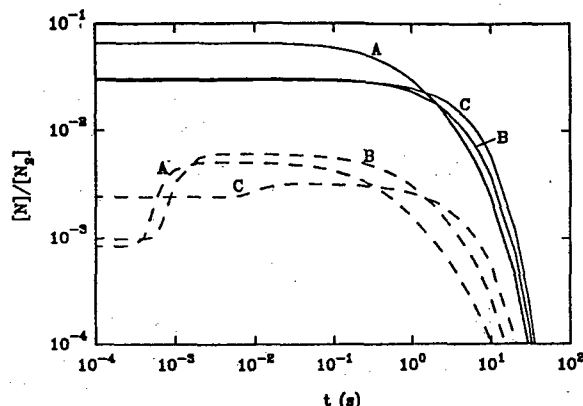


Fig. 2 -  $[N(^4S)]/[N_2]$  for  $p=2$  Torr (full), 10 Torr (broken), in pure  $N_2$  (A),  $N_2$ -50%Ar (B),  $N_2$ -90%Ar (C).

may be discarded from the model. Fig. 2 shows the temporal evolution of the relative concentration of  $N(^4S)$  atoms calculated for  $n_e=2 \times 10^{11} \text{ cm}^{-3}$ ,  $p=2$  Torr (full curves) and 10 Torr (broken), in a post-discharge in pure  $N_2$  (curves A), and in the case of the mixtures  $N_2$ -50%Ar (B) and  $N_2$ -90%Ar (C). The relative atomic concentration in the discharge remains with practically no modifications in the post-discharge up to  $t \approx 10^{-4} \text{ s}$ . After this time, two different situations take place depending on pressure. For the lower value  $p=2$  Torr, the relative concentration  $[N(^4S)]/[N_2]$  remains unchanged until  $\approx 10^{-1} - 1 \text{ s}$ , time at what this concentration starts to decay as a result of reassociation on the wall. However, if we consider the higher pressure  $p=10$  Torr, it is observed an increase of  $[N(^4S)]/[N_2]$  in the range  $\approx 5 \times 10^{-4} - 5 \text{ s}$ . This increase is more visible in the cases of the discharges in pure  $N_2$  and in  $N_2$ -50%Ar.

This corresponds, in fact, to additional dissociation in the post-discharge due to a vibrational mechanism, in which a  $N_2(X, v)$  molecule in the last bound level  $v=45$  is promoted to the continuum by the V-V and V-T exchanges. The different behaviours found here are explained by the appearance of overpopulated tails in the vibrational distributions of  $N_2(X, v)$  molecules during the relaxation process for the higher value of pressure. Fig. 3 and 4 show these distributions for  $p=2$  Torr and 10 Torr, respectively, in the case of a  $N_2$ -50%Ar mixture, and for the times  $t=0$  (A),  $10^{-5} \text{ s}$  (B),  $10^{-3} \text{ s}$  (C) and  $10^{-1} \text{ s}$  (D). In contrast, the less populated tails for  $p=2$  Torr result from a stronger vibrational deactivation by the V-T processes associated with  $N_2$ -N collisions. We note that the lower value of pressure corresponds to a higher maintenance reduced electric field and, hence, to a higher relative atomic concentration in the beginning of the post-discharge (see fig. 2). We still note that fig. 4

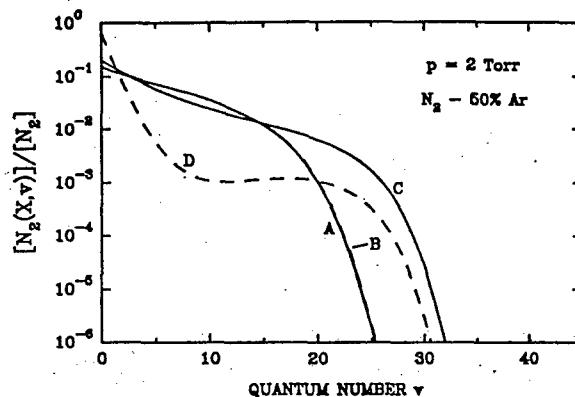


Fig. 3 -  $[N_2(X, v)]/[N_2]$  distributions for  $p=2$  Torr, at  $t=0$  (A),  $10^{-5} \text{ s}$  (B),  $10^{-3} \text{ s}$  (C),  $10^{-1} \text{ s}$  (D), in  $N_2$ -50%Ar.

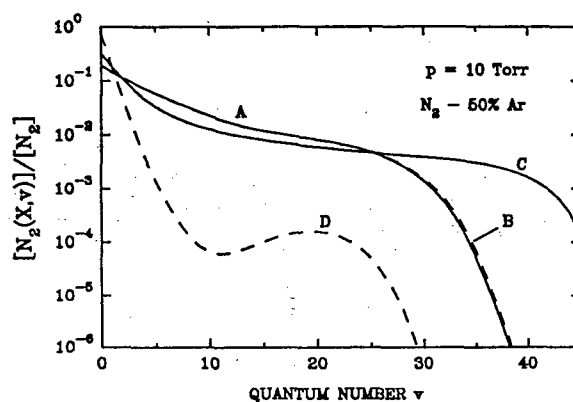


Fig. 4 - As in Fig. 3 but for  $p=10$  Torr.

shows an inversion of population during the relaxation as a result of pumping effects produced by the V-V exchanges. This is a consequence of the near-resonant V-V collisions are far more effective in the transfer of vibrational quanta than the non-resonant V-V and V-T collisions, which produces a pumping phenomena between the different levels of the anharmonic oscillator. Thus, the vibrational energy must be transferred up the vibrational ladder by near-resonant V-V exchanges rather than be immediately lost by V-T collisions. However, in the case of the lower value of pressure  $p=2$  Torr, the percentage of  $N(^4S)$  atoms in the discharge is high ( $[N(^4S)]/[N_2]=6.68\%$  in pure  $N_2$ ), so that a rapid deactivation by V-T( $N_2$ -N) exchanges occurs.

[1] - P.A. Sá and J. Loureiro 1996 Proc. 13th ESCAMPIG (Poprad), p.67; [2] - C. Gorse and M. Capitelli 1987 J. Appl. Phys. 62 4072.

This work has been carried out under the support of a PRAXIS XXI Research Grant (Portuguese Ministry of Science and Technology).

# COMPARATIVE STUDIES ON Xe(1s<sub>4</sub>) LASER LIGHT ABSORPTION AND ASSOCIATED OPTOGALVANIC SIGNAL IN A DC DISCHARGE IN Ne-Xe MIXTURES.

Y.Sakai, M.A.Bratescu\*, G.Musa\*, K.Myamoto,  
Hokkaido University, Dept.Electrical Eng. Sapporo, Japan  
\*Inst.Laser, Plasma and Radiation Physics, Bucharest, Romania

## 1.Introduction

In this paper we present a study on xenon-neon mixture dc discharge plasma, using diode laser absorption for the xenon transition from 1s<sub>4</sub> - 2p<sub>5</sub> at the wavelength of 828.239 nm.

Comparative analysis of the plasma modulation absorption signal and optogalvanic signal permitted us to introduce a new parameter, namely, optogalvanic efficiency -Eff<sub>OG</sub>- defined as the size of the optogalvanic signal corresponding to an atom optically pumped by laser. The experimentally observed dependency of Eff<sub>OG</sub> on the various parameters gives the possibility to obtain new useful data on the processes taking place at the atomic scale in neon-xenon discharges.

## 2.Experimental set-up.

Two experimental arrangements were used: a) dc plasma modulation detection system and b) optogalvanic spectroscopy mounting. In both cases we used the diode laser LTO 15 MDO from Sharp, with the wavelength range 815-845 nm and maximum optical power output of 30 mW. This diode was powered and its temperature was stabilized with a Melles Griot Laser Driver 06DLD203 and a Peltier element. The diode laser wavelength scanning over 75 GHz range with a 64 mHz frequency was performed by a triangular signal generator and marked with the interference fringes obtained from a confocal Fabry-Perot etalon (1.5 GHz free spectral range). The xenon absorption signal and the interference fringes were simultaneously recorded via an oscilloscope, and GPIB interface by a computer. The electrical discharge was ignited and maintained between two stainless steel electrodes with 50 mm in diameter, mounted inside a large metallic vacuum vessel, provided with two glass windows in line with the interelectrode space. The laser beam (cross section diameter being around 0.5mm) can be moved to various position between the cathode and anode, but remaining always parallel with the surfaces of the electrodes. A photodetector is provided at the exit window to measure the laser beam intensity.

In the dc plasma modulation detection system, the discharge is supplied by a high

voltage generator. The discharge current is modulated with a controlled frequency in the range 400 Hz-1500 Hz, the working frequency is 465 Hz. The plasma is periodically changed on and off, and consequently the absorption signal corresponding to the excited states will modulate with the same frequency with the plasma modulation frequency. Using phase sensitive detection of the absorption signal, the lock-in amplifier reference frequency will be just the plasma modulation frequency.

The optogalvanic signal obtained at resonant laser light absorption at 828.239 nm corresponding to xenon transition 1s<sub>4</sub> to 2p<sub>5</sub>, was detected as plasma impedance change and measured using wavelength modulation spectroscopy. The modulation frequency of the diode laser was 1.3 kHz, the measurements were done using the first harmonic signal

## 3.Experimental results and discussion.

Using the described experimental arrangements, we measured the absorption, through a dc discharge, of the laser light of 828.239 nm corresponding to xenon transition 1s<sub>4</sub>-2p<sub>5</sub> and also the induced optogalvanic effect at the passage of the laser beam through the discharge. The experimental parameters were: total gas pressure; 5 torr and 10 torr, xenon concentrations in neon-xenon mixture ; 5%, 10%, 20%, 100%, discharge current; 1mA, 3mA and 5mA. The laser beam along a diameter cord and parallel with the surfaces of the electrodes explored in the interelectrode of 5.5 mm. Using the obtained data, we represented the spatial distribution of the density of the excited xenon atoms Xe(1s<sub>4</sub>) and also the corresponding optogalvanic signals at various positions in the discharge space. Figs.1 and 2 respectively give, as examples, the spatial distribution curves for laser absorption signal I<sub>PM</sub> and OG signal I<sub>OG</sub>. In spite of the fact that both signals are obtained at the same laser light absorption (corresponding to the same xenon transition 1s<sub>4</sub>-2p<sub>5</sub>), the differences between the curves are significant due to the different nature of these two signals. Indeed, the signal I<sub>PM</sub> is directly proportional with the density of the excited xenon atoms on level 1s<sub>4</sub>.



Consequently, the curves given in fig.1 represent just the density distribution of the excited xenon atoms in the discharge space. OG signal represents the change of the plasma conductivity due to the ions generated from the excited xenon (2p5) state resulted from Xe(1s4) by laser light absorption.

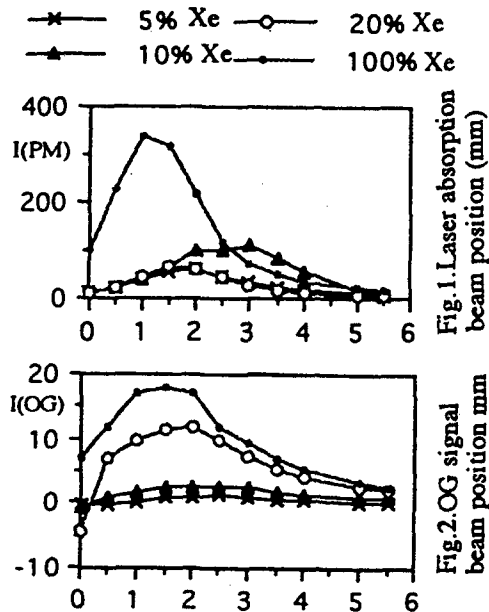


Fig.1.Laser absorption (mm)

Fig.2.OG signal beam position mm

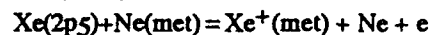
Starting from these data, we defined a new parameter **optogalvanic effect efficiency- (Eff<sub>OG</sub>)**, as the ratio between optogalvanic signal and the number of xenon atoms pumped to 2p5 state by laser absorption and responsible for generated OG signal. In present case we will have

$$\text{Eff}_{\text{OG}} = \text{I}_{\text{OG}} / \text{I}_{\text{PM}} \quad (1)$$

We must observe that the number of xenon atoms pumped optically to 2p5 state is proportional with the density of excited 1s4 xenon atoms, to which is proportional the absorption signal  $\text{I}_{\text{PM}}$ . The  $\text{Eff}_{\text{OG}}$  represents the size of the optogalvanic signal per absorbed photon for given experimental conditions, i.e., OG signal efficiency. Using the experimental data like those given in figs.1 and 2, we can study the dependence of the parameter  $\text{Eff}_{\text{OG}}$  on experimental conditions.

Interesting tendency is obtained (fig.3) if the dependence of  $\text{Eff}_{\text{OG}}$  on the content of xenon is evaluated. For all values of the experimental parameters (total gas pressures, discharge currents and laser beam positions), a clear optimum for  $\text{Eff}_{\text{OG}}$  is obtained for the same concentration of xenon 20%, as we can see in fig.3. Also, representing the values of  $\text{Eff}_{\text{OG}}$  corresponding to various points in the discharge space, we can clearly separate into two different cases for which the xenon concentrations are 5% and 100% and those for 10% and 20%. It is found that for

mixtures with close content of xenon and neon, the  $\text{Eff}_{\text{OG}}$  is much higher than that in the case of mixtures close to pure neon and xenon. Consequently, we can assume that a major contribution to generate ions from Xe(2p5) must be a process in which both neon and xenon atoms are taking part simultaneously. A preliminary analysis of the energy level structure for xenon and neon led us to an assumption that the responsible process is a second kind collision between metastable neon Ne(met) and excited xenon Xe(2p5) by a reaction



with an energy defect of +0.17eV. The lifetime of  $\text{Xe}^+(\text{met})$  is of the order of 1 s [1]. As a result of this reaction, short living Xe(2p5) (35ns) [2] are changed in long living  $\text{Xe}^+(\text{met})$ .

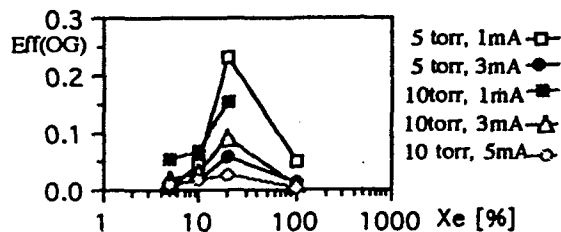


Fig.3.OG efficiency-xenon content

As an alternative explanation might be the change of electrons energy distribution (EDF) into favorable one to generate  $\text{Xe}^+(\text{met})$ , with high rate originating from the laser pumped xenon 2p5 when xenon concentration in Xe-Ne mixture is 10-20%. However, due to much higher values of the energy levels for neon than those for xenon, with increasing the concentrations of neon, the electron temperature may increase, which makes EDF less favorable to sustain this hypothesis.

#### 4. Conclusions

Laser absorption spectroscopy of dc discharges in Ne-Xe mixtures using both plasma modulation and optogalvanic signal measurements, suggested the existence of second kind collision processes generating long living xenon metastable ions.

This work was supported in part by a Grant-in-Aid of Scientific Research, Japanese Ministry of Education, Science and Culture.

#### 5. References

- [1] J.L. Delcroix, Propriétés Physico-Chimique des Gaz Simple, Int.Rept.Université Paris Sud, LPGP, 1982, Paris.
- [2] A.A. Radzizing, B.M. Smirnov, Reference Data on Atoms, Molecules and Ions, Edited, Springer-Verlag, Berlin, 1985.

# INFLUENCE OF THE H<sub>2</sub> ON THE NEON NEGATIVE GLOW SPECTRA IN Ne+1%Xe+H<sub>2</sub> MIXTURE

G.Musa, A.Baltog, C.P.Lungu

National Institute for Laser, Plasma and Radiation Physics  
P.O.Box MG-06 Magurele-Bucharest, Romania

## 1. Introduction

Studies of the narrow gap dielectric barrier discharges, generated in the Penning mixtures Ne+1%Xe or Ne+1%Ar, have shown that at the H<sub>2</sub> addition, in some experimental conditions (i.e. the hydrogen concentration and the total pressure of the gas mixture), the NeI spectrum is practically reduced to nearly one line. This is the neon yellow line with wavelength of 585.3 nm, corresponding to the optical transition 2p<sub>1</sub>-1s<sub>2</sub> [1].

We have denominated this behavior as M-effect ("monochromatisation" effect) and in order to characterize it, we have introduced the M parameter, defined as:  $M=I(\lambda_1)/I(\lambda_2)$  where  $\lambda_1=585.3$  nm and  $\lambda_2=614.3$  nm.

In the case of the d.c. luminescent discharges in the above mentioned triple gas mixtures this effect has been observed too, but exclusively in the negative glow region, the neon yellow line intensity being practically negligible in other regions of the discharge column.

The aim of this paper is to add new results on the H<sub>2</sub> contribution to the physical processes at atomic and molecular level which produce this effect.

## 2. Experimental and results

For this study we have used a d.c. discharge device with a controlled temperature cathode. The emitted radiation from the negative glow of the d.c. luminescent discharge was directed through an optical fiber on the entrance slit of a monochromator, provided at its exit slit with a photomultiplier. Between the experimental device and the optical fiber, a movable slit permits to select from the negative glow that radiating region which presents the highest value of the neon yellow line intensity ( $\lambda=585.3$  nm).

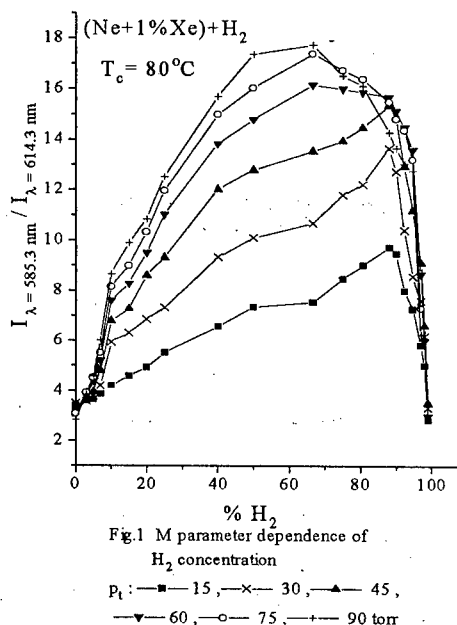
For each set of parameters (i.e. the total gas pressure, the H<sub>2</sub> or Ar concentration added to the Penning mixture Ne+1%Xe, the cathode temperature, the discharge current), the neon emission spectra (between 550 nm and 750 nm) from the negative glow have been recorded. For each recorded spectrum we have

calculated the value of the M parameter, which varies with the change of the working parameters.

This variation reveals the peculiarity of the 2p<sub>1</sub>-1s<sub>2</sub> transition and it is more important for the dielectric barrier discharge, in which M-effect is optimum at pressures of the order 200 torr, than in the d.c. luminescent discharge, because in this last case the maximum pressure has been of 90 torr.

All measurements have been done keeping the same value for the discharge current, namely 40 mA, finding that the limits for which the modification of the current changes not the M parameter value were between 35 mA-45 mA.

In Fig.1 it is given the dependence of the M parameter on the H<sub>2</sub> concentration (expressed in percentages from the total gas pressure), for different values of the pressure of the (Ne+1%Xe)+H<sub>2</sub> mixture. According to this dependence, the optimum concentration of H<sub>2</sub> to obtain an important value of the M parameter strongly depends on the total pressure of the gas mixture. The results presented in Fig.1 have been obtained.



maintaining the cathode temperature at the constant value of 80 °C.

In the other experiment we have proved the influence of the cathode temperature on the neon spectra [2]. In this work we have followed the M parameter modification versus the cathode temperature, for hydrogen or argon added to Ne+1%Xe. An example for (Ne+1%Xe):H<sub>2</sub>=1:1 and (Ne+1%Xe):Ar=1:1 mixtures at various total gas pressures is given in Fig.2., where can be seen that the M-effect is degraded by the increasing of the cathode temperature, but depending of the total gas pressure too. On the same figure it can be observed the different influence of the H<sub>2</sub> or Ar addition on the M parameter value, as well as the fact that the M-effect is negligible in the Ne+1%Xe Penning mixture alone.

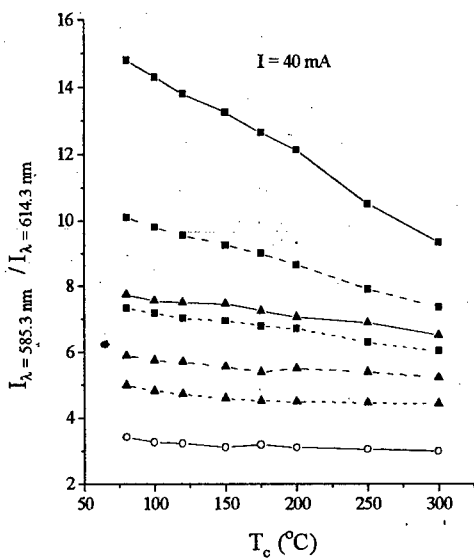


Fig.2 M parameter versus cathode temperature

(Ne + 1% Xe); —○—  $p_t = (15 - 60)$  torr  
(Ne + 1% Xe) + 50% H<sub>2</sub>; —■—  $p_t = 60$ ;  
—■—, 30; —■—, 15 torr  
(Ne + 1% Xe) + 50% Ar; —▲—  $p_t = 60$ ;  
—▲—, 30; —▲—, 15 torr

### 3. Discussions

In the case of the results presented in Fig.1, it can be observed that to have the M-effect is necessary an optimum concentration both of the neon atoms and of the hydrogen molecules. At low concentrations of  $H_2$  or Ne (0-10% $H_2$  and 90-100% $H_2$ ) the M-effect is practically negligible, suggesting an important participation of the hydrogen to the evidenced effect.

We can see that if the hydrogen is missing, the  $M$  parameter is not influenced of the cathode temperature. It results that the hydrogen is a necessary

partner together with the neon excited species generating the observed phenomena.

In the order to explain nearly one line spectra, we assume that in such a case we must have simultaneously two processes: the depleting of the lower level and the feeding of the upper level of the neon optical transition  $2p_1-1s_2$ . The first process is ensured by the Penning type collision of the excited neon atoms with the molecular hydrogen, having the reaction rate constant  $k=2.5 \times 10^{-10} \text{ cm}^3 \text{ s}^{-1}$  [3].

The second process is not clearly established. If we assume that both the argon and the hydrogen are taking part into the M-effect only through the Penning depletion of the neon lower level  $1s_2$ , this can not explain their so different influence on the M parameter, while their Penning reaction rate constants are practically equal [3]. In these circumstances we should assume that the hydrogen is taking part into a supplementary process of feeding of the neon upper level  $2p_1$  and this process is influenced by the cathode temperature and the gas pressure (Fig.2).

Consequently, we may assume that the hydrogen addition increases the population of the upper level  $2p_1$ . Such a process is possible due to the decrease of the electron temperature at the hydrogen addition [4]. In these conditions, the dissociative recombination of the neon molecular ions increases, due to the strong dependence of the reaction rate constant of this process on the electron temperature. The M parameter dependence on the cathode temperature and the total gas pressure sustains the importance of the process of dissociative recombination in the formation of the evidenced effect.

## 4. Conclusions

The results reported in this paper contribute to the understanding of the "monochromatisation" effect of the neon emission spectrum in neon-xenon-hydrogen mixture, from the negative glow of the d.c. luminescent discharge. These bring new arguments in favour of the existence of a selective feeding process of the upper level of the  $2p_1 - 1s_2$  transition of the neon to which the hydrogen is taking part.

## 5. References

- [1] G.Musa, A.Popescu, A.Baltog, C.P.Lungu: Romanian Rept. Phys., **45** (1993) 287
- [2] G.Musa, A.Baltog, A.Popescu, C.P.Lungu, E.Aldea, A.Ricard: Proc.XII-th ESCAMPIG (1994) 408
- [3] B.M.Smirnov: Excited Atoms (in Russian) Energoizdat Moscow (1982)
- [4] I.I.Muravev, E.V.Chernikova, A.M.Yancharina: Sov.J.Quantum Electron., **19** (1989) 123

# Measurement of Effective Diffusion Coefficient of Electrons in Low-Density Argon Afterglows

Tomio Okada<sup>+</sup>, Minoru Sugawara<sup>‡</sup> and Makoto Goto<sup>+</sup>

<sup>+</sup> Department of Electronic Technology, Gunma Polytechnic College, 918 Yamana, Takasaki 370-12, Japan.

<sup>‡</sup> Department of Electrical Engineering, Hachinohe Institute of Technology, 88-1 Ohbiraki, Myou, Hachinohe 031, Japan.

## 1. Introduction

The first theoretical research of the transition from free to ambipolar diffusion has been carried out by Allis and Rose[1]. Analyses under the condition of  $T_e = T_+$  ( $T_e$ : electron temperature,  $T_+$ : ion temperature) have been performed by using afterglows. Gusimov and Gerber[2] have theoretically derived temporal behavior of electron density using the ratio of diffusion coefficients of electrons to ions in the late hydrogen afterglows, from which they determined the effective diffusion coefficient. Their values of the coefficient were smaller than those obtained by Allis and Rose. Freiberg and Weaver[3] experimentally analyzed the transition in helium afterglows, and obtained that agreement with theoretical predictions by many authors was good when  $\text{He}_2^+$  ion was dominant ion species.

The aim of this research is to measure the effective diffusion coefficient of electrons and to verify the electron density dependence of the coefficient when atomic ion is dominant ion species. We examine argon plasma with large ratio of diffusion coefficients of electrons to the ions. In order to carry out the experiment under the condition of  $T_e = T_+$ , we use afterglow technique with a calibrated microwave resonant cavity.

## 2. Experiment and Results

### 2.1 Experimental conditions

We used a Pyrex-glass discharge tube with 31 mm inner diameter with a thermionic cathode and an anode. The distance between the two electrode was 560 mm. The tube current was supplied in dc pulsed operation of time interval of 80 ms, duration of 0.1 ms and peak current of 1.0 A. The discharge tube was baked out at 150 °C for one week before the experiments were carried out. The final vacuum attained was  $2.66 \times 10^{-5}$  Pa. Argon gas of purity 99.999% was used. Operating pressures were 46.6 and 66.5 Pa, at which diffusion cooling[4] does not occur and  $\text{Ar}^+$  ion is dominant ion species.

### 2.2 Measurement of electron number density and results

We have measured electron number density using a calibrated microwave resonant cavity (TM<sub>010</sub>-mode)[5]. Substituting the measured value of  $Q_0 = 587$  and  $f_0 = 2.7253$  GHz ( $f_0$ : resonant frequency of the empty cavity) into energy-response time  $t_r = Q_0/(2\pi f_0)$ , we obtain  $t_r = 3.4 \times 10^{-8}$  s. Since  $(\nu_c/\omega)^2 \ll 1$  ( $\nu_c$ : collision frequency of electrons,  $\omega (=2\pi f)$ : angular frequency of microwave field) is satisfied, we neglect the effect of collision terms. The relationship of electron density  $\langle n_e \rangle$  averaged over the volume of the cavity to the frequency shift  $\Delta f$  is therefore expressed as[5]

$$\langle n_e \rangle = 8.862 \times 10^{-2} f \Delta f \quad (1)$$

where  $\Delta f = f - f_0$ .

In order to minimize the disturbance due to the probing microwave, we adjusted the probing power so as to satisfy[6]

$$P_0 \ll 1.94 \times 10^{-30} \frac{\omega_0^3 V T_g}{Q_c A} \quad (2)$$

where  $P_0$  is microwave power,  $A$ : molecular weight of gas particles, and  $V$ : cavity volume. Substituting the experimental conditions of  $\omega_0 = 1.71236 \times 10^{10}$  rad s<sup>-1</sup>,  $V = 2.28 \times 10^{-4}$  m<sup>3</sup>,  $T_g = 300$  K,  $Q_c = 587$ , and  $A = 40$  into eq. (2), we obtain  $P_0 \ll 28.4 \times 10^{-6}$  W. We then applied the microwave power of 5  $\mu$ W.

Following the technique proposed by Freiberg and Weaver[4], we appended a synchronous detection circuit to a conventional apparatus for measuring  $\Delta f$ . With this improved apparatus we could measure very low  $\Delta f$  to 2.56 kHz, which is lower by about three orders of magnitude than  $\Delta f$  measured with the conventional technique. Substituting measured frequency difference into eq. (1), we obtained  $\langle n_e \rangle$ . Measured values of  $\langle n_e \rangle$  against time are shown in Fig. 1.

## 3. Analysis and Discussion

### 3.1 Relationship between $\langle n_e \rangle$ and axial electron density

In theories the effective diffusion coefficient  $D_s$  is calculated against axial electron density  $n_e(0)$ . In the experiments, however,  $\langle n_e \rangle$  is measured. In order to compare  $D_s$  determined from the experiment with that

obtained by theories, we must estimate  $n_e(0)$  from  $\langle n_e \rangle$ . Then, we calculated spatial distribution  $g_e$  of electrons in argon afterglow. Substituting  $g_e$  into eq. (3), we obtained a relationship between  $\langle n_e \rangle$  and  $n_e(0)$ .

$$\langle n_e \rangle = n_e(0) \frac{\int g_e E_m^2 dv}{\int E_m^2 dv} = \frac{n_e(0)}{1.47} \quad (3)$$

where  $E_m$  is microwave electric field in the empty discharge tube.

### 3.2 Electron density dependence of $D_s$

In present experimental conditions the rate equation of  $n_e$  is expressed by the following equation.

$$\partial n_e / \partial t = D_s \nabla^2 n_e - k_1 n_a^2 n_e \quad (4)$$

here  $k_1$ : the rate coefficient of conversion of atomic ions into molecular ions and  $n_a$ : gas density. Combining eqs. (3) and (4), we obtain  $D_s / D_e$  ( $D_e$ : electron diffusion coefficient),

$$\frac{D_s}{D_e} = - \left( \frac{n_a}{\langle n_e \rangle} \frac{\partial \langle n_e \rangle}{\partial t} + k_1 n_a^3 \right) \frac{\Lambda^2}{D_e n_a} \quad (5)$$

here  $\Lambda$ : characteristic diffusion length. Debye length  $\lambda_{D0}$  on the axis is obtained combined with eq. (3).

$$\lambda_{D0} = \sqrt{\frac{\epsilon_0 k_B T_e}{1.47 \langle n_e \rangle e^2}} \quad (6)$$

where  $\epsilon_0$ : the permittivity of free space,  $k_B$ : Boltzmann constant and  $e$ : electron charge.

Substituting  $\langle n_e \rangle$ ,  $D_e = 88.5 \text{ m}^2 \text{ s}^{-1}$  [7] and  $k_1 = 2.26 \times 10^{-43} \text{ m}^6 \text{ s}^{-1}$  [8] into eq. (5) we calculated the values of  $D_s / D_e$ . The values of  $\lambda_{D0}$  was obtained from eq. (6), where we set  $T_e = 300 \text{ K}$ . The relationship of  $D_s / D_e$  against  $\Lambda / \lambda_{D0}$  is shown in Fig. 2.

We introduced eq. (7) (dashed curve in Fig. 2) which fitted to the values calculated on the computer for  $T_e = T_+$  by Allis and Rose (▽).

$$\log \left( \frac{D_s}{D_e} \right) = \frac{1}{1 + 1.26 \left( \frac{\lambda_{D0}}{\Lambda} \right)^{1.17}} \log \left( \frac{D_a}{D_e} \right) \quad (7)$$

where  $D_a$ : ambipolar diffusion coefficient. We applied eq. (7) to present case, which is shown with a solid curve in Fig. 2. Good agreement between eq. (7) and present results is obtained over the range of  $4 \leq \Lambda / \lambda_{D0} \leq 500$ .

## 4. References

- [1] W.P. Allis and D.J. Rose: Phys. Rev. **93** (1954) 84
- [2] M.A. Gusinov and R.A. Gerber: Phys. Rev. A **5** (1972) 1802

- [3] R.J. Freiberg and L.A. Weaver: Phys. Rev. **170** (1968) 336
- [4] D. Smith, A.G. Dean and N.G. Adams: Z. Physik **253** (1972) 191
- [5] T. Okada and M. Sugawara: J. Phys. D: Appl. Phys. **26** (1993) 1680
- [6] H.J. Oskam: Philips Res. Rep. **13** (1958) 401
- [7] D.R. Nelson and F.J. Davis: J. Chem. Phys. **51** (1969) 2322
- [8] M. Sugawara, T. Okada and Y. Kobayashi: J. Phys. D: Appl. Phys. **19** (1986) 1213

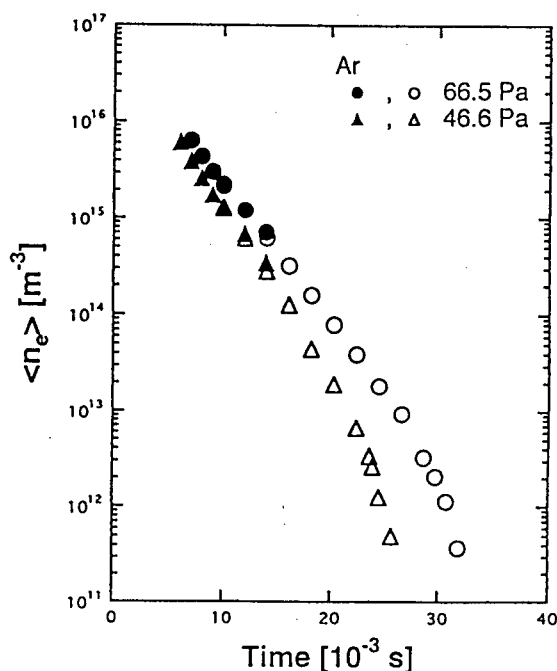


Fig. 1 Decay of  $\langle n_e \rangle$ .

●, ▲: measured with the conventional technique;  
○, △: measured with the improved technique.

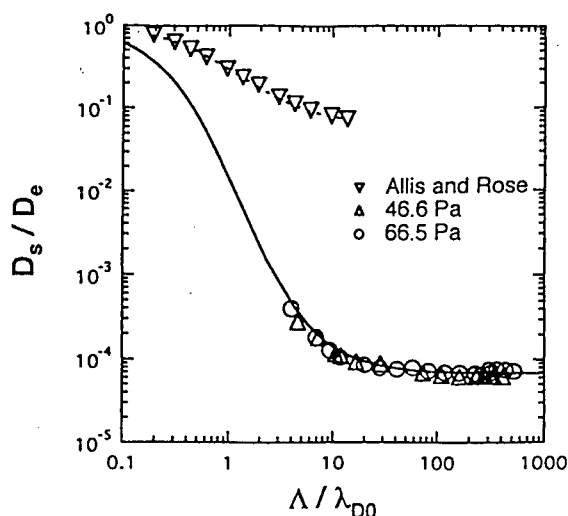


Fig. 2  $D_s / D_e$  vs.  $\Lambda / \lambda_{D0}$ .

---: eq. (7) for Hydrogen; —: eq. (7) for argon.

# EXCITATION OF 3p AND IONIC LEVELS IN ARGON TOWNSEND DISCHARGES

G.N.Malović, J.V.Božin\*, B.M.Jelenković and Z.Lj. Petrović

Institute of Physics, University of Belgrade, P.O.Box 57, 11001 Belgrade, Yugoslavia

\*Faculty of Physics, University of Belgrade, P.O.Box 550, 11001 Belgrade, Yugoslavia

## 1. INTRODUCTION

In this paper we present the excitation coefficients for 3p<sub>s</sub>, 3p<sub>6</sub>, 3p<sub>8</sub> levels of argon atom (in Paschen notation), and excitation coefficients for five ionized argon levels. Argon atoms play an important role in the kinetics of gas discharges and plasma processing [1], [2]. We apply a drift tube technique for measurement of the absolute emission intensities in low current self sustained Townsend type discharges. The excitation coefficients were obtained from the optical signal at the anode after correction for the detector quantum efficiency. The data were obtained for the electric field to argon number density ratio (E/N) from 30 Td to 6 kTd for atomic, and 400 Td to 11 kTd for ionic lines (1Td = 10<sup>-21</sup> Vm<sup>2</sup>)

## 2. EXPERIMENTAL SET-UP AND PROCEDURE

The experimental set-up has been described in an earlier publication [3]. The drift tube consists of a pair of parallel plane electrodes, with a diameter of 79 mm at a distance of 17.2 mm, placed inside a close fitting quartz tube. The cathode was made of stainless steel, while the anode was made of graphite in order to minimize the effect of backscattered electrons from the anode.

The pressure was measured by a capacitance manometer. Vacuum chamber (stainless steel) is evacuated by a turbomolecular pump typically to 3 · 10<sup>-7</sup> Torr. The quality of the vacuum system is sufficient to allow measurements of excitation coefficients over periods of up to 20 minutes without any effect of impurities. Research grade argon was used for the measurements.

The discharge current was measured by an electrometer, which was recalibrated before the experiment by using a standard current source. The current was kept below 2 μA, in order not to perturb the homogeneous electric field between the electrodes. Oscilloscope was continuously attached to the system to check for possible oscillations which occur even in the

Townsend regime. Pressure, current and voltage are continuously monitored and digitized by an AD interference card.

The light emitted from the discharge was detected using a collimator, a photomultiplier, and a photon counting chain. For the measurements of the light intensity the monochromator was positioned at the wavelength of the maximum of the line. The entire detection system was placed on the platform and moved by a stepper motor, which was controlled by a computer. The spatially dependent light emission was recorded with a spatial resolution of 1 mm.

The absolute calibration of the quantum efficiency of our detection system in the spectral region 330 - 830 nm was obtained by using a standard tungsten lamp, which was calibrated against the radiation from the blackbody radiation standard.

In Townsend discharges where electron excitation dominates over other processes of level population and where electrons are in equilibrium with electric field and gas collisions, the electron excitation coefficients of level m is related to the emission signal S<sub>a</sub> via

$$\frac{\epsilon_m}{N} = \frac{S_a}{j_e} \frac{e}{Q(\lambda)\Delta x N^{3/4}} \frac{A_m}{A_{mn}} \quad (1)$$

where j<sub>e</sub> is the current density at the anode, e is electron charge, Ω is effective solid angle of the detector, Q(λ) is the quantum efficiency of the detector, A<sub>mn</sub> is the transition probability for the level m, and A<sub>m</sub> is the total transition probability for the upper level, and Δx is the width of the entrance slit of the monochromator. The electron excitation coefficient given in Eq. (1) represent the average number of electron excitation collisions per unit distance as electron moves towards the anode. If the rate for the collisional quenching of an excited state is not negligible in comparison with the rate for the spontaneous emission, the correction to the measured S<sub>a</sub> can be done by multiplying the right-hand side of Eq. (1) by (1 + N/N<sub>0</sub>). Here N<sub>0</sub> is the quenching density

for the state  $m$  (equal to  $A_m/k_q$ , where  $k_q$  is the rate coefficient for collisional quenching).

### 3. RESULTS AND DISCUSSION

The data for absolute emission intensity were analyzed by the procedure outlined above to give the excitation coefficients. The results of the excitation coefficients for 3p levels are shown in Fig. 1.

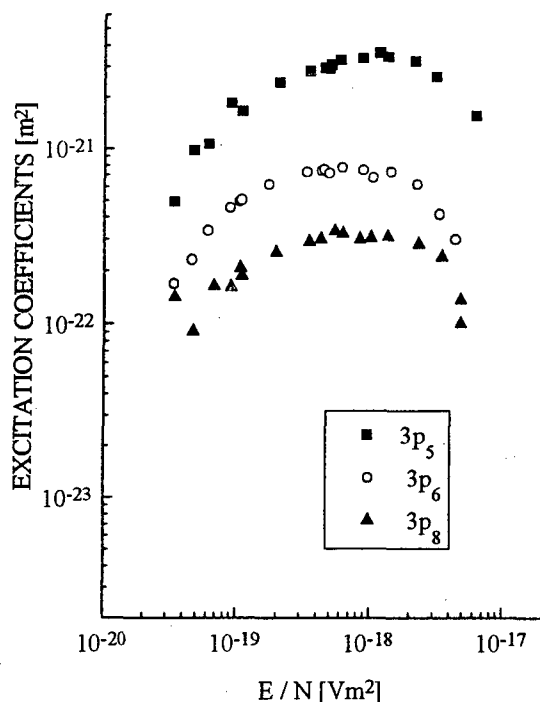


Fig. 1. Excitation coefficients for 3p level: 3p<sub>5</sub> - square, 3p<sub>6</sub> - circle, 3p<sub>8</sub> - triangle

The excitation coefficients were obtained using Eq.(1) and measured emission intensity of the anode  $S_a$  and corrected for quenching. The data for quenching are available in the [4]. The curves for different 3p levels have generally similar E/N dependence, with the maxima between 1 - 2 KTd.

In Fig. 2 the excitation coefficients of five ionized argon levels are shown. The transition probabilities of different transitions were taken from tables by Vujinović and Wiese [5]. Position of the maximum of the excitation coefficients for ionic levels of argon is shifted toward the region of lower pressures (0.1 - 0.2 Torr) i.e higher values E/N (3 - 4 KTd) if we compare with position of atomic argon. At lower pressures probability for excitation of ionic levels of argon increases with respect to atomic levels which causes shifting of these maxima curve.

To our knowledge these are the first absolute experimental results of excitation coefficients for ionized argon levels. The excitation coefficients for 3p<sub>5</sub>, 3p<sub>6</sub>, 3p<sub>8</sub> levels results of measurements are not available in the literature, so it was not possible to compare with another results. Data presented here are used very much in the plasma diagnostics [6], [7] so absolute values presented here may be of use in developing models and comparing them with experiments.

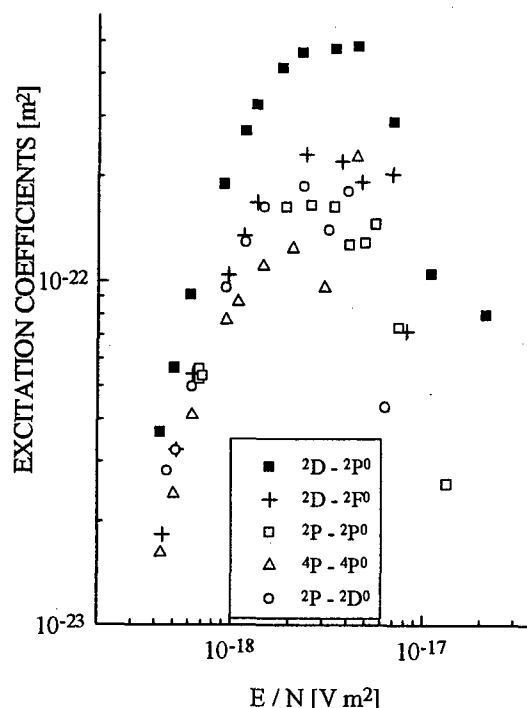


Fig. 2 Excitation coefficients for ionized argon levels: solid square -  $^2D - ^2P^0$  (413.7 nm); cross -  $^2D - ^2F^0$  (460.96 nm); open square -  $^2P - ^2P^0$ ; triangle -  $^2P - ^4P^0$  (480.6 nm); circle -  $^2P - ^2D^0$  (487.99 nm)

### 4. REFERENCES

1. Excimer Laser, edited by C.K.Rhodes (Springer Verlag, Berlin 1979)
2. H.F.Winters, J. Vac. Sci. Technol. A63 (1988) 1997
3. V. Stojanović, J.V.Božin, Z.Lj.Petrović and B.M. Jelenković, Phys.Rev.A 42 (1990) 4983
4. G.Inoue, D.W. Setser and N. Sadeghi, J. Chem. Phys. 76(2) (1982) 977
5. V.Vujinović, W.L. Wiese, J.Phys. Chem.Ref. Data, Vol. 21 No. 5 (1992)
6. A. Okigawa, T. Makabe, T. Shibagaki, N. Nakano, Z.Lj. Petrović, T. Kogawa and A. Itoh, Jpn. J. Appl. Phys. 35 (1996) 1890
7. F. Tochikubo, Z.Lj. Petrović, S. Kakuta, N. Nakano and T. Makabe, Jpn. J. Appl. Phys. 33 (1994) 4271

# Numerical study of low pressure argon discharges with ring-like cathode geometry

Ph. Belenguer and L.C Pitchford

Centre de Physique des Plasmas et Applications -ESA 5002-  
118, Route de Narbonne, 31062 Toulouse Cedex, France

## 1. Introduction

In this paper we present results from model calculations of the potential, density and ionisation rate distributions for a low pressure glow discharge in a ring-like cathode geometry.

This work is a preliminary step in the study of the electron beam that has been experimentally observed in similar discharge configurations. [1]

## 2. Model and discharge conditions

The calculations have been performed using a 2 dimensional hybrid, fluid-Monte Carlo model described in [2]. Briefly, the ion and 'bulk' electron density distributions are described by fluid equations in the drift-diffusion approximation. From these densities we calculate the space charge and hence the potential distribution from Poisson's equation. The ionization due to the cathode emitted electrons is determined from a Monte Carlo simulation.

The cell geometry is presented figure 1. The discharge cell consists of a cylindrical hollow cathode and a cylindrical anode. The electrodes are separated by a dielectric ring.

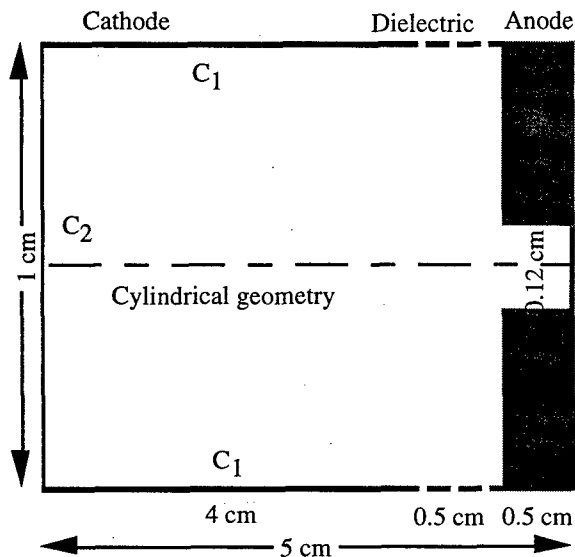


Fig.1. Cell geometry (not to scale).

The discharge conditions considered here are the following:

Gas: argon, pressure: 0.5 torr, applied voltage: 10 kV. The secondary electron emission coefficient has been set to 0.07. The total steady state discharge

current was calculated to be 4 A. The secondary emission has only been included for the cathode surface labelled C1 on figure 1. This was done as a first approach to simulate a ring-like cathode.

## 3. Results

The results presented in this section have been obtained at steady state for the discharge conditions described above.

Figure 2 shows the spatial distribution of the potential. The plasma formation leads to the penetration of the anodic potential into the cathodic cavity. The cathode surface is surrounded by a potential sheath that accelerates the ions towards it. These ions striking the cathode surface cause emission of secondary electrons (only from the surface C1) which are responsible for the gas ionization.

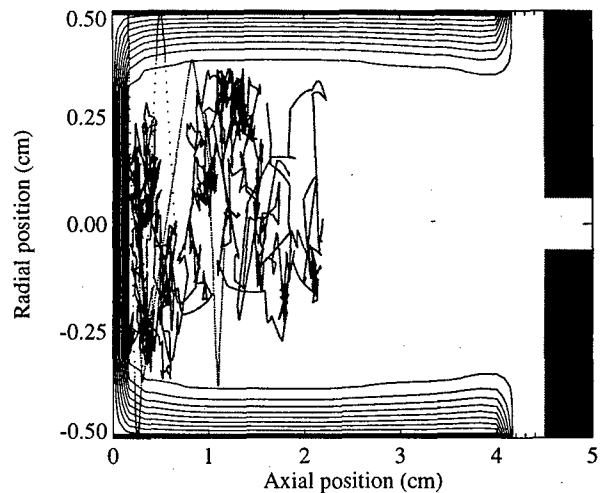


Fig.2. Equipotential contours. Each contour corresponds to 1/10 of the maximum potential (10005 V). The plasma potential is higher than the applied potential. Superimposed on these potential contours is the trajectory of one electron emitted from the cathode surface C1 at a point 0.3 cm from C2.

In this potential distribution, the electrons emitted from the surface C1 tend to be trapped in the discharge volume. This trapping increases the ionization ability of these electrons.



This trapping is also illustrated in figure 2 which displays the trajectory of an electron emitted from the surface C1 at an axial position 0.3 cm away from C2.

The ionization source term distribution is shown in figure 3. The maximum ionization occurs in the center of the discharge cell. We assume that this ionization is representative of the light emission, we can see that this emission will be maximum in the center.

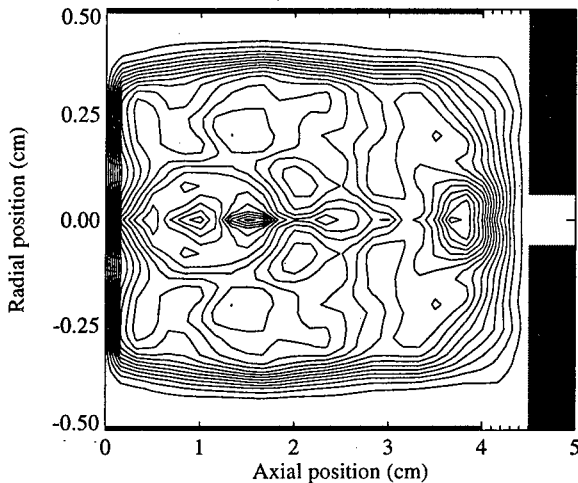


Fig.3. Contours of constant ionization source term. Each curve corresponds to 1/20 of the maximum of the ionization ( $5 \cdot 10^{19} \text{ cm}^{-3} \text{ s}^{-1}$ )

Figure 4 shows the velocity field distribution of the electron flux from the fluid equations, the electron flux on the axial direction versus the electron flux on the radial direction. The length of the arrows at each point is proportional to the amplitude of the flux. We can see on this figure that flux of the bulk electrons is directed toward the anode in the center of the cell discharge.

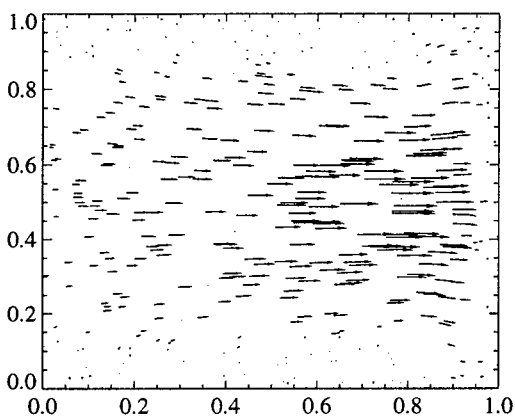


Fig.4 : Velocity field distribution of the electron flux from the fluid equations

Thus the bulk electrons form a 'beam' in the center of the discharge.

The spatial distribution of the bulk electron density is presented figure 5. As expected from the results presented above, the density shows a maximum in the center of the discharge.

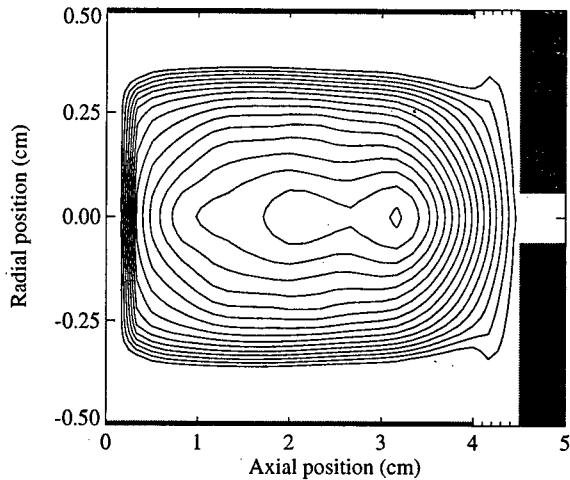


Fig.5 Contours of the electron plasma density. Each curve corresponds to 1/20 of the maximum of the density ( $6 \cdot 10^{13} \text{ cm}^{-3}$ )

Experimentally, a high energy component has been observed in the electron beam generated in this discharge configuration [1]. This beam of fast electrons is a transient phenomena and thus not included here in these steady state results. Calculations of the transient evolution of the discharge are now underway.

#### 4. Conclusion

The steady state properties of low pressure glow discharges in ring-like cathode geometries are studied here. For a range of conditions the bulk electrons form a beam in the center of the discharge.

This work is being extended to a study of the transient behavior of the discharge in order to identify the presence of a fast electron beam during the plasma formation and to make quantitative comparisons with the experiments of ref. [1].

#### 5. References

- [1] E. Dewald, K. Frank, D.H.H Hoffmann, R. Stark, M Ganciu, N.B. Mandache, M. Nistor, A.M. Pointu and I.-Iovitz Popescu. IEEE Trans. Plasma Sci. To be published
- [2] J.P. Boeuf and L.C Pitchford, IEEE Trans Plasma Sci, 19, 286, (1991).

# Influence of CH<sub>4</sub> Addition on Active Nitrogen Produced in a Low-Pressure DC Discharge

C.D. Pintassilgo, J. Loureiro and G. Cernogora<sup>†</sup>

Centro de Electrodinâmica, Instituto Superior Técnico, 1096 Lisboa Codex, Portugal

<sup>†</sup>Lab. de Phys. des Gaz et des Plasmas, Université de Paris-Sud, 91405 Orsay Cedex, France

## 1. Introduction

The methane decomposition in N<sub>2</sub>-CH<sub>4</sub> discharges has been the subject of different studies in these last years [1,2] due to its interest in different fields as metal nitriding, detection of small carbon impurities in N<sub>2</sub>, or for the purpose of gaining a better knowledge of the atmospheric chemistry of Titan. Therefore, in order to improve such applications there is a need for a deeper understanding of the influence of a small methane addition ( $\lesssim 5\%$ ) on the different species produced in the discharge such as N(<sup>4</sup>S), N<sub>2</sub>(A <sup>3</sup>Σ<sub>u</sub><sup>+</sup>), N<sub>2</sub>(X <sup>1</sup>Σ<sub>g</sub><sup>+</sup>, v), which constitute the active nitrogen.

## 2. Kinetic model

Here, we present preliminary results from a self-consistent kinetic model for a low pressure glow-discharge in N<sub>2</sub>-CH<sub>4</sub>, which solves the electron Boltzmann equation coupled to a system of steady-state rate balance equations for the vibrational levels N<sub>2</sub>(X <sup>1</sup>Σ<sub>g</sub><sup>+</sup>, v), the electronically excited states of N<sub>2</sub>(A <sup>3</sup>Σ<sub>u</sub><sup>+</sup>, B <sup>3</sup>Π<sub>g</sub>, C <sup>3</sup>Π<sub>u</sub>, a' <sup>1</sup>Σ<sub>u</sub><sup>+</sup>, a <sup>1</sup>Π<sub>g</sub>, w <sup>1</sup>Δ<sub>u</sub>), the N(<sup>4</sup>S) atoms, the most populated neutral species produced either from dissociation of CH<sub>4</sub> (CH<sub>3</sub>, CH<sub>2</sub>, H<sub>2</sub>, H) or in reactions with N<sub>2</sub> (HCN, H<sub>2</sub>CN, CN, NH), the most important ionic species (N<sub>2</sub><sup>+</sup>, N<sub>4</sub><sup>+</sup>, CH<sub>4</sub><sup>+</sup>, CH<sub>5</sub><sup>+</sup>, CH<sub>3</sub><sup>+</sup>), as well as some other species included in the model for mathematical convenience (C<sub>2</sub>H<sub>4</sub>, C<sub>2</sub>H<sub>5</sub>, C<sub>2</sub>H<sub>6</sub>) in order to ensure that the complete system of master equations has a non-zero steady-state solution. Further, the reduced electric field required for the maintenance of the plasma is self-consistently determined from this model. The Boltzmann equation is solved using a consistent set of electron-molecule cross sections for CH<sub>4</sub> derived in this work by comparing our predicted results with swarm data, whereas the electron cross sections of N<sub>2</sub> are taken from [3]. A complete list of the heavy-particle processes considered, along with the pertinent rate coefficients selected from the literature, will be made available at the conference.

## 3. Results and Discussion

Figs.1 to 4 show the relative concentrations of N(<sup>4</sup>S) atoms and of the triplet states of N<sub>2</sub>(A <sup>3</sup>Σ<sub>u</sub><sup>+</sup>,

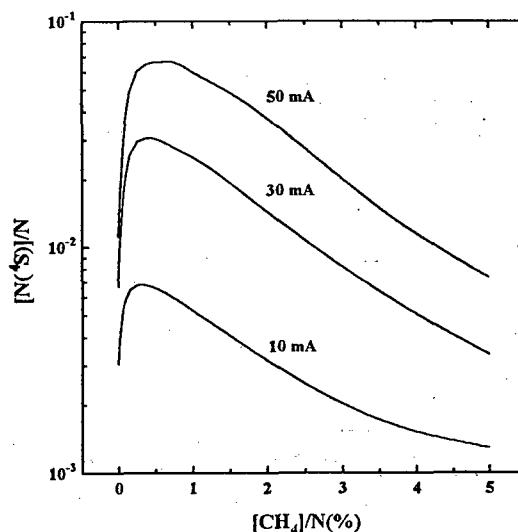
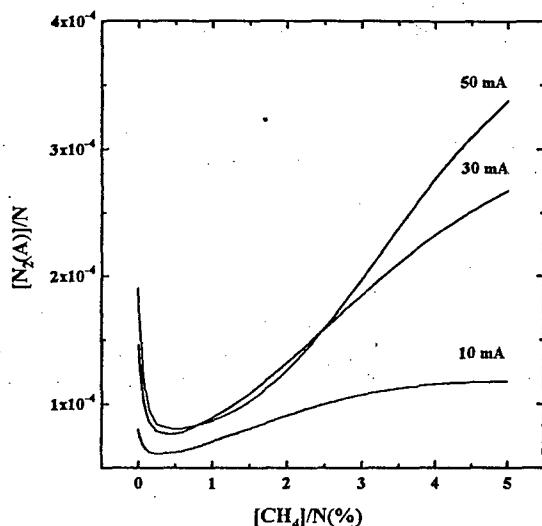
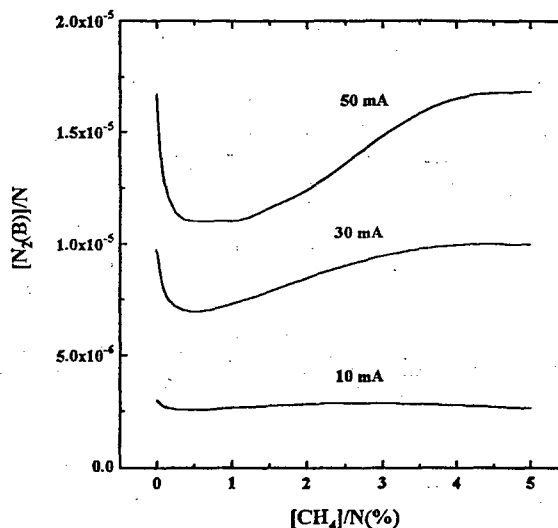
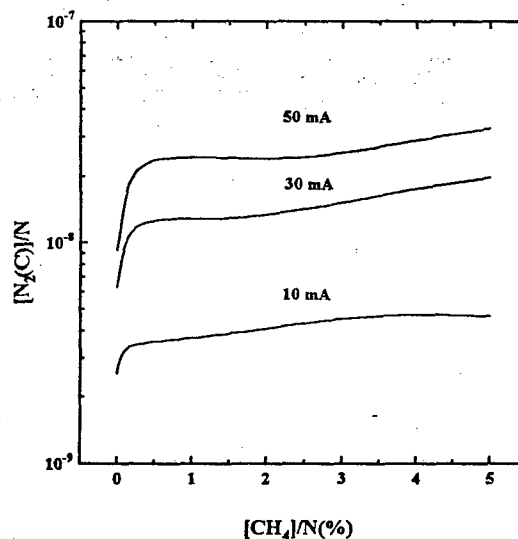


Fig.1 - Relative concentration  $[N(^4S)]/N$  vs.  $[CH_4]/N$ , for  $p=1.5$  Torr and  $I=10, 30, 50$  mA.

B <sup>3</sup>Π<sub>g</sub>, C <sup>3</sup>Π<sub>u</sub>) predicted here, as a function of the fractional concentration of CH<sub>4</sub> in the mixture, in a DC N<sub>2</sub>-CH<sub>4</sub> glow-discharge of tube radius  $R=1$  cm, for  $p=1.5$  Torr, and  $I=10$  mA, 30 mA and 50 mA. Fig.1 shows that the concentration  $[N(^4S)]/N$  (where  $N$  denotes the total gas density) rapidly increases as a small percentage of CH<sub>4</sub> is added to N<sub>2</sub> ( $\lesssim 0.5\%$ ) as a result of the increase of the maintenance electric field, which in turn is a consequence of the reduction of the contribution from associative ionization involving collisions between electronically excited states N<sub>2</sub>(A <sup>3</sup>Σ<sub>u</sub><sup>+</sup>)+N<sub>2</sub>(a' <sup>1</sup>Σ<sub>u</sub><sup>+</sup>) and N<sub>2</sub>(a')+N<sub>2</sub>(a'), since the N<sub>2</sub>(a') state is strongly quenched by CH<sub>4</sub> [4]. We note that as the associative ionization ceases to exist the electric field must increase in order to sustain the discharge. On the other hand, the decrease of  $[N(^4S)]/N$  for larger concentrations of CH<sub>4</sub> is associated with depopulation mechanisms through the following reactions: N(<sup>4</sup>S)+CH<sub>3</sub> → H<sub>2</sub>CN+H; N(<sup>4</sup>S)+H<sub>2</sub>CN → HCN+NH; N(<sup>4</sup>S)+NH → N<sub>2</sub>+H. This behaviour is in qualitative agreement with measurements in the flowing afterglow of a microwave N<sub>2</sub>-CH<sub>4</sub> discharge [5]. Fig.2 shows that the relative concentration of N<sub>2</sub>(A <sup>3</sup>Σ<sub>u</sub><sup>+</sup>) exhibits a reverse dependence on  $[CH_4]/N$  as compared to that shown in fig.1 for the N(<sup>4</sup>S) atoms, which is mainly associated with

Fig.2 - As in fig.1 but for  $[N_2(A \ ^3\Sigma_u^+)]/N$ .Fig.3 - As in fig.1 but for  $[N_2(B \ ^3\Pi_g)]/N$ .

the enhancement (for  $[CH_4]/N \lesssim 0.3\%$ ) and with the diminution ( $\gtrsim 0.3\%$ ) of the quenching of  $N_2(A)$  by  $N(^4S)$  atoms. The rapid decrease of the concentration of  $N_2(B \ ^3\Pi_g)$  molecules shown in fig.3, as very small percentages of  $CH_4$  are added to  $N_2$ , has the same origine as in fig.2, since both states are strongly correlated in the overall kinetics. Further, the increase of  $[N_2(B)]$  for larger percentages of  $CH_4$  occurs in a smaller extent than that observed for  $[N_2(A)]$ , due to an enhancement of the quenching of  $N_2(B)$ . We note that the rate coefficient for quenching of  $N_2(B)$  by  $CH_4$  is about one order of magnitude larger than that for quenching by  $N_2$  [6], while the rate coefficients for quenching of  $N_2(A)$  by  $N_2$  and  $CH_4$  are close. Finally, fig.4 shows an increase of the relative concentration of  $N_2(C \ ^3\Pi_u)$  as very small percentages of methane are added to  $N_2$ , which is a consequence of the increase of the maintenance electric field. Preliminary spectroscopic measurements on the  $1^+$  and  $2^+$  system bands of  $N_2$  are in agreement with these predicted behaviours for the concentrations of  $N_2(B)$  and  $N_2(C)$  states.

Fig.4 - As in fig.1 but for  $[N_2(C \ ^3\Pi_u)]/N$ .

[1] - A. Ricard et al 1995 Planet. Space Sci. 43 41; [2] - J.-C. Legrand et al 1995 Proc. 12th ISPC (Minneapolis) vol.2, p.601; [3] - L.C. Pitchford and A.V. Phelps 1982 Bull. Am. Phys. Soc. 27 109; [4] - L.G. Piper 1987 J. Chem. Phys. 87 1625; [5] - J.-C. Legrand et al 1994 Proc. 12th ESCAMPIG (Noordwijkerhout), p.324; [6] - L.G. Piper 1992 J. Chem. Phys. 97 270.

This work has been carried out under the support of a PRAXIS XXI Research Grant (Portuguese Ministry of Science and Technology).

# Experimental and numerical study of trapping and broadening of the $\text{Kr}(^3\text{P}_1 \rightarrow ^1\text{S}_0)$ resonance line in Kr-Ar mixtures

J. P. Gardou, N. Sewraj, F. Marchal, P. Millet, Y. Salamero

CPAT Université Paul Sabatier 118, route de Narbonne F-31062 Toulouse Cedex 4 France

## 1. Introduction

The present work deals with the experimental and numerical study of radiation trapping of the  $\text{Kr}(^3\text{P}_1 \rightarrow ^1\text{S}_0)$  resonance line in Kr-Ar mixtures. Theoretical studies have been done in the case of merely cylindrical and plane geometric vessels containing a pure gas [1], [2], [3].

Nonetheless, our experimental study concerns a brief laser excitation (5 ns) of the resonant state produced in a finite nearly cylindrical vessel at the focal point of a 40 mm focal length lens.

The simulation is done with a Monte-Carlo method.

## 2. Apparent lifetime determination by the Monte-Carlo method

The apparent radiative lifetime of an excited state is given by  $\tau_a = \frac{1}{g} \tau_n$ , where  $\tau_n$  is the natural lifetime of

the resonant state, and  $g$  the escape factor whose inverse represents the mean absorption-reemission processes undergone by a photon before reaching the detector.

The analysing cell containing the excited gas is rather complex. Indeed, this cell is a cylindrical one equipped with two observation windows, the laser entrance and exit and the gaz entry. In a first approximation it can be assimilated to a finite cylindrical volume whose wall's reflection coefficient for VUV photons is negligible.

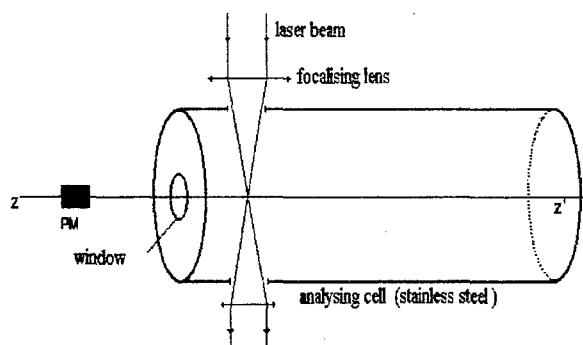


Fig 1 : The simplified analysing cell

The resonant states, initially created by short pulses of a 50 Hz pulsed tunable dye laser, are localized in the laser's confocal volume (Fig. 1). These excited atoms spontaneously lose their energy through emission of resonant photons whose treatment is based on the drawing of 4 random numbers  $X_1$ ,  $X_2$ ,  $X_3$  and  $X_4$  [4], where  $0 < X_i < 1$ .

The frequency of an emitted photon is determined by the pressure broadening assuming complete frequency redistribution :

$$\nu = \nu_0 + \frac{\Delta\nu_p}{2} \tan \left\{ \pi \left( X_1 - \frac{1}{2} \right) \right\}$$

$\nu_0$  and  $\Delta\nu_p$  are the line's central frequency and full-width at half maximum respectively.

Photons of negligible flight time are assumed to be in rectilinear motion between the emitting atom  $M_e$  and the absorbing one  $M_a$ . Each photon trajectory is defined, in polar coordinates, by its emission angles  $\theta$ ,  $\varphi_d$  and the distance  $D$  covered during one emission/absorption process. These geometrical parameters are given by :

$$\cos \theta = 2X_2 - 1$$

$$\varphi_d = 2\pi X_3$$

$$D = -mfp \cdot \ln(X_4)$$

$mfp$  is the mean free path of a photon at frequency  $\nu$ .

We follow each photon individually from its emission at the laser's focalising point to its exit. The absorbing position  $M_a$  is obtained from the emitting one  $M_e$ ,  $\theta$ ,  $\varphi_d$  and  $D$ . If the calculated absorbing position lies inside the cell then it is considered as the new emitting position of the following absorption/emission process. This procedure is repeated until the photon leaves the cell. Only those reaching the photomultiplier tube are considered for the escape factor determination.

The escape factor and hence the apparent lifetime are deduced from the overall photons and laser flashes.

Taking into account the frequency of each detected photon we can obtain the simulated emission line profile. The numerical method has been elaborated for the study of the imprisonment of resonance lines in rare gases mixtures.

## 3. Radiation trapping theory in mixtures

In the Kr-Ar mixtures, the line broadening is accounted by the Kr-Kr and Kr-Ar collisions, respectively described by the resonance broadening and the heteronuclear collision broadening of the  $\text{Kr}(^3\text{P}_1 \rightarrow ^1\text{S}_0)$  transition. These line broadenings are introduced by their respective coefficients  $\xi_{\text{Kr}}$  and  $\xi_{\text{Ar}}$  which allow the determination of the absorption coefficient and thus the apparent lifetime.

$\xi_{\text{Kr}}$  is given by [5] :

$$\xi_{Kr} = \left( \frac{g_1}{g_2} \right)^{1/2} \frac{e^2 f}{11,7 \cdot \pi^2 \cdot \epsilon_0 \cdot m_e \cdot \nu_0}$$

where  $g_1$  and  $g_2$  are the statistical weights of the lower and upper states respectively,  $f$  is the oscillator strength of the transition.

As far as  $\xi_{Ar}$  is concerned we don't have any theoretical expression. Its determination is done experimentally.

Indeed, the variation of the apparent lifetime  $\tau_a$  with the argon's concentration  $C$  is given by [6] :

$$\tau_a = A \sqrt{\frac{1-C}{(1-C)\xi_{Kr} + C\xi_{Ar}}} \quad (1)$$

where  $C = \frac{P_{Ar}}{P_{Ar} + P_{Kr}}$ . The constant  $A$  depends only on the cell's geometry and the atomic characteristics of the transition. Its exact theoretical determination is not easy. The measured apparent lifetime  $\tau_a$  of the resonant state can be deduced from the recorded temporal evolution of the luminescence decay. This determination has been realised by means of an experimental setup allowing selective excitation of the  $Kr(^3P_1)$  state by 3-photons absorption from the ground state ( $^1S_0$ ) [7].  $\xi_{Ar}$  is deduced from the measured value of  $\tau_a$ .

#### 4. Experimental results

$\left( \frac{1}{\tau_a} \right)^2$  varies linearly (Fig. 2) with  $\frac{C}{1-C}$ , in accordance to theoretical prediction (1).  $\xi_{Ar}$  is evaluated from this curve since  $\xi_{Kr}$  is theoretically determined.

$$\xi_{Ar} = 1,9 \cdot 10^{-16} \text{ m}^3 \text{ s}^{-1} \quad (\text{with } \xi_{Kr} = 9,8 \cdot 10^{-16} \text{ m}^3 \text{ s}^{-1})$$

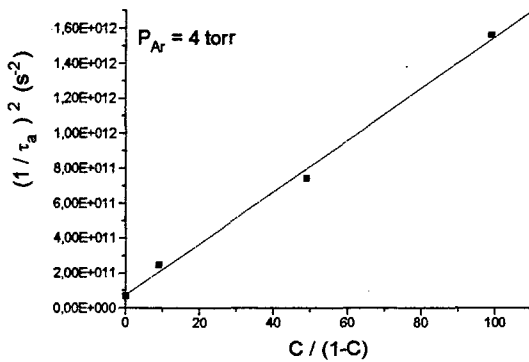


Fig 2 Measured values of  $\tau_a$  versus  $C/(1-C)$

#### 5. Numerical results

The apparent lifetime is obtained by using the natural lifetime of the  $Kr(^3P_1)$  state  $\tau_n$ , the theoretical value of  $\xi_{Kr}$  and the measured value of  $\xi_{Ar}$  (Table 1). The difference between experimental and simulated values of  $\tau_a$  can be explained by the simplified geometry

compared to the real one. Besides, the wall's reflection coefficient is not exactly zero.

C	Simulated values			Measured Values
	1	2	4	(Mean values)
0	4.78	4.79	5.00	4.01
0.9	2.68	2.69	2.64	2.00
0.98	1.32	1.32	1.30	1.08
0.99	0.91	0.91	0.93	0.82

Table 1 : Calculated and measured apparent lifetimes of the  $Kr(^3P_1)$  state ( $\mu\text{s}$ )

The emission profile of the  $Kr(^3P_1 \rightarrow ^1S_0)$  line has been simulated by our numerical method (Fig. 3). Its shape characterizes a high absorption of the resonance line. This is a very interesting result as well since our experimental setup does not allow its measurement.

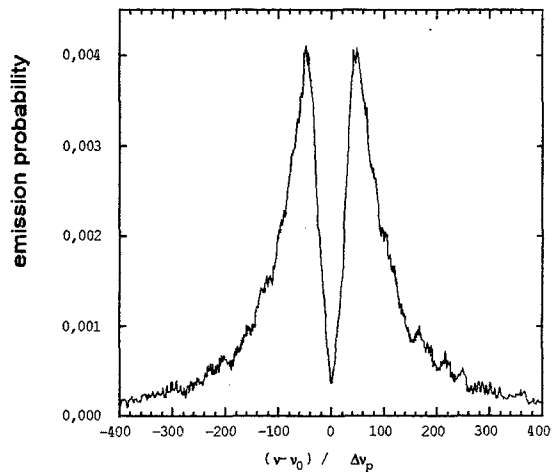


Fig 3 : Simulated emission profile for  $C = 0.99$

Actually we are improving this method. It should be used in our kinetic studies so as to determine apparent lifetimes corresponding to experimental situations where their measurements are rather difficult.

#### References

- [1] T. Holstein, Phys.Rev., **72**, (1947) 1212
- [2] T. Holstein, Phys.Rev., **83**, (1951) 1159
- [3] L.M. Biberman, Soviet Physic. JETP, **19**, (1949) 584
- [4] J.E. Lawler, G.J. Parker, W.N.G. Hitchon, JQSRT, **49**, (1993) 627
- [5] W. Lochte-Holtgreven, Plasma Diagnostics (North Holland Publishing Company, Netherlands, 1968)
- [6] K. Igarashi, S. Mikoshiba, Y. Watanabe, M. Suzuki and S. Muruyama, J. Phys. D-Applied Phys, **28**, (1995) 1377
- [7] P. Berejny, P. Millet, M. Saissac and Y.Salamero, J. Phys. B, **26**, (1993) 3339

# Determination of the radiative lifetime of the $^1P_1$ resonance state in Krypton by means of three photon excitation.

T. Van Bever and E. Desoppere

Department of Applied Physics, University of Ghent, Rozier 44, B-9000 Gent, Belgium

## 1. Introduction

Accurate knowledge of the natural lifetime  $\tau_n$  (inversely proportional to the optical oscillator strength) and the resonance interaction constant  $K$  is needed for applications in plasma physics and astrophysics. The determination of these values has been the subject of several experimental and theoretical studies performed with various methods (for an overview see [1]).

Multiphoton excitation processes offer a more selective excitation mechanism compared to a gas discharge and don't have the practical problems connected to excitation with intense VUV-light. These factors make it a favourable method to populate excited states in the vacuum ultraviolet spectral region [2]. We use this technique for studying the imprisonment of the ( $^1S_0$ - $^1P_1$ ) 116.49 nm resonance radiation in Kr. We present measurements of the lifetime of the Kr  $^1P_1$  resonance level by making use of three photon excitation. The measurements are compared with theory and Monte Carlo simulations. Fitting the theoretical curve to the experiment yields the resonance interaction constant.

## 2. Experiment

The measurements are performed in the 0.01-10 Torr pressure range. The  $^1P_1$  level of Kr is populated by means of a three photon excitation process. Therefore we use a pulsed dye laser, transversely pumped by a Nd-Yag laser. The dye laser is operated with pyridine 1 in the wavelength range around 698 nm: the 698 nm radiation is frequency doubled and focused into the centre of a cylindrical cell with a radius of 1.28 cm. The decay of the resonance radiation is measured with a resolution of 40 ns during 40  $\mu$ s after the laser pulse. The number of detected photons as a function of time after the laser pulse is registered with a multichannel analyser.

The measurements below 0.3 Torr can be fitted at late times by a single exponential decay term plus a constant. For higher pressures the second term gains importance and should be replaced by another exponential decay term to reproduce the measured curve. This indicates the occurrence of ionization processes caused by the laser interaction: the three photon excitation of the Kr  $^1P_1$  resonance level is

followed by a single photon transition from the resonance level to the continuum. These ions decay into the  $^1P_1$  level through radiative or dissociative recombination processes characterized by a slow decay rate. The decay of these excited atoms to the ground state is mainly determined by the slower recombination process and not by the lifetime of the  $^1P_1$  level.

As a consequence of successive emission and re-absorption processes before a photon leaves the cell, the resonance level acquires an apparent lifetime longer than the natural lifetime. The decay frequency  $\beta$ , computed from the first (largest) exponential, corresponds to the apparent lifetime and is plotted as a function of pressure.

## 3. Comparison with theory

The theory of Post [3] for radiation transport, takes into account the correlation between absorbed and emitted photon frequency (partial frequency redistribution) and describes the late time decay (fundamental mode) with:

$$\beta = \frac{1}{\tau_n} \int_{-\infty}^{+\infty} \frac{(1-P_c)L_d(x) + P_c L_v(x)}{1-a(x)(1-P_c)(1-\eta(\tau_x))} \eta(\tau_x) dx,$$

with  $x$  = reduced frequency,  $\eta$  the escape function and  $\tau_x$  the product of the absorption coefficient and the cylinder radius.  $P_c$  is the probability of a decorrelating elastic collision and  $a(x)$  is a fast varying function between 0 and 1 providing partial frequency redistribution in the line wings and complete redistribution in the centre of the line profile. We use a Voigt profile  $L_v(x)$  combining natural line broadening, Doppler and pressure broadening. The FWHM for pressure broadening (in the case of resonance broadening) depends on the interaction constant  $K$  [4]. A value of  $K = 2.09$  is supported by several authors and gives:

$$FWHM = 0.904 \frac{\lambda_0^3}{12\pi^3} \frac{g_u}{g_l} \frac{n_l}{\tau_n}.$$

Decay rates are calculated in an infinite cylindrical geometry using an approximation [5] for the escape function.

Varying the natural lifetime in the calculations, we search for the best agreement with measurements. The best fit with the experiment (Figure 1), not taking into account the second minimum, yields a value of  $\tau_n = 3.6 \pm 0.1$  ns which is in agreement with other experimental results [6].

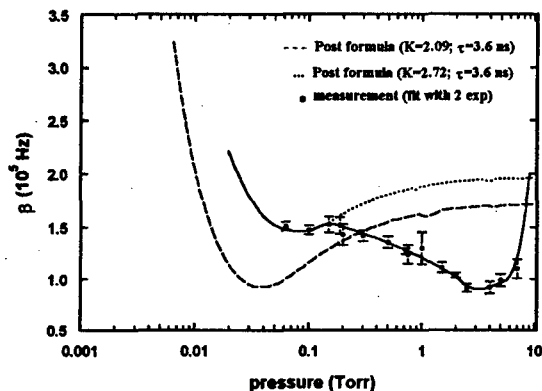


Figure 1: Decay rate as a function of pressure: comparison between analytical formula of Post and experiment

Using this  $\tau_n$  we vary the resonance interaction constant  $K$  towards the impact approximation limit [4] ( $K = 2.72$ ). Figure 1 shows this approximation is valid for pressures up to 0.2 Torr. For higher pressures the impact approximation nor the quasistatic limit ( $K = 1.81$ ) can explain the second dip around 3 Torr. We conclude that in the 0.2 - 10 Torr pressure range the apparent lifetime can no longer be determined based on the above line profile. A generalized line profile for pressure broadening, regardless of the duration of collisions, has to be applied [7].

#### 4. Monte Carlo simulations

The Monte Carlo code written in our laboratory [8] has proven to be a useful tool in describing the imprisonment of resonance radiation.

We search for the best agreement with the experiment (Figure 2). A natural lifetime of  $3.6 \pm 0.1$  ns is confirmed.

#### 5. Conclusions

- The natural lifetime  $\tau_n$  obtained in the present experiment differs from results where a constant  $\beta$  is assumed in the 0.2 - 10 Torr pressure range [9].
- Due to the good accuracy of the present experiment, the occurrence of a second minimum is established.
- Limiting the analysis to the first minimum, the experiment gives a natural lifetime in agreement with earlier theoretical work [10]:  $\tau_n = 3.6$  ns.
- We find a resonance interaction constant  $K = 2.09$

in good agreement with the experimental result of Hutcherson et al [11] and within the theoretical limits[4].

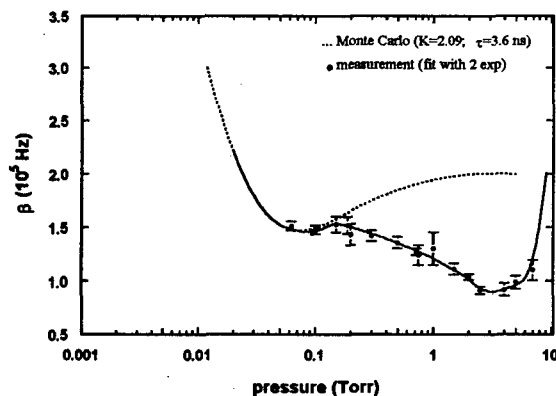


Figure 2: Decay rate as a function of pressure: comparison between Monte Carlo simulation and experiment.

#### 6. References

- [1] J.C. Molino Garcia, W. Böttcher, and M. Kock, J.Q.S.R.T. **55** (2) (1996) 169
- [2] F.H.M. Faisal, R. Wallenstein, and H. Zacharias, Phys. Rev. Letters **39** (18) (1977) 1138
- [3] H.A. Post, Phys. Rev. A **33** (3) (1986) 2003
- [4] R.P. Srivastava and H.R. Zaidi, Can. J. Phys. **53** (1975) 84
- [5] J. Heunneken and T. Colbert, J.Q.S.R.T. **41** (1989) 439
- [6] U.Hahn and N. Schwentner, Chem. Phys. **48** (1980) 53; J. Geiger, Z. Phys. A **282** (1977) 129 and Phys.Lett. **33A** (1970) 351; W.F. Ferrell, M.G. Payne and W.R. Garrett, Phys.Rev.A **35** (1987) 5020; J.M.Vaughan, Phys.Rev. **166** (1968) 13; E.L.Lewis, Proc. Phys. Soc. London **92** (1967) 817
- [7] N. Schoon, Experimental and theoretical investigation of the imprisonment of the Kr  $^1S_0 - ^3P_1$  123.58 nm resonance line, created by means of multiphoton excitation, Ph.D.-thesis, Gent University (1996)
- [8] F. Vermeersch, V. Fiermans, J. Ongena, H. A. Post, and W. Wieme, J. Phys. B: At. Mol. Opt. Phys. **21** (1988) 1933
- [9] P.G. Wilkinson, J.Q.S.R.T. **5** (1965) 503
- [10] P.F. Gruzdev and A.V. Loginov, Opt. Spectrosc. **38** (1975) 611 and Opt. Spectrosc. **22** (1967) 170; M. Aymar and M. Coulombe, At. and Nuc. Data Tables **21** (1978) 537; M. Aymar, S.Feneuille and M. Klapisch, Nucl. Instrum. Methods **90** (1970) 137
- [11] J.W. Hutcherson and P.M. Griffin, J.O.S.A. **63** (1973) 338

***Topic 6***

**High frequency discharges.**



# The asymmetrical capacitive HF low pressure discharge near-electrode plasma electron energy spectrum.

A.F.Alexandrov, V.P.Savinov, I.F.Singaevsky.

Physics Dept., Lomonosov University, Vorobiovy Hills, Moscow 119899, Russia.

The goal of the work is to study experimentally near-electrode plasma electron energy spectrum (EES) in capacitive HF discharge with gap between electrodes  $d=6$  cm, diameters active electrode 0.5 cm and earthed electrode 5.8 cm, HF voltage amplitude  $V_{\perp} \leq 2.5$  kV. The near earthed electrode region plasma created mainly by active electrode electron beam has been investigated. According to theoretical [1] and experimental [2] data, the aforesaid beam energy attains the value  $\varepsilon_{eb} \sim 2eV_{\perp}$ . The measurements performed with the aid of electrostatic and magnetic charged particle energy analyzers located beyond the earthed electrode. The energy analyzer output signals were recorded in quasistationary regime and oscillographically. The spectral line intensity emission space distribution  $I_{\lambda}(x)$  in the discharge is shown at Fig.1. General view of investigated plasma EES and its

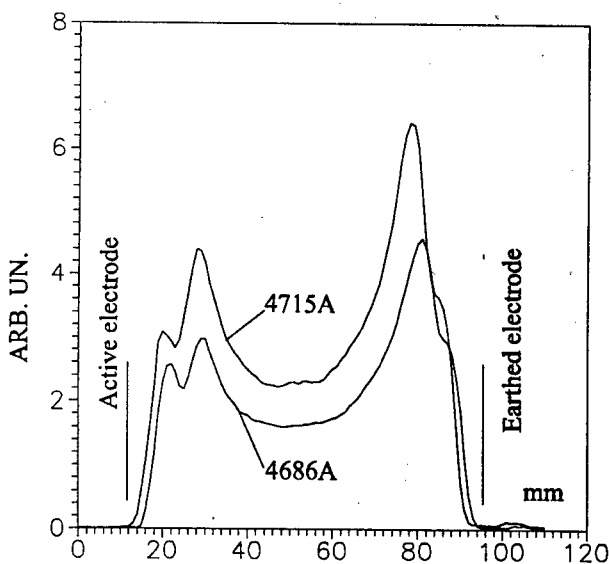


Fig.1. The spectral lines He I 4715A, He II 4686A intensity space distribution in CHFD. He,  $p=0.2$  Torr,  $f=2.1$  MHz,  $V=500$  V.

separate intervals are presented at Fig.2. The relation of chaotic and directed EES components obtained with the aid of the energy analyzers one can see at Fig.3. The electron flows at electrode oscillograms provided different energy analyzer collector retarding potentials  $V_k$  are shown at Fig.4. Since maximum emission

intensity observed near the earthed electrode not near the active one, then the main gas excitation near electrode cause appears not HF field but, evidently, the near-electrode electron beams (NEB). NEB being influence actively on gas in the opposite electrode neighbourhood. The evaluation showed that NEB free path length in gas was  $\lambda_{eb} \sim 10-15$  cm, hence  $\lambda_{eb} > d$ . However the distance from electrode to intensity emission maximum was  $\sim 5$  cm  $< d$ . The supposition was voiced that NEB relax rapidly as a result of excitation by them Langmuir oscillations in plasma. At experimental conditions the oscillation growth increment  $\gamma \sim (n_{eb}/n_e)^{1/3} \omega_{e0} \sim 10^8 s^{-1}$ , where  $n_{eb}$  and  $n_e$  - beam and plasma electron densities,  $\omega_{e0}$  - electron plasma frequency. The characteristic build-up of Langmuir oscillation length  $L_{eb} \sim u_{eb}/\gamma \approx 10^9/2 \cdot 10^8 = 5$  cm ( $u_{eb}$  - beam velocity), which corresponds experimental data. Thus, Langmuir oscillations excitation and NEB quick dying are possible. In such situation the beam electron peak in EES, observed in time-averaged measurements (Fig.2), must be absent. The peak presence may be explained by the near-electrode plasma physical processes time course. It was established that the pulse 1 at oscillogram Fig.4 caused by chaotic plasma electron input, but pulse 2 - by the directed beam electrons. The aforesaid beam exists in negative HF field half-period during which the space charge near-electrode sheath (SCNS) at earthed electrode undergo collapse. At the beginning the pulse 1 increases what shows the chaotic "hot" electron flow increase, but then - decreases and beam electron pulse 2 appears. During the pulses 1 and 2 coming, simultaneously the processes are going: 1) Langmuir oscillations building-up by electron beam and 2) the SCNS width and near-electrode potential barrier for electrons are decreasing. The last processes facilitate leaving of electrons to the electrode and values  $n_e$  and  $\gamma$  decreasing. As a result, Langmuir oscillations fade and the beam manifest itself as the pulse 2. Thus, the NEB arrives at the electrode only during the second half of the negative HF field half-period, when EES with "plateau" in the high-energy region turns into the energy distribution with the beam peak at its end.

The work was supported by the grant N 94-02-05194 of RFFI. References.

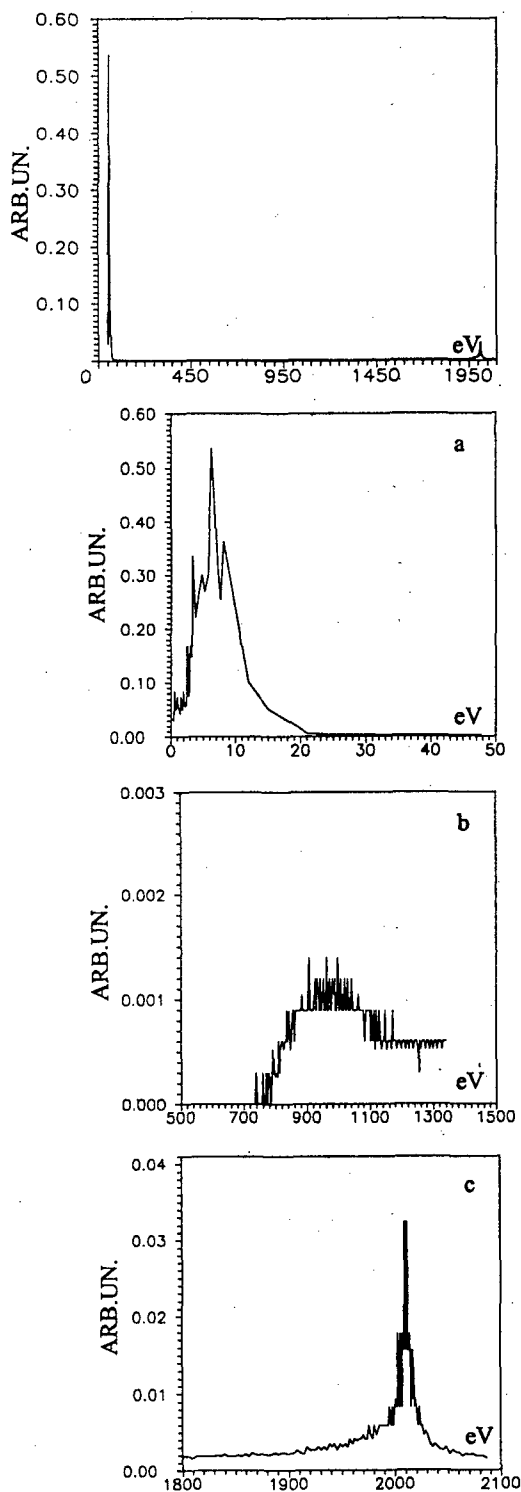


Fig.2. General view of CHFD near-electrode plasma EES and its separate energy intervals. Air,  $p=0.1$  Torr,  $f=1.2$  MHz,  $V=850$  V.

- a.  $0 < E_e < 50$  eV
- b.  $500 \text{ eV} < E_e < 1500$  eV
- c.  $1800 \text{ eV} < E_e < 2100$  eV

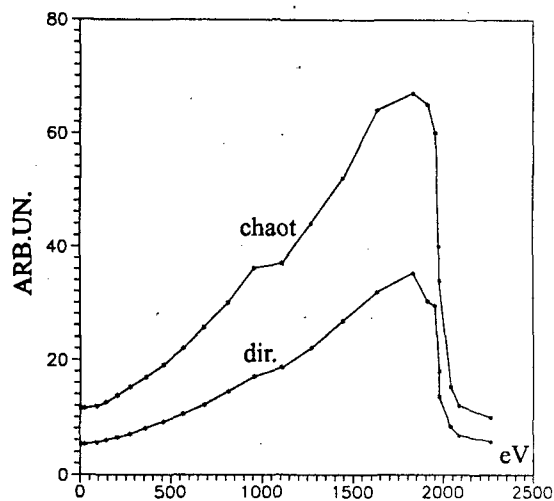


Fig.3. Near-electrode plasma CHFD EES chaotic and directed components. Air,  $p=0.1$  Torr,  $f=2.3$  MHz,  $V=800$  V.

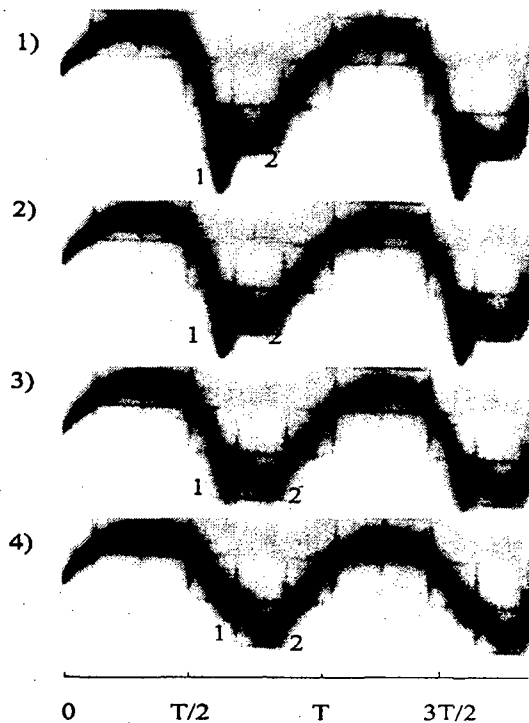


Fig.4. Oscillograms of the charge particles flows to electrode CHFD.

Air,  $p=0.07$  Torr,  $f=1.2$  MHz,  $V=1750$  V  
 1)  $V_k=-27$  V, 2)  $V_k=-300$  V, 3)  $V_k=-400$  V  
 4)  $V_k=-620$  V.

[1] Yu.P.Raizer, M.N.Schneider: Fizika plazmi, 18 (1992)1211 (in Russian).

[2] A.F.Alexandrov, V.L.Kovalevsky, V.P.Savinov, I.F.Singaevsky. Thes.rep.VIII confer. on phys.gas disch.Riazan. 1996, p.2, 48 (in Russian).

# INVESTIGATION ON THE AFTERGLOW OF PULSED MICROWAVE DISCHARGES IN Ar, N<sub>2</sub> AND AIR

Sudeep Bhattacharjee and Hiroshi Amemiya

*The Institute of Physical and Chemical Research & Saitama University  
Hirosawa 2-1, Wako-Shi, Saitama, 351-01, Japan*

## 1. Introduction

Microwave discharges in the atmosphere are now thought to have great environmental implications. Recently there have been a number of interesting proposals for eg. the removal of CFC's from the atmosphere [1], for ozone layer remediation [2]. There are models which predict that if the discharge is carried out at the ozone layer, the products of the plasma-chemical reactions could include the oxides of nitrogen (NO<sub>x</sub>), which would destroy the already existing ozone. Therefore it is considered advantageous to create the artificial ionization layer (AIL) slightly above the ozone layer, most suitably in the D layer at heights between 60 to 80 km, so that the generated ozone would sink down due to its mass. Furthermore, the D layer is known to be rich in negative ions, which may be beneficial both for the protection and generation of ozone, as there are some reactions involving negative ions which generate ozone [3]. In this work we study the processes in the afterglow of such pulsed plasmas at pressures corresponding to the height of the upper atmosphere above the ozone layer. We study the temporal afterglow and use pulsed microwaves as a continuation of a previous work [4]. The afterglow plasmas are very important because of the reactions between radicals and negative ions which needs to be well understood for overall ozone production and protection. We begin our studies with a simple monoatomic gas Argon, then going on to the molecular gas nitrogen and finally studying air discharge.

## 2. Experimental setup

Figure 1 shows a schematic of the experimental apparatus. It consists of a large space chamber inside which a multicusp type plasma bucket MC of 20 cm  $\phi$  was placed for plasma confinement. Ar, N<sub>2</sub> or air was introduced into the chamber and the experiment was performed at 0.2-1 Torr. Pulsed microwaves (MW) of 0.4  $\mu$ s pulse width, 60 kW peak power from a 3 GHz magnetron oscillator PM with a pulse repetition frequency of 546 Hz were introduced into the chamber through the attenuator ATT, matching element M, mode converter T for changing the rectangular TE<sub>10</sub> mode into the cylindrical TE<sub>11</sub> mode and finally through the quartz window W into the space chamber. Power

monitors Pf and Pr indicated the feed and reflected powers, C is a cylindrical waveguide to guide the waves into MC. Measurements of the plasma decay with time were made with Langmuir probes P1, P2 placed at the center and outside of the bucket. The transient probe current data at a particular probe voltage ( $V_p$ ) were taken by a digital oscilloscope and  $V_p$  was varied in the range -40-30 V.

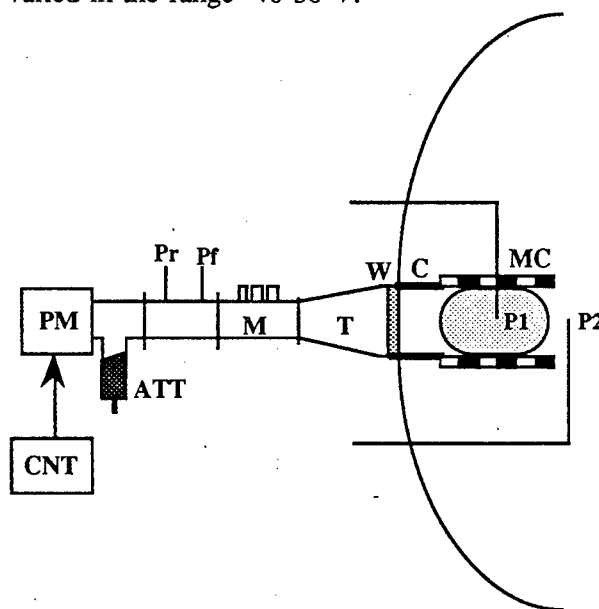


Fig.1 Schematic of the experimental apparatus

## 3. Results in Argon discharge

In figure 2 we show the plasma decay profile for  $p=0.24$  Torr and at  $V_p=-40$  V. The plasma decay could be fitted with

$$I(t) = I_0 \exp(-\beta t) / \{1 + (n_0 \alpha / \beta)(1 - \exp(-\beta t))\}$$

as shown by a solid curve, where  $\alpha$ : recombination coefficient,  $n_0$  ( $\approx 10^{10} \text{ cm}^{-3}$ ) is the initial plasma density,  $\beta = D_a / \Lambda^2$ ,  $\Lambda$  being the characteristic length and  $D_a$  the ambipolar diffusion coefficient. We obtained  $\alpha = (1.2) \times 10^{-6} \text{ cm}^3/\text{s}$  and  $\beta = (0.4-0.5) \times 10^6 \text{ s}^{-1}$ , at  $p=0.2-1$  Torr. While  $\alpha$  had almost the same values at all pressures,  $\beta$  became slightly lower at  $p > 0.9$  Torr. Moreover at lower pressures the decay could not be described by a single  $\beta$ , as during the final stage of the discharge the decay was very rapid (cf. Fig. 2). Figure 3 shows probe

characteristics at 0.24 Torr, for three different time periods after the end of the MW pulse. Variation of the electron temperatures  $T_e$ , with time as obtained from the electron current part of the probe characteristics are also shown in fig. 2. The observed temperature decrease with time could be due to the loss of electron energy due to electron-neutral collisions.

### 3. Results in Nitrogen discharge

Figure 4 shows the characteristics of the afterglow plasma in  $N_2$  at -16 V probe voltage and for  $p=0.24$  Torr and 0.92 Torr. The  $N_2$  afterglow has marked differences from the Ar afterglow. In this case the diffusion loss at the later stage of the discharge is alleviated, this is probably by the effect of metastable atoms (eg.  $N_2(A^3\Sigma_u^+)$ ,  $N^*$  etc) which accounts for the cumulative ionization after 5  $\mu s$ . This effect of metastable atoms leading to additional ionization is more profound at lower pressures and can be explained by the measured result of a higher  $T_e$  at lower p.

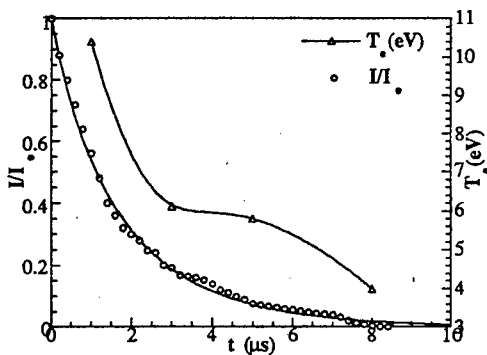


Fig.2 Decay of the ion current in Argon and variation of  $T_e$  with time

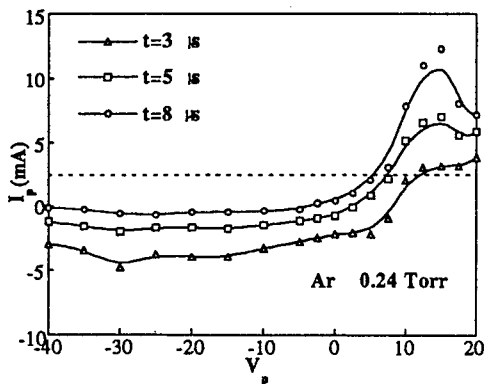


Fig.3 Probe Characteristics in Argon

### 3. Results in Air discharge

Figure 5 shows the case of air discharge, a double hump appears at  $t \approx 2 \mu s$  besides the hump at the later stage of the discharge as

observed in  $N_2$ . The first decay may be due to the electron-ion recombination while the second may be due to positive-negative ion recombination. The double hump appeared more conspicuously at  $p > 0.6$  Torr. It was very difficult to get a discharge above 0.6 Torr. This is a further support to the fact that the negative ions are profusely generated at higher pressures.

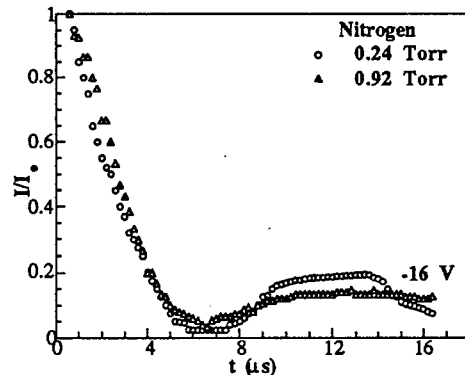


Fig.4 Decay of the ion current in Nitrogen

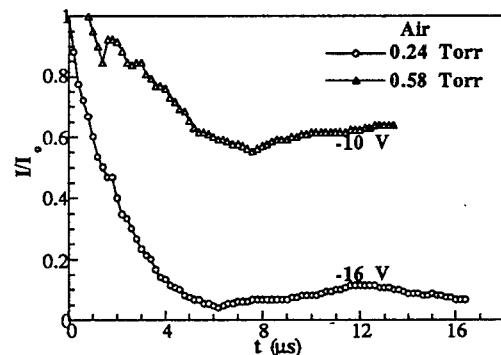


Fig.5 Decay of the ion current in Air

### 3. Conclusions

In pulsed microwave afterglow, the decay profiles of atomic rare gas, molecular gas, and a mixture gas containing an electronegative gas have been experimentally studied. The effects of recombination, diffusion, metastables and negative ions have been observed.

### References

- [1] G A Askaryan, G M Batanov et. al. : J. Phys. D: Appl. Phys. 27 (1994) 1311
- [2] G A Askaryan et. al. : Sov. J. Plasma Phys. 17(1) (1991) 48
- [3] G M Milikh and L M Duncan: *Controlled Active Global Experiments (CAGE)*, edited by E. Shidoni and A Y Wong, Editrice Composition Bologna, 1990
- [4] H Amemiya and M Maeda: Jpn. J. Appl. Phys. 34 (1995) 3718

# Influence of the assumptions on the EEDF in fluid models of RF discharges

A. Merad and J.P. Boeuf

Centre de Physique des Plasmas et Applications de Toulouse  
Université Paul Sabatier, 118 route de Narbonne  
31062 Toulouse Cedex, FRANCE

## I. Introduction

Fluid models of non equilibrium discharge plasmas are based on solutions of the electron and ion moment equations coupled with Poisson's equation. Using moment equations instead of Boltzmann equation to describe charged particle transport implies some assumptions on the charged particle velocity distribution functions. These assumptions have consequences on the form of the transport terms of the moment equations (e.g. pressure tensor or thermal flux) but also on the collision terms (ionization rate, energy loss rate, momentum transfer frequency). In this paper we focus on the consequences of two usual assumptions which can be made on the electron energy distribution function (EEDF) in fluid models of RF discharges and we present systematic comparisons between the two.

The models we consider are based on three moment equations for electron transport and two moment equations for ion transport, as in [1]. In this approach, the collision terms are estimated by assuming that the EEDF at a given position and time depends only on the local mean electron energy. We consider two possible shapes of the EEDF: 1) a «swarm distribution», i.e. an EEDF whose dependence on mean electron energy is the same as at steady state, under a uniform electric field («swarm experiment»), as in [1], and, 2) a Maxwellian EEDF.

It is expected that the «swarm» EEDF will be more adequate at higher pressure (above a few 100 mtorr, in a RF discharge in the  $\alpha$  regime) while the Maxwellian shape should be more appropriate at lower pressure. It is clear that the real EEDF are generally different from either a swarm or a Maxwellian distribution in these non equilibrium plasmas but 1) assumptions on the EEDF must be made in a fluid model, and 2), the aim of this paper is to estimate the consequences of these assumptions on the final results.

## II - Description of the fluid model

The 1D fluid model we use is similar to the one described (for a 2D geometry) in [1]. The momentum transport equation is written in the drift-diffusion form, i.e. inertia is neglected and the drift energy is supposed to be small with respect to the thermal energy. These assumptions are better for electrons than for ions in a 13 MHz RF discharge in the 100 mtorr range, and we shall discuss elsewhere the consequences of these assumptions in the ion momentum transport equation. The numerical model is fully implicit and the equations are discretized using an exponential scheme.

The momentum, energy loss, and ionization frequencies for the swarm case are obtained from a Monte Carlo simulation under uniform field conditions and are tabulated as a function of mean electron energy. In the Maxwellian case, these frequencies are tabulated as a function of mean electron energy using the known electron-molecule cross-sections.

## III - Discharge conditions

Calculations have been made for the two assumptions in a 13.56 MHz RF argon discharge for pressure between 50 and 500 mtorr with RF voltages ranging from 30 to 200 V and for a 2.5 cm gap length. Results from the swarm and Maxwellian models have been compared together and also with the results of Meyyappan et al [2] performed in the same conditions.

We also performed calculations at 12.0 MHz, for a gap length of 4 cm, in the 150-500 mtorr pressure range, and for applied RF voltages from 200 to 800V. These results were compared to those of Nitschke et al, [3] (for 250 mtorr only) in Ref. [4].

## IV - Results

In order to illustrate the discrepancies or similarities between the results for a swarm or a Maxwellian EEDF, the calculated parameters (electron density, ionization rate, power and current) are plotted only in a relative form: the ratio between the swarm calculation and the Maxwellian calculation is plotted for each parameter.

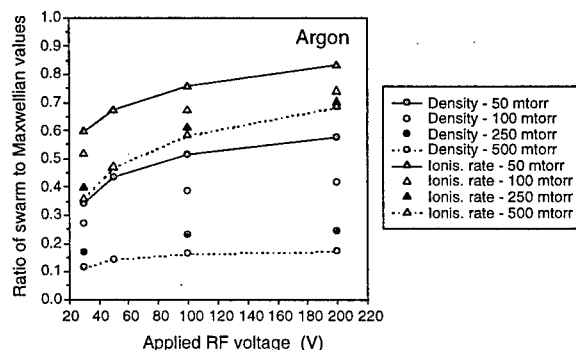
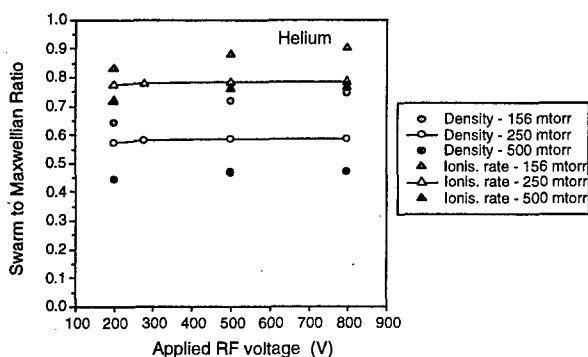


**Figure 1:** Ratio of Swarm to Maxwellian values for electron density and ionization rate vs. RF voltage amplitude and for different pressures in a 13.56 MHz, 2.5 cm gap length RF discharge

Figure 1 shows the variations with applied RF voltage and for different values of the pressure of the ratio of the swarm to Maxwellian calculated values of the time averaged electron density and ionization rate in

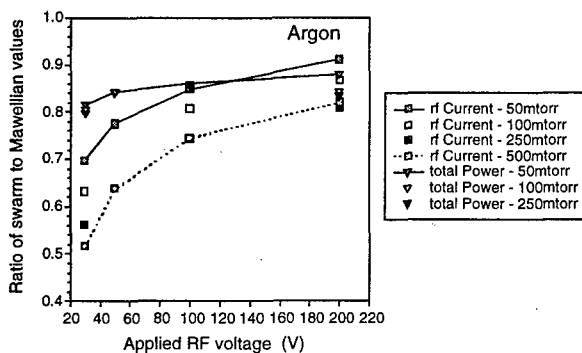
argon. We see that the discrepancy between the swarm and Maxwellian results tends to be smaller at lower pressure. At 50 mtorr, the plasma density deduced from the swarm model is about twice smaller than the one obtained with the Maxwellian EEDF, while the ratio can be as large as 6 at 500 mtorr.

Figure 2 shows the results obtained in helium. These results exhibits similar trends that in argon although the agreement between the swarm and Maxwellian results seems a little bit better in helium.



**Figure 2 :** Ratio of Swarm to Maxwellian values for electron density and ionization rate vs. RF voltage amplitude and for different pressures in a 13.56 MHz, 4 cm gap length RF discharge in helium.

Figure 3 shows a comparison between the calculated peak current and power in the same conditions as in Fig. 1. The calculated current and power in the swarm and Maxwellian cases are in better agreement than the calculated plasma densities displayed in Fig. 1.



**Figure 3 :** Ratio of the swarm to Maxwellian calculated current and power in the conditions of Fig. 1.

The results for the current and power in helium are plotted in Fig. 4. The Swarm and Maxwellian values of the current and power are very close together in that case.

Other results not presented here show that for both argon and helium, the electron mean energy adjusts to lower values in the case of Maxwellian EVDF, with smaller differences between swarm and Maxwellian results for helium. This was expected since for the same

mean energy, the ionization rate of a Maxwellian EEDF is much larger than the ionization rate of a swarm EEDF. Since the ionization rate (which depends on the tail of the distribution) has to adjust in order to compensate for ambipolar losses to the electrodes (which depend on the mean electron energy and thus on the bulk of the distribution) the mean energy for a Maxwellian distribution must be lower than for a swarm distribution.

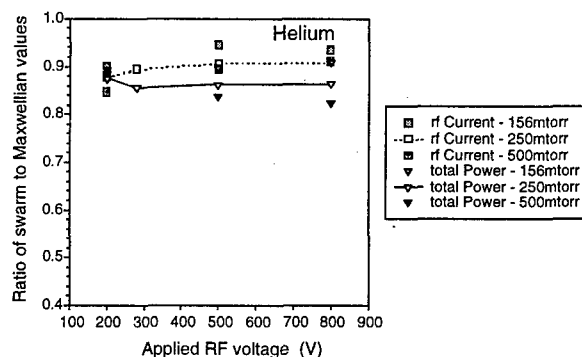


**Figure 4 :** Ratio of the swarm to Maxwellian values of the total current and powers as a function of RF voltage amplitude in helium, in the conditions of Fig. 1.

#### IV - Conclusions

The results presented in this paper can help quantify the error induced by the assumptions on the shape of the EEDF which must be done in a fluid model of a RF discharge.

It appears that although the difference between ionization rates from a swarm and a Maxwellian EEDF for the same mean electron energy can be orders of magnitude, the discrepancies induced by the choice of the shape of the EEDF in a fluid model are much more limited. This is due to the fact that the ionization rate in the discharge must adjust in order to compensate for ambipolar losses of charged particles to the electrodes (which depends on mean electron energy and reactor geometry).

#### References

- [1] J.P. Boeuf and L.C. Pitchford - "Two-dimensional model of a capacitively coupled RF discharge and comparisons with experiments in the GEC reference reactor", Phys. Rev. E, vol 51, p 1376 (1995)
- [2] M. Meyyappan and T.R. Godivan, J.Appl. Phys 74, 2250 (1993)
- [3] T.E. Nitschke and D.B. Graves , J.Appl. Phys 76, 5646 (1994)
- [4] J.P. Boeuf and A. Merad, «Fluid and Hybrid models of Low Pressure Discharges», NATO ASI on Plasma Processing of Semiconductors, Ed. P.F. Williams, to be published (Kruger).

# Heating Mode Transitions in a Capacitively Coupled Radio Frequency Discharge

C. M. Deegan and M.B. Hopkins

Plasma Research Laboratory,  
Dublin City University,  
Glasnevin,  
Dublin 9,  
Ireland.

## Introduction

In capacitively coupled rf discharges, it is now widely accepted that there are three main heating mechanisms. Transitions from one mechanism to another are effected by the external control parameters such as gas pressure, rf voltage, current density and the geometry of the discharge itself. These transitions in heating modes are observed as marked changes in the discharge properties such as light emission intensity and plasma parameters. The main motivation for this experiment was to study these heating modes in the plasma and investigate if they depend on discharge geometry.

In low pressure discharges a heating mode unique to rf discharges has been reported [1.] [2.]. This is in a low pressure, collisionless discharge, where electron heating is due primarily to the oscillating sheaths. Increasing the gas pressure effects a transition to a regime where the discharge is sustained by Joule heating of the electrons in the plasma bulk. The third heating mechanism is called the  $\gamma$  - mode regime which is due to secondary electron emission from the powered electrode.

Experiments were carried out at several electrode gaps over a wide range of input powers and pressures. Plasma parameters were measured using a Langmuir probe system. Corresponding current and voltage information was stored and analysed for its harmonic content. Therefore, the properties and behaviour of the plasma could be correlated with its external control parameters. In this way it is hoped that methods of proper optimisation of plasma processes may be devised.

## Experiment

Our experiment is an asymmetrically powered, capacitively coupled discharge with a powered electrode 20 cm in diameter. The gap width was varied from 3 to 7 cms. Two passively compensated Langmuir probes, positioned in the discharge midplane, are used to monitor plasma parameters. The first probe measures the I-V characteristic from which the plasma parameters are derived. The presence of an rf voltage across the probe sheath leads to a distortion

of the probe characteristic. This distortion is due to shifts in the plasma potential which increase with the measuring probe bias. The second probe compensates for this distortion by tracking the floating potential and allowing correction of the measured parameters. This system has been found to be essential in measurement of the low-energy electron component in such plasmas [3.]. An argon plasma generated in this type of system is non-equilibrium, the electrons and ions deviate from a Maxwellian distribution. Therefore, accurate measurement of the electron energy distribution function is important as there may be more than one temperature group in the plasma.

Monitoring of the primary control parameters was performed using a current and voltage monitor, connected to the powered electrode after the matching unit. Voltage and current information from this monitor was captured using a fast storage oscilloscope and downloaded to a computer for analysis.

Most of the data for this study was taken at gas pressures at or greater than 100 mTorr, though some data at lower pressures was also taken to study the collisionless heating mode. Plasma parameters (electron temperature, electron and ion density and electron energy distribution functions) were measured in argon at input powers ranging from 5 to 200 Watts.

## Results

This procedure was carried out on discharge gaps of 3, 5 and 7 cms. Current, voltage and power were evaluated for several harmonics of the fundamental driving frequency. An obvious transition was noted on increasing the gas pressure. At higher pressures and voltages another transition was apparent, the electron temperature dropping sharply while the density increased (see Figure 1.). This transition was observed at different input powers for different pressures (see Figure 2.). This is the  $\alpha$ - $\gamma$  mode transition in the plasma and it is coupled with an increase in the light emission intensity and variation in shape of the plasma voltage and current waveforms [1.].

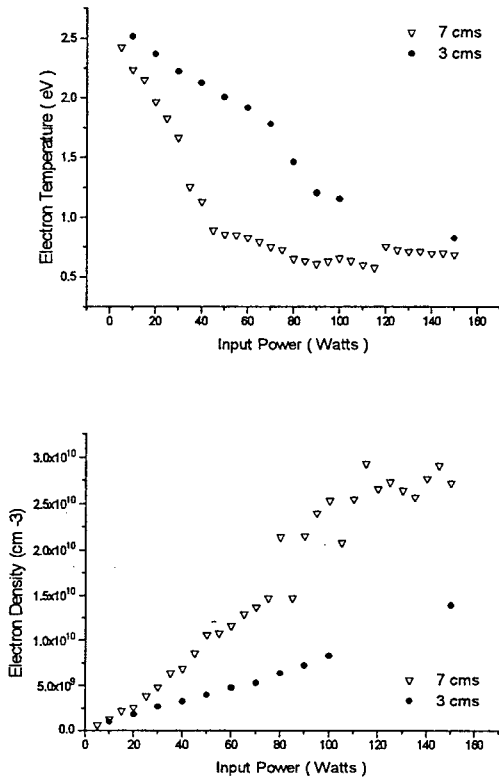


**Figure 1.** Electron temperature and density versus input power for two electrode gaps at 100 mTorr. The sharp drop in  $T_e$  and increase in  $N_e$  indicates a transition into the  $\gamma$  regime.

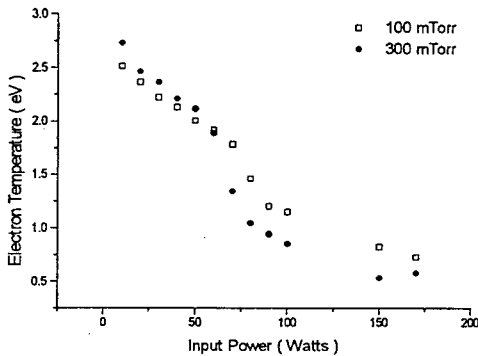


**Figure 2.** Electron Temperature Versus Input Power for 3 cm electrode gap at 100 and 300 mTorr. Transition to the  $\gamma$ -mode occurs at a lower input power at higher pressures.

## References

- [1.] V.A. Godyak *et al*, Plasma Sources Sci.Technol. 1 (1992) 36-58.
- [2.] M.M. Turner, R.A. Doyle and M. B. Hopkins, Appl. Phys. Lett. 62 (1993) 32.
- [3.] M. B. Hopkins and D. Vender, Poster MPA 11, Gaseous Electronics Conference, October 1996.



## The formation of RF sustained double layer in plasma resonance

B. M. Annaratone, J. E. Allen and A. E. Dyson  
*Department of Engineering Science, University of Oxford,  
 Parks Road, Oxford OX1 3PJ*

### Introduction

In the last decade semiconductor industry has required a big technological effort in order to match increasingly demanding requirements. Features below a tenth of a micron, shapes suitable for the optoelectronic devices or micro-size plasma technology can only be achieved by innovative plasma processing technique. In this context the non collisional regime has gained increasing importance. The mechanism described in the present paper may provide an alternative mode of operation for plasma reactors operating at low pressures. It is likely that RF sustained double layers could explain acceleration of charged particles in space plasmas. Typically double layers in plasma have only been observed in a DC context, either at electrode surfaces or between two different plasmas.

The enhancement of the DC floating bias on electrodes by a superimposed RF current is an effect much used in plasma processing to increase the energy of the impinging ions. The non linear IV characteristic of the plasma sheath is time averaged on the RF variation and this process effectively increases the electron current able to overcome the 'built in' negative voltage difference. In this contribution we propose an analogous mechanism to explain the observed double layers that appear in RF plasmas when the driving frequency coincides with the local plasma resonance on certain surfaces of a non uniform plasma.

The theory foresees a power absorption on these surfaces associated with an effective resistance<sup>1</sup> which depends on  $(d\omega_{pe}/dx)^{-1}$ . The  $\omega_{pe}$  profile, and the corresponding plasma density distribution,

can be modified in order to change the power transfer.

### Experiments

Measurements were carried out in a parallel plate reactor driven at 100V<sub>pp</sub> and 157MHz. At this frequency the reflected power to the amplifier, without matching unit, was minimised. Experiments were carried out in Argon and CF<sub>4</sub>, the electrode separation being 3cm and the gas pressure varying from 1 to 10<sup>-2</sup> Pa. On the grounded electrode a retarding field analyser, R. F. A., recorded the energy of the impinging ions. A probe in the plasma was connected alternatively to a divider circuit<sup>2</sup> for the measurements of the RF fluctuations, analysed by a spectrum analyser, and to a voltmeter, with active RF compensation for measurements of floating potential.

With decreasing pressure the harmonics of the voltage fluctuations in plasma develop a resonance which shifts towards lower frequencies. This resonance is attributed to the plasma-sheath resonance.

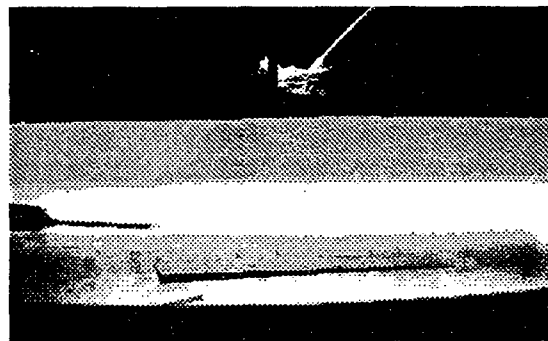


**Figure 1** Side view of the CF<sub>4</sub> plasma in plasma resonance. The upper electrode, grounded shows the connections for the R.F. A., a probe is inserted from side and on the lower electrode, driven, a sample to be etched can be seen. The bright disk corresponds to the white part in the centre of the discharges. No boundary sheaths can be seen here.

Approaching the fundamental frequency, and the local plasma frequency due to non uniformity of the plasma density the plasma undergoes a major change. A bright disk appears in the centre of the discharge surrounded by a much weaker plasma, see fig. 1.

Simultaneously the ion energy analyser records a shifting of the plasma potential to higher and higher values, up to 150V, which is associated with an increased energy of the ions. In coincidence with the formation of the bright disk the ion energy distribution splits in two peaks, see fig 2.

Usually the deviations from the typical, non collisional ion energy distribution, which are observed at low pressure and high driving frequency, are explained by the residual capacity of the ions to follow the RF fluctuations across the sheath when  $\omega_{pi}$  is smaller, but still comparable, with the involved frequencies. In our case the ratio  $f/f_{pi}$  is well above one hundred, so that this explanation is not applicable. An estimate can be obtained considering the driving frequency to hit the local plasma resonance in the middle point of the visible emission discontinuity. At that point the density will be  $3 \cdot 10^{14} \text{m}^{-3}$  giving  $f_{pi} < 1 \text{MHz}$ . A much higher density is expected inside the bright region. From the splitting of the two peaks the abrupt change in the space potential on the two sides of the light discontinuity is about  $10V_{DC}$ . The integral of the ion energy structure is more than double with respect to the single peak case. This integral represents the flux of ions and is proportional to the processing rate in technological applications.

Evidence of discontinuities in the DC and RF voltage on the two sides of the discontinuities by RF driven Langmuir probe will be presented. RF sustained double layers are more easily formed in electronegative gases,  $\text{CF}_4$  and Oxygen although in resonant conditions also appear in Argon and Helium.

### Discussion

The theory presented in [1] will need

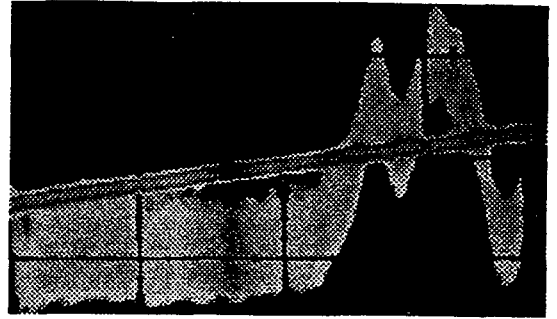


**Figure 2** Ion velocity distribution shown against the collector voltage from the R. F. A.. The ramp raises 50V/div., 0V is two divisions below the horizontal line (not shown) which cuts the noise. The smaller peak is at 150V and the larger one at about 160 positive with respect to the grounded electrode.

to be modified to take into account the finite nature of the discontinuity. The suggestion made here is that the non linear behaviour of the system leads to a localised D. C. voltage drop in addition to the localised A. C. voltage drop which is predicted by the linear theory. Electrons travel across the modulated double layer from the high potential to the lower and vice-versa. The net result is that energy is given to the electrons, the energy supply being that of the Pointing Vector. In addition energy is given to the outward-flowing positive ions in a similar fashion to that obtained in a radio-frequency enhanced sheath adjacent to an electrode[3].

Assistance in the experiment and discussions with W. H. Steel and S. N. Karderinis are acknowledged. The project is funded by the Engineering and Physical Sciences Research Council.

- 1) 'Recent work on the plasma sheath resonance in a non uniform plasma', B. M. Annaratone, J. E. Allen, D. A. Law and W. H. Steel, 1996, Proc. XIII ESCAMPIG, Poprad, Slovakia, 20E, 173.
- 2) 'Identification of plasma-sheath resonance in a parallel plate plasma reactor', B. M. Annaratone, V. P. T. Ku and J. E. Allen, J. Appl. Phys., 77, 5455.
- 3) 'Energy flow in a radio-frequency enhanced sheaths, J. E. Allen, 1987, Proc. XVIII IGPIG, 4, 808.

## RF HYDROGEN PLASMA DISCHARGE USED FOR CHLORIDE REMOVAL FROM CORRODED COPPER SAMPLES

M. El Shaer, M. Mobasher, M. Wüttmann\*

Faculty of Engineering, Zagazig university, Zagazig, Egypt

\* Institut Français d'Archéologie Orientale, Cairo, Egypt

### Introduction

RF discharges are now widely used in many technological applications. One of the promising field of use of such discharges is the treatment of corroded metals with hydrogen plasma discharges. An ideal case of corroded metal objects are those coming from archeological excavations. This method is successfully applied to different metal objects coming from the archeological field, [1-3]. The method consists on the use of hydrogen plasma to remove first the incrustation covering the metallic object by a reduction of the oxides in the incrustation layer, and then to passivate it against postcorrosion by the removal of the chlorides which act as a catalyser for corrosion. In this work we have treated artificially corroded copper samples in pure hydrogen plasma in order to study mainly the chloride removal process in copper by the effect of hydrogen plasma.

### Experimental setup

Fig. 1 shows the experimental arrangement.

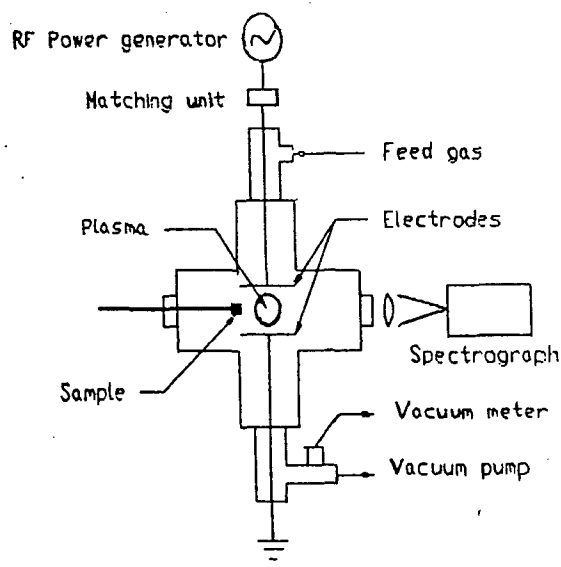


Fig.1 RF discharge experimental arrangement

The RF power at a frequency of 10 MHz, is coupled to two opposite stainless steel circular electrodes of 9.6 cm diameter. The discharge occurs in a symmetric cross shaped glass tube, of 10 cm inner diameter, the interelectrode distance is adjustable and can go up to 50 cm, which is the distance between two opposite ends of the glass tube. The discharge can be operated continuously with a power up to 300 W, applied to one electrode, while the other one is connected to the ground.

### Experimental investigations

Before proceeding on our investigation about the effect of the plasma on corroded copper, we have measured the physical parameters of the hydrogen plasma, namely the electron temperature and density. The electron temperature is determined spectroscopically by the measurement of the ratio of the line to continuum intensities of  $H_\beta$  line. In Fig. 2, the electron temperature variation is plotted versus the gas pressure for a RF power of 50 W. It appears that the electron temperature decreases rapidly with the increase of the gas pressure until a value of around 2 Torr and then seems to be maintained around a value of 2.4 eV.

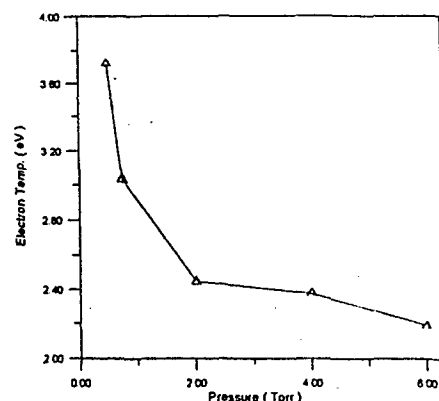


Fig. 2 Electron temperature variation with gas pressure for RF power of 50 W in hydrogen.

The electron density has been measured in a similar experiment using a microwave interferometer, /5/, the results show a density increase with gas pressure up to around 2 Torr, at which the density reaches a maximum and then decreases with the increase of the gas pressure. We take the value of 2 Torr as the operating gas pressure in our investigations on metal corrosion.

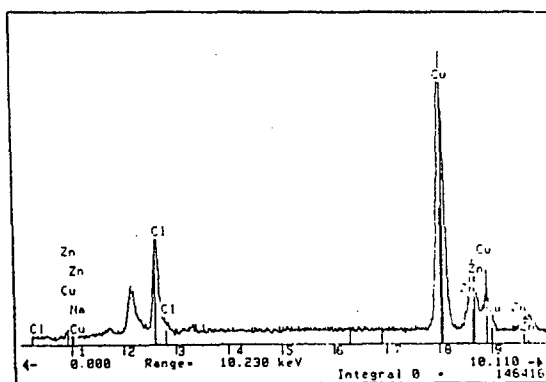
A copper sample is artificially corroded and then treated in pure hydrogen plasma for 150 hours, the plasma treated sample is then immersed in deionised water for one week with continuous stirring. Measurement of the chlorides contents on the surface of the plasma treated sample before and after washing in water by energy dispersion analysis of x rays (EDAX) shows a decrease in the chlorides after washing the sample, as shown in Fig.3- a and b. This result is coupled with the measurements of the chlorides concentrations in the water measured by an ion analyser with a  $\text{Cl}^-$  electrode which shows an increase in the concentration of chlorides in the water by approximately a factor 2 compared to the concentration obtained by untreated sample in the same conditions.

## CONCLUSION

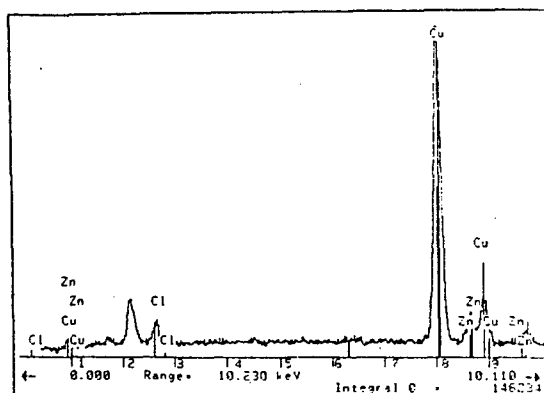
Those measurements show that the chlorides content in a corroded copper sample can be lowered using the hydrogen plasma which increase the porous nature of the oxide layer as a result of the ion bombardment, this was observed by scanning electron microscopy, and hence permitting the diffusion of the chlorides and their reduction from the insoluble to the soluble phase. This enhance their elimination after washing in deionised water.

## PLANS

More experimental measurements should be performed in order to determine quantitatively the effectiveness of this method on different corroded metals. Comparisons of the plasma effect in different types of plasma discharges as DC glow discharge, and microwave discharge are now in progress.



- a -



- b -

Fig. 3 - Spectrum by EDAX of the surface of a plasma treated corroded copper sample a- before washing b- after washing

## ACKNOWLEDGMENTS

A part of the Equipments used in this experiment are kindly offered by the Essen University, Germany.

## REFERENCES

- /1/ J. Patscheider, S. Veprek, Studies in Conservation, 31 (1986) 29-37.
- /2/ S. Veprek, Ch. Eckmann, J. Th. Elmer, Plasma Chemistry and Plasma processing, Vol. 8, No. 4, 1988.
- /3/ P. Arnould-Pernot, C. Forrières, H. Michel, B. Weber, Studies in Conservation, 39 (1994) 232-240.
- /4/ H.R. Griem, "Plasma spectroscopy", McGraw-Hill Book Company, 1964.
- /5/ M. El Shaer, V. Scultz- von der Ghaten, H. F. Döbele, XXI International Conference on Phenomena in Ionized Gases, Bochum, 1993

# Breakdown in a Hydrogen pulsed discharge created in a resonant cavity.

A. Draghici-Lacoste, L. Alves\*, C.M. Ferreira\*, Ph. Leprince, G. Gousset

Laboratoire de Physique des Gaz et des Plasmas, Université Paris-Sud, Bat 212, 91405 Orsay cedex FRANCE

\* Centro de Electrodinámica, Instituto Superior Técnico, Av. Rovisco Pais, 1, 1096 Lisboa codex PORTUGAL

## 1. Introduction.

The transient kinetics of  $H_2$  discharge has been investigated by the PICMIC technique. It consists of analyzing the motion of a particle swarm under the influence of an accelerating electric field, set up in a microwave cavity, in order to evaluate the statistical balance of its behavior.

The purpose of our study is to evaluate the breakdown time of the discharge, in order to compare it with that determined experimentally.

## 2. Experiment.

The  $H_2$  discharge (0.5-40 Torr) is created in a cylindrical quartz tube ( $d_{\text{e}} = 16/19$  mm) placed along the center axis of a microwave cavity ( $d = 257.1$  mm).

The  $TE_{111}$  excited cavity at frequency  $f = 1.12\text{GHz}$  ( $L_{\text{res}} = 168.4\text{mm}$ ) is supplied by a pulsed power ( $P_i \approx 1-15$  kW) with  $\Delta t \approx 10$   $\mu\text{s}$  width pulse and  $\alpha = 10^{-3}$  duty ratio.

The temporal distribution of the electric field at the critical coupling cavity and without plasma, working in the transient regime, can be written as :

$$E_0(t) = A_0 \times \sqrt{\frac{P_i \times \tau_{c0}}{\tau_{c0}^{\text{perfect}}}} \times [1 - e^{-t/\tau_{c0}}] \times \sin(\omega t) \quad (1)$$

where :

- the subscript '0' denotes that the cavity works without plasma.

-  $A_0$  is the electric field amplitude at steady state, normalized to 1W for a perfect cavity characterized by the padding time  $\tau_{c0}^{\text{perfect}}$ . Its value was found by electromagnetic analysis, which consists in solving the Maxwell's equations with appropriate boundary conditions.

-  $\tau_{c0} \approx 2.5 \times 10^{-6}$  s is the actual padding time for our cavity.

Figure 1 presents the temporal evolution of the electric field at the cavity walls.

At the beginning the field strength increases according to equation (1). The cavity works as if it is empty due to the weak electron density. Then, breakdown occurs and the rising electron density induces a change in the cavity  $\tau_{c0}$ , and consequently in the electromagnetic field configuration. This leads to the electric field peak shown in the figure 1.

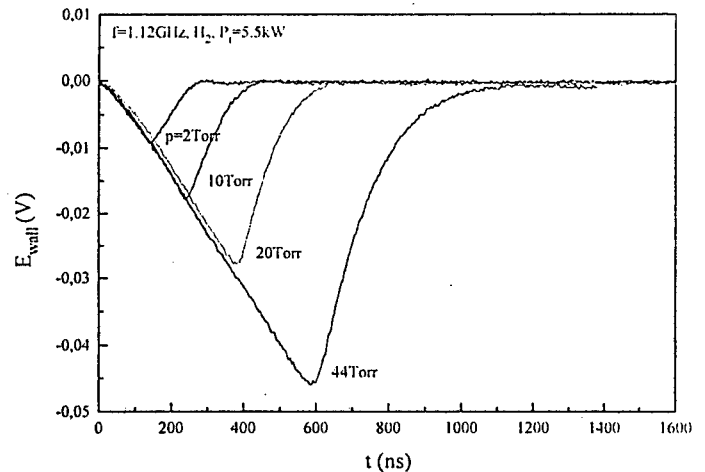


Figure 1. Temporal evolution of the electric field probe measurements at the wall of the cavity.

## 3. The numerical model.

The numerical simulation starts as soon as the HF power is supplied to the cavity. At this time a seed electron, stochastically chosen, and assumed to be produced by natural ionization, is considered present in the discharge tube.

Under these conditions it is not possible to use a fluid numerical code. On the contrary, a kinetic code is well adapted to describe the temporal evolution of a system starting at very low electronic density.

The primary electrons gain energy from the external electric field defined by equation (1) and lose it by collisions with molecules in ground state only. The chosen electron neutral collisions are rotational, vibrational, electronic excitation and ionization of  $H_2$  molecules. The electron kinetics is quite similar to the one described in [1]. The related cross sections are taken from [1] and [2].

In order to define the collision frequencies, the neutral density  $N$  must be defined from the working pressure and the gas temperature. Since the time duration under study is less than 1  $\mu\text{s}$ , the gas temperature is likely to be constant ( $T_g = 300$  K) presuming that the gas has not time to heat up, whatever the pressure is.

Due to the very low charged particle density at the beginning of the pulse, the ions are regardless and the discharge is controlled by electron free fall.

#### 4. Energy balance of the particles

The particle-field energy exchange is performed during the free flight (between two collisions), the system globally gaining energy at the expense of the field. Thus, the acquired global energy ( $\epsilon_{acq}$ ) is obtained by a sum over all electrons.

The global energy lost by collision processes ( $\epsilon_{lost}$ ) has been calculated in the same way. One contribution to this term is provided from the loss of electrons by diffusive flow to the walls.

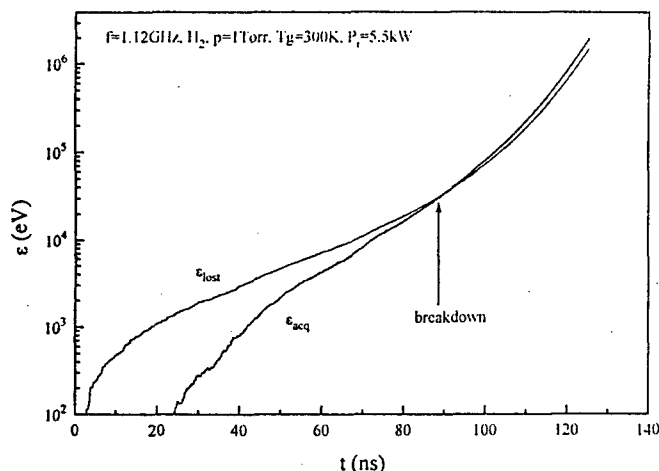


Fig. 2. Temporal variation of the acquired and lost energies.

According to Fig. 2, where the temporal energy evolution is shown, the system is initially relaxed (predominant energy loss) since the « hot distribution function » is not in equilibrium with the field. The weakness of the field and the small number of charged particles in the early stage of the discharge explain the predominance of the energy loss over the energy gain.

The increase of the field and of the number of collision events result finally in the equality of the energies ( $\epsilon_{acq} = \epsilon_{lost}$ ) at the instant which we will define as the breakdown time.

Beyond this time there is a positive energy balance followed by an exponential increase of the electronic density according to :  $n_e \propto e^{\nu \times t}$  where  $\nu$  may be considered as the net ionization rate (for instance  $\nu \cong 2.7 \times 10^8 \text{ s}^{-1}$  at  $p = 1 \text{ Torr}$ ).

#### 5. Results and discussion.

The comparison between the predicted and the experimental breakdown times has been performed for different pressures (0.5-10 Torr) and incident powers ( $P_i = 5.5 \text{ kW}$  and  $10 \text{ kW}$ ). They are in good agreement, as shown in figure 3.

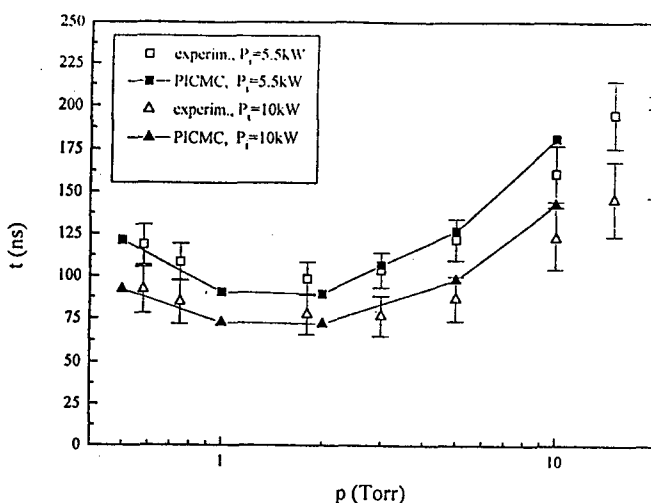


Fig. 3. Breakdown time values versus the gas pressures for two input powers  $P_i = 5.5 \text{ kW}$  and  $10 \text{ kW}$ .

The numerical effective field at breakdown also agrees well with the experimental one, according to figure 4.

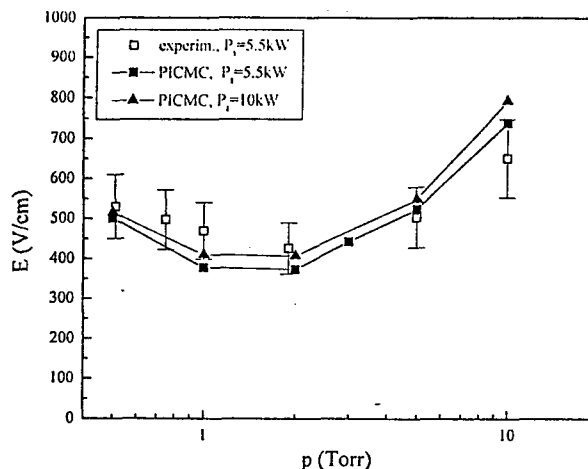


Fig. 4. Breakdown field values versus the gas pressures for two input powers  $P_i = 5.5 \text{ kW}$  and  $10 \text{ kW}$ .

It seems that the breakdown fields do not depend on input power which can be explained by the long padding time of the cavity relative to the characteristic breakdown times.

The sharp increase in the electron density after breakdown, makes that one has to consider the ambipolar diffusion regime of the free fall one and the ion kinetics. The work taking into account the plasma effect on the HF electric field is in progress.

- [1] Loureiro J., J. Phys D : Appl. Phys. 22 (1989) 1680.
- [2] Tawara H., Itikawa Y., Nishimura H. and Yoshino M., J. Pys. Chem. Ref. Data, 19 (1990) 617.

# Wave propagation characteristics in a low pressure nitrogen surface wave sustained discharge

F M Dias, E Tatarova<sup>†</sup> and C M Ferreira

Centro de Electrocinética, Instituto Superior Técnico, 1096 Lisboa Codex, Portugal

<sup>†</sup>On leave from Faculty of Physics, Sofia University, BG-1164 Sofia, Bulgaria

## 1. Introduction

Surface wave (SW) discharges link in a self-consistent way the wave electrodynamic characteristics and the behaviour of the plasma parameters. The wave field heats the electrons which ionize the gas ensuring in this way a continued wave propagation. Thus, the generated plasma column acts as a self-supporting waveguide [1]. The correlation between the different plasma balances and the wave propagation is a basic principle. For this reason, the present report is concerned with an experimental, space-resolved investigation of the electron energy distribution function (EEDF) and associated integral quantities together with the propagation characteristics of the surface wave. The aim is to show the essential correlation, for the SW discharge physics, between the EEDF behaviour and the electromagnetic wave characteristics.

## 2. Experimental procedures and results

The experiments have been performed in a stationary HF discharge sustained by an azimuthally symmetric SW of frequency  $\omega/2\pi = 500$  MHz. The plasma column is created in nitrogen at a pressure  $p = 0.5$  Torr in a Pyrex glass tube with an inner diameter  $2R = 4.5$  cm. Axially resolved EEDF measurements are performed by means of a computer controlled data acquisition system and numerical differentiation of the probe characteristics [2]. The ion saturation current at high negative voltages has been used to obtain the electron density. A radiophysics diagnostic method has been applied to obtain the SW propagation characteristics - phase and attenuation diagrams - (phase sensitive measurements along the wave path by a vector voltmeter).

The axial dependence of the measured EEDFs is depicted in figure 1. The measurements are performed at different axial positions ( $\Delta z$ ) from the end of the discharge at a fixed radial position  $r/R = 0$ . The scattered values at low and high energies indicate the limits of accuracy of the technique used, which is seen from fig. 1 to provide a dynamic range of nearly three orders of magnitude. Due to the well-known increase in the SW electric field intensity near the column end, a significant enhancement of the EEDF tail is observed

in this region, which yields higher energy averaged collision frequencies.

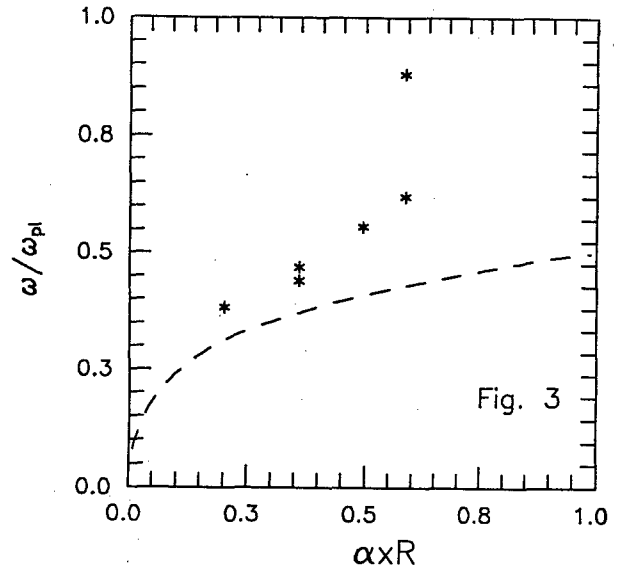
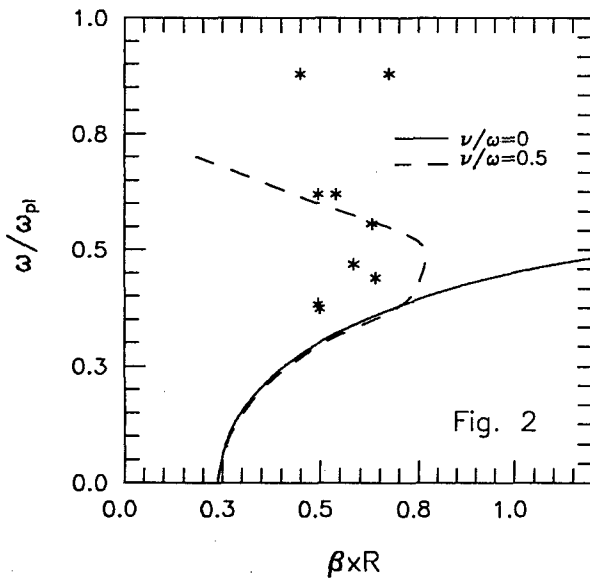
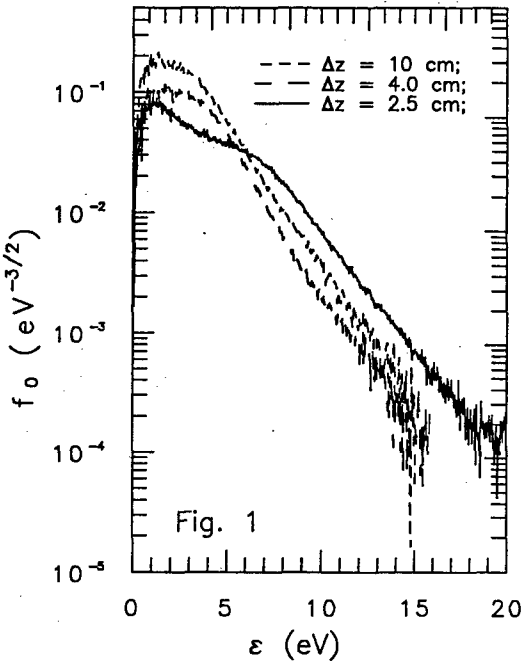
It is found that the electron density is a linear function of the axial co-ordinate with an axial gradient  $dn_e/dz = 2.12 \times 10^9 \text{ cm}^{-4}$ . Electron densities lower than the so called cut-off density [1] are obtained. The cut-off density is reached at about 5 - 7 cm from the end of the plasma column ( $L = 23$  cm under the conditions considered).

Figures 2, 3 show the phase ( $\omega/\omega_{pl}$  vs.  $\beta R$ ) and the attenuation diagrammes ( $\omega/\omega_{pl}$  vs.  $\alpha R$ ). In our experiment, the phase diagram is measured, i.e.,  $\omega$  remains constant and both  $\beta$  (axial wave number) and  $\omega_{pl}$  (electron plasma frequency) vary along the plasma column. The influence of collisions on the phase diagram is clearly observed [3]. The obtained experimental results follow the trends of the theoretical phase diagramme obtained for the collisional case, assuming a constant  $v/\omega = 0.5$  (where  $v$  is the electron neutral elastic collision frequency obtained by integration over the measured EEDFs [4]). Note however that this ratio slightly increases towards the column end due to the EEDF changes above described. It should be noted that the values of  $\beta R$  go through a maximum at  $\omega/\omega_{pl} \approx 0.5$  and tend to decrease afterwards. This "turning back" of  $\beta$  on the phase diagramme is a characteristic of SW propagation in a lossy medium. As it is seen, the axial damping coefficient  $\alpha$  increases continuously with increasing  $\omega/\omega_{pl}$  ratio. At about  $\Delta z = 5$  cm from the end of the column, the experimentally obtained  $\alpha$  values reach the axial wave number ones.

The observation that  $\alpha$  reaches the value of  $\beta$  at  $\Delta z = 5 - 6$  cm and the "turning back" appearing on the phase diagram are related to the fact that electron densities lower than  $n_{\text{cut off}}$  are obtained at a distance of about  $\Delta z = 5 - 7$  cm. In conclusion, collisions influence (in spite of the present low pressure conditions) the wave propagation characteristics and are responsible for the turning back of the axial wave number in the phase diagramme.

For a reliable description of the SW discharge physics, the investigation of the discharge electrodynamics should be coupled to a self-consistent

treatment of the plasma kinetics as the results demonstrate.



#### 4. References:

- [1] I. Zhelyazkov and V. Atanasov (1995) Phys. Reports 255 81.
- [2] F. M. Dias (1995) Plasma Sources Sci. Technol. 4 86.
- [3] J. Margot and M. Moisan (1993) J. Plasma Physics 49 357.
- [4] I. Ghanashev, I. Arestova, E. Tatarova, I. Zhelyazkov and Sv. Stoykov (1996) J. Plasma Physics 56 (in press)

#### Acknowledgments

This work was performed under a PRAXIS XXI Research Grant by the Portuguese Ministry of Science and Technology, with partial support of the Program FEDER of the European Commission. It was also partially supported by the Bulgarian National Fund for Scientific Research under Grant No. F-471/94. One of the authors (ET) gratefully acknowledges NATO for the award of a research Fellowship.



# SELF-CONSISTENT MODEL FOR KINETIC PROCESSES IN MICROWAVE $H_2$ DISCHARGES

B. F. Gordiets<sup>†</sup>, M. J. Pinheiro and C. M. Ferreira

Centro de Electrodinâmica, Instituto Superior Técnico, 1096 Lisboa, Portugal

<sup>†</sup> - On leave from Lebedev Physical Institute of the Russian Academy of Sciences, Moscow

## 1. Introduction

The low pressure hydrogen plasma created by a microwave discharge is widely used for different applications. The microwave power is efficiently absorbed and leads to strong heating of the gas and the discharge tube walls. Different theoretical models implemented in the past to describe  $H_2$  microwave discharges, do not take into consideration self-consistently this heating. The aim of our report is to present a self-consistent model taking into account these effects, which is able to calculate different plasma properties.

## 2. Description of the Model

The input parameters of the model are: angular frequency  $\omega$  of microwave generator; power  $P$  (watt) absorbed into discharge; radius  $R$  (cm) of discharge tube and length  $L$  (cm) of discharge; pressure  $p$  (torr); gas flow rate  $Q$  (sccm); and initial gas temperature  $T_0$  (at the gas inlet into discharge zone). The density of absorbed microwave power along and across tube is assumed homogeneous. It is also assumed that  $\omega \gg \nu_e$ , where  $\nu_e$  is the frequency for energy relaxation of plasma electrons. This condition permits us to use the stationary Boltzmann equation for free plasma electrons. The model enables to calculate the following plasma properties: concentrations of  $H_2$  molecules and  $H$  atoms,  $H^+$ ,  $H_2^+$ ,  $H_3^+$ ,  $H^-$  ions, populations of  $H(2)$ ,  $H(3)$ , vibrational levels of  $H_2(X^1\Sigma_g^+)$  and effective high Rydberg state  $H_2(R)$ ; density  $N_e$  of free electrons, their average kinetic and characteristic energies; electron drift velocity; electric field  $E$ ; average (across the tube) gas temperature  $T$  and wall temperature  $T_w$ .

For determination of the above mentioned plasma characteristics a coupled system of equations has been investigated for the kinetics of free electrons (stationary Boltzmann equation), vibrational kinetics of  $H_2$  molecules, kinetics of  $H_2$  Rydberg electronic state, chemical kinetics of heavy neutrals and charged particles (master equations for population densities), gas energy balance (equation for gas temperature) and reduced

maintenance electric field (equation relating the absorbed electric power to the effective electric field). The polyquantum vibration-translation energy exchanges  $H_2(v) + H \rightleftharpoons H_2(v - \Delta v) + H$ ;  $\Delta v \geq 1$  have been taken into account for investigation of vibrational kinetics and gas heating. A semi-empirical formula has been obtained and used for calculation of wall temperature  $T_w$  when forced outside cooling of discharge tube is absent, taking into consideration convective and radiative cooling of tube walls. This model extends to microwave discharge our model describing flowing  $N_2 - H_2$  low pressure DC discharges [1].

## 3. Typical Results

The behavior of different plasma characteristics (electric field; electron average and characteristic energies; gas, wall and vibrational temperatures; densities of particles and populations of excited states) has been investigated for different values of input parameters. As an example, the results of preliminary calculations for dependencies of  $H$  atom densities,  $H^-$  ion densities, gas temperature  $T_g$  and vibrational temperature  $T_v$  on gas pressure are given on Figs. 1 - 4, respectively, for different discharge powers (indicated on the curves) in pyrex glass tube. The calculations were carried out for  $\omega = 2.45$  GHz;  $R = 1.3$  cm;  $L = 15$  cm;  $Q = 200$  sccm;  $T_0 = 300$  K. It can be seen that maximal  $H$  atom density is reached for some gas pressure  $p \leq 1$  torr. The increase in  $H$  density with absorbed power is monotonous but smooth. The maximal  $H^-$  ion density is reached for low pressure and large discharge power. The gas temperature monotonously increases with pressure and absorbed power. The vibrational temperature changes little with pressure and power and has values in the range 1800 - 2800 K. It is interesting that it decreases with growth of discharge power in spite of the increased pumping of vibration levels in this case. This is explained by the increase in the rate for vibration-translation relaxation through the increase of gas temperature and  $H$  atom density.

It is necessary to note that the length  $L$  of a real microwave discharge is determined by the propagation and attenuation of the microwave electromagnetic field so it usually depends on absorbed power  $P$ , gas pressure  $p$ , radius  $R$  and material of discharge tube. Therefore the electrodynamics must be taken into account in the model for the choice of optimal working conditions. We plan to make this in the future.

**Acknowledgments.** Work supported by a contract with the Portuguese Ministry of Science and Technology under the Program PRAXIS XXI, partly funded by the EU Program FEDER.

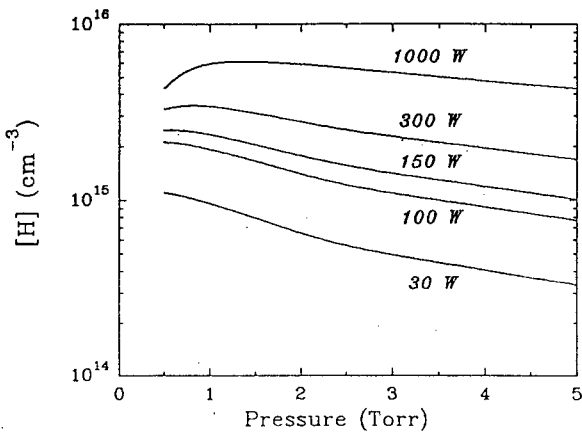


Fig. 1

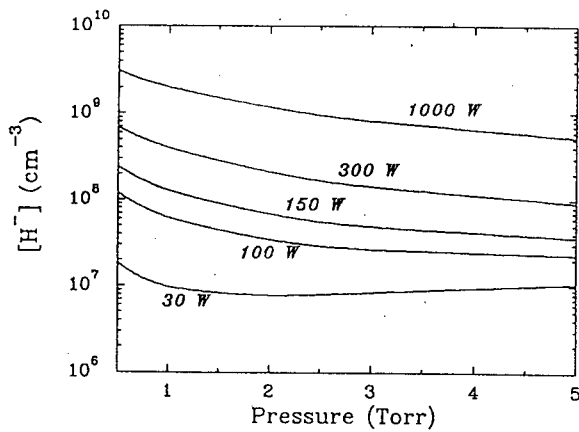


Fig. 2

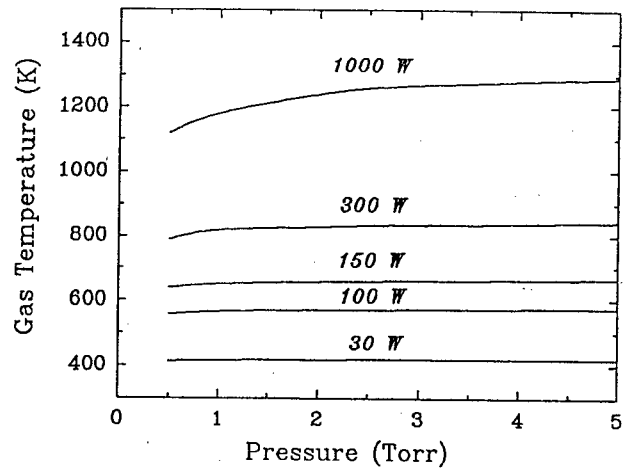


Fig. 3

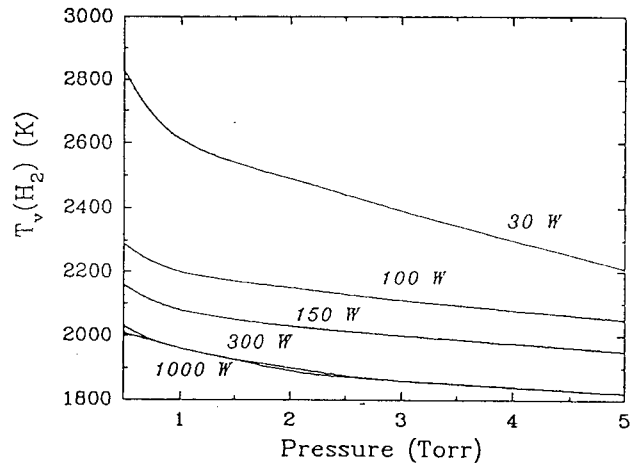


Fig. 4

#### 4. References

- [1] Gordiets B., Pinheiro M., Ferreira C. and Ricard A., ESCAMPIG 96, August 27-30, 1996, Poprad, Slovakia, v. 20 E, part A, p.147.

# Some results from hydrodynamic modelling of diffusion cooled radiofrequency sheath discharges

A. Harendt

Institut für Plasma- und Lasertechnik, TFH Wildau, D 15745, Friedrich-Engels Str. 63

## 1 The model

We examine capacitively coupled radio frequency (CCRF) discharges in systems with electrode spacing of some mm's, frequencies from 10 to 100 MHz at pressures of some kPa.

### 1.1 The equations

For the electrons and ions the continuity equation in the Lagrange and partial form is used (both are necessarily to use)

$$\frac{dn_i}{dt} = \frac{\partial n_i}{\partial t} + v_i \frac{\partial n_i}{\partial x} = -n_i \frac{\partial v_i}{\partial x} + n_e (n_0 X_i - n_i X_r) \quad (1)$$

with  $n_i = n_{e,i}$  and  $n_0$  the particle densities,  $v_i = v_{e,i}$  the drift velocities,  $X_i$  the ionisation rate coefficient and  $X_r$  the dissociative recombination coefficient. They are functions of  $E/n_0$ . The electron velocity is given by drift oscillation. For the ion velocity we solve the momentum balance omitting diffusion. [1]

$$v_e = -b_e (E/n_0) E$$

$$\frac{dv_i}{dt} = \frac{\partial v_i}{\partial t} + v_{e,i} \frac{\partial v_i}{\partial x} = \frac{e}{b_i m_i} (b_i (E/n_0) E - v_i) \quad (2)$$

We get the electrical field integrating the one dimensional Poisson equation

$$\frac{dE}{dx} = \frac{\rho}{\epsilon_0}, \quad \rho = e(n_i - n_e), \quad \int_{-d/2}^{d/2} -E dx = U_0(t) \quad (3)$$

To estimate the gas temperature  $\vartheta$  and  $n_0$  respectively we solve the stationary heat transfer equation

$$\frac{1}{T} \int_T j_\sigma(x, t) E(x, t) dt = -\frac{\partial}{\partial x} \left( \lambda(\vartheta) \frac{\partial \vartheta}{\partial x} \right) \text{ with} \quad (4)$$

$$j_\sigma = e(n_i(x, t) v_i(x, t) - n_e(x, t) v_e(x, t))$$

$\lambda$  ist the temperature dependent heat conductivity.

### 1.2 Discretisation, boundary and wall conditions.

Eq. (3) and (4) are easy to solve. They are real boundary value problems. Eq (1) and (2) are not of this type. As the result of the calculation we have to get  $n_{e,i}$  and  $v_{e,i}$  - not only in the volume, but also at the electrodes. Fig. 1 shows the discretisation process. The bold, bendet line is a front of charges (electrons or ions). Left the density of this species is zero and at right greater than zero. The boundary on the left represents the electrode. The time axis extends from top to bottom. At the top of Fig. 1 the velocity of the species points to the electrode at  $x = -d/2$ . The density and the velocity of each volume  $F$  is described by the *total* differentials from eq. (1) and (2). The position from each element

- including the front  $F$  of the species - is given by

$$\frac{dx_{e,i}^k}{dt} = v_{e,i}^k \quad (5)$$

$k$  is the number of the discretisation volume. This equation permits to estimate the time, at which the front  $S_i$  touches the electrode. The density of the species increases in this moment at the electrode

in a jump from zero to  $n_{e,i}$  and we get a current  $j_{e,i} = v_{e,i} n_{e,i}$  into the electrode. To continue our calculation we use the *partial* form of eq. (1) and (2) for the interval  $t_{con}$  and for the fixed point  $x = -d/2$ . This is not difficult since we have to make all derivatives to the right side. It is  $v_{e,i} \geq 0$  after the time  $t_{con}$ . We create for  $v_{e,i} = 0$  a volume  $S_0$  for calculations with the total differentials and initialize it with  $x = -d/2$ ,  $v = 0$  and  $n = n_p$ , with  $n_p$  as the result from the calculation with partial derivatives.

If the current into the electrode is an ion current then we get  $\gamma$ -electrons from the relation  $|j_e| = \gamma |j_i|$ . That gives the boundary value for the  $\gamma$ -electron density on the cathodic electrode

$$n_{eC} = \gamma n_i \frac{-v_i}{v_e} \quad (6)$$

## 2 Results

### 2.1 Results especially for CO<sub>2</sub> - slab - lasers

First we remember a result published previously [2]. Next we discuss some aspects concerning a CO<sub>2</sub>-slab-laser. We neglect  $\gamma$ -processes for this studies.

From eq. (1) using (2) and (3) follows

$$\frac{dn_e}{dt} \approx b_e n_e \frac{\partial E}{\partial x} + \dots = b_e n_e \frac{\rho}{\epsilon_0} + \dots \quad (7)$$

Eq. (7) means, that the density of electrons decreases for  $\rho < 0$  and increases for  $\rho > 0$ . Fig. 2 is showing that. The density in the front of the electron layer exceeds and at the rear falls below the ion density. From this follows that the electrons of the boundary layer see a higher electric field than the electrons of the bulk plasma. The conclusion is that all processes with a strongly dependence on the reduced field for example the production of charged particles are located in the boundary layer. On the other side the

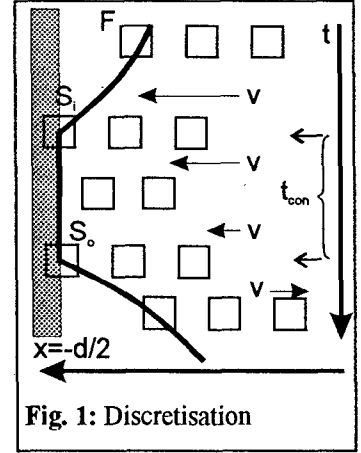


Fig. 1: Discretisation

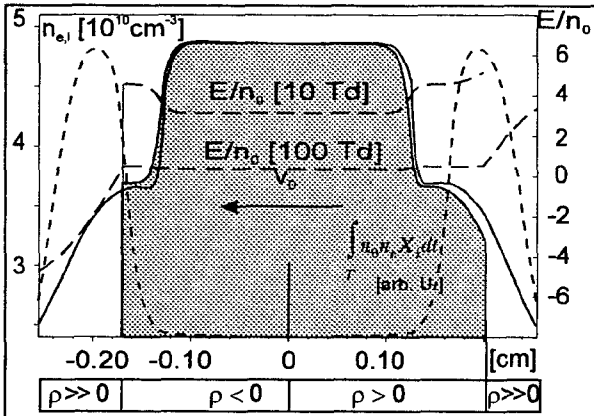


Fig. 2: Structure of a CCRF-discharge at 27 MHz,  $U_{\text{eff}} = 400\text{V}$ ,  $p = 4\text{ kPa}$ ,  $\text{CO}_2:\text{N}_2:\text{He} = 1:3:18$

ions in the boundary layer are under the influence of a very strong field during a long part of the period. The ion velocity is small in comparison with the electron velocity. But the power  $j_i E$ , which the ions extract from the electrical field can not be neglected. Fig. 3 shows this for two frequencies and some voltages: In the upper part the power absorption of the electrons, in the lower part that of the ions. This fact has to be taken in consideration for CCRF discharge systems.

## 2.2 Results including $\gamma$ -processes

We include now  $\gamma$ -processes with  $\gamma=10^{-2}$  in our calculations. The discharge skip from  $\alpha$ - to  $\gamma$ -mode if the voltage is high enough and the  $\gamma$ -mode is possible. Secondary electrons produced by ions at the electrode form an avalanche which is directed to the volume electrons. If the density in the electron avalanche drifting through the boundary layer reaches the density of the volume electrons then the discharge is changing to the  $\gamma$ -mode. Fig. 4 shows the structure of such a dis-

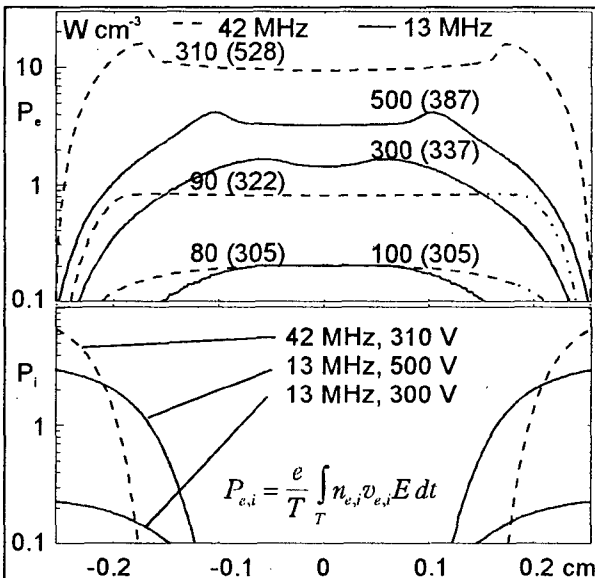


Fig. 3: Power absorption of electrons and ions. Parameters are the voltage and in parentheses the temperature in K on  $x = 0$ . All other are the same as Fig. 2.

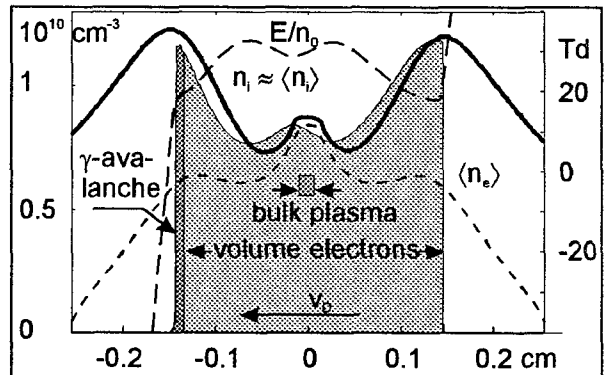


Fig. 4: 8 MHz,  $U_{\text{eff}} = 350\text{V}$ , all other is same as Fig 2

charge performing stationary oscillations. In front of the electrodes a space charge structure builds up being similar to a cathode fall region of a dc-discharge. It is important to mention that by the transition to the  $\gamma$ -mode the calculated voltage-current density characteristic does not fall. This demonstrate that the transition of a CCRF-discharge into the high current mode is not caused by  $\gamma$ -processes at the electrodes.

Fig. 5 shows that with an increase of the voltage the thickness of the boundary layer reaches a limit which is independent of the frequency. The simplest expressions of the ionisation rate coefficient and the electron drift velocity for high fields are

$$X_i = A e^{-B/E/n_0}, v_e \propto \sqrt{E/n_0}$$

We can see that the ionisation rate a efficient saturates while the drift velocity is increase monotonously indefinitely at high field. This is the reason for the limitation of the boundary layer thickness at high voltages. Comparing Fig.2 with Fig. 5 we can see that the boundary layer in the  $\alpha$ -mode at 27 MHz is much smaller than the layer in the  $\gamma$ -mode at 8 and 13 MHz. This means that at high frequency  $\gamma$ -processes alone are not enabled to initiate the transition into the  $\gamma$ -mode of the discharge.

Supported in parts by Deutsche Forschungsgemeinschaft SFB 191, project A10.

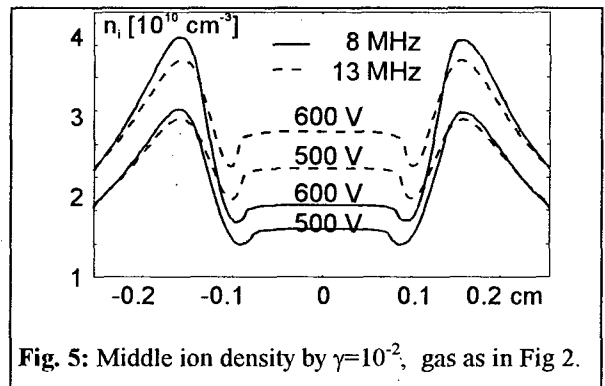


Fig. 5: Middle ion density by  $\gamma=10^{-2}$ , gas as in Fig 2.

- [1] A.Harendt: Hydrodynamische Modellierung ..., Dissertation, Bochum 1996
- [2] A.Harendt, H. Gündel: Num. Modellierung von HF - Schichtentladungen, DPG, Greifswald 1993

# Optical Diagnostics of the RF Discharge Burning at Atmospheric Pressure and Interacting with Water Solution

A. Brablec, P. Slavíček, M. Klíma and V. Kapička

<sup>1</sup>Department of Physical Electronics, Faculty of Science,  
Masaryk University, Kotlářská 2, 611 37 Brno, Czech Republic

## 1. Introduction

A combination of rf plasma jet burning at atmospheric pressure and liquid represents a system where are in contact all known state of matter - liquid, solid material (nozzle and other material), gas (carrier gas in the plasma jet) and ionized gas (the plasma). In the paper, we present our first experience with such system (in our case a pure water liquid) where a number of interesting phenomena can be found. It also evokes possible applications like are a new approach to the restoration of archeological artifacts, [1, 2], new therapy in medicine, new procedures in chemistry and in treatment of surfaces, etc.

## 2. Experiment

A schematic drawing of our plasma jet system driven at 13.56 MHz is given in Fig.1. As a working gas we used argon for two flow rates (1.5 l/min and 15 l/min) and two output power (150 and 200 W), respectively. Here, the plasma jet worked in the subsonic regime but a supersonic version is prepared.

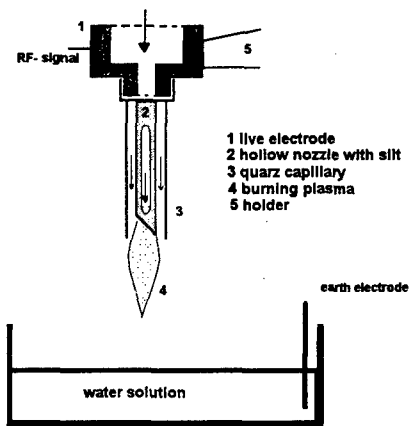


Figure 1: A schematic drawing of the RF discharge (length - 5 cm, inner diameter - 0.6 mm, outer diameter - 1.5 mm).

Spectra were recorded in the spectral range of 280 - 950 nm using the HR 640 monochromator and the Spectrum One CCD, air cooled (1024x128 pixels) by Jobin Yvon.

## 3. Results

The discharge was driven in flowing regime and visually we observe no difference between burning in open air and in pure water liquid. But in spectra recorded in water we found significant decrease of  $N_2$  and an increase of OH lines. A typical spectra are demonstrated in Fig.2, 3.

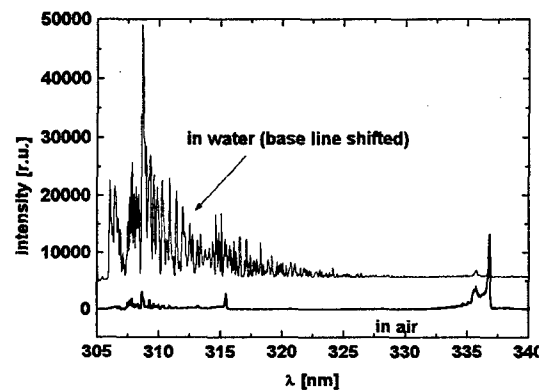


Figure 2: Typical spectra of the discharge burning at atmospheric pressure in water solution and in open air. The OH band (0,0) with rotational structure is observed in second order.

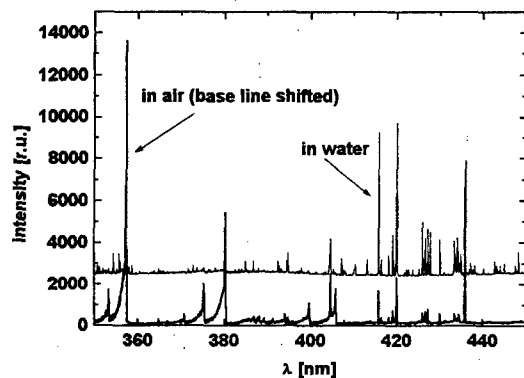


Figure 3: Typical spectra of the discharge burning at atmospheric pressure in water solution and in open air.

The plasma channel in air (for higher power and flow rate) was 1 cm long, very narrow (diameter - 1 mm<sup>2</sup>) and sharply space limited. The diameter of the discharge in water was practically the same but at low flow rate and output power the length was

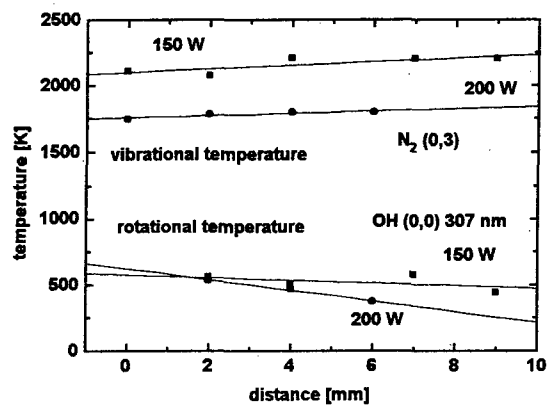


Figure 4: Vibrational and rotational temperature for the discharge burning in open air near the water level as a function of distance from the end of the nozzle.

about 1.5 cm.

In the spectra, there are identified important bands and lines as follows:

- nitrogen vibrational band for vibrational numbers (0,3), (0,2), (0,1), (0,0) - with observable rotational structure, (1,0)
- vibrational OH bands (0,0) with resolved rotational structure, bands are observed both in first and second order
- hydrogen lines - they are very dominant in the water liquid;  $H_{\alpha}$ ,  $H_{\beta}$  can be used for diagnostic purposes
- argon lines - argon is the carrier gas and for this reason the atomic lines are observed in all cases

Vibrational temperatures were determined from the  $N_2$  second positive system  $C^3\Pi_u-B^3\Pi_g$  using bands (0,3), (0,2). Rotational temperature estimated from the rotational lines of OH approximates temperature of neutral gas. From argon atomic lines we estimated excitation temperature. A comparison of the discharge with other ones investigated previously is done in Tab.1 (the data are from [3]).

	$N_2$ [K]	OH [K]	p [Pa]
RFPJ	4000 - 7000	500 - 650	100 - 2000
HCD	3500 - 4000	about 400	50 - 800
RFPJ*	1700 - 2200	400 - 800	$10^5$

Table 1: RFPJ - rf plasma jet burning at reduced pressure, HCD - hollow cathode discharge, RFPJ\* - rf plasma jet at atmospheric pressure

In Tab.1, there is also given results obtained from similar measurements realized in the system with hollow cathode running under the same conditions. Namely, there are physical reasons that in the hollow cathode discharge occur similar processes like in the plasma jet but in comparison with it the theory of the HCD is developed.

### 4. Conclusion

We present first results of so called "plasma pencil" which draws attention not only for unexpected phenomena appearing there but especially for hopeful technological and medical applications. Namely, we investigated interaction with liquid water (simple system) but it is evident that the experiment allows to modify many parameters like are working gas, electrical parameters, dimensions of the nozzle and composition of the solution. Particularly, the last parameter can bring new surprises.

The optical diagnostics will be supplemented by chemical analysis of the solution [4].

### Acknowledgements

This work was supported by the Grant Agency of Czech Republic, contract No. 202/94/0490 and has been done in the framework of the Association for Education, Research and Application in Plasma-chemical Processes and was financially supported by grant No. 202/95/1222 of the Grant Agency of Czech Republic and by project COST 515.50.

### 5. References

[1] Vepřek S., Eckmann Ch., Elmer J. Th.: Plasma Chem. and Plasma Processing, Vol. 8, No. 4, 1988, p. 455

[2] Klíma M., Zajíčková L., Janča J. and coll.: Conference of Conservation of Metal Objects in Low-Pressure Hydrogen Plasma, Zürich October 28. - 29., in press

[3] Brablec A., Kapička V., Slavíček P., Střecha M., Vaculík R.: Europhysics Conference Abstracts, Vol. 20 D, 28th EGAS, 1996, Graz, Austria, A4-98, p.196-197

[4] Kapička V., Šícha M., Klíma M., Novák M., Touš M., Jastrabík L., Soukup L., Behnke J., Tichý M., Brablec A., Slavíček P.: XXIII ICPIG, Toulouse 1997, France, in press

## Study of a gas flow in a two – nozzle plasma reactor

K. Kapoun<sup>1</sup>, Z. Hubička<sup>2</sup>, M. Šerý<sup>1</sup>, M. Šícha<sup>3</sup>

<sup>1</sup>Department of Physics, Faculty of Education, University of South Bohemia,  
Jeronýmova 10, 371 15 České Budějovice, Czech Republic, e-mail: kapoun@pf.jcu.cz

<sup>2</sup>Institute of Physics, Division of Optics, Academy of Sciences of Czech Republic,  
Na Slovance 2, 180 40 Prague 8, Czech Republic, e-mail: hubicka@fzu.cz

<sup>3</sup>Department of Electronics and Vacuum Physics, Faculty of Mathematics and Physics,  
Charles University, V Holešovičkách 2, 180 00 Prague, Czech Republic

### 1. Introduction

The low pressure RF plasma–chemical reactor with the multi–hollow cathode system is described in the papers [1] and [2]. We study a gas flow in the two nozzle system and we present the phenomenon of the substrate "paint".

### 2. Schlieren methods

The refractive methods of visualisation of inhomogeneities in gas use the dependence of refractive index  $n$  on density  $\rho$  or pressure  $p$  and temperature  $T$ :

$$n - n_0 = (n_0 - 1) \left( \frac{\rho}{\rho_0} - 1 \right)$$

$$\frac{\rho}{\rho_0} = \frac{T_0}{T} \cdot \frac{p}{p_0}$$

Gases with significant pressure inhomogeneities are especially suited to the well-known schlieren, interferometry or shadow schlieren methods. We have used the schlieren methods to the visualise of the interaction of gas flows from two nozzles.

Our experimental setup is described in paper [3]. This setup comprises a reactor chamber with a compressor, a vacuum pump and schlieren equipment Carl Zeiss. The images were taken by CCD camera and the procedure of DIPS was used.

### 3. Results

We have studied characteristics of the reactor with two hollow cathodes which were connected to the different RF generators. The working gas flow through both nozzles was supersonic. We could have changed electrical parameters of both generators, geometry and material of both nozzles and of substrate, and pressure of gas in both nozzles ( $p_1$  and  $p_2$ ) and in the reactor chamber ( $p$ ). We changed only pressure because we study the neutral gas flow in these experiments. The two nozzles in our experiments were placed in the reactor chamber perpendicularly to each other. The external diameters of both nozzles were 6 mm and the internal 3

mm. The substrate was placed in the angle  $45^\circ$  to both nozzles.

The figures 1 – 4 show a typical picture of schlieren image (and its equidensities) of supersonic flow from the nozzles, and the secondary flow. Pressure of gas in both nozzles ( $p_1$  and  $p_2$ ), pressure in recipient ( $p$ ) and position of substrate and nozzles are drawn in these figures. This flow is created due to the interaction of particles from both primary channels. It has been found out experimentally that the direction of the secondary gas channel depends on the pressure of working gases flows in the primary gas channels. It has been found out that it is possible to deviate the secondary gas (or plasma) channel by increasing of the gas flows in the nozzles (the phenomenon of "paint").

The deviation of the secondary plasma channel allowed to deposit a thin film on a particular part of substrate. For this reason by means of the multihollowcathode system it is possible to deposit the composite thin films and multilayer structures onto internal walls of cavities, tubes and on components with complicated shapes.

### 4. Acknowledgement

This work has been done in connection of the Association for Education, Research and Application of the Plasma–Chemical Processes and was particularly supported by grant 202/95/1222 of Grant Agency of Czech Republic.

### 6. References

- [1] Z. Hubička, M. Šícha, M. Novák, L. Soukup, L. Jastrabík, K. Kapoun, M. Šerý: Contrib. Plasma Phys., in print
- [2] Z. Hubička, M. Šícha, M. Novák, L. Soukup, L. Jastrabík, K. Kapoun, M. Šerý, V. Kapička: ICPIG XXIII
- [3] J. Blažek, K. Kapoun, M. Šerý: In Proceedings Digital Image Processing, JU České Budějovice 1996, 87

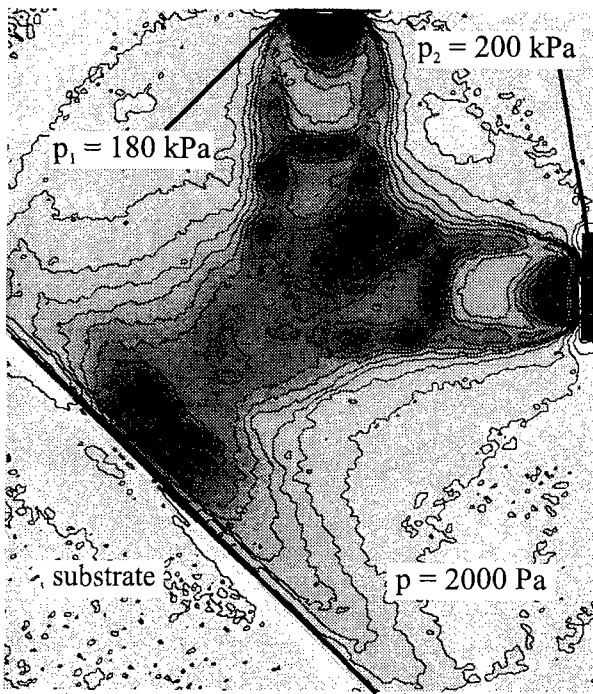


Fig. 1

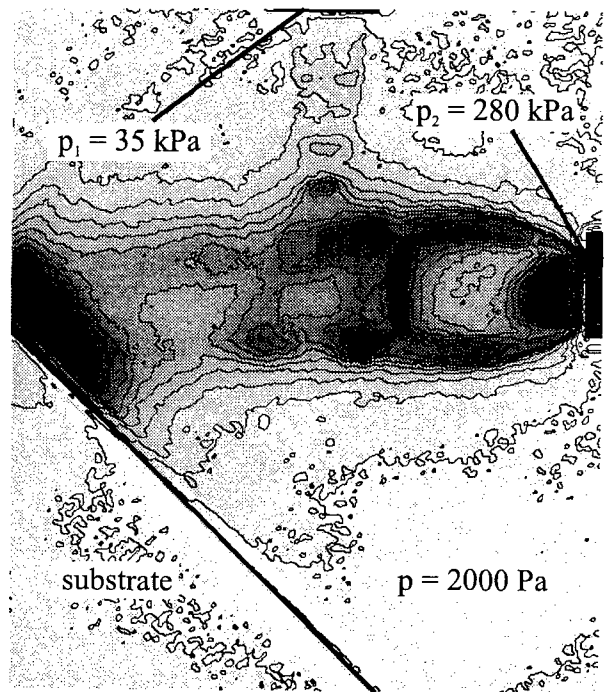


Fig. 2

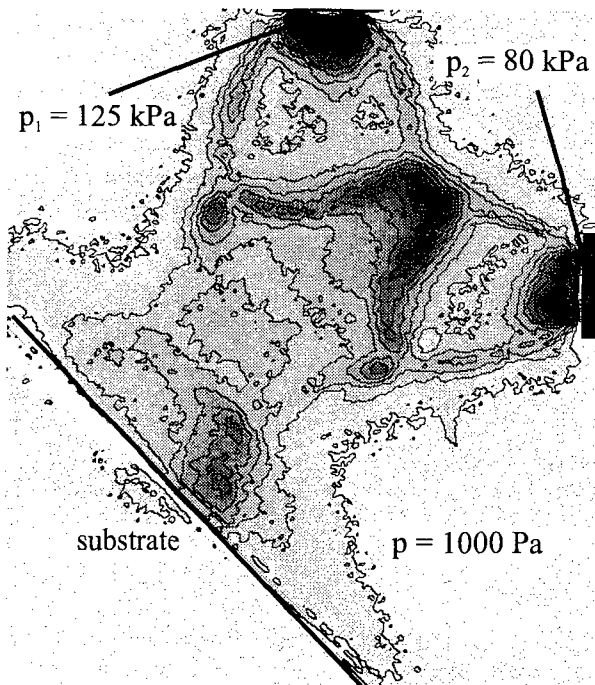
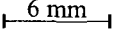


Fig. 3

scale:  6 mm

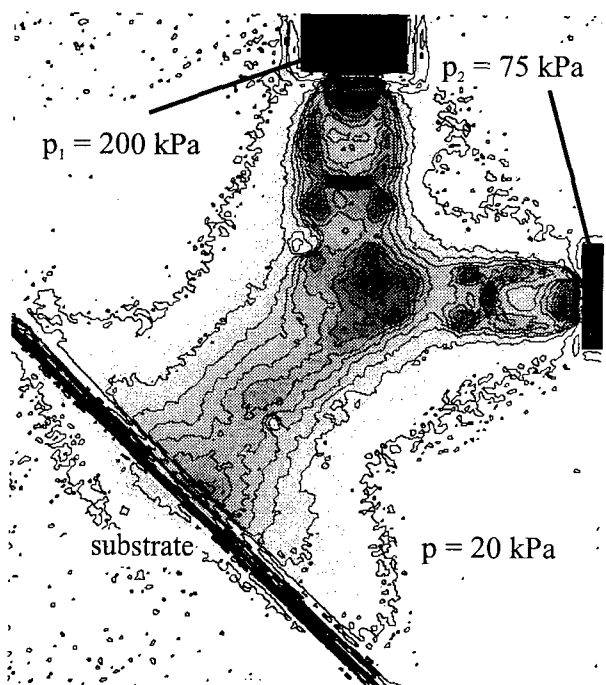


Fig. 4



## The structure of a capacitively coupled plasma

Sideris N. Karderinis, Beatrice M. Annaratone and John E. Allen  
Dept of Engineering Science, University of Oxford, Oxford, OX1 3PJ, UK

### 1. Introduction

Plasma processing has been an impetus for the very rapid growth of electronic industry, in recent years. The *Capacitively Coupled Plasma Reactor* is one of the most utilised tools for the development and study of plasma etching and deposition. In this contribution the aim is to characterise the plasma used in a variety of industrial processes using different diagnostics i.e. *Langmuir probes*, *Optical Emission Spectrometer* coupled to a *CCD detector* and a *Retarding Field Analyser*. In our experimental work many different gases have been used as: Ar, He and  $\text{CF}_4$ .

### 2. Experiment

The capacitively coupled plasma reactor is presented in figure 1.

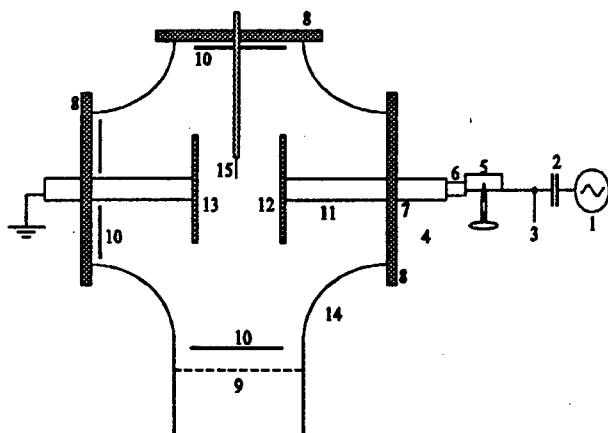


**Fig.1** Experimental apparatus: (1) rf amplifier, (2) blocking capacitor, (3) rf voltage probe, Tektronix P013A, (4) ac current probe, Tektronix P6022, (5) bridge for the rf guard, (6) rf guard, (7) grounded shield, (8) grounded flanges, (9) rounded grid to diffusion pump, (10) Teflon insulation, (11) ceramic insulation, (12) driven electrode, (13) grounded electrode, (14) glass vessel, (15) driven/voltage probe [1].

In the present paper the experimental work for the Ar case is presented, when the excitation to the driven electrode is  $300V_{pp}$  at a driving frequency of 13.56MHz with pressure varying between 0.8 to 20 Pa and an interelectrode distance of 80mm.

It is well known that when the plasma is in contact with a surface such as an electrode a positive *sheath* is formed to restrict the electron flux out of the plasma. As there is less collisional excitation of the gas neutrals in the sheath, this is less bright than the plasma. In our experimental arrangement the driven electrode has an area smaller than the combined earthed electrode and walls. A larger sheath with more RF volts, and as a consequence more DC volts, builds up at the driven electrode. A Langmuir probe provides information on the local electron density  $n_e$ , the electron temperature  $T_e$ , the ion density  $n_i$ , the plasma potential  $V_p$ , the floating potential  $V_f$  and, for isotropic plasma, the Electron Energy Distribution Function (EEDF). The spectrometer is used to monitor the line intensity of selected atomic transitions.

A spatial scan of the sheath and plasma regions has been performed with Langmuir probes and a fibre optic probe connected to the spectrometer /CCD. While the space resolution of the probe is about 1mm, the entrance angle of the optical fibre is  $23^\circ$  giving an error of 5mm on the optical emission. At pressures lower than 1Pa the plasma sheaths expand up to half the interelectrode separation. It should be noted that no information on the electron density can be obtained from the sheath regions with these diagnostics. At these low pressures the plasma between the sheaths is uniformly bright and of uniform electron density. As the pressure is increased the sheaths shrink in size and a less bright region develops in the middle of the plasma. This reduction in light emission is not followed by a reduction in electron density. At pressures in the range above 10Pa the sheaths are <3mm in size and the bright region is confined very near to the sheath edges. Figs 2,3 and 4 show the profiles of the intensity of the atomic line 415.86nm (excitation energy 14.53eV), the electron density profiles and the electron temperature profiles.

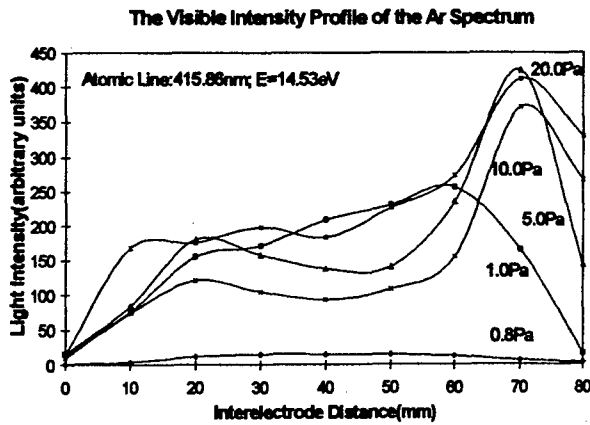


Fig.2 The intensity profile of the atomic Ar line 415.86nm at different pressures.

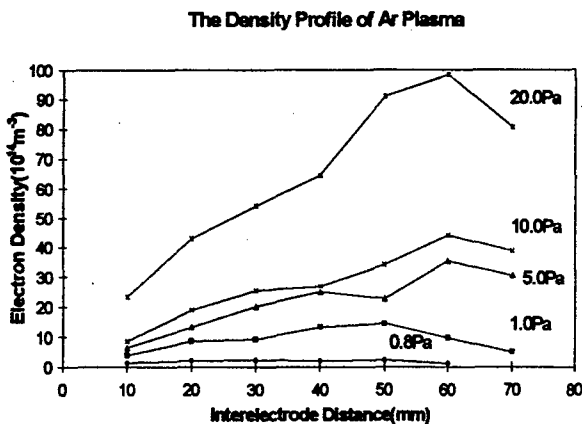


Fig.3 The density profile of the Ar plasma at different pressures.

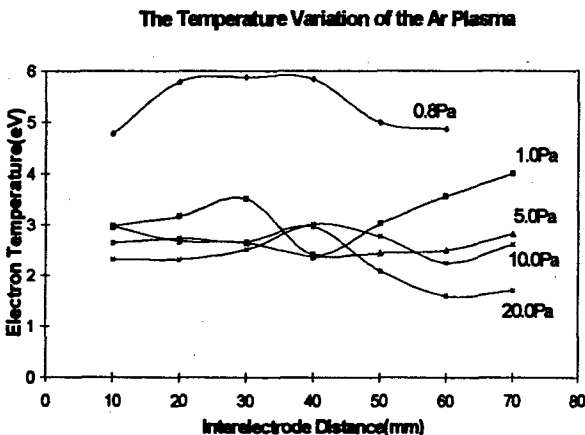


Fig.4 The electron temperature profiles of the Ar plasma at different pressures.

It is clear from Figs.2, 3 that as the pressure increases a peak in the line intensity profile and electron density profile develops near the driven electrode.

### 3. Discussion

It is intended to extend these observations to obtain information on various heating mechanisms that sustain the plasma discharge such as *plasma sheath resonance*[1], *secondary electron emission*[2] and *stochastic heating* at the sheath boundaries[3,4]. The last two mechanisms are both expected to be more important at the sheath adjacent to the driven electrode. The secondary electron emission depends on the larger D.C. voltage whereas the stochastic heating is associated with the larger A.C. voltage across the sheath. Separation of the two effects is therefore not a simple matter since the D.C. and A.C. voltages are closely related.

### 4. References

- [1] B.M., Annaratone, V.P.T., Ku and J.E., Allen, J. Appl. Phys., 77, 10,(1995), 5455.
- [2] Yu.P., Raizer, Gas Discharge Physics, (1991), Springer-Verlag.
- [3] M.A., Skorik, N. St. J., Braithwaite and J.E., Allen, Europhysics Conference Abstracts, 16C, (1992), III 1973.
- [4] J.E., Allen, Phenomena in Ionized Gases, XXII ICPIG, (1995), 316.

### 5. Acknowledgements

This project is supported by EPSRC. We would like to thank Dr A. Dyson for useful discussions. One of us (SNK) is supported partially by Solar Physics Corporation, USA.

# Temporal Evolution of an Inductively-Coupled RF Discharge during Mode Transition

Mamoru Matsuoka, Motoichi Kawaguchi and Mayuko Yoshida<sup>†</sup>

Department of Industrial and Technical Education, Mie University, Tsu, Mie 514, Japan

<sup>†</sup> Nagoya Memorial Hospital, Nagoya, Aichi 460, Japan

## 1. Introduction

It is generally known that a dark discharge plasma is first obtained and then the plasma is abruptly changed to a bright one in an inductively-coupled radio-frequency (rf) plasma when the applying rf power is gradually increased [1]. The brightness increases by an order of magnitude at such a mode transition. We observed the visible light profile during mode transition in detail in order to understand the mechanism of the transition.

## 2. Experimental Setup

The experimental setup is shown in Fig. 1, which is similar to that in the reference [2], in which three discharge modes were reported. The discharge tube was a glass sphere of 13 cm in diameter, filled with argon gas of 133 Pa. The plasma was obtained by a 13.56 MHz rf power which was fed by one turn coil wound around the tube on its equatorial plane. The continuous rf power up to 500 W was supplied to the coil via a matching network in an unbalanced way through the coaxial cable of which the outer conductor was grounded. The applied rf power was slowly varied and the matching network was always tuned manually to keep the voltage standing wave ratio (SWR) minimum ( $<1.5$ ). This is different with the experiment using a short pulse repetitive rf power source [3], where mode transitions occurred in each short pulse without quick tuning. Also in our experiment, however, the SWR transiently became a large value more than 3 just after mode transition since the tuning was unable to follow the discontinuous variations so quickly. The visible light profiles before, during and after mode transition were monitored by a CCD camera and digitized.

## 3. Experimental Result

The whole plasma behavior is described in detail in the reference [2]. The plasma was obtained with an rf power of 22 W. The intensity of visible light gradually increased with increasing the rf power up to 300 W. The most bright part was localized near the non-grounded feeding point and extended to the region near a semicircle of the non-grounded side of the coil. The mode transition occurred at 300 W. The connected rf power decreased to 200 W after tuning but the brightness of the visible light increased by about an order of magnitude compared with that just before transition. Further increase of the rf power up to 400 W

gave a brighter visible light but no essential change. When the rf power was decreased, the inverse mode transition occurred at 100 W, which decreased to 30 W after tuning. The discharge after the inverse mode transition was similar to the initial discharge but localized more than before. The matching condition was also different so that the latter discharge should be said in the "third" stage, not back in the initial stage [2]. The discharge disappeared at 10 W.

Temporal variation of the visible light profile during the first mode transition is shown in Fig. 2. The coaxial cable is connected to the left-hand side of the figure. Four profiles corresponding to different timings are shown in this figure; (a) just before transition, (b) just after transition but before tuning, (c) after transition and during tuning and (d) after transition and after tuning. Note that profile (a) was taken at a different experimental sequence with different camera iris so that the absolute light intensity cannot be compared with the others. The profile was still not axi-symmetric but localized to the other side of the feeding point just after transition (b). The profile became axi-symmetric during and after tuning (c and d). As the tuning proceeded, the bright region came close to the glass wall as well as the total light intensity increased. It is clear that the plasma behavior strongly depended on the tuning for reducing the SWR.

A periodic profile in azimuthal direction sometimes appeared transiently just before the profile (b) was established. The reproducibility of the appearance of the periodic profile was low. In a measured example, the

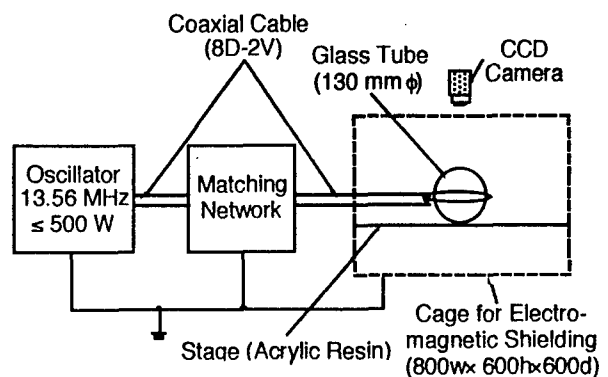


Fig. 1 Experimental setup.

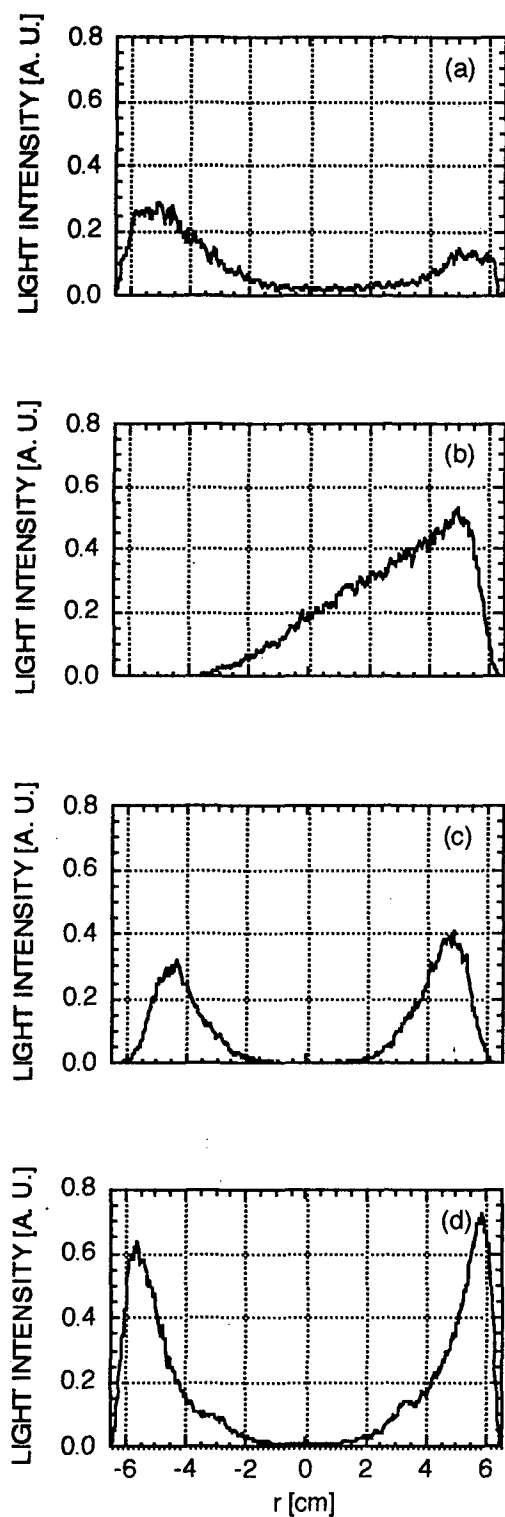


Fig. 2 Visible light profiles during mode transition; (a) just before transition, (b) just after transition but before tuning, (c) after transition and during tuning and (d) after transition and after tuning.

phenomenon was observed only in one frame of the video signal (1/30 s for NTSC). The periodicity quickly changed from 6 to 4. Similar but steady-state phenomenon was reported in the reference [4], where the periodicity was discussed in connection with striations generally known in dc electric discharges. It is not clear whether the phenomenon in our experiment is of the same type or not.

#### 4. Discussion

The measured profiles before, during and after the mode transition suggest that the mode transition is not the transition from an electrostatically-coupled discharge (E-discharge) to an inductively-coupled discharge (H-discharge). This comes from the fact that the plasma should be axi-symmetric if the discharge is coupled to the coil antenna completely inductively. The mode transition in this experiment should be the transition from an E-discharge (or an E-dominated discharge) to another E-discharge (or another E-dominated discharge). The latter E-discharge (or E-dominated discharge) would change to an H-discharge (or H-dominated discharge) as the tuning proceeded. The mode transition in this experiment was probably caused by a discontinuity in the coupling condition between the coil and the discharge due to a certain nonlinear response of the plasma on the production process itself. A circuit calculation including the nonlinear response of the plasma would be required for the exact description.

#### 5. Summary

We observed the visible light profile during mode transition and obtained the following results.

- (1) The plasma behavior strongly depended on the tuning for reducing the SWR.
- (2) A periodic profile in azimuthal direction sometimes appeared transiently just before the mode transition completed.

- [1] D. O. Wharmby: IEE Proceedings-A, **140** (1993) 465
- [2] M. Kawaguchi, M. Matsuoka and M. Yoshida: "Observation of Mode Transition in an hf Discharge Plasma Sphere", presented at 1996 International Conference on Plasma Physics, Nagoya, Sept. 1996
- [3] T. Takamoto, T. Mukoyama and H. Nagahama, J. I. E. E. Jpn, **91** (1971) 173
- [4] J. A. Stittsworth: IEEE Trans. Plasma Sci., **24** (1996) 125

# ROLE OF ELECTROMAGNETIC WAVES IN ECR PLASMA UNIFORMITY

Yoko UEDA and Yoshinobu KAWAI

Interdisciplinary Graduate School of Engineering  
Sciences,  
Kyushu University, Kasuga, Fukuoka 816, Japan

## 1. Introduction

Electron cyclotron resonance (ECR) plasma sources are widely used in the experiments or dry etching, plasma deposition and plasma assisted chemical vapor deposition (CVD). A significant advantage of ECR plasma sources is the high electron densities which can be achieved at low gas pressures. As wafers with large diameter like 200~300 mm and decreasing devices and features in size are required, it becomes increasingly important that the etch rate be uniform over the surface of a wafer in order to prevent charge-up damage or minimize the overetch. Hence, the production of a large diameter uniform ECR plasma has become one of the most important subjects in plasma processing. ECR plasma sources are fundamentally different from the conventional parallel plate or reactive ion etching configurations, in that ECR plasmas are sustained by electromagnetic waves. Furthermore, the behavior of electromagnetic waves in the ECR plasmas is determined by the plasma they support. This results in a highly nonlinear coupling of the waves to the plasma, with attendant problems in such areas as tuning and plasma uniformity.

It is well known that the uniformity of ECR plasmas depends on the experimental condition, such as incident microwave power, gas pressure and magnetic field configuration, that is, the radial profile of the ion saturation current density,  $I_{is}$ , changes the shape like concave, convex, uniform or wavy. The dependence of the radial profile of  $I_{is}$  on the gas pressure was reported by Gottscho *et al*[1]. Gorbatkin *et al*[2] showed the relation between the ECR plasma uniformity and the electron density jump. As for the effect of the magnetic field configuration on the plasma uniformity, it was reported[3] that the magnetic field lines should be set to be straight from ECR point to the periphery of the wafer.

As mention above, it was reported the uniform ECR plasmas with small diameter, where the electron density is in the range from  $5 \times 10^{10}$  to  $2 \times 10^{11} \text{ cm}^{-3}$ . Recently, we could achieve the very uniform large diameter ECR plasma, where uniformity was within 3% over 200 mm in diameter[4]. However, the mechanism of the uniformity of ECR plasma has not been clear yet. As one of the reasons, the complicated effect of electromagnetic waves propagation on the plasma uniformity could be proposed. Hence, to

understand the behavior of the electromagnetic waves in the ECR plasmas is indispensable for the control of the radial profile of electron densities. However, there are few reports on the propagation or absorption of electromagnetic waves in ECR plasmas with respect to plasma uniformity. In this paper, we reports the experiments on the plasma uniformity and electromagnetic wave propagation changing on input microwave power. Furthermore, the effects of the electromagnetic waves, specifically, ordinary waves(O-mode) or extraordinary waves(X-mode) in the plasma on the plasma uniformity is discussed.

## 2. Experimental apparatus

A detailed schematic diagram of the experimental apparatus was described in Ref.4. The vacuum chamber was made of stainless steel with an inner diameter of 290 mm and a length of 1200 mm. The magnetic coil assembly consisted of six coils; four to make a uniform magnetic field, and two to form the magnetic mirror, and control the current of the mirror. The frequency of the microwaves is 2.45 GHz and the microwave power could be varied up to 5kW. The used gas was He and the pressure was  $0.5 \sim 5 \times 10^{-3}$  Torr. The plasma parameters were measured with the movable Langmuir probes. The radial profiles of electric fields of electromagnetic waves were measured with a movable loop or dipole antenna with a crystal diode. The strength and wave pattern were measured by a crystal diode and interferometer, respectively. The amplitudes of wave patterns were given with arbitrary units because an uncalibrated loop antenna was used.

## 3. Results and Discussion

The dependence of the radial profile of the ion saturation current density on the input microwave power was in the following: The profile of  $I_{is}$  changed as convex, wavy, concave, uniform, and convex with changing the input microwave power.[4] In order to investigate this reason, the radial profile of electromagnetic waves was measured. Figure 2 shows radially propagating wave patterns observed by the interferometric method[4] for different input microwave powers,  $P_{in}$ . In the case of  $P_{in}=0.6\text{kW}$ , as seen from Fig.1, two waves with long and short wave length are excited, where solid lines of 1 - 4 mean wave length of  $P_{in}$  0.6kW and 1kW, and half-wave length of  $P_{in}$  1.5kW and 2kW, respectively. The wave length increased as the input microwave power was increased. The mode of these waves was confirmed to be O-mode as shown in Fig.2. With increasing the electron density, the wave number decreases, and becomes 0 at the cutoff.

Figure 3 shows a wave pattern and the output of a crystal diode. In the case,  $I_{is}$  shaped as shown in Fig.4. From Figs. 3 and 4, the profile of  $I_{is}$  was sure to be influenced by the waves propagating radially. However, the profile does not always correspond to the

radial profile of output of a crystal diode. In the case where electromagnetic waves remained strongly, the inserting antenna may disturb the profile of electromagnetic waves, which may be taken into consideration. Thus, the profile of the observed uniform plasma of the electron density,  $10^{11}\text{cm}^{-3}$  seems to be influenced by the remained electromagnetic waves such as X-mode. These waves in the plasma were found to disappear under the conditions that the electron density was higher than  $2 \times 10^{11}\text{cm}^{-3}$ . In this condition, only whistler waves were found to propagate before the ECR position, so focusing of whistler waves is supposed to make the radial profile peaking. The critical density where the waves of X-mode disappear changes according to the magnetic field configurations. A uniform ECR plasma of the high electron density around  $10^{12}\text{cm}^{-3}$  was already obtained at the incident power of 2kW in this experiment. In order to obtain such a ECR plasma stably, it is very important to understand the behavior of whistler waves before a ECR position. Recently, the ray tracing calculation in a plasma or 2D model for ECR plasma production have been proposed[6,7]. It is future work to measure the propagation of whistler waves in two dimension with changing external conditions.

#### 4. References

- [1] Eray S. Aydil, Jeffrey A. Gregus, and Richard A. Gottscho, Rev. Sci. Instrum., 64 (1993) 12
- [2] S.M. Gorbalkin, L.A. Berry, and J.B. Roberto, J. Vac. Sci. Technol., A8(3) (1990) 2893
- [3] S. Samukawa, J. Vac. Sci. Technol., A 11(5) (1993) 2572
- [4] Y. Ueda, M. Tanaka, S. Shinohara and Y. Kawai, Rev. Sci. Instrum., 66 (1995) 5423
- [5] Y. Ueda, and Y. Kawai to appear in Surface & Coating Technology
- [6] J. E. Stevens and J. L. Cecchi, Jpn. J. Appl. Phys., 32 (1993) 3007
- [7] Y. Yasaka, J. Appl. Phys., 72 (1992) 2652

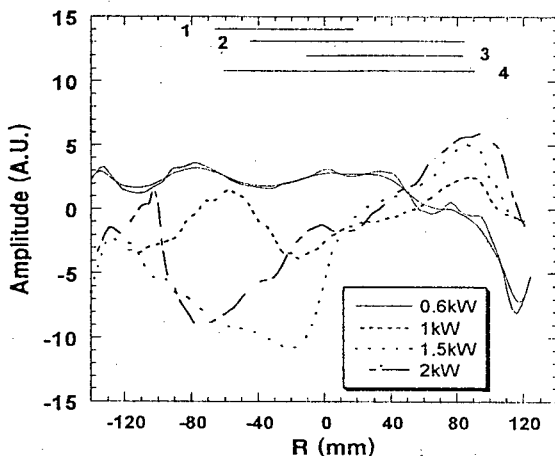


Fig.1 The interferometric wave patterns for different input microwave powers

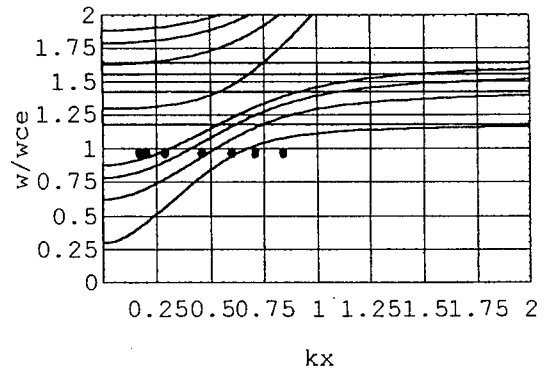


Fig.2 The dispersion relation of X-mode for different electron densities

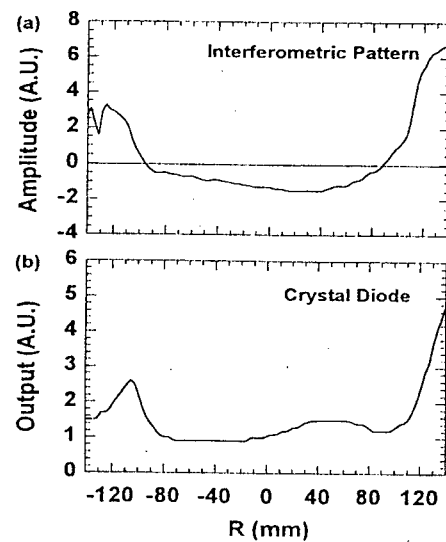


Fig.3 The radial profile of (a) the interferometric pattern (b) the output of a crystal diode

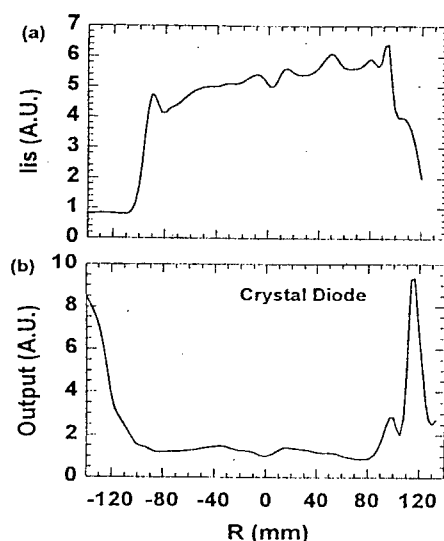


Fig.4 The radial profile of (a) the ion saturation current density (b) the output of a crystal diode

## Characteristic Properties of the Microwave Breakdown Wave in Electrically Negative Gases

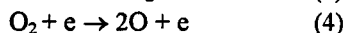
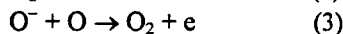
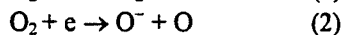
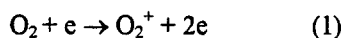
G.M.Batanov, I.A.Kossyi, N.I.Malykh\*, A.A.Matveev\*\*,  
A.V.Sapozhnikov, and V.P.Silakov\*\*

Institute of General Physics, Russian Academy of Sciences, 117942, Vavilov street, 38, Moscow, Russia,  
E-mail: sapoz@fp10.gpi.ru

\* Phys. Technical Institute, Sukhumi, Georgia,

\*\* Keldysh Institute of Applied Mathematics, Russian Academy of Sciences, Moscow, Russia.

Together with the electron impact ionization, the associative ionization and the electron detachment play an important role in the balance of charge particles in weakly ionized microwave plasmas [1,2]. One can expect that the accumulation of negative ions in discharges initiated in oxygen or water vapour can lead to the rapid growth of the electron density. For discharges in oxygen, the main processes are described by the following reactions:



the dissociative attachment (2) plays a dominant role at the first stage of the discharge, when the concentrations both of negative ions and oxygen atoms are low. As negative ions and atoms are accumulated, the dissociative detachment (3) becomes important (in particular, after the switching-off of the microwave pulse). For a pressure in the range 10 - 20 torr the discharge in these gases is a breakdown wave in character (see, for example, [3, 4]); in the case of weakly converging beams, the effect of ionization-field instabilities leading to the plasma stratification and increase in the electron density up to or even above the critical value is reduced. Therefore, in such discharges the role of the kinetic processes can manifest itself most clearly.

The experiments were conducted with a gyrotron radiation with a wavelength of 8 mm and a power of 500kW. A Gaussian beam was focused inside the vacuum chamber with a polystyrene lens; its radius in the focal plane was  $a_F = 1.8$  cm, and the caustic length was  $l_F = ka_F^2 = 25$  cm. In the experiments, the working-gas pressure was varied within the range 10 - 20 torr; the microwave pulse duration could be also varied. Characteristic of these experiments is that the field amplitude ( $E = 6$  kV/cm) was much greater than the threshold one; consequently, the gas breakdown occurred at the leading edge of the microwave pulse.

The plasma density was measured from the phase shift by using the interferometer with a wave length of 2 mm. The space resolution was 1cm. The diagnostic

beam intersected the caustic of the main beam at a distance of 5cm from the caustic center towards the lens. The time evolution of the electron density is seen in Fig. 1b which shows the oscilloscope traces of the interferometer phase detector signal; Fig. 1a shows the signal from the microwave detector measured the radiation passed through the discharge. As is seen, the electron density increases sharply and reaches its maximum at the leading edge of the gyrotron pulse (1μs); then, the density decreases smoothly during the pulse. After the switching-off of the microwave pulse, the density begins to grow, and the second maximum is usually twice as large as the first one. It should be noted that, if the duration of the microwave pulse is less than 3μs, then the second maximum isn't observed.

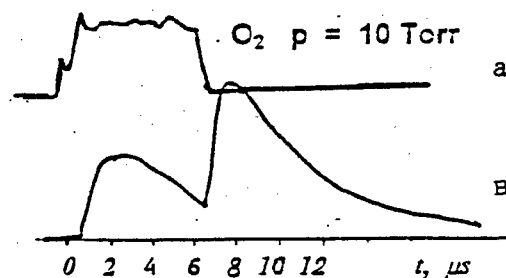


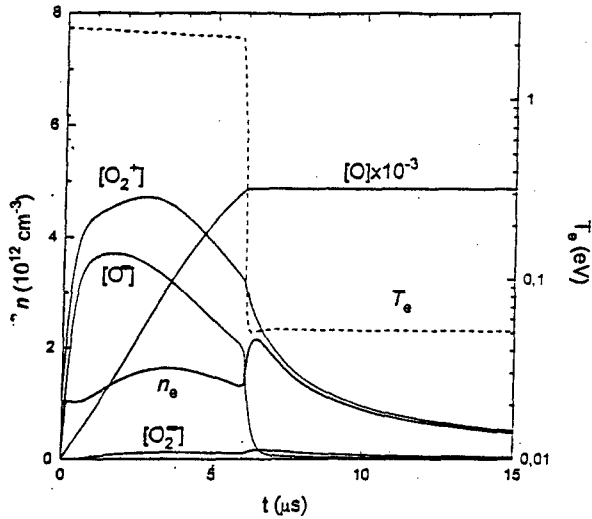
Fig.1. Oscilloscope traces of the signals (a) of microwave detector at the backside wall of the vacuum chamber and (b) the phase shift measured by interferometer.

The results similar to those obtained in the discharge in oxygen were observed also by using the air, water vapour as well as water vapour - nitrogen and water vapour - oxygen mixtures as a working gas.

For the discharge in oxygen the numerical simulation was performed for conditions similar to the experimental conditions (Fig. 2) by using the kinetic model [5], in which the vibrational kinetics of oxygen molecules was incorporated. The calculations show that the increase in the electron density after the switching-off of the microwave power is related to the electron detachment, since at this stage of the discharge, the

dissociative attachment, which occurred in the high electric field, is replaced by the weak three-particle attachment.

This work was supported by the Russian Foundation for Basic Research, project no. 96-02-16162a.



$p=10$  Torr,  $\langle E(t) \rangle / N = (6.9-3 \cdot 10^5 t) \cdot 10^{-15} \text{ V cm}^{-2}$ ,  $\lambda=8$  mm  
Isochoric discharge,  $\tau=6 \mu\text{s}$ .

Fig.2. Calculation of the discharge kinetics in oxygen.

## References

- [1] Bezmenov, I.V., Rusanov, V.V., and Silakov, V.P., Preprint of Keldysh Institute of Appl. Mathematics, Russ. Acad. Sci., Moscow, 1992, no. 30, p. 28, (in russian).
- [2] Baiadze, K.V., Kulikov, V.N., and Mitsuk, V.E., VIII All-Union Conf. on Physics of Low-Temperature Plasma, Minsk, 1991, p.45-46, (in russian).
- [3] Vikharev, A.L., Gil'denburg, V.B., Kim, A.V., Litval, A.G., and Semenov, V.E., High-Frequency Discharge in Wave Fields, Gorkii, 1988, p. 41-135, (in russian).
- [4] Inovenkov, I.N., Kim, A.V., Rakova, E.I., Semenov, V.E., Chukhin, A.E., Preprint of Inst. of Appl. Phys., Russ. Acad. of Sci., Moscow, 1990, no. 271, p. 28, (in russian)
- [5] Kossyi, I.A., Kostinskii, A.Ya., Matveyev, A.A., and Silakov, V.P., Pl. Sources Sci. Tekhnol., 1992, vol. 1, p. 207-220.



# Low-frequency periodic regime in the ECR Ion Sources

M. Lamoureux \*, A. Girard, H. Khodja and G. Melin

SI2A, Département de Recherche Fondamentale sur la Matière Condensée, CEA, 17 rue des Martyrs, 38054 Grenoble Cedex 9, France,

\* Laboratoire de Dynamique des Ions, Atomes et Molécules, Université P&M Curie, C75, 4 Place Jussieu, 75252 Paris Cedex 05, France.

## I. Introduction

A periodic regime (with a period on the time scale of about 1 s) has been revealed lately for the ECRIS (Electron Cyclotron Resonance Ion Source) Quadrumafios in Grenoble operated with pure krypton[1]; this regime was put into evidence by four types of signals: diamagnetism, bremsstrahlung, electron and ion end-loss currents. The appearance of this regime has been shown to limit the currents of highly charged ions produced. In order to provide further information on this phenomenon, Quadrumafios has been run very recently with other rare gases, again at 18 GHz, for the radio-frequency power  $P_{rf} = 100-1500$  W and the gas injection pressure  $p_{inj} = 0.5 \times 10^{-3} - 9 \times 10^{-3}$  mbar. We particularly investigate the borderline which corresponds to the appearance of this periodic regime in the  $P_{rf}-p_{inj}$  plane, more precisely, with increasing heating powers and decreasing injection pressures.

## II. Results obtained for He, Ne, Ar and Xe, and comparison with Kr.

When working with rare gases of increasing  $Z$ , only the He and Ne plasmas remain stable under the working conditions given in the introduction.

Ar is the first noble gas for which the periodic regime sets in within the range of our experimental working conditions. Figure 1 shows for Ar and Xe the borderline below which the plasma is stable, and compares it with the borderline previously obtained for Kr.

The comments made in [1] for the Kr border and ionic currents are qualitatively valid for the present Ar case. The most remarkable fact is that the linear section of the border of Ar overlaps pretty well with the linear section previously observed for Kr. The empirical law for the limit power  $P_{rf}^{(lim)}$  at which the periodic regime sets in is :  $P_{rf}^{(lim)} = a + b p_{inj}$  with  $b = 310 \pm 10$ , in both cases, in units of W and  $10^{-3}$  mbar respectively. We recall that for Kr the spare data points

relative to the periodic regime empirically lead to a period proportional to  $P_{rf} / (p_{inj})^{3/2}$ .

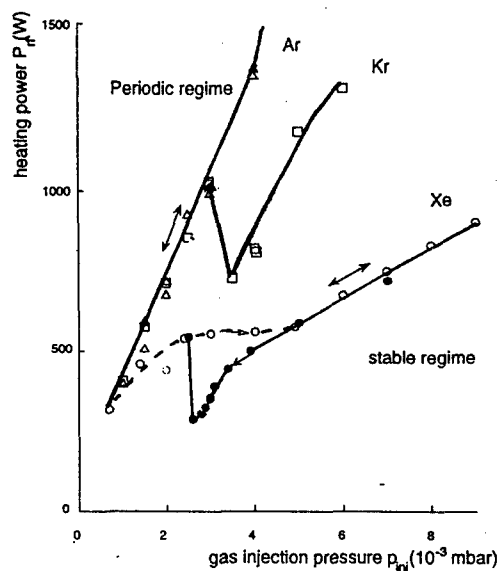


Fig. 1 The border between the domains of the periodic and stable regimes is indicated for Quadrumafios operated with three rare gases of increasing  $Z$ .

Triangles: Argon

Squares: Krypton

Circles: Xenon. The empty circles correspond to an upwards investigation (increasing the pressure and then the power until the switch to the periodic behavior is achieved), whereas the full circles correspond to a careful downwards mapping (decreasing  $p_{inj}$  and increasing  $P_{rf}$ ).

For Xe, the longest linear segment observed for the borderline lies between  $3 \times 10^{-3}$  up to  $9 \times 10^{-3}$  mbar, and corresponds to a different proportionality factor  $b = 75 \pm 5$ . When carefully investigating the borderline down from large pressures for Xe, the descent at the kink is smooth while the ascent is sudden and steep. At the lowest point, the period has become as high as 10 s.

### III. Concluding remarks

These results, obtained only in January 1997, are too recent to permit conclusions about the causes of the oscillations documented in ref.[1], but they are very useful for beginning a discussion. We have also just been aware that similar types of periodic regimes have been noticed in passing in other ECRIS sources around the world.

The present study finally offers a new interpretation of the gas-mixing strategy which is not inconsistent with the former interpretations which understand it as increasing the electron densities and/or the potential dip, decreasing the temperature of the heavier ions, etc [2-6]. We recall that this well known strategy consists in adding at the injection a gas moderately lighter than the element whose highly-charged ions are desired. Since the lighter elements lead to a border which lies higher in the  $P_{rf}-P_{inj}$  plane, the addition of the lighter adjuvant shifts the borderline to a more favorable location, and thereby allows for the production of larger currents. This was illustrated in ref.[1] for the production of  $Kr^{7+}$  currents increased by the addition of He.

Because of the smooth shape and long period of the oscillations observed in Quadrumafios (see Fig. 1 of ref.1), we tend not to ascribe the periodic phenomenon to instabilities, though whistler microinstabilities such in [7] have indeed been observed in our case and various loss-cone instabilities probably occur (we have in mind a loss cone instability which could grow only if the plasma size is above a few times the wavelength involved, and that would indeed favor the appearance of instabilities for the heavier elements). However, the fact that the border consists partly of stretches with a linear dependence of the limit power on the injection pressure suggests more a fluid-physics origin or sputtering by the wall. It is also possible that the sort of hysteresis illustrated in Fig.1 for Xe corresponds to different modes of the repartition of the electric fields in the cavity when the plasma is developing.

As a summary, these recent results confirm that the periodic regime is of a great practical importance, as its appearance limits the currents of highly charged ions produced. The striking features of this periodic regime are:

- (i) very low frequency (making, so to speak, the ECRIS plasma beat like a human heart)
- (ii) perfect regularity,
- (iii) the fact that the borderline of its appearance in the  $P_{rf}-P_{inj}$  plane is at times a linear segment but can also exhibit kinks.

Reasons for all these features remain an open plasma physics problem of great interest.

### Acknowledgments

We are grateful to P. Charles and R. Pras for preliminary results obtained in March 1996 on Ar; the spare data were contaminated by some unknown quantity of remnant He, so that unfortunately they could not be given here. One of us (M. L.) is also very grateful to M. Glass for effective encouragement in this work.

### References

- [1] M. Lamoureux, A. Girard, R. Pras, P. Charles, H. Khodja, F. Bourg, J. P. Briand and G. Melin, *Phys. Plasmas (Letter)*, **3**, 4307 (1996).
- [2] Z. Q. Xie and C. M. Lyneis, *Rev. Sci. Instrum.* **65**, 2947 (1994).
- [3] T. Nakagawa, T. Kageyama, M. Kase, A. Goto and Y. Yano, *Jpn. J. Appl. Phys.* **32**, L1335-1338 (1993).
- [4] C. C. Petty, D. L. Goodman, D. L. Smatlak, and D. K. Smith, *Phys. Fluids B3*, 705 (1991).
- [5] R. Friedlein, S. Herpich, H. Hiller, H. Wirth, Z. Zschornack and H. Tirroff, *Phys. Plasmas* **2**, 2138 (1995).
- [6] G. Melin, F. Bourg, P. Briand, M. Delaunay, G. Gaudart, A. Girard, D. Hitz, J. P. Klein, P. Ludwig, T. K. Nguyen, M. Pontonnier and Y. Su, *Proceedings of the 5<sup>th</sup> International Conference on Ion Sources*, August 31-September 4, 1993, Beijing, China, published in *Rev. Sci. Instrum.* **65**, 1051 (1994).
- [7] R. C. Garner, M. E. Mauel, S. A. Hokin, R. S. Post and D. L. Smatlak, *Phys. Fluids B2*, 242 (1990).

# RF heating of plasma between parallel plates by plasma-sheath resonance

T. Matsui, S. Tsuda, and K. Yamada

Hitachi Research Laboratory, Hitachi, Ltd., 7-1-1 Ohmika-cho, Hitachi-shi, Ibaraki 319-12 Japan

## 1. INTRODUCTION

We are developing an effective radio-frequency (RF) heating method for a low-temperature plasma without a magnetic field. Stochastic heating is one RF heating mechanisms [1], however, its energy conversion efficiency from the input RF power to the plasma temperature is low. In this work, we report a more effective heating method using plasma-sheath resonance.

## 2. EXPERIMENT

The experimental setup is shown in Fig. 1. In order to get the low temperature plasma, we used a gadolinium (Gd) plasma which was generated by electron impact when Gd in the crucible was vaporized by electron beam heating [2]. Since this plasma was generated near the Gd surface, the electron temperature decreases with collisions between the Gd atom and the electron when the Gd atomic density is high enough. The generated plasma expands and flows to the upper test section, which consists of a pair of parallel plate electrodes and the RF circuit. There was no magnetic field in the area of the electrodes. In this area, the electron density and electron temperature of the initial plasma were  $1 \times 10^{16} \text{ m}^{-3}$  and about 0.5 eV, respectively, while the atomic density was  $1 \times 10^{18} \text{ m}^{-3}$ . The ionization ratio, therefore, was about 1 %. Moreover, the drift velocity of the plasma was about 900 m/s.

The electrode height and the gap between electrodes were set at 17 cm and 5 cm, respectively. In Fig. 1,  $z$  is defined as the distance from the bottom of the electrode. The RF power was applied to one of the electrodes and RF frequency was set at 13 MHz or 150 MHz. A negative DC bias was applied to the same electrode in order to form the ion sheath in front of it. The sheath thickness was controlled by changing the amplitude of the DC bias. It also increases with the height because the plasma density decreases due to extraction of ions to the electrode. The other electrode was grounded. The electron density and electron temperature were measured by a single probe between the electrodes. The atomic flux was measured by a quartz crystal thickness monitor.

## 3. RESULTS AND DISCUSSION

### 3.1 Experimental results

The RF power dependence of the electron temperature is shown in Fig. 2. While the electron temperature ( $T_e$ ) for 13 MHz increased slightly, that for 150 MHz increased sharply. When  $T_e$  was more than 3 eV, light from plasma discharge was observed between the electrodes. The energy conversion ratio from the input RF energy to the plasma electron energy was estimated and was about 40 % when RF power was 1 W for 150 MHz. On the other hand, it was about 2 % when

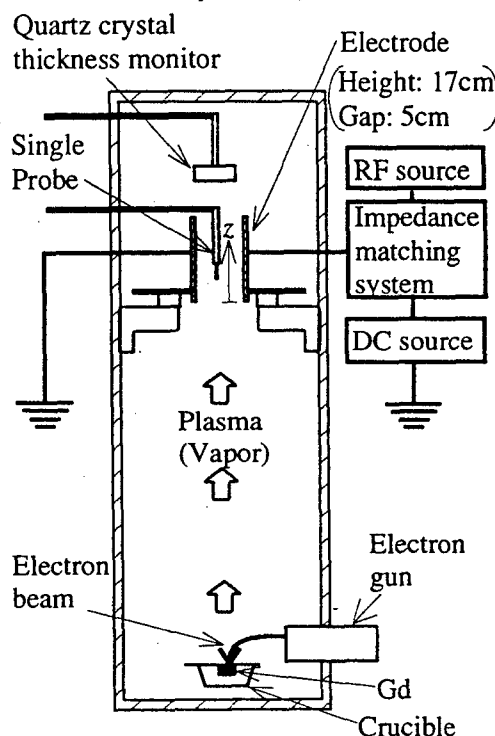


Fig. 1 Experimental setup

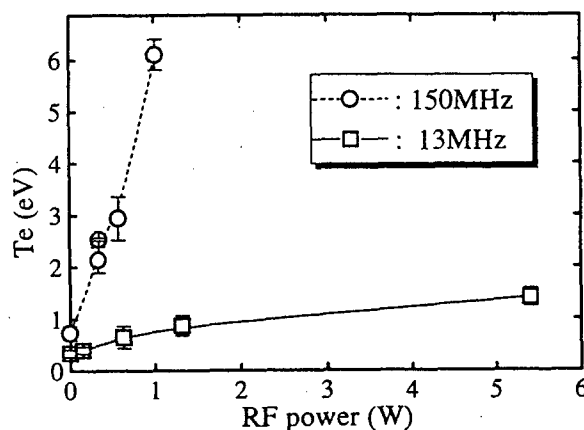


Fig. 2 RF power dependence of the electron temperature (DC bias: -100V)

RF power was 5.5 W for 13 MHz. The energy conversion efficiency was higher for the 150 MHz case.

### 3.2 Heating mechanism

In order to clarify the heating mechanism for 150 MHz, we studied the possibility of heating due to the plasma-sheath resonance. The angular frequency of the plasma-sheath resonance ( $\omega_r$ ) is described as follows [3, 4],

$$\omega_r = \sqrt{\frac{s}{d}} \omega_{pe} \propto s \cdot n, \quad (1)$$

where  $s$ ,  $d$ ,  $\omega_{pe}$ , and  $n$  are the sheath thickness, the gap between the electrodes, the electron plasma angular frequency, and the electron density, respectively. Therefore,  $\omega_r$  depends on  $s$  and  $n$ . Then, we investigated whether resonance would occur for the above experimental conditions. We estimated  $n$  and  $s$  for  $z$ , based on the theory of the Child-Langmuir sheath [5]. The results, when the initial electron temperatures were 0.5 and 5 eV, are shown in Fig. 3. In Fig. 3 (a),  $n_0$  is the initial electron density. When  $z$  increased,  $n$  decreased and  $s$  increased because the ions and the electrons in the plasma were extracted to the electrode by the DC bias. Although the resonance frequency ( $f_r$ ) decreased with  $z$ , we found that the resonance position for  $f_r = 150$  MHz was in the electrode area for  $T_e = 0.5$  eV. Even if  $T_e$  increased to 5.0 eV, the resonance position remained in the electrode area. On the other hand, the resonance position for  $f_r = 13$  MHz was not in the electrode area for  $T_e = 0.5$  eV.

Next, we simulated whether  $T_e$  rose in the above resonance condition, using a one-dimensional plasma particle simulation code, XPDP1 [6]. The initial density and the electron temperature were set at  $2 \times 10^{15} \text{ m}^{-3}$  and 0.5 eV, respectively, which were values at  $z = 0.1$  m in Fig. 3. The applied RF frequency was 150 MHz and its voltage ( $V_{rf}$ ) was changed. Figure 4 shows the time evolution of  $T_e$ . We found that  $T_e$  increased steeply at  $4 \mu\text{s}$  when  $V_{rf} = 10$  V. Since  $s$  at  $4 \mu\text{s}$  was about 4 mm, the resonance condition in Fig. 3 was satisfied.

In summary, we confirmed that the plasma was heated efficiently by RF heating based on the plasma-sheath resonance.

- [1] V. Vahedi *et al.*: Phys. Fluids B, 5 (1993) 2719
- [2] R. Nishio, K. Suzuki: Phys. Fluids B, 5 (1993) 2036
- [3] G. Bekefi: *Radiation Processes in Plasmas*, Wiley, New York, (1965) Chap.5.
- [4] T. Matsui *et al.*: Phys. Plasma, 3 (1996) 4367
- [5] F.F. Chen: Phys. Fluids, 25 (1982) 2385
- [6] C.K. Birdsall: IEEE Trans. Plasma Sci., PS-19 (1991) 65

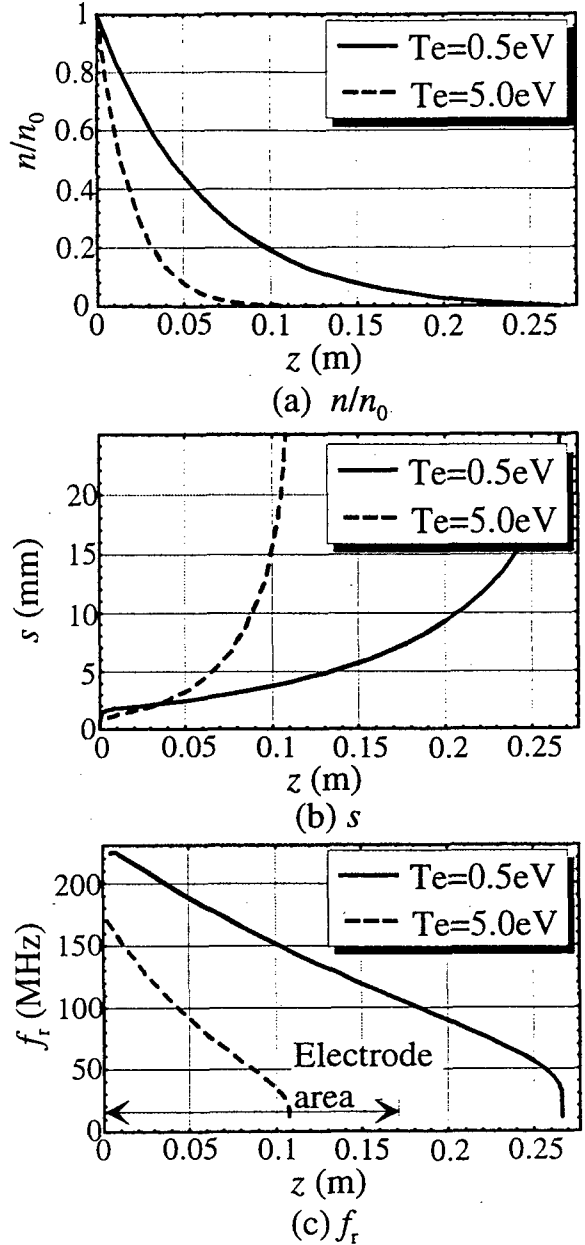


Fig. 3 Resonance characteristics of the plasma ( $n_0: 1 \times 10^{16} \text{ m}^{-3}$ , DC bias: -100V)

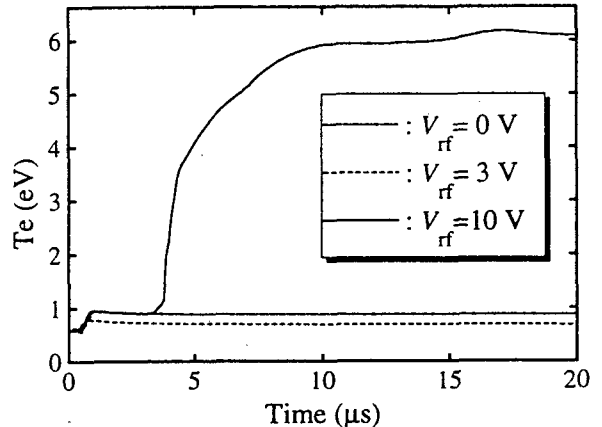


Fig. 4 Time evolution of  $T_e$  in the simulation ( $n_0: 2 \times 10^{15} \text{ m}^{-3}$ ,  $f_r: 150$  MHz)

# Measurement of Interaction between Plasma-Loaded Slow Wave Structure and High-Power Microwaves

Yuichi Naito, Atsushi Shiozaki, Hitoshi Onose, Nobukatsu Hangai and Kazuo Minami

Graduate School of Science and Technology, Niigata University, Niigata 950-21, Japan

## 1. Introduction

In recent years, high power backward wave oscillators (BWO's) utilizing intense relativistic electron beams have been considered to be an innovative approach for producing high-power microwaves.[1,2] Experiments [3-5] on plasma-filled BWO's have demonstrated the efficiencies up to 40%, which are of the same order as those obtained in conventional moderate power devices. The present work is a basic study of plasma microwave interaction in a slow wave structure (SWS) such as those used in plasma-filled BWO's. We have carried out an experiment to detect the density modulation in a plasma-filled corrugated metal wall waveguide caused by externally injected moderately high power microwaves. We describe the experimental results on "protuberance in plasma pressure" in a corrugated wall plasma waveguide.

## 2. Experimental Setup

The discharge plasma system is shown in Fig. 1. A weakly ionized steady-state plasma is produced by a gas discharge between a hot cathode of diameter 10 cm and a grounded corrugated wall SWS (anode). The latter is made of cast aluminum and has an axial length of 38.4 cm (12 periods). The inner wall radius of the SWS changes as  $R(z) = 1.4\cos(2\pi z/3.2) + 5.0$  (cm).

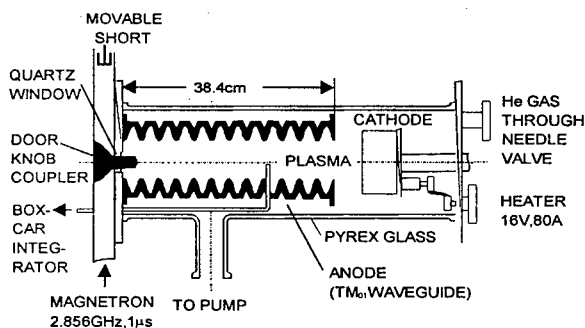


Fig.1. Discharge plasma system

The plasma is produced in pure helium gas of 50~100 mTorr using a stabilized direct current source (10~30V) up to  $I=30$ A. No external magnetic field is applied to the plasma, and no energetic electron beams which may result in BWO are present. A small size Langmuir probe

is inserted along the central axis of corrugated waveguide through a longitudinal slot cut to allow axial motion. No significant effects on the plasma parameters due to the corrugated wall are observed in the case without incident microwaves.

Microwave pulses in  $TM_{01}$  mode of frequency 2.856 GHz, power  $P$  less than 60kW and duration 1  $\mu$ s from a pulse magnetron are repeatedly injected through doorknob coupler (mode launcher) located at the left side of the apparatus shown in Fig. 1. The microwaves are completely reflected by the nonuniform plasma in the corrugated wall SWS. In Fig. 1,  $R(z)$  is designed so that the propagating 2.856 GHz microwaves have the nature of slow waves when no plasma is present near the mode launcher. Here, the term slow wave means that the phase velocity of the wave is less than the speed of light in vacuum. The refractive index in the axial direction is greater than unity, and the microwaves constitute a surface wave in the sense that  $E_z$  near the axis is approximately expressed in the form of a modified Bessel function  $I_0(r)$ .

## 3. Experimental results and discussions.

In Fig. 2, The ion saturation current (ISC) versus probe positions on the center axis is shown for the discharge current of 12A. Here, the zero probe position is taken as the position of the doorknob coupler in Fig. 1. The vertical axis shows the ISC of the probe with a bias voltage of -30V. The delay time  $\tau$  is set at 0.4  $\mu$ s after the cessation of the microwave pulse. The dashed horizontal lines indicate the zero ISC levels. In Fig. 2, it is noted that conventional cavitons [6] (local density decrease at the critical surface  $\omega=\omega_p$ ) are generated at various incident powers. Here,  $\omega$  and  $\omega_p$  are, respectively, the microwave angular frequency and local plasma frequency. An increase(decrease) in ISC is assumed to indicate a local increase(decrease) in plasma density. As far as cavitons are concerned, the results for the corrugated wall plasma waveguide are the same as those for smooth cylindrical plasma waveguides. [7,8]

For large incident microwave powers, a number of protuberances(rises) in ISC are generated as well as caviton. The protuberances are always located at the

positions which are at  $R(z)$  minimum in the underdense region ( $\omega > \omega_p$ ). Such protuberances in ISC have not been observed in conventional smooth cylindrical plasma waveguides. [8]

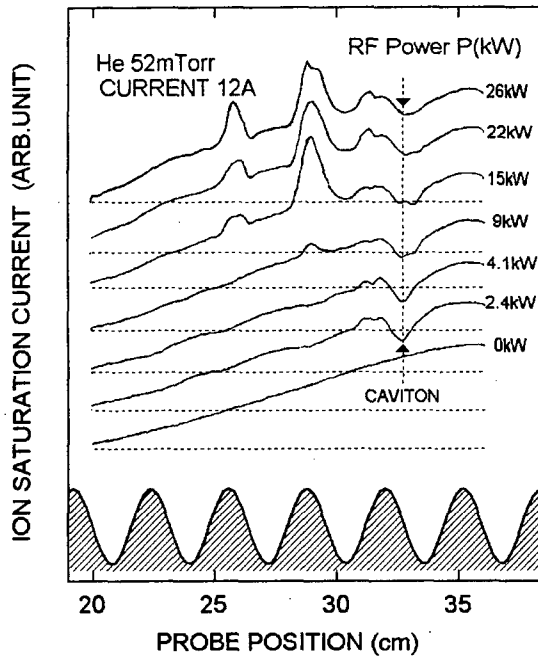


Fig.2. ISC vs. axial position. The profile of the corrugated waveguide is schematically shown at the bottom. The dashed horizontal line shows the zero level.

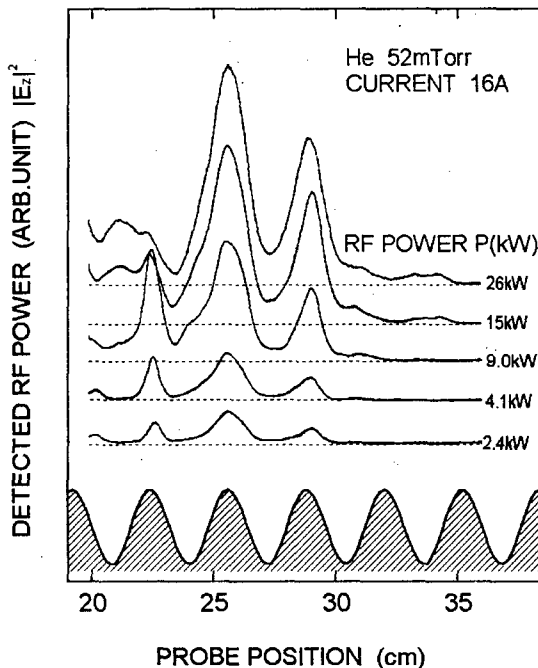


Fig. 3. The detected RF standing waves  $|E_z|^2$  vs. position of wire antenna on the waveguide axis.

The ponderomotive force of standing waves formed by incident and reflected microwaves can result in a caviton, i.e., a local decrease in plasma density. We need to clarify the relationship between RF axial electric field  $|E_z|^2$  and the measured result of ISC shown in Fig. 2. In Fig. 3, the  $|E_z|^2$  versus axial position is shown for  $I=16$  A and for various values of injected microwave power. The Langmuir probe is replaced by an RF thin wire antenna 2mm long along the center axis, and the RF signals are observed using a crystal detector. The dashed horizontal line is the zero level of the detected RF fields. It is confirmed experimentally that there are no  $E_r$  components on the axis, because the axisymmetric  $TM_{01}$  mode is excited in the plasma waveguide.

The maxima of RF standing waves are observed at the positions where  $R(z)$  is minimum, and the  $|E_z|^2$  maxima are never observed at  $R(z)$  maxima. Similar results are observed repeatedly under various conditions

In order to understand the physical mechanism of observed ISC protuberances, Langmuir probe characteristics at various positions are measured. In these results, the electron energy distribution is not exactly Maxwellian after the microwave incidence. Nevertheless, it is concluded that electron temperature is raised uniformly by incident microwaves, whereas the plasma density is depressed nonuniformly in axial positions. Decrease at  $R(z)$  minimum is less than those at other positions. Resultantly, ISC protuberances are observed at particular position:  $R(z)$  minima. We discussed some possibilities to explain the physical reason of the ISC protuberances.

#### 4. References

- [1] A. V. Gaponov-Grekhov and V. L. Granatstein: *High power Microwave Applications* (Artech House, Dedham, 1994).
- [2] J. Benford and J. Swegle: *High power Microwaves* (Artech House, Boston, 1992).
- [3] K. Minami, W. R. Lou, W. W. Destler, R. A. Kehs, V. L. Granatstein and Y. Carmel: *Appl. Phys. Lett.* **53** (1988) 559.
- [4] Y. Carmel, K. Minami, R. A. Kehs, W. W. Destler, V. L. Granatstein, D. Abe and W. Lou: *Phys. Rev. Lett.* **62** (1989) 2389.
- [5] X. Zhai, E. Garate, R. Prohaska and G. Benford: *Appl. Phys. Lett.* **60** (1992) 2332.
- [6] G. Morales and Y. C. Lee: *Phys. Fluids.* **20** (1977) 1135.
- [7] K. Minami, K. Izawa, M. Kaminaga and K. Ishii: *J. Phys. Soc. Japan.* **55** (1986) 1142.
- [8] K. Kato, A. Kunishima and K. Minami: *Jpn. J. Appl. Phys.* **28** (1989) 512.

# A NEW APPROACH TO RF DISCHARGE MODELLING AND THE EVALUATION OF RESULTING DISCHARGE PROPERTIES

Frank Praessler, Volker Hoffmann, Gunnar Suchanek<sup>1</sup>, Klaus Wetzig,

Institute of Solid State and Materials Research Dresden, P. O. B. 27 00 16, D-01171 Dresden, Germany

<sup>1</sup> Dresden University of Technology, IHM, Mommsenstraße 13, D-01062 Dresden, Germany

## Introduction

Glow Discharge-Optical Emission Spectroscopy is a rapid and very suitable quantitative in-depth profile technique for the elemental analysis of laterally homogeneous samples, layers and multilayer systems. The surface of solid and flat samples is sputtered in a low pressure glow discharge ( $p = 100 \dots 1000$  Pa) at a high ion current density ( $j \approx 200$  mA/cm<sup>2</sup>), where the sample is arranged as the cathode opposite to an anode tube (inner  $\varnothing = 2 \dots 8$  mm) in a distance of  $d \approx 0.25$  mm. The sputtered species are excited electronically in the plasma and the deexcitation processes can be used to detect intensities of certain spectral emission lines as a measure of the sample constituents if their concentration is larger than about 10 ppm.

Today, GD-OES is well established in analytical laboratories using the direct current mode (dc), because the measured emission line intensity-time profiles can reliably be converted into concentration-depth profiles of the sample investigated. In the radio frequency (rf) mode, which extends the field of analyzed samples to nonconductive materials, this quantification is more complicated because the unequivocal numerical description of the emission yields of spectral lines for changing discharge parameters requires at least two electrical parameters (voltage / current / power) of the discharge. For nonconducting materials at the backside of the sample, it is only possible to measure directly the power dissipated in the discharge. Therefore, the rf voltage at the nonconducting sample surface must be evaluated using, for instance, an equivalent electrical circuit whose analytical features for GD-OES have been introduced elsewhere [1].

The aim of this presentation is to introduce a new electrical engineering approach to rf discharge modelling and to evaluate the resulting physical properties of the equivalent circuit components.

## Experimental

The discharge volume and the cathode area are much smaller compared to usual plasma processing systems. That results in a relatively high ohmic equivalent resistance of the glow discharge of more than 10 k $\Omega$  and makes the use of commercial matching systems difficult. Using as an rf power supply a free-running generator (dashed rectangle 1 in Fig. 1), it is not necessary to match the discharge impedance to 50  $\Omega$  and this provides a sinusoidal rf voltage output of 200 to 1500 V at a frequency of 4.4 MHz [2].

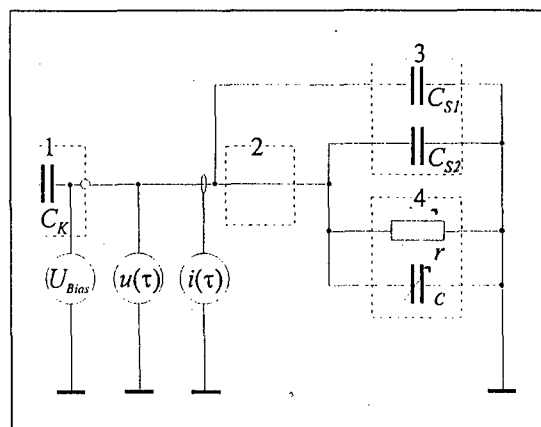


Fig. 1: Circuit diagram including rf generator (1), sample (2), discharge source (3), glow discharge (4) and the electrical measurements.

Voltage and current within the rf period  $T$  and the selfbias voltage are measured directly at the backside of the (conducting) sample (2) using probes connected to a digitizing oscilloscope (Tektronix 11201). The capacities of the source (3) optimized in this connection [2] represent those inside ( $C_{S1}$ ) and outside ( $C_{S2}$ ) the feedthrough. The sum of both capacities amounts to less than 15 pF. The arrangement of the electrodes (an anode tube very close to the cathode plate) results in an asymmetrical rf discharge (4) which in a first approximation can be represented by a parallel circuit of a nonlinear resistance and a nonlinear capacity.

## Results and Discussion

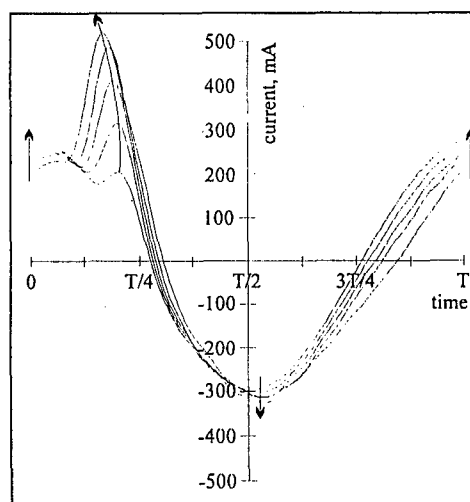


Fig. 2: Rf current measured for increased pressure values (550, 660 .. 990 Pa  $\uparrow$ ) at about 650 V.

Because of the rf current nonlinearity (Fig. 2 measured at an Al-sample), it is straight forward to assume a nonlinear glow discharge impedance which is parallel to the stray capacities of the glow discharge. This impedance can be completely described by a parallel circuit of a capacity, an inductivity and an ohmic resistance, all of them vary within the rf period. Because the linear stray capacities can be measured separately, at least two other assumptions are necessary to calculate all components of the glow discharge [3]:

1. The linear reactive components of the discharge source and the discharge itself can be separated from the measured rf current using the measured trigger time of the rf voltage. The resulting linear current is always slightly higher than the measured linear current through the stray capacities, which means that, it is not necessary to include an inductivity to describe the discharge. Furthermore, the difference between rf and linear reactive current represents the nonlinear components of the rf current through the discharge.
2. The resulting nonlinear current through the discharge can be separated into its active and reactive parts by assuming that in the discharge exist always enough charged particles. Therefore it can be concluded, that the active and the reactive currents are symmetrically to the time scale at  $T/4$  and  $T$ , respectively.

The calculated resistive current curves (Fig. 3) show typical u-i-characteristics of rf discharges and increase with pressure as expected.

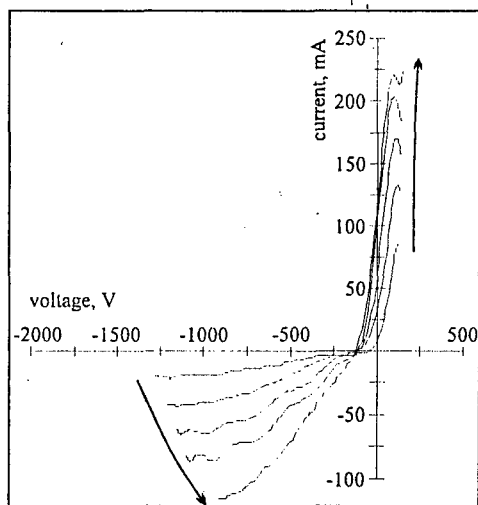


Fig. 3: Nonlinear resistive current through the discharge calculated from the rf current (Fig. 2) for different pressure values.

The calculated nonlinear reactive current through the discharge is in a first approximation due to the varying thickness of rf sheaths. Therefore, the varying sheath thickness during the rf period (Fig. 4) simply can be estimated by assuming rf sheaths in form of a plate capacity with the inner anode area and a dielectric number equal to one. The results are

in excellent agreement with published work [4, 5], but in our calculation only electrical engineering arguments are used without any physical modelling. Despite that, the average value of sheath thickness agrees with measured values [6] and the influence of both, cathodic (1) and anodic (2) dark space, can clearly be seen.

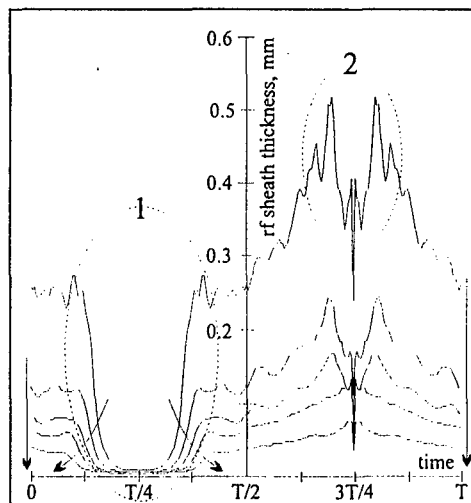


Fig. 4: Varying thickness of rf sheaths calculated of the rf current (Fig. 2). The oscillations in area 1 and 2 are due to the cathodic and anodic dark space, respectively.

Additionally, in the presentation we will discuss the possibilities to separate the discharge in a series circuit of cathodic dark space, plasma and anodic dark space using the discharge asymmetry. The physical properties of the equivalent electrical circuit components will be calculated according to the probe theory and compared to experimental data measured in the rf and dc mode.

- [1] F. Präßler, V. Hoffmann, C. Täschner, K. Wetzig: O7-4 Lecture at the European Winter Conference on Plasma Spectrochemistry, January 12-17, (1997) in Gent (Belgium)
- [2] V. Hoffmann, H.-J. Uhlemann, F. Präßler, K. Wetzig, D. Birus: Fresen. J. Anal. Chem., 355, 7-8 (1996) 826
- [3] F. Präßler: Thesis, Dresden University of Technology, Germany (1996) submitted
- [4] M. Klick: J. Appl. Phys., 79, 7 (1996) 3445
- [5] C. Beneking: J. Appl. Phys., 68 (1990) 4461
- [6] I. R. Videnovic, N. Konjevic, M.M. Kuraica. Spectrochim. Acta, 51B (1996) 1707



## Infrared Absorption Analysis of organosilicon plasmas in a Multipolar Microwave Plasma Reactor

P. Raynaud, C. Marlière, D. Berthomieu, Y. Segui and J. Durand.

GDR 1136 CNRS " Procédés de dépôts de couches minces par plasmas organosiliciés "

Laboratoire des plasmas et des Couches Minces - IMN

BP 3229 - 2 rue de la Houssinière - 44322 NANTES cedex 3

The deposits of  $\text{SiO}_x$  films from organosilicon precursors have been studied since a long time. The most common precursors being the Tetraethylorthosilicate (TEOS) and the Hexamethyldisiloxane (HMDS) in mixture with the oxygen. The deposits are most often obtained in radiofrequency (RF) or microwave plasma reactors. These molecules are complex, by their structure and their number of atoms. If the deposits from silane ( $\text{SiH}_4$ )-oxygen mixture have been widely studied in the plasma as well as in the solid phase, it is not the same case with the deposits obtained from the organosilicons. In particular, very little is known on the dissociation of these complex molecules in the plasma phase as well as on the recombination products or the fragments participating in the deposition. The standard diagnostics in the gaseous phase such as the optical emission spectroscopy (OES) the Mass Spectrometry or the Langmuir probe measurements do not give access directly to the bonds of the molecules. We have opted for an analysis by Fourier Transform Infra-Red (FTIR) spectrometry which permits the identification of the groups of the molecules and of the fragments as well as the radicals. An initial study in a low frequency (LF) plasma [1] permitted to compare the dissociation of HMDS with that of pure TEOS for pressures around 50 mTorr. A similar but more recent study has been made in a microwave reactor at 2.45 GHz and at a pressure of some mTorr [2]. These studies have shown a quasi total dissociation of the molecules even at low powers and the appearance of stable fragments such as the  $\text{CH}_4$  or  $\text{C}_2\text{H}_2$  and  $\text{C}_2\text{H}_4$ . However, the  $\text{SiO}_x$  layers are obtained in organosilicon-oxygen mixtures and not in pure organosilicon plasma. On the other hand, the dissociation products of the TEOS and the HMDS are different and the required powers for the total dissociation of each are also different.

The work presented here is related to the study by FTIR in a Microwave Multipolar Plasma (MMP) excited by a Distributed Electron Cyclotron Resonance (DECOR) of organosilicon monomers, of divers structures and compositions, pure and in mixture with oxygen and at different powers. Ten precursors have been selected, the first one being the HMDS [ $\text{O}(\text{Si}(\text{CH}_3)_3)_2$ ] which is the only one to present a  $\text{SiOSi}$  structure. Thereafter, we have defined two groups of precursors from Tetramethylsilane (TMS). The first group is derived from the TMS [ $\text{Si}(\text{CH}_3)_4$ ] substituting a methyl ( $\text{CH}_3$ ) group by a ( $\text{OC}_2\text{H}_5$ ) group each time. We obtain the trimethylethoxysilane (TMEOS) [ $\text{Si}(\text{OC}_2\text{H}_5)(\text{CH}_3)_3$ ], the dimethyldiethoxysilane (DMDEOS) [ $\text{Si}(\text{OC}_2\text{H}_5)_2(\text{CH}_3)_2$ ], the triethoxy-

methylsilane (TOMS) [ $\text{Si}(\text{OC}_2\text{H}_5)_3(\text{CH}_3)$ ], and finally, the TEOS [ $\text{Si}(\text{OC}_2\text{H}_5)_4$ ]. The second group derives from the TMS by substituting a  $\text{OCH}_3$  group for a methyl group. The precursors obtained are the trimethylmethoxysilane [ $\text{Si}(\text{CH}_3)_3(\text{OCH}_3)$ ] the dimethyldimethoxysilane [ $\text{Si}(\text{CH}_3)_2(\text{OCH}_3)_2$ ] that we do not possess, the methyltrimethoxysilane [ $\text{Si}(\text{CH}_3)(\text{OCH}_3)_3$ ] and finally the tetramethoxysilane (TMOS) [ $\text{Si}(\text{OCH}_3)_4$ ].

The analyses are carried out at a total pressure of 3.2 mT before plasma with the power ranging from 0 to 800 watts. The reactor is a MMP-DECOR reactor with 8 antennas and 8 ferrite magnets. The analysis of the gas and the plasma is made by IR absorption spectrometry, using a FTIR spectrometer Biorad FTS 60A with a resolution of  $0.5\text{ cm}^{-1}$ . The MCT detector permits an analysis of the spectrum in the range  $700\text{--}4000\text{ cm}^{-1}$ . The low pressure (3.2 mTorr) at which the discharge takes place imposes an increase of the optical path of the IR beam in the plasma in order to increase the detection sensitivity around 1 ppb or  $10^{-3}$  mTorr. This is obtained thanks to a White cell in which the beam traverses the optical path 44 times, i.e., around 40 m. A spectrum is acquired by doing the average of 64 scans. The monomer gas and oxygen feeds are separated. The experimental setup is shown on figure 1.

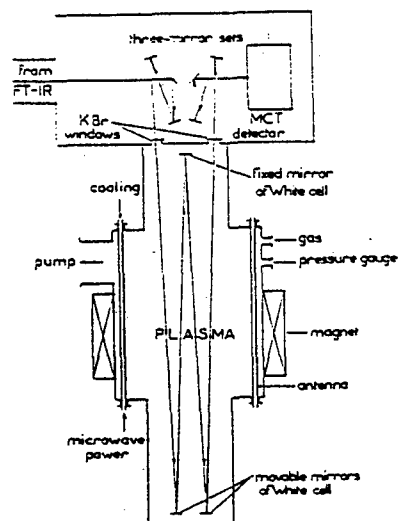


Figure 1 : Experimental setup

The analysis of the spectra of precursors in the gaseous phase can reveal the structural differences. Indeed, the compounds TEOS of the first group, TMS and TMOS of the second group, for example, give very different spectra in the  $700\text{--}1600\text{ cm}^{-1}$  range (fig.2).

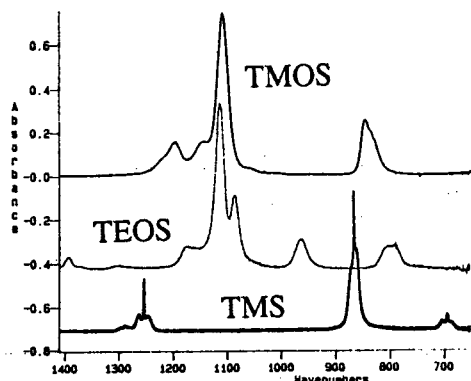


Figure 2 : IR spectra of TEOS, TMS and TMOS (gas phase) in the range  $700\text{--}1400\text{ cm}^{-1}$ . Pressure = 3,2 mTorr.

The CO structure present in the TEOS and the TMOS appears at  $1114.8\text{ cm}^{-1}$  and  $1110.1\text{ cm}^{-1}$  respectively (CO asymmetrical stretching) which is not the case for the TMS which does not possess any oxygen atom. The  $\text{SiO}_4$  asymmetrical stretching bond appears at  $792.9\text{ cm}^{-1}$  for the TEOS [3], whereas for TMOS it appears at  $847.9\text{ cm}^{-1}$ . This is due to the environmental difference around the  $\text{SiO}_4$  group in the two molecules. In the TEOS, the oxygen is bonded with  $\text{C}_2\text{H}_5$  while in TMOS it is only bonded with  $\text{CH}_3$ . As such, the vibration appears at a higher wavenumber for the TMOS. The  $\text{CH}_3$  bonded to Si produces peaks in the range  $1245\text{--}1290\text{ cm}^{-1}$  for the TMS. SiC bond not being present in the molecules of TEOS and TMOS, the above peaks are not detected for them. In this way, each precursor is well identified.

IR spectral analysis of the plasma phase of pure organosilicon compounds brings into evidence two important phenomena : the first is a very big decrease of the characteristic peaks (Fig.3) of the organosilicon molecules ( $\text{SiOSi}$ , CO, SiC or still CH)

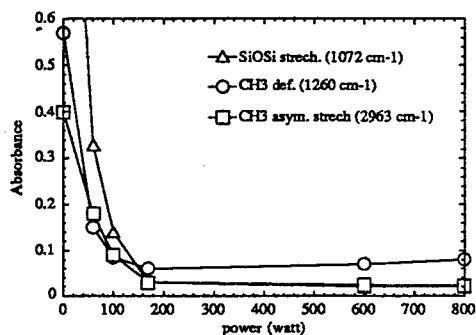


Figure 3 : Absorbance vs. microwave power for different absorption peaks of HMDS molecule.

The second phenomenon is the appearance of the new peaks related to the compounds such as  $\text{CH}_4$ ,  $\text{C}_2\text{H}_2$ ,  $\text{C}_2\text{H}_4$ , CO,  $\text{CO}_2$ . The characteristic peaks of the molecule are no longer detectable beyond 100 watts, which seems to prove that it has been totally dissociated. Moreover, the new peaks that appear from 50 watts are no longer detected above 100 watts. These remarks are valid for the 2 organosilicon groups analysed as well as for the TMS and the HMDS. However, it should be noted that the HMDS is dissociated with more difficulty than the other groups. This reflects the stronger chemical bonding in HMDS. The new peaks are characteristic of the organic molecules and are detected for all the precursors dissociated :  $\text{CH}_4$  ( $2960\text{--}3940\text{ cm}^{-1}$ ),  $\text{C}_2\text{H}_2$  ( $729\text{ cm}^{-1}$ ),  $\text{C}_2\text{H}_4$  ( $949\text{ cm}^{-1}$ ) [4]. On the contrary, free CO is not detected in either TMS or HMDS plasma, this group not being present in these molecules. It is detected in all other organosilicon groups. When the CO bond is present in the organosilicon molecule, CO and free  $\text{CO}_2$  are detected in the plasma phase, which is not the case with TMS and HMDS. A new structure centered at  $2125\text{ cm}^{-1}$  appears only for the HMDS plasma, while a new PQR structure ( $1700\text{--}1800\text{ cm}^{-1}$ ) is detected for all the groups except HMDS and TMS.

The 50 % oxygen mixture does not produce significant differences in the plasma phase spectra compared to the spectra recorded for pure organosilicon plasma. But now, all the spectra (including HMDS and TMS) show the characteristic structures of CO and free  $\text{CO}_2$  coming essentially from the etching and the recombinations on the wall. It should also be noted that in every case there is a very high increase of pressure in the plasma phase which confirms the very strong dissociation.

We can conclude that the DECR plasma induces, therefore, a very strong dissociation of the organosilicon compounds and the deposit is realized from simple compounds originating from this dissociation. These results confirm those obtained by Mass Spectrometry analysis in the same reactor [5]. This study has revealed the equivalent organosilicon groups in the plasma phase in terms of their structures, their dissociation modes and new species detected.

## References

- [1] P. Raynaud, Y. Segui, M. Latreche and R. Delsol Proceedings of the 11th Int.Symp.Plasma Chem. 4, (1993) 1487.
- [2] P. Raynaud, Y. Segui, G.Balmer, A. Boulanger and R.R. Burke, to be published.
- [3] M.G.M. Van der Vis, R.J.M. Konigs, A.Oskam and T.L. Snoeck, J.Mol.Struct. 274 (1992) 47.
- [4] T. Mitomo, T. Ohta, E. Kondoh and K.Ohtsuka, J.Appl.Phys. 70 (1991) 4532.
- [5] M. Latreche, Y. Segui, R. Delsol, and P. Raynaud, Proceedings of the 11th Int.Symp.Plasma Chem. 4, (1993) 1284.

# Kinetics of F atoms and CF<sub>x</sub> radicals in a pulsed CF<sub>4</sub> microwave plasma

W. Schwarzenbach, J. Derouard, N. Sadeghi

Laboratoire de Spectrométrie Physique, UMR CNRS 5588  
Université Joseph Fourier-Grenoble I, B. P. 87, F-38402 Saint Martin d'Hères, France

Appearance mass spectrometry has been applied to detect neutral radicals present downstream of a CF<sub>4</sub> microwave plasma. In a pulsed discharge, time resolved measurement has allowed to study the kinetics of these radicals in the afterglow. From the decay rate of their concentration, the sticking coefficient of these species on different surfaces was determined. The effect of the discharge parameters and of the nature of the surfaces introduced in the plasma chamber (aluminium, hexatriacontane polymer or silicon) were investigated. The influence of the UV and/or ions generated by the plasma in the reaction chamber was also investigated.

## 1. Introduction

CF<sub>4</sub> plasmas have a number of applications in the field of the etching of silicon for the microelectronics, or of the modification of polymer surfaces. Due to the complexity of the chemical processes occurring in the discharge, the knowledge of the kinetics of the radicals present in the plasma is essential. In particular, F atoms are considered as an important reactive agent. However, contrary to CF and CF<sub>2</sub>, the observation of F atoms and CF<sub>3</sub> radicals cannot be carried out by laser-induced fluorescence (LIF) [1].

In this work, the appearance mass spectrometry technique, first presented by Robertson *et al* [2], was applied to detect radicals produced by the plasma, with emphasis on F atoms and CF<sub>x</sub> radicals. Their kinetics were studied in the afterglow of a modulated plasma and related to the reactivity of the surfaces present in the discharge chamber.

## 2. Experimental apparatus

The flowing afterglow reactor used in our experiments is schematically shown in Fig. 1 and was presented extensively in a recent paper [3]. The 2.45 GHz microwave plasma was generated (with power from 15 to 75 W) in a pyrex tube open downstream to a reaction chamber where a sample holder can be introduced. A low CF<sub>4</sub> flow rate (1.25 to 5 sccm) was used and the pressure was adjusted between 15 and 100 mTorr by a throttle valve separating the reactor from a mechanical pump. To study the influence of the charged particles and the VUV radiation coming from the plasma on the surfaces reactivity, a metallic grid can be installed at the end of the discharge tube. It prevents the plasma to penetrate into the reaction chamber.

The detection of neutral particles was achieved by a Hiden HAL-EQP 500 quadrupole mass spectrometer. Differentially pumped, it collects the neutral particles from the reactor chamber via a

150 µm extraction orifice located in front of the discharge tube. The electron ionization energy was varied between 10 and 70 eV. For the time-resolved experiments, the microwave discharge was pulsed (plasma on 30 ms, off 98 ms) and the counting pulses provided by the mass spectrometer were supplied to a multichannel counter [4] to provide signal acquisition resolved in time.

To study the radicals kinetics in the presence of different materials, a sample holder can be introduced into the reaction chamber, in front of the discharge tube. Experiments were carried out with samples of bare aluminium, silicon or HTC film (hexatriacontane CH<sub>3</sub>-(CH<sub>2</sub>)<sub>34</sub>-CH<sub>3</sub>), a model molecule for high density polyethylene.

## 3. Kinetics of the radicals

In a pulsed plasma, the kinetics of the species can be observed from the evolution of the mass spectrometer signal along a modulation period. In the case of fluorine atoms (*m/e* = 19) the ionizing

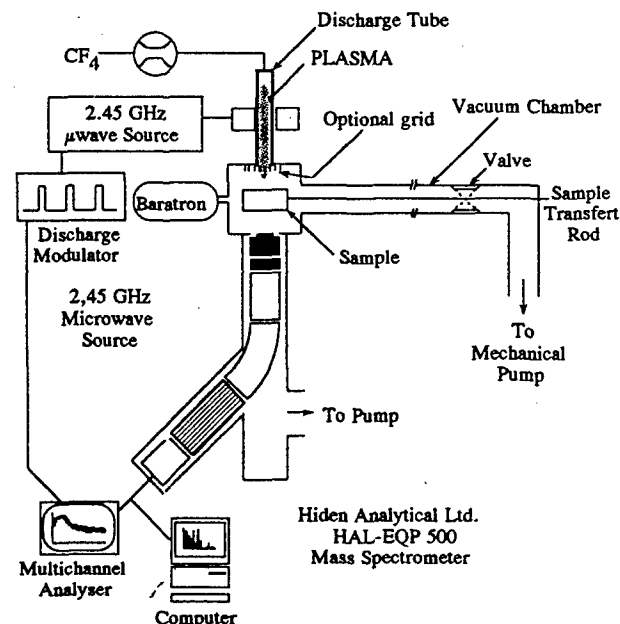


Fig. 1. Schematic view of the experimental set up

electron energy was set to 27 eV, in order to maximize the detected signal coming from the plasma itself (and containing the contribution from the F atoms) in front of the signal already present with the discharge "off" and coming from the dissociative ionization of CF<sub>4</sub> molecules in the ionization chamber of the mass spectrometer [5]. Like Hikosaka *et al* [6, 7] and Ito *et al* [8], the method has also been applied in the case of CF<sub>x</sub> radicals, where the ionizing electron energies were set close to the ionization potentials, at 18 and 15 eV for CF<sub>2</sub> and CF<sub>3</sub> respectively. Typical decay curves for these radicals are shown on Fig. 2.

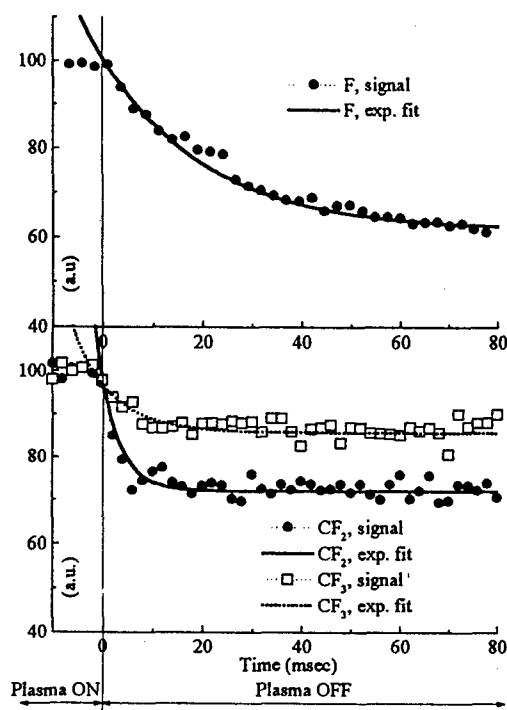


Fig. 2 Mass spectrometer signal and corresponding exponential fit for F, CF<sub>2</sub> and CF<sub>3</sub> radicals in the afterglow of a 15 mTorr, 35 W CF<sub>4</sub> plasma.

The time variation of the mass spectrometer signal of the radical X in the 98 msec afterglow can be described by the expression (plasma off at  $t = 0$ ):

$$I_X = [X_0] e^{-\Gamma t} + [A] \quad (1)$$

and our interest in the following will be focused on the decay rate  $\Gamma$ , which, in the case of Fig. 2, is equal to 45, 250 and 130 s<sup>-1</sup> for F, CF<sub>2</sub> and CF<sub>3</sub> respectively.

In the results presented on Fig. 2 the non-modulated part [A], whose relative importance compared to the modulated part [X<sub>0</sub>] depends on experimental conditions, can be attributed to the dissociative ionization processes occurring in the ionization chamber of the mass spectrometer, in addition to the background signal already present without plasma [5].

#### 4. Sticking coefficient of the radicals

In our low pressure conditions, the comparison between the decay rate  $\Gamma$  measured for F atoms and CF<sub>2</sub> and CF<sub>3</sub> radicals shows that the gas phase reactions are negligible in the removal of the radicals during the afterglow, as well as the influence of the gas removal by the pumping system. Consequently the decay rate  $\Gamma$  is attributed to the surface reactions. Following the analysis of Chantry [9],  $\Gamma$  can be related to the sticking coefficient  $\alpha$  of the radicals by:

$$\frac{1}{\Gamma} = \frac{\Lambda_0^2 p}{D_0} + \frac{V}{A} \frac{2(2 - \alpha)}{\alpha v_{th}} \quad (2)$$

where the first term represents the diffusion and the second one the surface reactions.

An application of this method to the results presented in Fig. 2 gives the sticking coefficient shown in Table 1, which are comparable to previous published results [6, 7].

Radical	$\Gamma$ [s <sup>-1</sup> ]	$\alpha$ [%]
F	45	0.32
CF <sub>2</sub>	250	3.02
CF <sub>3</sub>	130	1.79

Table 1: Sticking coefficient for F, CF<sub>2</sub> and CF<sub>3</sub> radicals on the discharge chamber walls of a 15 mTorr, 35 W CF<sub>4</sub> plasma.

Experiments described above are extended to study the influence (on the kinetics of the radicals and) on the surface reactivity of the discharge parameters, of the substrates introduced in the chamber, and of the UV and/or ions when the plasma penetrates into the reaction chamber.

#### References

- [1] A. Tserepi, J. Derouard, N. Sadeghi, J.-P. Booth: *J. Appl. Phys.* **81** (1997)
- [2] R. Robertson, D. Hils, H. Chatam, A. Gallager: *Appl. Phys. Lett.* **43** (1983) 544
- [3] A. Tserepi, W. Schwarzenbach, J. Derouard, N. Sadeghi: submitted in *J. Vac. Sci. Technol. B*
- [4] B. Pelissier, N. Sadeghi: *Rev. Sci. Instrum.* **67** (1996) 3405
- [5] W. Schwarzenbach, A. Tserepi, J. Derouard, N. Sadeghi: submitted in *Jpn. J. Appl. Phys.*
- [6] Y. Hikosaka, H. Toyoda, H. Sugai: *Jpn. J. Appl. Phys.* **32** (1993) L353
- [7] Y. Hikosaka, H. Sugai: *Jpn. J. Appl. Phys.* **32** (1993) 3040
- [8] S. Ito, K. Nakamura, H. Sugai: *Jpn. J. Appl. Phys.* **33** (1994) L1261
- [9] P. J. Chantry: *J. Appl. Phys.* **62** (1987) 1141

# Excitation mechanisms and ion kinetics in a 450 kHz capacitively coupled argon discharge

M. van de Grift, N. Sadeghi\*, T. Hbid, G.M.W. Kroesen and F.J. de Hoog  
Eindhoven University of Technology, P.O. Box 513, 5600 MB Eindhoven, The Netherlands

\*Laboratoire de Spectrométrie Physique (CNRS UMR 5588), Université Joseph Fourier-Grenoble I,  
BP 87, 38402 St. Martin d'Hères cedex, France

## 1. Introduction

Low pressure RF plasmas are widely used in the microelectronics industry for the production of integrated circuits. External conditions, like pressure, power, geometry and driving frequency determine the properties of the plasma and thus its practical use in various applications. The influence of the applied RF frequency has been studied by several authors [1-7]. When the driving frequency is in the order, or lower than the ion transit frequency across the sheath ( $\sim 1$  MHz), the discharge is then sustained by ionization due to the secondary electrons from the electrodes.

We applied a 450 kHz RF voltage to a capacitively coupled parallel plate plasma reactor filled with 158 mTorr argon. Time resolved emission spectroscopy is used to study the excitation mechanism. The movement of the ions near the sheath edge is investigated with Doppler-shifted laser induced fluorescence (DSLIF) [8]. Langmuir probe and optical absorption spectroscopy are used to determine the ion

density and the electron and neutral temperatures. The experimental results are compared with a 1D fluid model which includes both bulk and beam electrons.

## 2. Experimental Setup

The reactor consists of two parallel stainless steel cylindrical electrodes (E) with radii of 55 mm (see figure 1). All is surrounded by a cylindrical wall connected to the grounded electrode. The distance between the electrodes is 42 mm. Both electrodes contain slits to allow a laser beam to cross the reactor.

The detection system (L-MC-PM-PS) transforms the photons from the plasma to TTL pulses. A previously described pulse counting system, the CDP [9], stores these pulses with respect to the period of the applied RF voltage to obtain a time resolved emission or fluorescence signal.

DSLIF [8] is used to measure the velocity distribution function ( $vdf$ ) of argon metastable ions ( $Ar^{+*}$ ). The laser beam of a cw dye laser (DL) crosses the reactor. When the wavelength is scanned around the 611.492 nm absorption frequency of the metastable argon ions ( $^2G_{9/2} \rightarrow ^2F_{7/2}$ ), the 461 nm ( $^2F_{7/2} \rightarrow ^2D_{5/2}$ ) fluorescence signal intensity gives the velocity distribution function of the ( $Ar^{+*}$ ) ions.

A Langmuir double probe (LDP) can be inserted into the reactor. The electron density and temperature are derived from the analyzed probe characteristics. The probe can be moved between the electrodes to obtain the spatial dependence of the parameters.

A tunable diode laser beam ( $\lambda=772.4$  nm) can cross the reactor radially. From the Gaussian shaped absorption profile we obtain the density of the neutral metastable atoms and the gas temperature.

## 3. Model

We used a self consistent 1D fluid model to describe the excitation and transport of the particles in the discharge. The electric field and particle densities are derived simultaneously. We consider 3 kinds of charged particles (beam and bulk electrons and positive ions), and argon atoms in the ground, metastable and excited states. An electron from the beam (fast) becomes bulk electron (slow) when its energy is lower than the ionization threshold energy. Our model is similar to the one described previously by others [10,11].

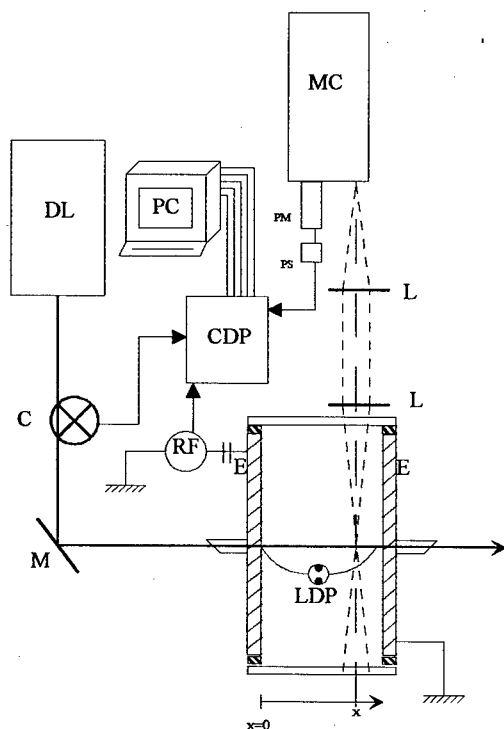
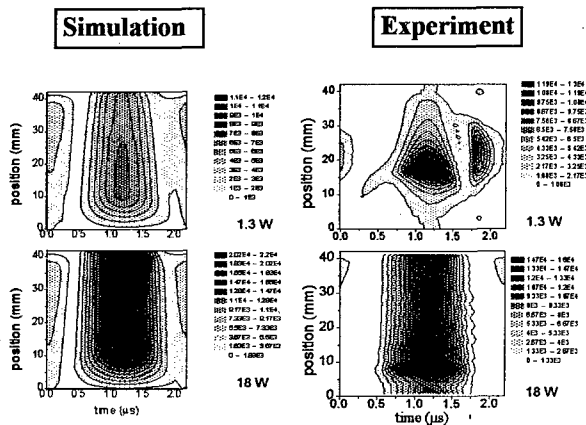


Figure 1 : Setup of the 450 kHz plasma reactor

We follow the space-time evolution of two excited levels of argon ( $2p_1$ ) and ( $2p_6$ ) and compare them with our experimental emission results. The source term in the model for the excited atoms arises from the excitation of ground and metastable states by electrons. The effect of metastable atoms in ionization is included in the model following the reaction scheme given by Tochikubo [12].

#### 4. Results

With the Langmuir double probe, temperatures of the bulk electrons of 1.1 eV are measured for 7.7 and 18 W dissipated RF power. The electron densities are  $0.4 \cdot 10^{16}$  and  $1.3 \cdot 10^{16} \text{ m}^{-3}$  respectively. Figure 2 shows the spatiotemporal emission of the 750.4 nm argon line ( $2p_1-1s_2$ ) at 1.3 and 18 Watts. The powered electrode is at position zero. The measurements are compared with the results of the 1D fluid model. A strong time



**Figure 2 : model results and emission measurements of the  $2p_1$  level**

dependence is observed due to the modulation of the beam electrons. These electrons are able to excite or ionize more than one atom during their trajectory from the cathode to the anode. The larger grounded surface in the plasma creates a higher negative bias voltage at the powered electrode than at the grounded electrode. This results in a lower energy of the beam electrons from the grounded electrode, during its cathodic half period. The measurements and the model clearly show this effect in terms of a lower intensity of the 750.4 nm line emission signal during the cathodic half period of the grounded electrode. The peak in the emission at 1.3 W around 2  $\mu\text{s}$  is an artifact from a micro-discharge localized inside the metal tube connecting the reactor to the pumping system. For the 763.5 nm line, originating from the  $2p_6$  atomic level, however, a non-zero background emission is observed. In fact, the  $2p_6$  level can be efficaciously populated from metastable states, whose population are not modulated during the RF cycle, by the bulk electrons.

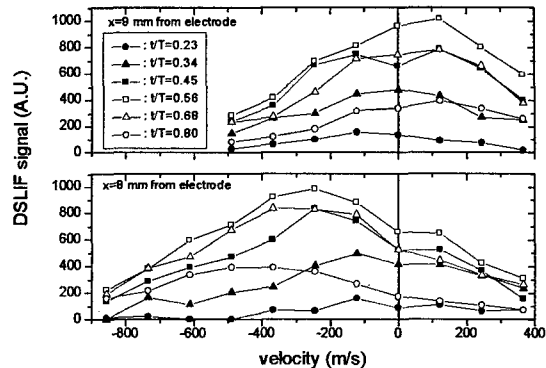


**Figure 3 : DSLIF measurement at two distances from the electrode for different phases ( $t/T$ ) in the RF period.**

The time resolved velocity distribution of the ( $\text{Ar}^{+*}$ ) ions is shown in figure 3. At 9 mm from the electrode, the ions are always inside the negative glow of the RF electrode and their mean velocity is zero. From the profile of their  $vdf$  we can deduce an ion temperature of about 400 K. At  $x = 8$  mm, however, the ions enter the sheath of the RF electrode during the most cathodic period of this later and are accelerated towards this electrode. It can also be seen clearly that the ions have a higher average velocity, particularly at  $t/T=0.8$ , when the electric field is the strongest at  $x = 8$  mm. Closer to the electrode the ion speed has increased, resulting in an ion density lower than the detection limit.

#### 5. References

- [1] K. Köhler, D.E. Horne, and J.W. Coburn, *J. Appl. Phys.* **58**, 3350 (1985)
- [2] R.H. Bruce, *J. Appl. Phys.* **52**, 7064 (1981)
- [3] D.L. Flamm and V.M. Donnelly, *J. Appl. Phys.* **59**, 1052 (1986).
- [4] V.M. Donnelly, D.L. Flamm, and R.H. Bruce, *J. Appl. Phys.* **58**, 2135 (1985)
- [5] R.A. Gottcho, G.R. Scheller, D. Stoneback, and T. Intrator, *J. Appl. Phys.* **66**, 492 (1989)
- [6] B.N. Ganguly and A. Garscadden, *IEEE transactions on plasma science* **24**, 115 (1996)
- [7] S. Kakuta, T. Makabe and F. Tochikubo, *J. Appl. Phys.* **74**, 4907 (1993)
- [8] N. Sadeghi, M. van de Grift, D. Vender, G.M.W. Kroesen, and F.J. de Hoog, *Appl. Phys. Lett.* **70**, 835 (1997)
- [9] B. Pelissier and N. Sadeghi, *Rev. Sci. Instrum.* **67**, 3405 (1996)
- [10] Ph. Belenguer and J. P. Boeuf, *Phys. Rev. A* **41**, 4447 (1990)
- [11] M. Surendra, D. B. Graves, and G.M. Jellum, *Phys. Rev. A* **41**, 1112 (1990)
- [12] F. Tochikubo, Z. Petrovic, S. Kakuta, N. Nakano and T. Makabe, *Jpn. J. Appl. Phys.* **33**, 4271 (1994)

## DYNAMICS OF THE FREELY LOCALIZED MICROWAVE DISCHARGE IN AIR

A.A.Kuzovnikov, V.M.Shibkov, L.V.Shibkova

Department of Physics, Moscow State University, 119899, Moscow, Russia

D.P.Singh, M.Vaselli

Istituto di Fisica Atomica e Molecolare. Via del Giardino, 7-56127, Pisa, Italy

Under effect of a powerful focused beam of electromagnetic waves of a microwave range, provided that the intensity of a electrical field exceeds threshold value, in focal area of a discharge chamber occurs a gas breakdown. At a microwave discharge in a beam with a reasonably small corner of convergence a wave of breakdown quickly leaves focus towards to a flow of energy. For many practical application it is required to localize the microwave discharge in a fixed place of the space. For it we offered the method of programmable pulse. The main point of a given method consists that the breakdown of a gas is executed by a powerful short pulse, during which forward front of the discharge has no time to leave focal zone, and the maintenance of a plasma is executed by the second pulse of small amplitude, which is not capable to stimulate of a gas breakdown independently, but if the breakdown is already carried out, the energy of a pumping pulse is sufficient for maintenance of the discharge in a fixed place of the free space for a long time.

In this work four types of the initiated microwave discharge in air atmospheric pressure were experimentally investigated: nonequilibrium running microwave discharge, created in a monopulse regime with a duration up to 1 ms, the energy flow density  $S=10^4\text{-}10^5$  W/cm<sup>2</sup>; localized microwave discharge, formed in programmable pulse regime with parameters:

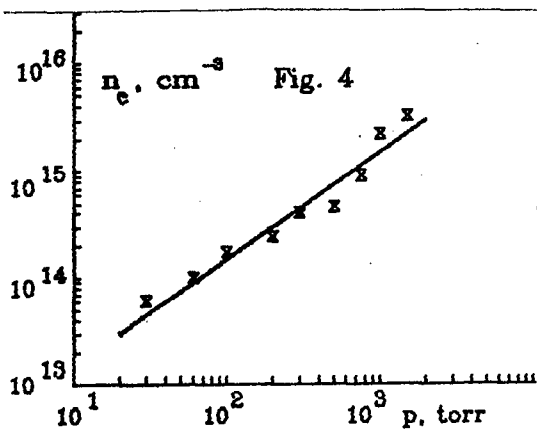
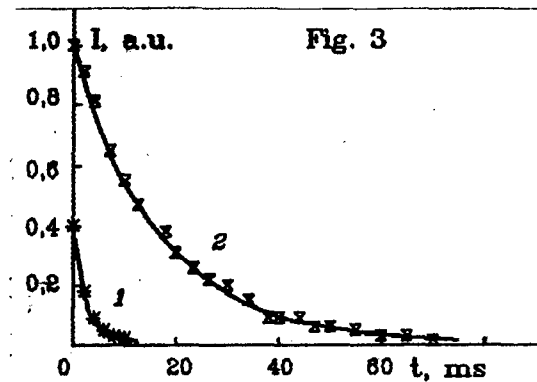
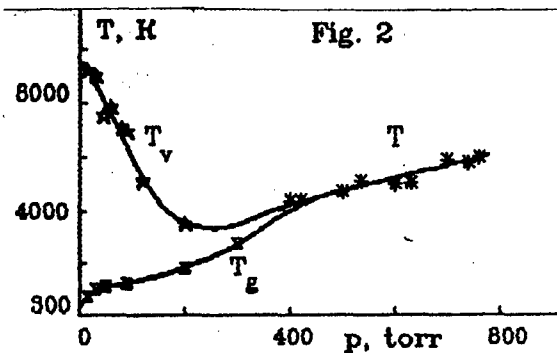
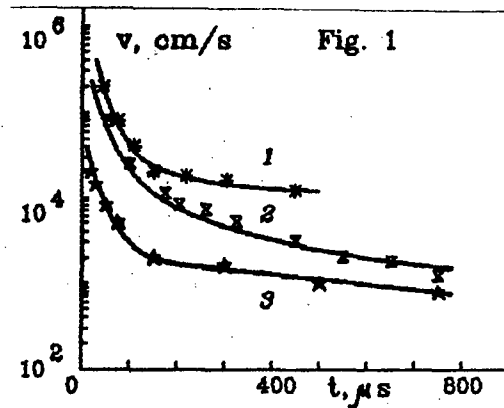
the breakdown pulse  $\tau_1 = 2\text{-}50$   $\mu$ s,  $S_1 = 10^4$  W/cm<sup>2</sup>, the pumping pulse  $\tau_2 = 1$  ms,  $S_2 = 10^3$  W/cm<sup>2</sup>; quasiequilibrium microwave discharge in a kind of uniformly radiated plasma formation, created at atmospheric pressure in a monopulse regime  $\tau \leq 10$  s and  $S=10^2\text{-}10^3$  W/cm<sup>2</sup>; initiated microwave discharge in a kind of a separate plasma channel at  $\tau = 1\text{-}20$   $\mu$ s and  $S = 10^4$  W/cm<sup>2</sup>.

The velocity of the running microwave discharge spreading reaches  $10^6$  cm/s in the beginning and reduces to  $10^4$  cm/s in the end of pulse, (Fig.1(1)). As the experiments were conducted in converging beam the discharge at the late stages of its existence consistently comes in places where  $S$  continuously decreases and accordingly velocity of the discharge spreading changes. The localized microwave discharge represents a example of non self maintained discharge. The electric field freely penetrates into a plasma. The discharge illuminates in all time of a pumping pulse on all area, engaged by plasma, unlike the running discharge, where only the thin plasma layer illuminates. The velocity of localized discharge decreases up to  $10^3$  cm/s to the end of a pulse (Fig.1(2)). On Fig. 1(3) the velocity of movement of the equilibrium discharge is indicated at various microwave pulse duration. The equilibrium discharge created in monopulse regime is

located in the space too, but in difference from of the programmable discharge at atmospheric pressure it represents homogeneous illuminated plasma formation during whole a time of existence. The velocity of this discharge reduces up to 5 cm/s at  $S=2 \cdot 10^2$  W/cm<sup>2</sup>. On Fig. 2 vibrational and gas temperatures in dependence on the pressure of air in a plasma of the localized microwave discharge are showed. One can see, that at low pressure strong vibrationally-translational nonequilibrium  $T_v/T_g \approx 10$  is observed, with growth of pressure  $T_v$  decreases, and  $T_g$  increases, so at  $p > 400$  torr  $T_v \approx T_g$ . If microwaves energy puts off in this condition the radiation of a plasma proceeds yet during several milliseconds in a visible range and order 100 ms in infrared of the area of a spectrum (Fig.3(2)), in difference from the non-localized microwave discharge (Fig.3(1)). The initiator, used in work, has allowed also to receive the initiated microwave discharge in a kind of a separate plasma channel. The channel is formed for times 1-2  $\mu$ s, the velocity of its regrow reaches  $(0,5-1) \cdot 10^6$  cm/s. The electron density in channel of microwave discharge is indicated in double logarithmic scale on fig.4 (points -experiment, line -calculation [2]). At the atmospheric pressure  $n_e = (1-2) \cdot 10^{15}$  cm<sup>-3</sup>,  $T_e = 0,7-1,0$  eV. Experiment and calculation give dependence of the electron density from pressure close to linear and well agree with each other.

#### References

1. Zarin A.S., Kuzovnikov A.A., Shibkov V.M. Freely localized microwave discharge in air. -M.: Oil & Gas, 1996, 204p (Rus).
2. Babaeva N.Y., Mnatsakanyan A.X., Naidis G.V. - Fizika Plazmi, 1992, v.18, N8, p.1055-1063 (Rus).





# Surface wave sustained discharges in pulsed regime operation

D. Grozev, K. Kirov, K. Makasheva and A. Shivarova  
Faculty of Physics, Sofia University, BG-1164 Sofia, Bulgaria

## 1. Introduction

Besides some advantages with respect to applications, the pulsed discharges giving results on the dynamics of the gas breakdown, provide information necessary for better understanding of the discharge production. The experimental study presented here contributes to the research started [1-4] on pulsed mode operation of surface wave (SW) sustained discharges.

## 2. Experimental arrangements

A pulsed discharge is produced (Fig.1) by using a surfatron device [5]. The parameters of the applied

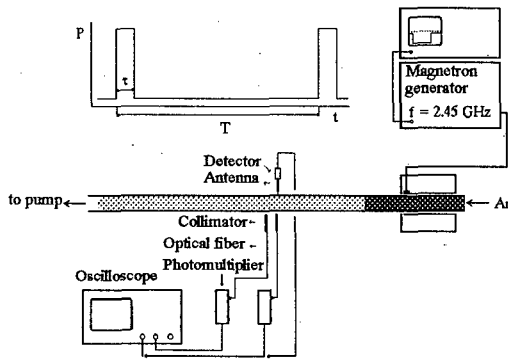


Fig. 1. Experimental arrangements

signal are: rectangular pulses with carrier wave frequency of  $f = 2.45$  GHz, pulse width  $\tau_p = (0.8-2)$  ms, repetition frequency of 10 Hz, peak power  $P_0 = (80-360)$  W. The discharge is in Ar at pressure  $p = (0.1-10)$  Torr and flowing gas.

The microwave power  $P$  of the SW electric field sustaining the discharge and the total light emission of the produced plasma considered as giving information about its density  $n$  are the registered signals. They are picked by a microwave antenna and by photomultipliers through collimators.

## 3. Results

### 3.1 Shape, energy and rise time of the pulses

The microwave pulses and the pulses of the plasma density are measured simultaneously at the same axial ( $z$ ) positions. Depending on  $p$  and  $P_0$ , the shape of the pulses changes in a different manner along the discharge length. From the measurements of the microwave pulses, their total energy  $W(z)$  is obtained. The rise time  $\tau_n$  of the pulses of the plasma density, i.e.

the time interval of reaching the stationary state, is also determined.

At low  $p$  and comparatively high  $P_0$ , the pulses keep their rectangular shape over a long distance (Fig.2).

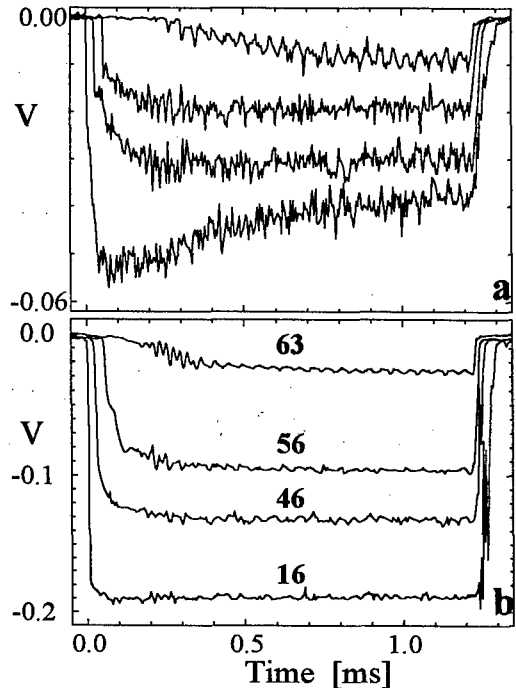


Fig. 2. Pulses of the plasma density (a) and of the electric field power (b) at different positions  $z$  in cm (denoted in (b)) read from the gap of the surfatron:  $p = 0.5$  Torr,  $P_0 = 310$  W

The leading edge is sharp. Starting with a value of  $3 \mu\text{s}$  in the beginning of the discharge,  $\tau_n$  is almost constant over a long distance. With increasing  $z$ , the amplitude of the pulses decreases and their width slightly diminishes from the side of the leading edge. The strong changes are in the very end of the column (Fig.1) where  $W$  drops fast (Fig.3) and  $\tau_n$  increases (Fig.4). The delay in the response of  $n$  (Fig.2) to  $P$  could be associated with a threshold field intensity [6] necessary to be reached for creating a discharge.

At higher  $p$  (and the same—comparatively high— $P_0$ ), the pulse parameters change quite more drastically (Fig.5). Changes to a triangular shape are observed towards the discharge end where only that part of the pulses which is at the side of their trailing edge is kept. The leading edge of the pulses is inclined even at the beginning of the discharge.  $\tau_n$  there is about  $9 \mu\text{s}$  and strongly increases.  $W(z)$  decreases exponentially fast (Fig.3). The difference in the  $W(z)/W_0$  -dependencies at low and high pressures is an indication that the discharge production is at different gas-discharge

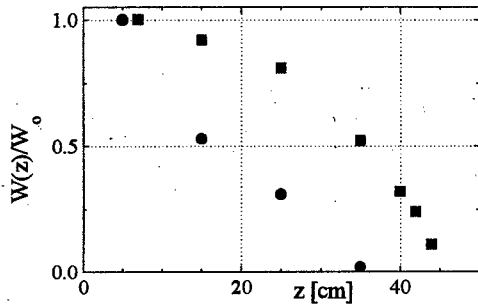


Fig. 3.  $z$ -variation of  $W$  (normalized to the energy  $W_0$  of the applied pulse) at low (■) and high (●) gas pressures: cases, corresponding respectively to those in Figs. 2 and 5.

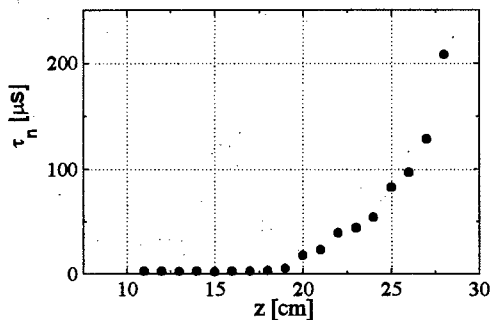


Fig. 4.  $z$ -variation of  $\tau_n$  ( $p = 0.3$  Torr,  $P_0 = 100$  W).

regimes [7]: different contributions of diffusion and recombination to the charged particle losses.

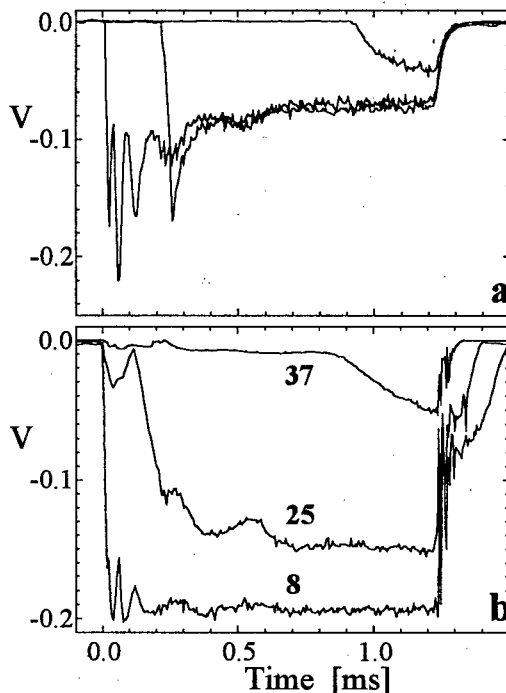


Fig. 5. The same as in Fig. 2 but at  $p = 9$  Torr.

### 3.2 Ionization front velocity

$V_f$  decreases along the discharge length (Figs. 6 and 7).

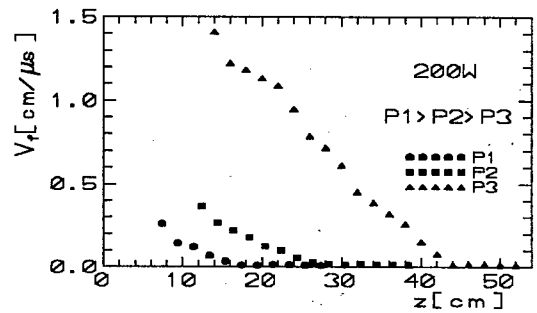


Fig. 6.  $z$ -variation of  $V_f$  at different  $p$ -values in the limits of  $p = (0.4-5)$  Torr;  $P_0 = 200$  W.

At  $p \geq 0.3$  Torr,  $V_f$  is smaller (Fig. 6) at higher  $p$ . An increase of  $P_0$  leads (Fig. 7) to an increase of  $V_f$ .

The measurements show that there is an optimum—for discharge production—value of  $p$  at which  $L$  is large,  $\tau_n$  is small and  $V_f$  is high. Its value ( $p_{opt} \approx 0.3$  Torr) is in the range of discharge maintenance in a diffusion regime. Existence of  $p_{opt}$  can be associated with the minimum of the maintenance field intensity which appears [6], in a diffusion regime, at the transition from predomination of the nonlinear process of stepwise ionization to that of recombination.

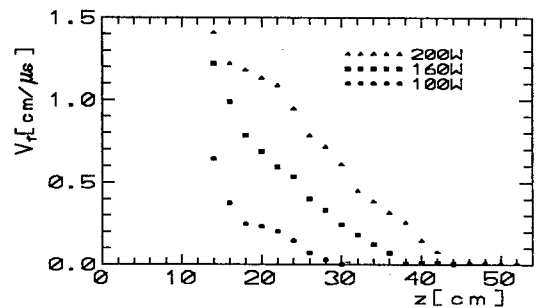


Fig. 7.  $z$ -variation of  $V_f$  at different  $P_0$ -values;  $p = 0.4$  Torr.

In conclusion, the obtained results cover different conditions of maintenance of pulsed SW sustained discharges. Specificities in their behaviour showing development of modulation instability on the stationary level of the pulses and separation of the leading edge of the pulses are discussed in Ref. [8].

**Acknowledgements.** This work was supported by EC-project n0 CIPA-CT-93-0101 and NFSR-project n0 F-409.

### References

- [1] E. Bloyet *et al.*: *Phys. Lett. A*, **83** (1981) 391
- [2] M. Llamas *et al.*: *J. Phys. D: Appl. Phys.*, **18** (1985) 2169
- [3] A. Gamero *et al.*: *J. Appl. Phys.*, **65** (1989) 2189
- [4] A. Böhle *et al.*: *J. Phys. D: Appl. Phys.*, **29** (1996) 369
- [5] M. Moisan *et al.*: *Phys. Lett. A* **50** (1974) 125
- [6] Yu. M. Aliev *et al.*: *Phys. Plasmas* **3** (1996) 3162
- [7] Yu. M. Aliev *et al.*: *Plasma Sources Sci. Technol.* **2** (1993) 145
- [8] D. Grozev *et al.*: *IEEE Trans. Plasma Sci.* (1996) in press.

# Gas-discharge maintenance by guided mode propagation in strong magnetic field

A. Shivarova and Kh. Tarnev\*

Faculty of Physics, Sofia University, BG-1164 Sofia, Bulgaria

\*High Military School "Vassil Levski," BG-5007 Veliko Tarnovo, Bulgaria

## 1. Introduction

Self-consistent longitudinal structure of high-frequency gas discharges maintained in a diffusion controlled regime by Trivelpiece-Gould mode propagation in strong external magnetic field is obtained. The study is stimulated by the extension of the experimental research on surface wave sustained discharges to magnetized plasma production [1-3] and the development [4-6] of the fluid theory of waveguided discharges of isotropic plasmas. It is shown that nonlocality due to longitudinal diffusion is a process which ensures the self-consistent variation of discharge parameters (plasma density  $n$  and electron temperature  $T_e$ ) and wave characteristics (maintenance field intensity) along the discharge length.

## 2. Formulation of the problem

Maintenance of magnetized plasmas of high-frequency gas discharges produced by the field of travelling waves is modelled on the basis of the fluid theory. The discharge is sustained in a diffusion controlled regime. The waveguided structure consists of the produced plasma column (of radius  $R$ ), free space region ( $R < r < R_1$ ) and a metal shielding of radius  $R_1$ . The external magnetic field  $B_0$  is fixed in the direction ( $z$ ) of the wave propagation. The produced plasma is strongly magnetized ( $\omega_{ce} \gg \omega, \omega_p, \nu$  where  $\omega_p$  and  $\omega_{ce}$  are respectively electron-plasma and gyro-frequencies,  $\nu$  is the electron-neutral elastic collision frequency and  $\omega$  is the field frequency). The wave sustaining the discharge is an azimuthally symmetric Trivelpiece-Gould mode [7] with field variation  $\propto \exp(-i\omega t + ikz)$ ;  $k$  is the wavenumber. As it is known [4-6], the longitudinal structure of the waveguided discharges should be obtained as a solution of a closed set which combines equations of the gas discharge physics and electrodynamical relations.

The electrodynamical part of the problem described by the wave energy balance equation

$$dS/dz = -Q \quad (1)$$

and the wave dispersion law

$$D(\omega, k, \varepsilon(n)) = 0, \quad (2)$$

although involving tedious calculations, is quite transparent. In (1),  $S = -(k\varepsilon_{33}R^2\omega gE^2)/(8\kappa_v^2)$

and  $Q \cong (\nu R^2 q E^2)/(8n_e)$  are respectively the wave power flux and the Joule losses in the discharge. Obtained in the case of a Trivelpiece-Gould mode in a strong magnetic field ( $E_r, B_\phi, E_z \neq 0$ ) they are determined by  $k, n$  and  $E = |E_z(r=R)|$ ;  $\varepsilon_{33}$  and  $\sigma_{33}$  are the longitudinal components of the permittivity and conductivity tensors,  $n_e = (m\omega^2)/(4\pi e^2)$  is the critical density and  $\kappa_v = [k^2 - (\omega/c)^2]^{1/2}$ . The functions  $g$  and  $q$  are slowly varying functions with values between 2 and 3 and their ratio is  $q/g \cong 1$ . The function  $f(N) = (kR)/(\kappa_v R)^2$  where  $N = n/n_e$  can be approximated by  $f(n) \cong \alpha N$  with  $\alpha = 0.23$ . Therefore the electrodynamical part of the problem (eqs. (1) and (2)) gives the following equation:

$$\frac{d}{d\xi}(\bar{N}^2 V) = -\bar{N} V \quad (3)$$

where  $\xi = (\nu/\omega)(q/g)(z/\alpha R)$  is a normalized axial co-ordinate. Eq.(5) relates the averaged (over the plasma column cross-section) normalized density  $\bar{N}$  to a normalized field intensity  $V = E^2/E_i^2$ ;  $E_i$  appears here as a constant (its meaning is defined below).

The description of the gas-discharge part of the problem is based on the particle balance equation:

$$D_{A1}\Delta_1 n + D_{Az} \frac{d^2 n}{dz^2} + \nu_i n = 0 \quad (4)$$

and the electron energy balance equation

$$(3/2)n\nu_* U_* = Q' \cong (1/2)\sigma_{33}|E_z|^2 \quad (5)$$

taken in a local approach. Here  $\nu_i = \nu_i \exp(-U_i/T_e)$  and  $\nu_* = \nu_* \exp(-U_*/T_e)$  are respectively the frequencies of direct ionization and excitation;  $U_i$  and  $U_*$  are the corresponding threshold energies. The ambipolar diffusion coefficients in transverse ( $D_{A1}$ ) and longitudinal ( $D_{Az}$ ) directions are taken as constants. The gas discharge part of the problem adds the electron temperature  $T_e$  to the other three unknown quantities ( $k, n, E^2$ ). The four relations (1), (2), (4) and (5) are the closed set of equations which describes

the structure of the discharge composed by a self-consistent variation of plasma ( $n, T_e$ ) and wave ( $k, E^2$ ) characteristics.

### 3. Results

The solution of eq. (5):

$$T_e = -U_* / \ln V \quad (6)$$

relates  $T_e$  to the field intensity  $|E|^2$  and expresses the effect of the thermal nonlinearity. The normalizing

$$\text{field intensity } E_i^2 = (3m\omega^2 v_i U_*) / (qe^2 v)$$

determines its efficiency. With  $v_i = v_i V^s$  obtained by using relation (6), eq. (4) gives the second equation

$$\frac{d^2 \bar{N}}{d\xi^2} + F(V) = 0 \quad (7)$$

which relates the field intensity  $V$  and the plasma density  $\bar{N}$  (the averaging of the density in radial direction is over the profile  $N_r(r) = J_0(2.4r/R)$  obtained from eq. (4). In eq. (7),  $F(V) = \beta V^s - \delta$  and its first and second terms account respectively for charged particle gain through ionization and particle losses due to diffusion in a transverse direction;

$$\beta = v_i \mu / D_{Az}, \quad \delta = \lambda^2 \mu / D_{Az} \quad \text{with} \\ \mu = (\omega g \alpha R / v q)^2, \quad \lambda = (2.4/R) \sqrt{D_{A\perp}}$$

Equations (3) and (7) coupling the electrodynamical and gas discharge parts of the problem, constitute the final set of equations (for  $n$  and  $E^2$ ) which describes the self-consistent plasma ↔ wave behaviour. It includes the strong thermal nonlinearity (eq. (6)) responsible for the discharge creation and nonlocality due to axial diffusion responsible for self-consistent interrelation of  $n(z)$  and  $E^2(z)$ .

With the small value of  $F(V)$  ( $F(V) < 10^{-2}$ ), the solution of the set of eqs. (3), (7) is

$$\bar{N} = 1 - \frac{1}{2} [1 - 2F(V_{th})] \xi - \frac{1}{2} \xi^2 F(V_{th}) (1 - \frac{1}{6} \xi) \quad (8)$$

$$V = V_{th} [1 + 2F(V_{th})(\bar{N}^2 - 1)]. \quad (9)$$

A boundary condition for  $y = 0$  at  $\bar{N} = 1$ , i.e. at the resonance of the Trivelpiece-Gould mode (in strong magnetic field) considered as a discharge end ( $\xi = 0$ ) is applied. Here  $y = (V - V_{th}) / V_{th}$  is the deviation of the field intensity from its threshold value  $V_{th}$  at the discharge end. Given by

$V_{th}^s = (2D_{A\perp} / v_i)(2.4/R)^2$  it is determined as a field intensity which creates plasma of critical density by compensation of the losses (diffusion in transverse and longitudinal direction) by ionization. The results

(8) and (9) for the axial structure of the discharge are presented in Figs. 1 and 2.

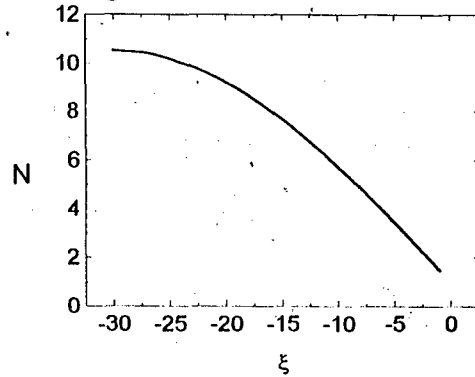


Fig. 1. Axial variation of the plasma density.

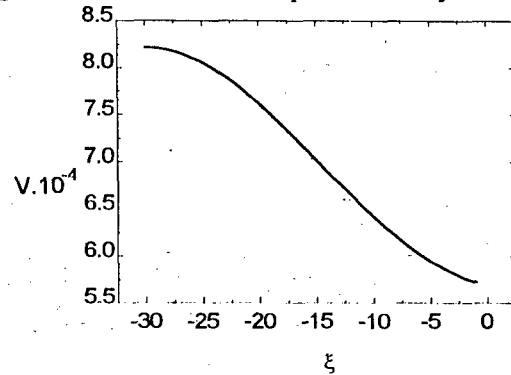


Fig. 2. Axial variation of the field intensity.

In conclusion, the axial structure of the gas discharges maintained in a diffusion controlled regime by Trivelpiece-Gould mode propagation in a strong magnetic field is constituted by decreasing (from the wave launcher towards the discharge end) self-consistent variations of the plasma density  $n$ , electron temperature  $T_e$  and maintenance field intensity  $E^2$ . This axial structure of the discharges is obtained on the basis of the effects of strong thermal nonlinearity and nonlocality due to longitudinal diffusion.

**Acknowledgements.** This work was supported by EC-project n° CIPA-0101 and the NFSR-project n° F-409.

### References

- [1] R. Anghelova et al: J. Phys. D: Appl. Phys. **21** (1988) 1371
- [2] S. Pasquiers et al: J. Appl. Phys. **65** (1989) 1465
- [3] J. Margot et al: J. Vac. Sci. Technol. A **13** (1995) 2890
- [4] Yu. M. Aliev et al: J. Phys. D: Appl. Phys. **28** (1995) 1997
- [5] Yu. M. Aliev et al: Contr. Plasma Phys. **36** (1996) 573
- [6] Yu. M. Aliev et al: Phys. Plasmas **3** (1996) 3162
- [7] A. W. Trivelpiece: Slow-Wave Propagation in Plasma Waveguides (San Francisco, San Francisco Press, 1967)

# Effects of non-local electron kinetics in a RF capacitive discharge in nitrogen

E. Stoykova, E. Tatarova, K. Bachev and I. Zhelyazkov  
Faculty of Physics, Sofia University, BG-1164 Sofia, Bulgaria

## 1. Introduction

An important aspect of RF capacity discharges comes from the type of the RF inhomogeneous field structure and electron energy distribution function (EEDF) coupling into discharge. Two different approaches of electron kinetic treatment are usually considered in analysis of inhomogeneous bounded plasma. In the limits of so called *local* regime the EEDF and its moments are local functions of the maintaining electric field, i.e. the energy gain from the field is locally balanced by the energy loss in elastic and inelastic collisions with neutral particles. In opposite, the *non-local* approach takes into account the non-locality of the problem, i.e. the fact that information is distributed by the electrons over the whole cross-section of the discharge, due to their diffusive motion [1]. The transition between local and non-local plasma response in molecular gases differs from that in atomic gases for the vibrational and rotational levels of molecules are excited. The aim of this work was to observe the non-local properties of the EEDF in molecular gases. To this end the space resolved (along the RF electric field) behaviour of the EEDF and its moments has experimentally been investigated. A single Langmuir probe by appropriate methods and techniques that provided the unperturbed probe characteristics in the presence of RF electric field has been used [2]. The measurements are performed by means of a computer controlled data-acquisition system with cross-modulation second derivative technique applied. The probe diagnostic methods are accompanied with accurate measurements of the electrical discharge characteristics (RF discharge current density, RF voltage, etc.). In a capacity discharge, nearly all of the applied voltage is dropped across the oscillating electron sheaths that form near the electrodes. These sheaths heat the electrons through a process in which electrons reflected from the moving sheath edge gain energy on average. This process, usually referred to as "stochastic heating" is the dominant source of electron heating at low pressures [3].

## 2. Experimental results and discussion

The experiments have been carried out in an asymmetrically driven capacity discharge at a frequency of 27 MHz. The plasma device consists of parallel plate aluminium electrodes with a diameter of 8.2 cm and electrode separation  $L = 2.6$  cm. The bottom electrode is grounded and the top electrode is the powered one. The cylindrical glass discharge chamber is evacuated down to a pressure of 0.35 Torr. Typical curves of the

measured EEDF are shown in Fig. 1 at various discharge current densities  $j$ , when the probe is at the midplane of the discharge axis. The obtained EEDFs are markedly non-Maxwellian. Their energy variations show dominant influence of the electron-molecule energy exchange processes. A strong decrease of the curves in the energy range of 2–5 eV is observed. This behaviour mirrors the rapid rise of the cross-sections for vibrational excitation of  $N_2$  molecules by approximately two orders of magnitude in that energy interval. Figure 2 demonstrates the evolution of the EEDF as the axial distance  $x$  (referred to the grounded electrode) is changed along the RF electric field. The measured EEDFs reveal a "widening" towards the discharge center where the heating inhomogeneous RF field decreases. This behaviour correlates with the average electron energy variations (Fig. 3). The spatial scanning of  $\langle \epsilon \rangle$  exhibits a nonuniformity along the RF field with a well pronounced decrease towards the electrodes, where the heating electric field is larger. Thus, the non-local coupling between the EEDF and the inhomogeneous RF electric field is an obvious experimental result. The axial electric field in such a discharge increases towards the electrodes due to a decrease of the electron density by ambipolar diffusion. The axial distribution of the electron density, estimated by measuring the ion saturation current is shown in Fig. 4. For comparison a theoretical profile given by the relation

$$n(x)/n(x=L/2) = (1 - (2x/L)^2)^{-1/2}$$

is also shown.

The obtained EEDF's axial variations may also be interpreted in terms of the electron energy relaxation length  $\lambda_e$ . For low electron energies (2–5 eV), the electron collisions leading to vibrational excitation of nitrogen molecules is the main process significantly affecting  $\lambda_e$ :  $\lambda_e(\epsilon) \equiv \lambda_e(v_{ev}(\epsilon)/v_{em}(\epsilon))^{-1/2}$  [4]. Here  $\lambda_e$  is the electron mean free path,  $v_{ev}$  and  $v_{em}$  are the frequencies of vibrational excitation and electron-molecules elastic collisions, respectively. An estimation shows that for mean electron energies in the range 2–5 eV,  $\lambda_e \approx 0.5\text{--}0.8$  cm  $\sim L/2 = 1.3$  cm. Thus, the *non-local plasma response* should be certainly consider as an approximation which finds its range of validity under conditions when the energy relaxation length  $\lambda_e$  is of the order or large compared to the discharge dimensions ( $L/2$ ) as the results obtained demonstrate.

Another important problem for a RF discharge is the nature of the electron heating mechanisms. At low-pressure conditions, one occurs the so called "collisionless" regime for plasma electrons where stochastic

electron heating in the oscillating RF sheaths at the plasma boundaries dominates. Since the sheath voltage is generally much larger than the mean electron energy, the sheaths usually present an impenetrable potential barriers for electrons: electrons can escape to an electrode only when the adjacent sheath is fully collapsed or nearly so. Thus when an electron strikes a sheath it will generally be reflected, and because of the sheath motion the electron will generally change its energy on reflection. Although this energy change can be positive or negative, the average effects is positive.

The total dissipation power  $P_{\text{disch}}$  in the discharge at conditions considered is composed of the Ohmic  $P_v$  and stochastic  $P_{\text{st}}$  heatings. By comparing  $P_{\text{disch}}$  and  $P_v$  one can estimate the contribution of the noncollisional dissipative process in the RF energy transferred to plasma electrons.  $P_{\text{disch}}$  is obtained by measuring the RF discharge current  $I_{\text{disch}}$ , RF voltage  $U_{\text{disch}}$  and phase shift between them. The RF power  $P_v$  imparted to plasma electrons in the plasma bulk through electron-neutral-atom collisions may be found as [3]:

$$P_v = \frac{2I_{\text{disch}}^2 v_{\text{em}} L}{\omega_{e0}^2 \bar{K}_x \bar{K}_r R^2}.$$

$\omega_{e0}^2$  is the electron-plasma frequency at the center of plasma volume,  $R$  is the discharge plasma radius,  $\bar{K}_x$  and  $\bar{K}_r$  are geometrical factors of plasma axial and radial inhomogeneities [3].  $\bar{K}_r$  is obtained under the assumption of a Bessel plasma density profile in radial direction, while  $\bar{K}_x$  is calculated from the experimentally obtained electron density profile shown in Fig. 4. The estimation shows that the ratio  $P_v/P_{\text{disch}}$  is 0.05 for a pressure  $p = 0.35$  Torr and RF discharge current density  $j = 4.49 \text{ mA cm}^{-2}$ . Thus, one may conclude that the dominant heating mechanism for such conditions is the stochastic heating.

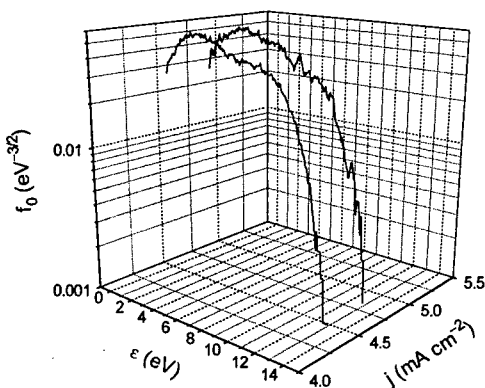


Fig. 1. EEDFs measured at different RF discharge current densities ( $x = L/2$ ).

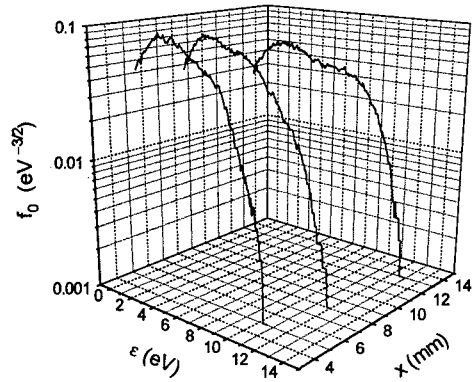


Fig. 2. EEDF's variations along the RF field.

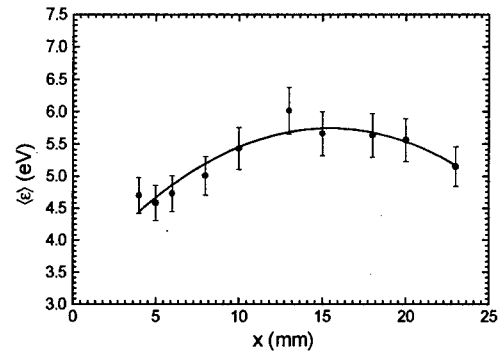


Fig. 3. Axial variation of the mean electron energy.

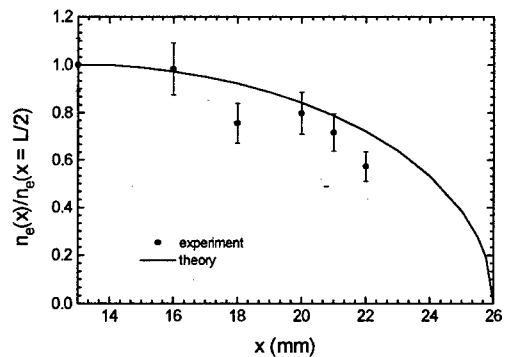


Fig. 4. Axial electron density profile ( $j = 4.49 \text{ mA cm}^{-2}$ ).

**Acknowledgement.** This work was supported by the National Fund for Scientific Research under Grant No. F-538/95.

## References

- [1] V. I. Kolobov, V. A. Godyak: IEEE Trans. Plasma Sci., **PS-23** (1995) 503
- [2] V. A. Godyak, R. B. Piejak and B. M. Alexandrovich: Plasma Sources Sci. Technol., **1** (1992) 36
- [3] O. A. Popov, V. A. Godyak: J. Appl. Phys., **57** (1985) 53
- [4] N. A. Gorbunov, K. O. Iminov and A. A. Kudryavtsev: Zh. Tekn. Fiz., **58** (1988) 2301

# Transition from $\alpha$ - to $\gamma$ -regime in a RF capacitive discharge in nitrogen

E. Stoykova, E. Tatarova, K. Bachev and I. Zhelyazkov

Faculty of Physics, Sofia University, BG-1164 Sofia, Bulgaria

## 1. Introduction

The specific feature of capacitively coupled RF discharges is the existence of two operational modes which essentially differ in a light emission and in the main governing ionization mechanism. At low discharge voltages, ionization is provided by plasma bulk electrons and the discharge is in an  $\alpha$ -mode, while at high discharge voltages (or high RF current densities) the ionization is maintained by fast electrons initiated at the RF electrodes and the discharge is in a  $\gamma$ -mode [1]. The experimental study of RF discharges in the  $\gamma$ -regime in inert gases (argon, helium) showed that the transition into  $\gamma$ -regime is accompanied by a sharp change in the electron energy distribution function (EEDF) and as a consequence a strong drop in the electron temperature and a steep rise in the electron number density is observed [2].

The aim of this work is to demonstrate some specific features of a RF capacitively coupled discharge (E-type) in molecular gas (nitrogen), when it goes from  $\alpha$ - to  $\gamma$ -regime. The transition between  $\alpha$ - and  $\gamma$ -mode is investigated by measuring the EEDF and its moments' changes with the increase of the RF discharge current density. For that purpose a single Langmuir probe by appropriate methods and techniques that provided the unperturbed probe characteristics in the presence of RF electric field has been used [3]. Along with this, integral light emission measurements by using an optical fibre and photo multiplier are also made to confirm the results obtained through a probe diagnostics. The probe measurements are accompanied with accurate measurements of the electrical discharge characteristics (RF discharge current densities, RF voltage, ect.).

## 2. Experimental results

The experiments have been carried out in an asymmetrically driven capacity discharge at a frequency of 27 MHz. The discharge is sustained between two parallel plate aluminium electrodes separated by a distance of 2.6 cm and confined by a cylindrical glass tube with a diameter of 8.2 cm. The bottom electrode is grounded and the top electrode is the powered one. All measurements are made in the midplane of the axis in the discharge chamber which is evacuated down to a pressure of 0.2 Torr.

Figure 1 demonstrates the evolution of the EEDF with RF discharge current density variation. The corresponding variation of EEDF moments together with corresponding discharge parameters (voltage and power

density) are shown in Figs. 2 through 4. As can be seen over a limited range of discharge currents (up to 4 mA cm<sup>-2</sup>) the EEDF does not change, the average electron energy  $\langle \epsilon \rangle$  remains constant and the electron density  $n_e$  grows linearly. The electron energy spectrum is far away of being Maxwellian with a shape which reflects the influence of collisions leading to vibrational excitation of nitrogen molecules. When the discharge current is further increased a sharp change in the EEDF's shape with a corresponding drop in  $\langle \epsilon \rangle$  and a rapid increase of  $n_e$  is observed. As can be seen (Figs. 1 through 3) the transition to a  $\gamma$ -regime has a threshold-like nature. The transition point where the discharge changes the mode of operation (from  $\alpha$ - to  $\gamma$ -mode) corresponds to a transition current density  $j_{\text{trans}} = 4.9 \text{ mA cm}^{-2}$  and a transition voltage  $U_{\text{trans}} = 35.4 \text{ V}$ . The high voltage ensures conditions for a secondary electron multiplication in the RF plasma sheaths. After acceleration in the sheaths these  $\gamma$ -electrons gain a high ionization efficiency which leads to much faster electron density growing than at a linear rate. Figure 2 shows that  $n_e$  increases by two orders of magnitude as the discharge current density changes from 3.3 to 5.6 mA cm<sup>-2</sup>. The steep rise in the electron density due to the  $\gamma$ -electron ionization results in a sharp fall (about 5 times) of the mean electron energy (Fig. 3). Both the drop in  $\langle \epsilon \rangle$  and jump in  $n_e$  lead to a drastic increase of the electron-electron collision frequency  $\nu_{ee} \propto n_e / \langle \epsilon \rangle^{3/2}$  [2]. While the discharge current density increases twice (from 3 to 6 mA cm<sup>-2</sup>), which causes a transition from  $\alpha$ - to  $\gamma$ -regime,  $\nu_{ee}$  increases by a factor of 800, thus giving conditions for a thermalization of the electron energy spectrum. The observed in Fig. 1 trend of measured EEDF (in  $\gamma$ -mode operation) to Maxwellian distribution can be explained by this increased influence of the electron-electron energy exchange processes.

The sharp changes in the EEDF and in the plasma parameters—well known in literature as a transition into  $\gamma$ -regime—are accompanied with a change in the discharge luminosity distribution (Fig. 5). The increase of integral light emission near the electrodes when the discharge goes from  $\alpha$ - to  $\gamma$ -mode correlates well with the observed abrupt transition on EEDF and its moments.

## 3. Discussion and conclusion

The experiments show that in the  $\gamma$ -mode the physical processes occurring in the RF sheaths and in the bulk plasma are rather complicated. Their dynamics is

determined mainly by the character of the electric field variation in the plasma sheaths during the RF period [1]. The RF field main part is concentrated in the plasma sheaths where due to the nonlinear interaction a strong additional quasi-stationary field arises. This field creates a potential barrier for plasma electrons in the most part of the RF period. However during the whole period a continuous stream of positive plasma ions is directed towards the electrodes. The ion bombardment initiates a secondary electron emission, which plays an important role in the maintenance of the discharge. The secondary electron current grows under the action of the large electric fields inside the sheaths. After electrons multiplication and acceleration in the sheaths towards the plasma, electron beams are formed. They reach the plasma bulk and dissipate their energy mainly through inelastic collisions. By contrast with an  $\alpha$ -mode, in the  $\gamma$ -mode the production of excited and charged particles is controlled by the fast electrons generated in RF sheaths and as a result a strong increase of the discharge luminosity near the electrodes is observed. Due to the high efficiency of the  $\gamma$ -electrons the electron density rises sharply and as a consequence a reducing of the RF field in the bulk plasma and a fall of the mean electron energy is registered.

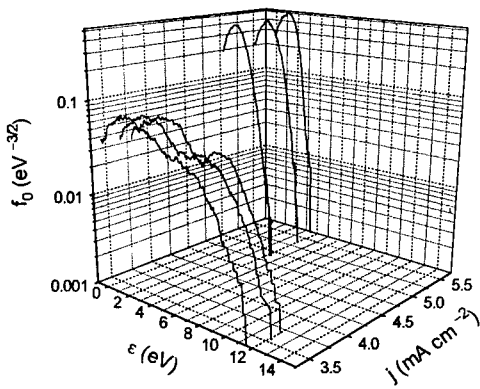


Fig. 1. EEDF evolution during RF discharge transition to a  $\gamma$ -mode.

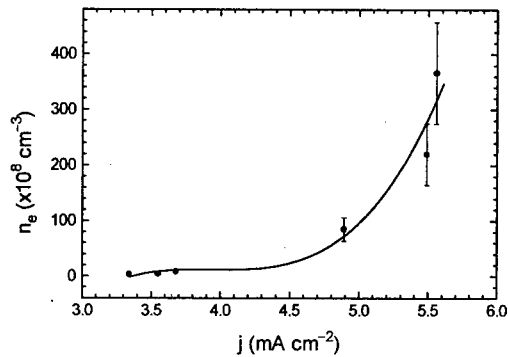


Fig 2. Electron density variation during RF discharge transition to a  $\gamma$ -mode.

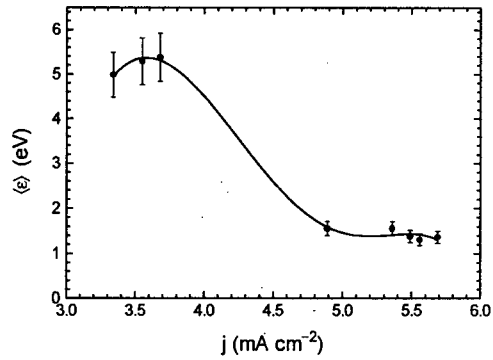


Fig. 3. Average electron energy variation during RF discharge transition to a  $\gamma$ -mode.

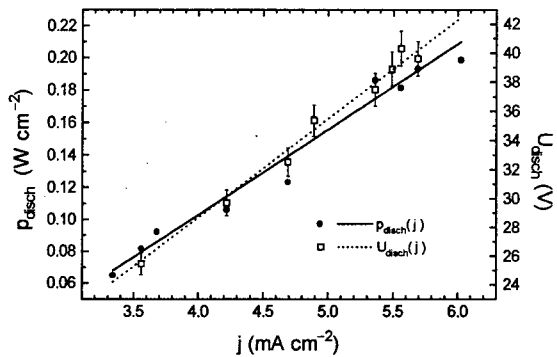


Fig. 4. Voltage and power density variations as a function of the discharge current density.

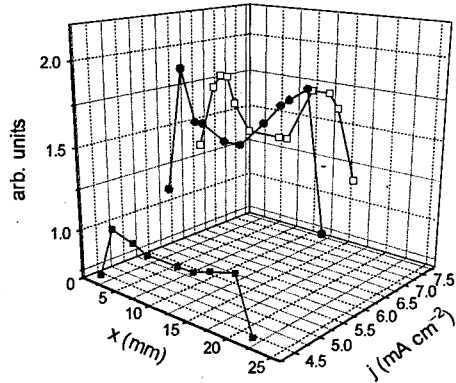


Fig. 5. Axial distribution of the integral light emission density.

**Acknowledgement.** This work was supported by the National Fund for Scientific Research under Grant No. F-538/95.

**References**

[1] V. A. Kovalevskii, V. P. Savinov: *Fizika Plazmy*, **20** (1994) 322  
 [2] V. A. Godyak, R. B. Piejak and B. M. Alexandrovich: *Phys. Rev. Lett.*, **68** (1992) 40  
 [3] V. A. Godyak, R. B. Piejak and B. M. Alexandrovich: *Plasma Sources Sci. Technol.*, **1** (1992) 36



## Diagnostic Study of R.F. Parallel Plate Reactor

Y. Kobayashi, K. Sando<sup>A</sup> M. Sugawara<sup>B</sup> and T. Sato<sup>B</sup>

Gunma National College of Technology, 580, Toriba-cho, Maebashi, Gunma, JAPAN

<sup>A</sup>Gunma University, Department of Electrical Engineering, 1-5-1, Tenjin-cho, Kiryu, Gunma, JAPAN

<sup>B</sup>Hachinohe Institute of Technology, 88-1, Obiraki, Myou, Hachinohe, Aomori, JAPAN

### 1. Introduction

When R.F. voltage is applied between parallel-plate electrodes, sheaths are found in front of each electrodes and a plasma connects these sheaths. The purpose of this research is to measure distribution of electron temperature and electron density by using a double probe compensated R.F. potential variation in R.F. discharge. Sheath is exist in front of electrodes. Potential on earthed electrode is earthed and potential on powered electrode is lower than earth by self-bias voltage.

### 2. Experimental Methods

The discharge system consists of cylindrical vacuum chamber (diameter: 20 [cm], length: 29 [cm]), parallel-electrodes that are 10 [cm] in diameter and spaced 4 [cm] apart (Fig. 1). The discharge between two electrodes is confined in glass tube. The lower electrode is earthed. From the upper electrode R.F. power is supplied. The frequency of the R.F. power is 13.56 [MHz]. An impedance matching unit is comprised of two variable capacitors and one variable inductor which transfers the R.F. power to the discharges. The cylindrical vacuum chamber is formed a vacuum at  $10^{-6}$  [torr] by a turbo molecular pump and a rotary pump. Argon gas is supplied via a massflow controller. The pressure is varied between 0.01 and 0.5 [torr], which is monitored with a capacitance manometer.

### 3. Results and Discussion

Fig. 2 shows electron temperature ( $T_e$  [eV]) and probe current ( $I$  [ $\mu$  A]) versus distance from the axis of the discharge. At input power ( $P_w = 60$  [W]) and pressure ( $p = 0.1$  [torr]) probe current ( $I$  [ $\mu$  A]) are decreases as the distance from the axis increase. Fig. 3 shows electron temperature ( $T_e$  [eV]) and electron density ( $n_e \cdot 10^{17}$  [ $m^{-3}$ ]) on the axis of discharge as a function of the pressure. Electron density ( $n_e \cdot 10^{17}$  [ $m^{-3}$ ]) increases as pressure ( $p$  [torr])

increases. Electron temperature ( $T_e$  [eV]) decrease as pressure ( $p$  [torr]) increases. This agrees with Schottky's theory. Fig. 4 shows that electron temperature ( $T_e$  [eV]) and electron density ( $n_e \cdot 10^{17}$  [ $m^{-3}$ ]) on the axis of discharge varies with input power at  $p = 0.1$  [torr]. As input power increases, electron density ( $n_e \cdot 10^{17}$  [ $m^{-3}$ ]) increases sharply and electron temperature increases gradually.

Input power ( $P_w$ ) is consumed only at bulk plasma.

$$P_w = R_p \times I^2 \quad (1)$$

Discharge current ( $I_d$ ) is

$$I_d = e \times s \times n_e \times v \quad (2)$$

( $s$ : size of electrode [ $m^2$ ],  $v$ : velocity of electrons [m/s])

Therefore,

$$n_e^2 \propto P_w \quad (3)$$

This results reflect on measurements of Fig. 5.

### 4. Conclusions

Electron density ( $n_e$ ) decreases as pressure increases and increase of electron temperature ( $T_e$  [eV]) is caused by increase of ionization collision frequency. Electron density ( $n_e$ ) is proportional to  $P_w^{1/2}$ . And electron temperature ( $T_e$  [eV]) increases gradually as input power ( $P_w$  [W]) increases.

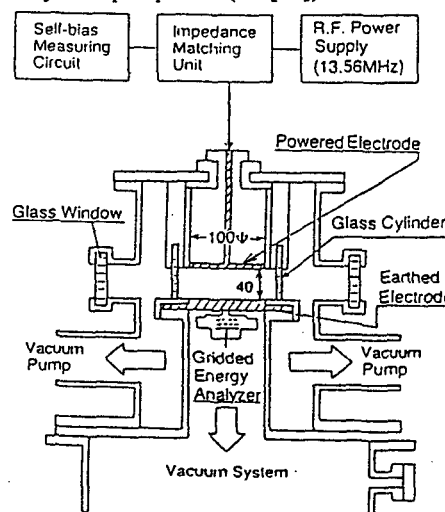


Fig. 1

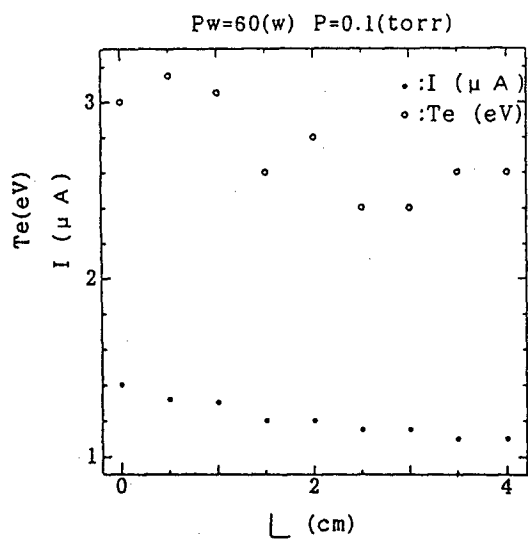


Fig. 2

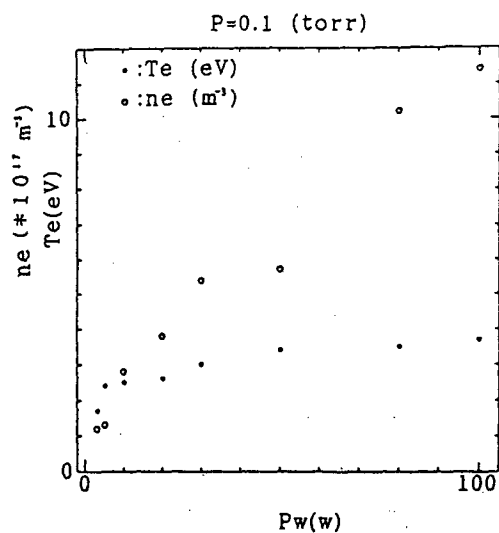


Fig. 4

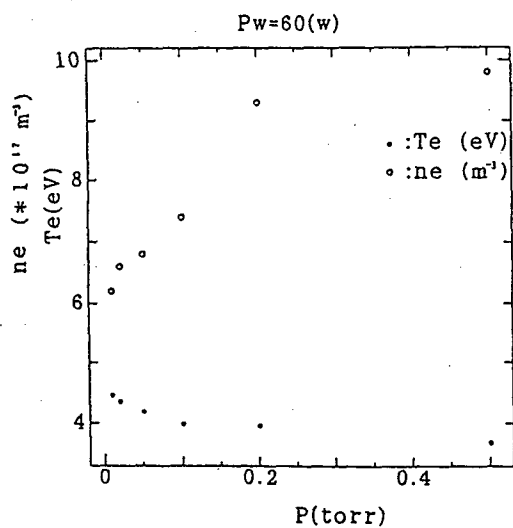


Fig. 3

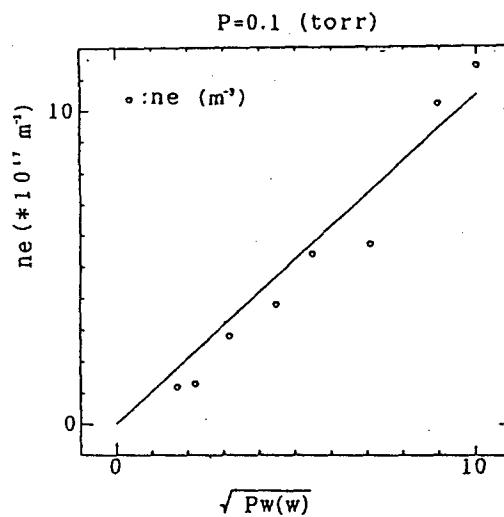


Fig. 5

# A Surface-wave-based High-density Plasma Source operated near 200 MHz

M. Tabbal, O. Pauna\*, M. Chaker and J. Margot \*

INRS-Énergie et Matériaux, 1650 boul. Lionel Boulet, Varennes, Qc, Canada, J3X 1S2.

\* Département de Physique, Université de Montréal, C.P. 6128, Succ. Centre-Ville, Montréal, Qc, Canada H3C 3J7.

## 1. Introduction

Newly developed high density magnetized plasma sources such as microwave sustained discharges at electron cyclotron resonance (ECR at 2.45 GHz) [1] are very attractive for the ever more stringent requirements imposed on the etching processes in microelectronics and optoelectronics. In comparison with the conventional RF capacitive discharges, such sources have the advantage of independent control of ion flux and ion energy; they also provide high densities at extremely reduced gas pressures. Recently, J. Margot et al. [2] have developed a new large diameter high density magnetoplasma reactor based on a Surface Wave Discharge which, in contrast to common magnetized plasmas, can be operated over a large range of magnetic field intensities and of field frequencies (10 MHz-2.45 GHz).

Operated at 2.45 GHz in SF<sub>6</sub>, this reactor has been characterized [2] and used to replicate 0.2  $\mu\text{m}$  W etched patterns with an excellent anisotropy [3]. In this communication, we examine the characteristics of the plasma sustained at a lower frequency, namely 190 MHz in argon. Preliminary results on the influence of gas pressure and magnetic field intensity on the electron temperature,  $T_e$ , and ion density,  $n_i$ , are presented.

## 2. The experimental setup

The plasma is created by an electromagnetic surface wave propagating in a 15 cm diameter fused silica tube and penetrates into a 28 cm diameter stainless steel vessel. A characteristic of this reactor is that the magnetic field is uniform over a large part of the reactor vessel. The surface wave is launched at the gap of a 16 cm inner diameter Ro-box operated at 190 MHz. The plasma is produced in Ar at pressures varying from 0.3 to 20 mTorr and a gas flow rate of 25 sccm. When no magnetic field is applied, the plasma can be sustained at pressures as low as 1 mTorr.

A RF driven cylindrical Langmuir probe was used to determine the electron temperature  $T_e$  and the positive ion density  $n_i$ . The RF signal was sampled from the 190 MHz HF power supply and superimposed to the d.c voltage applied to the probe. Its phase was adjusted so that it compensates for plasma potential RF fluctuations. This procedure enables to minimize the

distortion of the probe characteristics which can thus be used to retrieve  $T_e$  and  $n_i$  [4]. The effect of the magnetic field were reduced by orienting the probe perpendicularly to the magnetic field lines. The good linearity of  $\ln(i_e)$  ( $i_e$  is the electron current collected by the probe) observed when plotted against the probe potential suggests that (i) the bulk of the electron distribution function is very close to a Maxwellian and (ii) the magnetic field does not significantly affect the repelling electron current. In these conditions, a reliable value of  $T_e$  can be obtained. The influence of B shows up more strongly when considering the electron saturation current. For this reason, the plasma density was derived from the ion saturation current using the ABR theory [5]; under our experimental conditions, the ions are always weakly magnetized. The measurements reported below have been obtained on the axis ( $r=0$ ) of the large diameter portion of the reactor at 20 cm from the wave launcher gap and for a HF power of 275 W.

## 3. Results

Figure 1 shows the ion density  $n_i$  measured at the plasma axis as a function of the operating argon pressure, for two extreme cases namely, when no magnetic field is applied ( $B=0$  Gauss) and at  $B=875$  Gauss which the value of the magnetic field intensity used in conventional ECR discharge operated at 2.45 GHz. When  $B=0$  Gauss,  $n_i$  increases from  $4.10^{10}\text{cm}^{-3}$  at 1 mTorr until it saturates at about  $15.10^{10}\text{cm}^{-3}$  at an operating pressure of 10 mTorr and above. When the 875 Gauss magnetic field is applied,  $n_i$  increases with gas pressure to reach a maximum value ( $1.7 \cdot 10^{12}\text{cm}^{-3}$ ) at about 3 mTorr; further pressure increase yields a decrease of the ion density down to  $9 \cdot 10^{11}\text{cm}^{-3}$  at 10 mTorr. The increase of the plasma density with pressure can be related to a more favorable power balance which results from a reduction of charged particles losses [6]. For non-zero B, the fact that  $n_i$  decreases for  $p > 3$  mtorr presumably results from a spatial redistribution of the plasma (Probe measurements are local and do not provide a spatially average density).

Figure 2 presents the electron temperature at the plasma axis for the same conditions as in Fig.1. In absence of magnetic field,  $T_e$  decreases slowly from 2.5 eV at 1 mTorr to about 1.75 eV at 20 mTorr. When the magnetic field is applied,  $T_e$  is higher than

for  $B=0$  (about 4.0 eV) at low pressures while it reaches a comparable value at 10 mTorr. The decrease of the electron temperature with increasing pressure results from the reduction of the diffusion coefficient; at steady-state, this implies the ionization frequency and consequently  $T_e$  will both decrease. Because the diffusion coefficient is also further reduced for non-zero  $B$ -field, one should also expect a lower  $T_e$  at  $B=875$  Gauss than at  $B=0$ . Figure 3 shows that it is not the case at low pressure. Very different spatial distributions of the plasma with and without  $B$ -field could explain this result. This is well supported by our observation that the radial extent of the plasma decreases as  $B$  increases.

Finally, Fig. 3 presents the ion density measured at 1 mTorr as a function of the applied magnetic field. The ion density increases from  $4 \cdot 10^{10} \text{ cm}^{-3}$  when no field is applied and to about  $8 \cdot 10^{11} \text{ cm}^{-3}$  for  $B > 400$  G. Such an increase by more than one order of magnitude was also observed at higher pressures, namely 10 mTorr. These results seem to indicate that there is no significant gain in applying a magnetic field larger than 400 Gauss. In addition, preliminary comparison with results previously obtained at 2.45 GHz show that similar plasma densities can be achieved in both plasmas. The 190 MHz magnetized plasma thus seems to be advantageous as compared to the 2.45 GHz discharge in terms of magnetic field intensity required to achieve a high-density plasma.

#### 4. Conclusion

We have designed a surface-wave-based magneto-plasma reactor operated at 190 MHz. The experimental results show that high plasma densities can be achieved at gas pressures as low as 0.3 mtorr. The density obtained in argon is comparable to that of ECR reactors but requires a lower magnetic field. This work will be now pursued by studying a  $\text{Cl}_2$  or an  $\text{Ar}/\text{Cl}_2$  plasma intended for anisotropic etching of thin films.

#### 5. References

- [1] O. A. Popov: High Density Plasma Sources: Design, Physics and Performances, Noyes, New Jersey (1995).
- [2] J. Margot, M. Chaker, M. Moisan, L. St-Onge, F. Bounasri, A. Dallaire and E. Gat : Lecture for NATO ASI on Plasma Processing of Semiconductors, to be published in the NATO ASI Series B, Kluwer (1997).
- [3] F. Bounasri, E. Gat, M. Chaker, M. Moisan, J. Margot and M.F. Ravet : J. Appl. Phys. 78 (1995) 6780.

- [4] T.I. Cox, V.G.I. Deshmukh, D.A.O. Hope, A.J. Hydes, N.St.J. Braithwaite and N.M.P. Benjamin : J. Phys. D : Appl. Phys. : 20 (1987) 820.
- [5] J.E. Allen, R.L.F. Boyd and P. Reynolds: Proc. Phys. Soc. B, 70 (1957) 297.
- [6] I. Pérès and J. Margot : Plasma Sources Sci. Technol., 5 (1996) 653.

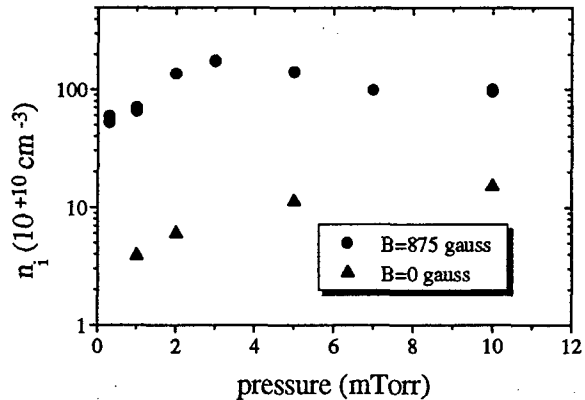


Fig.1. Influence of pressure on the ion density with and without magnetic field.

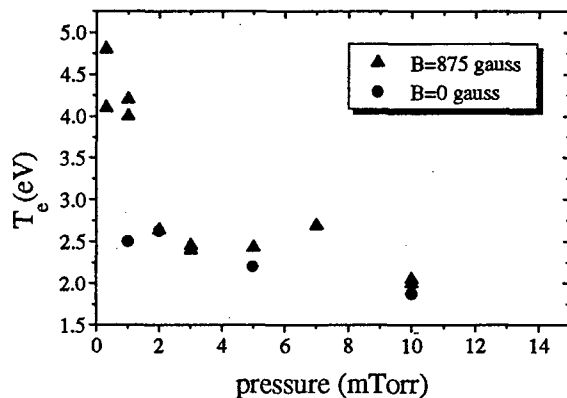


Fig.2. Influence of pressure on the electron temperature with and without magnetic field.

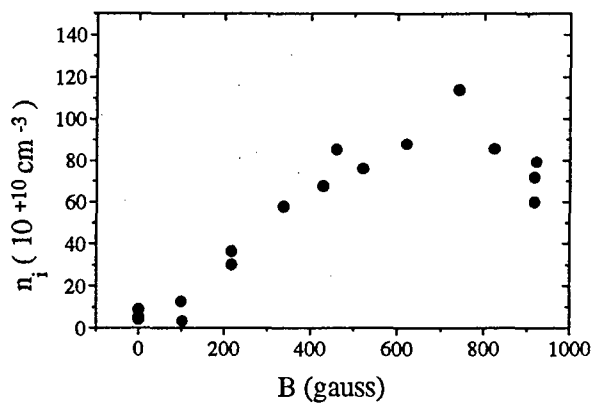


Fig.3. Influence of the magnetic field intensity on the ion density.

# A high flux source of N atoms based on a N<sub>2</sub> HF discharge

P. Mérel, M. Tabbal, M. Chaker, M. Moisan<sup>1</sup>, A. Ricard<sup>2</sup>

INRS- Énergie et Matériaux, 1650 boul. Lionel Boulet, Varennes, Québec, Canada, J3X 1S2.

<sup>1</sup>Département de Physique, Univ. de Montréal, C.P. 6128 Succ. Centre-Ville, Montréal, Québec H3C 3J7, Canada.

<sup>2</sup>CAPT, Université Paul Sabatier, 118 Route de Narbonne, 31062 Toulouse CEDEX, France.

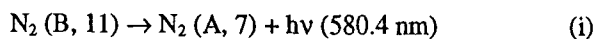
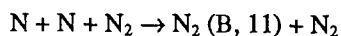
## 1. Introduction

There has been recently considerable interest in flowing post-discharge reactors for surface coating processes. In microelectronics, deposition of Si<sub>3</sub>N<sub>4</sub> films has been obtained in N<sub>2</sub> CVD post-discharges with SiH<sub>4</sub> [1]. Surface activation of polymers [2] and nitriding of metals (steel) [3] have also been achieved in post-discharge reactors. Correlations have been established between the active species density and film properties such as wettability for polymers and resistance to corrosion for metals [2,3]. It is the purpose of the present work to report on N atom production in a flowing post-discharge used for CN<sub>x</sub> film deposition [4].

A surface-wave discharge is produced with a Ro-box field applicator [5] at frequencies  $f$  ranging from 13.56 to 2450 MHz in a N<sub>2</sub> discharge tube (dia. 4.5 mm) at powers up to 200 watts. The N<sub>2</sub> flux  $Q$  and pressure  $p$  in the discharge tube are in the range 0.1-2 slm and 1-10 Torr, respectively. Standard values of  $Q = 0.55$  slm,  $p=4$  Torr in the post-discharge tube (dia. 3 cm) and 7 Torr in the discharge tube are selected since we found that the N atom density increased with pressure and reached a saturation at  $p=4$  Torr. The N atom density is determined by NO titration in the post-discharge tube.

## 2. Post-discharge characterization

A Nitrogen post-discharge is formed by an early and a late afterglow. The early or "pink" afterglow which is formed right after the discharge, is characterized by the N<sub>2</sub> vibrationally excited molecules which are producing self-ionization reactions (Penning effect). The "pink" afterglow is followed by a late or "Lewis-Rayleigh" afterglow where reaction (i) is dominant. The late afterglow in a N<sub>2</sub> post-discharge is well characterized by the emission of the N<sub>2</sub> (B, 11) - (A, 7) spectral band at 580.4 nm, which results from the following recombination reactions:



The afterglow intensity at  $\lambda = 580.4$  nm is proportional to  $[N]^2$  and this classical method has been

calibrated by NO titration [6]. Depending on HF power, gas pressure and flux, the early and late afterglows are more or less separated. An emission spectroscopy method has been proposed recently [7] to separate the contributions of the pink and late afterglows in the recorded spectrum in order to determine accurately the N atom density. For that purpose, the normalized  $r_{B,v}$  distribution of the N<sub>2</sub> (B, v') population:

$$r_{B,v'} = \frac{[N_2(B, v')]}{\sum_{v=7}^{12} [N_2(B, v')]} \quad (1)$$

has been calculated.  $r_{B,v}$  is the sum of contributions from  $r_{B,v}$  (N+N) in the late afterglow and  $r_{B,v}$  (pink) in the early afterglow:

$$r_{B,v'} = a r_{B,v'}(N + N) + b r_{B,v'}(\text{pink}) \quad (2)$$

Abacus of  $r_{B,v}$  are then determined by choosing well confirmed values of  $r_{B,v}$  (N+N) and  $r_{B,v}$  (pink) distributions [7]. Then, the "a" parameter in eq. 2 is determined for each experimental  $r_{B,v}$  distribution and the N atom density can be determined by:

$$[N] \propto (a I_{\lambda=580.4 \text{ nm}})^{1/2} \quad (3)$$

We now use the NO titration method to validate the above abacus method.

## 3. Abacus method experimental validation

The post-discharge optical emission is observed using a Jobin-Yvon HR 320 spectrometer with a Hamamatsu R955 photomultiplier, a picoameter amplifier and a chart recorder. Using equation 3, we evaluated the relative N atom density, for different pressures and powers ( $f=440$  MHz), and compared the results to the absolute density values obtained by NO titration. The correlation of the two techniques is reported in fig.1. In the plot, data points corresponding to  $a < 0.5$  represent a dominating "pink" afterglow while data points corresponding to  $a \geq 0.5$  represent a dominant "late" afterglow. For both cases, the correlation of the two N atom density measurement methods is quite good, thus validating the  $r_{B,v}$  technique.

Figure 2 shows the N atom density as a function of absorbed power in the pink afterglow ( $a < 0.5$ , as detected 25cm away from the Ro-Box) and in the late afterglow ( $a = 0.9$ , 40cm away from the Ro-Box). Little variation in the N atom density values are detected in going from the pink to the late afterglow indicating few losses and creations of N atoms in the post-discharge region.

#### 4. Influence of frequency on N atom production

The effect of wave frequency on N atom production is reported in fig.3 for  $p=4$  Torr. Plots of N atom density as a function of absorbed power are presented for four wave frequencies (13.56, 40.68, 440 and 2450 MHz). For all frequencies, the N atom density increases with the absorbed power and then reaches a saturation region ( $1.3 \times 10^{15} \text{ cm}^{-3}$ ). Furthermore, the power required to attain saturation decreases with increasing wave frequency. We can relate this to the electron density which increases as a function of wave frequency for a traveling surface wave [8]. It can also be noted that in the saturation region, values of N atom density are equivalent for 40.68, 440 and 2450 MHz. At 13.56 MHz, the saturation region is not yet reached at 120 Watts. The measurements were limited to this value to avoid the injection of plasma inside the post-discharge tube.

In conclusion, the optimum discharge conditions for N atom production were found to be  $p=4$  Torr with absorbed power as low as 40 Watts at 2450 MHz. This N atom source was successfully used for  $\text{CN}_x$  thin film deposition where a high flux of atomic nitrogen is essential [4].

#### 5. References

- [1] I. Kato, K. Noguchi and K. Numada: J. Appl. Phys., 62 (1987) 492.
- [2] F. Normand, A. Granier, I. Leprince, J. Marec, M. K. Shi and F. Clouet: Plasma Chem. and Plasma Process., 15 (1995) 173.
- [3] A. Ricard, J. Oseguera-Pena, H. Michel and M. Gantois: IEEE Trans. Plasma Sci., 18 (1990) 940.
- [4] M. Tabbal, P. Mérel, S. Moisa, M. Chaker, M. Moisan and A. Ricard: Appl. Phys. Lett., 69 (1996) 1698
- [5] M. Moisan and Z. Zakrzewski: Rad. Process in Dich. Plasma, (1986) 381.
- [6] I. M. Campbell and B. A. Thrush: Proc. Roy. Soc., A296 (1967) 201.
- [7] S. Bockel, A. M. Diany and A. Ricard: Surface and Coating Tech., 74-75 (1995) 474.
- [8] M. Moisan and J. Pelletier: Microwave Excited Plasmas, sec. 5.8, Elsevier (1992).

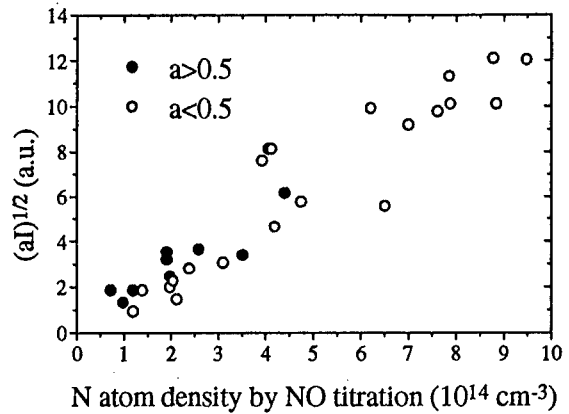


Fig.1. Correlation of NO titration with the abacus method  $(al)^{1/2}$  obtained from optical emission measurements ( $f=440$  MHz).

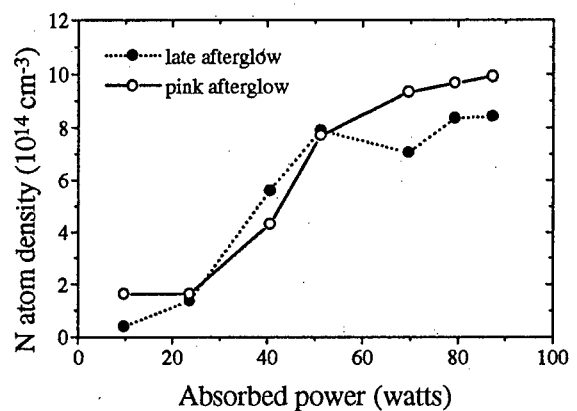


Fig.2. Variation of N atom density as a function of absorbed power in conditions of late and early afterglow ( $p=4$  Torr,  $f=40.68$  MHz).

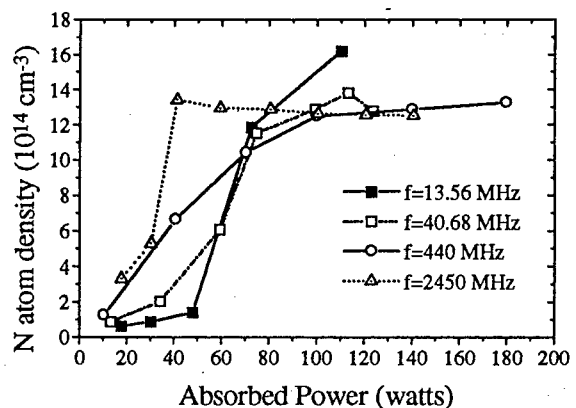


Fig.3. Variation of N atom density with absorbed power for different HF frequencies ( $p=4$  Torr).

# Estimation of Electron Density Distribution in Inductively Coupled Electrodeless Discharge

Yoshio Watanabe, Makoto Yasuda\*

Kanagawa University,

\*Hitachi Ltd.

Yokohama, Japan

## 1. Introduction.

An inductively coupled electrodeless discharge has various advantages since it is free from electrode damage. If electron density distribution in the discharge tube can be determined, discharge power and current distribution in the tube will be estimated.[1] Then the optimum dimensions of the discharge tube and the excitation coil can be designed.

## 2. Electron density distribution.

The employed discharge tube consists of an inner tube and an outer tube in a coaxial configuration and is shown in Fig.1. The excitation coil is located inside the inner tube. The discharge forms in the space between the inner and the outer tube in circumferential direction.

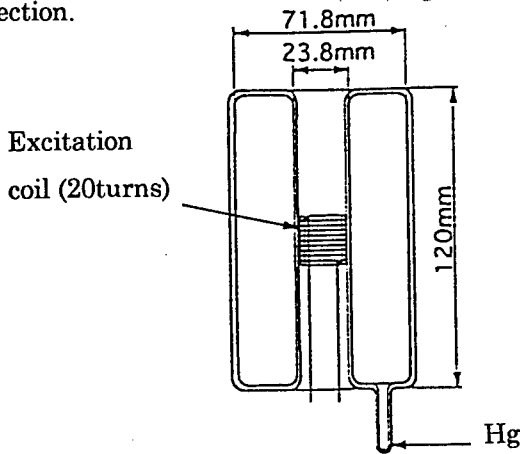


Fig.1 Experimental discharge tube configuration

The rate equation for electron density,  $n_e$ , is:

$$\frac{\partial}{\partial t} n_e = \text{div}(n_e \mu_e E - D_e \text{grad} n_e) + \nu_i n_e, \quad (1)$$

where  $\mu_e$ : electron mobility,  $E$ : electric field,  $D_e$ : electron diffusion coefficient,  $\nu_i$ : ionization

frequency. Cylindrical coordinates  $(r, \theta, z)$  are employed and  $\partial/\partial \theta = \partial/\partial z = 0$  are assumed. Under the assumption of  $\partial/\partial t = 0$  due to MHz operation and  $E_r = E_z = 0$ , eq.(1) is rewritten as follows:

$$\frac{D_e}{r} \frac{\partial}{\partial r} \left( r \frac{\partial}{\partial r} n_e \right) + \nu_i n_e = 0, \quad (2)$$

where  $D_e$  is replaced by the ambipolar diffusion coefficient,  $D_a$ . Assuming that  $\nu_i$  is proportional to electric field,  $E_\theta$ , and  $E_\theta$  is almost proportional to the inverse of the radius outside the region of the excitation coil, the expression,  $\nu_i = A/r$ , is employed where  $A$  is constant. Then eq.(2) is rewritten as follows:

$$\frac{\partial^2}{\partial x^2} n_e + \frac{1}{x} \frac{\partial}{\partial x} n_e + \frac{B}{x} n_e = 0, \quad (3)$$

where  $x = r/r_m$  ( $r_m$ : inner tube radius) and  $B = r_m A / D_a$ .

The electron density distribution is calculated with constant  $B$  by eq.(3) and shown in Fig.2 with  $r_m = 11.9\text{mm}$ ,  $r_D = 35.9\text{mm}$  ( $r_D$ : outer tube radius) and  $B = 4.4328$ .

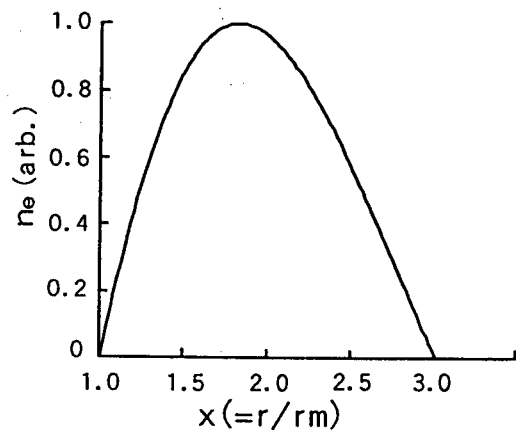


Fig.2 Calculate electron density distribution.

The density has a maximum at  $x=1.81$  ( $r=21.5$  mm).

The value of  $B$  is determined by the boundary condition,  $n_e=0$  at  $r=r_D$ .  $B$  as a function of  $(r_D/r_m-1)$  is shown in Fig.3. The relationship between  $B$  and  $(r_D/r_m-1)$  is approximated by,

$$B \doteq 15.45(r_D/r_m-1)^{-1.77}. \quad (4)$$

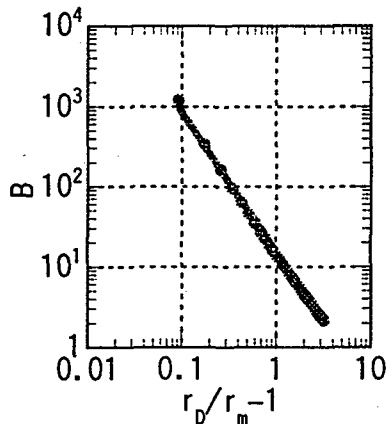


Fig.3  $B$  as a function of  $(r_D/r_m-1)$ .

### 3. Measurement of distributions of the excited mercury atom at $6^3D$ and $7^3S$ states.

The discharge tube was filled with argon of 67Pa and mercury. The distributions of the excited mercury atom at  $6^3D$  and  $7^3S$  states were measured instead of electron density, since the direct measurement of electron density distribution is difficult. The power radiated in a transition between the  $k$ th and  $j$ th state of the atom,  $I_{kj}(r)$ , is:

$$I_{kj}(r) = \frac{1}{4\pi} C_{kj} N_k(r) E_{kj}, \quad (5)$$

where  $C_{kj}$ : emission constant,  $N_k(r)$ : atom density at the  $k$ th state,  $E_{kj}$ : energy difference between the  $k$ th and  $j$ th state. Thus  $N_k(r)$  distribution can be determined by measuring  $I_{kj}(r)$  distribution using Abel inversion.

Four non-imprisonment emission lines from mercury, 312.6nm ( $6^3D_2 \rightarrow 6^3P_1$ ), 365.0nm ( $6^3D_3 \rightarrow 6^3P_2$ ), 404.7nm ( $7^3S_1 \rightarrow 6^3P_0$ ), 435.8nm ( $7^3S_1 \rightarrow 6^3P_1$ ), were employed for the measurement. The

obtained results are shown in Fig.4. Each distribution of the excited atom density has a maximum around  $r=21$ mm.

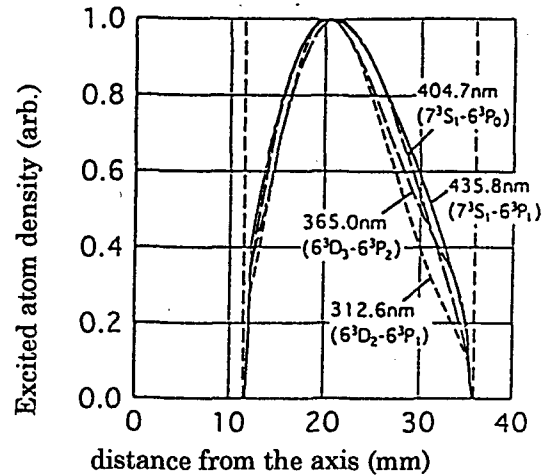


Fig.4 Measured distribution of the excited mercury atoms at  $6^3D$  and  $7^3S$  states.

### 4. Discussion.

The electron density distribution shown in Fig.2 obtained by eq.(3) and the distributions of the excited mercury atom shown in Fig.4 show good agreement both in shape and maximum position. Since the excited mercury atoms at  $6^3D$  and  $7^3S$  states (non-imprisonment level) are produced by collision between electrons and mercury atoms, it can be considered that the electron distribution should be proportional to the distributions of the excited mercury atom at  $6^3D$  and  $7^3S$  states.

### 5. Conclusion.

The electron density distribution in the inductively coupled electrodeless discharge which is calculated by eq.(3) shows good agreement with the measured distributions of the excited mercury atom at  $6^3D$  and  $7^3S$  states.

### 6. Reference.

- [1] Y.Watanabe: Jpn.J.Appl.Phys. Part 1, Vol.35, No.8, pp.4498-4502 (1996)



# Theoretical Study of Electromagnetic Phenomena in Plasma Layers and Thin Films

Ayşegül Yılmaz and Sinan Bilikmen  
Middle East Technical University,  
İnönü Bulvarı, 06531 Ankara, Türkiye .

Anri Rukhadze  
Russian Academy of Sciences, General Physics Institute 711333,  
Moscow, Russian Federation

## 1. Introduction

Our aim is to investigate the propagation of quasi-longitudinal waves in the surface layer of a magnetically confined plasma by using the scalar potential derived from Poisson equation which is independent from the distribution function of particles.

## 2. Modeling

For a collisionless, inhomogeneous, semi-bounded, magnetically confined anisotropic plasma with the characteristic length exceeding the Larmor radii of the particles (i.e.  $V_{T\alpha}/\Omega_\alpha \ll L$  :  $\alpha = i, e$ ) the following Poisson equation is derived using kinetic theory:

$$\begin{aligned} \nabla\phi = & -4\pi \sum e_\alpha^2 \int d\vec{P}_\alpha \frac{\partial F_{0\alpha}(\mathcal{E}_\alpha, x)}{\partial \mathcal{E}} \phi(x) \\ & + \sum_n 4\pi \frac{e_\alpha^2}{m_\alpha} \int d\vec{P} \int dk_x e^{ik_x x} \phi(k_x) \\ & \times \left[ \left( m_\alpha w \frac{\partial F_{0\alpha}}{\partial \mathcal{E}_\alpha} + \frac{k_y}{\Omega_\alpha} \frac{\partial F_{0\alpha}}{\partial x} \right) J_n^2(b) \right. \\ & + \frac{m_\alpha}{\Omega_\alpha^2} v_\perp^2 \frac{w}{w - k_z V_z - n\Omega_\alpha} \\ & \left. \times \frac{\partial^2 F_{0\alpha}}{\partial x^2} \left( n \frac{J_n^2(b)}{b^2} k_y - ik_x \frac{J_n(b) J'_n(b)}{b} \right) \right] \end{aligned} \quad (1)$$

where  $b = \frac{k_\perp V_{\perp\alpha}}{\Omega_\alpha}$ ,  $F_{0\alpha}(\mathcal{E}_\alpha, x)$  is either Maxwellian or Fermian, and  $J_n$  &  $J'_n$  are Bessel function and its derivative, respectively. Here one dimensional inhomogeneity is chosen along  $x$ -axis, and uniform external field is oriented along  $z$ -axis (i.e.  $\Omega_\alpha = \text{constant}$ ).  $V_{T\alpha}$  is thermal speed of particles,  $\Omega_\alpha$  is particle-cyclotron frequency,  $\vec{P}_\alpha$  is particle-momentum, and  $\mathcal{E}_\alpha$  is particle-kinetic energy.

New phenomena is expected when  $w \leq \frac{k_y}{L\Omega_\alpha} V_{T\alpha}^2 \sim \frac{V_{T\alpha}}{L^2\Omega_\alpha^2}$ . At this limit only  $n = 0$  term is essential in Eq.(1). Moreover, at long wavelengths, only  $\frac{k_\perp V_{\perp\alpha}}{\Omega_\alpha} \ll 1$  is of interest.

Then, Eq.(1) is reduced to

$$\nabla\phi = \left[ \frac{\partial}{\partial x} \gamma \frac{\partial}{\partial x} + \frac{\partial \beta}{\partial x} + \alpha - k_y^2 \gamma \right] \phi = 0 \quad (2)$$

where

$$\alpha = \sum 4\pi e_\alpha^2 \int d\vec{P}_\alpha \frac{\partial F_{0\alpha}}{\partial \mathcal{E}_\alpha} \frac{k_z V_z}{w - k_z V_z}$$

$$\beta = \sum 4\pi e_\alpha^2 \int d\vec{P}_\alpha \frac{F_{0\alpha}}{m_\alpha \Omega_\alpha} \frac{1}{w - k_z V_z}$$

$$\gamma = \sum 4\pi e_\alpha^2 \int d\vec{P}_\alpha \frac{V_{\perp\alpha}^2}{2\Omega_\alpha^2} \frac{w}{w - k_z V_z}$$

Eq.(2) is valid for all inhomogeneous plasma like media. Therefore various kinds of problems can be studied by means of Eq.(2).

We restrict ourself to the case where

$$\begin{aligned} \nabla\phi_1 = & \left[ \gamma \left( \frac{\partial^2}{\partial x^2} - k_y^2 \right) + \alpha \right] \phi_1 ; \quad x \leq |d| \\ \nabla\phi_{2,3} = & 0 ; \quad x < 0, \quad x > d \end{aligned} \quad (3)$$

Then related boundary conditions are

$$\begin{aligned} \phi|_{x=0,d} = & 0, \quad \left[ \xi \frac{\partial \phi}{\partial x} - \Lambda \phi \right]_{x=0,d} = 0, \\ \phi|_{x \rightarrow \pm\infty} = & \infty \end{aligned} \quad (4)$$

where  $\xi = 1 - \gamma$ , and  $\Lambda = k_y \beta$ . Hence solution of Eq. (3) is

$$\phi = \begin{cases} C_1 e^{-\kappa x} + C_2 e^{\kappa x}; & |x| < d \\ C_3 e^{-\eta x} & x < 0 \\ C_4 e^{\eta x} & x > d \end{cases} \quad (5)$$

where  $\kappa^2 = \frac{\alpha + k_z^2}{\xi}$ ,  $\eta = \sqrt{k_y^2 + k_z^2}$ .

## 3. Results

Eq.(5) leads to following dispersion equation:

$$\begin{aligned} (\kappa^2 \xi^2 + \eta^2 - \Lambda^2)(e^{\kappa x} - e^{-\kappa x}) \\ + 2\eta \kappa (e^{\kappa x} + e^{-\kappa x}) = 0 \end{aligned} \quad (6)$$

We observe that

- If  $Im\kappa > Re\kappa$ , Eq.(6) describes the bulk waves and coincide with  $\sin(i\kappa d) \approx 0$  at the short wavelength limit,  $\eta d \gg 1$ .
- In the case of  $Re\kappa \gg Im\kappa$ , there are two cases:  
 (a) If  $\kappa d \gg 1$  (i.e. semi bounded media) we have surface waves which are one direction with

$$\kappa\xi + \eta \pm \Lambda = 0 \quad (7)$$

(b) If  $\kappa d \ll 1$  (i.e. long wavelength limit) the surface waves are represented by the following dispersion relation

$$(\kappa\Lambda\xi^2 + \eta^2 - \Lambda^2)d + \eta\xi = 0 \quad (8)$$

Our study continues to find  $w$  at the limit of

- $w \ll \Omega_i, \quad n = 0$  and
- $k_z V_{Ti} \ll w \ll k_z V_{Te}$

for Maxwellian ion and Fermian electrons.

#### 4. References

- [1] A. Yilmaz, A. A. Rukhadze and S. Bilikmen, in preparation

***Topic 12***

**Non ideal plasmas.**

**Clusters and dusty plasmas.**

# underwater laser sparks spectroscopic characterisation using hydrogen Balmer emission lines

Alexandre ESCARGUEL\*, Alain LESAGE\*\*, Jacques RICHOU\*

\*Laboratoire d'Optoélectronique, Université de Toulon et du Var, BP 132, 83957, LA GARDE, FRANCE

\*\* Laboratoire de Physique des Plasmas, Observatoire de Meudon, 5 place Janssen 92195 MEUDON, FRANCE

## 1. Introduction

Laser breakdown, in which a substance is transformed explosively to a plasma by a focused pulsed laser beam has been studied extensively [1, 2]. The spark is a result of dielectric breakdown of the medium induced by the strong electric fields of the pulse. In the high temperatures of the spark plasma, material is reduced to elemental form and is excited and ionised. In gases and on solid samples the main spectrum feature of such plasma is the appearance of atomic and ionic lines. These lines can be used to determine plasmas parameters as temperature or electronic density [3, 4]. In pure water, laser plasmas produce a quite different sort of spectrum because of the important medium density. Indeed, atomic or ionic emission lines is less evident and the spectrum is mainly composed of an intense continuum which vanishes a few hundreds of nanoseconds after the laser pulse. Then, spectroscopic characterisation of such plasma becomes more difficult. To our knowledge, no hydrogen emission lines have been yet observed in underwater laser spark spectra. D.A. Cremers and al. studied such spectra with an experimental configuration comparable to ours [5]. They did not observe any emission from H I and only at early times a weak O I (777.4 nm) signal. In the following sections, we study time resolved spectra in different zones of underwater laser plasma, and we observe Balmer emission lines in some zones. Continuum radiation is studied and temporal evolution of electron density is calculated using Stark broadening of H $\alpha$  emission line. Results are in good agreement with D.A. Cremers and al. Results [5].

## 2. Experimental

### a. Spectroscopic measurements

We used a Nd:YAG laser of 10 ns duration with an energy  $E_l$  ranging from 10 mJ to 310 mJ. The beam was focused into the liquid by a 50 mm focal length plano-convex fused silica lens. The cell containing the samples was constructed of quartz to provide an inert environment for the liquids. The spark light was monitored at right angles to the path of the laser pulses through an achromatic cemented doublet and an optical fiber up to a Jobin-Yvon spectrometer. A 1024 pixels time-gated photodiode array provided simultaneous detection of the spark light over the whole visible region. This photodiode array was intensified with a pulse generator which was monitored with an Optical Multichannel Detector (OMA2000) connected to a personal computer.

### b. Data handling

Spark light intensity is much less intense in water than in gases. Then, to avoid too noisy line emission spectra, we had to sum over several hundreds of shots. Moreover, to have a better estimation of the noise to subtract to a series of shots, we alternately acquire the noise and the signal. We used a reconvolution method based on a least square curve fitting technique to retrieve lines parameters. Such reconvolution method has several advantages over deconvolution techniques : first, it is possible to retrieve positions, shapes and intensities of several lines overlapping each other. Secondly, the continuum which can distort in an important way emission lines spectra is fitted at the same time and then, does not need any additional treatment. Aqueous solutions were prepared with ultra-pure water having resistivity equal to 18 M $\Omega$ /cm.

### c. Size measurements

We measured plasma size using a single-mode fiber-optic connected to an achromatic cemented doublet. The other end of the fiber was connected to a photodiode directly connected to an oscilloscope. The doublet was fixed on a x-y-z micro-positioning system with a 1  $\mu$ m precision. The spark size diameter was taken to be the distance between the one half intensity points. Each measurement was averaged over several hundreds of sparks.

## 3. Laser spark characteristics in water

### a. Global spectral characteristics

The focal point, where the plasma is initiated, is dominated by an intense continuum. At a given delay  $t_p$  after plasma beginning, its intensity decreases when the observation zone shifts parallel to the laser beam towards the focusing lens. At the same time, hydrogen and oxygen emission lines (H $\alpha$  : 656.2 nm ; H $\beta$  : 486.1 nm ; O I : 777.4 nm) intensities increase and become narrower, which indicates a plasma electronic density lowering when moving from the focal point to the incident laser pulse. Hydrogen and oxygen lines are hardly visible in the focal point zone essentially for two reasons : first, concerning the O I at 777.4 nm, it is located in a low sensitive zone of the photodiode array so that the signal has to be much more intense than towards 550 nm to be detected, whatever zone is observed. Secondly, because of the high electronic density, hydrogen Balmer lines are very broad and merge easily into the background light.

## b. Continuous radiation

If we suppose that no other radiative process than Bremsstrahlung, as recombination radiation, contribute significantly to the background light spectrum before the emission lines apparition, i.e. during the first 40 ns, it is possible to estimate the plasma diameter  $d$  for which the radiative energy loss equals the radiation of a blackbody of the same diameter and temperature as the plasma during this period. If we suppose that the plasma shape is cylindrical [5], we can equal Bremsstrahlung and Planck loss rates (energy per unit time) to obtain the plasma diameter  $d$  versus electronic density and temperature ( $d(\text{m}) = 3.98\text{E}32 \cdot T^{3.5}(\text{°K})/N_e^2(\text{m}^{-3})$ ). Barnes and Rieckhoff [6] deduced a temperature of 15.000 °K at  $t_p = 15$  ns after plasma formation from the black-body-like spectrum of the continuum. Using Ca traces added to water, Cremers and al [5] measured a temperature of 11.600 °K at  $t_p = 250$  ns, which is consistent with Barnes and Rieckhoff measurements. With the help of hydrogen Balmer  $\alpha$  line Stark broadening (see paragraph d), we measured electronic densities equal to  $3.2 \times 10^{19} \text{ cm}^{-3}$  50 ns after the plasma beginning. Then we deduce that, during the first tens of nanoseconds after the laser pulse,  $d \sim 320 \mu\text{m}$ . Now, for an incident laser pulse energy  $E_l$  of 70 mJ, we experimentally measured the following plasma diameter :  $(260 \pm 10) \mu\text{m}$ , at  $t_p = 10$  ns and  $(240 \pm 10) \mu\text{m}$  at  $t_p = 100, 200$  and  $300$  ns. Then, we can conclude that the plasma spectroscopic and spatial characteristics allow it to approach the black-body spectrum intensity before the emission lines apparition, i.e. during the first 40 ns.

## c. Apparition times of hydrogen lines

The  $H\alpha$  and  $H\beta$  averaged apparition times we experimentally obtained are respectively equal to 40 ns and 100 ns. The corresponding electron densities for  $E_l = 22$  mJ are :  $N_e(t_p=40 \text{ ns}) = 4.7 \times 10^{19} \text{ cm}^{-3}$  and  $N_e(t_p=100 \text{ ns}) = 5.3 \times 10^{18} \text{ cm}^{-3}$ . We observed that when laser energy is increased, these times increase, the lines being merged into the continuum longer and longer. Now, if we consider the Inglis and Teller formula [7, 8] that gives electron density  $N_e$  versus principal quantum number  $n_m$  of the last resolved hydrogen Balmer line, the other lines with higher  $n_m$  being completely merged into continuum, we obtain the following theoretical electron density above which emission lines must be merged into continuum :  $N_e(\text{th}) = 7.6 \times 10^{19} \text{ cm}^{-3}$  (Balmer  $\alpha$  :  $n_m = 3$ ), and  $N_e(\text{th}) = 8.8 \times 10^{18} \text{ cm}^{-3}$  (Balmer  $\beta$  :  $n_m = 4$ ). Considering that Inglis and Teller formula only gives a coarse estimation, these results are in rather good agreement with  $N_e(t_p=40 \text{ ns})$  and  $N_e(t_p=100 \text{ ns})$ .

## d. Emission lines

In underwater laser sparks, Stark broadening due to the high electron density is the major contributor

to the width of most spectral lines [3, 4]. Temporal evolution of electron densities at different laser energies were calculated with the use of the Griem theory [3, 4]. We used hydrogen Balmer  $\alpha$  emission line Stark broadening, assuming that Doppler broadening is negligible compared to Stark broadening. hydrogen Balmer  $\beta$  emission line was too broadened and too weak to be analysed. We did not take into account line self-absorption. According to Cremers and al [5], we inferred that local thermodynamic equilibrium (LTE) would be established more quickly than 15 to 20 ns into the plasma lifetime. The very important electron densities found, up to  $4 \times 10^{19} \text{ cm}^{-3}$ , support this assumption. The electron density uncertainties have been estimated to be  $\pm 25\%$ . The spatial zone studied was 1 mm before the focal point, and the temporal resolution of the detection system was 10 ns. Results are shown in figure 1.

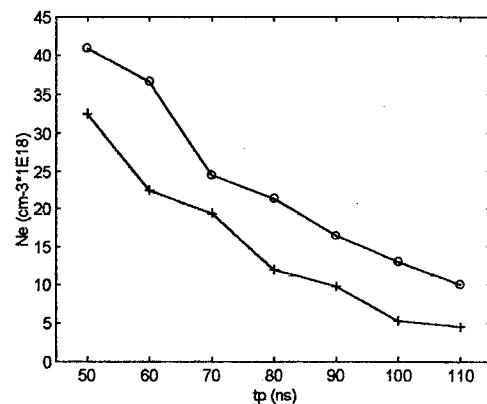


Fig. 1 : electron density as a function of delay time in underwater laser spark at two different laser energy :  $E_l = 22$  mJ (+), and  $E_l = 70$  mJ (o).

Cremers and al. [5]; using elements traces, measured the following electron densities :  $5 \times 10^{18} \text{ cm}^{-3}$  at  $t_p = 250$  ns,  $2.3 \times 10^{18} \text{ cm}^{-3}$  at  $t_p = 500$  ns and  $9 \times 10^{17} \text{ cm}^{-3}$  at  $t_p = 1 \mu\text{s}$ . Considering that they used a Nd:YAG laser with 45 mJ energy and 15 ns pulse duration, their results are in good agreement with ours.

## References

- [1] C. Grey Morgan, Rep. Prog. Phys. **38** (1975) 621.
- [2] Leon J. Radziemski, David A. Cremers, *Laser-induced plasmas and applications*, Marcel Dekker, Inc., New York and Basel, (1989).
- [3] H. R. Griem, *Plasma spectroscopy*, Academic Press, New York, (1974).
- [4] H. R. Griem, *Spectral line broadening by plasmas*, McGraw-Hill, New York, (1964).
- [5] D. A. Cremers, L. J. Radziemski and T. R. Loree, App. Spec., **38** (1984) 721.
- [6] P. A. Barnes and K. E. Rieckhoff, Apl. Phys. Lett., **13** (1968) 282.
- [7] D. R. Inglis and E. Teller, Astr. J., **90** (1939) 439.
- [8] L. H. Aller, *Gaseous nebulae*, Chapman and Hall, (1956).

# Observation of Ordered Structure in Thermal Dusty Plasmas

A.V.Chernyshev, V.E.Fortov, A.P.Nefedov, and O.F.Petrov

High Energy Density Research Center, Russian Academy of Sciences  
Izhorskaya 13/19, Moscow, 127412, Russia

## 1. Introduction

It was found in laboratory rf plasmas that negatively charged particles tend to self-organize in ordered structures [1,2]. Previously an experimental realization of the crystal-like structures has been already achieved in similar non-neutral systems of macroscopic charged particles and atomic ions in different type of traps.

The thermal plasma under study is at a low temperature, with electrons, ions, and gas all having the same temperature. When we introduce dust particles into thermal plasma, they will become charged by collecting electrons and ions, as they do in low-pressure discharges, but also by emitting electrons. The latter process can lead to a positive electric charge, unlike the negative charges in low-pressure discharge experiments.

We present here an experimental study of the formation of a macroscopic ordered structure in a weakly ionized thermal dusty plasma under atmospheric pressure and temperatures of 1700-2200 K. This is the classical neutral and extended thermal plasma that is not confined in a trap. The plasma volume and the number of particles being investigated are about of 10 cm<sup>3</sup> and 10<sup>8</sup>, respectively. The effect of boundary conditions on the plasma state may be neglected and, in consequence of this, the conditions of the structure formation are close to that in the infinite plasmas.

## 2. Experimental Setup and Procedure

The experimental facility incorporated the plasma device and the diagnostic instrumentation for the determination of particle and gas parameters [3]. The dusty plasma device uses as the basic plasma source a two-flame propane-air Meeker burner with combustion gases seeded with dust particles. Two types of the weakly ionized thermal plasmas with chemically inert dust have been studied in our experiments. The basic constituents of one type were Al<sub>2</sub>O<sub>3</sub> particles, electrons, and singly charged Na<sup>+</sup> and K<sup>+</sup> ions, and the other were formed from CeO<sub>2</sub> particles, Na<sup>+</sup> ions, and electrons. We are able to make a number of measurements of plasma parameters such as the electron and ion number densities, plasma temperature, and the diameter and number density of the particles. Employing a laser time-of-flight system, we can compute the radial pair correlation function  $g(r)$  and analyze the particles structure in the plasma spray.

## 3. Results and Discussion

The particle structure measurements were compared with a random particles distribution obtained at room temperature when only air was supplied to the burner producing the aerosol flow. This simulates a dusty plasma in its "gas phase".

Typical pair correlation functions  $g(r)$  for a spray of CeO<sub>2</sub> particles at room-temperature conditions ( $T_g \approx 300$  K) and at plasma-temperature conditions ( $T_g = 2170$  K and  $T_g = 1700$  K) are shown in Fig. 1.

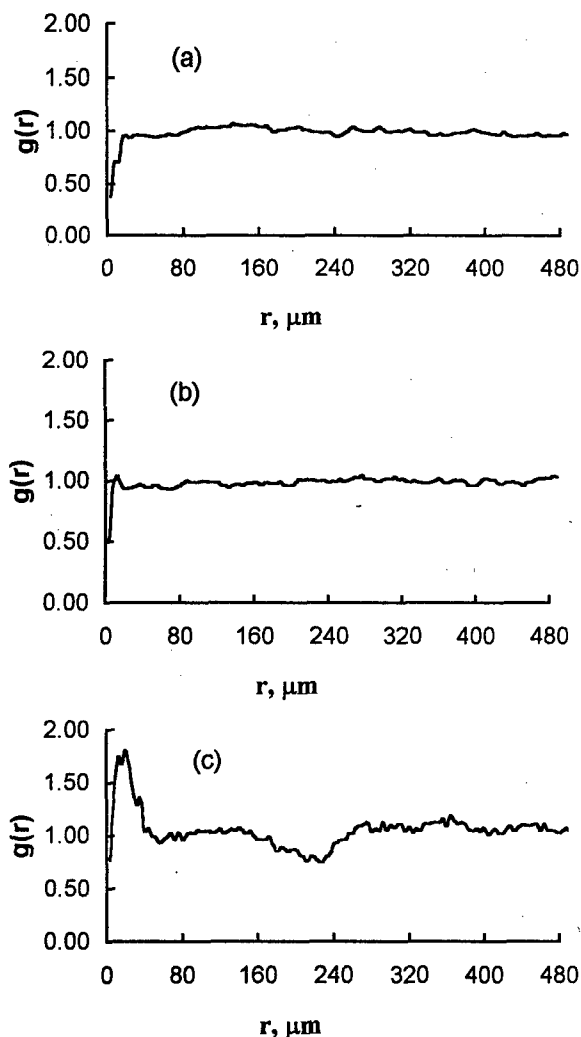


Fig. 1. Pair correlation function  $g(r)$  for spray of CeO<sub>2</sub> particles ( $Z_p=500$ ): (a) at room temperature  $T_g \approx 300$  K and  $\gamma_p=0$  ( $Z_p=0$ ); (b) at plasma temperature  $T_g=2170$  K and  $\gamma_p=40$  ( $\Gamma_s=1$ ); (c) at plasma temperature  $T_g=1700$  K and  $\gamma_p=120$  ( $\Gamma_s=40$ )

The measured mean diameter of particles was  $0.8\ \mu\text{m}$ . The  $\text{CeO}_2$  particles were charged positively and have of about  $10^3$  electron charges. It was found that pair correlation function computed at a plasma temperature  $T_g=2170\ \text{K}$  (Fig. 1a) and number density  $n_p=2.0\cdot 10^6\ \text{cm}^{-3}$  is very similar to those observed at room temperature (random gaslike distribution). Therefore the plasma is weakly coupled and does not exhibit the formation of ordered structure. This fact is also verified by plasma diagnostics. From our optical and probe measurements we obtain that the mean interparticle distance ( $\langle r \rangle = 50\ \mu\text{m}$ ) is approximately four times the Debye length ( $r_D = 14\ \mu\text{m}$ ) and that the Coulomb coupling parameter  $\gamma_p$  is about 40. The estimated value of parameter  $\Gamma_s = Z_p^2 e^2 \exp(-\langle r \rangle / r_D) / \langle r \rangle k T_g$  is about 1.

Figure 2 shows the range of  $n_e$  and  $n_p$  where ordered structure takes place. The theoretical boundaries of the OCP and Yukawa model are indicated [4,5].

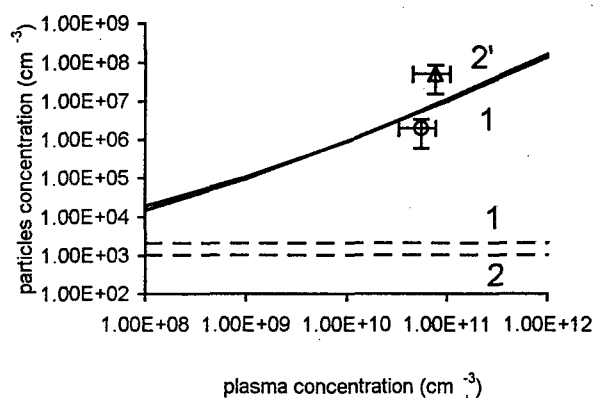


Fig. 2. The range of plasma density ( $n_e+n_p$ ) and particle density  $n_p$  in which an ordered structure is formed when  $Z_p=500$ . The curves 1 (1') and 2 (2') correspond to  $\gamma_p=4$  ( $\Gamma_s=4$ ) at  $T_g=1700\ \text{K}$  and  $2200\ \text{K}$ , respectively:  $\gamma_p=40$  ( $\Gamma_s=1$ ) ( $\circ$ ) and  $\gamma_p=120$  ( $\Gamma_s=40$ ) ( $\Delta$ ) for the plasma with  $\text{CeO}_2$  particles

The short-range order condition is satisfied in the region above curves 1 and 2 (OCP model) and curves 1' and 2' (Yukawa model). The boundary curves 1 (1') ( $T_g=1700\ \text{K}$ ) and 2 (2') ( $T_g=2200\ \text{K}$ ) correspond to  $\gamma_p=4$  ( $\Gamma_s=4$ ). The Yukawa model predicts higher values of  $\gamma_p$  for the observed interparticle distance  $\langle r \rangle$  and the Debye length  $r_D$ . The experimental data point (circle) lies between the curves 1(2) and 1'(2'). The appropriate pair correlation function  $g(r)$  is shown in Fig. 1b. It can be seen that the state of the strongly coupled plasma is found with corresponding values of  $\Gamma_s=4$  and  $\gamma_p=160$ . This value of the coupling parameter  $\gamma_p$  is approximately 40 times larger than the critical value for the OCP model. By this means the experimental data are in accordance with the Yukawa model.

In the case of the lower plasma temperature ( $T_g=1700\ \text{K}$ ) and particle number density  $n_p=5.0\cdot 10^7\ \text{cm}^{-3}$ , Fig. 1(c) shows the pair correlation function  $g(r)$ , in which the distinctive short-range order of a liquid system is apparent. The calculated values of  $\gamma_p$  and  $\Gamma_s$  are about 120 and 40, respectively. That corresponds to a strongly coupled system of positively charged particles and electrons. The particles form an ordered structure, which is in agreement with the diagram of plasma states as shown by the triangle in Fig. 2. The corresponding pair correlation function is shown in Fig. 1(c).

Decreasing the density of  $\text{CeO}_2$  particles increases the mean interparticle distance and causes a reduction in the Coulomb energy. The spatially ordered structure no longer holds, as is seen in Fig. 1(b) for  $n_p=2.0\cdot 10^6\ \text{cm}^{-3}$ .

The plasma with  $\text{Al}_2\text{O}_3$  particles was studied at temperatures in the range  $T_g=1900-2200\ \text{K}$ . The mean size of particles was about  $1.5\ \mu\text{m}$ . Due to the larger numbers of alkali ions and electrons, the Debye screening reduces the Coulomb interaction. For example, taking  $T_g=2035\ \text{K}$ ,  $n_i=8.6\cdot 10^{10}\ \text{cm}^{-3}$ ,  $n_e=1.3\cdot 10^{11}\ \text{cm}^{-3}$ , and  $n_p=1.0\cdot 10^6\ \text{cm}^{-3}$ , we obtain the values  $r_D = 6.5\ \mu\text{m}$  and  $\langle r \rangle = 60\ \mu\text{m}$ . Since  $\langle r \rangle \cong 9r_D$ , the particles are significantly shielded from each other and do not form a space-ordered structure.

#### 4. References

- [1] J.H.Chu and L.I, Phys Rev. Lett. 72, 4009 (1994).
- [2] H.Thomas, G.E.Morfill, V.Demmel et al., Phys Rev. Lett. 73, 652 (1994).
- [3] V.E.Fortov, A.P.Nefedov, O.F.Petrov et al., Phys. Rev. E: 54, R2236 (1996).
- [4] S.Ichimaru, Rev. Mod. Phys. 54, 1017 (1982).
- [5] M.O.Robbins, K.Kremer, and G.S.Grest, J. Chem. Phys. 88, 3286 (1988).

# Dusty plasma ordered structures in the stratified dc glow discharge

V.E.Fortov, A.M.Lipaev, V.I.Molotkov, A.P.Nefedov, O.F.Petrov, V.M.Torchinskii

High Energy Density Research Center, Russian Academy of Sciences,  
Izhorskaya 13/19, Moscow, 127412, Russia  
Tel: (095)4842300, Fax: (095)4857990, E-mail: ipdust@hedric.msk.su

## 1. Introduction

It was found in 1994 [1, 2] that dusty plasmas could be made to "crystallize" under certain conditions. These conditions were realized in radio-frequency discharges. A plasma crystal forms near the bottom electrode at the boundary of the cathode sheath. Dusty plasma crystals have some unique properties and promise to be an indispensable research tool both in the investigation of properties of strongly coupled plasmas and in the investigation of fundamental properties of crystals.

Here we report the results of experiments that open up the new field of existence of dusty plasma ordered structures and a new area to the experimenter. We have discovered [3] the formation of macroscopic ordered structures of the negatively charged dust particles in the standing striations of a direct current glow discharge in Ne. Subsequent experiments revealed several interesting features of these structures.

## 2. Results and discussion

The glow discharge was produced in a cylindrical vertically positioned glass tube with cold electrodes. The inner diameter of the tube was 3 cm and the distance between electrodes was 40 cm. The discharge current ranged from 0.1 to 10 mA and the neon pressure ranged from 0.2 to 2 Torr. Discharge regimes with natural standing striations existed in this range. Micron sized particles were injected from a container located on the top of the discharge tube. Falling particles were trapped and suspended in the striations. Two kinds of dust grains were used: berossilicate glass microballoons 50-63 microns in diameter with wall thickness of 1-5 microns (particle mass  $M_p$  is in the range  $3 \cdot 10^{-8}$  -  $8 \cdot 10^{-8}$  g), and alumina particles 3-5 microns in diameter ( $M_p$  is in the range  $6 \cdot 10^{-11}$  -  $3 \cdot 10^{-10}$  g). Particles were illuminated by a horizontal or vertical sheet of Ar laser light and imaged with a CCD video camera. Dust particles were seen as a cloud levitated in the centre of luminous part of a striation. Usually a few clouds were observed in adjacent striations. The cloud diameter was in the range of 5-20 mm. The particles were organised in 10-20 (for glass particles) and more (for alumina particles) planar layers. Distances between layers were in the range of 200-400 microns. Interparticle distances in the horizontal plane were 250-600 microns.

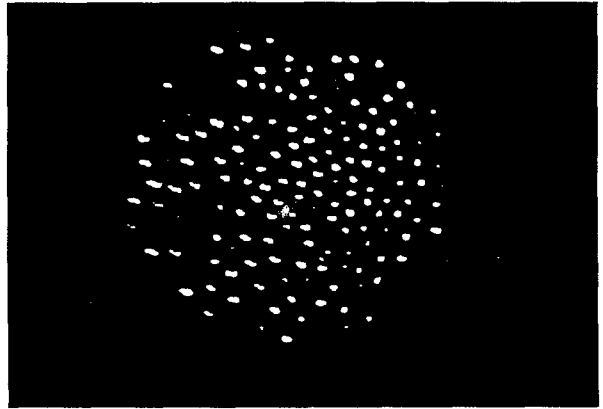
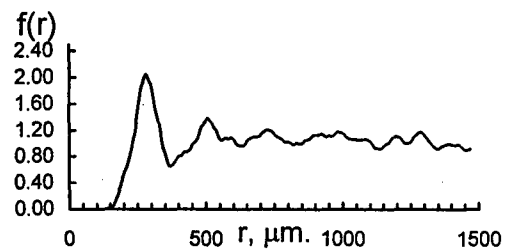
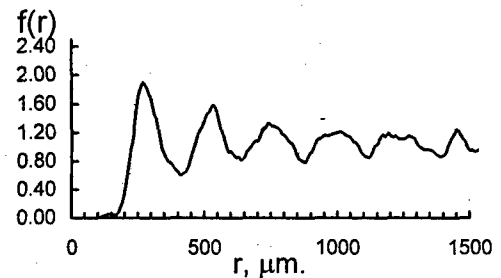


Figure 1

Fig.1 displays an example of the structure observed in the horizontal plane for alumina particles at  $p = 0.3$  Torr and discharge current  $I_d = 0.4$  mA.





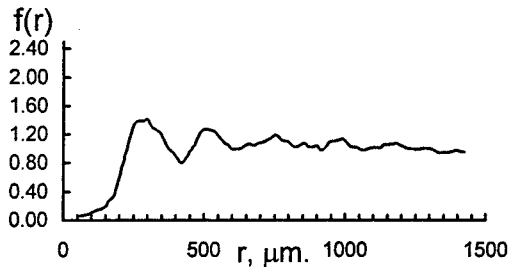


Figure 2

Fig.2 shows pair correlation functions obtained from images at discharge currents equal, correspondingly, to 0.4; 0.9; 3.9 mA at the above mentioned pressure. It is seen that at  $I_d = 0.4$  mA there are at least five peaks that testifies an existence of long-range order in the dusty plasma. This corresponds to the crystallike structure. It follows from the correlation functions obtained that with increasing current the long-range order is being disturbed. In the case of  $I_d = 3.9$  mA only the short-range order is observed. It is noteworthy that the nearest neighbour distance  $a_p$  which is equal to 270 microns is nearly unchanged during the current increase (that is, during ion and electron density increase almost by an order of magnitude) This behaviour is quite different in comparison with investigations in radio frequency dusty plasma [4] where a change of ion density caused a significant variation of  $a_p$ . Let's make estimations of plasma parameters in these experiments. It follows from measurements in neon glow discharges [5,6] that in the case of  $I_d = 0.4$  mA parameters in the striation head are as follows: electron density  $n_e = 10^8 \text{ cm}^{-3}$ , electron temperature  $T_e = 6 \cdot 10^4 \text{ K}$ , electron Debye length  $1700 \mu\text{m}$ , ion Debye length  $120 \mu\text{m}$ . The particle charge can be estimated from the value of floating potential in the striation head [6] and from the balance of gravity and electrical field. For alumina particles we have the particle charge  $Z_p = 2 \cdot 10^4$ . Taking this into account we obtain the Coulomb coupling parameter  $\Gamma = 10^5$ . Assuming that the screening is due to ions we have with an account of screening  $\Gamma_{scr} = 10^4$ . In the case of  $I_d = 3.9$  mA:  $n_e = 8 \cdot 10^8 \text{ cm}^{-3}$ , electron Debye length  $600 \mu\text{m}$ ; ion Debye length  $40 \mu\text{m}$ . Here, we obtain  $\Gamma = 10^5$  and  $\Gamma_{scr} = 10^2$ . These estimations correlate with the behaviour of the structures observed.

Notice that for glass particles  $Z_p$  is equal to  $2 \cdot 10^6$  electrons. So, for both kinds of particles used in our experiments the ratio of the particle charge to its mass has  $\sim 10^{14}$  electrons/g. This is almost one order of magnitude greater than in the case of radio frequency discharge plasmas.

Note one more interesting feature of the dc glow discharge dusty plasma. By properly adjusting the plasma parameters it was possible in these experiments to modify a shape of the particle cloud from an

ellipsoidal structure to the threadlike structure extended up to 60 mm. The magnified fragment of such structure observed for glass particles is given as an example in Fig.3 (The bar is equal to 1 mm).

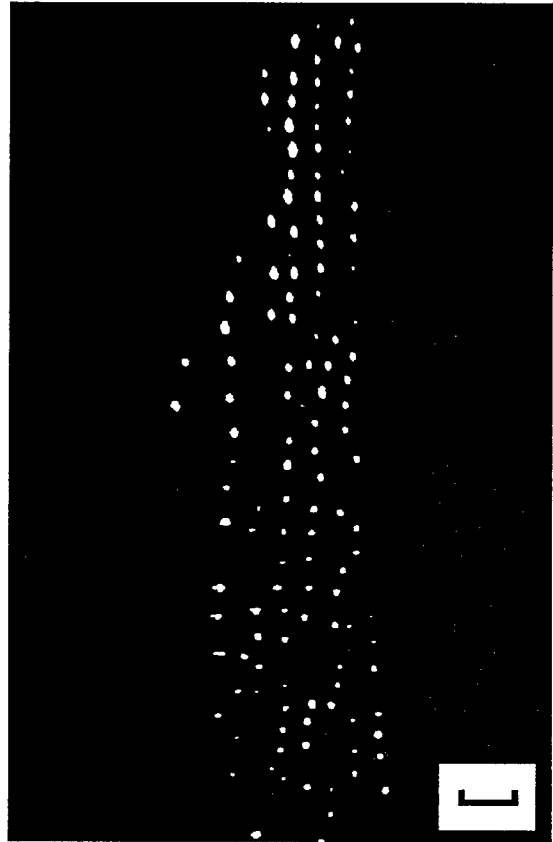


Figure 3

### 3. References

- [1] H.Thomas, G.E.Morfill, V.Demmel, J.Goree, B.Feuerbacher, and D.Mohlmann:Phys.Rev.Lett.,73 (1994) 652
- [2] J.Chu, and I.Lin: Phys.Rev.Lett.,72 (1994) 4009
- [3] V.Fortov, A.Nefedov, V.Torchinskii, V.Molotkov, A.Khrapak, O.Petrov, and K.Volykhin;JETP Lett.,64 (1996) 92
- [4] Th.Trottenberg, A.Melzer, and A.Piel; Plasma Sci. Technol.,4 (1995) 450
- [5] J.Behnke, Yu.Golubovsky, S.Nisimov, I.Porokhova:Contrib. Plasma Phys.,36 (1996) 75
- [6] Yu.Golubovsky, S.Nisimov:Jour. Techn. Phys. (Russia),65 (1995) 46

# Shell Structure of Pure Ion Plasmas

A.M. Ignatov

General Physics Institute, 117942, Moscow, Russia

## 1. Introduction

Pure ion plasma is an unneutralized cloud consisting of some number of ions (up to few thousands) confined by external electromagnetic fields. The thermal energy of such a cloud may be extremely low, so that the gaseous parameter, that is, the ratio of average potential and kinetic energies of a particle, is much larger than unity.

Both physical and computer experiments indicate that pure ion plasmas at sufficiently low temperature exhibit a number of phase states resembling crystall or smectic liquid crystal. (It should be noted that many habitual concepts like temperature are rather conventional in application to this plasma. Strictly speaking, it is a nonthermodynamic system.) In the present paper we focus on the phenomenon discussed in Refs. 1-3. It was found that a uniform ion cloud tends to split in a few concentric shells like those shown in Fig.1. Here we present a simple theory describing some of the features of this transition.

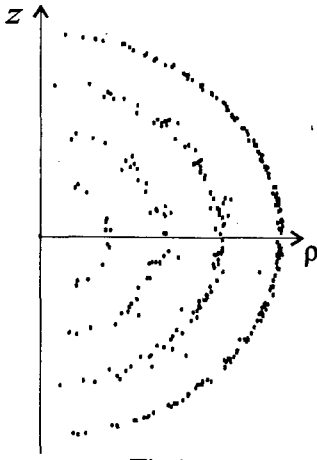


Fig.1.

## 2. Basic equations

The model we study is just a set of  $N$  charged particles placed in a potential well without any neutralizing background. For simplicity, we consider a spherically symmetric well with the potential

$$\psi(\mathbf{r}) = \frac{m}{2e} \omega_0^2 \mathbf{r}^2 \quad (1)$$

This potential well is a reasonable approximation for the Penning trap. Fig.1 shows the spatial distribution in polar coordinates for 300

ions obtained by computer minimization of the total potential energy:

$$U = \sum_i e \psi(\mathbf{r}_i) + \frac{1}{2} \sum_{i \neq j} \frac{e^2}{|\mathbf{r}_i - \mathbf{r}_j|} \quad (2)$$

It is clearly visible that particles tend to concentrate near 5 spheric shells (the first shell consists of a single ion placed exactly at the origin). The similar results were obtained in Refs.[1-3] using molecular dynamics simulations. This means that this structure is rather due to the electrostatics than due to the dynamics.

Our main purpose is to evaluate the minimum of the total potential energy of the particle set and to estimate the character of the distribution over the shells. We assume that the particles organize themselves in  $M$  concentric spheric shells of growing radii  $R_i$  ( $R_1 < R_2 < \dots$ ) each containing  $N_i$  ions ( $i=1..M$ ,  $N = \sum_{i=1}^M N_i$ ). In ignoring the structure and the thickness of the shells, we treat each shell as a uniformly charged thin spheric layer and find that the approximation for the total potential energy (2),  $W(R_i, N_i, M)$ , consists of three parts:

$$W = \sum_{i=1}^M \left[ \frac{1}{2} m \omega_0^2 R_i^2 N_i \quad (\text{External energy}) \right. \\ \left. + \frac{1}{2} \frac{e^2}{R_i} N_i^2 \quad (\text{Self energy of the } i\text{-th shell}) \right. \\ \left. + \frac{e^2}{R_i} N_i \sum_{j=1}^{i-1} N_j \right] \quad (\text{Energy of the } i\text{-th shell in the field of all inner shells}) \quad (3)$$

Our task here is to find the minimum of this energy with respect to  $R_i$  and  $N_i$ .

Force balance is determined by the condition  $dW/dR_i = 0$  resulting in the expression for equilibrium radii of the shells:

$$R_i^3 = \frac{e^2}{m \omega_0^2} \left( \frac{1}{2} N_i + \sum_{j=1}^{i-1} N_j \right) \quad (4)$$

The next step is to minimize the potential energy (3) with  $R_i$  given by Eq.(4) with respect to shell charges  $N_i$  at fixed  $N$  and  $M$ . This yields rather bulky equations, which, however, may be explicitly solved:

$$N_i = \frac{\Lambda_i - \Lambda_{i-1}}{\Lambda_M} N \quad (5)$$

where  $\Lambda_i$  form a sequence of numbers:  $\Lambda_0=0$ ,  $\Lambda_1=1$ ,  $\Lambda_2=2.808$ ,  $\Lambda_3=5.342$ ,  $\Lambda_4=8.554$  etc. For large  $i \gg 1$ ,  $\Lambda_i \approx 0.602i^{9/5}$ , where the pre-exponent factor is a result of numeric adjustment, while the exponent (9/5) is exact. This results in the following asymptotic dependence for shell charge and radius:

$$N_i \approx \frac{9}{5} \frac{i^{4/5}}{M^{9/5}} N$$

$$R_i \approx \left( \frac{e^2}{m\omega_0^2} \right)^{1/3} \frac{i^{3/5}}{M^{3/5}} N^{1/3} \quad (6)$$

The results of numeric minimization of the potential energy (2) for  $N = 4 \div 330$  are depicted in Fig. 2 and 3. Evidently, the dependences of  $N_i$  (Fig.2) and  $R_i$  (Fig.3) on  $N$  correspond to analytical expressions (6). However, the number of runs we performed is not enough to determine the dependencies on the shell number,  $i$ .

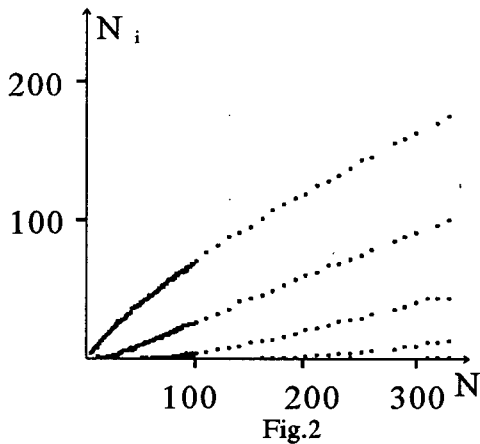


Fig.2

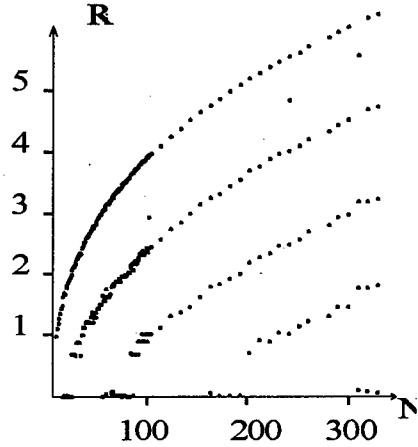


Fig.3

Within the approximations we have used, the energy,  $W$ , does not take any extremal values as a function of number of shells,  $M$ , but was found to be a very slowly growing sequence. Seemingly, this means that in order to pick the optimal value of  $M$  one should take into account the inner structure of the shells. However, we can estimate their number in a following manner. Computer runs show that with the growing number of particles,  $N$ , the number of shells also grows. Since the smallest shell have to contain at least one particle, we must impose the constrain  $N_1 \geq 1$ , that is, the number of shells is estimated as  $M \propto N^{5/9}$ .

### References

1. A.Rahman and J.P. Schiffer, Phys. Rev. Lett. **57**, 1133 (1986).
2. J.P. Schiffer, Phys. Rev. Lett. **61**, 1843 (1988).
3. D.H.E. Dubin and T.M. O'Neil, Phys. Rev. Lett. **60**, 511 (1988).

# Electron energy distribution function in a dusty plasma.

V.V. Ivanov, T.V. Rakhimova

119899, Nuclear Physics Institute, Moscow State University, Moscow, Russia

Physical processes in dusty plasmas are studied intensively because of their importance for a number of applications in various technologies (plasma etching, plasma deposition, etc). The particles of dust created in the plasma volume by gas polymerisation or by plasma - surface interaction can change plasma features and therefore technology processes. On the other hand, studying the ability of microparticles to form the solid phase structure (Coulomb crystal) may contribute not only to the plasma physics and chemistry, but also the solid state physics. A number of theoretical and experimental efforts were focused on investigation of plasma electrodynamics with microparticles, the role of negative ions in nucleation of critically large clusters and particle growth [1-3].

One of the main problems in plasma with microparticles is their influence on electron distribution function.

The influence of microparticles on the electron energy distribution function (EEDF) in the electropositive gas is considered in the report. The research is based on solving the Boltzman equation in the two-term approximation (TTA) [4]. The Debye radius is supposed to be less than the distance between microparticles. Microparticles can be considered as volume drains for positive and negative charges. The positive charge flux to microparticles related to their drift was considered in the assumption of their Maxwellian velocity distribution. The flux of electrons to microparticles (depending on electron energy) was determined in assumption of Coulomb potential of microparticles (with charge  $z_d$ ). The cross section of this process was written as follows:  $\sigma_e^k = \eta \pi r_d^2 (1 - e^2 k / (r_d \epsilon_e))$ , where  $r_d$  is the radius of a microparticle,  $\epsilon_e$  - electron energy,  $\eta$  - the probability of electron attachment to microparticle. The stationary EEDF corresponds to the distribution of microparticles with respect to charges, in which the fluxes of electrons and ions on microparticles are equal one to another.

In the common case, the stationary EEDF in a given gas is determined by large number of parameters, such as gas density  $N$ , the reduced electrical field  $E/N$ , density of electrons  $n_e$ , different types of ions  $n_i^j$ , density of microparticles  $n_d$  and their size distribution. Even if we limit ourselves to microparticles of only one size  $r_d$ , the number of the parameters appears to be unreasonably large.

The number of the parameters may be considerably reduced, assuming that all the microparticles in plasma have the same average charge  $z_d$ . In this case, the EEDF determined from

the Boltzman equation solution in TTA depends only on three parameters:  $E/N$ , potential of the microparticle  $\phi = e z_d / r_d$  and the reduced microparticle surface

$S_d = \eta \pi r_d^2 N_d / N$ . Therefore, it is possible to solve this problem even on PC AT. Parameter  $\phi$  can be determined from the continuity equations for electrons, ions and microparticles taking into account the losses of electrons and ions on microparticles. In the case of homogeneous quasineutral plasma, these equations are reduced to the following:

$$dn_e/dt = n_e N \langle \sigma v \rangle_{ion} - n_e n_d \langle \sigma v \rangle_{esc}^e, \quad (1)$$

$$dn_i/dt = n_e N \langle \sigma v \rangle_{ion} - n_i n_d \langle \sigma v \rangle_{esc}^i, \quad (2)$$

$$z_d = (n_i - n_e) / n_d. \quad (3)$$

The ionization rate constant  $\langle \sigma v \rangle_{ion}$  and the attachment rate constant of electrons to microparticle  $\langle \sigma v \rangle_{esc}^e$  were taken from the results of the EEDF calculations, attachment rate constant of ions to microparticle  $\langle \sigma v \rangle_{esc}^i$ , supposing that their Maxwellian velocity distribution may be written as follows:

$\pi r_d^2 (T_i / (2\pi m_i))^{1/2} (1 + e^2 k / (r_d T_i))$ , where  $T_i$  and  $m_i$  are the temperature and mass of the ion.

To close this equation set, an additional condition, for example, the constancy of the current density, is necessary. These equations are integrated numerically until a steady-state regime is reached. As a result, the values of ion and electron density, the reduced electrical field and average charge of a microparticle may be determined.

The dependences of the EEDF on the electron energy  $\epsilon$  and microparticle potential  $\phi$  in plasma of helium at  $E/N = 30$  Td are shown on Fig. 1

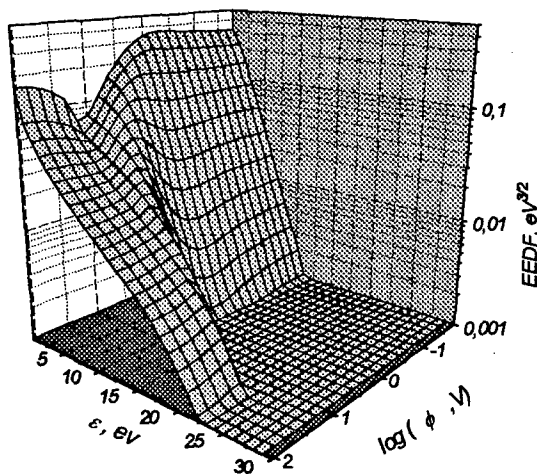


Fig.1 EEDF at  $S_d = 10^{-17} \text{ cm}^2$  and  $E/N = 30$  Td in dependence of microparticle potential and electron energy.

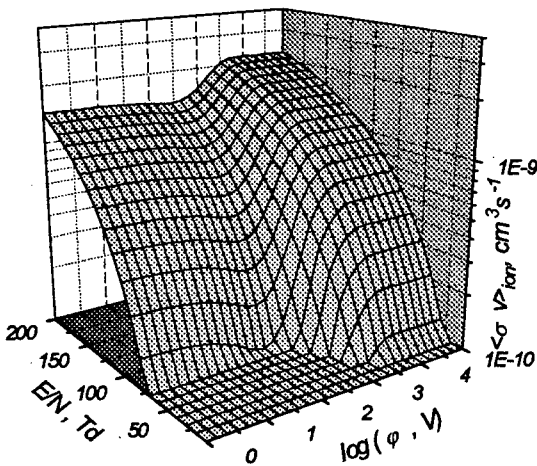


Fig.2  $\langle \sigma v \rangle_{\text{ion}}$  dependence on microparticle potential and reduced electric field at  $S_d = 10^{-17} \text{ cm}^2$

for  $S_d = 10^{-17} \text{ cm}^2$ . As it is seen from the figure, the EEDF significantly varies with  $\varphi$ . The flux of high energy electrons on microparticle significantly decreases this part of the EEDF at low  $\varphi$ . It is more evident for the processes that depend on a high energy part of the EEDF, for example, for ionization. In Fig. 2, the dependence of the ionization coefficient on  $\varphi$  and  $E/N$  is shown for  $S_d = 10^{-17} \text{ cm}^2$ . It is worth noting that this dependence is not monotonous. The ionization rate constant has a minimum at a medium value of  $\varphi$ . Such a behaviour is explained as follows. For large  $\varphi$ , the electron flux on microparticles is absent and the ionization rate constant reaches its maximum value. The decrease of  $\varphi$  results in reaching the microparticles by the high energy electrons. As a result, the high energy part of the EEDF decreases and the ionization rate constant falls. Further downturn of  $\varphi$  results in losses on microparticles of the low energy electrons, which are unable to ionize gas. Owing to the EEDF normalization, it is equivalent to the increase of the high energy part of the EEDF and some increase in the ionization rate constant.

The EEDF is calculated in the assumption of equal charges of all the microparticles. Nevertheless, it allows one to determine the distribution of microparticles on charges  $F(z)$  in the case of weak EEDF dependence of  $\varphi$ . In fact, considering only integer  $z$ , we can determine the frequencies of electron losses of on microparticles with different charges,  $v_e^z$ . The frequencies of losses of positive ions on microparticles of different charges  $v_i^z$ , may be determined in the assumption of their Maxwellian velocity distribution [5]. The frequencies obtained allow us to determine  $F(z)$  from the stationary balance equation:  $F(z+1) = F(z) * v_e^z / v_i^{z+1}$  with normalization

condition  $\Sigma F(z) = 1$ . Fig. 3 shows  $F(z)$  distributions for the ion temperature  $T_i = 0.1 \text{ eV}$  and  $E/N = 10 \text{ Td}$ . For comparison, we have also plotted the  $F(z)$  calculated in the assumption of the Maxwellian distribution for electrons. The electron temperature needed for these calculations was calculated using the EEDF for given  $E/N$  and  $\varphi$ .

Fig.3 shows that the results of  $F(z)$  calculation have practically the same behavior for different EEDF. As was expected, deviation of the EEDF shape from the Maxwellian one results in a small reduction of average charge of a microparticle. It is possible that in molecular gases (for example,  $\text{N}_2$ ), or in the region of strong  $\varphi$ , the dependence on the EEDF and the deviation of  $F(z)$  shape from the Maxwellian one will be more pronounced.

This work was supported by grant 96-02-18938 from the Russian Foundation of Fundamental Research.

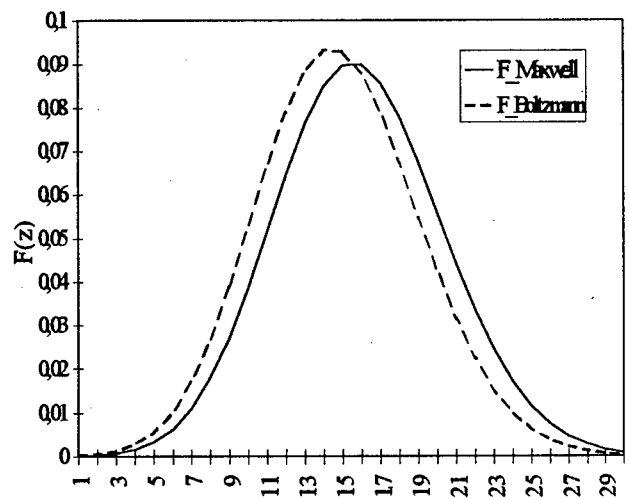


Fig3 Microparticles charge distribution function at  $T_{\text{ion}} = 0.1 \text{ eV}$  and  $E/N = 10 \text{ Td}$

#### References

- [1]. G.S.Selwyn, J.E.Heidenreich, K.L.Haller Appl. Phys. Lett. 57 (1990) 1876.
- [2]. J. P. Boeuf Phys. Rev. A 46 (1992) 7910
- [3]. S.J.Choi, M.J.Kushner J.Appl. Phys. 74 (1993) 853
- [4]. Yu. P. Raizer The physics of gas discharge. (Russ). Moscow, Nauka, 1987
- [5]. V.A. Schweigert and I.V. Schweigert: J.Phys. D 29 (1996) 655

# Spectral Diagnostics of Optical Constants of Particles in Dusty Plasma

A. Kirillin, A. Samarian, O. Vaulina.

High Energy Density Research Center, Russian Academy of Sciences,  
Izhorskaya 13/19, Moscow, 127412, Russia

Tel: (095)4842355, Fax: (095)4857990, E-mail: ipdustpl@redline.ru

## 1. Introduction

A presence of the disperse phase in ionized gas may considerably influence on its optical properties, electrical conduction, processes of radiative heat transfer and proceeding of the chemical reactions. The development of techniques for non-intrusive determining the particle sizes and optical constants provides a means for studying different physical processes in the dusty plasma. As an example the complex refractive index of particles contains information regarding their physical properties such as chemical composition, temperature, state of aggregation of matter, type of conduction. The primary difficulty associated with diagnostic optical methods is inverting the measurements for particle size and optical constants simultaneously. The analytical techniques for solving inverse problems usually do not possess a unique solution. Because of this, most diagnostic methods require the use of a priori information regarding the size distribution or optical constants of particles.

The purpose of this work was to develop a practicable technique for spectral diagnostics of particle in dusty plasma flows. Here we present two optical methods developed for determining the particle temperature, mean size, concentration and complex refractive index. The complex use of these methods does not require a priori knowledge of the particle sizes, complex refractive index or its spectral dependence. One of the methods is based on measurements of forward scattering transmittance (FST) at the different aperture angle of detector. This method has been successfully used to retrieve the particle mean size, concentration and real refractive index of the polydispersions in the dusty plasma [1].

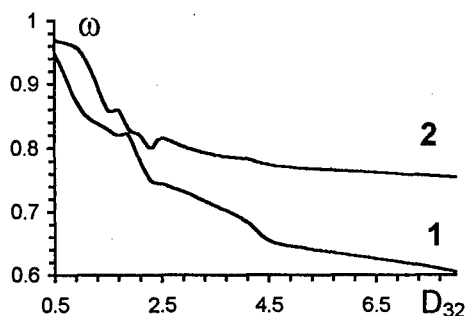
In this work we consider the particles which are optically non-grey at the measurement wavelengths. The temperature of these particles is measured by the spectroscopic method involving the approximate relationships for the spectral dependencies of the single scattering albedo [2]. The temperature  $T_p$  of the particles is measured by the spectroscopic method. The method is based on solving a system of radiative transfer equations for light intensity measurements at several wavelengths  $\lambda$  [2]:

$$I(\lambda) = \varepsilon(\lambda) B(T_p, \lambda) \quad (1)$$

Here,  $I(\lambda)$  is the radiation intensity,  $B(T_p, \lambda)$  is the Planck blackbody function,  $\varepsilon(\lambda)$  is the emissive ability of the particles suspended in a plasma. This method was advanced, owing to the developed technique for inverting the measurements. We propose a novel spectroscopic method for determination of the particle Sauter mean size and image part of the refractive index.

## 2. Theory

We concentrate on the empirical inversion of spectral measurements here. Empirical inversion techniques are based on computer simulations of the scattering or extinction processes. Then, the particle parameters can be obtained by minimizing a mean-squares error between measured and calculated data. Calculations are performed by using the Mie theory here. The inversion technique for determining the particle Sauter mean size  $D_{32}$  and image part  $k$  of the refractive index is based on the measurements of a single scattering albedo  $\omega$  for weakly absorbed particles ( $k < 0.1$ ). The spectral distribution of the albedo  $\omega(\lambda)$  is uniquely determined by the particle sizes under the assumption that the particle refractive index is independent of measurement wavelengths. The values of the single scattering albedo at one of measurement wavelengths contains information on the image part of the particle refractive index. Therefore, with a knowledge of the particle sizes and real refractive index, the spectral dependence of  $k$  can be easily measured. Dependencies of the single-scattering albedo  $\omega(\lambda)$  on the particle Sauter mean diameter  $D_{32}$  and the image part  $k$  of the particle refractive index are shown in Figs. 1a,b for the Gaussian distribution with the standard deviation  $\delta = 25\%$ .



a)

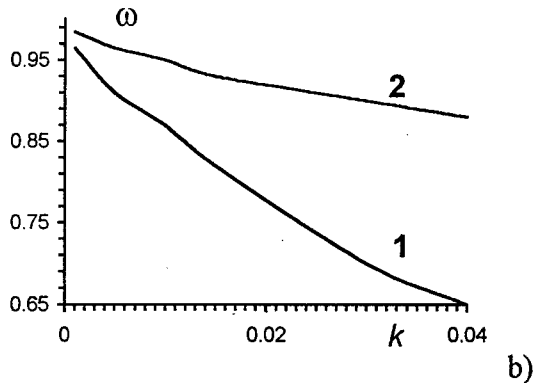


Fig.1 Dependencies of the single-scattering albedo  $\omega$  on the particle Sauter mean diameter  $D_{32}$  (a) and the image refractive index  $k$  (b) for the Gaussian distribution with the standard deviation  $\delta=25\%$ :

a)  $m=1.7-0.01i$ ,  $1-\lambda=0.5\mu\text{m}$ ,  $2-\lambda=1\mu\text{m}$ ;

b)  $n=1.7$ ,  $\lambda=1\mu\text{m}$ ,  $1-D_{32}=0.5\mu\text{m}$ ,  $2-D_{32}=1\mu\text{m}$ .

The values of the single scattering albedo can be obtained from the emissive ability  $\epsilon(\lambda)$  of the dusty plasma. Assuming that multiple in-scattering is negligible yields [2]

$$\epsilon(\lambda) = (1 - \omega(\lambda)) (1 - \exp\{-\tau(\lambda)\}) \quad (2)$$

where  $\tau(\lambda)$  is the optical depth of the suspended particles. Thus the measurements of the particle temperature and optical depth provide a means for determining the  $\omega(\lambda)$  values from Eqs. 1 - 2.

### 3. Experiment

The polydispersions of weakly absorbing particles of  $\text{CeO}_2$ , and ash in the flow of the propane-air flame combustion products were measured at the spectral range from 0.5 to 1.2  $\mu\text{m}$ . The particle temperature was varied from 1800 to 2250 K. The particles were introduced in the inner flame of the Mekker combustor. The optical instrument consists of two parts: the FST channel and the spectroscopic channel. The particle temperature ( $T_p$ ), complex refractive index ( $m=n-ik$ ) and mean diameter ( $D_{32}$ ) are obtained. The results of measurements are given in Table 1.

Table 1. The results of measurements for the particles of ash and  $\text{CeO}_2$ .

particles	$T_p$ , K	$D_1$ , $\mu\text{m}$	$D_2$ , $\mu\text{m}$	$k, 10^{-2}$	$n$
ash	1927	1.73	1.78	0.88	1.68
	2086	1.57	1.60	1.05	1.68
$\text{CeO}_2$	2025	1.23	1.26	1.76	2.05
	2227	1.17	1.20	1.98	1.98

The mean Sauter diameter of the particles are measured by several techniques such as the FST technique ( $D_1$ ), the novel spectroscopic method ( $D_2$ ) and the spectral

transmittance method. The obtained values of particle Sauter mean diameter are in close agreement. The use of the FST technique also provides a means for estimating the dispersion of particle sizes. The ratio  $\mu=D_{32}/D_{10}$ , where  $D_{10}$  is the particle mean diameter, for the ash particle is about 1.08. For the model Gaussian distribution, this value of  $m$  corresponds the standard deviation  $\delta G=20-25\%$ . The  $\mu$  value for the  $\text{CeO}_2$  particles is about 1.02 ( $\delta G=12-15\%$ ). Thus, the measured particle size distributions are the narrow functions. The real part of the particle refractive index is measured by the FST technique. The image part of the particle refractive index is determined by the novel spectroscopic method. A dispersion of the particle refractive index is not founded. The obtained values of complex refractive index for the ash particles are in good agreement with the data [3].

### 4. Summary

A simple method for determining the particle mean size, and the image part of the refractive index of weakly absorbing particles in a dusty plasma flows is proposed. A schematic of the instrument realized the complex of optical methods for determining the particle temperature, mean size, concentration and complex refractive index is presents. The complex use of the presented optical methods does not requires a knowledge of the particle mean size, complex refractive index and its spectral dependence. The developed methods have been successfully used in the dusty plasma flows for determining the particle temperature, mean size, concentration, complex refractive index and radiative properties (the emissive ability, the single-scattering albedo). The measurements have been made for the particles with the different sizes and refractive indices. The complex refractive index of  $\text{CeO}_2$  particles for high temperatures was obtained first.

### 5. References

- [1] A.P.Nefedov, O.P.Petrov, O.S.Vaulina: Appl. Opt., 36 (1997).
- [2] A.P.Nefedov, O.P.Petrov, O.S.Vaulina: JQSRT, 54 (1995) 435.
- [3] Wall T.F. and al.: Combust. Sci. and Tech., 26 (1981) 107.

# High power density dusty matter collected as a source of hard x-ray

Yu.K.Kurilenkov \*, M.Skowronek, G.Louvet, and P.Romeas

Laboratoire des Plasmas Denses, Universite P. & M. Curie, F-75252 Paris Cedex 05, France

\*Institute for High Temperatures (IVTAN), Russian Academy of Sciences, Moscow 127 412, Russia.

## 1. Introduction

We consider the creation of a high power density matter (HPDM) configured in a low pressure discharge. Our prime goal is to produce and study a "dusty" - like plasma followed by an intense energy deposition into this medium. The anomalous absorbing (stopping) power phenomena related provide to use this media as a working one for high power sources of radiation including hard x-ray. We present below the basic physics used to create HPDM. This is followed by a brief description of the experiments related and results obtained on hard x-ray generation.

The never-ending and exciting physics of pulse electrical discharges in vacuum and at low pressure have allowed to study even dense plasma phenomena like cathode micro drops and hot spots [1-3]. The occurrence and physics of anode spots are less investigated [2,4]. Theory is led by experiment here, and the summing up both the knowledge available for particular processes in discharges and hot dense matter physics itself allows hopefully to formulate the set of conditions for getting a new quality, in particular, for the possible simple ways of HPDM production.

## 2. Basic remarks.

We are looking for to realize few cumulative (or high local power density) effects for our aim: to collect HPDM originated from clusters or dust grains in the inter electrode space [5]. As a reference system we consider the hollow cathode ns discharge scheme at low air pressure [4] which have been modified reasonably.

First, a well known fact is that the initial electronic beams issued from hollow cathode are converging at a near-axis area. This feature together with a variation of the cathode - anode distance is a way to get a maximum current density  $j_{\max}$  at the axis for particular electrode configuration.

Second, the choice of the anode configuration itself may essentially increase the efficiency of its heating by pre-breakdown electron beams. In fact, the anode power density related may be higher than known values  $10^{8-9}$  W/cm<sup>2</sup>, being effectively close up to laser action of  $10^{17-19}$  W/cm<sup>2</sup> [1,2]. For example, it can be realized as a result of "scanning" of ring-like anode sharp edge by avalanche beams with high power density delivered on a small surface ( $w_a \sim 10^{5-6}$  J/cm<sup>3</sup>). Additionally, the special choice of the anode geometry may provide the focusing of explosive evaporated matter on the axis during their expansion into vacuum

(its cooling associated partially with the adiabatic one). The expansion process of the anode flare and oversaturation of concentrated anode vapours on the axis is accompanied by the compact collecting of clusters, nucleated microdrops, accelerated microparticles, etc. at the fixed place beyond the electrodes. The degree of condensation is estimated as high as 0.2 - 0.5 [1]. The analysis of the experiments shows that the dust grain (cluster, microparticles) size may typically vary from 0.01 to 1  $\mu$ m under certain conditions [2,6]. Thus, an unique combination configured of both solid density and gas-plasma "target" medium may be "prepared" behind of anode flare front directly before breakdown.

Just after, the further anomalous deposition of external energy into this condensed phase obtained in vacuum (beams-clusters interactions and their ns heating by postbreakdown current), may provide a large number of well-collected micro plasmas with extreme temperatures and densities inside of each ones (mult-keV electrons,  $n_e \sim 10^{20-21}$  cm<sup>-3</sup>). In fact, Joule heating  $j_{\max}^2 / \sigma_{\min}$  under anomalous low conductivity  $\sigma_{\lim} \approx \omega_{pe} / 4\pi$  [7] ( $\omega_{pe}$  is the plasma frequency) due to current- and beams-driven instabilities have to allow the very effective energy deposition (up to  $10^{7-8}$  J/cm<sup>3</sup>): the plasma spot conductivity  $\sigma_{\lim}$  (T) will decrease at any stages of the hydrodynamic expansion ( $\tau_{\text{expand}} \leq 1$  ns), supporting the overheating of dense plasma. Correspondingly, the process of destruction of dusty grains by high density currents ( $\sim 10^8$ - $10^9$  A/cm<sup>2</sup>) have to be accompanied by x-ray radiation during expansion, cooling and recombination of the dense hot microplasmas created (see figures 1-3 below).

Note that the x-ray production and the energetics related is of similar origin as that due to the volume irradiation of clusters by intense laser pulses [8], but differ of high current z-pinchs. The role of intracuster processes, inner-shell excitations and anomalous x-ray emission under direct e and i beams deposition have to be discussed also [9], as well as some elements of other cluster ionization mechanism models [10].

## 3. Experiment

The application of the general scheme described above is performed using a hollow cathode, a cylindrical anode and a low inductance ns discharge at low pressure ( $10^{-6}$ - $10^{-2}$  mbar). The electrode typical diameter is 5 mm. A Marx generator provides a 70 kV, 50 ns,  $I_{\max} \approx 1$  kA pulse and a stored energy of 1 J [4,5]. The spatial distribution of the emitting hot spots



has been determined using a sensitive imaging device and a rapid scintillator. The exposure time may be as short as 5 ns. During a single pulse, when the voltage is applied, the "dusty" anode matter is first created and focused in the interelectrode space. After breakdown, this dusty plasma-like medium is transformed into HPDM (on the background of rather dilute post breakdown plasma). The radiation with wavelength  $\lambda < 0.1$  nm of this HPDM is registered during 10 to 40 ns, through appropriate attenuators. It may have the shape of a 1 to 4 mm diameter "ball" (figures 1-3) of collected micro plasma hot spots. To illustrate, figure 1 shows an example of initial stage, figure 2 the maximum of hard x-ray intensity (which correspond to current maximum) and figure 3 represents the end of the x-ray "ball" emission (intensities are inverted).

The shape and space structure of the "ball", its duration, the intensities, the microplasma parameters, the microstructure of anode surface after few hundreds shots, etc. have been studied and will be presented.

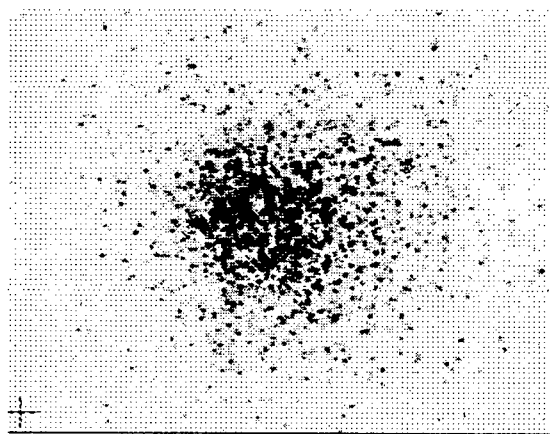


Fig.1 Hard x-ray from anode hot spots collected

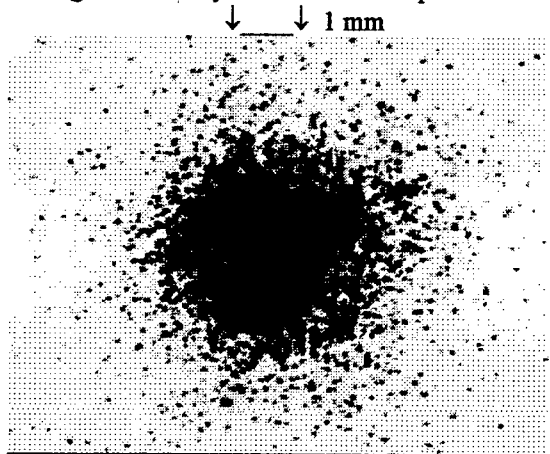


Fig.2. Radiative maximum (hard x-ray "ball")

#### 4. Concluding remarks

Thus, absorbing (stopping) power of media of dust grains (clusters) with very small volumes and near solid densities is essentially higher compared to both

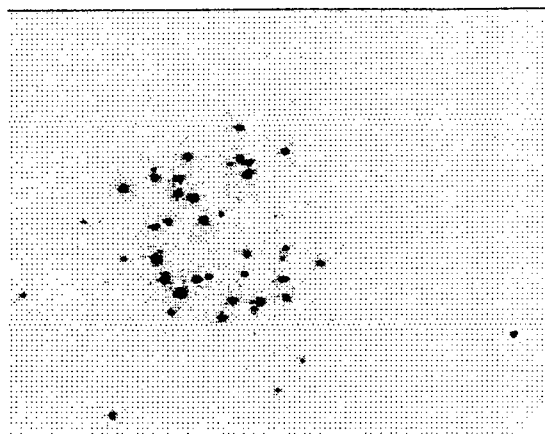


Fig.3. Recombination of the rest of "ball" formation.

plasma (gas) and solid sample targets, i.e. looks more optimal for HPDM production. A relatively small and cheap low energy device provides the well reproducible generation of high power density matter configured (with energy densities up to  $\sim 10^{15-18}$  J/cm<sup>3</sup>).

This result is similar to high-intensity laser ( $10^{15-18}$  W/cm<sup>2</sup>) focusing on clusters [8-10], but the way used here seems as a more effective and simple. (In terms of [4], fig.2 view looks as the "anode ectons" collection). HPDM obtained may play the role of working media both for technologies and basic studies (electronics, x-ray lasers, energy conversion, astrophysical simulations, etc.). In particular, this compact table-top design, flexibility, with a sufficient photon number at efficiencies about 0.1-0.3% (with power  $\sim 10^5$ - $10^6$  W) looks promising for special types of hard x-ray sources (for example, the x-ray images of living organisms may be captured before any absorption kinetics can happen).

We acknowledge with thanks the stimulating discussions with A.A.Rukhadze, G.Maynard, J.Duffy, partial support of this work by NATO Linkage Grant HTECH.LG 960803, and technical support of Kodak Corp. for special films presented.

#### References

1. G.A.Mesyats, D.I.Proskurovsky: Pulsed Electrical Discharge in Vacuum. Springer-Verlag (1989)
2. G.A.Mesyats: Ectons. "Nauka", Ekaterinburg (1993)
3. A.Anders, S.Anders, B.Juttner, H. Luck: IEEE Transactions on Plasma Science, 24 (1996) 69
4. M.Skowronek, A.Ikhlef *et al.*: Plasma Sources Science and Technology, 5 (1996) 70
5. M.Skowronek, Yu.K.Kurilenkov *et al.*: Int. Conf. on Physics of Dusty Plasmas, Goa, India (1996) Abstracts.
6. T.Witke, A.Lenk, P.Siemroth: XVII Int. Conf. on Physics of Vacuum Discharges and Insulation in Vacuum, Berkeley, USA (1996)
7. Yu.K. Kurilenkov, M.A. Berkovsky: in Transport and Optical properties of Nonideal Plasma, ed. by G.A. Kobzev *et al.*, NY, Plenum (1995) 215.
8. T. Ditmire *et al.*: Phys.Rev.Lett. 75 (1995) 3122
9. A. McPherson *et al.*: Phys.Rev.Lett. 72 (1994) 1810
10. E.M.Snyder *et al.*: Phys.Rev.Lett. 77 (1996) 3347

## The density effect in opacity of pure hydrogen plasma

T. Gavrilova<sup>1</sup>, V.P. Averyanov<sup>1</sup>, Y. Vitel<sup>2</sup>, C. Le Guen<sup>2</sup>, L. D'yachkov<sup>3</sup> and Yu. Kurilenkov<sup>3</sup>

<sup>1</sup>Vavilov State Optical Institute, Birzhevaya 12, 190034 St.-Petersburg, Russia

<sup>2</sup>Laboratoire des Plasmas Denses, Tour 12E5, Université P et M Curie, 4 Place Jussieu, 75252 Paris Cedex, France

<sup>3</sup>Institute for High Temperature, Russian Academy of Sciences, Izhor'skaya 13/19, 127412 Moscow, Russia

### 1. Introduction

A goal-oriented experiment to the quest and research for specific manifestation of interparticle interactions in optical spectra of non-ideal hydrogen plasma has been realized. The absorption spectra in Balmer region (250–750 nm) have been studied in two conditions characterized by temperatures 18000 K and 23000 K and densities  $6.6 \times 10^{18} \text{ cm}^{-3}$  and  $1.6 \times 10^{19} \text{ cm}^{-3}$ , respectively. Spectral distribution of plasma absorption coefficient turned out different of principle in these two cases. In the first case the absorption spectrum of plasma answered the conception [1], conventional for weakly non-ideal plasma, according to which a disappearance of spectral series highest members is totally compensated by continuum enlargement in the same spectral region. In the second case we observed the pronounced "clearing-up" effect predicted [2], when this compensation does not happen, and the plasma absorption in a disappearing lines region is substantially lower than expected one (on the basis of unperturbed density of oscillator strengths [1]). The effect observed may be caused by collective modes and plasma microfields action on atoms under strong Coulomb correlations between free charges in a dense plasma (Section 4 and refs therein).

### 2. Experiment

Plasma "clearing-up" was revealed previously in air and noble gases [3], but all attempts to get this in hydrogen plasma suffered a reverse [4]. A main problem was a creation of the pure hydrogen plasma with high electron density and well-diagnosed parameters. In this work we succeed in getting it due to use of specially constructed plasma source based on a pulse discharge in closed quartz capillary [5]. The plasma obtained by this discharge is quasi-stationary and fairly volume. To avoid the wall ablation we reduce pulse duration to 3  $\mu\text{s}$ . Capillaries of square cross section of  $1 \times 1 \text{ mm}^2$  and a length of 10 mm are used in experiment. Small transversal size of the capillary provides the optical plasma transparency sufficient for direct transmission measurements in visible spectral region. All optical measurements are made at the temperature pulse maximum with time resolution of 0.3  $\mu\text{s}$ . Spectra are recorded by optical multichannel analyzer coupled with a spectrograph giving a spectral resolution of 0.6 nm.

Plasma temperature  $T$  is evaluated from

independent measurements of brightness  $b_\lambda$  and transparency  $t_\lambda = \exp(-k_\lambda l)$  at wavelength  $\lambda = 632.8 \text{ nm}$  corresponding to the generation line of He-Ne laser. Transversal profiles of  $b_\lambda$  and  $t_\lambda$  (with spatial resolution of 0.1 mm) are used to obtain the temperature profile. The temperature is fairly homogeneous within hot near axis zone having a width of  $l_{\text{eff}} = 0.75 \pm 0.05 \text{ mm}$ . The radial distribution of plasma neutral density  $N$  is found from the temperature profile and from the conditions [5] for invariance of the mass and the constancy of the pressure over cross section. The electron concentration  $N_e$  in the hot zone of discharge is calculated from Saha equation at the known  $T$  and  $N$ . The relative error in the definition of plasma temperature is estimated as 3 %, of density and electron concentrations around 6%.

### 3. Method of calculations

To clarify the possible density effects we have to compare the measured absorption with the calculation based on consequent weakly non-ideal plasma conception. In the spectral range investigated the main contribution to the emission (absorption) comes from the Balmer spectrum. The line intensities are calculated taking into account the dissolution due to destruction of the bound states under the influence of the quasi-static plasma microfields. The probability  $W$  that the state is still bound, is defined as the integral of the quasi-static microfield distribution function from zero to the critical value of the field  $F_c$  for which the state is found at the top of the potential barrier formed by the interaction of the ionic microfield with the atomic core Coulomb field. If the microfield is assumed as uniform on the atomic scale, then for the state with the ionization energy  $E$  in the case of isolated atom, we have  $F_c = E^2/4e^3$ . In the calculation we use the Hooper's distributions for a neutral point [6]. Profiles of  $H_\alpha$  and  $H_\beta$  are calculated according to [7], while the following Balmer lines are almost completely dissolved and their profiles are not important.

The Balmer photoionization cross sections are calculated from the exact quantum mechanical equations [8]. Other photoionization and inverse bremsstrahlung cross sections are calculated in the Kramers approximation with the corresponding Gaunt factors from [9] and [10], respectively. The Balmer photoionization cross section is continued over the long wavelength threshold with the factor  $1 - W(\lambda)$ , assuming that the total (lines + continuum) density of oscillator strengths is conserved (the loss in the line

oscillator strengths is compensated by the continuum extension).

#### 4. Results and discussion

As an example, spectral emission intensity measured in the case of higher temperature and density is presented in Fig. 1 by curve 1. The optical thickness here is closed to 1 and more than 1 in the region of  $H_{\alpha}$ . Curve 2 shows the intensity under the assumption that the plasma is optically thin (i.e. all the radiation goes away from the capillary).

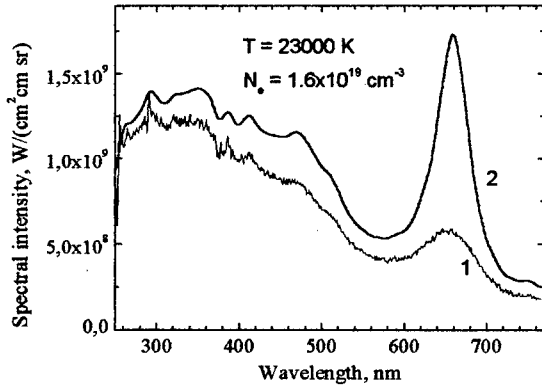


Fig. 1. Emission from the short pulse discharge.

Absorption spectra, obtained from plasma emission spectra by Kirchhoff-Planck equation, are presented in the Figs. 2 and 3 in comparison with calculations. The relative experimental error is about of 7%. For highest density (Fig. 3) we present two experimental curves for different discharges under the same conditions (for curve 2 smoothing is applied). Analysis of the results obtained shows that deviation of experimental absorption from calculated one starts for hydrogen plasma at  $n_e \approx 10^{19} \text{ cm}^{-3}$ .

This density effect in opacity of pure dense hydrogen plasma can be interpreted as the manifestation of essential perturbation of density of oscillator strengths in comparison with isolated atom picture. It is characterized by relative "clearing-up" of hydrogen plasma spectra as the density grows. Note, that the data presented in Fig. 3 correspond to maximal value of  $N_e$  achieved up to now [4, 11]. The effect observed now at first for hydrogen reliably has been discussed during last two decades as well as the "transparency windows" for plasmas of complex elements [2,4,11]. Obviously, this phenomenon registered (redistribution of absorption along the spectrum) for hydrogen even under rather moderate plasma density may provide the new stage for true description of radiative opacities and energy transport in laboratory and astrophysical dense(coupled) plasmas.

This work is supported by a contract of the 'Club Arc Electrique' of the Electricité de France, by NATO Linkage Grant HTECH.LG 960803, PECO CEI program and RFBR Grant 94-02-05464.

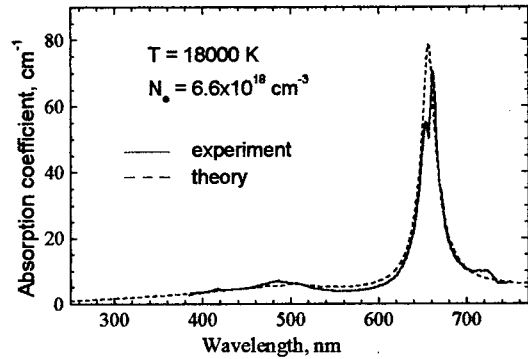


Fig. 2. Absorption coefficient (lower density).

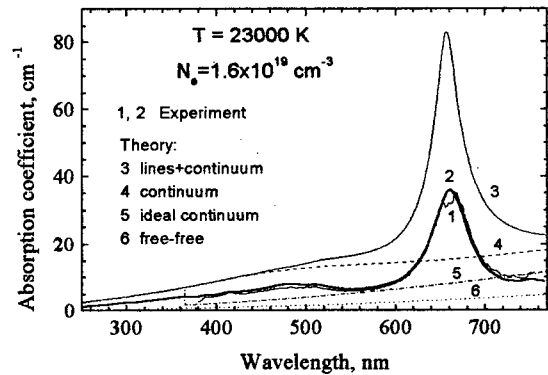


Fig. 3. Absorption coefficient (higher density).

#### References

- [1] L.M. Biberman, G.E. Norman: *Sov. Phys.-Usp.*, **10** (1967) 51
- [2] G.A. Kobzev, Yu.K. Kurilenkov, G.A. Norman: *High Temp.*, **15** (1977) 163; G.A. Kobzev, Yu.K. Kurilenkov: *High Temp.*, **16** (1978) 385; G.E. Norman: *High Temp.*, **17** (1979) 382; Yu.K. Kurilenkov, P.V. Minaev: *Zh. Eksp. Teor. Fiz.* **74** (1978) 563
- [3] T.V. Gavrilova: *Sov. Phys. Tech. Phys.*, **24** (1979) 374; V.E. Gavrilov, T.V. Gavrilova, V.E. Fortov: *High Temp.*, **28** (1990) 453
- [4] G.A. Kobzev, Yu.K. Kurilenkov: III Int. Workshop on Nonideal Plasmas, Biesenthal, GDR, Proc. (1984) p. 42; Y Vitel et al.: *Physica B* **228** (1996) 161
- [5] S.I. Andreev, T.V. Gavrilova: *High Temp.*, **12** (1974) 1138
- [6] C.F. Hooper, Jr.: *Phys. Rev.*, **165** (1968) 215
- [7] H. Griem: *Spectral Line Broadening by Plasmas*. NY, Plenum (1974)
- [8] H.A. Bethe, E.E. Salpeter: *Quantum Mechanics of One- and Two-Electron Atoms*. Berlin, Springer (1957)
- [9] J.R. Roberts, P.A. Voight: *J. Res. Nat. Bur. Stand.*, **75A** (1971) 291
- [10] L.G. D'yachkov: *J. Phys. B*, **23** (1990) L429
- [11] Yu.K. Kurilenkov, M.A. Berkovsky: in *Transport and Optical properties of Nonideal Plasma*, ed. G.A. Kobzev et al., NY, Plenum (1995) p. 217; Yu.K. Kurilenkov et al.: *Physica B* **228** (1996) 158

# Radiation of dense helium plasma produced in flashlamps

Y. Vitel<sup>1</sup>, M. El Bezzari<sup>1</sup>, L. D'yachkov<sup>2</sup> and Yu. Kurilenkov<sup>2</sup>

<sup>1</sup>Laboratoire des Plasmas Denses, Tour 12E5, Université P et M Curie, 4 Place Jussieu, 75252 Paris Cedex, France

<sup>2</sup>Institute for High Temperature, Russian Academy of Sciences, Izhorskaya 13/19, Moscow 127412, Russia

## 1. Introduction

Non-ideality effects in dense plasma radiation of different elements have been under investigation for during recent years. However, continuous spectra of helium plasma presented in this paper, were investigated earlier rather poorly because of the problems of plasma generation. Being between hydrogen and complex atoms, helium has the defined principal advantages for studying the plasma density effects in radiation due to spectra simplicity and absence of the linear Stark effect. In this work, helium high pressure arcs are created in linear flashlamps. Those plasmas have a good cylindrical symmetry, are very reproducible and in local thermodynamic equilibrium. On axis electron densities achieved are in the range  $2 \times 10^{17} - 1.7 \times 10^{18} \text{ cm}^{-3}$  and temperatures in the range  $(2-3) \times 10^4 \text{ K}$ . In these conditions, the mean interaction potential energy between charged particles  $E_p$  is not small compared to their kinetic energy  $E_k$ . The ratio  $\Gamma = E_p/E_k$  is in the range 0.1–0.2. The number of particles in the Debye sphere is small and around unity. Then, flashlamp as plasma source is a very convenient and efficient tool to study non-ideality effects in moderately dense plasmas spectra [1,2].

## 2. Experiment

The plasmas are produced in fused quartz linear flashlamps whose inner diameter is 5 mm and distance between electrodes 100 mm. These lamps are filled with pure helium at initial pressures from 50 to 500 Torr. The gas breakdown is performed by applying a high voltage pulse (30 kV, 1  $\mu\text{s}$ ) on an auxiliary electrode. Then a low current ( $\approx 1 \text{ A}$ ) simmer is maintained during 12 ms before triggering the main discharge to ensure the discharge centring on tube axis, and to minimise the plasma-wall disturbance phenomena [3,4]. The main discharge has a maximum current intensity in the range 0.5–1.5 kA and its pulse duration at half height is around 100  $\mu\text{s}$ . Three spectrographs with different dispersions are used to measure the spectrum. Each of them is coupled to an intensified optical multichannel analyser mono- or bi-dimensional. All spectral measurements are performed during a short period of time (less than 1  $\mu\text{s}$ ) at the maximum of the current, when the best filling of the plasma is obtained inside the flashlamp. For standardisation purposes, we use a calibrated deuterium lamp in the wavelength range  $\lambda < 350 \text{ nm}$  and a tungsten ribbon lamp for  $\lambda > 350 \text{ nm}$ . The wavelength

scale is absolutely calibrated using spectral lamps. The different methods of diagnostics used to determine the radial profiles of particles and temperature are based on measurements of continuum intensities, neutral line intensities and opacities, and infrared laser interferometry (3.39  $\mu\text{m}$ ). The plasma parameters deduced from continuum and line intensities on the basis of ideal plasma calculations, are in disagreement with those deduced from opacity measurements (for  $T$ ) and interferometry (for  $N_e$ ). But, if we take into account the effect of the statistical ionic microfields on the atomic levels in the calculation of the continuum and the line intensities, a good agreement is obtained in the evaluation of the plasma parameters by those different methods.

## 3. Theory

Radiation spectrum of helium in the considered conditions, is formed from bound-bound (spectral lines), free-bound (photorecombination) and free-free (bremsstrahlung) transitions in neutral atoms. The line broadening and shift are calculated according to Griem [5], while the line intensities are estimated taking into account the line dissolution due to destruction of the radiating levels  $E$  under the influence of the quasi-static plasma microfields. If the microfield  $F$  in the point of the radiating atom placed is strong enough, more than a certain critical value  $F_c(E)$ , the level is destroyed. The probability of the level realization is then defined as the integral of the microfield distribution function

$$W(E) = \int_{F_c(E)}^{\infty} P(F) dF.$$

We use the quasi-static distribution function of Hooper [6] for a neutral point and take  $F_c(E) = E^2/16e^3$  assuming that the microfield is mainly created by nearest ion [7].

The photorecombination and bremsstrahlung are calculated using the semiclassical approximation in the framework of the quantum defect theory [8,9]. Assuming that the density of oscillation strengths in the near-threshold region is conserved [10] and redistribution of oscillation strengths along the spectrum is impossible, we continue the photorecombination continuum multiplied by the factor  $1-W$  over its long-wavelength threshold in order to compensate the decrease of the line intensities. Near the ionization threshold  $W \rightarrow 0$ , while  $W \rightarrow 1$  far off it. Therefore, the line series passes gradually to a continuum. The free-bound  $\xi$  function is shown in Fig 1

for a few values of the electron density. In the case of  $N_e \rightarrow 0$  our calculation is in a good agreement with that of Hofsaess [11].

The emission coefficient have been calculated for 36 points on the tube radius taking into account the temperature and density profiles obtained. By integrating the results, we can then estimate the total spectral intensity from the flashlamps, since the plasma is optically thin for all the wavelengths, except the core of the 587,6 nm line, where the measured data have been corrected, and so the whole spectrum can be considered for the effectively thin plasma.

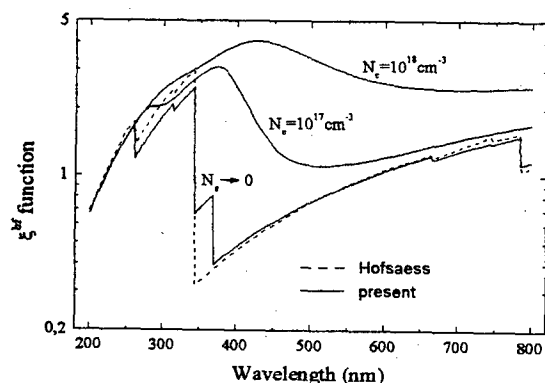


Fig. 1. Free-bound  $\xi$  function of helium,  $T = 15000$  K.

#### 4. Results and discussion

In Fig. 2 the measured and calculated radiation intensities from the flashlamp are presented. In whole a satisfactory agreement is found, which is better for the red part of the spectrum. This may be explained by the fact that the quantum defect method is more accurate for small frequencies. However, other reasons are possible too. Indeed, for the diagnostic we use the 587,6 nm line and 780 nm continuum intensities. So it is not surprised that the neighbouring region is more accurately estimated. We have got a good agreement for the 587,6 nm line intensity, while for other the lines it is underestimated or overestimated. One of the possible reasons is the dependence of the critical value  $F_c(E)$  on the orbital quantum number  $l$ , which is not taken into account in the present calculations. Near-threshold area at  $\lambda > 400$  nm needs further analysis at higher density.

#### 5. Conclusions

The radiation of helium plasmas measured at first at  $N_e \approx 10^{18} \text{ cm}^{-3}$  is in a good agreement in whole with the calculations based on the unperturbed densities of oscillator strengths and statistical action of microfields on radiators [10]. Last one provides smooth extension of the continuum and may be considered as a density effect itself, namely under moderate plasma densities. The consequent taking into account of this effect is

necessary to obtain a good agreement in the determination of the plasma parameters between the methods based on emitted radiation and other ones, and then – between the measured spectra and calculations.

This work is supported partially by NATO Linkage Grant HTECH.LG 960803.

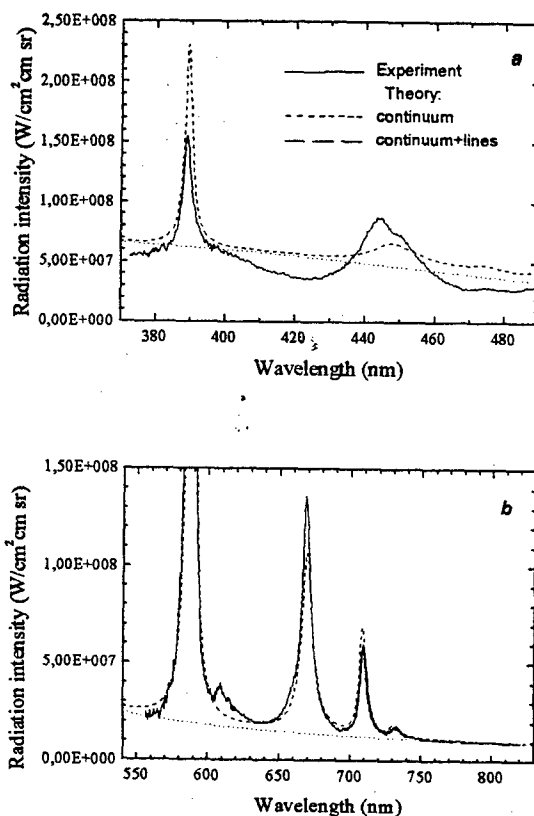


Fig. 2. Radiation intensity of helium plasma in spectral regions 370–490 nm (a) and 540–830 nm (b) from a discharge with axis temperature 23000 K and electron density  $1.05 \times 10^{18} \text{ cm}^{-3}$ .

#### References

- [1] K. Gunther, M.M. Popovic, S.S. Popovic, R. Radtke: J. Phys. D, 9 (1976) 1139
- [2] K. Gunther, S. Lang, R. Radtke: J. Phys. D, 16 (1983) 1235
- [3] Y. Vitel, M. Skowronek, K. Benisty, M.M. Popovic: J. Phys. D, 12 (1979) 1125
- [4] Y. Vitel, M. Skowronek: Proc. 8th ESCAMPIG, Greifswald, GDR, (1986) ed A. Bethke, p. 297; p. 299
- [5] H. Griem: Spectral Line Broadening by Plasmas. NY, Plenum (1974)
- [6] C.F. Hooper, Jr.: Phys. Rev., 165 (1968) 215
- [7] V. Sevastyanenko: Contrib. Plasma Phys., 25 (1985) 151
- [8] L.G. Dyachkov, P.M. Pankratov: J. Phys. B, 24 (1991) 2267; 27 (1994) 461
- [9] L.G. Dyachkov: High Temp., 30 (1992) 709
- [10] G.A. Kobzev, I.T. Yakubov, M. Popovich, ed: Transport and Optical properties of Non-ideal Plasma, NY, Plenum (1995)
- [11] D. Hofsaess: JQSRT, 19 (1978) 339

# Probe Induced Interpenetration and Circulation in Plasma-Dust Crystals\*

D. A. Law<sup>†</sup>, W. H. Steel, B. M. Annaratone and J. E. Allen  
*Department of Engineering Science, University of Oxford,  
Parks Road, Oxford OX1 3PJ*

## Introduction

Dust particles injected into a low pressure, capacitively coupled RF plasma collect negative charge as they fall through the plasma due to the greater mobility, and hence flux, of the electrons with respect to ions. Particles continue to fall until the force of gravity is balanced by the force due to the electric field in the sheath, and by the drag forces present due to asymmetric ion and neutral bombardment. Under certain conditions a suspension becomes strongly coupled, where the energy of interaction between the charged particles significantly exceeds their kinetic energy and the particles arrange themselves into solid, 2-D crystalline structures of several layers.

A Langmuir probe introduced above such a crystal is found to affect its structure and properties significantly — inducing convection-like circulation amid solid, crystalline islands.

## Experiment

Spherical melamine formaldehyde particles,  $\phi = 15\mu\text{m}$ , are injected into a 13.56 MHz plasma of argon sustained between two parallel electrodes, through a hole in the top, grounded electrode (as in [1, 2]). Pressure is in the  $10^{-1}$  torr range, with power  $\sim 5W$ . The particles gather 1cm above the lower, driven electrode, within the slight potential well of a copper gasket placed on the electrode (see figure 1). They lie within 2mm below the visible plasma-sheath edge. The probe,  $Ta$ ,  $\phi = 0.125, 0.25$  or  $0.5\mu\text{m}$ , is placed roughly 5mm above the plasma-sheath boundary. The potential on the probe is variable, between  $-20$  and  $20V$  to ground. Parameters which can be adjusted include the pressure, power, probe voltage and diameter, dust material and density.

The dust suspension is illuminated with a HeNe laser, made planar by an arrangement of lenses, focused to a line through the suspension. Scattered light is recorded in real-time using a video camera, connected to a computer. This data is analysed using a workstation, providing information about the velocity

and trajectories of the particles, as well as their temperature. In some cases, the camera is set up to record the probe-crystal interaction from the side, giving information about the vertical properties.

## Observation

Figures 2 and 3 display a single image, and two seconds of overlapping frames respectively, of a crystal with a probe above (seen as a diagonal line). This single image does not provide much information, but viewed over time the features become quite clear.

Below the probe, a rigid elliptical crystalline area is formed, comparable in shape to the probe (indicative of the probe sheath), toward which the surrounding crystal continually streams; interpenetrating 1 – 2 intergrain distances. The increased density resulting

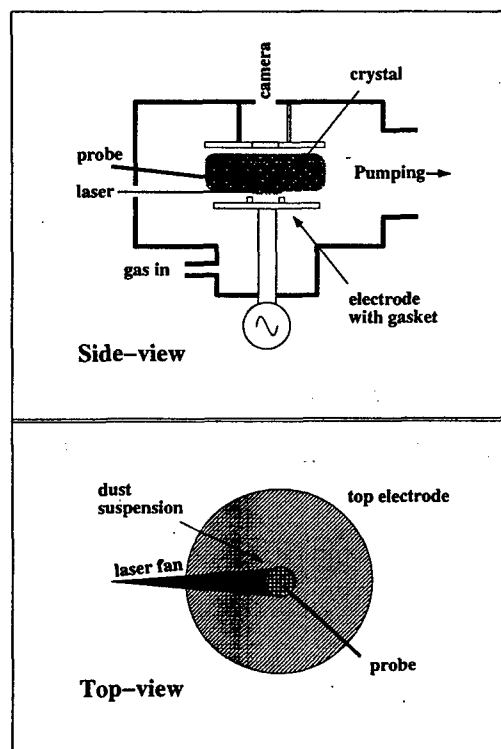


Figure 1: Schematic of the Experiment

\*Funded by the EPSRC

<sup>†</sup>Supported, in part, by an Overseas Research Scholarship administered by the CVCP.

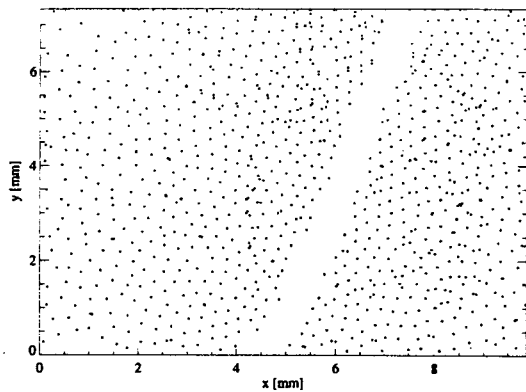


Figure 2: Probe-Crystal interaction – Top view. One video frame is displayed.

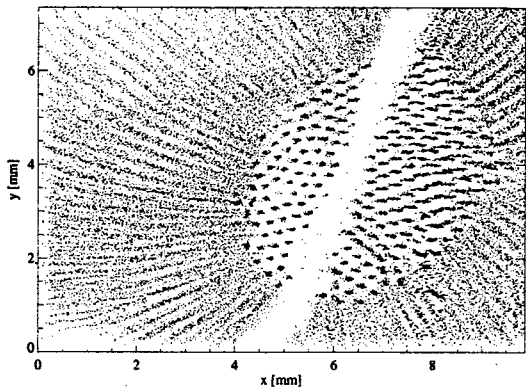


Figure 3: Probe-Crystal interaction – Top view. Two seconds of overlapping video frames (50 frames) are displayed.

from the geometry forces the interpenetrating grains to fall to lower layers where a new crystal is constructed (see figure 4), suggesting that, for small inter-particle distances, the charge balance on each grain is not sufficient for levitation within the local electric field.

Once in the lower layers, particles counter-stream, closing the loop, far from the probe disturbance at the boundary of the suspension (see figure 4). Adjustment to probe voltage alters these properties: when more positive, the crystalline 'island' becomes smaller and more tightly bound, with the particles around streaming much more quickly; when more negative, the 'island' is larger, less bound, and the particles circulate more slowly. At a certain point, the island is no longer obvious, and the particles are repelled from below the probe.

Convection-like circulation has also been observed near the boundary of the suspension, with a probe, likely due to the horizontal component of the electric field; and without a probe, possibly caused by a non-uniformity in gas-flow.

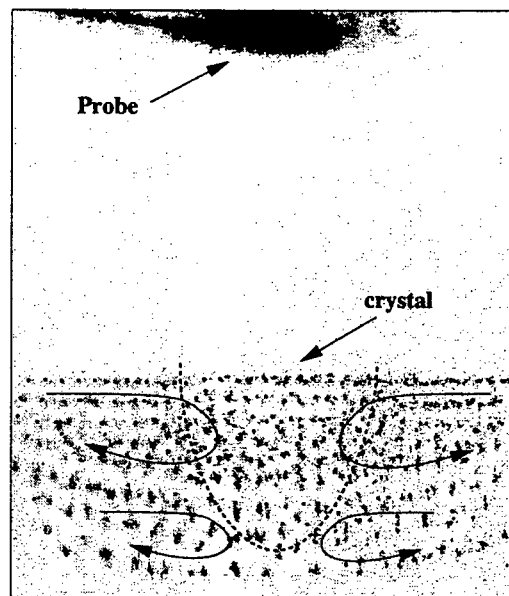


Figure 4: Probe-Crystal interaction – Side view. Inverted (single) image with marked features.

## Discussion

A possible explanation for this phenomenon is that the flow of ions, with the Bohm velocity at the sheath edge, is perturbed by the presence of the probe, increasing the ion density (in a specific region) above the value predicted in the absence of a probe [3]. This would alter both the potential distribution and the horizontal electric field. Another possibility is that the negative particles are attracted to a positive probe, creating a solid region by compression; due to the 'pressure' associated with the inwardly streaming particles. A detailed study of the effects of probe voltage, position, and diameter — with simultaneous measurements of the field around the perturbing probe (using another, smaller probe) — are necessary to explain the phenomenon, conclusively. Further experimental and theoretical work is currently underway.

## References

- [1] D A Law, B M Annaratone, J E Allen and W H Steel 1996, *13th European Sectional Conference on the Atomic and Molecular Physics of Ionised Gases* Vol. 20E, Part A, p.187
- [2] Thomas, H M and Morfill, G E 1996, *Nature*, **379**, 806
- [3] P C Stangeby and J E Allen 1971, *Journal of Plasma Physics*, **6**, 19

# Laser induced motion of micrometre size particles in rf plasma sheaths \*

W H Steel, D A Law, B M Annaratone, J E Allen  
Department of Engineering Science  
University of Oxford, Parks Road, Oxford OX1 3PJ

## Introduction

The increase of interest in dusty plasmas has led to observations of 2-D *dust* or *plasma crystals*[1][2] and to demonstrations of crystal phases, and how these phases are induced. These dust assemblies are typically viewed by illumination with a laser line (ie a 2-d plane of light) and a camera, positioned so as to collect the scattered light. We have seen that, as well as providing illumination, a laser beam can also be used to *fracture* a plasma crystal. The extent to which fracturing occurs is dependent upon the morphology of the particles which make up a crystal.

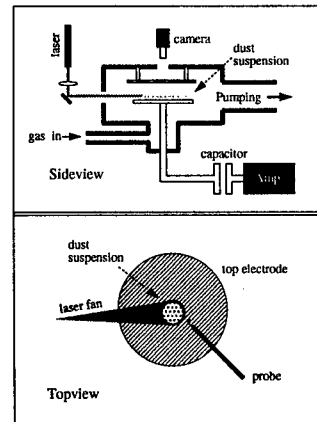


Figure 1: Experimental arrangement.

## Experimental setup

A capacitively coupled rf system at 13.56MHz is used to suspend various particles in an argon discharge. Dust, dropped through a hole in the top (grounded) electrode, charges negatively due to the higher electron fluxes over the ions. A balancing of forces (electrical and gravitational) causes the dust to suspend in flat layers just inside of the positive space charge sheath at the lower (driven) electrode (see figure 1). A 5mW HeNe laser line is used to illuminate the layers of dust and a second 16mW HeNe laser beam is used to fracture dust crystals (see figure 2).

## Plasma crystals

Plasma crystal formation is dependent upon the inter-particle Coulomb potential energy, determined by dust charge, and the kinetic energies of the dust and the thermal motion of the particles, determined by the amount of neutral gas cooling, as well as by other factors. The Coulomb

coupling parameter  $\Gamma$ , the ratio of these two energies, controls the phase of a crystal[3]. Melting (a decrease in  $\Gamma$ ) is brought about either by raising the rf power or lowering the gas pressure, and solidification either by lowering the power or raising the pressure. For a solid crystal the regularity of the lattice depends upon the uniformity of its constituent particles. The less homogenous the dust, the less order there will be, as charge, suspension height, etc., vary from one particle to the next.

## Crystal Fracturing

By using a focused, moderate power laser beam (a few milliwatts) we have demonstrated that it is possible to fracture certain solid crystal lattices. Particles in the path of the laser beam are forced out of their lattice sites and pushed in the direction of the beam. Using several types and sizes of dust we observe that the morphology, physical properties, surface properties, etc., of particles in a crystal determines the extent to which laser fracturing can occur. Four particles

\*Funded by the EPSRC



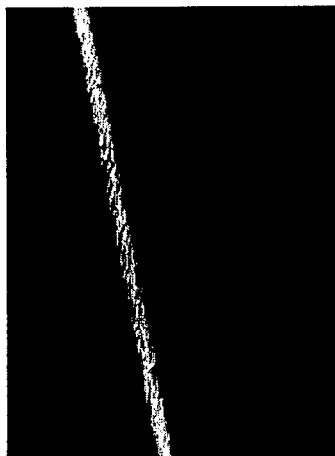


Figure 2: Fracturing a plasma crystal.

which have been used are:

- tungsten powder, 1 to 5  $\mu\text{m}$  diameter
- tungsten powder, maximum diameter 100  $\mu\text{m}$
- carbon toner particles, 0.3 to 30  $\mu\text{m}$  diameter
- melamine formaldehyde MF spheres, 14  $\mu\text{m}$  diameter.

Using a variable neutral density filter and laser we find that a crystal of the highly dispersive carbon is the easiest to fracture (laser intensity less than  $\sim 8\text{mWmm}^{-2}$ ). A crystal of the smaller tungsten powder breaks with a focused laser beam of greater than  $\sim 40\text{mWmm}^{-2}$ . Crystals of the larger particle size, 100  $\mu\text{m}$  tungsten and the highly uniform lattice of MF particles, do not fracture (maximum focused laser intensity is  $\sim 150\text{mWmm}^{-2}$ ). An examination of the nature of the fracturing force lead us to discount thermal forces, due to temperature differences across the dust, because of the small dimensions involved. A more likely mechanism is radiation pressure — A beam of 10mW,  $\phi = 1\text{mm}$ , will exert on a 30  $\mu\text{m}$  grain a force of  $3 \times 10^{-14}\text{N}$ , and give an unbounded grain of mass  $10^{-11}\text{Kg}$  an acceleration of about  $3\text{mm/s}^2$ .

## Determination of Inter-Particle Forces

Using a laser beam, measurements will be made of the force required to fracture a crystal, see

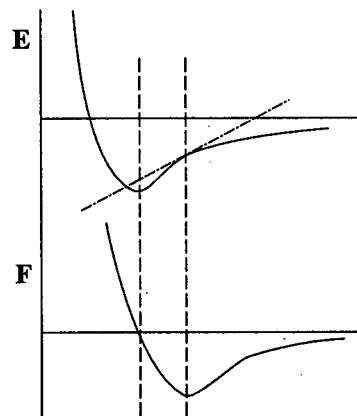


Figure 3: Energy and Force between two charged particles.

figure 3. The nature of the repulsive force is clear but it is intended to obtain information on the attractive forces which are believed to be present. The possibilities include:

- (a) a bond associated with localised ion space charges, and
- (b) an attractive force due to the imbalance of ion impacts on the surface of the particles.

## References

- [1] M Thomas, G E Morfill 1996 *Nature* **379**, 806
- [2] D A Law, B M Annaratone, J E Allen, W H Steel 1996 *13th European Sectional Conference on the Atomic and Molecular Physics of Ionised Gases* Vol. 20E, Part A, p187
- [3] M Thomas, G E Morfill, V Demmel 1994 *Physical Review Letters* Vol. 73, Number 5, p652

# Numerical Analysis on Fine Particle's Behavior in an Ion-Beam Plasma System

N. Ohno, M. Nakamura, S. Nunomura, and S. Takamura

Department of Energy Engineering and Science  
Graduate School of Engineering, Nagoya University, Nagoya 464-01, Japan

## 1. Introduction

The investigation of dusty plasmas has received considerable attention in various fields of plasma physics. In order to do a comprehensive study of dusty plasmas, it becomes quite important issue to generate the dusty plasmas with a large volume in a steady state[1-5].

We have constructed a modified double-plasma (D.P) device equipped with the feeder of fine particles as shown in Fig. 1(a), which can make an ion-beam plasma system where the gravity force on a fine particle could balance the friction force between the particle and the ion beam. Figure 1(b) shows the typical distributions of ion beam density  $n_b$  and plasma density  $n_0$ . The  $n_b$  decreases due to an elastic and a charge exchange collisions. The mean free path of an argon ion is estimated to be about 5cm at 1mtorr of argon gas pressure. The detail of this device is described in Ref. [6]. The main purpose of the present paper is to discuss conditions to sustain fine particles in the ion-beam plasma system by using simple model.

## 2. Numerical Analysis

In this section, we show numerical analysis on the forces acting on a fine particle. The ion drag force  $F_i$  acting upon a charged particle generated by a Coulomb interaction has two parts, the collection force  $F_{ic}$  showing an effect of the direct collision between a fine particle and an ion, and the orbit force  $F_{io}$  due to the deflection of the ion orbits [4]. Figure 2(a) shows the dependence of the ion drag force on the ion beam velocity  $V_b$ . In this figure, we assume the argon target plasma with  $T_e \sim 2\text{eV}$ ,  $T_i \sim 0.1\text{eV}$ ,  $n_0 \sim 10^{15}\text{m}^{-3}$ , and the fine particles with  $r_d \sim 1.0 \times 10^{-7}\text{m}$  and  $\rho = 1.8 \times 10^3\text{kgm}^{-3}$ . The beam density  $n_b$  is assumed to be  $10^{14}\text{m}^{-3}$ . These parameters can be obtained in our device as shown in Fig. 1.  $F_i$  is found to have a strong dependence on  $V_b$ .  $F_i$  increases with an increase in  $V_b$  to have a peak at  $V_b \sim 6 \times 10^2\text{ m/s}$ . Further increase in  $V_b$  leads to decrease in  $F_i$ , because the impact parameter is rapidly decreasing as increases  $V_b$ . It is

found that the  $F_i$  overcomes the gravity force in two ranges of beam velocity from 73m/s to 2800m/s and more than 17000m/s. In Fig. 2(b), the ion drag force is plotted as a function of ion beam density  $n_b$  at  $V_b \sim 1.0 \times 10^4\text{m/s}$ .  $F_i$  is found to be proportional to  $n_b$  and

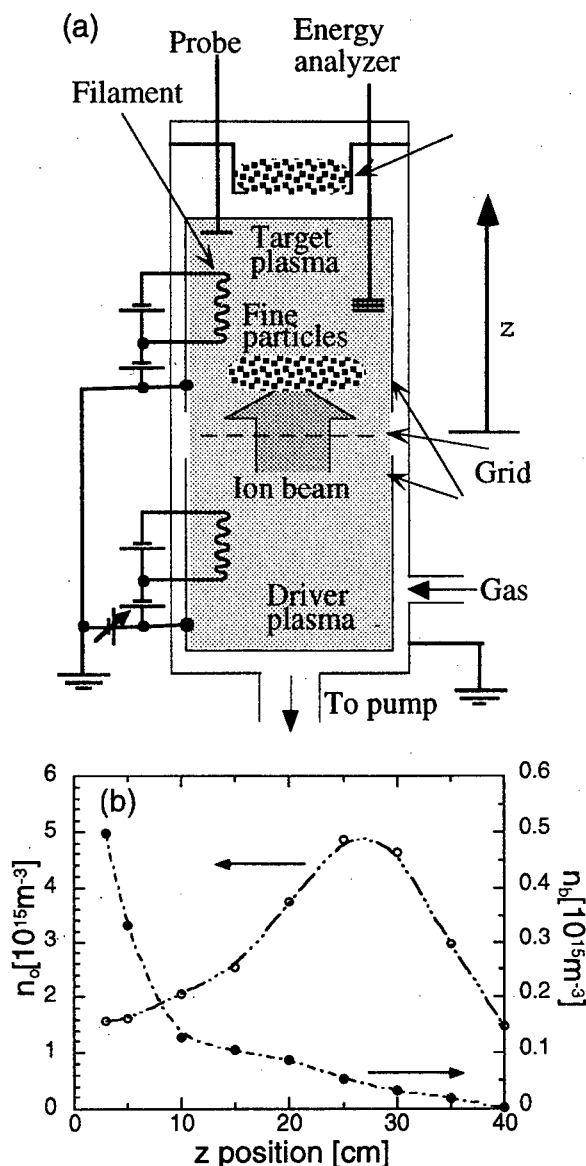


Fig. 1 Experimental setup: (a) schematic of experimental apparatus, (b) typical profiles of plasma density  $n_0$  and ion beam density  $n_b$  at 30eV of ion beam energy.

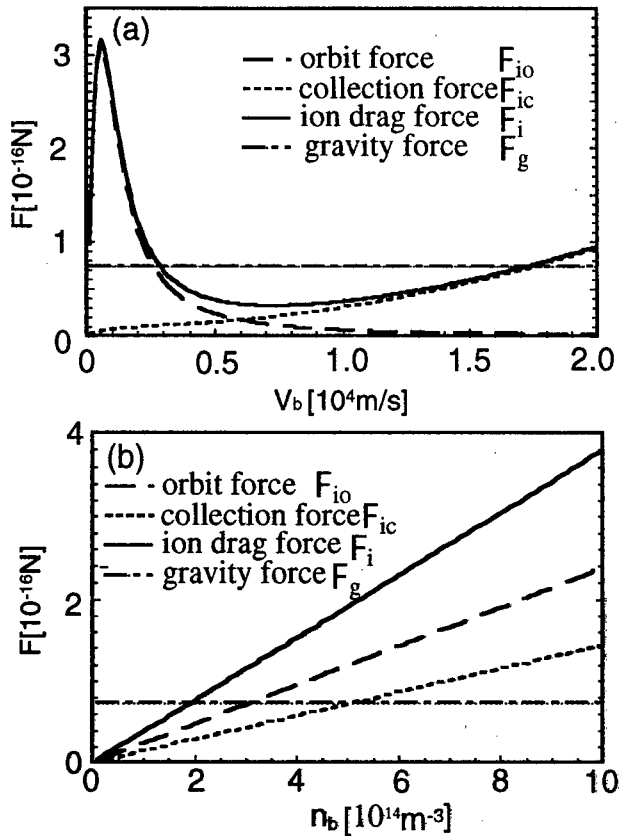


Fig. 2 Dependence of ion drag force on: (a) the ion beam velocity  $V_b$  and (b) ion beam density  $n_b$ .

overcomes the gravity force above  $n_b \sim 2.0 \times 10^{14} \text{ m}^{-3}$ .

Figure 3 shows the threshold value of ion beam density  $n_b$ , which is necessary to sustain a fine particle, as a function of  $V_b$ . At the region above each line in the figure,  $F_i$  is larger than the gravity force for a fine particle with each  $r_d$ . The threshold value is dramatically increasing with an increase in  $r_d$ , because the mass of the fine particle is proportional to the cubic of the  $r_d$ . Comparing between Fig. 3(a) and (b), at higher electron temperature  $T_e$ , the threshold beam density is found to be getting smaller, which is due to a  $T_e$  dependence on the charge of the fine particle through the magnitude of floating potential. These analysis indicate that fine particles could be sustained in the target plasma due to the ion drag force in our device.

### 3. Conclusion

In order to investigate basic physics in dusty plasmas, a new dusty plasma generator has been constructed. Numerical analysis shows us the condition of balance between the gravity force and the ion drag force on the fine particle. Plasma parameters in this device shows suitability for dusty plasmas generation.

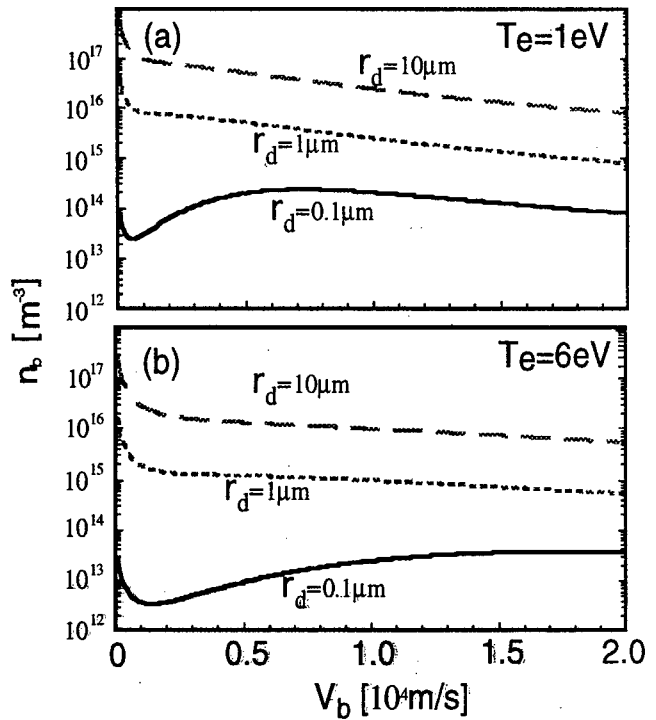


Fig. 3 Threshold value of ion beam density  $n_b$  to balance the ion drag force  $F_i$  and the gravity force as a function of ion beam velocity  $V_b$  at: (a) electron temperature  $T_e \sim 1 \text{ eV}$  and (b)  $T_e \sim 6 \text{ eV}$ .

### Acknowledgments

The authors would like to thank Dr. Y. Uesugi (Nagoya University) for many useful discussions and Mr. M. Takagi (Nagoya University) for his technical help. One of the author (S.N.) would like to thank a Grant-in-Aid of the Scientific Research from the Japan Ministry of Education, Science and Culture (JSPS Research Fellow No. 3254).

### References

- [1] N. N. Rao, P. K. Shukla and M. Y. Yu, *Planet. Space Sci.* **38** (1990) 543.
- [2] F. Melandso, T. Aslaksen and O. Havnes, *Planet. Space Sci.* **41** (1993) 321.
- [3] A. Barkan, R. L. Merlino and N. D'Angelo, *Phys. Plasma.* **2** (1995) 3563.
- [4] Michael S. Barnes et. al., *Phys. Rev. Lett.* **68** (1992) 313.
- [5] S. Nunomura, N. Ohno, and S. Takamura, *Jpn. J. Appl. Phys.*, to be published.
- [6] M. Nakamura et. al., *Proc. of 1996 Int. Conf. Plasma Physics, Nagoya, Japan, 1996*, to be published.

# GENERATION OF CARBON CLUSTERS AND FULLERENES IN ARC JET.

G.I.Sukhinin, O.A.Nerushev

Institute of Thermophysics, Novosibirsk, 630090, Russia

Since the discovery of fullerenes, it is still a miracle why fullerenes (the most symmetric spheroidal molecules) have very large yield in the graphite contact arc reactor with helium atmosphere but low yield in graphite laser ablation experiments? Why carbon clusters have very specific non-monotonic mass-spectrum with the pronounced gap in the region of  $n=25-35$  atoms per cluster  $C_n$ , even-odd alternation that is different for small and large clusters? Usually, the answer is searched in fullerenes stability and different possibilities of reactions of various carbon clusters. In this paper, we present a model of carbon clusters formation, which connects the above mentioned peculiarities of carbon clusters mass-spectrum with their spatial structures and related effective collisional cross sections of carbon clusters.

Carbon clusters exist in different isomeric forms [1]: linear chains, mono- and poly-cyclic rings, and spheroidal forms (fullerenes). Collisional cross sections,  $\sigma_{ik}$ , between all these structures and constants,  $K_{ij}$ , for clusters formation in the process  $C_i + C_j$  were calculated taking into account their rotation during collisions. For example, the effective cross sections of carbon atoms collisions with  $C_k$  clusters change linearly with the  $k$  number and depend on the structure of clusters; the dependence of cross sections of linear and plane

$C_k$  clusters on  $k$  is quadratic; the dependence of  $C_k$  fullerenes cross sections on  $k$  is linear again. Therefore, carbon clusters are dramatically different from compact clusters, whose collision cross sections are proportional to  $k^{2/3}$ .

Obtained cross sections and some simple assumptions on clusters and fullerenes reactivities were used for calculation of Smoluchowski equations for clusters formation in a flow of carbon vapour in helium after graphite contact arc. For description of the flow of C-He mixture from inter-electrode gap, it was assumed that the turbulent radial jet is formed. The Görtler theory for turbulent mixing is applied to the problem of a radial jet. Magneto-hydrodynamic model [2] of flow in the high current arc were used for taking into account the real parameters of plasma reactor for fullerene production and finding of flow velocity in arc jet,  $v_a \sim I^2/\rho$ . This model is used as a basis for transition from nonstationary kinetic equations to the description of the radial dependent stationary fields of relative concentrations  $c_k$  at the distance  $r$  from interelectrode gap with the initial condition in that gap for the density of carbon vapour and initial velocity of carbon-helium mixture at the exit from the inter-electrode gap of the radius  $r_0$  ( $N_c$  and  $u_0$ ). As a result the following system of equations for clusters relative concentration  $c_k$  were obtained:

$$\frac{dc_k}{dr/r_0} = \frac{N_c r_0}{u_0} \left( \sum_{j=1}^{k_m} K_{k-j,j} c_{k-j} c_j - \sum_{j=1}^{\infty} K_{kj} c_k c_j - K_{kk} c_k^2 \right) \quad (1)$$

The analysis of system (1) and the hydrodynamics of the flow in an arc and reactor allows us to find out the modelling parameter of

the problem that determines the fullerene yield at the reactor walls,  $R_c$ :

$$X = \frac{\langle P \rangle (n_0 v_c \sigma_{11} P_c)}{u_0} = \frac{Q \langle P \rangle v_c \sigma_{11} P \mu_g \pi R_c J_0}{m_c \chi^2 \mu_0 R T I^2 b_0}, \quad (2)$$

where  $Q$  is the carbon mass flow rate,  $p$  is the gas pressure,  $R_c$  - is the radius of reactor chamber,  $I$  is the arc current,  $\mu_g$  is the molar mass of buffer gas,  $\sigma_{11}$ ,  $m_c$  and  $v_c$  are the collisional cross sections, the mass and thermal velocity of carbon atoms,  $r_0$  and  $b_0$  are the parameters of the inter-electrode gap, initial velocity of gas is  $u_0 = \chi v_a$ ,  $\langle P \rangle / \chi^2 \approx 1$ .

Figure 1 shows cluster size distributions at  $X=25$  for different initial conditions: curve 1 -  $c_1^0=1$ ,  $c_k^0=0$  for  $k>1$ ; curve 2 -  $c_1^0=0.1$ ,  $c_2^0=0.45$ ,  $c_k^0=0$  for  $k>2$ . (Note here, that  $\sum k \cdot c_k = 1$ , in accordance to the total carbon mass conservation). It is found that the initial distribution of clusters is relatively unimportant for large cluster size distributions.

Figure 2 shows the comparison of fullerene yield on the modelling parameter,  $X$ , with the experimental data [3,4] for different arc currents, helium pressures, and inter-electrode gaps,  $b_0$ .

Figure 3 shows the partial rate constants of the  $C_{60}$  formation in  $C_k + C_{60-k}$  pair collisions for different radial distances  $X = 25, 50, 100$ . This constants were defined from the known cluster structure and solutions of (1).

Thus, the present results reveal the crucial role of collisional cross sections of carbon clusters and gas dynamic processes on the evolution of carbon clusters and fullerene formation.

### Acknowledgement.

The research described in this publication was made possible in part by Grant No 96-03-33770a from Russian Foundation for Basic Researches.

### References.

- [1] G.von Helden, et al. *J.Phys.Chem.*, 97(1993) 8182.
- [2] S.Ramakrishnan, et al. *J.Phys.D: Appl.Phys.* 1978, 11, 2267.
- [3] Y.Saito, et al. *Chem.Phys.Lett.*, 1992, 200, 643.
- [4] D.Afanasyev, et al. *Zh.Techn.Fiz.*, 1994, v.64, No.10, p.76 (in Russian)

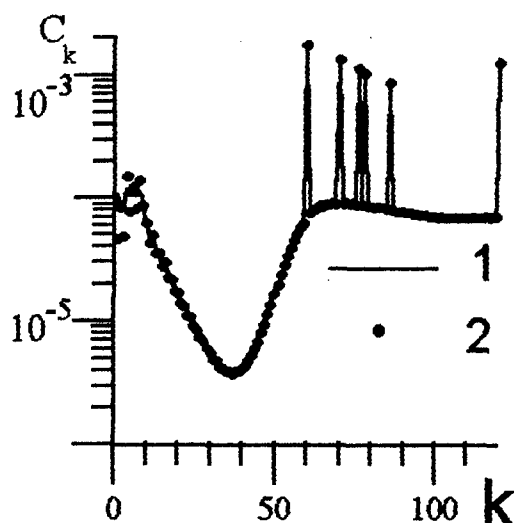


Fig.1 Calculated mass-spectra for two sets of initial conditions

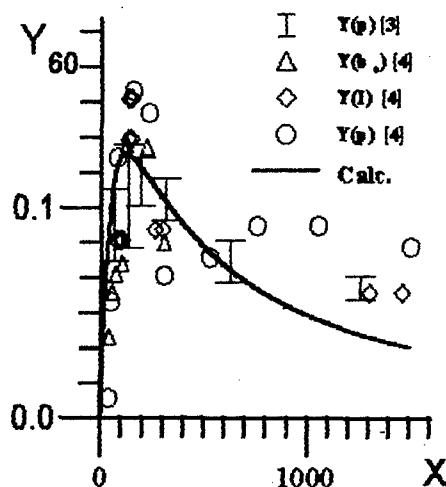


Fig 2. Fullerene yield

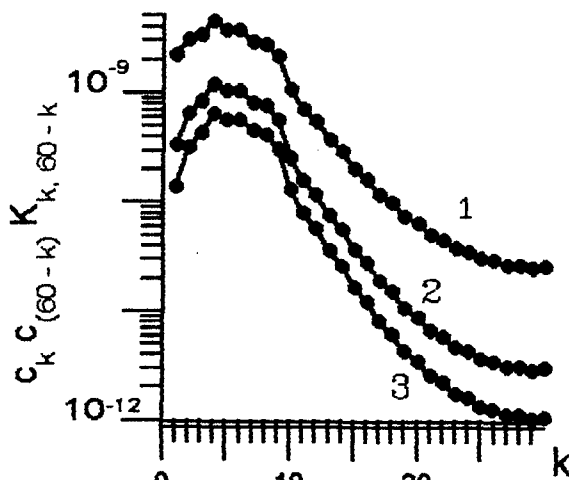


Fig.3 Partial rate constants for equation (1)

# Submicronic $\text{Si}_x\text{C}_{1-x}$ powder synthesis and Palladium coating by using low pressure dusty plasma properties

F. Vivet, A. Bouchoule

Groupe de Recherche sur l'énergétique des Milieux Ionisés, Unité de Recherche Associée au CNRS (URA 831), UFR Sciences, Université d'Orléans, BP 6759, 45067 Orléans cedex 02, FRANCE

## Introduction

Silicon carbide is interesting for its high thermal conductivity and high temperature stability when looking at it as a support for catalysis material and Palladium has catalytic properties which are close to these of platine (Pt), for a lower cost. An integrated process for elaboration of silicon carbide ultrafine powders, coated by thin Pd films, is described

## Powder synthesis and characterization

The first step is the synthesis of the powders by a 13.56 Mhz silane /methane mixture diluted in argon low pressure discharge. Two growth routes were investigated which led to different types of materials in terms of cristallinity and size distribution. These differences are due to the RF power level and the introduction time of the methane which are not the same in both cases. We used infra-red (FTIR) spectroscopy to detect  $\text{Si-CH}_3$  bonds. X-ray photoelectron spectroscopy (XPS) allowed us to obtain the surface composition of the powders and a measurement of the specific surface by BET technical showed these powders are very porous.

In the first way of production (called process n°1), we used a rather high power (80 W,  $V_{p-p} = 850$  V) and the silane ( $\sim 2.3$  sccm) and methane ( $\sim 9$  sccm) were introduced simultaneously. The typical plasma-on time was 20 s. The collected powders were analyzed by XPS, focussing our interest on the C(1s) and Si(2p) shapes. The fitting result are summarized on table I.

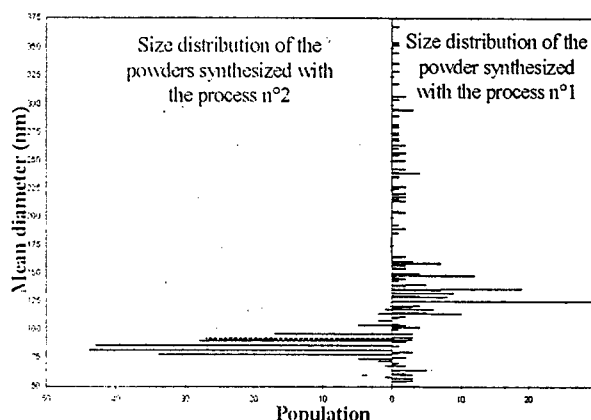
Table I: XPS results (calibration with respect to C(1s) binding energy at 284.6 eV)

	position	percentage	attribution
	99.7 eV	10 %	Si-Si
Si (2p)	100.8 eV	65.8 %	Si-C
	102 eV	24.2 %	Si-O
C (1s)	284.6 eV	100 %	C-C.C-H.C-Si

As can be seen, the Si-C bonds represent 66% of the whole bonds which involve Si atoms. An excess of carbon is proved by the value of

the ratio  $1-X = [\text{C}]/\{[\text{Si}]+[\text{C}]\}$  which is equal to 0.6. Information on the particles material is also obtained through FTIR spectroscopy. The obtained spectrum presents vibration modes attributed mainly to  $\text{Si-CH}_3$  and  $\text{Si-H}_2$  groups. Finally the size distribution as studied by MET (see fig. 1) is found to be a broad one: the mean size is equal to 152 nm and the standard deviation is equal to 70 nm. A further inspection of the distribution highlighted three main classes of particles sizes (48-85 nm; 105-185 nm and 205-335 nm) which correspond to successive generations of powders [1].

Figure 1: size distribution of powders collected with the two processes



An electronic diffraction analysis on these different generations led to the same diffuse rings corresponding to  $\alpha$ -SiC (hexagonal network). The fact that the diffraction rings are diffuse suggests that the material is only partially crystalline, embeded in a general amorphous structure.

As we were primarily interested to synthesize particles with a restricted size distribution, we moved to the second process described below.

This second process (called process n°2) is a sequential one. An initial particle growth (5 s long) is obtained in Argon (36 sccm) / Silane (2.3 sccm) discharge and the Methane flow is added for 5 s for further growth to SiC larger size particles. We avoid the multi-generation of powder using lower RF power: it was reduced to 20 Watts ( $V_{p-p} = 450$  V) for the whole 10 s growth sequence.

We first studied the chemical surface properties with XPS analysis. The peaks decomposition results are summerized on table II.

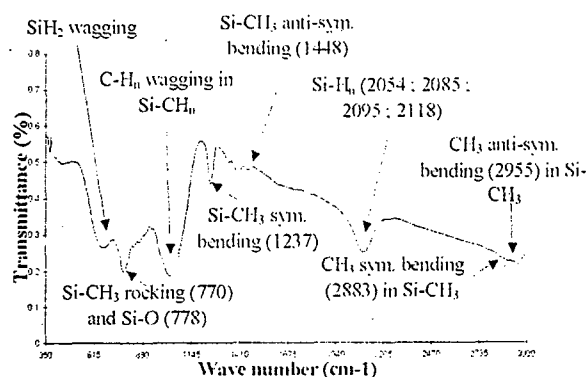
Table II: XPS results( calibration with respect to C(1s) binding energy at 284.6 eV)

	position	percentage	attribution
	99.5 eV	27.9 %	Si-Si
Si (2p)	100.5 eV	30.8 %	Si-C
	101.8 eV	24.5 %	Si-O
	103.1 eV	16.8 %	Si-O <sub>2</sub>
C (1s)	284.6 eV	100 %	C-C, C-H, C-Si

The rate of Si-C bonds fall down to 31% and in the same time the Si-Si bonds percentage increased to 28%. Moreover, the surface of the powders presented an excess of silicium: the ratio 1-X is equal to 0.4 and the presence of Si-O<sub>2</sub> was detected which was not the case for the powders collected with the first way of production. We explain the appearance of silicium dioxide by the fact the surface is no more saturated with carbon atoms which preserve from oxydation. They are probably oxydized during air exposure before analysis. Conversely the Si-O percentage appears stable whatever experimental conditions we use, suggesting that these bonds could be created in the reactor during the growth phase.

FTIR spectrum (see figure2) presented the same vibration modes as obtain in the first case.

Figure 2: FTIR spectrum of the powder collected using the process n° 2



A monodisperse size distribution is obtained, with a standard deviation always lower than 30 nm. Electronic diffraction rings are not observed for these powders, as was the case in the higher power N°1 synthesis.

Their specific area, as measured by BET, is very high (115m<sup>2</sup>/g), a useful property for further Palladium coating.

## Coating of the powders with Pd

The Palladium coating step is achieved in the same RF reactor ( integrated process).

The procedure is based on the electrostatic trapping of the powders in the plasma glow [2]. When the particles reach the wanted size, we stop the reactive gas flows (Methane and Silane) keeping the Ar flow and the RF power on. Thus the powders are trapped in an Ar plasma. After 1 mn which is the required time to pump all the reactive radicals (SiH<sub>Y</sub> and CH<sub>Y</sub>), we introduce 6 Pd wires through slits in the discharge box and we bias them at - 300 V. Then the Ar<sup>+</sup> ions bombardment of the wires surface produces an efficient sputtering as proved by the spectroscopic measurement which allowed to observe atomic Pd emission. To obtain a better Pd diffusion in the discharge box, we stop the Ar flow and the pumping during the Pd coating to be in a stable plasma. Another important point is that powders, which are negatively charged in the plasma, are repelled by the biased wires as observed by Mie scattering. To reduce this phenomena, we pulse the wire bias at a frequency f equal to 1 Hz and thus the powders swing at the same frequency. XPS spectrum presented two shapes in addition to C(1s), Si(2p) and O(1s) which binding energy positions correspond to metallic Pd. A high resolution MET analysis showed that the powders present 5 nm large Pd islands on their surface. However, some of them are well coated and other are not which is due to the volumic distribution of the particles which is not homogeneous in the discharge box. This result shows that the goal of an homogeneous coating on all the particles trapped in the reactor requires a special care in order to insure homogeneous distributions both for particles and palladium vapor.

## Conclusion

This study shows that SiCH particles can be grown within a broad range of properties in terms of size distribution and material characteristics. Particles of mean diameter 70-80 nm have been obtained with narrow size dispersion in a two steps process and then coated with Pd in the same reactor. Catalytic tests are now in progress.

## Aknowledgement

This work has been supported by BRITE-EURAM Contract N° 7328

## References

- [1] L. Boufendi, A.Plain, J.Ph. Blondeau, C.Laure and M.Toogood: Appl. Phys. Lett., 60 (1992)
- [2] A.A.Freedman, L.Boufendi, T. Hbid, B.V.Potapkin and A.Bouchoule: J.Appl.Phys., 79 (1996)

# Observation of dust levitation in a thermoionic low pressure discharge

C. Arnas Capeau, M. Mikikian and F. Doveil

Equipe Turbulence Plasma, UMR 6633 CNRS/Université de Provence

IMT, Technopôle de Chateau-Gombert

13451 Marseille cedex 20 - France

## 1. Introduction

Space plasmas [1-2] and laboratory plasmas [3-5] are often contaminated by charged solid particles from ten nanometers to ten micrometers in size. In particular, these dust particles have been observed in rf plasmas for etching [3] or deposition processes [4], at high gas pressure ( $\sim 0.1$  Torr). They are trapped in the plasma or at plasma-sheath boundaries and tend to self-organize in ordered structures [6-7]. Analytic models give the charge of the dusts and the forces acting [8-9] on them to explain their trapping.

We report here, a new example of dust levitation in a collisionless plasma produced by a hot cathode discharge, in a multipolar device, at low argon pressure ( $5 \cdot 10^{-4}$  -  $1.3 \cdot 10^{-3}$  Torr). The localization of the dust trajectories over a negatively biased plate (not necessarily in the center) is assigned to the variation of the fast electron flux, due to the multipolar magnetic field lines.

## 2. Experiment

### 2.1. Experimental set up

The plasma device consists of a stainless steel cylinder (30 cm diameter and 40 cm length). The argon plasma is produced by a dc discharge between the grounded wall and two heated, negatively biased, tungsten filaments (20 cm long and 0.03 cm diameter). The fast electrons (emitted by the filaments) confinement is provided by: i) fixed separated permanent magnets, parallel to the chamber axis, with alternate polarization and ii) two floating potential plates, parallel to the two chamber doors. A stainless steel plate (12 cm diameter) negatively biased (at floating potential or biased by a power supply) is located in the center of the chamber. Glass micro-balloons ( $110 \text{ kg/m}^3$  mass density and radius  $\sim 50 \text{ }\mu\text{m}$ ) are injected by a small dust dropper located over the plate. This electrode intercepts the magnetic fields of the multipolar device. So, the inhomogeneous fast electron flux (gyro-radius of 1, 2 cm) produce perturbations of the electrode potential - the different location of the dusts trajectories being a signature of the potential variations -.

### 2.2 Situation and results

We have plotted the magnetic field variation in the vicinity of the electrode and the corresponding fast electron flux variation. A moving Langmuir probe gives the plasma parameters variation according to the magnetic field or according to the position on the electrode.

Varying the three discharge parameters: i) the argon pressure (probability of ionization), ii) the fast electrons emission and iii) the fast electrons energy, we can observe different dust behaviors: 1) gas, 2) "liquid" and 3) solid (at pressure  $\sim 1.3 \cdot 10^{-3}$  Torr) phases and in special conditions: 4) individual dust low frequency oscillations in the vertical plane, during their motion in the gas phase.

Moreover, it is possible to trap a single micro-balloon in the sheath edge. In that case, a model for the charging of an isolated dust can be applied. This model must take into account the fast electrons [10] emitted by the heated cathodes and their secondary emission.

The oscillation frequency of the dust can be measured and associated to their charge [7] in the potential sheath electrode.

The forces acting on the dust grains in the electrode sheath [8-9] are also estimated. We show that the gas drag force as well as the thermophoretic force are negligible with respect to the gravity force and to the balancing forces: i) electric field force and ii) ion drag force.

## 3. Conclusion

The first experimental results of dust levitation obtained in a hot cathode continuous discharge look very promising. In particular the solid phase obtained at low pressure ( $1.3 \cdot 10^{-3}$  Torr) is rather new and opens a new field of study as well as the observed vertical oscillations of the dust grains during their motion, in the gas phase.

- [1] E.C. Whipple, T.G. Northrop and D.A. Mendis, *J. Geophys. Res.* **90** (1985) 7405
- [2] C.K. Goertz, *Rev. Geophys.* **27** (1989) 271
- [3] G.S. Selwyn, J. Singh and R.S. Bennet, *J. Vac. Sci. Technol. A* **7** (1989) 2758
- [4] K.G. Spears, T.M. Robinson and R.M. Roth, *IEEE Trans. Plasma Sci.* **14** (1986) 179
- [5] A. Bouchoule, A. Plain, L. Boufendi, J.P. Blondeau and C. Laure, *J. Appl. Phys.* **70** (1991) 1991
- [6] H.M. Thomas and G.E. Morfil, V. Demmel, J. Goree, B. Feuerbacher and D. Mohlmann, *Phys. Rev. Lett.* **73** (1994) 652
- [7] A. Melzer, T. Trottenberg and A. Piel, *Phys. Lett. A* **191** (1994) 301
- [8] M.S. Barnes, J.H. Keller, J.C. Forester, J.A. O'Neill and D.K. Coultas, *Phys. Rev. Lett.* **68** (1992) 313
- [9] T. Nitter, *Plasma Sources Sci. Technol.* **5** (1996) 93
- [10] B. Walch, M. Horanyi and S. Robertson, *Phys. Rev. Lett.* **75** (1995) 839



***Topic 13***

**Waves and instabilities,  
including shock waves.**

# Ion-electron instability in an electron-collecting contactor

V. Lapuerta and E. Ahedo

E.T.S.I. Aeronáuticos, Universidad Politécnica, Madrid, Spain

Laboratory experiments with hollow-cathode based plasma contactors [1] show that the structure of the plasma around the contactor consists of a double-layer(DL) that confines a quasineutral plasma cloud (the core), mainly constituted by plasma emitted by the contactor, from the external quasineutral plasma (the presheath). Since the DL produces two counterstreaming beams of energetic particles, it is thought that current-driven instabilities are launched on both DL sides. Our aim is to analyze the kinds of instabilities that set up, taking into account the characteristics of the plasma structure around the contactor, like the presence of the DL, the quasispherical geometry, and the boundary conditions. We proceed along the usual way in linear stability theory, analyzing the reaction of a stationary state of the plasma field to small disturbances. Here, the analysis is restricted to electron-collecting (anodic) contactors and to frequencies in the range of the ion-electron instability.

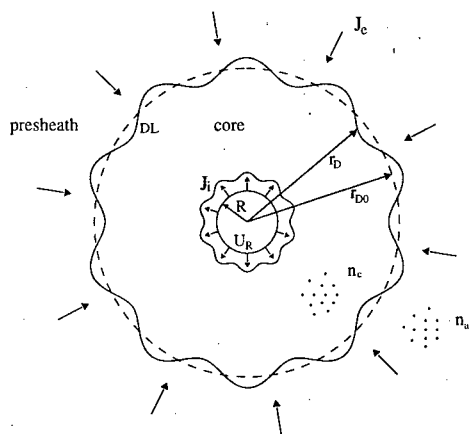


**Figure 1.-** Sketch of the model:  $J_i$  and  $J_e$  are the emitted and collected currents, respectively;  $n_c$  and  $n_a$  are the densities of confined electrons and ambient ions, respectively;  $r = r_D$  and  $r = r_{D0}$  are the actual and mean position of the DL.

In order to get a tractable model, we consider that the contactor is a sphere of radius  $R$ , biased to a positive potential,  $U_R$ , relative to the ambient, quiescent plasma, that emits a plasma current,  $4\pi J_i$ , high enough to sustain a thin double-layer, separated from

the contactor, and a quasineutral core between the DL and the contactor. The potential barrier on the DL prevents ambient ions(a) from reaching the core, confines emitted electrons(c) within the core, and accelerates ambient electrons(e) inwards and emitted ions(i) outwards, Figure 1.

The set of macroscopic equations that describe the dynamics of the four plasma species, admits, for  $U_R$  and  $4\pi J_i$  uniform and time-independent, a stationary, spherically symmetric solution that reproduces the core/DL/presheath structure we are interested in. That solution determines the dimensionless collected current,  $j_e$ , and DL position,  $\xi_{D0} = r_{D0}/R$ , as function of the dimensionless contactor potential,  $\chi_R = eU_R/T_c$ , emitted ion current,  $j_i$ , and plasma temperature ratio,  $\theta_{ac} = T_a/T_c$ . As  $\xi_{D0}$ , i.e. the core size, increases with  $j_i$ , we find convenient to use  $\xi_{D0}$ , instead of  $j_i$ , as parameter.

For the perturbation analysis, the appropriate normal mode decomposition for a generic plasma variable, let us say  $f$ , is

$$f(r, \theta, \phi, t) \simeq f_0(r) + f_1(r; \ell, m, \gamma) Y_{\ell m}(\theta, \phi) \exp \gamma t$$

where  $f_0$  is the known stationary solution,  $Y_{\ell m}(\theta, \phi)$  is any spherical harmonic, and  $\gamma = \gamma_r + i\gamma_i$  is a complex frequency.

Within each quasineutral region: core and presheath, each normal mode verifies a set of differential equations on the radial variable  $r$  that includes  $\ell$  and  $\gamma$  as eigenvalues. Here, we restrict the instability analysis to values of  $|\gamma|$  much smaller than the response frequency of electrons. We find that the perturbation equations and, hence, the dispersion relation, are independent of the azimuthal number,  $m$ .

As boundary conditions for the perturbation equations we have: i) the solution is bounded in all space, and, in particular, at  $r = R$ ,  $r = r_D^\pm$  and  $r = \infty$ ; ii) the jump conditions across the DL derived from the plasma equations; iii) perturbations are zero at  $r = R$  and  $r = \infty$  (for the stability analysis). The perturbation modes produce a ripple of the DL,  $r = r_{D0} + r_{D1}(\theta, \phi, t)$ , that must be determined. At the same time, to impose correctly conditions at the DL boundaries,  $r_D^\pm$ , requires to expand the plasma variables around the DL mean position,  $r_{D0}$ .

For  $eU_R/T_a \gg 1$ , we can solve the perturbation problems on presheath and core separately. The solution for the presheath shows that, at least for the

above parametric limit, no ion-electron instability sets up in this region and the presheath response depends only on the ripple of the DL.

In the core, we first obtain the general solution of the perturbation equations. Then, we impose the set of conditions at both boundaries, and, for zero-perturbation at  $r = R$ , we find that non-trivial solutions exist if and only if a certain eigenvalue or dispersion relation,

$$D(\gamma, \ell, \xi_{D0}, \chi_R, \theta_{ac}) = 0.$$

is satisfied [3]. For each stationary state,  $(\chi_R, \theta_{ac}, \xi_{D0})$ , the dispersion relation yields a family  $(\ell, \gamma)$  of self-excited modes. They are unstable if  $\gamma_r > 0$ , and neutrally stable if  $\gamma_r = 0$ ; they are non-oscillatory or oscillatory (in time) if  $\gamma_i$  is equal to 0 or not, respectively.

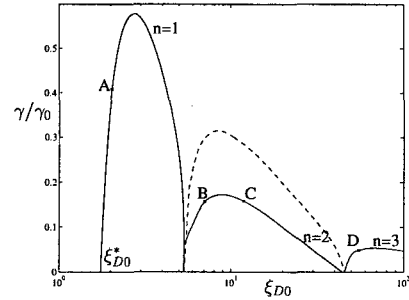
Figure 2 shows the unstable modes,  $\gamma(\xi_{D0})$ , with  $\ell = 5$ , for given values of  $\chi_R$  and  $\theta_{ac}$ . The number  $n$  refers to the sequence of loci of non-oscillatory ( $n$  odd) and oscillatory ( $n$  even) modes, alternatively. For each  $\ell$ , there are no unstable modes below a certain core size,  $\xi_{D0}^*(\ell)$ , and the most unstable mode occurs for  $n = 1$ , always. Figure 3 shows the  $n = 1$  mode for different  $\ell$ . For  $\ell$  increasing, the threshold,  $\xi_{D0}^*(\ell)$ , decreases, and the modes are more unstable. For the purely-longitudinal case,  $\ell = 0$ , (the only one discussed in previous works) there are not unstable modes. For  $\xi_{D0}$  fixed,  $\gamma_r$  does not attain a maximum for any  $\ell$  but the model is not valid beyond certain  $\ell$ , unless space-charge effects are considered throughout the core and presheath. In general, the instability growth rate decreases with  $\chi_R$  increasing and  $\theta_{ac}$  decreasing; the second effect is due to the increasing 'rigidity' of the presheath.

Figure 4 shows potential profiles of several unstable modes; observe that  $n$  is related to the number of radial oscillations of the mode. In the figure, the perturbed potential does not go to 0, at  $r = R$ : this is a consequence of the core quasineutrality; in fact, there exists a thin non-neutral sheath (of thickness about the core Debye length up to the 4/5 power) attached to the contactor that carries the perturbation to 0.

The above unstable modes correspond to a three-streaming ion-electron macroinstability [4] where the electrons streaming into the core provide the destabilizing effect and the confined electrons tend to stabilize. This competition explains the evolution of the growth rate with  $\ell$  and  $\chi_R$ .

#### Acknowledgments

This work was supported by the Comisión Asesora de Investigación Científica Técnica of Spain, Project PB94-0417-C3-03.



**Figure 2.-** Complex frequency,  $\gamma_r$  (---) +  $i\gamma_i$  (- -), of unstable modes with  $\ell = 5$ ;  $\gamma_0 = \sqrt{T_c/m_i}/R$ ;  $\chi_R = 50$ ,  $\theta_{ac} = 0.1$ .

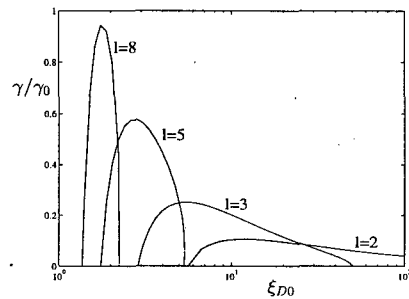


**Figure 3.-** Complex frequency of unstable modes with  $n = 1$  and different values of  $\ell$ ;  $\chi_R = 50$ ,  $\theta_{ac} = 0.1$ .

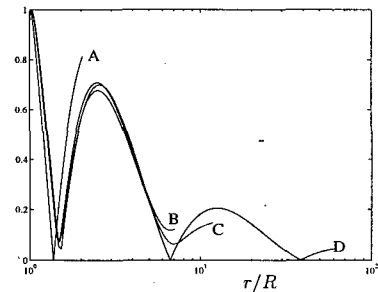


**Figure 4.-** Radial profiles of the perturbation on the potential (modulus), corresponding to points A, B, C, and D in Fig.2.

#### References

- [1] J.D. Williams and P.J. Wilbur: *J. Spacecraft* **27** (1990) 634; L. Conde and L. León: *Phys. Plasmas* **1** (1994) 2441.
- [2] E. Ahedo, M. Martínez-Sánchez, and J.R. Sanmartín, *Phys. Fluids B* **4** (1992) 3847.
- [3] E. Ahedo and V. Lapuerta, *Phys. Plasmas* **2** (1995) 3252.
- [4] A. Krall, A. Trivelpiece, *Principles of Plasma Physics* (San Francisco Press, San Francisco, 1986).

# Hall effect as the producer of effective gravity and of quasi-acoustic-gravity waves in plasma flows

Liliya M. Alekseeva

Institute of Nuclear Physics, Lomonosov Moscow State University,  
Moscow 117234, Russia

Rosenau, Tataronis and Conn [1] studied the non-linear partial differential equations of magnetohydrodynamics (MHD) in which allowance was made for the Hall effect. They found real characteristics for this system of equations, which show no trace of fast, slow, and Alfvén waves known in non-Hall MHD but describe sound waves absent in non-Hall MHD. The characteristic surfaces  $\phi(\mathbf{r}, t) = \text{const}$  are given by the equation  $\mathbf{H} \cdot \nabla \phi = 0$ .

It is unclear to what extent this system of MHD equations with the Hall effect is evolutionary and represents physical phenomena, although this question has been discussed for a long time. However, it is beyond doubt that taking into account the magnetic viscosity  $\nu$  makes the Hall MHD equations evolutionary [2].

We obtain here an analytical solution to the equations of resistive Hall MHD (or RHMHD). This solution proves to be of the form of purely acoustic waves (certain stages of this work have already been presented in [3–5]). Our results correlate with a prediction made in [1].

In a Cartesian coordinate system  $x, y, z$  with the  $x$ -axis streamwise, we consider planar flows of the form

$$\mathbf{v} = (v_x, v_y, 0), \quad \mathbf{H} = (0, 0, H), \quad \partial/\partial z = 0. \quad (1)$$

As the unit of length, we take an appropriately chosen characteristic scale  $l$ ; as the units of density  $\rho$  and magnetic field  $H$ , the values  $\rho_*$  and  $H_*$  of these variables at some upper point  $(x_*, y_*)$  of the stream within the region at hand for some time moment  $t_*$ . The Alfvén velocity  $v_* = (H_*^2/4\pi\rho_*)^{1/2}$  at this point is adopted as the unit of velocity  $v$ , and the magnetic pressure  $H_*^2/(4\pi)$ , as the unit of the pressure  $P$ . The ratio of the unit length to the unit velocity is of the order of the transit time and serves as the unit of time  $t$ . The equation set (obtained in [2]) thus takes the form

$$\frac{\partial \rho}{\partial t} = -(\nabla \cdot \rho \mathbf{v}), \quad (2)$$

$$\frac{d\mathbf{v}}{dt} = -\frac{1}{\rho} \nabla \left( P + \frac{H^2}{2} \right), \quad (3)$$

$$P = c^2 \rho, \quad (4)$$

$$\frac{\partial \mathbf{H}}{\partial t} = \nu \Delta \mathbf{H} + \text{curl}(\mathbf{v} \times \mathbf{H}) + \xi \nabla \frac{1}{\rho} \times \nabla \frac{H^2}{2}. \quad (5)$$

We assume the plasma to be isothermal. In this case, plasma dynamics is determined by three constants: the

magnetic viscosity  $\nu = R_m^{-1}$  (where  $R_m$  is the magnetic Reynolds number), the ratio  $\beta$  of the characteristic value of gas pressure to that of magnetic pressure ( $\beta = 2c^2$ , where  $c$  is the gasdynamic speed of sound), and the parameter  $\xi = c_0 m_i / e l \sqrt{4\pi\rho_*}$  that characterizes the influence of the Hall effect ( $c_0$  being the speed of light).

We denote a solution of Eqs. (2)–(5) as  $\Pi(x, y, z, t) = (\rho, \mathbf{v}, H)$  and seek it in the following form:

$$\Pi(x, y, t) = \Pi^0(x, y/\delta) + \tilde{\Pi}(x, \gamma \delta x, y/\delta, \gamma y, \gamma ct). \quad (6)$$

Here,  $\Pi^0$  is the known (background) steady-state flow with the characteristic transverse scale  $\delta$  (the relationship  $v_y^0/v_x^0 \sim \delta$  being valid for its velocity components);  $\tilde{\Pi}$  is a time-depending deviation from it; and the gamma factor

$$\gamma \equiv \gamma(\Pi^0) = -\Gamma \left( \frac{H^0}{\rho^0} \right)^2 \frac{\partial H^0}{\partial x}, \quad \Gamma \equiv \frac{\xi}{\nu c^2} \quad (7)$$

characterizes  $\tilde{\Pi}$ . We choose  $\Pi^0$  to be fairly uniform across the stream, so that  $\partial \Pi^0 / \partial y \lesssim 1$ . We assume that  $c \ll 1$ . Then, in the adopted units,

$$\frac{\partial \rho^0}{\partial x} \sim \frac{\partial H^0}{\partial x} \sim \frac{\partial v^0}{\partial x} \sim \rho^0 \sim H^0 \sim v^0 \sim 1. \quad (8)$$

Let us also put

$$\xi \gg c \gg \delta. \quad (9)$$

(hence, we evidently restrict ourselves to considering flows  $\Pi^0$  with smooth streamlines). Further, we put  $(\xi/c)(\delta/c) \gg \nu$ . The above-assumed conditions imply that

$$\Gamma \delta \gg 1, \quad \Gamma \gg 1, \quad \Gamma c \gg 1. \quad (10)$$

Let all operators acting on  $\tilde{\Pi}$  change the order of magnitude of this quantity in the following way:

$$\frac{\partial \tilde{\Pi}}{\partial x} \sim \Gamma \delta \tilde{\Pi}, \quad \frac{\partial \tilde{\Pi}}{\partial y} \sim \Gamma \tilde{\Pi}, \quad \frac{\partial \tilde{\Pi}}{\partial t} \sim \Gamma c \tilde{\Pi}, \quad 0 \leq t \lesssim \frac{\delta}{c}. \quad (11)$$

We also assume that  $|\tilde{H}|$  is small, setting

$$\frac{1}{\nu \Gamma^2} \Phi(\Pi^0) \ll |\tilde{H}| \ll \min \left( \frac{1}{\Gamma \delta}, c^2 \right), \quad (12)$$

where

$$\Phi(\Pi^0) \equiv \left| \nu \Delta H^0 + \text{curl}(\mathbf{v}^0 \times \mathbf{H}^0) + \xi \nabla \frac{1}{\rho^0} \times \nabla \frac{(H^0)^2}{2} \right| \quad (13)$$

Obviously, such fields of variables can exist only if

$$\frac{1}{\nu \Gamma^2} \Phi(\Pi^0) \ll \min \left( \frac{1}{\Gamma \delta}, c^2 \right) \quad (14)$$

This is another condition for the parameters  $\xi$ ,  $\nu$ ,  $\beta$ , and  $\delta$  but, unlike the above-listed conditions, it depends on the structure of  $\Pi^0$ . [This condition is not too restrictive, and in some cases it does not appear at all. In particular, we can choose as  $\Pi^0$  a solution  $I^0$  to Eqs. (2)–(5) for the case  $\partial/\partial t = \xi = \nu = 0$ . Among them, there are solutions representing isomagnetic streams ( $H^0/\rho^0 = 1$ ), in which  $\Phi(\Pi^0) = \nu |\Delta H^0|$ . If, in addition, such a  $\Pi^0$  is an iso-Bernoulli stream, for it  $j_x^0 = \partial H^0/\partial y \sim \delta$  (see [4] and references therein) and  $\Phi(\Pi^0) \sim \nu$ . Then condition (14) is satisfied automatically, being a consequence of (10). In some cases, we shall use as a simple and representative form of  $\Pi^0$  an isomagnetic, iso-Bernoulli background flow  $I^0$  with the same  $\beta$  as assumed for  $\Pi$ . It is known that the streamlines of  $I^0$  can have diverse configurations. Therefore, the flow  $I^0$  is a good model for practically important streams.]

The substitution of (6) into the  $x$ -component of the Euler equation shows that if the terms nonlinear in  $\tilde{\Pi}$  are small (which will be seen below), then

$$\tilde{v}_x \sim \max \left\{ \frac{|\tilde{\rho}|}{\gamma c}, \frac{|\tilde{v}_y|}{\gamma c}, c\delta|\tilde{\rho}|, \frac{\delta|\tilde{H}|}{c} \right\}. \quad (15)$$

This relation allows us to conclude that the  $y$ -component of the Euler equation reduces to

$$\frac{\partial \tilde{v}_y}{\partial t} = -\frac{1}{\rho_0} \left( c^2 \frac{\partial \tilde{\rho}}{\partial y} + H^0 \frac{\partial \tilde{H}}{\partial y} \right), \quad (16)$$

and the induction equation (5) integrated over  $y$  has the form

$$\frac{\partial \tilde{H}}{\partial y} = \frac{c^2}{H^0} \gamma(\Pi^0) \tilde{\rho}. \quad (17)$$

Now the order of  $\tilde{H}$  in  $\tilde{\rho}$  is known. By direct substitution, we can check that  $|\tilde{\rho}| \ll 1$ ,  $|\tilde{v}| \ll 1$ , and the nonlinear terms of all the equations used are indeed small.

Using Eq. (17) makes it possible to close the gasdynamic part of the equation set at hand and shows that in the given situation electromagnetic processes generate a force proportional to  $\tilde{\rho}$ , which appears in Eq. (16). In other words, the perturbations  $\Pi$  "sense" an effective gravitational force with acceleration  $g = -c^2 \gamma(x, y)$ , which acts in  $y$ -direction.

The obtained gasdynamic system still remains to be solved. The analysis of orders of magnitude shows that the continuity equation reduces to  $(\partial \tilde{\rho}/\partial t) =$

$-(\partial \tilde{v}_y/\partial y)/\rho^0$  and, on eliminating  $v_y$  with the use of (16) and (17), gives

$$\frac{1}{c^2} \frac{\partial^2 \tilde{\rho}}{\partial t^2} = \frac{\partial^2 \tilde{\rho}}{\partial y^2} + \gamma(x, y) \frac{\partial \tilde{\rho}}{\partial y}. \quad (18)$$

We see that this equation coincides in form with the equation of acoustic-gravity waves propagating vertically in a neutral atmosphere [6, 7]. In accelerated plasma flows  $\gamma$  is positive, and the upward direction in the atmosphere corresponds to the negative direction of the  $y$ -axis (i.e., counter to the  $y$ -component of the field  $\mathbf{E}$ ). The quantity  $1/\gamma$  plays the role of the local scale height. Waves of this sort in RHMHD media, described by Eq. (18), can be called quasi-acoustic-gravity (QAG) waves.

If  $\gamma$  does not depend on  $y$  (which is ensured by  $I^0$  taken as  $\Pi^0$ ), there exists a solution of the plane-wave type  $\tilde{\rho} = \chi(x) \exp(-\gamma y/2) \exp[i(\omega t - ky)]$  ( $\chi$  being an amplitude factor). Its amplitude increases in the case of "upward" propagation (i.e., in accelerated flows, toward the anode). The dispersion relation for QAG waves has the form  $k^2 c^2 = \omega^2 - \omega_L^2$ , where  $\omega_L = c\gamma/2$  is the lower frequency limit for traveling waves (the analog of the Brunt-Väisälä frequency for atmosphere). The phase and the group velocity of QAG waves are respectively  $v_p = \omega/k = c/Q$  and  $v_g = cQ$ , where  $Q = [1 - (\omega_L/\omega)^2]^{1/2}$ .

If  $\gamma(y)$  is variable, a wave of frequency  $\omega$  should be reflected from the region where  $\omega \approx \omega_L$ .

As  $\gamma(y)$  varies rather slowly over a distance of the order of the QAG-wave length, Eq. (18) can be solved by the Wenzel-Kramers-Brillouin technique.

## References

- [1] P. Rosenau, J. A. Tataronis, and G. Conn, *J. Plasma Phys.* **21**(3), 385–399 (1970).
- [2] K. V. Brushlinskiĭ and A. I. Morozov, in: *Voprosy teorii plazmy*, ed. by M. A. Leontovich, vol. 8, Moscow: Atomizdat, 1974, pp. 88–163 [Engl. transl.: *Reviews of Plasma Physics*, vol. 8, New York: Consultants Bureau, 1980, p. 105].
- [3] L. M. Alekseeva, *Dokl. Akad. Nauk SSSR*, **310**(3), 567–571 (1990). [Engl. transl: *Sov. Phys. Dokl.*, **35**, 51 (1990)].
- [4] L. M. Alekseeva, *Zh. Tekh. Fiz.*, **62**(2), 64–73 (1992). [Engl. transl.: *Sov. Phys. Tech. Phys.*, **37**(2), 146–151 (1992)].
- [5] L. M. Alekseeva, *Pis'ma Zh. Tekh. Fiz.* **19**(5), 34–88 (1993). [Engl. transl.: *Sov. Tech. Phys. Lett.* **19**(3), 145–147 (1993)].
- [6] H. Lamb, *Hydrodynamics*, 6th ed., Cambridge University Press, 1932.
- [7] C. O. Hines, *Can. J. Phys.* **38**, 1441–1471 (1960).

# Electric field waves inside the positive column of the self-pulsed gas discharge

L.S. Alexandrov, M.V. Chirkin, D.A. Morozov, V.A. Stepanov  
 Department of Physics, Pedagogical University  
 46 Svoboda St., 390000 Ryazan, Russia  
 e-mail: yastreb@ttc.ryazan.ru

## 1. Introduction

One of the most important mechanisms of weakly ionized plasma instability is the influence of the ion spatial charge upon charged particle flows onto the discharge tube wall [1]. It was experimentally shown [2] that this mechanism is the cause of the current wave amplification in the positive column of the low pressure DC helium discharge, which is surrounded by the grounded metallic screen. Instability development inside the distributed-parameter line "low temperature plasma - external screen" provides the existence of several non-stationary self-conformed regimes for gas discharge maintenance in a narrow lengthy channel. The characteristic feature of these regimes is the generation of a periodical sequence of short current impulses with large amplitudes (see Fig. 1). The purpose of the present paper is to find a way of self-pulsed discharge maintenance.

## 2. Experimental technique

The electric circuit under examination consists of DC power supply, ballast resistor and discharge tube (1 mm in internal diameter, 8 mm in external diameter, 125 mm in length). The tube is filled with helium (3 Torr in pressure). The metallic screen surrounding the tube consists of several isolated sections in the form of hoops (25 mm in diameter) (Fig. 2).

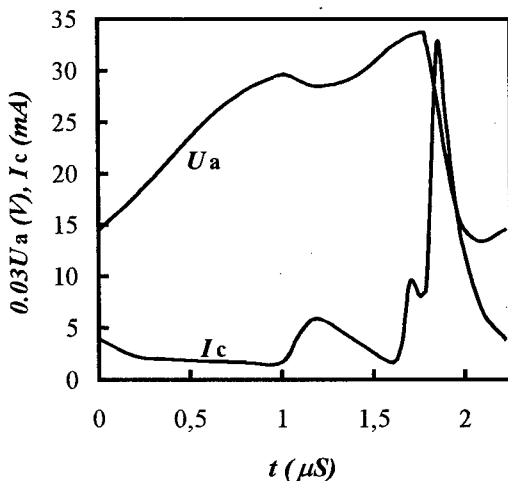


Figure 1: Oscillations of the anode voltage and the cathode current in the case of the self-pulsed gas discharge in helium

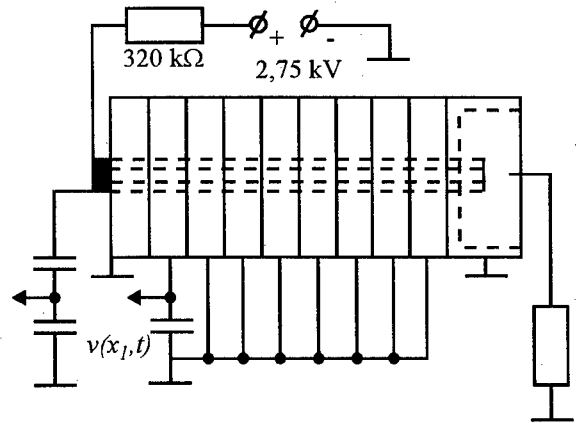


Figure 2: Outline of the experimental system

In accordance with the problem under research there have been reconstructed on the basis of experimental data the instantaneous distributions of the electric field potential along the positive column axis  $U(x, t)$ . The data were obtained by means of measuring the voltage  $v(x_i, t)$  on the capacitor  $C$  connected with an isolated section of the metallic screen. The voltage on the capacitance detector was induced by electric field oscillations inside the positive column:

$$v(x_i, t) = \int_0^l K(x_i, x') U(x', t) dx' \quad (1)$$

where axis  $Ox$  is directed to the cathode of the tube from the anode,  $l$  is the discharge channel length,  $x_i$  - the coordinate of the  $i$ -th screen section.

The kernel of the integrated equation (1)  $K(x_i, x')$  was analytically determined by means of the Shockley - Ramo theorem [3]:

$$K(x_i, x') = \frac{8\pi\epsilon\epsilon_0 r_0}{Cl} \sum_{n=1}^{\infty} a_n \sin \frac{n\pi x_i}{l} \sin \frac{n\pi x'}{l} \quad (2)$$

where  $r_0$  is the internal radius of the discharge tube,  $\epsilon$  - the glass permittivity,  $a_n$  - the coefficients depending on the geometry of the screen and the discharge tube.

## 3. Results of the electric field measurements

The results of the solution to the reverse problem (1) are given in Fig. 3 in the form of the electric field potential distributions inside the plasma for various temporal stages of the self-oscillations. The recon-

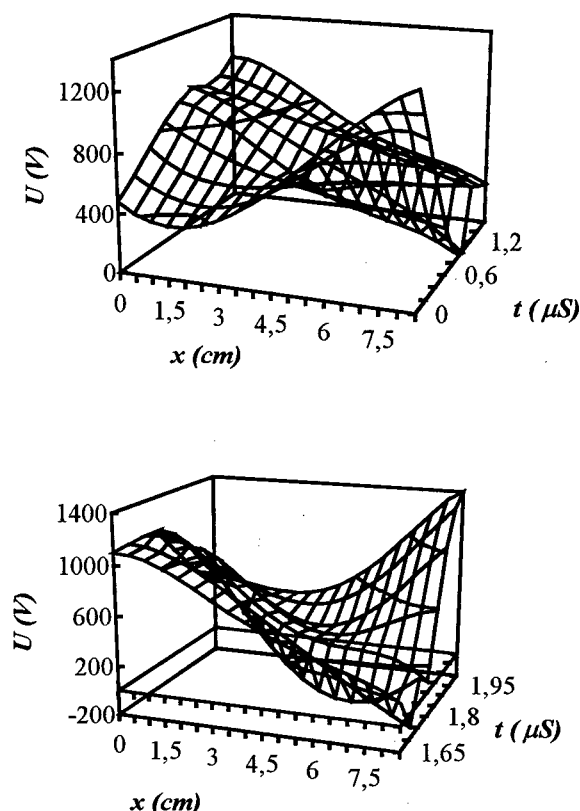


Figure 3: Reconstructed distributions of the electric field along the discharge channel axis

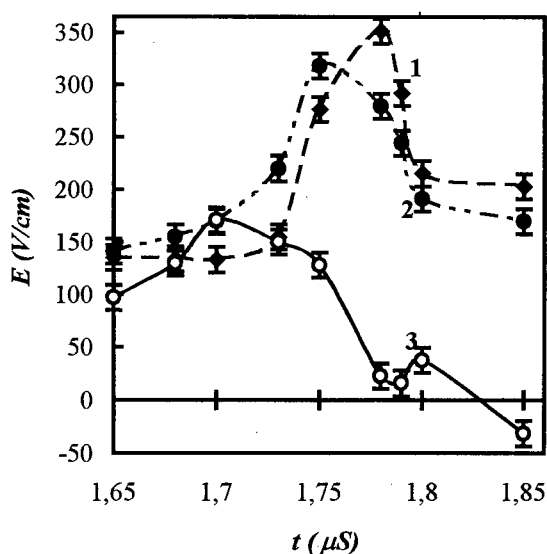


Figure 4: Propagation of the strong longitudinal electric field area inside the positive column. Distance from the anode  $x$  (cm): 1 - 2.0, 2 - 3.5, 3 - 5.5

structed process resembles a standing wave. The distance between the nodes of the wave is about 8 cm.

However there has been discovered a local area (4 cm in length) with a strong longitudinal electric field intensity (300 V/cm) that appears inside the short temporal interval ( $\sim 150$  ns) immediately preceding the current impulse. The temporal dependences of the longitudinal electric field intensities are shown in Fig. 4 for various points of the positive column. The results obtained demonstrate the propagation of the strong electric field area to the anode from the cathode with the velocity about  $10^8$  cm/S.

There has been observed a local impulse of a displacement current (about 70 nS in duration) which flows from the screen sections. This impulse propagates together with the strong electric field area. Inside a gap between the discharge tube and the screen the peak value of displacement current density is about  $1 \text{ mA/cm}^2$  during the impulse.

#### 4. Conclusions

The self-pulsed gas discharge under research is in immediate proximity to a standing wave in the active distributed-parameter line the length of which is approximately equal to  $3/4$  of the wavelength. The necessary condition of this regime maintenance is the formation of the moving ionization front appearing as a result of transient processes, which are accompanied by a redistribution of the potential in the discharge channel. The observed propagating area with the strong electric field and high ionization rate is analogous with a fast ionization wave [4]. However in the case observed the ionization front propagates from the grounded electrode of the discharge tube to the high voltage one; that makes a difference.

For the moving ionization front to appear as a result of pulsed breakdown it is necessary to provide the discharge voltage growth rate ( $dU/dt$ ) of about  $10^{12}$ - $10^{13}$  V/s. In the case of the self-pulsed discharge there appears a local area with an electric field of large intensity even if the temporal growth of the anode voltage between the discharge current pulses is relatively slow ( $dU/dt \sim 10^9$  V/s). High energies of electrons inside the ionization front and a slight heating of the gas make self-pulsed form of the gas discharge maintenance applicably attractive.

#### 5. References

- [1] L. Alexandrov, M. Chirkin, V. Stepanov: XXII ICPIG Contr. Papers, Part 3 (1995) 56
- [2] M.V. Chirkin, D.A. Morozov, V.A. Stepanov: XIII ESCAMPIG Contr. Papers, Part B (1996) 415
- [3] W. Shockley: J. Appl. Phys., 9 (1938) 635
- [4] L.M. Vasilyak, S.V. Kostyuchenko, N.N. Kudryavtsev, I.V. Filyugin: Uspekhi Fizicheskikh Nauk, 164 (1994) 247

# Nonlinear Plasma Wave Propagation

Carlo Lancellotti and J. Dorning  
University of Virginia, Charlottesville, VA 22903

## 1. Introduction

One of the oldest and most fundamental problems in plasma kinetic theory is the study of small-amplitude longitudinal wave propagation in a plasma described by the Vlasov-Poisson-Ampère (VPA) system

$$\frac{\partial f_\alpha}{\partial t} + v \frac{\partial f_\alpha}{\partial x} + \frac{q_\alpha}{m_\alpha} E \frac{\partial f_\alpha}{\partial v} = 0 \quad (1a)$$

$$\frac{\partial E}{\partial x} = 4\pi \sum_\alpha q_\alpha \int dv f_\alpha \quad (1b)$$

$$\frac{\partial E}{\partial t} = -4\pi \sum_\alpha q_\alpha \int dv v f_\alpha \quad (1c)$$

where  $E(x, t)$  is the electric field and  $f_\alpha(x, v, t)$  is the distribution function for the species  $\alpha$ ,  $\alpha = 1, \dots, N$ . This system has played a major role in the analysis of plasma instabilities and wave propagation in a wide variety of settings, ranging from astrophysical, solar and magnetospheric plasmas to laboratory and fusion plasmas. However, due to the extreme analytical difficulties associated with the nonlinear Vlasov equation, Eq. (1a), much of the theory, starting with the classic works of Vlasov [1] and Landau [2], has been based on the linearized version of the model. Unfortunately, this limits the validity of most of the results to a relatively short time-scale, on which the linearization is accurate. This is the case, in particular, for the most famous result of the linear theory, namely Landau damping. Whereas Landau's solution to the linearized initial value problem predicts the exponential damping of  $E(x, t)$  for every small disturbance to a thermal distribution, already in 1965 T.M. O'Neil [3] argued that nonlinear effects can prevent the complete damping of a sinusoidal wave and lead to a time-asymptotic traveling-wave mode, sustained by the oscillations of the particles trapped in the wave's potential well. Even though this phenomenon, known as nonlinear Landau damp-

ing, is now qualitatively well understood, a satisfactory quantitative analysis has never been possible, because of the formidable nonlinear nature of the VPA system. Recently, some rigorous nonlinear results have confirmed that Vlasov plasmas can sustain small-amplitude waves in spite of the predictions of the linear theory. Holloway and Dorning [4] have used the BGK formalism [5] in order to construct exact nonlinear, periodic, undamped traveling wave solutions to the VPA system with arbitrarily small amplitude. Buchanan and Dorning [6,7] have reformulated and extended the analysis to include small-amplitude solitary waves [7] and multiple periodic waves [6]. The question still open, though, is whether and how such undamped-wave solutions can be generated from given initial conditions.

## 2. General Development

We have carried out a fairly general mathematical analysis of the VPA initial value problem, which has enabled us to study the long-time amplitude of the electric field as a function of the initial amplitude. Our approach is based on the decomposition  $E(x, t) = A(x, t) + T(x, t)$ , where  $T$  and  $A$  denote, respectively the transient and time-asymptotic parts of the electric field. This decomposition makes it possible to focus on the time-asymptotic part of the problem and to obtain important results on  $A$  independently of the details of the transient  $T$ . Under mild assumptions, we have shown that  $A$  is given at leading order by a finite superposition of wave modes, whose phase velocities satisfy a Vlasov dispersion relation [1]. Whereas the usual Vlasov dispersion relation is determined by an initial, unperturbed Vlasov equilibrium, the one for  $A$  depends on a time-asymptotic Vlasov equilibrium, modified by the action of  $T$ . Based on this general form of the solution for  $A$ , we obtained an approximate solution to the nonlinear Vlasov equation by linearizing only



the term containing the transient, and then integrating the resulting equation along the nonlinear characteristics corresponding to  $A$ . These were determined explicitly via the methods of Hamiltonian perturbation theory, in the manner of Buchanan and Dorning [6]. At this point, we were able to obtain the transient  $T$  using a standard perturbation technique because the decay properties of  $T$  neutralize most of the secularities that would otherwise plague the perturbative solution of the original VPA system. Then, a simple projection procedure allowed us to reduce the problem to a finite set of nonlinear algebraic equations – relating the amplitudes of the time-asymptotic wave modes to that of the initial electric field – which we studied as a bifurcation problem. Thus, we obtained both vanishing and non-vanishing solution branches for the time-asymptotic amplitudes; which one of these is realized depends on the initial condition.

### 3. Two-Wave Case

We considered the classic problem of a sinusoidal perturbation to a single-humped (e.g. Maxwellian) Vlasov equilibrium, with  $f_\alpha(x, v, 0) = \mathcal{F}_\alpha(x, v) \equiv F_\alpha(v) + \epsilon h_\alpha(v) \cos x$ . For  $\epsilon \ll 1$ , we can assume the Langmuir modes with wavenumber one to be dominant at long times (whereas all other modes can be neglected, see Buchanan and Dorning [6]). It follows that the asymptotic field  $A$  can be represented as a pair of counter-propagating waves of the form

$$A(x, t) = a \sin(x - v_f t) + a \sin(x + v_f t). \quad (2)$$

After substituting the representation  $E = A + T$  into Eq. (1a), we approximate the term  $T(\partial f_\alpha / \partial v)$  by the “linearized” quantity  $T(\partial \mathcal{F}_\alpha / \partial v)$  and obtain

$$\frac{\partial f_\alpha}{\partial t} + v \frac{\partial f_\alpha}{\partial x} + \frac{q_\alpha}{m_\alpha} A \frac{\partial f_\alpha}{\partial v} = -\frac{q_\alpha}{m_\alpha} T \frac{\partial \mathcal{F}_\alpha}{\partial v}. \quad (3)$$

Unlike the traditional linear Vlasov equation, we expect this modified equation to be a uniformly good approximation in time, since by definition  $T$  vanishes at long times (when  $\mathcal{F}_\alpha$  ceases to be a good approximation for  $f_\alpha$ ), whereas the full nonlinear interaction between the long-time field  $A$  and  $f_\alpha$  is maintained. Eq. (3) was solved exactly, since the characteristics for  $A$  in Eq. (2) could be computed explicitly by

the method of [6]. The solution for  $f_\alpha$  was substituted into the Ampère equation, Eq. (1a), which was then broken into its transient and asymptotic parts (see Frechét [8]). The transient part was solved perturbatively for  $T$  in terms of the small amplitude  $a$ , and the solution substituted into the time-asymptotic part of the Ampère equation, which was projected on the one-dimensional space spanned by  $A$  in Eq. (2). This yielded a closed scalar equation for  $a$  in terms of  $\epsilon$ . We omit this lengthy development, and also the ensuing expansion procedure, that finally allowed us to express the problem in the form

$$[\beta \epsilon - \Gamma(\epsilon)] a^{\frac{1}{2}} + \sigma(\epsilon) a^{\frac{3}{2}} = O(a^2) \quad (4)$$

where  $\beta$ ,  $\Gamma(\epsilon)$  and  $\sigma(\epsilon)$  are known, and  $\Gamma(0) = 0$ . Eq. (4) has the trivial solution branch  $a = 0$ , which corresponds to all the zero asymptotic states that are attained when  $E(x, t)$  Landau-damps completely to zero before the nonlinear effects become important. Our elementary bifurcation analysis showed that non-zero solutions for  $a$  can exist only for initial amplitudes  $\epsilon$  near values  $\epsilon_0$  which satisfy  $\beta \epsilon_0 = \Gamma(\epsilon_0)$ . Near any such “critical initial amplitude”, Eq. (4) has the local non-zero solution

$$a = -\frac{\beta - \Gamma'(\epsilon_0)}{\sigma(\epsilon_0)} (\epsilon - \epsilon_0) + O(\Delta^2 \epsilon, a^{\frac{3}{2}}) \quad (5)$$

which (when positive) corresponds to non-zero time-asymptotic travelling-wave solutions. Since  $\Gamma(0) = 0$ ,  $\epsilon = 0$  is a critical amplitude; a Taylor expansion in  $\epsilon$  shows that, if there is a small non-zero critical amplitude, it must be at  $\epsilon_1 = 2(\beta - \Gamma'(0))/\Gamma''(0)$ .

### 4. References

- [1] A. Vlasov: J. Physics, 9 (1945) 25
- [2] L.D. Landau: J. Physics, 10 (1946) 25
- [3] T.M O’Neil: Phys. Fluids, 8 (1965) 2255
- [4] J.P. Holloway, J.J. Dorning: Phys. Rev. A, 44 (1991) 3856
- [5] I.B. Bernstein, J.M. Greene, M.D. Kruskal: Phys. Rev., 108 (1957) 546
- [6] M. Buchanan, J. Dorning: Phys. Rev. E, 50 (1994) 1465
- [7] M. Buchanan, J. Dorning: Phys. Rev. E, 52 (1995) 3015
- [8] M. Frechét: Rev. Sci., 79 (1941) 341

## EXPERIMENTAL STUDY OF AL LINE IN DENSE XENON PLASMA

M. Kulish, V. Gryaznov, A. Mezhiba, V. Mintsev, V. Fortov

Institute of Chemical Physics, Chernogolovka;

D.H.H. Hoffmann

Universität Erlangen;

C. Stöckl, M. Roth

Institut für Angewandte Physik, T H Darmstadt;

B. Sharkov, A. Golubev

Institute of Theoretical and Experimental Physics, Moscow.

Measurements of contours of resonance spectroscopic lines of aluminum atom admixture in dense Xe plasma in dependence on the electron concentration were carried out. To generate the dense plasma the explosively driven generators of rectangular shock wave were used, based on the acceleration of metal impactors by the detonation products. The shock waves generated by the impactors in targets spreaded in gas investigated, creating plasma. In such experiments it was measured the dependence of plasma radiation spectral intensity on time. Simultaneously in every experiment it was registered the shock front velocity and plasma brightness temperature. The pressure, temperature and plasma composition were calculated by the experimental data on shock wave velocity within the Debye approximation in the grand canonical ensemble of statistical mechanics. Registration of plasma radiation was performed with application of measuring complex of devices, such as a spectrograph, electron-optical streak camera, readout CCD camera and four photoreceivers with bandpass optical filters and resolution up to 3 ns. In the last works we have noted already the appearance in the investigated plasma radiation spectrum of the lines of target materials. In the present work it was used the aluminum targets with a mirror surface with a goal of lowering the possible influence of target material admixture on the plasma parameters. The particle velocity of targets was 5.3 km/s. A duplex Al I 394.4-396.1 nm (transition  $4^2S - 3^2P$ ) was observed in the region accessible in the experiments. The

undisturbed spectrum line positions were determined by the standard spark spectrum. The spectrum line contours were calculated by electron concentrations from Grime's work and were compared with the experimental data. The line contours for optically thin layers were approximated by the spectrum for plasma layers of finite ( $<0.5$ ) optical width. Concentration of atoms involved in the absorption process was estimated by the absorption coefficient in the line and was  $N < 10^{17} \text{ cc}^{-3}$ . Fig.1 shows results of the measurements. It is readily seen that the broadening of the lines at  $n_e > 10^{19} \text{ cc}^{-3}$  largely exceeds the distance between them. Therefore, the lines of duplex are not resolved and only one broadened contour is observed. Fig 1 presents below the form of the observed lines of aluminum in the spark discharge plasma. The vertical stroke-lines demonstrate the position of undisturbed lines and also dotted contours of lines there are the contours calculated by Stark tables for neutral atom isolated lines. Fig.2 shows the broadening and shift dependence of the lines on concentration of electrons. The experimental and theoretical values of width of the contours at their half-height are presented here. The line shifts were determined by the line width center position at its half-height. The experimental data for the electron densities  $n_e < 1.3 \cdot 10^{19} \text{ cc}^{-3}$  are in a good agreement with theory and the maximal relative disagreement between them was found to be for  $n_e > 2.4 \cdot 10^{19} \text{ cm}^{-3}$ .

*This work was supported by grants INTAS-94-1638 and RFBR No 96-02-18828.*

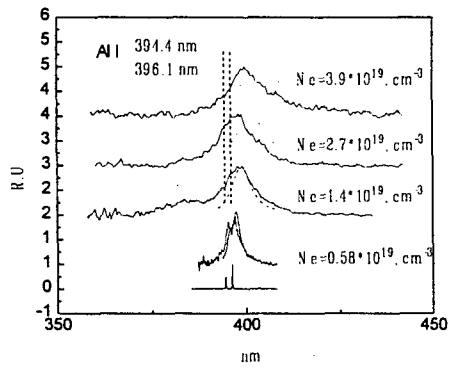


Fig.1. The contours of Al-lines in Xe plasma

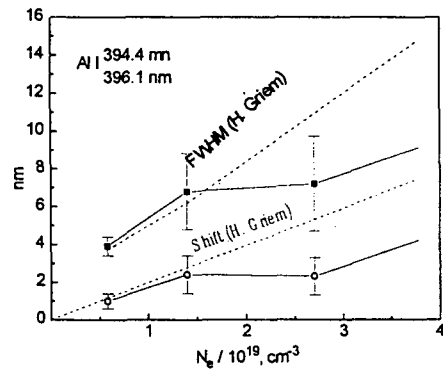


Fig.2. The width and shift of Al lines

# Electron Shock Waves: Wave Profile for a Range of Speeds

Mostafa Hemmati

Head, Physical Science Department, Arkansas Tech University, Russellville, AR 72801, USA

## Abstract

We have integrated the electron fluid-dynamical equations through the dynamical transition region for several wave speeds of breakdown waves. This article will also report on the variation of the wave profile, i.e., electric field intensity, electron number density, electron temperature, and ionization rate inside the sheath region as a result of the changes in wave speed.

## Model and Theory

The propagation of electron driven shock waves (breakdown waves) has been previously investigated by employing a one-dimensional, steady-state, three-component fluid model. A three-fluid hydrodynamical model with a shock front, driven by electron gas partial pressure was first presented by Paxton and Fowler (1962). In their model, they considered both photoionization and electron impact ionization as two important ionization processes. Their approximate solutions had a limited success.

Breakdown waves are assumed to consist of a shock front followed by a dynamical transition region. The transition region, which is somewhat thicker than a Debye length, will be referred to as the sheath region. In the sheath region, electrons come to rest relative to neutrals, and the net electric field falls to zero at the trailing edge of the sheath. The large difference in electron and ion mobility results in the establishment of space charge and, therefore, of a space charge field inside the sheath. The net electric field is the sum of the applied field and the space charge field.

In our investigation of the problem, we will use a set of three-component fluid equations which were completed by Hemmati and Fowler (1984). The set of equations consists of equations of conservation of mass, momentum, and energy, coupled with Poisson's equation. In dimensionless variables they are respectively:

$$\frac{d(\nu\psi)}{d\xi} = \kappa\mu\nu, \quad (1)$$

$$\frac{d}{d\xi} \{ \nu\psi(\psi-1) + \alpha\nu\theta \} = -\nu\eta - \kappa\nu(\psi-1), \quad (2)$$

$$\frac{d}{d\xi} \{ \nu\psi(\psi-1)^2 + \alpha\nu\theta(5\psi-2) + \alpha\nu\psi + \alpha\eta^2 - \frac{5\alpha^2\nu\theta}{\kappa} \frac{d\theta}{d\xi} \} = -\omega\kappa\nu \{ 3\alpha\theta + (\psi-1)^2 \}, \quad (3)$$

$$\frac{d\eta}{d\xi} = \frac{\nu}{\alpha} (\psi-1). \quad (4)$$

The dimensionless variables are:

$$\omega = \frac{2m}{M}, \kappa = -\frac{mVK}{eE_0}, \mu = \frac{\beta}{K}, \alpha = \frac{2e\phi}{mV^2}, \nu = V\psi$$

$$n = \frac{\epsilon_0 E_0^2}{2e\phi} \nu, T_e = \frac{2e\phi}{k} \theta, E = \eta E_0, x = -\frac{mV^2}{eE_0} \xi.$$

In the above equations,  $\nu$ ,  $\psi$ ,  $\theta$ ,  $\mu$ ,  $\kappa$ ,  $\eta$ , and  $\xi$  are the dimensionless electron concentration, electron velocity, electron temperature, ionization rate, elastic collision frequency, electric field, and position inside the wave, respectively. The symbols  $m$ ,  $e$ ,  $n$ , and  $T_e$  represent electron mass, charge, number density, and temperature inside the sheath, and  $\beta$ ,  $\phi$ ,  $V$ ,  $M$ ,  $E_0$  are ionization frequency, ionization potential, wave velocity, neutral particle mass, and electric field at the wave front.

## Analysis

In our approach to solving the equations, we have been able to place the singularity inherent in the equations in the denominator of the momentum integral.

$$\frac{d\psi}{d\xi} = \frac{\kappa(1+\mu)(1-\psi)\psi - \kappa\mu\alpha\theta - \eta\psi - \alpha\psi\theta'}{\psi^2 - \alpha\theta} \quad (5)$$

A zero denominator in the momentum integral represents an infinite value for the electron velocity derivative with respect to the position inside the sheath. This condition requires the existence of a shock inside the sheath region, which is not allowed. The numerator in the equation, therefore, has to become zero at the same time that the denominator becomes zero. In the process of integration of the equations through the sheath region, comparing the numerator and denominator values allows us to choose correct initial parameters by trial and error.

## Results

For nitrogen gas and for proforce waves moving into a nonionized medium we have been able to integrate the set of electron fluid-dynamical equations for five different values of  $\alpha$ : 0.01, 0.1, 0.25, 0.5, and 1.  $\alpha = 0.01$  represents a fast moving wave with a speed of  $3 \times 10^7$  m/s, and  $\alpha = 1$  represents a slow moving wave with  $V = 3 \times 10^6$  m/s. For slow waves, the singularity becomes very sharp and the passage through the singularity becomes very time consuming. We were able to integrate the set of equations for  $\alpha = 4$ ; however, the passage through the singularity required keeping the values of numerator and denominator in equation 5 constant for up to 40 integration steps. This introduces a large kink at the singularity and; therefore, we have discarded  $\alpha = 4$  ( $V = 1.48 \times 10^6$  m/s) from the range of wave speeds in our graphs.

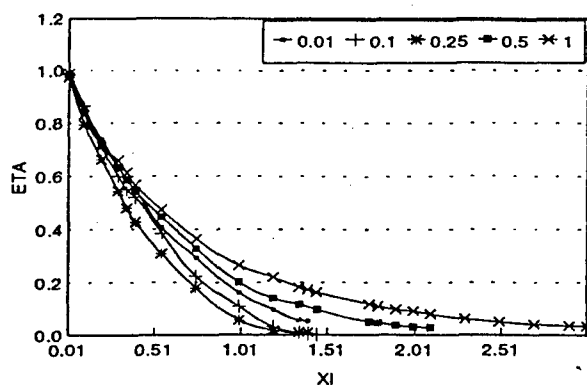


FIG. 1. Electric field as a function of position inside the sheath.

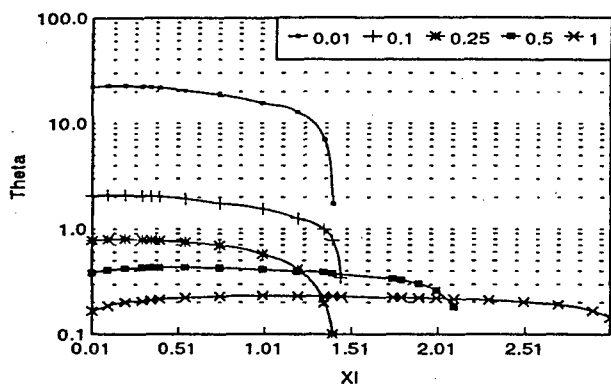


FIG. 2. Electron temperature as a function of position inside the sheath.

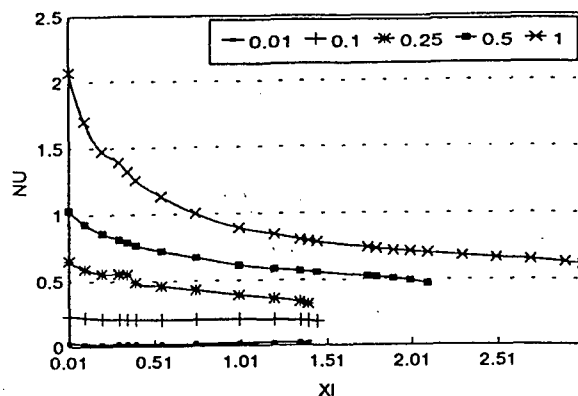


FIG. 3. Electron number density as a function of position inside the sheath

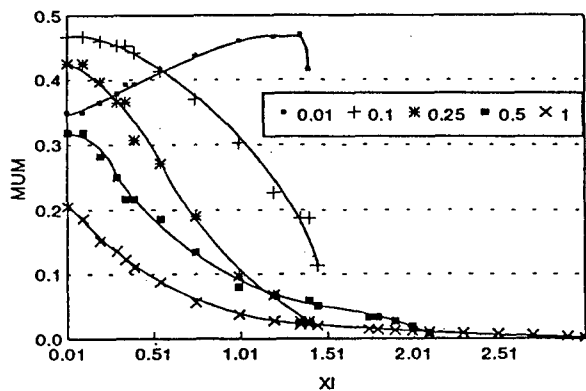


FIG. 4. Ionization rate as a function of position inside the sheath

The solution for the electron fluid-dynamical equations seems to present a cut-off point in the wave speeds at approximately  $10^6$  m/s. Scott's (1976) report is the result of extensive experimental measurements of initial electric breakdown wave speed in nitrogen and argon as a function of local electric field at the wave front. His reported lowest speed magnitude is of the order of  $10^5$  m/s.

For a fast moving wave, Hemmati (1995) has presented the wave profile for current bearing waves at the XXII International Conference on Phenomena in Ionized Gases. The four diagrams, however, represent the complete wave profile for the above mentioned range of wave speeds. Figure 1 represents the dimensionless electric field,  $\eta$ , as a function of dimensionless position,  $\xi$ , inside the sheath. For all wave speed values, as required by physical conditions, the net electric field approaches a minimal value at the end of the sheath and its derivative with respect to position approaches zero ( $\frac{d\eta}{d\xi} \rightarrow 0$ ). The next three graphs represent wave profiles for: electron temperature,  $\theta$ , electron number density,  $\nu$ , and ionization rate,  $\mu$ , as a function of position,  $\xi$ , inside the sheath.

At the shock front, for selected wave speeds,  $\alpha$ , the values of electron number density,  $\nu_1$ , electron velocity,  $\psi_1$ , and the values of wave constant,  $\kappa$ , for successful integration of the electron fluid-dynamical equations are:

$$\begin{aligned}\alpha = 0.01, \kappa &= 1.239718, \nu_1 = 0.023, \psi_1 = 0.327 \\ \alpha = 0.1, \kappa &= 1.071818, \nu_1 = 0.235, \psi_1 = 0.29125 \\ \alpha = 0.25, \kappa &= 0.959363, \nu_1 = 0.666, \psi_1 = 0.26016 \\ \alpha = 0.5, \kappa &= 1.08576, \nu_1 = 1.05, \psi_1 = 0.25375 \\ \alpha = 1, \kappa &= 1.0426635, \nu_1 = 2.1, \psi_1 = 0.2071\end{aligned}$$

#### Conclusion

The graphs indicate that for slow waves: a) the sheath thickness is larger, b) the electron number density is larger at the shock front and decreases toward the end of the sheath, c) the ionization rate has a small value at the shock front and it reduces to very small values at the trailing edge of the wave. The electron temperature,  $\theta$ , at the shock front for fast waves has a large value, and as expected, it reduces to small values at the end of the sheath.

#### References

- HEMMATI, M. 1995. Wave profile for current bearing proforce waves. Proceedings of the International Conference on Phenomenon in Ionized Gases. 1:45-46.
- HEMMATI, M. AND R. FOWLER. 1985. Electrical breakdown waves: Exact solutions. Part II. Phys. Fluids. 28:2744-2750.
- PAXTON, G.W. and R.G. FOWLER. 1962. Theory of breakdown wave propagation. Phys. Rev. 128:993-997.
- SCOTT, R.P. and R.G. FOWLER. 1976. Breakdown waves in argon and nitrogen. Phys. Fluids. 20:27-31.

# ION SHEATH INSTABILITY IN MULTI-COMPONENT PLASMAS CONTAINING NEGATIVE IONS

K. Koga, N. Hayashi and Y. Kawai

Interdisciplinary Graduate School of Engineering Sciences,  
Kyushu University, Kasuga, Fukuoka 816, Japan

## 1 Introduction

There are few reports on dynamic behavior of a sheath, especially the sheath instability. Stenzel [1,2] reported on the instability nearby the electron plasma frequency in the electron sheath. On the other hand, Ohno *et al.* [3,4] observed the chaotic phenomenon of the ion sheath instability in the dc current system using a double plasma (D.P.) device. As an excitation mechanism of this instability, they proposed a bunching model that the ion sheath instability is excited by the bounce motion of ions in an asymmetric sheath potential and the frequency of this instability is given by a reciprocal of their sheath transit time. Piel *et al.* [5] reported the oscillations of the ion sheath on the low density side of the negatively biased grid in D.P. device, and called "virtual anode oscillations" in analogy to virtual cathode formation in electron diodes. They concluded that the frequency locking among three oscillations (the virtual anode oscillation, the reciprocal of the sheath transit time and the ion plasma frequency at the sheath) provides the coherent frequency spectrum of the ion sheath oscillation.

It is well known that negative ions play an important role in space plasma and processing plasma. Studies of the static sheath were reported by many researchers [6]. However, there are no reports on the dynamic behavior of the sheath in a negative ion plasma. In this paper, we report the experimental results on the ion sheath instability in multi-component plasmas containing negative ions.

## 2 Experimental Apparatus

We use a D.P. device whose diameter and length are 50 cm and 100 cm, respectively. The dc discharge between the filaments and the chamber wall produces an argon plasma. Negative ions are generated by electron attachment to  $\text{SF}_6$  and, as a result, a multi-component plasma is formed. The fine-meshed grid at the center of this device divides the plasma into two regions. Plasma parameters are measured with a 6 mm diam. plain Langmuir probe. In the target region, the electron temperature and plasma density is 1.0~1.5 eV and  $(1\sim3) \times 10^8 \text{ cm}^{-3}$ , respectively. In the driver region, the plasma density is below one tenth of that. The negative ion concentration  $\alpha$ , is estimated from the ratio of the electron saturation current with negative ions to that

without those. The separation grid is grounded through the power supply  $V_g$  and the resistor. Perturbations of the current are obtained from the voltage drop across the resistor and are analyzed with a spectrum analyzer. The chamber is evacuated to below  $1.0 \times 10^{-6}$  Torr. Gases are correctly introduced into the chamber with the mass flow controller (MFC). In this experiment, the argon gas and the  $\text{SF}_6$  gas are introduced with the flow rate 9.0 sccm ( $3.0 \times 10^{-4}$  Torr) and 1.0 sccm max, respectively.

## 3 Experimental Results and Discussion

We investigate the change of the static sheath width with  $\alpha$ , where this width is obtained by the axial profile of the ion saturation current. When  $\alpha$  is increased, the sheath width widens. The existence of negative ions causes the shield of the ion movement to the sheath, and the ion current flowed into the sheath decreases, suggesting that the sheath widens.

When the plasma density of the target region in the D.P. is more dense than the driver region and the separation grid is biased negatively, the ion sheath instability is excited. In this case, we observe oscillating components of the grid current with the spectrum analyzer. A very sharp peak of the oscillation is found near the half of the ion plasma frequency. We investigate the

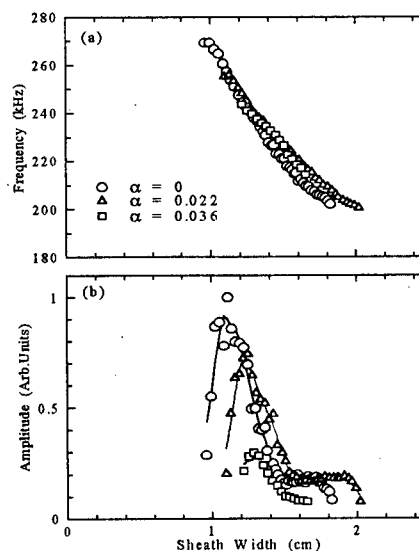


Fig.1: Dependence of (a) frequency and (b) amplitude of the instability on the sheath width. The sheath width is changed by the bias voltage  $V_g$ .

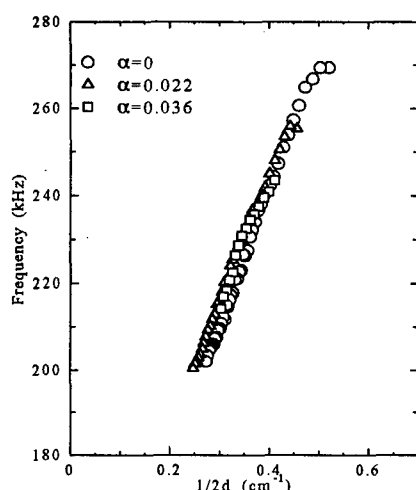


Fig.2: Dependence of the frequency on a reciprocal of twice sheath width.  $d$  is the sheath width

dependence of the frequency and amplitude of this instability on  $\alpha$ , where the bias voltage to the grid is kept constant. As  $\alpha$  becomes larger, both the frequency and amplitude decrease. Since the sheath transit time is prolonged by the sheath widening, the frequency decrease. Figure 1 (a) shows the dependence of the frequency of the instability on the sheath width for various  $\alpha$ . The sheath width is changed by the bias voltage  $V_g$ . Figure 2 indicates the dependence of the frequency on a reciprocal of twice sheath width. As seen from Fig. 1 (a) and 2, the measured frequency is in inverse proportion to the width and the dependence of the frequency on the sheath width is independent of  $\alpha$ . The relationship between the frequency of the instability and the sheath width suggests that the excitation mechanism of the observed instability is explained by the ion bunching model. Figure 1 (b) shows the dependence of the amplitude on the sheath width. Increasing  $\alpha$ , the region where the instability is excited tends to become narrow. If the negative ions contribute only to the change of the static sheath width, such behaviors of the instability is not observed. Figure 1 (b) shows that the negative ions change the dynamic behavior of the sheath. As a result, the growth rate of the instability becomes small and the instability finally disappear at a certain small  $\alpha$ . Furthermore, its excitation region become narrow.

Figure 3 shows the potential gaps  $\Delta\phi (= \phi_D - \phi_T)$  between the plasma potential of the driver region  $\phi_D$  and the target region  $\phi_T$  as functions of grid bias  $V_g$ . Here, the plasma potentials are measured with the Langmuir probes which are located in the plasma region. When the instability is excited,  $\phi_D$  increases and  $\Delta\phi$  becomes positive value, while,  $\phi_T$  does not change so much. That is, the ions injected from the target region are reflected by the potential wall on the driver side and, as a result, the instability is excited. This indicates that the driver plasma potential depend on the grid bias and there is possibility that the local swell as the virtual anode oscillations at the sheath of the driver side exist. This swell

or the average of this swell rise the plasma potential. Therefore, the potential gap  $\Delta\phi$  comes to a positive value at a certain  $V_g$  and the sheath instability is excited, although  $\Delta\phi$  is a negative value at low  $V_g$ . The similar behaviors are also observed in a negative ion plasma.

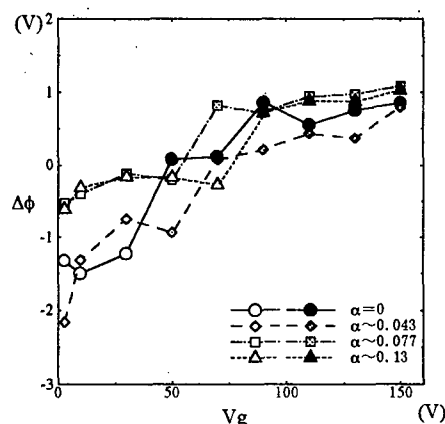


Fig.3: The potential gaps  $\Delta\phi (= \phi_D - \phi_T)$  as functions of  $V_g$ . (Filled marks: instability is excited)

#### 4 Conclusion

We observe the ion sheath instability in a negative ion plasma. The frequency of this instability is in inverse proportion to the sheath width and the dependence of the frequency on the sheath width is independent of  $\alpha$ . We conclude from these results that the excitation mechanism of the observed instability is explained by the ion bunching model. When the negative ion concentration  $\alpha$  is increased, the growth rate of the instability become small. As a result, the region where the instability is excited tends to become narrow. The plasma potential of the driver side depends on grid bias  $V_g$  and there is possibility that the dynamic behavior of the sheath on driver side change. From this result, the behavior of the sheath on the driver side also play an important role in the excitation of this instability.

#### 5 References

- [1] L. Stenzel: Phys. Rev. Lett. **60**(1988) 704
- [2] R. L. Stenzel: Phys. Fluids **B1**(1989) 2273
- [3] N. Ohno, A. Komori, M. Tanaka and Y. Kawai: Phys. Fluids, **B3**(1991) 228
- [4] N. Ohno, A. Komori, M. Kono and Y. Kawai: Phys. Fluids, **B5**(1993) 796
- [5] A. Piel, H. Klostermann, A. Rohde, N. Jelic, R. W. Schrittwieser: Phys. Lett. A, **216**(1996) 296
- [6] For example, see  
H. Amemiya: J. Phys. D, **23**(1990) 999  
H. Shindo and Y. Horiike: Jpn. J. Appl. Phys., **32**(1993) 5109 etc.

## A 30 kHz - 1 MHz fast sweeping method for Langmuir probes applied to turbulent plasmas

L. Leborgne, J.C. Goulet, B. Van Ootegem, P. Vervisch  
UMR 6614 CNRS CORIA - 76821 Mont-Saint-Aignan Cedex, France

Langmuir probes are generally used to determine the electronic temperature and density [1] in plasmas. In order to measure these quantities, an I-V characteristic curve is obtained by sweeping the probe voltage. When the plasma is unstable or turbulent, fast sweeping is required. To measure the electron density fluctuations in turbulent plasmas, the scanning frequency has to vary from 30 kHz to 1 MHz. For frequencies greater than 100 Hz, the noise due to the RC characteristics of coaxial cables is not negligible. This is all the more true since the probe electronic saturation is weak. To reduce this phenomenon, a dual-cable method has been developed by Yang *et al* [2] for frequencies less than 1 kHz. The method consists in doubling the measuring circuit. The second circuit supplies a dummy cable. The noise due to dummy cable is removed from the measured signal. The objective of this work is to adapt this method to the 30 kHz - 1 MHz frequency range.

an equivalent circuit which supplies the dummy probe. The probes are a 0.2 mm diameter tungsten round tip, insulated by an alumina tube. The BNC coaxial cable is soldered with a tinned copper wire which is twisted around the probe. This setting is inserted in a stainless-steel tube. The active and dummy probes are of the same type, equal in length. To prevent ground loop, the ground of each instrument is connected to the same reference. The probes signals are recorded by the differential comparator of the DSA 602A Tektronix numerical oscilloscope.

Fig. 1. General scheme of the dual-cable circuit

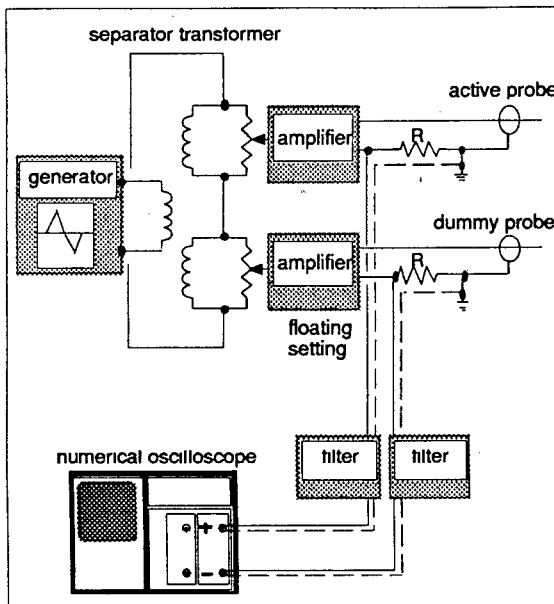
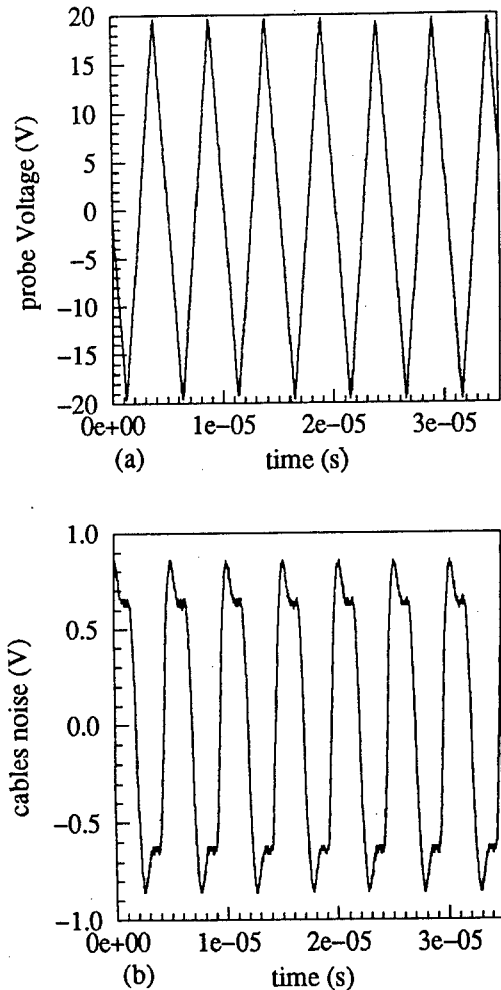


Figure 1 shows the general scheme of the measuring circuit. The sweeping voltage of 14 V amplitude is generated by a TG501 THANDAR function generator. Its frequency range is from 0.005 Hz to 5 MHz. In order to insulate the measuring set-up, the power supply output is fed to the primary winding of a transformer which has two secondary windings. The voltage of the first secondary winding is applied to the probe circuit. The tension is amplified three times before being applied to the probe. The other winding is connected to

Fig 2 : (a) triangular sweeping voltage (b) induced noise from the dummy or active probe

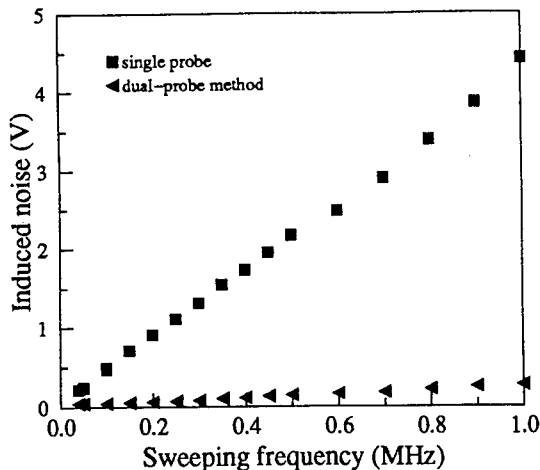


However the characteristics of the two circuits are slightly different, since the components (resistors, amplifiers...) are not exactly the same. Thus the active and dummy probes noises are slightly different. The



adjustment of two variable resistors in each circuit compensates the difference in impedance, in order to make equal the noises in amplitude and in form. Figure 2b shows the noise signal without plasma when a 200 kHz sweeping voltage (Figure 2a) is applied. The superimposing of the two noises on the oscilloscope allows the tuning of the setting. The fine adjustment is made by minimising the difference between the noises. The uncompensated noise amplitude increases as a function of the sweeping frequency as shown in Figure 3.

Fig 3 : Evolution of the induced noise as a function of the sweeping frequency



This method has been validated in a low pressure  $\text{CO}_2$  -  $\text{N}_2$  arc plasma jet and has been used to study a low pressure supersonic turbulent argon inductive plasma. The aim of this work is to understand the electron density behaviour in the turbulent jet. The latter is determined by several interacting processes. Especially, coupling between kinetics and turbulence seems to be of great importance. In order to focus on this interaction, the argon gas has been chosen for its well-known simple chemistry. The argon gas is injected in a distilled water-cooled double-wall quartz chamber which is the discharged chamber. The plasma is produced at atmospheric pressure. The generator has a 100 kW power and a 1.70 MHz frequency. The injected power is 40 kW. After a water-cooled copper convergent nozzle, the plasma jet is expanded in the test vacuum chamber at a pressure of 50 mbar. The turbulence is created by a tungsten grid fixed 10 cm downstream the nozzle exit. The Langmuir probe is placed behind the grid. Radial and axial I-V characteristics have been obtained, but are perturbed by the electromagnetic effects of the inductive torch. Currently, the 1.5 - 1.8 MHz frequency range rejected filters are under construction to eliminate this electromagnetic noise.

In conclusion, this work has shown that for the 30 kHz - 1 MHz frequency range the use of a dual-cable method allows to reduce the RC induced noises. By adding a dummy probe and adjusting the impedance of the circuits, the noises are minimised. This method allows to measure the fluctuations of the electron density by Langmuir probes in turbulent plasmas.

This work was sponsored by the Commissariat à l'Energie Atomique (C.E.A. C.E.S.T.A.).

[1] F.F.Chen in Plasma diagnostics techniques, edited by R.H. Huddleston and S.L. Leonard, (Academic Press, New-York, 1965) p113

[2] T.F. Yang, Q.X; Zu, Ping Liu : Rev. Sci. Instrum. 66 (1995) 3879

# Computer simulation of two-plasmon decay instability excited by a strong running pump wave in two-species plasma

Vadim D. Levchenko and Yuri S. Sigov

M.V.Keldysh Institute of Applied Mathematics, Miusskaya Square 4, Moscow 125047, Russia

## 1. Introduction

Two dimensional problem on parametric excitation of plasma at  $\omega_0$  near the double frequency is investigated in the frame of Vlasov-Poisson equations via particle simulation using a special highly optimized version of the object-oriented code SUR [1].

Two cases of (3.1.) pure electron and (3.2.) electron-ion plasmas are compared to one other to study the joint action of both the two plasmons' decay and modulation instabilities.

## 2. Computational model

We simulate the plasma with electrostatic PIC model in 2D space-bounded double periodic region ( $64\lambda_D \times 64\lambda_D$ ). Pump wave has the form  $E_x(x, y, t) = E_0 \cos(\omega_0 t - k_y y)$  and its amplitude was linearly increasing from 0 up to  $E_0$  value over first 3 plasma oscillations. For the sake of computational succession the runs' parameters  $\omega_0/\omega_p = 2.027$ ;  $cE_0/mV_T\omega_0 = 2$  were chosen to be close to ones used in pioneer computer simulation [2] by Dawson and Kruer (1971) for the special case of the one-species electron plasma with the fixed positive ion background. For the case of original simulation with mobile ions (3.2.) the model relation  $m_e/m_i = 1/100$  was chosen.

## 3. Results

### 3.1. Pure electron plasma with homogeneous ion background

Under an appropriate pump wave intensity the parametric instability develops with the threshold and the growth rate being in a satisfactory agreement with Jackson's theory [3].

The spectrum of excited electric field modes is discrete. This fact, along with decay conditions of energy and moment conservation. Essentially affects the choice of growing unstable modes with maximal growth rates. For example, in the computational region under consideration the pure diagonal mode (1,1) of maximal growth rate is accompanied by the (0,-1) mode with a lower amplitude.

The curve of time dependence for the  $x$ -component of electrostatic energy lies higher than one for the  $y$ -component (Fig.1). The first break (to side of decreasing) on the curves of time dependence of the dimensionless average and maximal wave energy den-

sities corresponds to the achieved level of the order of unite, i.e. to transition to a strong nonlinear stage. Growth of the dimensionless average and maximal wave energy densities continues up to the values 1.5 and 9. correspondingly. Saturation, followed by a sharp exponential sloping down towards the corresponding values 0.1 and 0.2-0.3, is conditioned by the beginning of nonlinear waves' overturning (Fig.2).

A significant growth of the electron kinetic energy begins with the strong nonlinear stage, realizes mainly at the stage of a pronounced overturning, and then achieves (for the  $x$ -component) the ten times increase (for the  $y$ -component it is 20% lower). The great bulk of this energy is concentrated at an asymmetric cloud of fast electrons with maximal velocities being 16-18 times higher than thermal ones.

The formation of such prolonged high-energetic electron 'tails' in the velocity space, from one hand, and a relative nearness of the initial pump wave intensity to its threshold value, from other hand, lead to an effective 'switching off' the pump wave, i.e. transform our system into 'sub-threshold' regime.

### 3.2. Simulation with mobile ions

Linear stage of parametric instability appears in the same modes, but with a bit smaller growth rate, as compared to case 3.1. (Fig.1).

The pronounced formation of density cavities is observed at the strong nonlinear stage: the movement of the electrostatic waves' envelope dies down, the number and shape of quasi-one-dimensional cavities meet a ponderomotive force profile, the cavities become deeper (Fig.3,4). Therewith, as contrasted to case 3.1., the observed growth rate becomes to be approximately the modulation instability growth rate value higher. (Fig.1)

The saturation stage begins earlier then in the case 3.1. Correspondingly the saturation level is lower, and tends approximately to 1.5 for the maximal dimensionless wave energy density value.

The saturation process is conditioned by formation of a 'continuous' short wave spectrum (connected with the modulation self-focusing of cavities) accompanied by a quick generation of high-energetic electron 'tails' due to Landau mechanism. The number of superthermal electrons is considerably higher then in case 3.1., though their maximal energies are lower. As result the total income of kinetic electron energy is almost twice lower then in case 3.1.

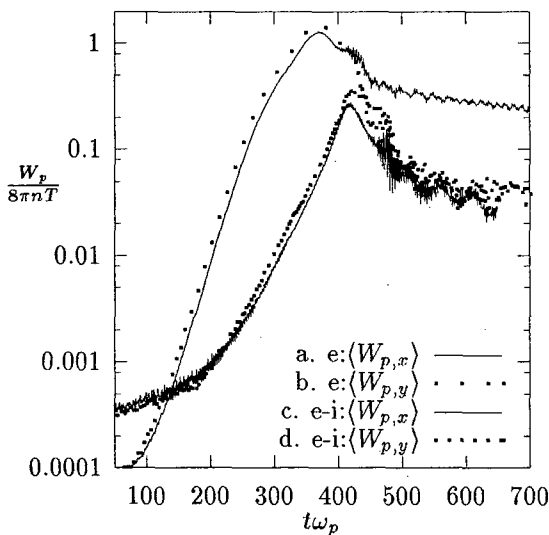


Fig 1. Time dependence of average electrostatic energy for 3.1. (a., b.) and 3.2. (c., d.) cases.

Absorption of the hf contents of cavities is accompanied (with a corresponding initial ions' delay) by generation of quasi-one-dimensional oblique ion sound waves (Fig.4). At this stage it is easy to observe a relatively slow heating mechanism caused by a direct conversion of the pump wave into short wave plasmons with the help of the ion density 'comb'.

Like the case 3.1. for the similar reasons the system comes to a 'sub-threshold' regime.

#### 4. Conclusions

Thus in our first 2D computer experiments on the parametric two plasmon decay taking into account the ions' mobility we observed in detail practically all the variety of nonlinear effects caused by the joint action of parametric and modulation instabilities as known in general from the strong Langmuir turbulence's theory and some related computer simulation [4]. The work is in progress [5]

#### References

- [1] V.D. Levchenko and Yu.S. Sigov: Object-oriented code SUR for plasma kinetic simulation, in K.H. Becker, W.E. Karr, and E.E. Kunhardt, editors, *XXIII ICPIG. Contributed papers 4*, pp 221-222, Hoboken, New Jersey, USA, (1995).
- [2] J.M. Dawson and W.L. Kruer: *Phys. Fluids*, **14** (1971) 1003.
- [3] E.A. Jackson: *Phys. Rev.*, **153** (1967) 235.
- [4] Yu.S. Sigov and V.E. Zakharov: Strong turbulence and its computer simulation, *J.de Physique suppl*, **40** (1979) 63.
- [5] V.D. Levchenko and Yu.S. Sigov. '2D Computer simulation of two-plasmon decay instability. preprint, Keldysh Inst. of Appl. Math. RAS, Moscow, (1997), in print.

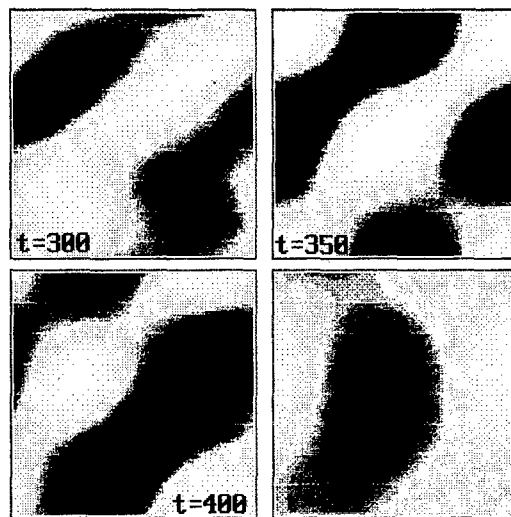


Fig 2. Case 3.1. Snap shots of electrostatic potential  $\varphi(x, y)$  for sequential time moments.

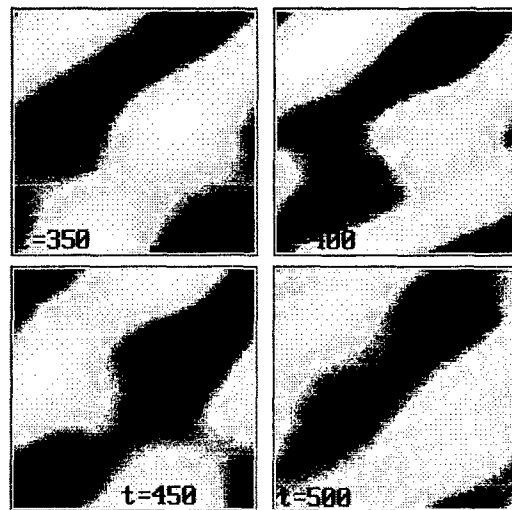


Fig 3. The same value for the mobile ions simulation (3.2.)

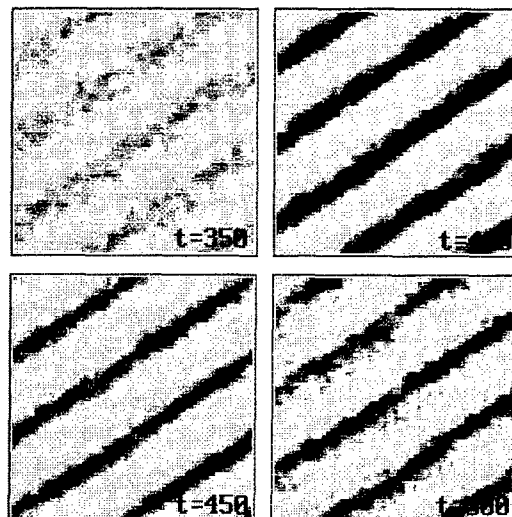


Fig 4. Snap shots of ions density  $n_i(x, y)$  for sequential time moments.

# On the influence of relative ion concentrations on QPESIC modes in weakly ionized plasmas with singly, doubly and triply charged ions

D.Ž. Gajić\* and B.S. Milić\*\*

\*Faculty of Philosophy, Dept. of Physics, P.O.B. 91, YU-18001 Niš, Yugoslavia

\*\*Faculty of Physics, P.O.B. 368, YU-11001 Beograd, Yugoslavia

In a recent paper [1], the processes of spontaneous excitation of instabilities in the long-wave part of certain quasi-perpendicular electrostatic ion-cyclotron (QPESIC) modes in weakly ionized plasmas containing singly, doubly and triply charged ions originating from the same atomic species were analysed. It was assumed that the ions have Maxwellian distribution functions characterized by a common temperature  $T_i$ , which may be different from that of electrons  $T_e$  (e.g. this is encountered in gas discharges). It was also assumed that a "strict" billiard-ball model for collisions ( $\nu_e/\nu_{is} = v_{Te}/v_{Tis}$ ,  $s = 1, 2, 3$ ) may be applied [2,3], and that a small percentage of the ions is in the state of double or triple ionization, which corresponds to comparatively low ion temperature.

In the present paper, the same problem is reconsidered using the same evaluation procedures and focusing attention on the same six IC modes ( $\omega \approx \Omega_l = l\omega_{B1}$ ,  $l = 1, 2, \dots, 6$ ). Thus, the ions  $A^+$  are "resonant" with all these modes, whereas  $A^{2+}$  and  $A^{3+}$  may be either "resonant" or "non-resonant", depending on  $l$ . However, here one assumes that the ion temperature has higher values than in [1] (e.g. the electric field in the discharge is of larger intensity). Thus, the relative ionic concentrations  $\bar{n}_s = n_s/(n_1 + n_2 + n_3)$  are now different; in particular, the concentration of triply ionized atoms is augmented. The results arrived at, if juxtaposed with those of [1], are expected to allow a better quantitative insight in the role of relative ion concentrations in the processes of spontaneous excitation of the instabilities studied.

From the general dispersion equation for the long-wave part of the QPESIC modes in multi-ion plasmas [1,3], applied to the situation studied, one obtains the spectra and the threshold electron drifts. The results for the spectra are illustrated by Figs. 1 and 2, which show  $\omega/\omega_{B1}$  vs.  $\mu_1 \equiv k_{\perp}^2 v_{Ti}^2 / \omega_{B1}^2$  for the six modes analysed, in plasmas with  $\bar{n}_1 = 0.60$  and either  $\bar{n}_2 = \bar{n}_3 = 0.20$  (unbroken lines) or  $\bar{n}_2 = 0.30$ ,  $\bar{n}_3 = 0.10$  (dotted lines), for two non-isothermality,  $\tau = 5$  and  $\tau = 10$  ( $\tau \equiv T_e/T_i$ ); the dotted lines in Fig. 2 reproduce the results of [1],

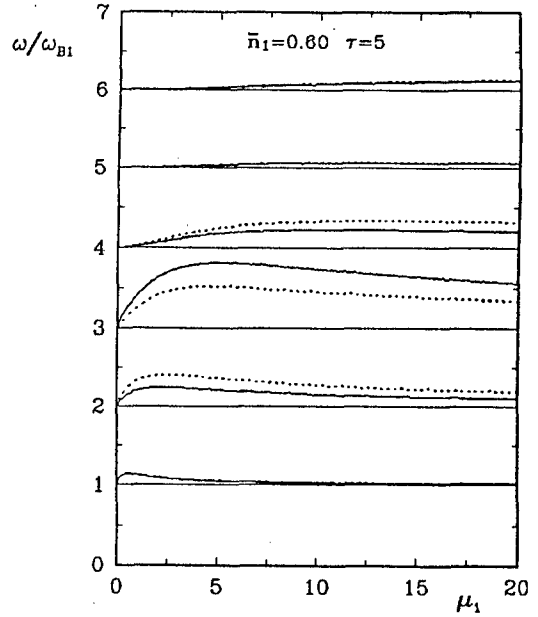


Figure 1.

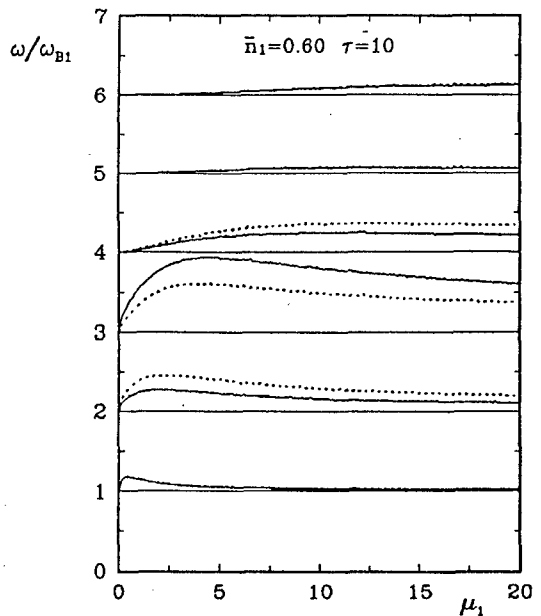


Figure 2.

and are given here for the sake of comparison. It can be seen that the increase (doubling) of  $\bar{n}_3$  (unbroken lines) alters noticeably the spectra of the modes  $l = 2, 3$  and  $4$ . More precisely, one sees diminishments of maximum deviations of  $\omega$  from  $l\omega_{B1}$  for  $l = 2$  and  $l = 4$  (ions  $A^{3+}$  are "non-resonant"), and to its enhancement for  $l = 3$  (ions  $A^{3+}$  are "resonant"). This trend agrees with the previous results [3] for the two-ion plasmas with singly charged ions of two atomic species.

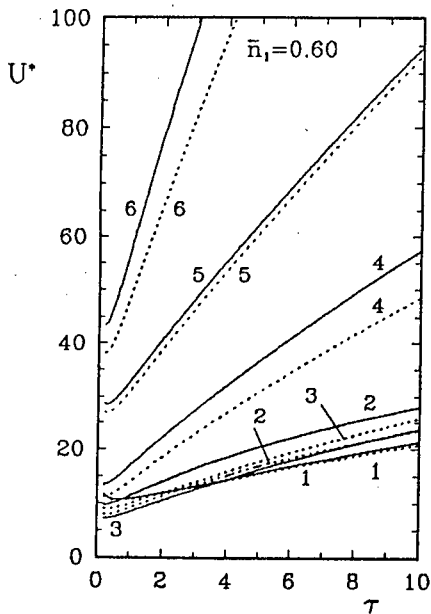


Figure 3.

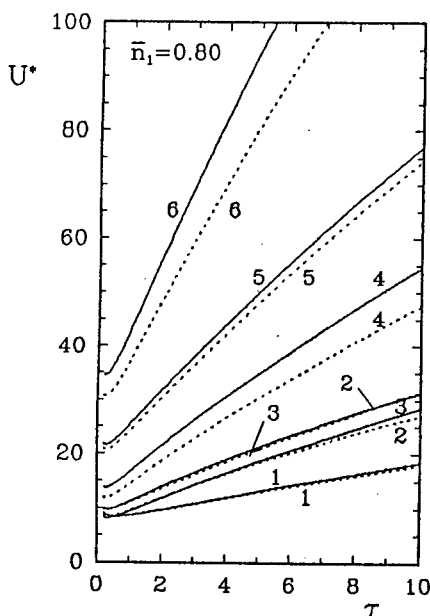


Figure 4.

Figures 3 and 4 show the results for the threshold drifts,  $U^* = (u/v_{Ti})_{thr}(m_e/m_i)^{1/4}$ . Figure 3 corresponds to the plasma compositions in Figs. 1 and 2 (with the same meaning for unbroken and dotted lines), and Fig. 4, corresponding to  $\bar{n}_1 = 0.80$  and either  $\bar{n}_2 = \bar{n}_3 = 0.10$  (unbroken lines) or  $\bar{n}_2 = 0.15$  and  $\bar{n}_3 = 0.05$  (dotted lines), is given for comparison with Fig. 3. Apart from the fact that the curves shown exhibit the well-known general behaviour (a minimum for  $\tau \approx 1$ , and a monotonic increase for  $\tau > 1$ ), it can be seen that the doubling of  $\bar{n}_3$  raises the threshold drifts, the effect being more prominent in even harmonics. However, a comparison of the unbroken curves in Fig. 4 with the dotted ones in Fig. 3 (both sets of curves correspond to  $\bar{n}_3 = 0.10$ ) shows that the increase of  $\bar{n}_2$  (with ensuing decrease of  $\bar{n}_1$ ) tends to diminish the threshold drifts of  $l = 5$  and  $l = 6$ , and to enhance it in the case of lower harmonics. This effect, together with the drift inversion at the lower harmonics (for  $1 < \tau < 4$ , the gradual increase of the drift results in the onset of  $l = 3$  first, then  $l = 1$  and  $l = 2$ ; for  $4 < \tau < 10$ , the order of appearance of the instabilities is  $l = 1$ ,  $l = 3$ ,  $l = 2$ ), can be attributed to the influence of the off-resonance terms [1,3].

## References

- [1] N.R. Brajušković, D.Ž. Gajić and B.S. Milić: Contr. Papers of the SPIG 18 (Kotor, 1996), p. 556
- [2] B.S. Milić and N.R. Brajušković: J. Plasma Phys., 29 (1983) 31
- [3] B.S. Milić and D.Ž. Gajić: Plasma Phys. and Contr. Fusion, 33 (1991) 1161

# Some properties of the QPESIC instabilities in weakly ionized plasmas with ions $A^+$ and $A^{++}$ possessing different temperatures

D.Ž. Gajić\* and B.S. Milić\*\*

\*Faculty of Philosophy, Dept. of Physics, P.O.B. 91, YU-18001 Niš, Yugoslavia

\*\*Faculty of Physics, P.O.B. 368, YU-11001 Beograd, Yugoslavia

It was shown previously that both different ion charge numbers [1,2] and different ion temperatures [3,4], taken separately, are factors of importance in the processes of spontaneous excitation of instabilities in the long-wave parts of certain quasi-perpendicular electrostatic ion-cyclotron (QPESIC) modes by an electron drift parallel to the magnetic lines of force. It seems, therefore, worthwhile to study the situation in which both factors act simultaneously. The present paper deals with weakly ionized plasmas containing ions  $A^+$  and  $A^{++}$ , originating from the same atomic species and having Maxwellian distributions with temperatures  $T_1$  and  $T_2$ . It is assumed that a "strict" billiard-ball model for collisions ( $\nu_e/\nu_{is} = v_{Te}/v_{Tis}$ ,  $s = 1, 2$ ) is valid. The analysis is based on linear perturbation theory and, more specifically, on the results of the theory corresponding to multi-ion plasmas [1,3,5]. Two modes are studied in detail: (A)  $\omega \approx \Omega_A = \omega_{B2} = 2\omega_{B1}$  (both ion species are "resonant" with the wave), and (B)  $\omega \approx \Omega_B = \omega_{B1}$  (doubly charged ions are "non-resonant").

From the general dispersion equation for the long-wave parts of the QPESIC modes in multi-ion plasmas [1,3,5], adapted for the two modes studied presently, the expressions for the modal spectra and for the threshold electron drifts are obtained. As an illustration of these results, Figs. 1 and 2 show graphs of  $\omega/\Omega$  vs.  $\mu_1$  ( $\mu_1 = k_{\perp}^2 v_{T1}^2 / \omega_{B1}^2$ ) for  $T \equiv T_1/T_2 = 0.2$  (bold lines) and  $T = 5$  (thin lines), with  $\tau \equiv T_e/T_1 = 10$ . The curves shown pertain to three selected compositions, as specified by the values of the parameter  $\bar{n}_1 \equiv n_1/(n_1 + n_2)$ ,  $n_1$  and  $n_2$  being the number densities of  $A^+$  and  $A^{++}$  respectively, viz.  $\bar{n}_1 = 0.25$  (unbroken lines, both bold and thin),  $\bar{n}_1 = 0.50$  (dashed lines) and  $\bar{n}_1 = 0.75$  (dotted lines). It should be noticed that the maximum deviations of  $\omega$  from corresponding  $\Omega$  are particularly large and occur at very large values of  $\mu_1$  in the case of mode (A), provided that the ions  $A^+$  are hotter of the two ion species.

The threshold drifts are obtained from the imaginary parts of the dispersion equations studied, and are of the form  $(u/v_{T1})_{thr} = (m_i/m_e)^{1/4} U^*$  (ions

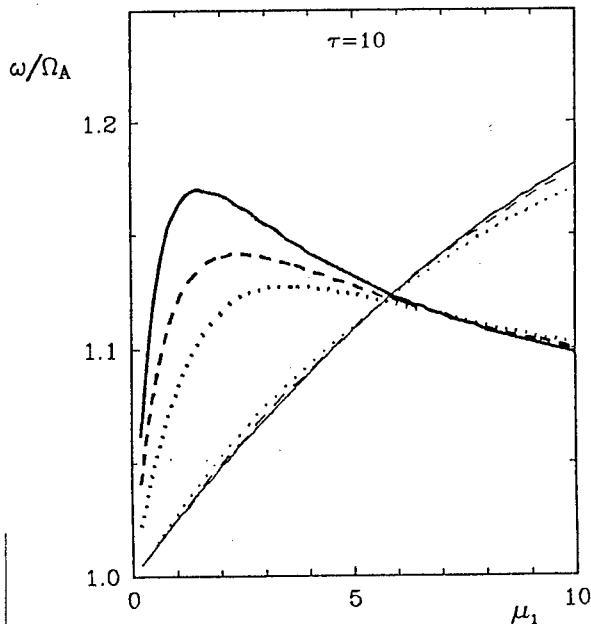


Figure 1.

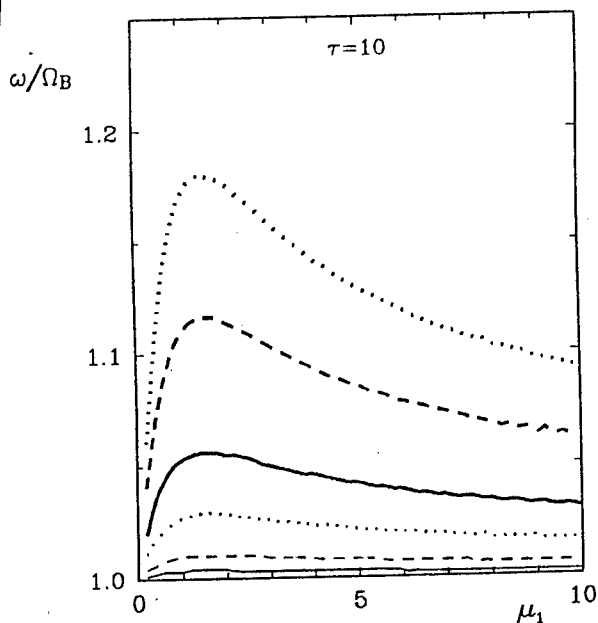


Figure 2.

$A^+$  and  $A^{++}$  have practically the same mass,  $m_i$ ). Figure 3 shows the graphs of  $U^*$  vs.  $\bar{n}_1$ , again for  $\tau = 10$  and  $T = 0.2, 1$  and  $5$  (curves for  $T = 1$

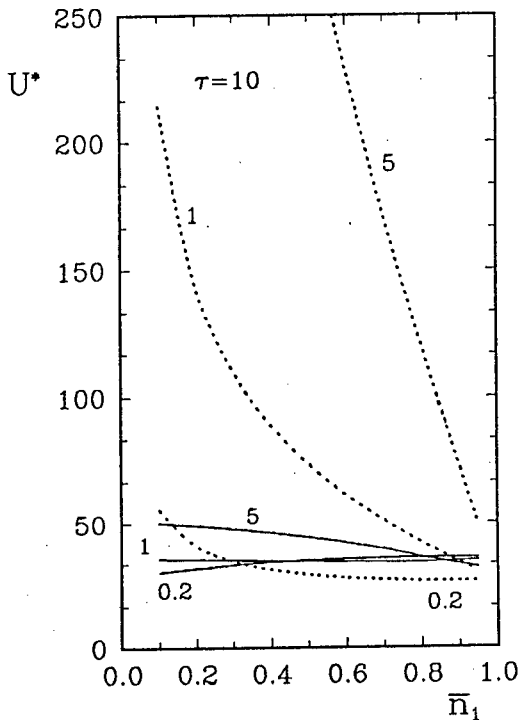


Figure 3.

are included for the sake of comparison with the previous results); unbroken lines pertain to mode (A), dotted lines to mode (B). Apart from the easily recognized feature of the excitation being facilitated (the threshold drift lowered) if the percentage of the "resonant" ions is augmented (or that of the "resonant" ions with lower IC harmonic, if both species are "resonant"), a somewhat unusual trait can be seen in the curve pertaining to the mode (A) if  $T = 5$ . Namely, here the augmentation of  $\bar{n}_1$  entails a decrease of the threshold drift, although this augmentation means the gradual transition from the first IC harmonic (for  $\bar{n}_1 = 0$ ) to the second (for  $\bar{n}_1 = 1$ ). This can be obviously attributed to the fact that, in this particular instance, the singly charged ions are much hotter.

## References

- [1] B.S. Milić: J. Plasma Phys., **43** (1990) 23
- [2] N.R. Brajušković, D. Ž. Gajić and B.S. Milić: Contr. Papers of the SPIG 18 (Kotor, 1996), p. 556
- [3] B.S. Milić and D.Ž. Gajić: Plasma Phys. and Contr. Fusion, **33** (1991) 1161

- [4] B.S. Milić and D.Ž. Gajić: Contr. Papers of the SPIG 17 (Belgrade, 1994), p. 358
- [5] B.S. Milić and D.Ž. Gajić: Contr. Papers of the SPIG 15 (Dubrovnik, 1990), p. 354

# SPATIAL ATTENUATION OF LANGMUIR WAVES IN GAS-DISCHARGE NEON AND ARGON PLASMAS

V.J. Žigman and B.S. Milić

*Faculty of Physics, University of Belgrade, P.O.B. 550, Belgrade, Yugoslavia*

Kinetic studies of the spectral properties of high-frequency fast ( $\omega^2/k^2 v_{te}^2 \gg 1$ ) longitudinal electron Langmuir waves, excited in weakly ionized, weakly collisional gas-discharge plasma, indicate that, generally, two mechanisms of attenuation of the waves, i.e. the Landau (collisionless) and the collisional dampings compete. Both of these mechanisms depend on the reduced electric field (the Townsend parameter)  $E_0/n_n$ , and on the transport coefficients, characterizing the steady-state background plasma bulk. The Landau damping, in particular, also exhibits strong dependence on the specific form of the steady-state electron distribution function (SSEDF)  $f_e^0(\vec{v})$  [1,2]. When the anisotropy of the SSEDF due to the drift of the electrons is taken into account, by way of the two-term EDF approximation,  $f_e(\vec{v}) = f_e^0(v) + f_e^1(v) \cos \chi$ , the Landau attenuation of Langmuir waves is shown to depend on their *direction* with respect to that of the electron drift [2]. This fact makes it interesting to regard the damping process in space, rather than in time.

Therefore, in the present paper attention is focused on the weak *spatial* attenuation, by taking the wave vector  $\vec{k}$  as complex ( $\vec{k} = \vec{k}_r + i\vec{k}_i$ ,  $k_i \ll k_r$ ) and keeping  $\omega$  purely real. The spectrum is taken in the longwavelength ( $k^2 r_{De}^2 \ll 1$ ) Bohm-Gross approximation

$$\omega^2 = \omega_{pe}^2 \left( 1 + \frac{k^2 v_{te}^2}{\omega_{pe}^2} \mathcal{E} \right), \quad (1)$$

yielding isotropic group velocity, related to the phase velocity by  $v_g v_f = \mathcal{E} v_{te}^2$ . Here  $v_{te}$  is the electron thermal velocity, and  $\mathcal{E}$  is a dimensionless functional of the SSEDF defined previously [3]. Following the gen-

eral procedure [3], and taking into account the collisional attenuation as well, one, presently, obtains the spatial decay rate for Langmuir waves with spectrum (2), propagated at an angle  $\theta$  with respect to the electron drift. Namely,  $k_i$ , as function of the phase velocity  $\omega/k$  and scaled to the electron Debye radius  $r_{De}$  is expressed in the following form:

$$k_i r_{De} = \frac{1}{2D\mathcal{E}} \left[ \sqrt{\frac{\pi}{2}} C \Omega(\omega/k) \frac{\omega^4}{k^4 v_{te}^4} \times \frac{f_e^{00}(\omega/k) + f_e^{01}(\omega/k) \cos \theta}{f_e^{00}(0)} + \frac{\nu_{en}}{\omega_{pe}} \mathcal{B} \right], \quad (2)$$

where

$$\Omega(\omega/k) = \left( 1 - \mathcal{E} \frac{k^2}{\omega^2 v_{te}^2} \right)^{-1/2},$$

with  $\nu_{en}$  being the electron-neutral effective collision frequency,  $\mathcal{B}$  being another dimensionless functional of the SSEDF; both of these, along with the quantities  $D$  and  $C$ , are defined previously [3,4].

It is easily seen that the first and second term in (2) can be readily interpreted as the purely Landau  $k_i^L r_{De}$  and the purely collisional  $k_i^C r_{De}$  decay rates, respectively, both contributing to the overall  $k_i r_{De}$ .

On the ground of (2), comparison of the decay rates of Langmuir waves of a given phase velocity, as they evolve in argon and neon gas-discharge plasmas under analogous conditions, i.e. at equal values of  $E_0/n_n$  (10 Td and 50 Td), degree of ionization  $X$  ( $10^{-3}$ ), and neutral number density  $n_n$  ( $10^{21} \text{ m}^{-3}$ ), is elaborated presently. The selected interval of phase velocities examined ( $2.2 \times 10^6, 3.0 \times 10^6 \text{ m/s}$ ) corresponds to the region of weak attenuation, and only *direct* waves, propagated in the direction of



the electron drift ( $\theta = 0$ ) are considered. The evaluations were performed with two-term SSDEFs pertaining to Ar [4], and Ne [5], that have been shown previously, to yield reliable transport coefficients for the plasmas in question.

Table 1:

$\omega/k$	$E_0/n_n$	$k_i r_{De}$	$k_i^L/k_i^C$	$f_e^{01}/f_e^{00}$	$k_i r_{De}$	$k_i^L/k_i^C$	$f_e^{01}/f_e^{00}$
$[10^6 \frac{m}{s}]$	[Td]	ARGON			NEON		
2.2	10	$2.52 \cdot 10^{-3}$	0.90	0.24	$5.00 \cdot 10^{-1}$	$2.2 \cdot 10^3$	0.092
	50	$1.87 \cdot 10^{-1}$	$1.4 \cdot 10^2$	0.28	$6.68 \cdot 10^{-1}$	$3.5 \cdot 10^3$	0.27
2.4	10	$1.56 \cdot 10^{-3}$	$1.1 \cdot 10^{-5}$	0.37	$2.77 \cdot 10^{-1}$	$1.0 \cdot 10^3$	0.21
	50	$2.30 \cdot 10^{-2}$	$1.4 \cdot 10^1$	0.41	$6.11 \cdot 10^{-1}$	$2.7 \cdot 10^3$	0.36
2.6	10	$1.80 \cdot 10^{-3}$	$\approx 10^{-12}$	0.51	$3.37 \cdot 10^{-2}$	$1.1 \cdot 10^2$	0.38
	50	$2.69 \cdot 10^{-3}$	0.5	0.54	$4.48 \cdot 10^{-1}$	$1.7 \cdot 10^3$	0.48
2.8	10	$2.04 \cdot 10^{-3}$	0	0.64	$1.16 \cdot 10^{-3}$	2.2	0.51
	50	$2.05 \cdot 10^{-3}$	$6.5 \cdot 10^{-3}$	0.68	$2.48 \cdot 10^{-1}$	$8.1 \cdot 10^2$	0.58
3.0	10	$2.27 \cdot 10^{-3}$	0	0.78	$4.08 \cdot 10^{-4}$	$1.1 \cdot 10^{-2}$	0.62
	50	$2.29 \cdot 10^{-3}$	$2.9 \cdot 10^{-5}$	0.83	$1.04 \cdot 10^{-1}$	$2.9 \cdot 10^2$	0.67

The results arrived at show that the collisional decay rate,  $k_i^C r_{De}$ , increases very slowly with  $v_{fs}$ , remaining of the order  $10^{-3}$  and  $10^{-4}$ , in Ar and Ne plasma, respectively, on the whole interval of  $v_{fs}$  examined, at both 10 Td and 50 Td. On the contrary, the Landau decay rate,  $k_i^L r_{De}$ , decreases towards higher  $v_{fs}$ , more distinctly at the lower  $E_0/n_n$  value and more markedly in Ar.

The values of the resulting overall decay rate,  $k_i r_{De}$ , as well as of two other conveniently chosen parameters,  $k_i^L/k_i^C$  and  $f_e^{01}/f_e^{00}$ , on the specified range of  $v_{fs}$  and  $E_0/n_n$ s are listed in Table 1. The parameter  $k_i^L/k_i^C$  indicates the relative significance of the two mechanisms of attenuation, and the ratio  $f_e^{01}/f_e^{00}$ , taken at the velocity of electrons resonant with the wave, estimates the relevance of the two-term SSDEF approximation in determining the Landau damping.

It is clearly seen from Table 1 that

the Landau mechanism is dominant at the lower limit of the  $v_{fs}$ 's interval, and at the upper limit collisional attenuation prevails. In Ar, where  $k_i^L r_{De}$  goes to zero for the largest  $v_{fs}$  considered, the overall  $k_i r_{De}$  goes through a minimum attaining subsequently the slowly increasing  $k_i^C r_{De}$  value. In this case the attenuation of the wave is purely collisional and determined by the

bulk properties of the plasma. It is interesting to note that, in all the cases examined, the evaluation of the  $k_i^L r_{De}$  with the anisotropic part of the SSDEF included, is of unquestionable importance. The ratio  $f_e^{01}/f_e^{00}$  increases as the distribution approaches the high energy tail, but it is also far from being negligible at the lower  $v_f$  limit, where  $f_e^{01}$  amounts to roughly 30% of the  $f_e^{00}$  value in both Ne and Ar at 50 Td.

### References

[1] Žigman V.J., *Contr. Papers*, 17th SPIG, p. 366, Belgrade (1994).  
 [2] Žigman V.J., Milić B.S., *Proceed. I Contr. Papers*, 321 XXII ICPIG, Hoboken, (1995).  
 [3] Žigman V.J., Milić B.S., *Contr. Papers*, 18th SPIG, p. 552, Kotor (1996).  
 [4] Žigman V.J., Milić B.S., *J. Plasma Phys.* **38**, 223 (1987).  
 [5] Golant V.E., *Zhurn. Tekhn. Fiz. (USSR)*, **27**, 1482 (1957).

# High-Power Backward-Wave Oscillator Operating far from Upper Cutoff

Koji Tanaka, Xiaodong Zheng, Kazuo Minami, Takao Nagahama and Hisashi Tokumasu  
Graduate School of Science and Technology, Niigata University, Niigata 950-21, Japan

## 1. Introduction

Usually, high-power backward-wave oscillators (BWOs) operate near upper cutoff edge of the transmission band i.e.  $\pi$ -mode[1] shown in Fig.1. The reason is that the starting current usually has its lowest value in  $\pi$ -mode. In an ideal case, the guiding magnet field is so strong that the electrons are restricted to move only in the axial direction. In this case, the electrons only interact with TM modes in the slow-wave structure (SWS). However, in the actual experiments, the strength of guiding magnetic field was finite and the effects of electrons rotation have to be considered. When the beam currents are less than a threshold, hybrid  $TE_{11}$  mode plays a dominant role instead of symmetrical  $TM_{01}$  mode in BWOs[2]. Because the starting current for the latter is greater than that of the former. There is a possibility of mode selection of  $TE_{11}$  from BWO by controlling the beam current. In this investigation, we report the experimental results about the BWO operating far from  $\pi$ -mode.

## 2. Experimental setup

We designed and constructed a SWS which consisted of aluminum modules and can be varied in length up to 9.5 periods. The inner structure wall radius,  $R(z)$ , varies sinusoidally according to the relation

$$R(z) = R_0 + h \cos(k_0 z)$$

where  $k_0 = 2\pi / z_0$ ,  $z_0$  is the length of the corrugation period,  $R_0$  and  $h$  are mean radius and the amplitude of corrugation. The parameters of SWS in this experiment are chosen as follows:  $R_0 = 1.445$  cm,  $z_0 = 1.67$  cm and  $h = 0.445$  cm. Schematic drawing of SWS and annular beam are shown in Fig.2. The dispersion diagram for  $TM_{01}$  and  $TE_{11}$  modes in an infinitely long SWS with the same dimensions is shown in Fig.1. Marx generator is used as a high voltage source to generate and to accelerate the intense pulsed electron beam. The annular electron beam is generated by a beam diode that consists of an aluminum cathode with circular edge and a foilless stainless steel anode. The operating voltage of Marx generator is varied between 70-130 kV with a pulse length of about 100 ns. The dot dashed line in Fig.1 indicates a beam line with energy 110keV. The beam diode and SWS are installed in a stainless steel pipe which is evacuated by a turbo molecular pump and a

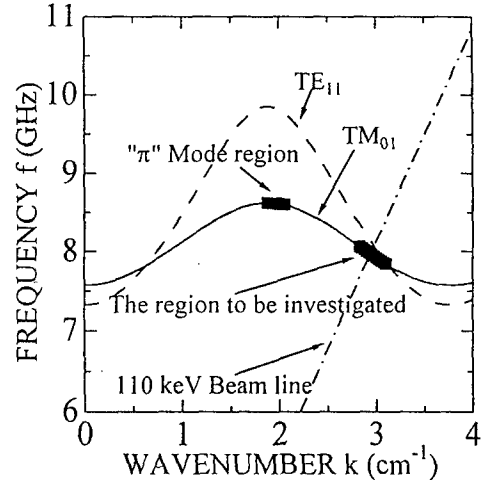


Fig.1 The calculated dispersion diagram of the sinusoidally corrugated waveguide.

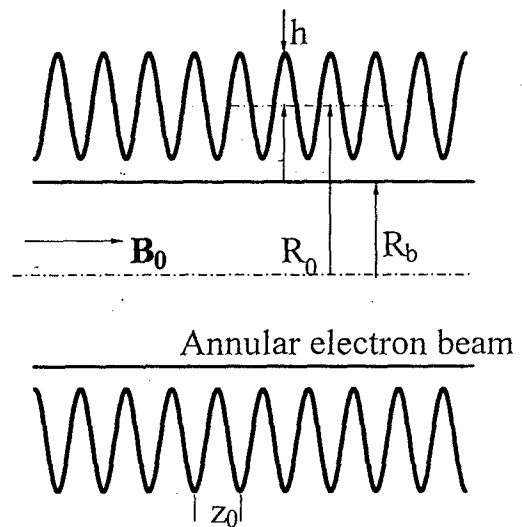


Fig.2 Schematic drawing of slow-wave structure and annular beam.

diffusion pump to pressure less than  $2 \times 10^{-5}$  Torr. The electron beam is guided by axial magnetic field,  $B_0$ , of 0.05-1.0 T. The beam current is measured with Rogowski coil at the upstream side of SWS and the

diode voltage is diagnosed with a resistance voltage divider positioned at the upstream of the diode.

### 3. Results

In the experiments, we measured the output power, frequency versus the following parameters: the length of SWS, the magnitude of the axial magnetic field, and the diode voltage. The tests with different lengths of SWS, 9.5 periods, 7.5 periods and 5.5 periods are performed to clarify the influence with decreasing the length of interaction. Microwave output power as a function of diode voltage is shown in Fig.3 for a given magnetic field of 0.97 T. The power is seen to increase monotonically with the diode voltage over the range of 80-125 kV, and is increasing with the length of SWS. The starting currents are decreased with the longer SWS which contributes to an increase in microwave output power and efficiency.

The radiation pattern is measured by scanning the receiving antenna in horizontal direction[3]. Typical mode patterns under the condition of two different beam currents are measured. Figure 4 (a) and (b) show the results for 300 A and 500 A, respectively. The distance between the output window and the horn antenna is 1.5 m. The diode voltage and the magnetic field are 110kV and 0.97 T, respectively. The shape of measured radiation pattern under the condition of 300 A indicates that the dominant oscillation mode of BWO is  $TE_{11}$  mode. The calculated  $TE_{11}$  radiation pattern is also shown by the solid curve in Fig.4 (a). On the other hand, the measured radiation pattern under the condition of about 500 A indicates that the dominant oscillation mode is  $TM_{01}$  mode. A solid curve in Fig.4 (b) indicates the calculated  $TM_{01}$  radiation pattern at 8.5 GHz. Usually, the  $TM_{01}$  mode always are dominant oscillation mode for BWOs, because an axisymmetric annular beam is used and operation is made near  $\pi$ -mode oscillation. For the BWO operating in far from  $\pi$ -mode, a large current is needed for starting oscillation. However, in our experiment,  $TM_{01}$  mode is not observed even in the case of 300 A beam currents.

In conclusion,  $TE_{11}$  and  $TM_{01}$  modes are, for the first time, observed separately by changing the operation condition of beam current in a BWO.

### 4. References

- [1] S.M. Miller *et al.*: Phys. Plasma **1**(1994)730.
- [2] V.L. Bratman *et al.*: Sov. Tech. Phys. Lett. **9**(1983)266.
- [3] K. Ogura *et al.*: Phys. Rev. E **53**(1996)2726.

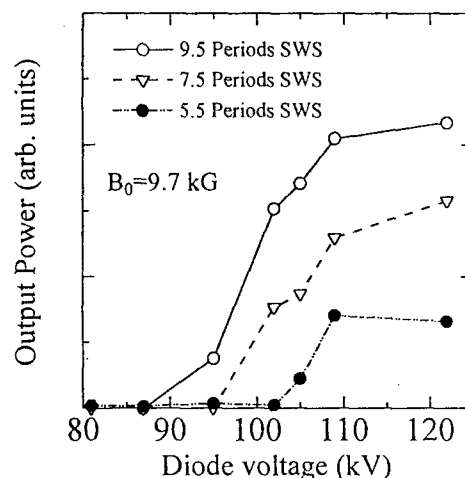


Fig.3 Output power vs. Diode voltage

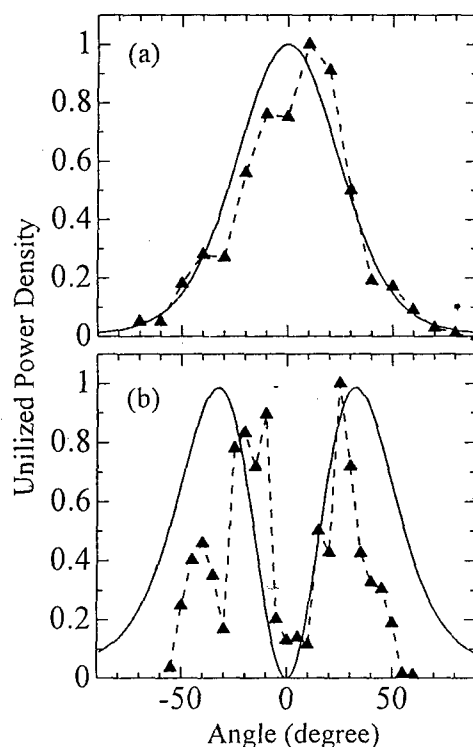


Fig.4 Radiation pattern

# Experiments on Nonneutral Plasmas in Multi-Ring-Electrodes Traps

A. Mohri, T. Michishita, Y. Yamazawa<sup>†</sup>, H. Higaki<sup>‡</sup>, T. Yuyama, H. Tanaka<sup>†</sup>, A. Hirota, H. Oishi

Department of Fundamental Sciences, Faculty of Integrated Human Studies, Kyoto University

<sup>†</sup> Graduate School of Energy Science, Kyoto University

<sup>‡</sup> Graduate School of Human and Environmental Studies, Kyoto University

Sakyo-ku, Yoshida, Kyoto 606-01, Japan

## 1. Introduction

Experiments on nonneutral electrons and positrons have been performed by using developed three traps, each of which is composed with aligned multiple ring electrodes (MRE). These traps can generate many types of electrostatic configurations for confining nonneutral plasmas of different shapes, according to the purpose of experiment. Figure 1 shows a schematic drawing of the MRE. Each ring electrode can be biased independently to generate a desired electrostatic field inside the confinement region, and also the electrodes are used either to excite electrostatic modes or to detect their signals.

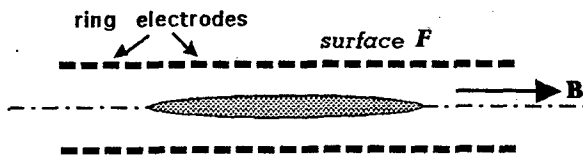


Fig.1 Multi-Ring-Electrodes Trap.

This report describes the recently obtained results using the MRE traps concerning subjects as:

- Spheroidal plasma
  1. Cancellation of the image charge effects to realize an ideal rigid rotor equilibrium.
  2. Relaxation phenomena after ECRH.
- Nonlinear couplings among electrostatic modes in a cylindrical plasma column.
- Formation of positron plasma.

## 2. Cancellation of image charge effects

A cold spheroidal plasma is settled in a uniform axial magnetic field and a hyperbolic electrostatic potential well written by  $\phi_h = A(r^2 - 2z^2)$ , if the surrounding wall is far away from the plasma. On the other hand, when the wall is present near the plasma, the image charges induced on the wall deteriorate the external electric field and thereby the rigid rotor equilibrium breaks. However, if the potential distribution on the wall surface  $\phi_T|_F$  is given as

$$\phi_T|_F = \phi_h|_F + \phi_s|_F,$$

where  $\phi_s|_F$  is the self field potential of the plasmoid, then the image charge effects on the plasmoid disappear. This method to cancel the effects is possible in the MRE trap. It was experimentally proved that this cancellation of the image charges much improves the confinement [1,2]. The confinement time became the longest when the parameters of the confined spheroidal plasma coincided with those given by  $\phi_s|_F$ .

Under this cancellation, the electrostatic modes changes their frequencies since the electric field generated by  $\phi_s|_F$  works as an additional field at the oscillation. Therefore, mode frequencies differ from the Dubin's dispersion relation found for free boundary case<sup>3)</sup>. Figure 2 shows the observed dependence of  $(\ell = 1, m = 0)$  mode frequency on the trapped total electron number  $N$ . Here is also shown the calculated mode frequency including the additional field, which is well in agreement with the observed one.

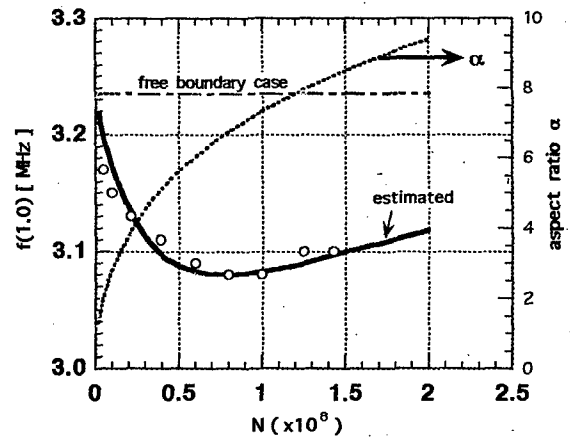


Fig.2 (1,0) mode frequency at the cancellation of the image charge effects in the MRE trap.

## 3. Relaxation of electrons heated by ECRH

The several ring electrodes of MRE trap are azimuthally cut to segments so as to apply asymmetric perturbations for heating, or to excite and observe axially asymmetric oscillation modes. An rf power of  $\sim 609$  MHz and  $\leq 3$  mW was applied to one segment of the electrode at the midplane in order to heat a spheroidal electron plasma by ECRH. This power level was sufficient to see the heating effect. The plasma to be heated had the total electron number of  $N = 1.8 \times 10^8$  with the radius of 9 mm and the

aspect ratio of 9. The high energy tail side of the parallel components of the heated electrons was measured by detecting the electrons leaked from the potential well when its depth was promptly shallowed a little, as usually done for measuring the temperature. In this way, the equivalent  $T_{\parallel}$  was deduced. Figure 3 shows the obtained time variations of  $T_{\parallel}$  for different input rf powers.

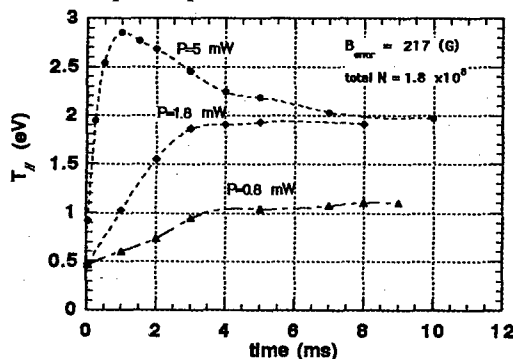


Fig.3 Time variations of  $T_{\parallel}$  after 0.5 ms application of ECRH for different input powers  $P$ .

Here, it is clearly seen that electron energies heated perpendicularly to the magnetic field relax to the parallel energies or to a thermalized state. At the higher input powers, there appear overshoots in  $T_{\parallel}$ , which correspond to the presence of two components of the temperature, i.e., the presence of non-thermalized energy tail. This tail disappears as the thermalization proceeds.

#### 4. Nonlinear mode coupling in a cylindrical plasma column

The MRE trap can form the configuration like the Malmberg trap which plugs a plasma by electric potential barriers at the both ends. The plasma confined in this type of trap is nearly a cylindrical column and axial modes of electrostatic oscillations are present since the column length is finite. In the MRE trap axisymmetric modes can be excited easily by applying rf perturbations which resonate with the modes. It was found that nonlinear couplings among the modes occur and its threshold of the occurrence depends on the electron temperature. [4]. Here is presented the reconfirming results of such a mode coupling. The trap used is a new MRE trap which is accurately machined and set in a more uniform magnetic field with the spatial fluctuation less than  $10^{-4}$  over the whole confinement region.

The mode is indicated by the number of nodes along the plasma column  $\ell$ . A typical example of the mode coupling is shown in Fig. 4. In this case,  $N = 3 \times 10^8$  electrons,  $B = 215G$  and the radius and the length of the plasma was 1 cm and 24 cm, respectively. The observed mode frequencies were 2 MHz for  $\ell = 1$ , 3.9 MHz for  $\ell = 2$ , 5.6 MHz for  $\ell = 3$ , 7.1 MHz for  $\ell = 4$  and 8.4 MHz for  $\ell = 5$ . The figure shows the time variations of power spectra

when  $\ell = 4$  was excited by applying a burst of 7.1 MHz perturbations for 4  $\mu$ s. Immediately after the end of the burst,  $\ell = 4$  mode was quite dominant and its spectrum was broad. As time elapsed, this mode disappeared while different modes  $\ell = 3, 2, 1$  and 5 came out. These modes were changing their relative amplitudes with time and at the later stage  $\ell = 1$  and  $\ell = 3$  modes survived for a long time. This mode coupling changed its feature with the amplitude of the initially excited pump mode.

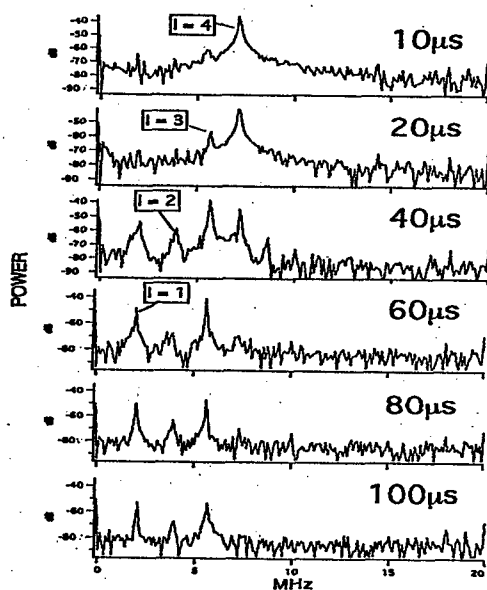


Fig.4 Observed time dependence of the power spectra when the nonlinear mode coupling was induced by the pump mode  $\ell = 4$ .

#### 5. Formation of a positron plasma in a superconducting magnet

An MRE trap is set in the 8 T superconducting magnet. This MRE trap has the inner diameter of 4 cm and the axial length of 14.8 cm. The confinement time of electrons reached about 4000 s at  $B = 7$  T. As a source of positrons, a  $^{22}\text{Na}$  isotope of 0.1 mCi was set outside the trap region. To include a non-adiabatic process, an axial rf electric field of the positron bounce frequency was applied on the edge of the trap. This rf field works as a decelerating kicker to incoming positrons and, in addition, a resonator to damp the bouncing oscillation was attached. The particle number of trapped positrons after the accumulation for 400 s was  $7 \times 10^5$ . Here, the cyclotron radiation cooled down the positrons to the room temperature. The ratio of the plasma size to the Debye length was about 7 at the minimum. This cloud satisfies the plasma condition.

#### 6. References

- [1] A. Mohri, H. Tanaka, H. Higaki, Y. Yamazawa: Proc.12th ICPG, 3(1995)63.
- [2] A. Mohri et al.: to be submitted.
- [3] D. H. E. Dubin: Phys. Rev. Lett.66(1991)2076.
- [4] H. Higaki: submitted to Plasma Phys and Cont. Fusion.

## Nonstationary parametric processes in a relativistic semi-bounded plasma

V.N. Pavlenko

Institute for Nuclear Research,  
prospect Nauki 47, 252028, Kiev, Ukraine.

In recent years many papers on parametric instabilities in plasmas of relativistic electron beam (REB) have appeared [1-5]. These investigations are very important for plasma electronics and free-electron lasers because the nonlinear wave interaction processes may lead to up-conversion of the frequency of the scattered wave as compared to the frequency of the incident electromagnetic wave. Previously have been studied space-time evolution of three nonlinearly interacting wave packets in infinite plasma [4,5].

In present report we consider the nonstationary parametric interaction of three waves packets in the semi-bounded plasma of REB. We assume that electron beam is filling the region  $z > 0$  and moved with velocity  $V = V_0 \vec{e}_z$ . The region  $z > 0$  is filling the media with dielectric constant  $\epsilon_r > 0$ .

We analyzed three-wave resonant interaction two s-polarized volume waves

( $E_{1,2,y} = E_{1,2}$ ,  $E_{1,2x,z} = 0$ ) with frequency  $(\omega_{1,2}, k_{1,2})$  and surface wave  $(\omega_3, k_3)$ ,  $\vec{k}_{1,2,3} = \{k_{1,2,3x}, 0, k_{1,2,3z}\}$ . The matching conditions are written in the form:

$\omega_3 = \omega_2 + \nu \omega_1 + \Delta\omega$   
 $\vec{k}_3 = \vec{k}_2 + \nu \vec{k}_1 + \Delta\vec{k}$ ,  $\nu = \pm 1$  is sign function,  $\Delta\omega$  and  $\Delta\vec{k}$  is represent the frequency and wave-number mismatch. We consider waves satisfying the dispersion relation:

$$\omega_{1,2} = N_{1,2}^{-1} (k_{1,2}^2 c^2 + \omega_p^2 \gamma_0^{-2})^{1/2},$$

$$\omega_3 \approx k_3^2 \vec{V}_0 - r \omega_p \gamma_0^{-3/2} (2\epsilon_r)^{-1/2} \quad (2)$$

where  $r = 1$  correspond to the surface with negative (and  $r = -1$  positive) energy,

$\gamma_0 = (1 - V_0^2/c^2)^{-1/2}$ ,  $\omega_p$  is electron plasma frequency,  $N_{1,2} = [\epsilon(\omega_{1,2})]^{1/2}$ , where  $\epsilon(\omega_{1,2})$  - are the dielectric constant of media, filling the region  $z > 0$ . From (1) and (2) it is easy to show that  $\omega_2 > \omega_1$  (up-conversion of the frequency), if  $N_1 V_0 / c > 1$ .

We obtain the system of equations described the different nonlinear wave interactions the surface wave with ele-

ctromagnetic waves ( the technique to derive these equations has been described in [2,4,6]). We shall study these equations in parametric approximation, i.e. we assume that the pump wave amplitude  $E_1 = E_{1,0}$  ( $\gg E_{2,3}$ ) is constant.

We analyzed the propagation of an electromagnetic signal wave packet with a Gaussian amplitude profile in the presence of a REB with initial modulation. It is shown that a diffusion broadening in space of the wave packet occurs. The diffusion length  $l_d$  is determined. After a distance that is much larger than the  $l_d$ , a phase locking will take place, however, and the growth rate has then reached its maximum value.

We think that the results of the present report can be useful for some free-electron laser work, as three-wave interaction processes are important in the generation of ultra-high frequency radiation.

#### References

- [1] R.C.Davidson and Y.Z.Yin: Phys.Rev. **A30** (1984) 3078.
- [2] S.V.Davydov, V.P.Zakharov, V.N.Pavlenko: Radiophys. Quantum Electronics, **32** (1990) 999.
- [3] V.N.Pavlenko, S.V.Davydov, L.Stenflo: Soviet J. Plasma Phys., **18** (1992) 398.
- [4] S.V.Davydov, V.N.Pavlenko, L.Stenflo and I.Weiland: Physica Scripta, **45** (1992) 257.
- [5] V.N.Pavlenko, S.V.Davydov: Abstr.Intern.Conf.on Plasma Phys. (Nagoya, Japan, 1996), p.124.
- [6] A.G.Sitenko, V.N.Pavlenko: Sov.Phys.JETP, **74** (1978) 128.

# Propagation of Whistler Wave Packets in a Collisional Plasma

E. Sonnenschein<sup>1</sup>, I. Rutkevich<sup>2</sup> and D. Censor<sup>1</sup>

<sup>1</sup> Department of Electrical and Computer Engineering

<sup>2</sup> Department of Mechanical Engineering

Ben-Gurion University of the Negev, Beer Sheva 84105, Israel

The theory of wave packets (WP) in dispersive media without wave energy absorption has been extensively developed and discussed in the literature [1, 2]. For a homogeneous medium a WP is constructed by the continuous superposition of the elementary waves which have close values of their wave vectors. Usually such a superposition is presented in the form of the integral of the function  $A(\mathbf{k})\exp[i(\mathbf{k} \cdot \mathbf{x} - \omega t)]$  over the  $\mathbf{k}$ -space. The frequency  $\omega$  and the wave vector  $\mathbf{k}$  are related by the dispersion equation  $D(\omega, \mathbf{k})=0$  characterizing the properties of the medium with respect to wave propagation. The Fourier transform of the spatial WP at  $t=0$  is the function  $A(\mathbf{k})$  concentrated in some vicinity of the carrier wave vector  $\mathbf{k}_c$ . The spatial maximum of the WP envelope propagates with the group velocity  $\mathbf{W}=\partial\omega/\partial\mathbf{k}$  where the derivative is calculated at  $\mathbf{k}=\mathbf{k}_c$ . As can be shown by the saddle-point method for calculating the Fourier integrals [2], for large times each small section of the WP can be characterized by the instantaneous values of the local wave vector  $\tilde{\mathbf{k}}(\mathbf{x}, t)$  and the local frequency  $\tilde{\omega}(\mathbf{x}, t)=\omega[\tilde{\mathbf{k}}(\mathbf{x}, t)]$  where the relation  $\omega(\mathbf{k})$  is determined by the dispersion equation. These local characteristics of the WP maintain constant values along the straight-line trajectories  $\mathbf{x} = \mathbf{X}(t)$  called rays. The description of the rays associated with the WP propagation admits the Hamiltonian formalism: The vectors  $\mathbf{X}(t)$  and  $\tilde{\mathbf{k}}$  determine the position of the dynamic system in coordinate space and in momentum space, respectively.

In dissipative (absorbing) or active (amplifying) media the elementary waves that are sinusoidal in space ( $\text{Im } \mathbf{k}=0$ ) decay or grow in time ( $\text{Im } \omega \neq 0$ ), while the time-periodical waves ( $\text{Im } \omega =0$ ) decay or grow in space ( $\text{Im } \mathbf{k} \neq 0$ ). This leads to a complex group velocity vector. When the medium is absorbing, the WP acquires some new features in comparison with its behavior in non-absorbing media. Thus, the velocity of the WP envelope maximum  $\mathbf{V}$  changes with time even in the case when the medium is homogeneous [3-5]. In addition, the local wave number which can be determined in the point of the envelope maximum also changes with time [3]. These circumstances provide the difference of the vectors  $\mathbf{V}$  and  $\mathbf{W}$ . In an absorbing medium vector  $\mathbf{W}$  is complex at the point of the envelope maximum. Although the velocity  $\mathbf{V}$  can be expressed in terms of both real and imaginary parts of  $\mathbf{W}$ , the concept of the

complex group velocity remains obscure from the physical point of view. On the other hand, several examples existing in the literature show that  $\mathbf{W}$  may represent a real physical velocity in an absorbing medium [4-7], if for some real or complex values of the wave vector  $\mathbf{k}$ , the vector  $\mathbf{W}$  becomes real.

The purpose of the present paper is to examine role of the real rays provided by the requirement  $\text{Im } \mathbf{W}=0$  in the propagation of one-dimensional WP in homogeneous absorbing media and to show that such rays determine all local characteristics of the WP for large times and distances. To illustrate the features of the WP that are associated with the local group velocity which remains real in the presence of absorption, we investigate the exact analytical solution for a Gaussian WP in a medium characterized by the quadratic complex law of dispersion  $\omega=(\alpha - i\beta)k^2$ . This dispersion equation is commonly used for whistlers propagating along the magnetic field lines in a collisional magnetosphere. The parameters  $\alpha$  and  $\beta$  which are responsible for the dispersion and absorption of the whistlers are determined by  $\alpha = c^2\omega_{ce}/\omega_{pe}^2$ ,  $\beta = \alpha v_e/\omega_{ce}$ . Here  $c$  is the vacuum light velocity,  $\omega_{ce}$  is the electron gyrofrequency,  $\omega_{pe}$  is the electron plasma frequency,  $v_e$  is the mean collision frequency of electrons. When the initial distribution  $u(x,0)=\text{Re } f(x)$  is a Gaussian WP given by

$$f(x) = C \exp(ik_c x - x^2/h^2) \quad (1)$$

after introducing the dimensionless variables and parameters

$$\xi = k_c x, \quad \tau = \beta k_c^2 t, \quad N = k_c h/2, \quad a = \alpha/\beta \quad (2)$$

the solution of the Cauchy problem is given by

$$u(x, t)/C \equiv \bar{u}(\xi, \tau) = E(\xi, \tau) \cos[\theta(\xi, \tau)], \quad (3)$$

$$E(\xi, \tau) = \frac{\exp[-\psi(\xi, \tau)]}{[(1 + \tau/N^2)^2 + a^2 \tau^2/N^4]^{1/4}}$$

where  $\psi(\xi, \tau)$  is given by

$$\psi(\xi, \tau) = \frac{(1 + \tau/N^2)[\xi - \xi_m(\tau)]^2}{4[(N + \tau/N)^2 + (a\tau/N)^2]} + \frac{\tau}{1 + \tau/N^2} \quad (4)$$



Here  $\xi_m(\tau) = 2a\tau/(1+\tau/N^2)$  is the normalized coordinate of the WP envelope maximum. The phase function  $\theta$  in Eq. (3) has the form

$$\theta(\xi, \tau) = \vartheta(\xi, \tau) - \frac{1}{2} \arctan\left(\frac{a\tau}{\tau + N^2}\right), \quad (5)$$

$$\vartheta = \frac{\xi(1+\tau/N^2) - a\tau + a\xi^2\tau/(4N^4)}{(1+\tau/N^2)^2 + a^2\tau^2/N^4}$$

When  $N^2 \gg 1$ , i.e. the characteristic number of spatial oscillations inside the WP is sufficiently large, the local complex wave number  $k^*$  can be defined as

$$k_r^* = \frac{\partial \vartheta}{\partial x}, \quad k_i^* = \frac{\partial \psi}{\partial x} \quad (6)$$

The exact solution presented here shows that only at  $t=0$  the real part of the local wave number  $k_r^*$  is spatially uniform and equals the carrier wave number  $k_c$ . For any small  $t > 0$  the WP acquires an inhomogeneous filling: Any given value of the wavelength can be found within the WP. Away from the WP center for  $t > 0$  very short local wavelengths appear. The family of the trajectories  $k_r^* = \text{constant}$  in  $(x, t)$  plane is shown in Fig.1. As is seen from this figure, for small times  $t$ , sufficiently large values of  $|k_r^*|$  propagate from the wings to the central part of the WP and after reaching the turning points where  $dx/dt=0$  they propagate back to the wings, so that for  $t \rightarrow \infty$  the velocity of propagation of a given value of  $k_r^*$  tends to the real group velocity

$W^* = W(k_r^* + i\beta k_r^*/\alpha)$ . The straight-line trajectory  $\Gamma$  corresponding to  $k_r^* = k_c$  is exceptional since along  $\Gamma$  both real and imaginary parts of the local wave number  $k^* = (1+i\beta/\alpha)k_c$  all time remain constant and propagate with the real constant group velocity  $W(k^*)$ .

The obtained solution indicates that in a homogeneous medium the initial carrier wave number may propagate with the real group velocity at all times if the requirement  $\text{Im } W=0$  is satisfied in some point of the WP profile at  $t=0$ . The velocity of the envelope peak is an important characteristic of the WP. However, in an absorbing medium the peak velocity is not the group velocity: The wave group is marked by its wave number or frequency and these quantities change with time in the center of the WP. For large times the group of spatial oscillations with the initial carrier wave number  $k_c$  can be found far away from the WP center. Such a behavior is displayed even in the case of weak absorption.

To estimate the influence of the collisional wave damping on the typical whistler WP in the Earth's magnetosphere we used the following parameters: the

carrier wave length is 2 km, the initial WP width is 8.9 km, the characteristic frequencies are  $\omega_{pe} = 1.8$  MHz,  $\omega_{ce} = 0.26$  MHz,  $\nu_c = 1.3$  kHz. These parameters were used in calculations of the trajectories shown in Fig. 1. The wave absorption provided by the collisions results in the localization of the wave group with  $k_r^* = k_c$  ahead of the envelope peak. Thus, after time  $t=0.014$  s the distance between the spatial envelope maximum and the position of the carrier wave number reaches 60 km and the lowering of the central wave number is close to 9%.

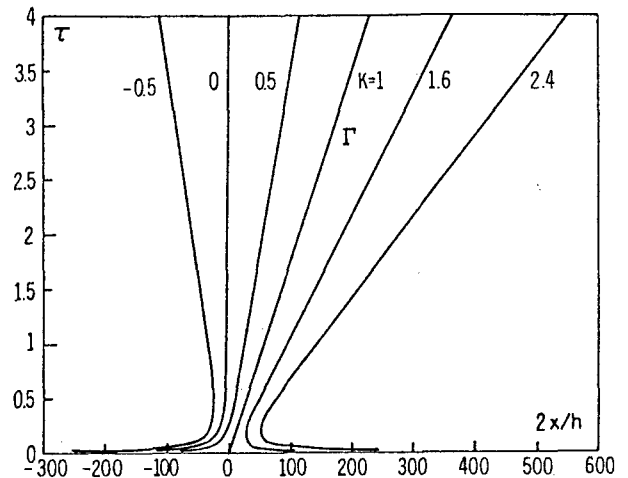


Fig. 1. The space-time trajectories along which the real part of the local wave number  $k_r^*$  is constant for various values of the parameter  $\kappa = k_r^*/k_c$  with  $a=200$ ,  $N=7$ . The time variable is defined as  $\tau = \beta k_c^2 t$ . The straight line  $\Gamma$  shown for  $\kappa=1$  is the solution of Hamiltonian equations corresponding to the initial carrier wave number.

## References

- [1] L.B. Felsen, N. Markuvitz. Radiation and Scattering of Waves, Vol.1. Prentice-Hall, New Jersey (1973).
- [2] G.B. Whitham. Linear and Nonlinear Waves. Wiley and Son, New York (1974).
- [3] L. Muschietti, C.T. Dam. Phys. Fluids B, **5** (1993), 1383.
- [4] K. Suchy. Proc. IEEE, **62** (1974), 1571.
- [5] K.A. Connor, L.B. Felsen, Proc. IEEE, **62** (1974), 1586.
- [6] D. Censor. Int. J. Heat Mass Transfer, **21** (1978), 813.
- [7] D. Censor, J.J. Gavan. IEEE Trans. Electromagn. Compat., **31** (1989), 262.

# Analysis of Stability of Strong Shock Waves in Metals

I. Rutkevich, E. Zaretsky and M. Mond

Pearlstone Center for Aeronautical Engineering Studies  
Department of Mechanical Engineering  
Ben-Gurion University of the Negev, Beer Sheva 84105 Israel

1. Strong shock waves in metals provide an important dynamic method for the generation of a dense plasma [1]. The possibility of the spontaneous emission of sound from such shocks [2] is of interest for the physics of shock waves and for various applications, including the experimental studies of a dense plasma and the problems related to inertial fusion.

For shock waves in metals the experimental Hugoniot adiabetic (HA) is commonly presented as the relationship between the shock velocity  $D$  and the particle velocity behind the shock  $U$ . For most metals the empirical dependence  $D(U)$  is a straight line:  $D=c_0+SU$  [3]. On the other hand, when the problem of stability of a shock wave in an arbitrary medium is considered, the criteria of instability are formulated in terms of the Hugoniot adiabetic  $p_2=p_H(\rho_2)$  connecting the pressure  $p_2$  and the density  $\rho_2$  of the shock-compressed material and in terms of the Mach number  $M_2=(D-U)/c_2$  for the subsonic flow behind the shock in the frame of reference, in which the shock is at rest [2]. Here  $c_2$  is the sound velocity behind the shock.

As is well-known [4], for a given dependence  $D(U)$ , the function  $p_H(\rho_2)$  can be determined from two of the Rankine-Hugoniot relationships which express the conservation laws for mass and momentum across the shock. However,  $p_H(\rho)$  alone cannot determine the sound velocity which is a thermodynamic quantity. To find this quantity and, subsequently, to apply the stability criteria one has to obtain the equation of state (EOS) for the shock-compressed material. The fundamental principles of thermodynamics can be employed to find the EOS providing such a form of the specific internal energy  $\epsilon(T, \rho)$  that would be consistent with the law of variation of  $\epsilon(\rho)$  along the HA. The latter follows from the third of the Rankine-Hugoniot relationships, which expresses the conservation of energy across the shock. In addition, if a connection between two unknown functions of density, which are the cold compression pressure and the Grüneisen parameter, is specified (for example, see the Slater - Landau model [4]), then a complete thermodynamic description of the material can be obtained.

This paper considers the possibility of spontaneous emission (SE) of sound and entropy-vortex waves from strong shocks in metals. The occurrence of SE means the existence of such two-dimensional sinusoidal sound waves impinging on the shock, for which the reflection

coefficient becomes infinite. This results also in spontaneous corrugation of the planar shock front. The problem of corrugation instability of a planar shock was first addressed by Dyakov [5] and Kontorovich [6].

During long time since the formulation of the classical criterion for SE, appropriate physical conditions for which this criterion is satisfied have not been found. Only recently [7,8] it has been shown that SE, indeed, may occur behind very strong ionizing shocks propagating in inert gases. A simple thermodynamic consideration of the conditions for SE from strong shocks in metals was given in [9] where it was shown that SE may appear for sufficiently strong shocks.

In this paper the three-term EOS presenting the total pressure as a sum of the cold elastic pressure, the thermal atomic pressure and the thermal pressure of free electrons is employed. The numerical solutions that allowed calculating the sound velocity, the shock temperature and the threshold for SE are obtained. The occurrence of SE from strong shocks depends on the slope  $S$  of the straight-line HA. It has been found that strong shocks propagating in such metals as molybdenum characterized by relatively low values of  $S$  are susceptible to SE.

2. When an experimental dependence  $D(U)$  is known, two of three Rankine-Hugoniot relations representing the conservation of mass and momentum allow determining the Hugoniot adiabetic in the plane of variables  $(\rho_2, p_2)$  [4]. The problem considered below is formulated as follows: For a given form of the HA find the EOS determining the pressure  $p$  as a function  $\rho$  and  $T$ . In addition, find the specific internal energy  $\epsilon$  and the specific entropy  $s$  as functions of  $\rho$  and  $T$ . The solution of this problem should satisfy the condition

$$\epsilon_2 - \epsilon_1 \equiv \epsilon_H(\bar{\rho}) = p_H(\bar{\rho})[1 - \bar{\rho}^{-1}]/2\rho_1 \quad (1)$$

Here  $\bar{\rho} = \rho_2/\rho_1$  is the densities ratio across the shock. The following three-term EOS [4] is assumed

$$p(\rho, T) = p_c(\rho) + p_T(\rho, T) + p_e(\rho, T) \quad (2)$$

$$[p_T = \rho\Gamma(\rho)\epsilon_T, \quad p_e = \rho\Gamma_e(\rho)\epsilon_e]$$

where  $p_c$  is the cold elastic pressure,  $p_T$  is the thermal atomic pressure,  $p_e$  is the contribution of free electrons to the total pressure. In Eqs. (2)  $\epsilon_T$  and  $\epsilon_e$  are the thermal parts of the specific internal energy due to the atoms and the electrons, respectively. These quantities are given by

$$\varepsilon_T = C_V T, \quad \varepsilon_e = \beta(\rho) T^2 / 2 \quad (3)$$

where  $C_V$  is the specific heat of atoms and  $C_{Ve} = \beta(\rho)T$  is the electronic specific heat. The functions  $\Gamma(\rho)$  and  $\Gamma_e(\rho)$  are the Grüneisen parameters for atomic and electronic subsystems, respectively. The function  $\beta(\rho)$  is the electronic specific-heat coefficient which is connected with  $\Gamma_e(\rho)$  by the relation  $\Gamma_e = -d \ln \beta(\rho) / d \ln \rho$ . The total specific internal energy is presented in the form similar to Eq.(2)

$$\varepsilon(\rho, T) = \varepsilon_c(\rho) + \varepsilon_T(\rho, T) + \varepsilon_e(\rho, T) \quad (4)$$

where  $\varepsilon_c$  is the elastic potential energy:  $d\varepsilon_c / d\rho = p_c / \rho^2$ . The specific entropy  $s$  is calculated from the identity  $Tds = d\varepsilon - (p/\rho^2)d\rho$ . Then Eqs. (2)-(4) allow calculating the sound velocity  $c(\rho, T) = \sqrt{(\partial p / \partial \rho)_s}$  and the shock temperature  $T = T_H(\rho_2)$ . To obtain a closed thermodynamic description of the shock-compressed medium the Slater - Landau model [4] was used

$$\Gamma(\rho) = -\frac{2}{3} - \frac{1}{2} \frac{d \ln [d(p_c v) / dv]}{d \ln v}, \quad v = \frac{1}{\rho} \quad (5)$$

Along the HA the internal energy is a known function of the density. Inserting Eq. (1) into Eq. (4), setting  $T = T_H$  and differentiating the result with respect to  $\rho = \rho_2$  leads to the equation:

$$\frac{d\varepsilon_H}{d\rho} = \frac{p_c}{\rho^2} + (C_V + \beta T_H) \frac{dT_H}{d\rho} + \frac{d\beta}{d\rho} \frac{T_H^2}{2} \quad (6)$$

Thus, a system of coupled equations (5), (6) was obtained for functions  $\Gamma(\rho)$  and  $p_c(\rho)$ . The initial values at  $\rho = \rho_1$  were chosen from the requirement that in the plane  $(p, \rho)$  the HA and the initial isentrope  $s = s_1$  have a second order touching in the initial point.

3. The criterion for SE [4] reads as follows:

$$h_c(\bar{\rho}, M_2) < h = -V_2^2 \left( \frac{dp_2}{dp_1} \right)_H < 1 + 2M_2 \quad (8)$$

$$M_2 = V_2 / c_2 < 1, \quad h_c = \frac{1 - M_2^2(\bar{\rho} + 1)}{1 + M_2^2(\bar{\rho} - 1)}$$

Here  $h_c$  is the critical value of the Dyakov parameter  $h$  determining the threshold of SE. Numerical calculations of the lattice Grüneisen parameter and the cold elastic pressure allowed us to calculate the sound velocity behind the shock. As a result, the critical parameter  $h_c$  and the criterion for SE were calculated. It

was found that SE from shock fronts may occur in metals, for which the slope  $S$  of the straight-line HA is less than  $4/3$  (for example, in molybdenum where  $S = 1.26$ ). The Dyakov parameter  $h$  and the critical parameter  $h_c$  as functions of the density ratio  $\bar{\rho}$  along the HA for molybdenum are shown in Fig. 1. The thermodynamic model which neglects the electronic contributions to the total energy and to the total pressure always predicts the occurrence of SE for sufficiently strong shocks [9]. Taking account of the thermal pressure and the thermal energy of free electrons may have stabilizing effect with respect to SE for metals with relatively large values of the parameter  $S$  (such as copper, for which  $S = 1.5$ ).

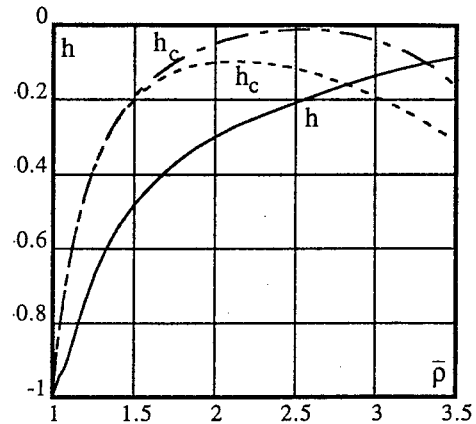


Fig. 1. The Dyakov parameter  $h$  (solid curve) and the critical parameter  $h_c$  for molybdenum ( $S = 1.26$ ) calculated along the HA from the three-term EOS (dot-dashed curve) and the two-term Mie-Grüneisen EOS (dashed curve). The critical degree of shock compression  $\bar{\rho}$  corresponding to the threshold of SE is equal to 2.8 and 3.3 for the two-term and three-term EOS, respectively.

## References

- [1] V.E. Fortov, I.T. Iakubov. Physics of Nonideal Plasma. Hemisphere, New York (1990).
- [2] L.D. Landau, E.M. Lifshitz. Fluid Mechanics. Pergamon Press (1987).
- [3] A.C. Mitchell, W.J. Nellis. J. Appl. Phys., **52** (1981), 3363.
- [4] Ya.B. Zel'dovich, Yu.P. Raizer. Physics of Shock Waves and High-Temperature Hydrodynamic Phenomena, Academic Press (1984).
- [5] S.P. Dyakov. Zh. Eksp. Teor. Fiz., **27** (1954), 288.
- [6] V.M. Kontorovich. Sov. Phys.-JETP, **6** (1957), 1179.
- [7] M. Mond, I.M. Rutkevich. J. Fluid Mech., **275**, (1994), 121.
- [8] I. Rutkevich, M. Mond and E. Toffin. Proc. XXII ICPIG, Hoboken, New Jersey. Contributed Papers, Vol.3 (1995), 41.
- [9] I. Rutkevich, E. Zaretsky and M. Mond. J. de Physique IV, **C8** (1994), 728.

# Restricted Density Perturbations in a Magnetized Electronegative Gas Positive Column

H. Satoh and M. Matsumoto\*

Faculty of Textile Science and Technology, Shinshu University Tokita 3-15-1, Ueda 386, JAPAN

\* Teraodai 1-18-4-901, Tama-ku, Kawasaki 214, JAPAN

## 1 Introduction

A plasma in the electronegative gas positive column contains generally some kinds of positive ions and negative ones. Now, the discharge tube is long enough and in a longitudinal magnetic field  $B$ . For simplicity, the plasma with one species each of positive and negative ions is treated, and assumed collision dominant. The presence of the negative ions usually causes the plasma to constrict into a region near the tube axis. This constriction is remarkable when the negative ion density is comparable to the electron one [1], [2].

The density distributions  $n_{j0}(r)$  in steady state are assumed to depend on only the distance  $r$  from the axis, where  $j = p$  for the positive ion,  $j = n$  for the negative ion and  $j = e$  for the electron. At the ratio  $g(r) = n_{n0}(r)/n_{e0}(r)$  of the order 1 as mentioned above, the distributions  $n_{j0}(r)$  can be obtained numerically only. However, at some strength of the field  $B$  fortunately those  $n_{j0}(r)$  are determined analytically.

## 2 Analysis

The charged particle flow densities  $\Gamma_{j0}$  in steady state can be obtained from

$$0 = -D_j \nabla n_{j0} + \mu_j n_{j0} E_0 + \frac{\Omega_j}{v_j} (\Gamma_{j0} \times \hat{Z}) - \Gamma_{j0}, \quad (1)$$

which is based on the momentum conservation of  $j$ -type particles in the field  $B$ . Here,

$$\mu_j = \frac{q_j}{m_j v_j} \quad \text{and} \quad \Omega_j = \frac{q_j B}{m_j c_j}, \quad (2)$$

$v_j$  being the momentum transfer collision frequency and  $\hat{Z}$  the unit vector along the tube axis. It should be noted that  $|\mu_j|$  and  $|\Omega_j|$  are respectively the mobility and Larmor frequency.

Putting the  $r$ -component of the current density derived from eq.(1) to zero, i.e.  $0 = \sum_j q_j \Gamma_{j0}^{(r)}$ , we can

obtain the ambipolar field  $E_A^{(r)}$ , used in eqs. (4) and (11) later. We here assume that the ambipolar diffusion mentioned, and the space charge neutrality are still effective when the present plasma comes to be with low frequency perturbations. The flow density perturbations  $\Gamma_{j1}$  are obtained in linear approximation about  $n_{j1}$  and  $E_1$  from eq.(1) which is replaced  $\Gamma_{j0}$  with  $\Gamma_{j0} + \Gamma_{j1}$ ,  $n_{j0}$  with  $n_{j0} + n_{j1}$  and  $E_0$  with  $E_0 + E_1$ .

First, the assumption of the ambipolar diffusion leads to

$$\begin{aligned} 0 &= \sum_j q_j \Gamma_{j1}^{(r)} \\ &= e |\mu_e| n_0 \left[ \frac{E_1^{(r)}}{A^\perp} + \left\{ \frac{D_e^\perp}{|\mu_e^\perp|} \frac{\partial}{\partial r} \left( \frac{n_1}{n_0} \right) \right. \right. \\ &\quad \left. \left. + E_A^{(r)}(r) \sum_{j=e}^{\perp} \epsilon_j^\perp \frac{n_{j0}}{n_0} \left( \frac{n_{j1}}{n_{j0}} - \frac{n_1}{n_0} \right) \right\} \right] \end{aligned} \quad (3)$$

We simply put  $n_0 = n_{e0}(r)$  and  $n_1 = n_{e1}(r, t)$  for the electrons, and

$$\begin{aligned} A^\perp &= \left( 1 + \sum_{j=e}^{\perp} \epsilon_j^\perp \frac{n_{j0}}{n_0} \right)^{-1}, \quad \epsilon_j^\perp = \frac{|\mu_j^\perp|}{|\mu_e^\perp|}, \\ D_j^\perp &= \frac{D_j}{1 + s_j^2}, \quad \mu_j^\perp = \frac{\mu_j}{1 + s_j^2}, \quad s_j = \frac{\Omega_j}{v_j}. \end{aligned} \quad (4)$$

Further,  $\sum'_{j \neq e}$  stands for the sum of  $j$  except  $j=e$ . The ratios  $\epsilon_j^\perp$  are of the order 1 for  $s_e^2 \lesssim 10$ , of which values correspond to the field strengths near but less than the critical field  $B_c$  for the helical instability.

Second, taking account of eq.(3) and azimuthally uniform perturbations, the assumption of the space charge neutrality leads

$$0 = \frac{\partial}{\partial z} \sum_j q_j \Gamma_{j1}^{(z)} = e |\mu_e| n_0 \frac{\partial}{\partial z} \left\{ E_1^{(z)} + \left( \frac{n_1}{n_0} \right) E_0^{(z)} + \frac{D_e}{|\mu_e|} \frac{\partial}{\partial z} \left( \frac{n_1}{n_0} \right) \right\} \quad (6)$$

Here,  $E_0^{(z)}$  is the discharge field. We have put the charge  $q_p = -q_n = -q_e = e$ , for simplicity.

Then, we express  $n_1$  for the electrons and  $E_1 (= -\nabla V_1)$  as

$$\begin{aligned} n_1(r, t) &= \tilde{n}_1(r) \exp\{i(kz - \omega t)\}, \\ V_1(r, t) &= \tilde{V}_1(r) \exp\{i(kz - \omega t)\}. \end{aligned} \quad (7)$$

Using the above expansions, eq.(6) leads to

$$\frac{\tilde{n}_1}{n_0} = \frac{iK}{1 + iaK} \frac{\tilde{V}_1}{RE_0^{(z)}}, \quad (8)$$

where  $K = kR$  and  $a = T_e / (R_e E_0^{(z)})$ ,  $R$  being the tube radius. We have used Einstein's relation,  $D_e / |\mu_e| = T_e / e$ ,  $T_e$  being the electron temperature in energy unit.

From the charge neutrality assumption, on the other hand,  $\Delta V_1 = 0$ . This leads to a solution

$$\tilde{V}_1(r) = V_a I_0(kr), \quad (9)$$

where  $V_a$  is the perturbed potential at the axis and  $I_0(z)$  the zeroth order modified Bessel function. We may regard  $\tilde{V}_1$  as constant, i.e.  $E_1^{(r)} \approx 0$  in the constricted plasma as stated in the introductory part. Therefore, eq.(4) with eq.(8) leads to the following restricted density perturbations.

$$\frac{n_{p1}}{n_{p0}} = \frac{n_{n1}}{n_{n0}} = \frac{n_1}{n_0} \quad (10)$$

at the strong field  $B$  which gives  $\epsilon_j^\perp = O(1)$ . We call this restriction a same ratio approximation.

### 3 Discussion

We have considered the positive column of  $CF_4$  gas at pressure (1 ~ 2) Torr with the tube radius  $R = 1$  cm. For  $\epsilon_j^\perp = O(1)$ , the ambipolar field concretely given as

$$E_A^{(r)} = -A^\perp \frac{D_e}{|\mu_e|} \frac{1}{n_0} \frac{dn_0}{dr} \quad (11)$$

becomes weak in the bulk of the constricted column, but strongly the periphery, compared with that for usual inert gas discharges. Further, all  $j$ -type particles' mobilities across the field  $B$  are of same order in their magnitudes.

Under the above circumstance, the density perturbations are kept in space charge neutrality by same order drift speeds of each  $j$ -type particles.

These perturbations may be proportional to their own steady densities. Then, the restriction(10) must be maintained sufficiently. If the field  $B$  is weak enough ( $\epsilon_j^\perp \ll 1$ ), the perturbations are preserved in their charge neutrality by a quick response of the electrons and eq.(10) is not necessary to hold (See eq.(4)).

### 4 References

- [1] M.Matsumoto and K.Sakai ; J. Phys. Soc. Japan 63 (1994) 4027
- [2] M.Matsumoto and S.Takeuchi ; J. Phys. Soc. Japan 65 (1996) 1125

## Negative charge in anode-side region of plasma arc as basis of initiation mechanism of high-frequency instability

Andrei P. Smakhtin, Valentin V. Rybakov  
Moscow State Aviation Institute (Technical University)  
4, Volokolamskoe Shosse, Moscow, 125871, Russia

In present time lots of different types of plasma arc instabilities are known [1]. These instability types each are determined by inherent characteristics both to the frequency and to the intensity of electromagnetic oscillations. It is obvious that some one of these plasma instabilities has the individual initiation mechanism.

In this paper we consider the possible mechanism of electromagnetic high-frequency instability initiation conditioned by formation of the three-dimensional electrical negative charge near the anode of the plasma arc. Kindred instability is exhibited by an experimental approach in different technical systems using the plasma arc. For example, under appropriate conditions this type of the instability is initiated in the plasma arc of such electro-rocket engine as magnetic plasma dynamic (MPD) thruster. This process is called as the limiting operating conditions of the MPD thruster.

As is known there is a thin layer near the anode inside which the electro-neutralization of the plasma arc is broken and through which the electronic current traverses only. This fact allows to consider the anode-side region of the plasma arc as a ordinary vacuum-diode. In this case the plasma arc plays a role of the cathode which can be called the plasma cathode. Contrary to the metallic cathode of the ordinary vacuum-diode which emits electrons from its surface the plasma cathode generates the emission current by the whole volume of the plasma arc. Hereafter we shall use the term "the anode current"  $J_a$  to mean the discharge current of the plasma arc and the term "the cathode current"  $J_c$  to mean the emission current from the plasma cathode as is conventional in the literature descriptive of processes in the vacuum-diode.

As in case of the ordinary vacuum-diode, the cathode current in the anode-side region of the plasma arc may be unequal to the anode current. The quantity of the cathode current depends on the operating conditions of the plasma arc, namely, geometrical sizes, the voltage and the current of the discharge, the distribution of the pressure and the temperature in the plasma arc.

We consider the plasma arc scheme which is diagrammed in Fig. 1.

The kinetic model of the emission current generation from the plasma arc bases on following notion. Each point of the plasma volume has Maxwell's electronic speed distribution because of the electrical field inside of the plasma arc is absent practically and almost whole plasma arc voltage concentrates in the cathode-side and in the anode-side regions. As is known Maxwell's speed distribution depends of the plasma temperature which is radius variant  $T(r)$ . By virtue of the fact that the

thickness of the anode-side region of the plasma arc in the order of the Debye's screening radius is far less than the plasma arc radius  $R$ , the radius of the plasma cathode is set equal to  $R$ .

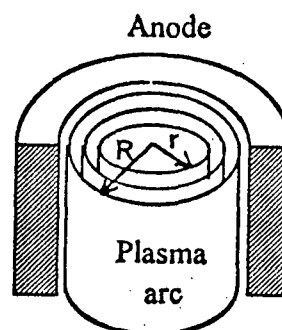


Fig. 1 Scheme of plasma arc for calculation of electron emission current  $J_a$  to anode-side region

It is apparent that thermal electrons of the plasma arc do not all have the speed and the corresponding free track length which makes possible to reach the anode-side region. For the calculation of the emission current quantity it is essential to split the plasma cathode radius  $R$  into the several parts, to determine the plasma temperature  $T$  in these regions with constant radiuses  $r$ . Using the Maxwell's electronic speed distribution with designated temperature  $T$  and the relationship between the electron speed  $V$  and its free track length  $\lambda$  we determine  $\lambda$  as a function of parameters  $T$ ,  $V$  [2]. In the calculation of the emission current with thermal electrons from each of selected plasma parts the electrons having  $\lambda$  longer than the distance  $R-r$  should be taken into account only. These electrons are among the electrons from "the energy tail" of the Maxwell's distribution from some electron speed  $V_r$  depending on the plasma parameters at a point on the cylindrical surface with the radius  $r$ . After integration we determine the whole emission current from the plasma cathode in the anode-side region.

These calculations were performed for the plasma arc with following conditions: working substance - argon at operating pressure of  $10^4$  Pa; plasma arc radius  $R = 5$  millimeters.

The calculations of the radius temperature distribution of the plasma arc were performed by the known procedure [3].

The results of these calculation under a variety of discharge current of the plasma arc are shown in Fig.2.

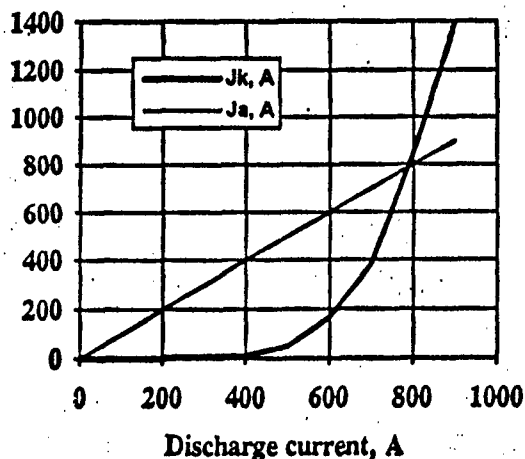


Fig.2 Plasma arc discharge current  $J_d$  dependence of the electron emission current  $J_e$  to anode-side region of plasma arc.

From these curves it will be obvious that the electronic emission current from the plasma arc increases with increasing of the anode current. The place of emission increasing is more rapid than the same parameter of the anode current. The emission current becomes more the anode current starting with some value. This mode of operation of the vacuum-diode is called as a virtual cathode behaviour. In this case there is a minimum of electrical potential distribution between the plasma cathode and the anode of the plasma arc. As it is in the vacuum-diode this electrical potential distribution is not stable and this mode of plasma arc operation is accompanied by electromagnetic instability of plasma arc.

The analysis of the problems discussed above shows that the situation when the emission current is greater than the anode current reveals itself more effective with decreasing of plasma density in the plasma arc. This fact has been confirmed experimentally because of arising of the limiting operating condition of the MPD thruster with smaller anode current if plasma flow rate through the MPD thruster decreases.

### References:

- [1] A. B. Mikhailovsky: Theory of Plasma Instabilities, Atomizdat, Moscow, 1975.
- [2] W. Finkelnburg und H. Maecker: Electricische Bogen und thermisches Plasma, Handbuch der Physik, Bd. XXII, S (1956) 254-444.
- [3] Earl W. McDaniel: Collision Phenomena in Ionized Gases, John Wiley & Sons, Inc., New York - London - Sydney, 1964.

# Amplification of Subsonic Ion Acoustic Envelope in a weakly Magnetized Plasma

Isao Tsukabayashi, Sugiya Sato and \*Yoshiharu Nakamura

Nippon Institute of Tech., 4-1 Miyashiro, Saitama 345 Japan

\*Inst. of Space and Astro. Science, 3-1-1 Yoshinodai, Sagamihara, Kanagawa 229 Japan

## 1. Introduction

Observations of double layers (DLs) and solitary waves in the auroral or magnetospheric plasma made to be a origin[1], there has been great deal of interest in studying the electrostatic solitary waves in a magnetic field. Many of works related to this subject have been done in a plasma with two electron temperatures, ion beam, negative ions species, and oblique magnetic field. Main characteristics of the DLs or the solitary waves in a magnetic field can be summarized as follows, "containing magnetic -field -aligned electric field", "V shape rarefactive perturbations" and "moving with slower velocity than the ion acoustic velocity".

In this paper, we present for the experimental evidence of subsonic ion acoustic envelopes in a weakly magnetized plasma.

## 2. Experimental setup

The experiments were performed in a magnetic multi-pole plasma device with 80cm length and 60cm diameter as shown in Fig. 1. The plasma is produced by a dc discharge in argon at  $1 \sim 2 \times 10^{-4}$  Torr. The typical plasma parameters are: plasma density  $n_e = 3 \sim 5 \times 10^8 \text{ cm}^{-3}$ , electron temperature  $T_e = 1 \sim 1.5 \text{ eV}$  and ion temperature  $T_i < T_e/10$ . A Helmholtz coil (36cm diam) provides for a region of uniform weak magnetic field ( $B_0 < 20 \text{ G}$ ), which direction can be changed by rotation of the coils.

The double plasma ( DP ) method is conventionally employed to excite the large amplitude electrostatic ion

perturbations, e.g., ion acoustic solitons, ion beam and DLs. In this experiment, the grid excitation method has been adopted in order to avoid the creation of ion beam by the DP method. A movable one-side plane Langmuir probe (10mm diam) and an emissive probe have been used to detect the density perturbations and the plasma potential.

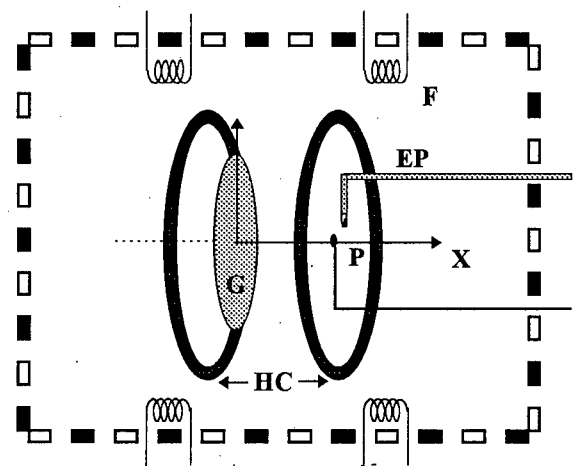


Fig. 1. Schematic of the magnetic multi-pole device. G ; an excitation grid (30cm diam). HC ; a Helmholtz coil (36cm diam). F ; filaments. P ; an electrostatic probe, EP ; an emissive probe.

## 2. Experimental results

One period of sinusoidal negative potential pulse ( $V_{pp} = 3 \sim 5 \text{ v}$ ,  $f = 100 \sim 120 \text{ kHz} \approx f_{pi}/5$ ) has been applied to the grid. The ion acoustic perturbations detected by the probe at  $X=20 \text{ cm}$  from the grid are shown in Fig.2 as a parameter of parallel magnetic field.

A leading rarefactive perturbation (A) is excited by the initially applied negative pulse, and large amplitude



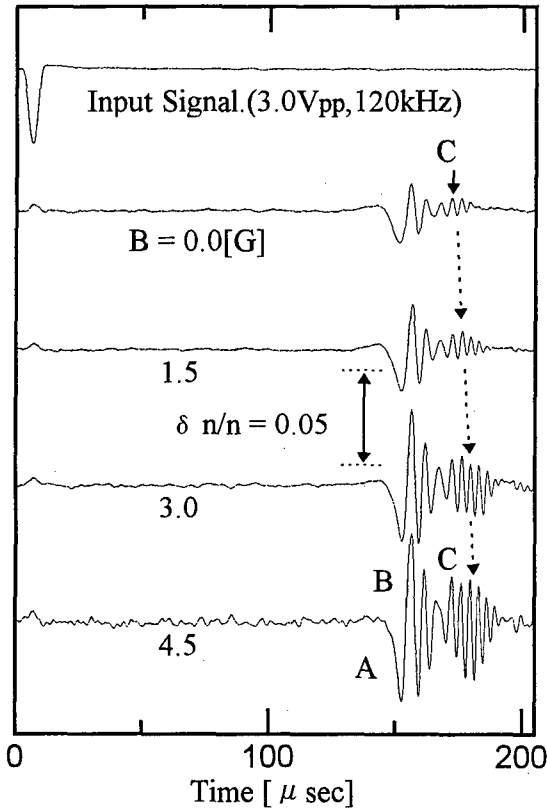


Fig.2 . Variation of the ion acoustic perturbations in a parallel magnetized field.

oscillating waves (B) are followed by the first rarefactive perturbation. Both waves A and B are propagated to coalesce with the ion acoustic velocity ( $C_s$ ). Behind the oscillating waves, a small trailing perturbation (C) which is also observed in upper trace ( $B=0$ ) of Fig.2. increases the amplitude and forms an envelope in parallel weak magnetic fields ( $B=3 \sim 5$  Gauss). The group velocity of the envelope is slower than the  $C_s$ . These characters of the wave excited by a negative potential pulse are almost equal to the previous experiment which was performed in a DP device [2].

Rarefactive ion acoustic waves excited by a negative pulse were investigated by E.Okutsu et. al [3]. But they had not noticed the trailing slow envelope, because their experiment was performed in a magnetic field free plasma.

Spatial and temporal scale of the plasma in a parallel magnetic field of 5 Gauss are as follows;

$R \sim r_{ci}(60\text{cm}) > r_{pr} \sim r_{ce}(0.5\text{cm}) > \lambda_D(0.5\text{mm})$  and  $f_{ci}(200\text{Hz}) < f_{pi}(600\text{kHz}) < f_{ce}(14\text{MHz})$ , where  $R$ ,  $r_{pr}$  are device dimension and probe radius, respectively. Motion of the electron is only restricted in a weak magnetic trough with the electron gyro-radius. The dispersion relation of ion acoustic waves derived from a fluid model is,

$$C_s = \frac{\omega}{k} = \left( \frac{\gamma_e \kappa T_e}{M} \frac{1}{1 + k^2 \lambda_D^2} + \frac{\gamma_i \kappa T_i}{M} \right)^{1/2} \quad (1)$$

where  $\gamma_i$ ,  $\gamma_e$  are the ratio of specific heats of ion and electron. The frequency of envelope is composed of the second harmonic of the precedent oscillating waves. The phase velocity of the waves in the envelope can be estimated by the dispersion relation (1). The time lag of the envelop which is proportioned to the group velocity increases in a magnetized plasma as shown in Fig.2.

#### 4. conclusion

Characteristic features of the ion acoustic envelope are summarized as follows; the envelope is generated behind a rarefactive perturbation, the group velocity of the envelope is slower than  $C_s$  and the envelope increases the amplitude in a weak parallel magnetic field. The existence of the ion acoustic envelope solitons in a plasma with nonisothermal electrons has been predicted by H.Schamel and P.K.Shukla[4].

#### References

- [1] F.S.Mozer, C.W.Carlson, M.K.Hudson, R.B.Torbeert, B.Parady, J.Yatteau and M.C.Kelley, Phys.Rev.Lett.**8**, 292(1977).
- [2] I.Tsukabayashi and Y.Nakamura, Proc. Of ICPP. **3**,253 (1994).
- [3] E.Okutsu and Y.Nakamura, Plasma Phys.**21**,1053 (1979)
- [4] H.Schamel and P.K.Shukla, Phys.Rev.Lett.**36**,968 (1976).

# EFFECTS OF NEGATIVE IONS ON DISPERSION RELATIONS OF ION WAVES

S.Yoshimura<sup>1</sup>, K.Koga<sup>1</sup>, Y.Nakamura<sup>2</sup>, T.Watanabe<sup>3</sup> and Y.Kawai<sup>1</sup>

<sup>1</sup> Interdisciplinary Graduate School of Engineering Sciences,  
Kyushu University, Kasuga, Fukuoka 816, Japan

<sup>2</sup> Institute of Space and Astronautical Science, Sagami-hara, Kanagawa 229, Japan

<sup>3</sup> National Institute for Fusion Science, Chikusa-ku, Nagoya 464-01, Japan

## 1. Introduction

When ion waves propagate in a negative ion plasma, there are two mode of propagation: a fast mode and a slow mode[1]. The fast mode wave was observed by Wong *et al.* using a Q-machine [2]. Only a few observations of the slow mode wave have been reported, to our knowledge. So far, there are many investigations of ion waves in a negative ion plasma, however, the dispersion relation has not yet been so clear, especially in high frequency region.

Here, we have studied detailed dispersion relation of ion waves in a negative ion plasma. In the case of  $T_e \approx 0.1\text{eV}$ , it was found that the phase velocity of the fast mode wave does not agree with the theoretical dispersion relation, when exciting frequency approaches to a positive ion plasma frequency. It was also found that the measured phase velocity increase in proportional to  $f^{1/3}$ , where  $f$  is an exciting frequency. This dependence suggests that the *free-streaming* [3] effect appears in the negative ion plasma. Furthermore, we measure the detailed dispersion relation of ion waves in a negative ion plasma in order to examine the effect of negative ions in the case of  $T_e \approx 1\text{eV}$  and compare with the previous results in the case of  $T_e \approx 0.1\text{eV}$ .

## 2. Experimental

The experiments were performed using a negative ion double plasma (D.P.) device, 200cm in axial length and 100cm in diameter in case  $T_e \approx 0.1\text{eV}$ . It has two pairs of magnetic cages and is separated into a source and a target region with an electrically floating grid. The plasma is produced by a dc discharge in the outer region and diffuses across the cage into experimental region where  $\text{SF}_6$  molecules form negative ions ( $\text{SF}_6^-$ ) due to electron attachment. A Schematic diagram of the negative ion double plasma device is shown in Fig. 1. In the case of  $T_e \approx 1\text{eV}$ , a usual D.P. device, 100cm in axial length and 50cm in diameter was used. It has one pair of magnetic cages and is separated into source and target region by similar way. Typical plasma parameters in experimental region were as follows :  $n_e \approx 10^7 - 10^8 \text{ cm}^{-3}$ ,  $T_e \approx 0.1\text{eV}$  or  $T_e \approx 1\text{eV}$ . In order to determine the negative ion concentration, we measured the ratio of the negative

saturation current of the Langmuir probe characteristics before and after introducing  $\text{SF}_6$  gases. The same method was used previously by, for example, Wong *et al.* [2]. Ion waves were excited by applying 40mV or 200mV sinusoidal voltages to the anode of the source plasma or separation grid respectively. Plasma parameters and wave signals were measured with a plane Langmuir probe. The dispersion relation of ion waves was obtained from the wave pattern which is measured using the interference method.

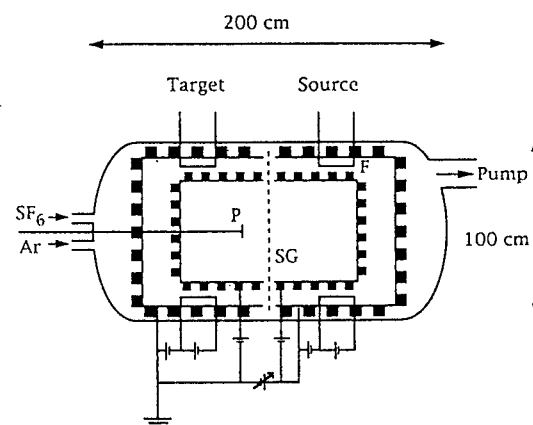


Fig.1 Schematic diagram of the negative ion double plasma device.

## 3. Results and Discussion

First, we show the results in the case of  $T_e \approx 0.1\text{eV}$ . By introducing  $\text{SF}_6$  gases, we observed increases in the wave length and damping length. The fast mode wave in a negative ion plasma is known to have the same tendency. In order to identify the waves which we observed, we compared the dispersion relation of these waves with the theoretical dispersion curves of the fast mode wave. Here we assumed  $T_e/T_i = T_e/T_i = 1/6$ . The result is shown in Fig. 2. Figure 2-(a) shows that the experimental results deviate from the expected dispersion curve in high frequency region. This deviation is caused by an increase in the phase velocity of the observed ion waves. If observed waves are *bursts*, the phase velocity should increase with increasing exciting voltages.

However it remained constant when applied voltages are changed from 40mV to 400mV. Thus the observed waves are not *bursts*. Figure 2-(b) shows that the dependence of the increase in the phase velocity on exciting frequency in high frequency region is about  $f^{1/3}$ . This experiment is considered to be the first observation of the *free-streaming* in a negative ion plasma from above result. We mention that no slow mode wave was found in our experiments, which is explained by taking into account strong Landau damping of the slow mode wave for the parameters which we used.

Next, we show the results in the case of  $T_e \approx 1\text{eV}$ . In this device, the negative ion species is also identified as  $\text{SF}_6^-$  by preliminary experiments. By introducing  $\text{SF}_6$  gases, we also observed the fast mode wave in a negative ion plasma. We examined the dependence of the phase velocity of the wave on exciting frequency. The result is shown in Fig. 3, where  $T_+/T_- = T_e/T_i = 1/10$  was assumed. Figure 3 shows that the phase velocities of observed waves, when negative ion concentration was low, agree with the expected one obtained from a kinetic dispersion relation. When negative ion concentration is high, however, the observed phase velocities deviate from expected one in high frequency region, though we could not confirm the power-law type dependence of the phase velocity on the frequency.

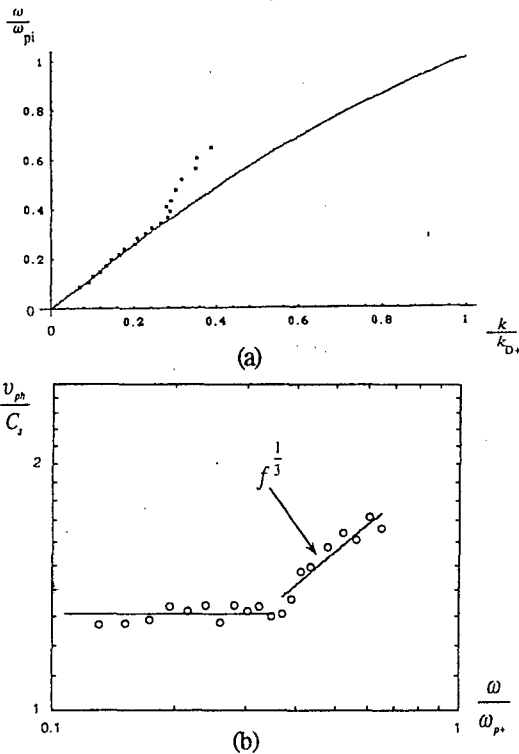


Fig.2 (a) Dispersion relation of ion waves. Solid curve is the theoretical dispersion relation of fast mode waves. Negative ion concentration  $\gamma = 0.23$ . (b) Phase velocities of ion waves in fig.1 (a) as a function of frequency. In high frequency region, the dependence of phase velocities on frequency is about  $f^{1/3}$ .

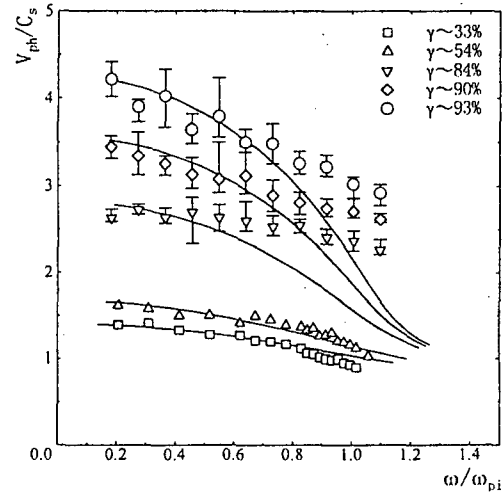


Fig.3 Phase velocities of the ion waves as a function of frequency. Solid curves are theoretical values of phase velocity of fast mode wave. Negative ion concentration  $\gamma = 0.33, 0.54, 0.84, 0.90, 0.93$ .

#### 4. Conclusion

The fast mode wave in a negative ion plasma was observed in two electron temperature cases  $T_e \approx 0.1\text{eV}$  and  $T_e \approx 1\text{eV}$ . In the case of  $T_e \approx 0.1\text{eV}$ , we observed the *free-streaming* like dependence of the phase velocity on exciting frequency ( $v_{ph} \propto f^{1/3}$ ) in high frequency region. In the case of  $T_e \approx 1\text{eV}$ , when the negative ion concentration was low, the observed phase velocities showed the good agreement with expected one. However, when the negative ion concentration was high, the observed phase velocities deviated from expected one in high frequency region.

Here, we are only concerning with the real part of the dispersion relation, but for more detailed examination of the fast mode wave propagation, it is necessary to compare the imaginary part of theoretical values with experimental results. It would be also necessary to estimate the magnitude of *free-streaming* effect and the excitation coefficient of each modes and the contribution of electron temperature to the wave excitation, which are our future work. The excitation of the slow mode wave in a negative ion plasma is still an interesting subject in plasma physics.

#### References

- [1] N.D'Angelo, S.v.Goeler and T.Ohe, Phys. Fluids 3, 1605 (1966)
- [2] A.Y.Wong, D.L.Merlino and D.Arnush, Phys. Fluids 18, 1489 (1975)
- [3] G.M.Sessler and G.A.Pearson, Phys. Rev. 162, 108 (1987)

***Topic 18***

**Plasmas for environmental issues.**

# Simultaneous treatment of iron, ash and wood simulating miscellaneous radioactive solid wastes by thermal plasma

Tadashi AMAKAWA, Shinji YASUI and Kazuo ADACHI

Central Research Institute of Electric Power Industry  
2-6-1 Nagasaka, Yokosuka, Kanagawa 240-01 JAPAN

## 1.Introduction

The final disposal of low level radioactive miscellaneous solid waste produced by nuclear power plants will start around the year 2000 in Japan. Electric utilities have imposed that wastes must be solidified before final disposal. Thermal plasma technology offers advantages for the miscellaneous waste treatment such as stable heating at high processing rate as well as high volume reduction rate and long stabilization of radionuclides. We have investigated the migration behavior of cold tracers during melting and the material properties of solidified products in case of metallic and incombustible materials[1-3]. This paper describes the results concerning the migration behavior of cold tracers and material properties of solidified products in case of simultaneous melting of metallic, incombustible and combustible wastes[4].

## 2.Experimental Procedure

We selected carbon steel, fly ash and wood as representatives of metallic, incombustible and combustible waste respectively. Also we selected Co, Cs and Sr as the cold tracers. 10kg of carbon steel and 3kg of fly ash were set with cold tracers in the crucible of the 100kW class plasma melting system shown in Fig.1. Then these materials were melted by transferred type of the thermal plasma at the power of 30kW (200A) for 30min., 38-44kW (300A) for 30min. and 45-53kW (500A) for 15min. in the order. The feeding of 2g of wood started after 5min. of the arc ignition and continued for 55 min. The air ratio (the ratio of the amount of air needed theoretically for complete combustion to that injected experimentally into the furnace) was adjusted by changing the feeding interval of wood and air injection flow rate. Carbon steel and fly ash were melted in the N<sub>2</sub> and CO atmosphere simulating reductive gases generated by pyrolysis of combustible waste. Table 1 shows the experimental conditions. In the table, CO gas concentrations are the mean value during melting. The reason why CO gas was not detected under the conditions of the air ratio of 0.5 and 1.0 is because of consumption of the oxygen in the water cooled chamber.

We clarified the migration behavior of cold tracers from the weight and composition of solidified products. Distribution of cold tracers and specific gravity, uni-axial compressive strength of slag layers and statistic leaching rates of cold tracers were investigated as

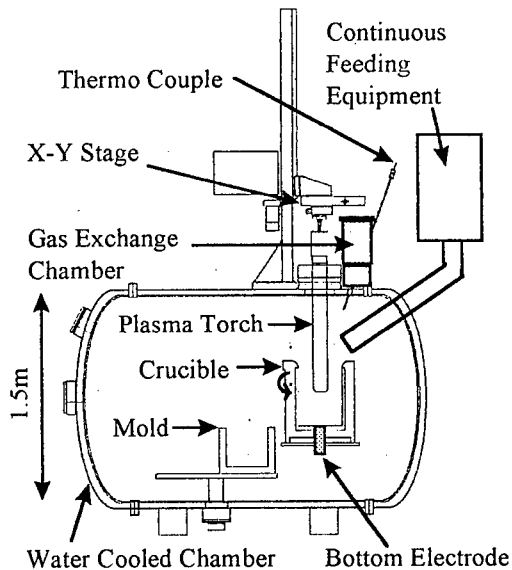


Fig.1. 100kW class plasma melting system

Table 1. Experimental conditions.

No.	Weight of feeding materials			Air Ratio	Feeding interval of wood (sec)	Injected air flow rate (m <sup>3</sup> /h)	CO gas conc (%)
	Iron	Ash	Wood				
1	9.66	3.00	0.44	2.09	14.9	4	ND
2	10.6	3.00	0.46	1.01	14.3	2	ND
3	10.6	3.00	0.49	0.52	14.7	1	ND
4	9.78	3.00	1.320	0.17	5.0	1	1.9
5	9.84	3.00	-	-	-	-	3.4
6	10.05	3.00	-	-	-	0.6	ND

ND : not detected

material properties of solidified products. The statistic leaching tests were based on MCC-IP standards, that is, test specimens were immersed into deionized water at constant temperatures of 10 and 40 °C for 3, 7, 14 and 28 days. The value of SA/V (surface area of specimen / leachant volume) was 0.1cm<sup>-1</sup> for slag layers and 100cm<sup>-1</sup> for metallic layers. The normalized elemental mass loss (N<sub>Li</sub>) is calculated using Eq.(1) and leaching rate is calculated by dividing N<sub>Li</sub> by leaching periods.

$$N_{Li} = \frac{m_{si} - m_{bi}}{f_i \cdot SA} \quad (1)$$

In this equation,  $m_{si}$  and  $m_{bi}$  are mass of element  $i$  in the leachate and in the blank leachate, respectively and  $f_i$  are mass fraction of element  $i$  in the specimen.

### 3. Results

#### 3.1 Migration behavior of the cold tracers

The general migration behavior of an element during melting can be explained from its thermodynamic properties, such as the standard free energy for oxide formation and the saturated vapor pressure. It is experimentally confirmed that Co, of which the standard free energy value is larger than that of Fe contained as a main component of metallic layer, migrated into metallic layer and that Sr, of which the standard free energy is lower than that of Fe, migrated into slag layer as shown in Fig.2. Cs high in saturated vapor pressure partially migrated into the dust. Even though the boiling point of Cs is lower than the molten bath temperature, it can be captured in the slag layer. One possible reason is that Cs ions are trapped in the random tetrahedron structure of  $\text{SiO}_4$  in the same mechanism as Na ions are trapped in the  $\text{SiO}_2\text{-Na}_2\text{O}$  glass. The most important result in the figure is that the migration ratios of Cs into the slag layer decrease when CO gas was detected constantly in the off gas (No.4,5). This suggests that continuous reductive atmosphere in the furnace should be avoided from the viewpoint of Cs migration behavior.

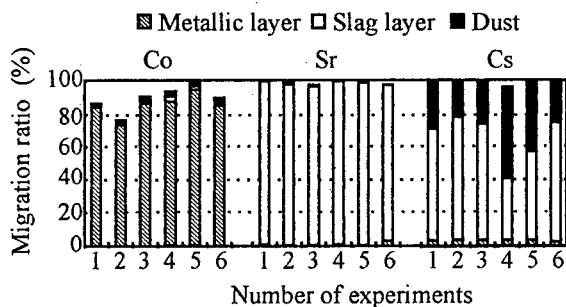


Fig.2. Migration behavior of cold tracers.

#### 3.2 Material properties of solidified products

Fig. 3 shows the distributions of cold tracers' concentrations and specific gravity in the solidified product in a case where the air ratio was 2. The values of the relative standard deviations (standard deviation / mean value) of concentrations or specific gravity are less than 5% in each solidified products. We can confirm that these distributions are uniform. This result indicates that it will be easy to measure the total radioactivity of the waste forms before final disposal without distracting them.

The uni-axial compressive strength of slag layers are more than  $500\text{kg}\cdot\text{cm}^{-2}$  in each solidified products. These values are larger than those of solidified cement waste forms ( $200\text{--}400\text{kgf}\cdot\text{cm}^{-2}$ ) already used for final disposal of liquid waste. So these values are high enough to bear the weight of waste forms themselves stacked up to 9 layers in the disposal site.

Only Sr was detected in the leachate of slag and leaching rates are of the order of  $10^{-8}\text{g}\cdot\text{cm}^{-2}\cdot\text{day}^{-1}$  for 28 days periods. This value indicates that slag layers has

a good performance to stabilize the radionuclides. The leaching rates of Co and Cs are calculated using the values of detectable limits. They are of the order of  $10^{-6}$ ,  $10^{-7}\text{g}\cdot\text{cm}^{-2}\cdot\text{day}^{-1}$ , respectively.

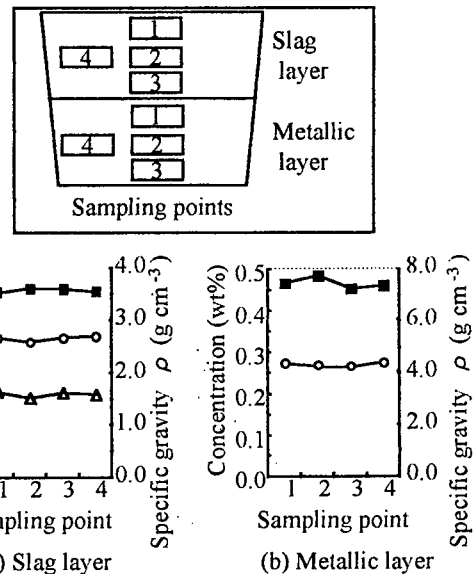


Fig.3. Distributions of cold tracers' concentrations and specific gravity in the solidified products

### 4. Conclusion

Carbon steel, fly ash and wood were selected as representatives of metallic, incombustible and combustible wastes generated from nuclear power plants. They are melted simultaneously with the cold tracers by thermal plasma heating by changing the air ratio. Solidified products show good properties for final disposal such as high uni-axial compressive strength of slag layers, uniform distributions of the cold tracers' concentrations and gravity in both metallic and slag layers and low leaching rate of cold tracers from both layers. But the results of migration behavior of Cs suggest that proper treatment conditions should be chosen in order to avoid extremely reductive atmosphere when combustible wastes are treated.

### 5. References

- [1] T. Amakawa, S. Yasui and K. Adachi: UIE XIII Congress on Electricity Applications WTI20 1996
- [2] T. Amakawa, K. Adachi and S. Yasui: CRIEPI REPORT No. W95005 1996 (in Japanese)
- [3] S. Yasui, K. Adachi and T. Amakawa: CRIEPI REPORT No. W94017 1995 (in Japanese)
- [4] T. Amakawa, S. Yasui and K. Adachi: CRIEPI REPORT No. W95019 1996 (in Japanese)

# Coaxial underwater pulsed corona discharge as a source of non-thermal plasma

M. Člupek, P. Šunka, V. Babický and M. Černák\*

Inst. of Plasma Physics, Academy of Sci. of the Czech Republic, P.O. Box 17, 182 00 Prague, Czech Republic

\*Institute of Physics, Comenius University, Mlynská dolina F2, 842 15 Bratislava, Slovakia

## 1. Introduction

Recent development in the domain of water treatment have led to so-called Advanced Oxidation Processes. AOPs are ambient temperature water treatment processes that involve the generation of highly reactive radicals (in particular  $\text{OH}^\bullet$ ) and transient species, which destruct organic pollutants in water without any secondary disposal requirements.

The use of non-thermal plasma generated in the liquid water matrix has been demonstrated to be an alternative to other AOPs as UV photolysis and e-beam treatment. The starting step in the development of a non-thermal plasma AOP was the pioneering work of Clements et al. [1] on pulsed positive streamer corona generated in water using a point-to-plane geometry of electrodes. Recently, the pulsed positive point-to-plane streamer corona discharges has been demonstrated to be effective in the production of the radicals [2-5]. However, the studies have revealed that in the point-to-plane geometry the streamers fill the reactor volume inhomogeneously, and the corona discharge exists within only a narrow range of applied pulsed voltages. In addition, discharge characteristics were found to be extremely sensitive to changes in water conductivity and scaling of such type of reactor is difficult.

As a solution of the above mentioned problems a coaxial type pulsed corona reactor has been constructed [6], where a homogeneous high-density streamer discharge is generated using a special ceramics-metal composite anode. This contribution describes basic electrical characteristic of an improved model of this reactor type. The results of tests of chemical effectivity of the reactor will be published elsewhere.

## 2. Experimental set-up and results

Experimental set-up used is schematically shown in Fig. 1. The 6 mm-diam. anode coated by porous layer of  $\text{Al}_2\text{O}_3$  is immersed in the cylindrical stainless steel chamber with a diameter of 30 mm and length of 200 mm. Fast rising high voltage pulses are produced by a cable generator. A pulse

forming line ( $12.5 \Omega$ ) made from four 50  $\Omega$  coaxial cables was charged up to 50 kV from a DC power supply. The forming line output was switched to the discharge chamber by means of rotating spark gap. The discharge gap voltage and current were measured by a capacitive divider and Rogowski coil. The measurements were made for the pulse voltage amplitudes up to 30 kV, corresponding current maxima up to 1750 A, and the HV pulse frequency up to 200 Hz. Figure 2 shows a typical couple of HV voltage and current pulses measured.

The fundamental characteristics of the discharge that should be known for determination of its chemical effectivity and for optimisation of the reactor is the instant ratio of the power used in the discharge to the total power input. This can be estimated from V/A characteristics measured at different values of the time delay  $t'$  as those shown in Fig. 3. A typical value of this ratio estimated for tap water of 5  $\text{k}\Omega\cdot\text{cm}$  resistivity used is some 30%.

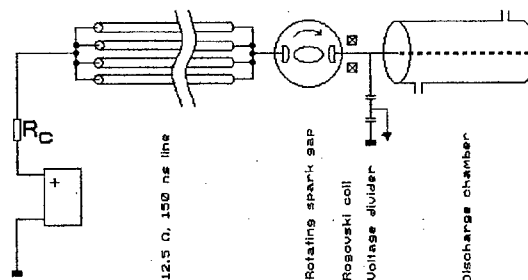


Fig.1 Experimental arrangement

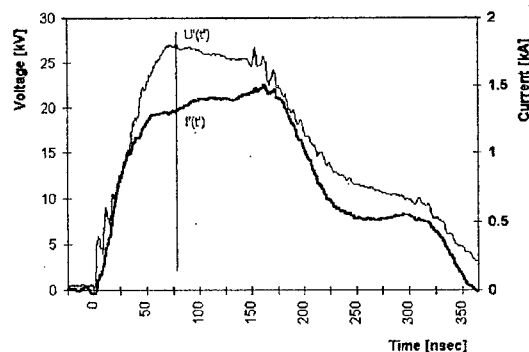
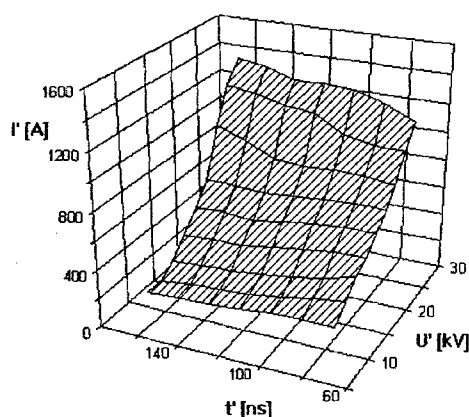


Fig.2 Typical voltage  $U'$  and current  $I'$  waveforms



**Fig.3**  $U'$ - $I'$  characteristics at measured at different time points  $t'$  (see Fig.2).

### 3. Discussion

Physical tests of the coaxial reactor have shown that using the composite anode together with coaxial geometry makes possible to generate a bushlike coaxial streamer discharge filling homogeneously the reactor volume without depending critically on the water conductivity and applied voltage stability. In addition, such coaxial discharge can easily be scaled up to practical applications.

Preliminary measurements of the decomposition of small amounts of phenol in aqueous solution have indicated that in this case study the energy effectiveness of the reactor is higher than that of e-beam treatment and UV photolysis. In determination of the energy effectiveness especially helpful would be a direct measurement of the  $\text{OH}^\bullet$  densities by a CARS experiment.

To optimise the streamer corona reactor of prime importance is the understanding of the streamer ionisation mechanism [7]. Unfortunately, there is little data available on the streamer formation and propagation, in particular, on the question whether or not an electron avalanche can occur in liquid water without changing density of water. There seems to be a difference in this opinion. According to the recent paper [8] the streamer front develops via heating by electron injection, lowering of the liquid density, and the subsequent avalanche growth, i.e., a bubble process. On the other hand, it has been suggested that an avalanche can growth in liquid water by an electronic process without a significant density change under the influence of high amplitude pulsed electric field. To explain it,

the mechanisms as collision ionisation [9], field ionisation [10], and ionised waves associated with proton hopping [11] have been suggested. Since in [10] at the anode fields higher than 700 kV/cm during the streamer propagation no hydrodynamic phenomena were observed in the streamer front and due to transparency of such fast primary streamer we favour this hypothesis.

### Acknowledgements

The work has been supported by the Grant Agency of the Czech Republic under the contract No. 202-96-0746, by the Slovak Scientific Grant Agency under the contract No. 95-5195-136, and by the NATO under Grant ENVIR.LG.9505729.

### 4. References

- [1] Clements J S, Sato M and Davis R H 1987 *IEEE Trans. Ind. Appl.* **IA-23** 224
- [2] Joshi A A, Locke B R, Arce P and Finney W C 1995 *Journal of Hazardous Materials* **10** 3
- [3] Sharma A K, Locke B R, Arce P and Finney W C 1993 *Hazardous Waste & Hazardous Materials* **10** 209
- [4] van Veldhuizen and Rutgers W R 1995 *12th Int. Conf. on Plasma Chemistry, XXX*, pp 691-5
- [5] Sato M and Clements J S 1996 *Trans. Ind. Appl.* **IA-32** 106 ]
- [6] Šunka P, Člupek M and Babický V and Černák M 1996 *13th European Sectional Conf. on the Atomic and Molecular Physics of Ionised Gases, Poprad, Slovakia*, pp 125-6
- [7] Černák M, Šunka P, Člupek M and Babický V., *ibid.*, pp LVII-LX
- [8] Jones H M and Kunhardt E E 1995 *J. Appl. Phys.* **77** 795
- [9] Alkhimov A P et al. 1971 *Soviet Phys.-Doklady* **77** 795
- [10] Petrov P G, Kukhta V P, Lopatin V V 1988 *Sov. Phys. Tech. Phys.* **33** 697
- [11] Kuskova N I 1983 *Sov. Phys. Tech. Phys.* **28** 591



# KINETICS OF NITRIC OXIDE REMOVAL FROM $N_2:O_2:CO_2:NO$ IN A POINT-TO-PLATE CORONA DISCHARGE

Mirosław Dors, Genrietta V. Nichipor\*, Jerzy Mizeraczyk

Institute of Fluid Flow Machinery, Polish Academy of Sciences,  
Fiszera 14, 80-952 Gdansk, Poland

\*Radiation Physics and Chemistry Problems Institute,  
Academy of Sciences of Belarus,  
Minsk, Sosny, 220109, Republic of Belarus

## Abstract

In this paper results of modelling of chemical processes in a dry or humid mixture of  $N_2:O_2(5\%):CO_2(15\%)$  with addition of 400 ppm NO subjected to a dc corona discharge are presented. The results show that  $NO_x$  removal in the dry operating gas is less effective than that in the humid one. In the humid operating gas (8%  $H_2O$ , i.e. concentration of water vapour typical of exhaust gases) the dc corona discharge decreases  $NO_x$  concentration about 65%, while in the dry operating gas the  $NO_x$  removal is about 35%. The removal of  $NO_x$  from the humid operating gas is possible owing to OH and  $HO_2$  radicals produced from  $H_2O$  in the corona discharge.

## INTRODUCTION

For over twenty years researches have been trying to remove  $NO_x$  from exhaust gases by subjecting them to a corona discharge [1]. Apart from experimental investigations computer models of chemical processes are being developed for clarifying a mechanism of  $NO_x$  removal [2, 3].

In this paper a model of chemical processes in a dry or a humid mixture of  $N_2:O_2(5\%):CO_2(15\%)$  with addition of 400 ppm NO subjected to a dc corona discharge are presented. The mixture simulates the exhaust gas emitted by fossil fuel power plants. To clarify the role of  $H_2O$  in the process of  $NO_x$ , concentration of  $H_2O$  in the operating gas was varied in the range 0-50%. Special attention was put to the variation of concentrations of NO,  $NO_2$ ,  $NO_x$  and  $HNO_3$  produced in the discharge.

## MODELLING

A model of chemical processes in the  $N_2:O_2:CO_2:NO$  mixture subjected to a dc corona discharge considered basic parameters of dc corona discharge and chemical reactions occurring in the exhaust gases and known from literature.

It was assumed that a dc corona discharge is generated in the reactor with the electrodes of the point-to-plate geometry. The analysis is local. No spatial dependence, i.e. neither diffusion nor a hydrodynamic expansion of the corona discharge column, was taken into account. It

was also assumed that the discharge is consisted of a series of rectangular current pulses which correspond to primary streamers. Each current pulse produces the same electrons concentration in the operating gas. On the base of previous experiment and model [4] it was assumed that typical duration time of current pulse is 20 ns, repetition time is  $10^{-4}$  s and electrons concentration is  $10^{13} \text{ cm}^{-3}$ . During the pulses electrons collide (primary reactions) with  $N_2$ ,  $O_2$ ,  $CO_2$  and  $H_2O$  producing chemical active species which react with all components of the operating gas (secondary reactions). The reaction rate coefficients of the primary reactions depend on electric field in the discharge [5]:

$$k_i = 10^{-A-B/(E/N)} \quad (1)$$

where:  $k_i$  - rate coefficient for  $i$  primary reaction ( $\text{cm}^3 \cdot \text{s}^{-1}$ ),

A, B - coefficients,

E - electric field ( $\text{V} \cdot \text{cm}^{-1}$ ),

N - gas density at 273 K and 1 at ( $\text{mol} \cdot \text{cm}^{-3}$ )

The value of the electric field in the discharge was taken from [2]. The reaction rate coefficients of the secondary reactions were taken from the literature [6]-[8]. The model includes 242 reactions with 39 radicals, ions and molecules.

## RESULTS AND CONCLUSION

The results of modelling are presented in Fig. 1. In general, the results show that NO is removed from the operating gas while  $NO_2$  and  $HNO_3$  (in humid gas) are produced by the dc corona discharge. The  $NO_x$  removal in the dry operating gas is less effective than that in the humid one. In the case of the operating gas with 8%  $H_2O$  the dc corona discharge processing decreases  $NO_x$  concentration from 400 ppm to 130 ppm. The removal of  $NO_x$  from the humid operating gas is possible owing to OH and  $HO_2$  radicals produced from  $H_2O$  in the corona discharge. The rates of the reactions between these radicals and nitrogen oxides are much higher than those between N and O radicals produced in the dry operating gas and nitrogen oxides. The main product of  $NO_x$  removal in the humid operating gas is  $HNO_3$ . It can be easily removed from the exhaust gas by adding  $NH_3$ ,

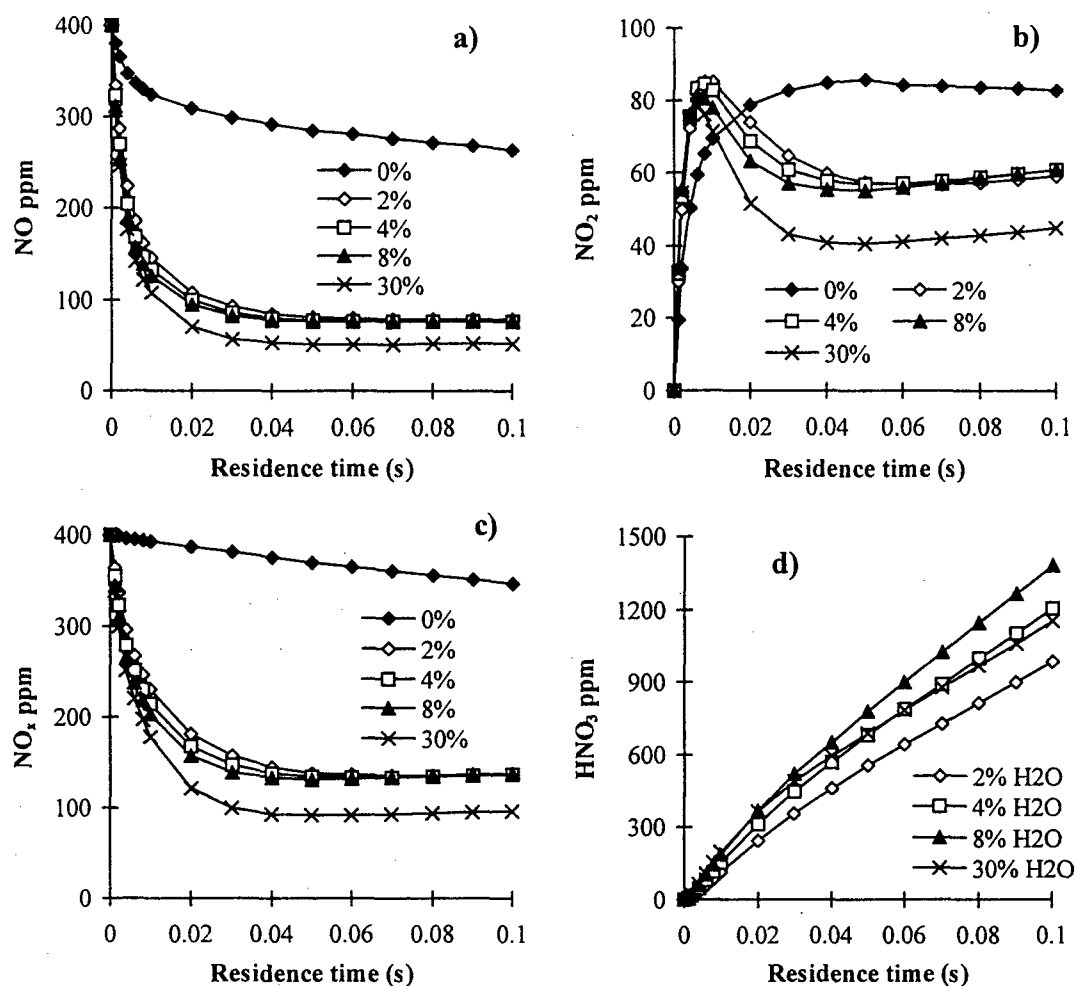


Fig. 1. Concentrations of NO, NO<sub>2</sub>, NO<sub>x</sub> and HNO<sub>3</sub> in the N<sub>2</sub>:O<sub>2</sub>(5%):CO<sub>2</sub>(15%) + NO (400 ppm) mixture as a function of residence time for different H<sub>2</sub>O concentrations.

which reacts with HNO<sub>3</sub> producing ammonium salts NH<sub>4</sub>NO<sub>2</sub> and NH<sub>4</sub>NO<sub>3</sub> which can be used as fertilisers in agriculture. The optimal conditions of the NO<sub>x</sub> removal process by the dc corona discharge processing, regarding the efficiency of NO<sub>x</sub> removal, lowest production of HNO<sub>3</sub> and low energy consumption, are: the residence time of 0.04 s and 8% H<sub>2</sub>O. This means that exhaust gases usually contain water vapour enough for the optimal removal of NO<sub>x</sub> by corona discharge processing.

## References

- [1] Chang J.S., NATO ASI Series, G 34 (A), 1-32, 1993
- [2] Bastien F., Marode E., Gaseous Dielectrics III, Ed.: L.G. Christophorou, Pergamon, New York, 1982, p. 119
- [3] Penetrante B., NATO ASI Series, G 34 (A), 65-91, 1993
- [4] Dors M., Mizeraczyk J., Nichipor G.V., Proc. 5th Int. Symp. on High Pressure Low Temperature Plasma Chemistry, Milovy, Czech Rep., 1996, p. 72
- [5] Aleksandrov N.L., Wysikailo F.I., Islamov R.S., Kochetov I.W., Napartovich A.P., Pevlov W.G., Teplofizika Wysokich Temperatur, 19, 3, 485-489, 1981
- [6] Atkinson R., Baulch D.L., Cox R.A., Hampson Jr. R.F., Kerr J.A., Troe J., J. Phys. Chem., Ref. Data, 18, 2, 881-1108, 1989
- [7] Gentile A.C., Kinetic processes and plasma remediation of toxic gases, Thesis, Ed.: University of Illinois at Urbana-Champaign, USA, 1995, p. 154-169
- [8] Mätzing H., Advances in Chemical Physics, 58, 315-402, 1991

# Influence of neutral dynamics on chemical kinetics for flue gas discharge modeling

O. Eichwald, M. Yousfi, P. Bayle\*, M. D. Benabdessadok

CPAT-ESA du CNRS n° 5002, 118 Route de Narbonne, 31062 Toulouse, FRANCE

\*Cemes-Loe, 118 Route de Narbonne, 31062 Toulouse, FRANCE

## 1. Introduction

As is known, pulsed corona discharges are used for flue gas pollution control. The ionized channel created by the successive streamers crossing the flue gas is a highly reactive medium in which the toxic oxides ( $\text{NO}_x$  or  $\text{SO}_2$ ) are removed. Indeed, the inelastic collisions between charged and neutral particles induce during a first phase, the excitation, dissociation and ionization of the flue gas. These primary ( $\text{OH}$ ,  $\text{O}$ ,  $\text{N}$ ) and secondary ( $\text{O}_3$ ,  $\text{HO}_2$ ) radicals thus created are involved in the oxide transformation into acid (e.g.  $\text{HNO}_3$ ) in a second phase and then into mineral salt (e.g. nitrate) in the last phase discharge. Moreover, the elastic collisions and the thermal energy relaxation of excited states increase the gas temperature due to the neutral gas dynamics.

The aim of this communication is to study this flue gas temperature rise and to analyze its effects on the chemical kinetics for particularly the  $\text{NO}$  removal in the case of a wire-cylinder<sup>1</sup> (gap=35mm, anode voltage=30KV, maximum current=20mA) corona discharge at atmospheric pressure for an initial gas temperature of 300K in a flue gas involving 74% $\text{N}_2$ , 15% $\text{CO}_2$ , 6% $\text{H}_2\text{O}$ , 5% $\text{O}_2$  and a few ppm of  $\text{NO}$ .

## 2. Flue gas discharge models

Present calculations are based on a chemical kinetics model<sup>2</sup> coupled to a neutral dynamics model<sup>3</sup> for gas temperature estimation and to an analytical model<sup>1</sup> for electric field and electron current density evaluations in the ionized channel. This electric model includes the effects of the primary and secondary streamers during a time  $t_{\text{dis}}=140\text{ns}$ . The initial radius of the ionized channel is chosen equal to 100  $\mu\text{m}$  in coherence with streamer propagation models<sup>4</sup>. The kinetics model involves 39 species (electrons, ions and neutral species excited or not) interacting following 287 selected reactions<sup>2</sup>. The electron-neutral reaction coefficients are calculated from a Boltzmann equation model<sup>5</sup> and those corresponding to ion-neutral interactions from a Monte Carlo model<sup>6</sup>. In the case of gas dynamic model<sup>3</sup>, we include the gas heating via the direct Joule effect and the excited states (electronic and vibrational) relaxation. The radiative state relaxation is assumed instantaneous while the vibrational relaxation time  $t_{\text{vib}}$  is close to 100 $\mu\text{s}$ .

## 3. Results and discussion

For the electric field  $E/N$  magnitude in the ionized channel (10 up to 100Td), the major part of the dissipated energy is stored in the gas under a vibrational mode (Fig1). The energy restored to the gas obviously depends on time and gap position. Fig2 show the spatial variation of the gas temperature for  $t=140\text{ns}$

and  $t=100\mu\text{s}$ , i.e. for a time equal to  $t_{\text{dis}}$  and  $t_{\text{vib}}$ . As expected, the maximum temperature is in middle of the ionized channel ( $r=0$ ) and near the anode ( $z=35\text{mm}$ ). The temperature decreases at the approach of the cathode ( $z=0$ ) and the borders of the ionized channel. In this figure, we also observe a radial extension of the discharge channel which increases its radius from 100 $\mu\text{m}$  up to 200 $\mu\text{m}$ . It is due to the thermal diffusion and energy vibrational relaxation modes. The thermal shock wave due to excitation modes (electronic and then vibrational excitation) can be observed in Fig2 or Fig3 where the gas temperature, starting from the initial value (300 K), can reach 750K (after 140ns) and then 550K (after 100 $\mu\text{s}$ ). These sharp temperature increases near the anode generate a wave pressure which propagate along the gap. The gas pressure relaxation leads to the temperature decrease observed near the anode in Fig2. The pressure inside the ionized channel (not given here) reaches its initial value after about 2 $\mu\text{s}$ .

As a consequence of this temperature rise, the chemical kinetics results present several non negligible differences in comparison to the classical case where the gas temperature is assumed constant ("T=300K" case). First, the temperature rise restricts the  $\text{O}_3$  and  $\text{HO}_2$  radical formation (see Fig4). In fact, the temperature rise reduces the gas density thus partly limiting the effect of certain three body reactions responsible of the radical formation (e.g.  $\text{H}+\text{O}_2+\text{N}_2 \rightarrow \text{HO}_2+\text{N}_2$ , or  $\text{O}+\text{O}_2+\text{N}_2 \rightarrow \text{O}_3+\text{N}_2$ ). The drop of  $\text{O}_3$  density is also due to the reaction " $\text{O}_2(\text{a}\Delta\text{g})+\text{O}_3 \rightarrow 2\text{O}_2+\text{O}$ " which is more efficient for higher temperature. This reaction limits the  $\text{NO}$  reduction due to the competition with another reactions (as e.g.  $\text{NO}+\text{O}_3 \rightarrow \text{NO}+\text{O}_3$ ). Furthermore, this reaction creates around  $10^{-3}$ s a large part of  $\text{O}$  atoms involved in the  $\text{NO}$  creation via:  $\text{NO}_2+\text{O} \rightarrow \text{NO}+\text{O}_2$ . This have a direct effect (via  $\text{HO}_2+\text{NO} \rightarrow \text{NO}_2+\text{OH}$ ) on the  $\text{NO}_2$  and  $\text{NO}$  densities which are respectively lower (Fig5) and higher (Fig6) than the "T=300K" case.

As a conclusion, the gas temperature rise (due to gas dynamics) can modify up to 100% the evolution of certain chemical species (radical or oxides). Such results show that a more rigorous modeling of the non thermal plasma devices for flue gas pollution control must absolutely includes the gas dynamics.

## 4. References

- [1] Y. Creighton, PhD Thesis of Eindhoven, 1994
- [2] J. Hart, Rapport DEA (Yousfi's Group), 1994
- [3] Eichwald, Jugroot, Bayle, Yousfi, J.Appl.Phys., 80, 694, 1996
- [4] A. Hamani, Thèse Univ. Paul Sabatier, Toulouse 1996
- [5] M. Yousfi, M. Benabdessadok, J.Appl.Phys., 80, 6619, 1996
- [6] A. Hennad, Thèse Univ. Paul Sabatier, Toulouse, 1996

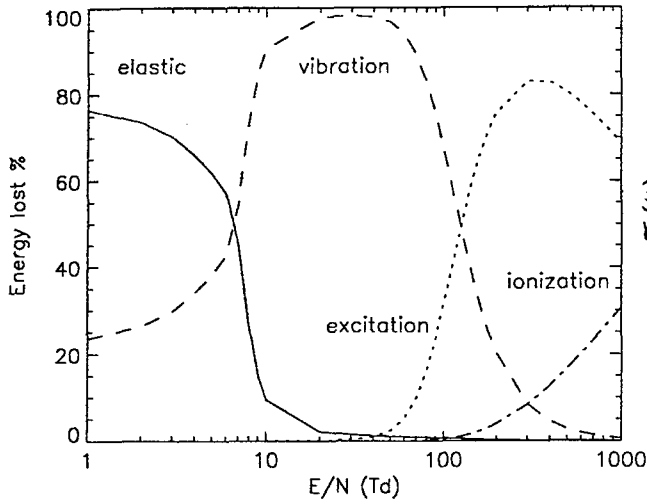


Fig1: Energy lost by different electron-molecule processes in N<sub>2</sub>-O<sub>2</sub>-CO<sub>2</sub>-H<sub>2</sub>O flue gas

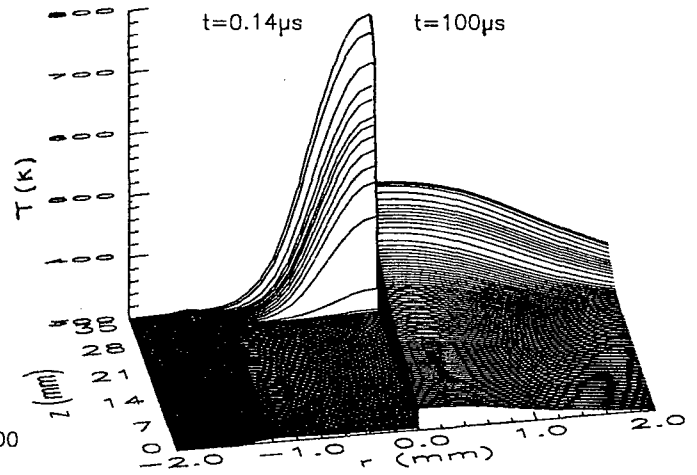


Fig2: Temperature profile for two  $t$  values

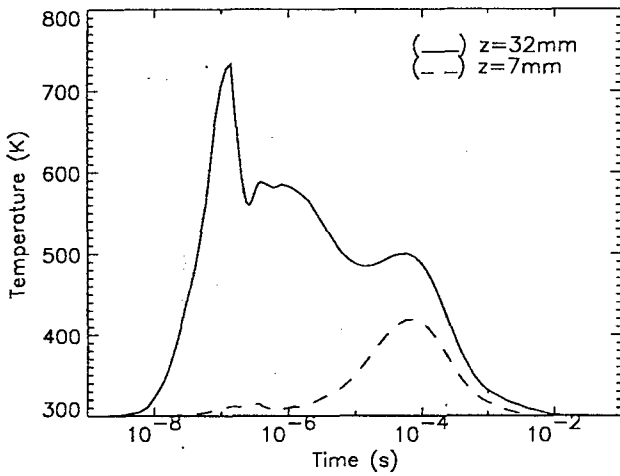


Fig3: Evolution of gas temperature for two axial positions

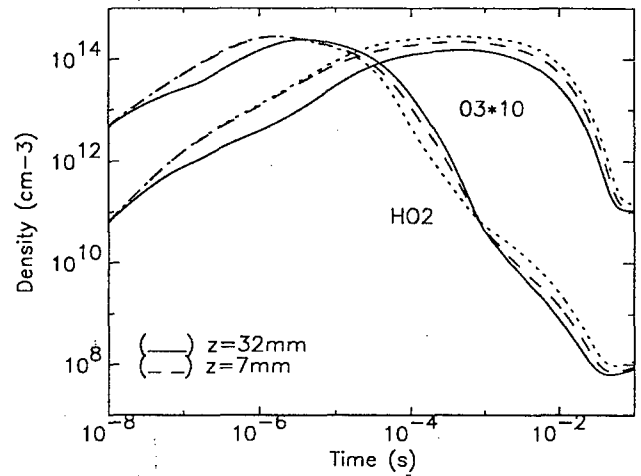


Fig4: Density evolution of HO<sub>2</sub> & O<sub>3</sub> for "T=300K" case (...) and two cases including the gas dynamics

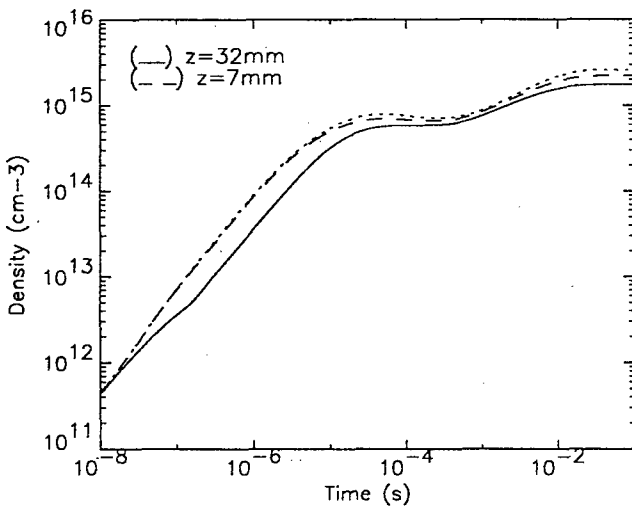


Fig5: Density evolution of NO<sub>2</sub> for "T=300K" case (...) and two cases including the gas dynamics

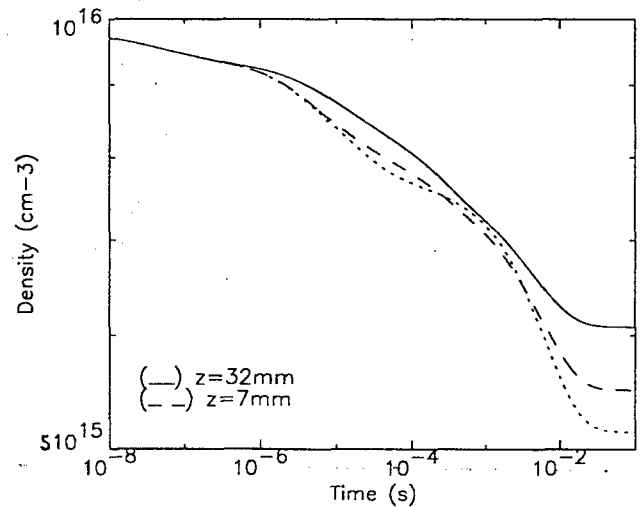


Fig6: Density evolution of NO for "T=300K" case (...) and two cases including the gas dynamics

# An apparatus for on-line monitoring of metal traces in atmospheric air :

## The influence of some pertinent parameters on detection.

A.Almi, J.P.Sarrette and A.M.Gomes

Centre de Physique des Plasmas et leurs Applications ESA 5002  
Université Paul Sabatier, 118 route de Narbonne  
31062 Toulouse Cedex, FRANCE

### 1. Introduction

Most metals and their compounds in the form of airborne particles are toxic for public health and the environment. Metals aerosols are becoming increasingly abundant more and more important in particular with the greater use of waste incinerators. Before being implemented, these thermal processes for waste treatment have to comply with norms concerning environmental pollution. From this point of view, the control of gaseous effluents is an important task. Furthermore, new regulations concerning the environment have recently been issued. In the case of heavy metals in gaseous effluents, they call for regular monitoring. For these reasons an apparatus for on-line and in situ measurements of metals aerosol concentrations directly in ambient air was developed.

This apparatus for continuous emission monitoring (CEM) is based on atomic emission spectrometry (AES) in an inductively coupled plasma (ICP).

The electron temperature  $T_e$  is a pertinent parameter to improve the sensitivity of the method.

The results presented in this work show the radial evolution of  $T_e$  with some characteristic parameters of the discharge such as input power  $P$ , air flow rate  $D_{air}$  and the amount of water in the ambient air. Determination of the optimum conditions lowers the detection of the apparatus limit (DL).

### 2. Experimental set up and diagnostic

The air plasma was produced by a tuned-line oscillator with a frequency of 64 Mhz (ROC. DURR Model 8600); the electrical power dissipated by the generator are varied from 1.0 to 1.5 kW. The discharge was not only an inductive plasma; a capacitive effect, involving an axial component of the electric field, was also clear. The characteristics of the torch are rather different from the analytical processes using argon as plasmagenic gas. The ambient air to be analyzed was sucked directly by a high throughput pump placed downstream, through a 20 mm i.d quartz tube surrounded by the seven-turn water cooled coil inductor. The air flow rate  $D_{air}$  was adjustable between 10 and 20 NI/mn. Introduction of gas into this torch occurred tangentially above the coil to produce a vortex. The vortex both protects the walls of the tube and stabilized the discharge. The discharge was

amorced directly in ambient air by heating a movable graphite rod through a 12 mm i.d central quartz tube. Spectroscopic measurements were performed using a 640 mm focal length monochromator (Jobin-Yvon HR 640) with a 3600 groove  $\text{mm}^{-1}$  grating. The detector was a photodiode array (Hamamatsu S2304-512Q). The geometric exploration of the discharge was performed using a fixed mirror on two axes (horizontal and vertical) and a stepping motor-driven rotator. The motions of the motor-driven mirrors and the grating of the monochromator were controlled by a computerized laboratory system, which also allows data acquisition and treatment. Calibration is achieved by nebulizing known quantities of standard aqueous solutions containing known concentrations of salts of the relevant metals. The experimental set-up is shown schematically in Fig 1.

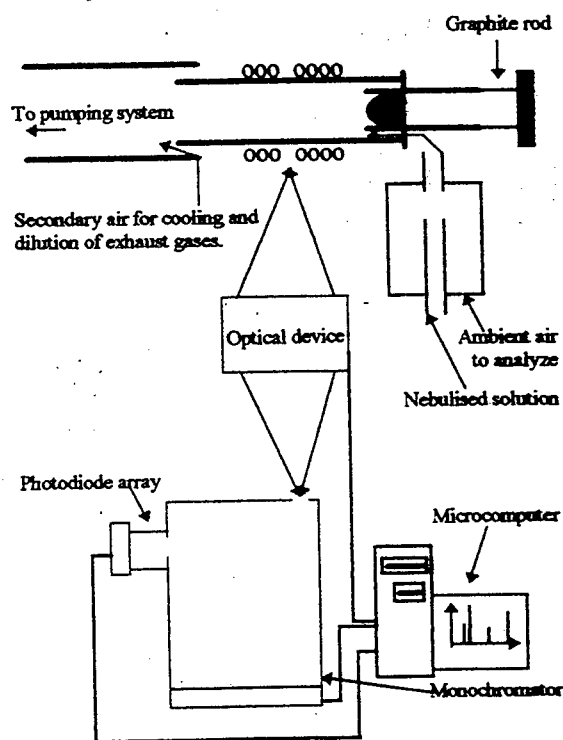


Fig 1: Schematic diagram of the experimental set-up

The air ICP spectra was essentially composed of molecular bands. The strongest emissions of the ambient air ICP between 200 and 350 nm that were

identified correspond to the  $\gamma$  system of NO [ $A^2\Sigma-X^2\Pi$  transition] and a band emitted by the OH radical [ $^2\Sigma-^2\Pi$  transition].

A method was developed [1] to determine the local electron temperatures. It is based on the comparison of the local emissivities of the (0-1) vibrational transition of the NO  $\gamma$  system and the (0-0) band of the  $A^2\Sigma-X^2\Pi$  transition in OH.

### 3. Results and discussion

Measurements were carried out in the central zone of the inductor coil, between the fourth and the fifth turns of the inductor coil. This area has been shown to be the most suitable for analytical purposes.

#### 3.1 Electron temperature measurements

The variation of  $T_e$  across a radius is shown in fig 2 for an input power  $P$  of 1.5 KW and for different values of the flow rate  $D_{air}$ . A monotonic decrease was obtained in all the cases, due to the axial component of the electric field in this particular discharge.

In the central area ( $r < 1\text{ mm}$ )  $T_e$  increased with  $D_{air}$ ; simultaneously, the radius of the discharge decreased. The intermediate value  $D_{air}=15\text{ NL/mn}$  was found to be the best suitable analyte detection.

The effect of increasing  $P$  is shown in fig 3. Larger values of  $P$  produce both higher  $T_e$  values and a broadening of the discharge. In this case improvement of the sensitivity and lower DL can be obtained by increasing  $P$ .

Another problem encountered in this sort of discharge is the matrix effect caused by variable amounts of atmospheric water. This water produces the large OH spectral band mentioned above. We have shown that the incidence of water is a decrease of  $T_e$  of about 80 K in the plasma center. As a consequence, the analyte line intensities are lowered by between 20-30%, depending on the value of the excitation energy of the emitting level.

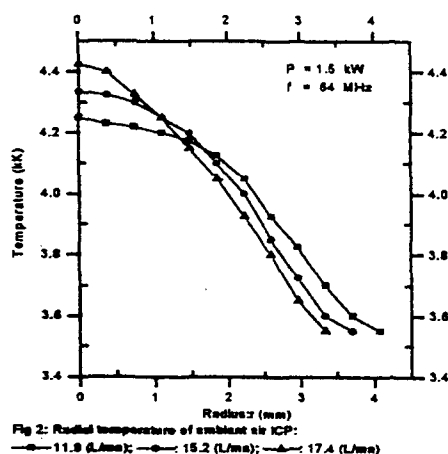


Fig 2: Radial temperature of ambient air ICP:  
— 11.8 (L/mn); — 15.2 (L/mn); — 17.4 (L/mn)

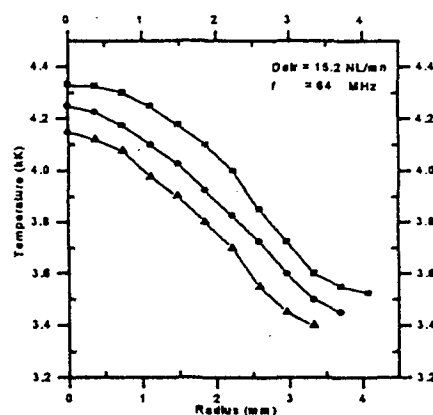


Fig 3: Radial temperatures for an ambient air ICP:  
— 1.5 kW; — 1.2 kW; — 1.0 kW

#### 3.2 Detection limits DL

The DL obtained in this work were, in all cases lower than the recommended threshold limit values (TLV). Except in the case of metals whose analytic lines exhibit high excitation energies like Zn and Cd, DL lower than  $1\text{ }\mu\text{g.m}^{-3}$  were obtained (table 1).

Table 1: Comparison of the best detection limits obtained in this work with the other CEM methods in air-argon mixtures.

Element	LD ( $\mu\text{gm}^{-3}$ ) This work	LD ( $\mu\text{gm}^{-3}$ ) Meyer[3]	LD ( $\mu\text{gm}^{-3}$ ) Trassy[2]
Zn	39.4	-	1
Cd	10.8	0.1	0.5
Mg	0.48	-	3
Cu	0.09	1	0.3
Co	0.24	-	0.5
Ni	0.14	5	3
Cr	0.19	1	0.2
Pb	8.16	10	6
Fe	0.33	-	0.3

### 4. Conclusions

This apparatus avoids any manipulation susceptible to produce modifications of the degree of air pollution. It enables representative sampling of the atmosphere to be analyzed and was relatively low running costs. The DL obtained are in good agreement with the results of alternative CEM methods in air or in air-argon mixtures.

### Bibliography

- [1] A.M.Gomes, J.P.Sarrette, L.Madon and A.Epifanie; J. Anal. At. Spectrom., 10 (1995)923.
- [2] C.Trassy, R.Diemiashzoneck; J. Anal. At. Spectrom., 10 (1995)661.
- [3] G.A.Meyer, K.W.Lee; (paper presented at ANATECH conference, 1994) Process Control and Quality, 6(1994)187.

# Oxidation Processes in the Liquid Solutions by means of Gliding Arc at Atmospheric Pressure

J. Janča<sup>1</sup>, A. I. Maximov<sup>2</sup>

<sup>1</sup>Department of Physical Electronics, Faculty of Science,  
Masaryk University, Kotlářská 2, 611 37 Brno, Czech Republic

<sup>2</sup>Institute of Non-aqueous Solutions Chemistry,  
Russian Academy of Sciences, 1. Akademicheskaja, Ivanovo 153460, Russia

## 1. Introduction

There is a rather limited number of the investigations of chemical reactions in liquid solutions under the discharge plasma applications [1-3]. In these papers the chemical changes after application of low pressure plasma excited between metallic electrode and water solution surfaces were investigated. The connection of the kinetics of these processes with the parameters of the discharge plasma used was found. The usual engineering processes of textile bleaching are carried out in the solutions and based on the experimental selection of the solution composition. Therefore the use of selective processes accelerated or stimulated by the discharge plasma is possible [4-6]. Besides that the interaction of the plasma with the solution may be used for water cleaning and for the modification of material surface without using the complicated vacuum equipment.

## 2. Experiment

The gliding arc was sustained between the plasma treated solution surface and the stainless steel cooled tube (horn shape) electrode - Fig.1.

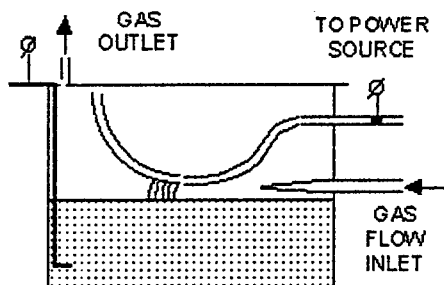


Figure 1: A schematic drawing of the experimental arrangement

The alternating voltage source (50 Hz) produced the voltage 10 kV and the discharge current up to 100 mA. The dc source with similar parameters was also used. The experimental device allows experiments with air, nitrogen and argon as working gases. The reactor has the form of a rectangular vessel made of polymethylmetacrylate; the solution volume was about 1500 ccm. The investigation of the liquid solution reactions during and after the plasma treatment

was carried out by means of its continuous transmittance measurement. The absorption spectra of solutions before and after the plasma treatment were recorded by means of the UV-VIS spectrophotometer.

## 3. Results

Our experiments show the increase in water conductivity during the plasma treatment of the solution surface. The effect is very great, stable and depends on the the employed working gas. At the same time, pH of the water decreases from 6.5 to approx. 3-4. The formation of nitrogen oxides in the plasma volume is possible [6]. Their dissociation in the water leads to the acid origin and partially explains the increase in conductivity. The gliding discharge plasma application on the water leads to the generation of hydrogen peroxide which dissociates in water under formation of hydroxonium ions  $H_3O^+$ . The hydroxonium ion mobility is ten times higher than that of other positive ions. The increase in water acidity mean first of all the change of the hydroxonium and hydroxyl ions balance. Therefore some other negative ions except  $OH^-$  have to be produced under the plasma treatment.

The application of the gliding arc on the neutral water solution KI causes a rather intensive generation of molecular iodine which is accompanied by a remarkable change in the absorption spectra and in the transmittance - Fig.2.

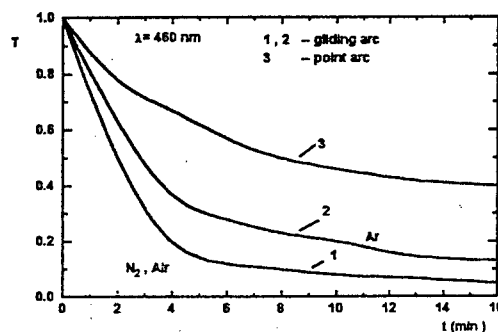


Figure 2: Transmittance of the water solution of KI as a function of plasma treatment time

The plasma treatment of the transparent colourless  $N_2S$  solution leads to the appearance of its green

colour. The transmittance of the solution in the visible and in the UV-regions decreases during the plasma treatment. The treatment of organic substrates as some water soluble dyes and sodium huminate have also been examined. The gliding arc plasma treatment of the dye water solution leads to its gradual discolouration. If the dye molecule has two independent optically absorbing components, in the initial period only the absorption in the intermediate VIS region increases but in the near UV-region the absorption increases in any case - Fig. 3.

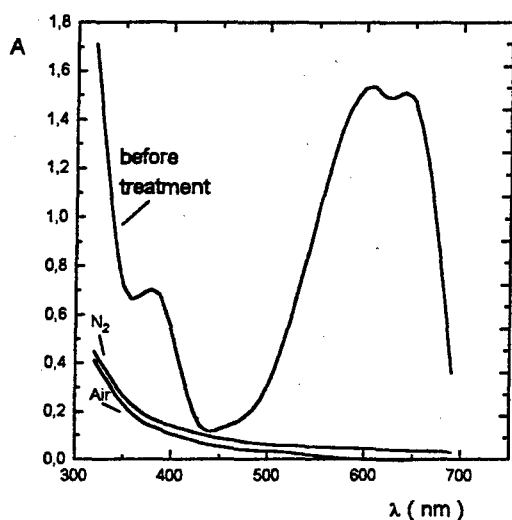


Figure 3: Absorbance as a function of wavelength of oxazine blue colour (concentration 0,025 g/l) before and after 2 hour plasma treatment

So the time dependent gradual displacement of the absorption maximum indicates multi-step processes of the oxidation destruction of organic substances. The estimation of the destruction rate may be done on the basis of the measured transmittance change at the wave length corresponding to the maximum absorption of the initial molecule. Assuming that the absorption coefficient does not change during the plasma treatment we have estimated the dye molecule destruction rate. The maximum destruction rate is reached in 15-20 min of the gliding arc action and it is about  $10^{16}$  molecules/s. Taking into consideration the mean value of the energy dissipated in the gliding arc (100 W) we can get the mean energy consumption on one molecule destruction  $10^2$  eV. In the case of nitrogen and argon the destruction rates are approximately the same, in the case of air as working gas it is somewhat higher. However, many of the destruction processes occur simultaneously and the kinetics of the destruction of initial dye molecules is accompanied by the reactions of all the intermediate species.

#### 4. Conclusion

The use of the ac and dc gliding arc shows that the process evolution in all these cases is in general identical. However the destruction rate and the destruction degree depends on the arc type rather strongly. It confirms the comparison of the absorption spectra of the blue dye treated by the different arc types at the fixed discharge power and treatment time. The positive gliding arc (solution surface is negative) has the maximum efficiency similarly to the case of the iodine oxidation. It is necessary to emphasize that the long plasma treatment of different organic substances leads to the accumulation of the products which have similar absorption spectra in the UV-region. Probably they are aromatic substances containing the phenol groups. The oxidation effect of the gliding arc may be connected with the generation of hydrogen peroxide in the water solutions. The water solution of  $H_2O_2$  has the absorption maximum near 260 nm. The measurements show that plasma treatment by the gliding arc leads to the increase in the absorption in this region.

#### Acknowledgements

This work was supported by the Grant Agency of the Czech Republic, contract No. 202/96/0139 and MŠMT Czech Rep. project No. VS96084.

#### 5. References

- [1] A.R. Dinaro and A. Hickling, *J. Electrochem. Soc.* **105** (1958) 265.
- [2] A. Hickling and G.R. Newnes, *J. Chem. Soc.* **12** (1961) 5186.
- [3] A. Hickling and M.G. Ingram, *Trans. Farad. Soc.* **60** (1964) 783.
- [4] J.L. Brisset, J. Lelievre, A. Doubla, and J. Amouroux, *Analisis* **18** (1990) 185.
- [5] K. Susanta, O. Sengupta, S. Prakash, *J. Electroanal. Chem.* **30** (1991) 189.
- [6] A. Czernichowski, *Pure & Appl. Chem.* **66** (1994) 1301.



# Production of chemically active species by positive streamer in air

A.A.Kulikovsky

Moscow State University, Research Computing Center (NIVC)

Moscow 119899, Russia

e-mail: akul@oberon.phys.msu.su

During a past decade streamer corona discharge is considered as a promising tool for cleaning of polluted gas flows. A small region – streamer head plays central role in technological applications of streamer corona. The electrons in the head gain energy which is sufficient to ionize, dissociate and excite molecules. These products of electron–molecules collisions, which will be referred to as chemically active species (CAS) initiate then multiple chemical reactions in the ambient gas which lead to removal of harmful components.

The efficiency of streamer corona strongly depends on various factors; probably the most important are voltage rise time [1] and geometry of the electrode system [2]. To investigate the role of different factors on streamer corona purification efficiency a realistic model of single positive streamer in nonuniform field is required. Here we present the results of two-dimensional simulation of generation of chemically active species by cylindrically-symmetric positive streamer between a point anode and a plate cathode.

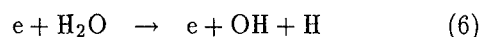
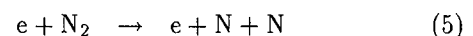
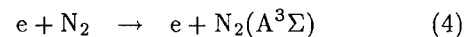
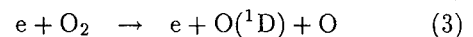
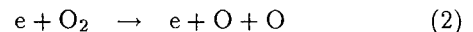
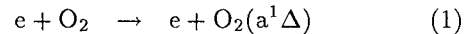
Consider a point anode placed over the plate cathode at the distance  $d = 1$  cm. To initiate streamer a small spot of quasineutral plasma is placed at the tip of the anode. A voltage  $V_0 = 11$  kV is applied to the anode at the moment  $t = 0$  and kept fixed.

The dynamics of streamer is described within the scope of diffusion–drift approximation for the three charged fluids: electrons, positive and negative ions. Ions were treated as immobile. We took into account electrons drift and diffusion, collisional ionization and photoionization in a gas volume, two-body and three-body attachment of electrons to oxygen molecules and electron–ion and ion–ion recombination. The full description of the model and the details of numerical procedure are given in [3,4].

Knowing the 2D distributions of electron density and electric field in the course of streamer propagation one may calculate the number densities  $X(r, z, t)$  of chemically active species produced by the streamer using the rate equations:  $\partial X/\partial t = sKn_e P_X$  where  $K$  being reaction rate constant,  $P_X$  number density of parent molecules and  $s$  stoichiometric coefficient.

A following electron–molecule reactions were taken

into account [5]:



The results presented below were obtained for the following conditions: pressure  $p = 760$  Torr, gas temperature  $T = 300$  K. The gas is air with 1% of water content:  $N_2 : O_2 : H_2O = 79.2 : 19.8 : 1$ .

Under these conditions after short period of formation ( $\approx 5$  ns) streamer propagates with the constant velocity ( $\approx 2.7 \times 10^7$  cm/s), constant field at the tip ( $\approx 140$  kV/cm) and produces constant current in the external circuit ( $\approx 0.025$  A).

Fig.1 shows streamer at the moment 25 ns. The distribution of space charge (a) and absolute value of electric field (b) gives a qualitative picture of streamer structure. Fig.1c,d illustrates the ability of streamer to produce chemically active species. Contour lines of rate of dissociation of (c) oxygen (in reactions (2) and (3)) and (d) nitrogen molecules (in reaction (5)) are shown. As it seen, the dissociation of nitrogen molecules occurs mainly around the head of the streamer. The dissociation of oxygen molecules requires less energy and it occurs also at the lower  $E/N$  values around plasma channel.

Integrating  $X$  over the space one obtain total number of a given species  $N_X$ :

$$N_X(t) = 2\pi \int_0^\infty r dr \int_0^d X(r, z, t) dz$$

Fig.2 shows dependencies of a total number of generated in the gap species on time. We note that after  $\approx 5$  ns all values increase linearly with time, (except  $O_2(a^1\Delta)$ ). This result correlates with the constant velocity of propagation and constant field at the tip of the streamer. The deviation of  $O_2(a^1\Delta)$  growth from linear one is attributed to the fact that excitation of oxygen occurs also around streamer channel, where radial field is about 40 – 50 kV/cm (Fig.1b).

As mentioned above, the current in the external circuit produced by the streamer is almost constant

in time. Under constant applied voltage this means that energy delivered by power supply varies almost linearly with time. The most part of the species produced by the streamer are O atoms and excited nitrogen molecules and their amount also varies linearly with time (Fig.2). Therefore, for streamer of the length  $\leq 1$  cm it is reasonable to introduce time-independent mean energy cost of one chemically active specie. The calculation gives the value 35 eV per specie.

- [1] E.M. van Veldhuizen, M.A.Tas and W.R.Rutgers *Proc. of Int. Workshop on Plasma Techn. for Pollution Control and Waste Treatment*, China, Beijing, May 1996.
- [2] A.Jaworek, J.Mizeraczyk, A.Krupa, T.Czech, L.Karpinski, J.Jakubowski *Czech.J.Phys.* 1995 45(12) 1049-61
- [3] A.A.Kulikovskiy *J.Phys.D* 1995 28 2483
- [4] A.A.Kulikovskiy *J.Comp.Phys.* 1995 119 149
- [5] I.A.Kossyi, A.Yu.Kostinskii, A.A.Matveev and V.P.Silakov *Proceedings of Institute of General Physics* 1994 47 37 (in Russian).

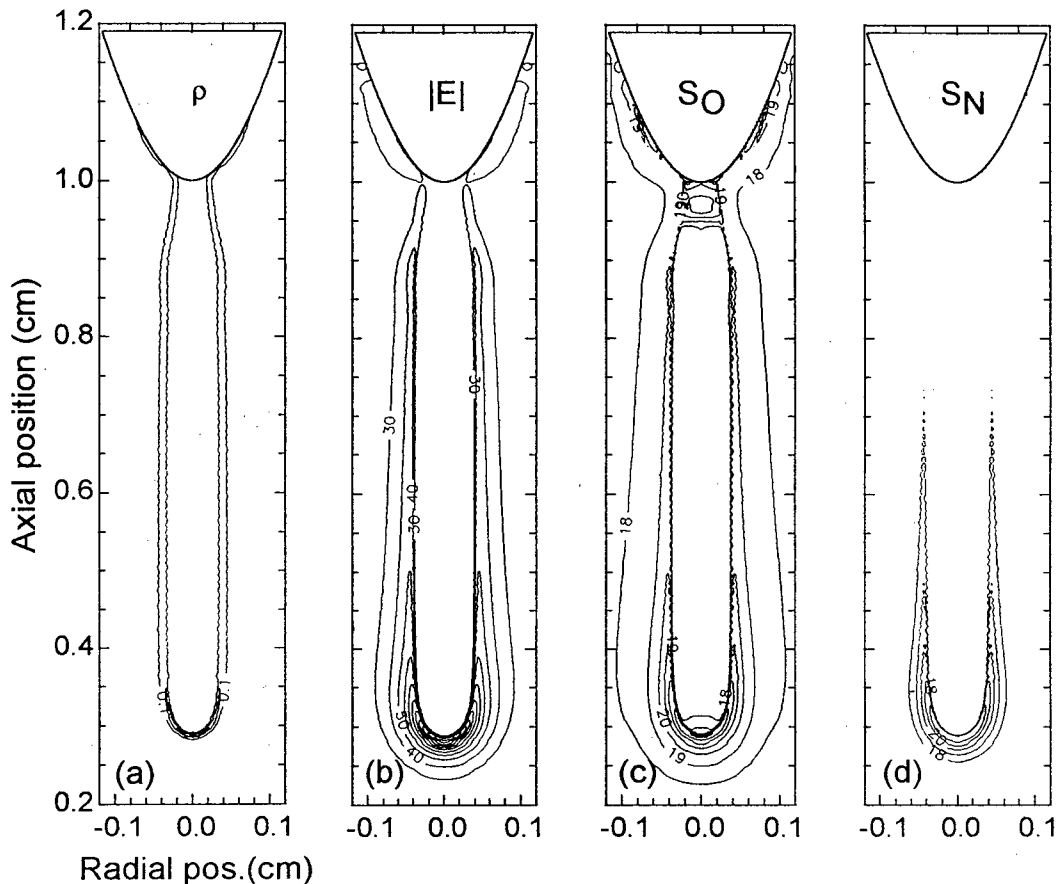


Figure 1: Contour plots for time 25 ns. (a) space charge density in  $10^{13} \text{ cm}^{-3}$  units, contours 0.1, 0.9, 1.7 and 2.5 are shown. (b) absolute value of electric field (30 to 140 kV/cm, step 10 kV/cm), (c) rate of oxygen dissociation ( $\text{cm}^3/\text{s}$ , logarithmic scale, contours  $10^{18}$ ,  $10^{19}$ ,  $10^{20}$ ,  $10^{21}$  and  $10^{22}$  are shown), (d) rate of nitrogen dissociation ( $\text{cm}^3/\text{s}$ , also contours from  $10^{18}$  to  $10^{22}$  are shown).

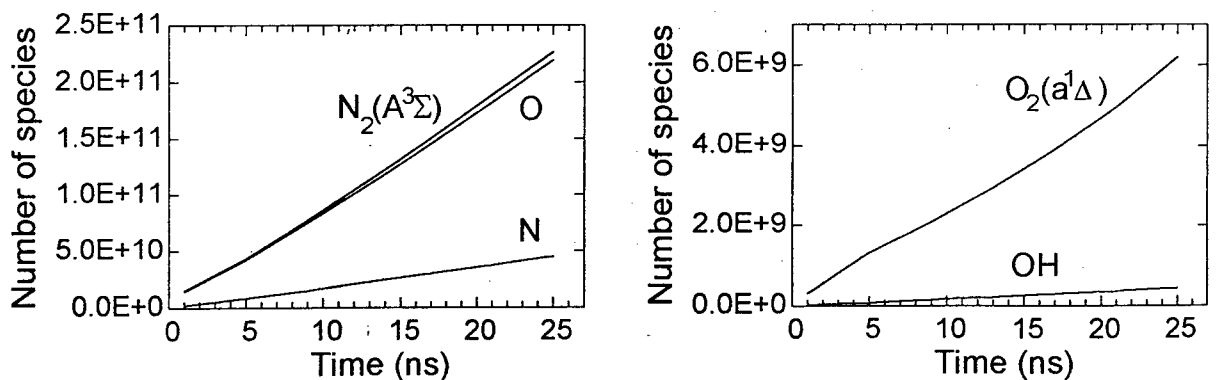


Figure 2: The dependence of total number of chemically active species produced by the streamer on time (ns).

# On-line Monitoring of Volatile Organic Compounds by Proton Transfer Reaction Mass Spectrometry (PTR-MS)

W. Lindinger, R. Holzinger, P. Prazeller, A. Jordan, and A. Hansel

Institut für Ionenphysik, Technikerstraße 25, 6020 Innsbruck, Austria

## 1. Introduction

We have shown the applicability of proton transfer reaction mass spectrometry PTR-MS for on line trace gas analysis in the ppb regime in extensive investigations of human breath[1],[2],[3]. In the present paper we report an extension of the PTR-MS technique for analysis of volatile organic compounds (VOCs) in urban air sampled near a road traffic intersection. Air samples were taken by filling a preevacuated glass bulb (ca. 6 l) which was directly connected to the PTR-MS system, and the air was then analyzed without further handling.

The PTR-MS technique most simply involves the protonation of sample species by proton transfer from  $\text{H}_3\text{O}^+$  in a weak drift field, followed by mass analysis of the resulting positive ions. The proton affinity [4] of  $\text{H}_2\text{O}$  is 7.2 eV, a value which is greater than the proton affinities of the dominant atmospheric components of clean air but less than those of many likely pollutants. Thus proton transfer from  $\text{H}_3\text{O}^+$  to many atmospheric pollutant species is exothermic and occurs rapidly, while proton transfer to the principal components of clean air is endothermic and does not occur.

## 2. Experimental and Results

When attempting to measure trace components at the ppb level, we observed as expected that the ion count rates were frequently too low to allow use of isotopic abundance to distinguish isomeric components of the samples. We have therefore developed a collision induced dissociation (CID) technique for identification of species of the same mass. This technique involves imposing an electric field at the downstream end of the drift tube. The field is generated by applying

a variable potential between the last drift ring and the entrance orifice of the quadrupole mass spectrometer. In this electric field the ions are strongly accelerated and may suffer energetic collisions with the air buffer gas, causing dissociation of the protonated species and generation of characteristic daughter ions. An example of the results of this CID technique is shown for protonated ethylbenzene (107 amu) in fig. 1.

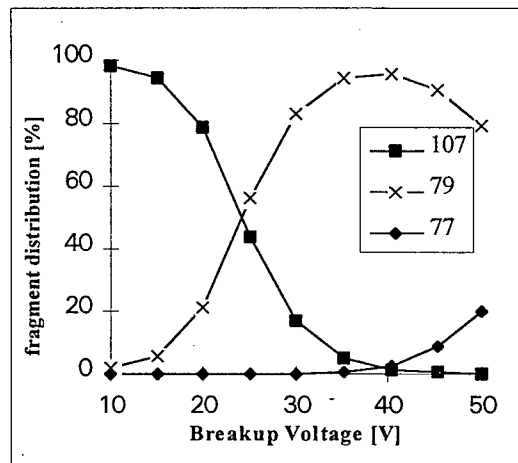


Fig. 1: Breakup pattern of protonated ethylbenzene 107 amu

In contrast a similar plot for protonated xylene (107 amu) shows that the intensity does not begin to diminish significantly until a breakup voltage of 30 Volts or greater is applied. Thus we determined that no significant amount of ethylbenzene was present in the air at this particular traffic intersection, and the signal observed at mass 107 amu had to be attributed to protonated xylene.

Fig. 2 shows the typical daily variation of concentrations of various aromatic compounds in the air at a traffic crossing situated at the west entrance of Innsbruck. Assuming that these compounds are emitted directly from the exhausts of cars and lorries, i.e., that none of them is created by photochemical reactions, the densities of these compounds are proportional to the density of the traffic. Fig. 2 shows a broad maximum in the morning from 7:30 to 9:00, a sharp maximum at lunch time and a pronounced peak at about 17:30. Additional compounds have also been investigated but are not shown in the figure.

### 3. Conclusions

The wide applicability of PTR-MS for fast on-line measurements of trace constituents especially VOCs has been demonstrated by examples in the field of medicine and also environmental research. Potential for further exploitation of this method could be in on-line monitoring of plasma-based environmental technologies e.g. parameter optimization for plasma processing of VOCs or efficiency control of plasma assisted waste cleaning.

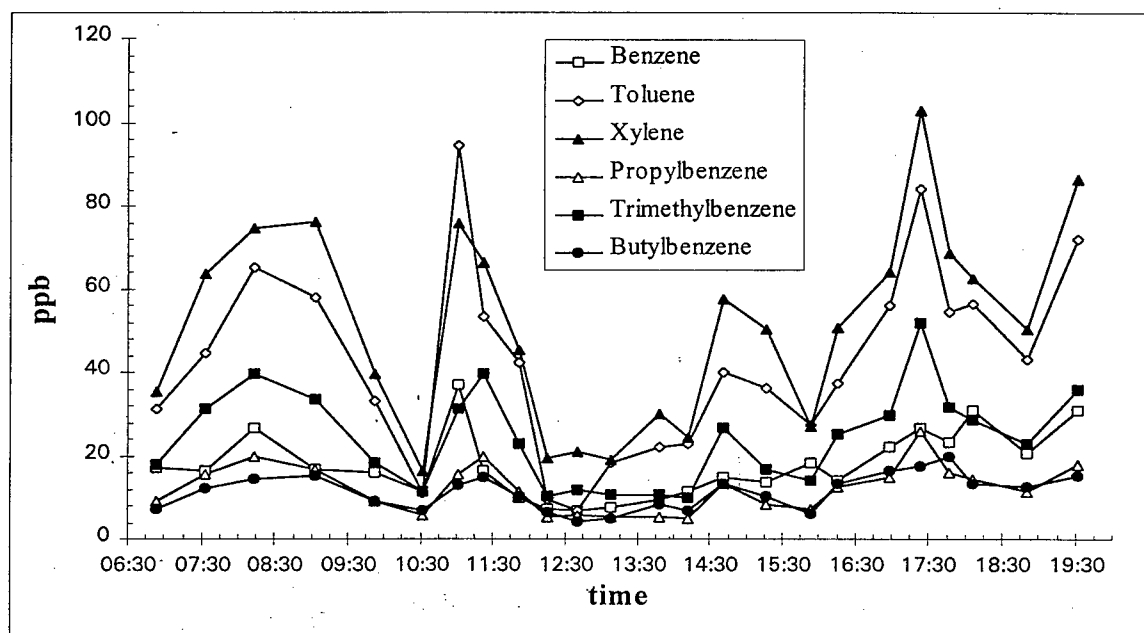


Fig. 2 Concentrations of aromatic compounds during a day

### 4. References

- [1] A. Hansel, A. Jordan, R. Holzinger, P. Prazeller, W. Vogel, W. Lindinger, *Int. J. Mass Spectrom. Ion Processes*, 149/150 (1995) 609-619
- [2] A. Jordan, A. Hansel, R. Holzinger, W. Lindinger, *Int. J. Mass Spectrom. Ion Processes*, 148 (1995) L1-L3.
- [3] J. Taucher, A. Hansel, A. Jordan and W. Lindinger, *J. Agric. Food Chem.* 44 (1996) 3778-3782
- [4] S.G. Lias, J.E. Bartmess, J.F. Liebman, J.L. Holmes, R.D. Levin and W.G. Mallard, *J. Phys. Chem. Ref. Data*, 17 (1988) Suppl. 1.

# REMOVAL OF ETHYLACETATE USING CORONA DISCHARGE

Z. MACHALA\*, M. MORVOVÁ

Institute of Physics, Faculty of Mathematics and Physics, Comenius University, Mlynská Dolina F2,  
842 15 Bratislava, Slovak Republic

\*Department of Plasma Physics, Faculty of Mathematics and Physics University of Comenius,  
Mlynská dolina F2, 842 15 Bratislava, Slovak Republic

## ABSTRACT:

The effect of „anomal“ dc corona discharge on removal of ethyl acetate was investigated. The originated products and removal efficiency were estimated by IR absorption spectrometry. The influence of ultrasonic aerosolization of water on process efficiency was tested. The main product was solid polymer mixture in powder form and as by products methanol, ethanol and CO<sub>2</sub> especially in negative polarity.

## Introduction:

Ethyl acetate is a volatile organic compound with ester-type odour present in paintings (especially on the basis of cellulose nitrates, ethylcellulose, acrylonitril, rubber chlorid, polyvinyl chlorid and many resins) and solution for paintings and rust removers. So sources of ethyl acetate are production, treatment and use of painting, celluloid industry, artificial leather industry, shoe industry, pharmaceutical industry. The boiling point is 77 °C, vapour pressure at 20 °C is 73 mm Hg i.e. 9,7 kPa. Maximum allowable concentration is 150 p.p.m. Ethyl acetate causes skin irritation, is narcotic from concentration 400-600 p.p.m after 2-3 hour of exposure, it was reported also fatal case after inhalation with high concentrations. But is less toxic than propyl, butyl and amyl acetate [1].

## Experimental:

For measurements we have used spontaneously pulsing d.c. powered „anomal“ type of corona discharge stabilised by resistance. This form of corona discharge arises at higher currents after regular dc corona pre-discharge. The process is connected with the fall of voltage from about 10 kV to several hundreds of volts and current rise up to ~ 2 mA. The frequency of „brush-like“ streamer type of current pulses with frequency about 1 kHz is accompanied by an intensive sound.

The stressed electrode was in form of internal thread from copper, non stressed plate electrode also from copper. The both electrode surfaces were modified due to action of corona pre-discharge. Measurements were made in static regime in gas cell discharge tube described on Fig.1

Necessary mixture of air with ethylacetate was realised by bubbling of air from pressure tank through

flowmeter with needle valve and temperable bubbler with studied solution. The necessary water for process was introduced via ultrasonic aerosolator. After 10 minutes of flowing the mixture was closed in gas cell.

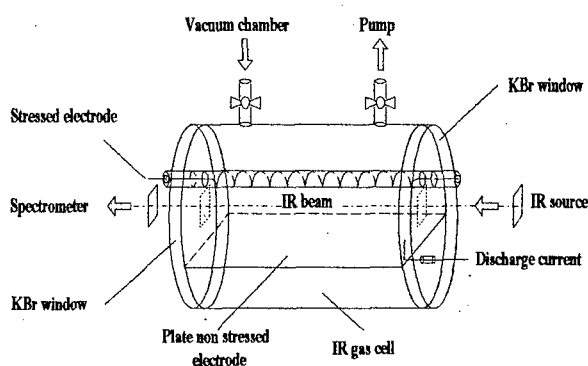
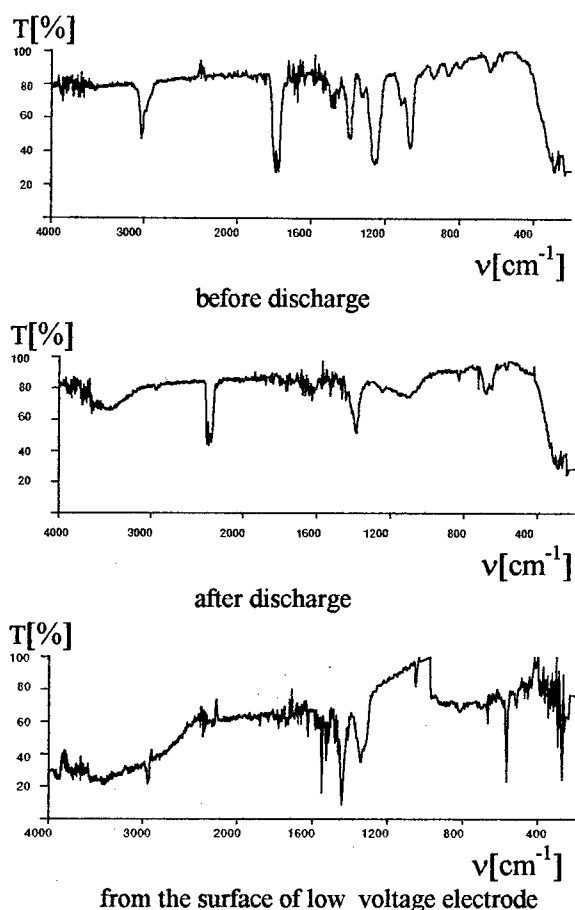


Fig. 1 Gas cell discharge tube

The composition of gas mixture before/after the discharge and the surface of used plane non stressed electrode was analysed using IR absorption spectrometry for gas and reflection IR spectrometry for surface. The water from process was accumulated and liquid or solid products soluted or suspended in water were analysed by ATR reflection spectrometry on KRS5 crystals with 45° reflecting angle. The solid product was separated from water, dried and treated by the KBr pellet making technology for scanning of IR absorption spectra. To see the structure and size of solid products the microscopic photography of solid product was made.

## Results and discussion:

We present the influence of d.c.corona discharge in anomal regime and both polarities on the removal efficiency of air-ethyl acetate mixture. As diagnostic method we have used IR absorption spectrometry. The ultrasonic aerosolization of water into discharge tube lead to the increase of removal efficiency for both positive and negative polarity of the discharge for about 15-20% comparing to dry process and also change the type of product, especially gas by products and solid products.



**Fig. 2** IR absorption spectra of gas before and after negative corona discharge in the mixture of air plus ethyl acetate and reflection IR absorption spectrum of the surface of low voltage electrode

From IR absorption spectra on Fig.2 for mixture of air-ethyl acetate after action of negative corona discharge the sharp decrease of hydrocarbon groups -CH<sub>3</sub> and CH<sub>2</sub> is seen. In the same time the decrease of carbonyl group -C=O seen from 1742 cm<sup>-1</sup> and -C-O- seen from 1182 cm<sup>-1</sup> occurred.

Due fragmentation process initiated by water aerosolization in air-ethylacetate mixture ethanol was produced as the by product. In IR absorption spectrum of gas products rise the band group at 1300-1450 cm<sup>-1</sup>. Activated nitrogen created in the discharge broke the hydrocarbon string and past into carbonyl group to produce -C=N=O group, or oxim group -C=N-O-. Due to dimerization bright group of compounds with IR bands in the described region of IR spectrum are produced. These group of gas and liquid compound after reaction with water and its dissociation products (-OH radical and H) are responsible for origin of copolymers on the surface of non stressed electrode containing polyimide, polyaminoacid, polyurethan and polyamid groups.

In positive polarity the removal efficiency is about 85%, CO<sub>2</sub> methanol and ethanol byproduct are not produced and more solid product is originated and

content of poly amino acids oxamidato complexes in solid product are greater.

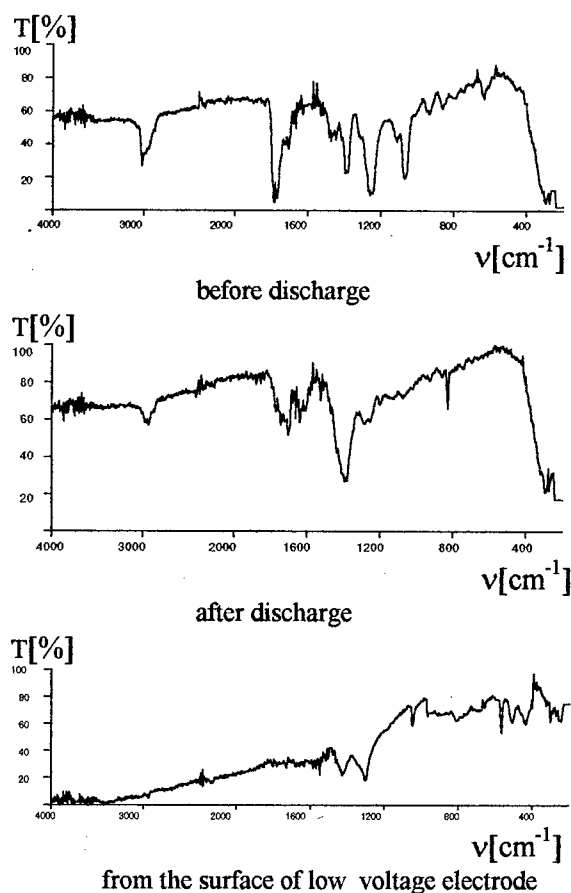
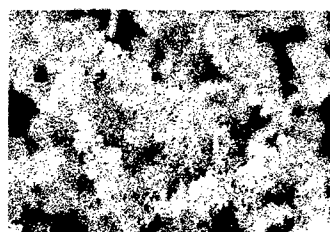


**Fig. 3** IR absorption spectra of gas before and after positive corona discharge in the mixture of air plus ethyl acetate and reflection IR absorption spectrum of the surface of low voltage electrode



The microscopic photography of the solid dark white product created in „anomalous“ corona discharge.

### Conclusions:

The investigated form of discharge is suitable especially for ethyl acetate removal. Energy content of anomalous corona is lower comparing to glidarc and consequently only a particular destruction of organic compound occurs. The process is followed by further polymerisation, which has a great importance from the point of view of CO<sub>2</sub> minimisation in atmosphere.

### References:

- [1] E. Browning: Toxicity and metabolism of industrial solvents, Elsevier, Amsterdam London New York, 1965

# The Influence of Hydrocarbons on the Removal of NO<sub>x</sub> from Exhaust Gas by Dielectric Barrier Discharges

Wolfgang Niessen, Reiner Schruft, Oliver Wolf and Manfred Neiger

LTI (Lighting Technology Institute), University of Karlsruhe, PO Box 6920, D-76128 Karlsruhe, Germany

## 1. Introduction

The introduction of economic car engines with direct injection will help reducing the CO<sub>2</sub>-emission into our atmosphere and therefore combat the greenhouse effect. The problem of cleaning the exhaust of such engines is, however, an unsolved one as yet, because due to the high air-to-fuel ratio conventional catalytic converters cannot remove the NO<sub>x</sub> in the exhaust gas. New methods for the remediation of toxic compounds in car exhausts have to be developed. Apart from techniques like the so-called DeNO<sub>x</sub>-scheme, the major drawback of which is the need of reducing additives, plasma assisted conversion of NO<sub>x</sub> in a dielectric barrier discharge is a promising treatment whose applicability has been studied for several years. Most of the theoretical and experimental work was based on „synthetic exhausts“ – well defined mixtures of nitrogen, oxygen, water and NO, without hydrocarbons (HCs) [1], [2]. A systematic experimental investigation of the influence of a number of HCs on the conversion of NO was carried out by Wolf et al. [3]. A sound understanding of the plasma chemical processes that come into play when HCs are present in the exhaust is still lacking. The present work is a contribution towards filling this gap by discussing the most important chemical reactions that play a role in the conversion of NO when unburned ethene (C<sub>2</sub>H<sub>4</sub>) is part of the exhaust gas.

## 2. Model

The spatially homogeneous model used for this work comprises three parts:

1. A coupled system of ordinary differential equations represents the rate equations describing the changes of the species concentrations due to chemical reaction, ionisation, recombination and charge exchange.
2. The temporal change of the electric field strength due to the accumulating charge on the surface of the dielectrics is taken into account.
3. From the solution of the Boltzmann equation the rates of electron collision reactions (ionisation, electron impact dissociation) are derived.

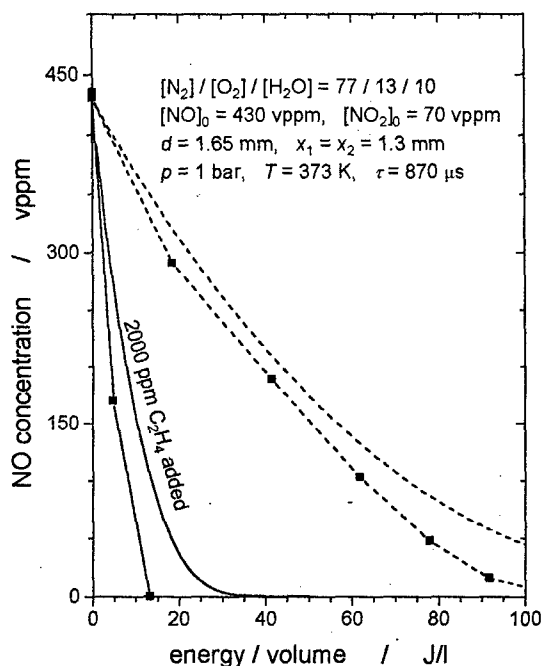
A total of 367 reactions are implemented in the model, including 148 chemical reactions involving HCs and 14 electron impact reactions.

## 3. Results

The model was used to calculate the conversion of NO and NO<sub>2</sub> in an exhaust gas of following composition: [N<sub>2</sub>] / [O<sub>2</sub>] / [H<sub>2</sub>O] = 77 / 13 / 10 with an initial concentrations of NO<sub>x</sub> of 500 vppm. C<sub>2</sub>H<sub>4</sub> as HC was used at an initial concentration of 2000 vppm. Temperature and

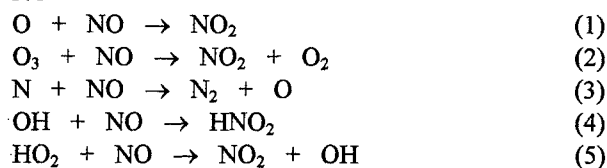
pressure were chosen 100°C and 1 bar. The time interval between two consecutive discharge pulses was set to 870 μs, the gap distance to 1.65 mm, the thickness of the dielectrics to 1.3 mm and the dielectric constant to 4.7. A total of 100 to 200 pulses are needed to reach NO conversion of over 90 %.

Figure 1 shows the concentration of NO as a function of the input energy for two cases: exhaust gas without HCs (dashed lines) and exhaust gas with C<sub>2</sub>H<sub>4</sub> (solid lines). Along with the computed curves experimental data are plotted as well in order to show the fair agreement between both.



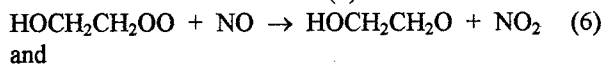
**Figure 1:** Concentration of NO as function of input energy. The dashed curves represent data for a gas mixture with no C<sub>2</sub>H<sub>4</sub>, while the solid lines represent data for a gas mixture that contains 2000 vppm C<sub>2</sub>H<sub>4</sub> at the beginning of the treatment. Curves with solid squares are obtained from experiment [3].

Analysis of the turnovers of the different reactions shows that without the presence of C<sub>2</sub>H<sub>4</sub> following reactions are mainly responsible for the conversion of NO

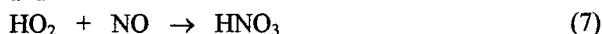


The ratio of there turnovers from (1) to (5) is 8.0 / 3.0 / 2.1 / 1.5 / 1. Apart from reaction (3) conversion is achieved by oxidation turning NO into NO<sub>2</sub> or HNO<sub>2</sub>. Latter product is volatile and decomposes partly into NO, NO<sub>2</sub> and H<sub>2</sub>O.

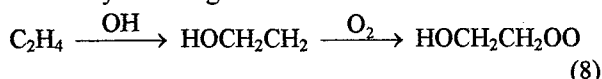
When C<sub>2</sub>H<sub>4</sub> is added NO conversion is much more efficient. This can be contributed mainly to the increased turnover of reaction (5) and



and



The ratio of the turnovers (6) / (5) / (7) is 6.7 / 4.0 / 1. The peroxyradical on the left hand side of reaction (6) is formed by following chain



The product HOCH<sub>2</sub>CH<sub>2</sub>O of reaction (6) in turn quickly reacts with O<sub>2</sub>:



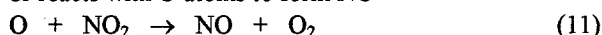
The increased formation of HO<sub>2</sub> supports reaction (5).

The concentration of NO<sub>2</sub> as a function of input energy is displayed in **Figure 2** – again, derived from measured and calculated data. In order to obtain better coherence between experiment and model in the case when C<sub>2</sub>H<sub>4</sub> is added, [NO<sub>2</sub>] is replaced by the concentration of all oxidation products of N minus the concentration of [NO], ie the total concentration of NO<sub>2</sub>, HNO<sub>2</sub>, HNO<sub>3</sub>. This had to be done because the decomposition of HNO<sub>2</sub> and HNO<sub>3</sub> into NO and NO<sub>2</sub> was not properly described by the kinetic data from the literature.

Without the presence of C<sub>2</sub>H<sub>4</sub> much less NO<sub>2</sub> is built up because it is oxidised by OH to HNO<sub>3</sub> after its formation



or reacts with O atoms to form NO



The much more desired reduction of NO<sub>x</sub> to N<sub>2</sub> can only be achieved by sufficient concentrations of the radicals N, CN, C [4] and NH<sub>2</sub>. Although N is produced during the discharge phase its concentration of about 1 vppm is too low in order to compensate for the oxidation of NO.

#### 4. Conclusions

The presence of ethene (C<sub>2</sub>H<sub>4</sub>) has a large effect on the plasma assisted removal of NO. Due to the presence of the peroxy radical HOCH<sub>2</sub>CH<sub>2</sub>OO it is much more efficiently oxidised than without C<sub>2</sub>H<sub>4</sub>, where oxidation is mainly achieved by O atoms. End products are mostly HNO<sub>3</sub> (no C<sub>2</sub>H<sub>4</sub> added) and NO<sub>2</sub> (with C<sub>2</sub>H<sub>4</sub>). In both cases the net reduction of NO<sub>x</sub> to N<sub>2</sub> is low.

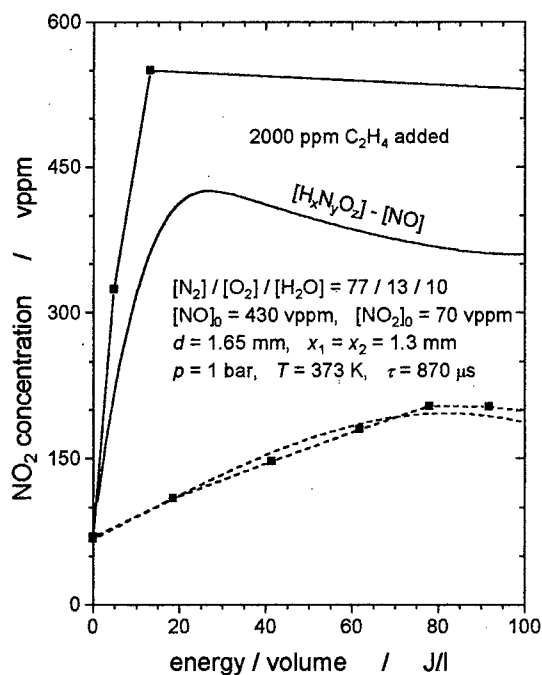


**Figure 2:** Concentration of NO<sub>2</sub> as function of input energy. The dashed curves represent data for a gas mixture with no C<sub>2</sub>H<sub>4</sub>, while the solid lines represent data for a gas mixture that contains 2000 vppm C<sub>2</sub>H<sub>4</sub> at the beginning of the treatment. Curves with solid squares are obtained from experiment [3].

#### 5. Acknowledgement

This work was supported by the German Ministry of Education and Research BMBF (Grant FKZ 13 N 6370).

#### 6. References

- [1] Sun W, Pashaie B and Dhali S K 1996 *Journal of Applied Physics* 79 No. 7 p 3438
- [2] Niessen W, Neiger R and Schruft R 1995 *Proceedings of the 12<sup>th</sup> International Conference on Plasma Chemistry* p 677, Minneapolis, USA, 8 / 1995
- [3] Wolf O, Listl S and Neiger M 1996 *Contributed Papers of the 5<sup>th</sup> International Symposium on High Pressure Low Temperature Plasma Physics* p 324
- [4] Niessen W, Russ, H, Schruft R and Neiger M (1996) *Contributed Papers of the 5<sup>th</sup> International Symposium on High Pressure Low Temperature Plasma Physics* p 102



# ATMOSPHERIC PRESSURE ELECTRIC DISCHARGE IN FAST FLOWING AIR

S. Pekárek, J. Rosenkranz, F. Hanitz, V. Kříha

Czech Technical University in Prague, FEE, Technická 2, 166 27 Prague 6, Czech Republic

For a wide range of modern ecological applications of electric discharges, like cleaning of flue gases, destruction of pollutants or toxic molecules, etc., it is necessary to produce in the volume of a gas sufficient number of free electrons having energies in the range 5-20 eV. These electrons generate free radicals, which diffuse through the gas and preferentially oxidise nitrogen and sulphur oxides to form acids that can be neutralised to form non-toxic, easily collectible compounds. Electrons might be produced in different types of electric discharges: corona discharge [1,2], dielectric barrier discharge, surface discharge, discharge in a ferroelectric material or an electric discharge at atmospheric pressure in a fast flowing medium [3,4].

Electric discharge at atmospheric pressure in a fast flowing medium is studied at our laboratory. First electrode system used consisted from a thin plane which was perpendicular to a massive plane electrode. The system was placed in a rectangular channel through which there was a flow of air. Volt-ampere characteristics of the discharge together with the generation of ozone and nitrogen oxides were measured [4].

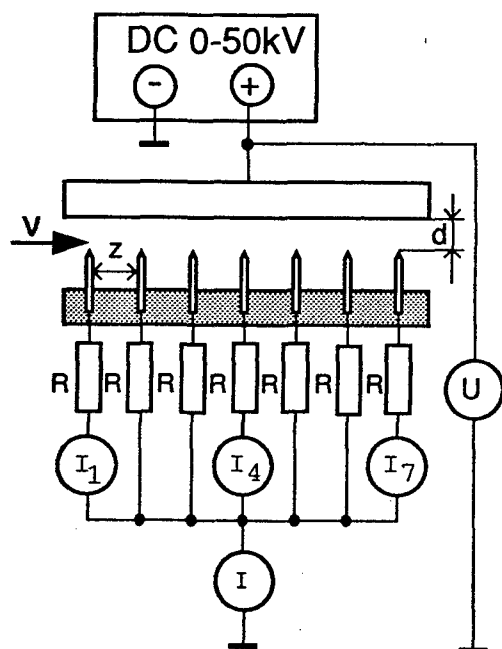


Fig.1 Experimental set-up.

For the purposes of practical applications the important role is played by the efficiency of the

discharge in producing atoms and free radicals. This efficiency certainly depends on the ratio of the power dissipated in the ballast resistors to that deposited into the bulk of plasma. As far as this ratio was in our experiments very high the electrode system was changed. Following the results presented in [3] this ratio never exceeds 10% for an electrode system consisting from the anode plate and a multi-pin cathode.

The electrode system, see Fig. 1, consists from a set of 7 pins arranged linearly against a plane anode. As far as the discharge with positive pins is difficult to control with sparking occurring frequently, the experiments were carried out with negative polarity of pins. To stabilise the discharge each pin is individually ballasted by a resistor  $R=1M\Omega$ . Pins, which are separated one from the other at equal distances  $z$  are made from iron. The distance  $z$  was either 7 or 10 mm. Pins protrude 9.5 mm from the holder. The discharge gap  $d$  between the tips of pins and a plane anode can be varied up to 1.5 cm. The electrodes in the discharge chamber were cooled by flow of air. DC power supply provides voltage up to 50 kV.

The experiments were devoted to the study of the influence of the distance  $d$  between the tips of the pins and the plane anode and the interpins distance  $z$  on the volt-ampere characteristics of the discharge together with the study of the current distribution among separate pins. Experiments were carried out with two velocities of the flowing air  $v_1=30\text{m/s}$  and  $v_2=70\text{ m/s}$ . The typical experimental results are shown in Figures 2-5. The curves were drawn by the least squares method.

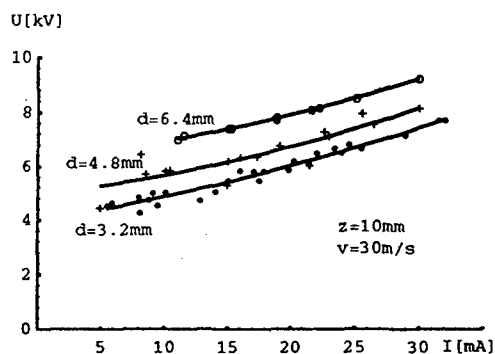


Fig.2. V-A characteristics

Discharge voltage  $U$  as a function of the total discharge current  $I$  for different distances  $d$  between the tips of pins and the plane anode is shown in Fig. 2.

It is seen that for a given current  $I$  discharge voltage increases with the increasing  $d$ . This dependence is obtained for both values of air velocity and both interpins distances  $z$ .

V-A characteristics of the discharge as a function of air flow velocity are shown in Fig.3. It is seen that for a smaller interpins distance  $z=7$  mm discharge voltage for a given current slightly increases when velocity increases. This dependence is more significant for greater  $d$ . Full lines correspond to the air flow velocity 70 m/s and dashed lines correspond to the air flow velocity 30 m/s. For the interpins distance  $z=10$  mm distance voltage does not change, within the experimental error, with velocity.

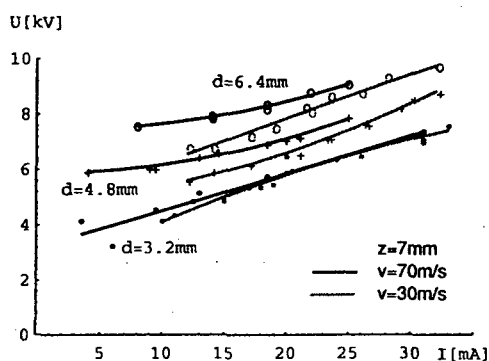


Fig.3 V-A characteristics

The results of experiments concerning the dependence of the V-A characteristics on the interpins distance  $z$  are shown in Fig. 4. As it is seen for the air flow velocity 70 m/s the discharge voltage for  $z=7$ mm increases with respect to interpins distance  $z=10$ mm for all values of distances  $d$ . For velocity 30 m/s V-A characteristics do not depend essentially on  $z$ .

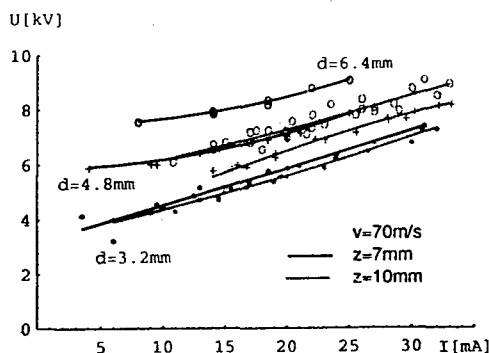


Fig.4 V-A characteristics

Finally in Fig.5 are shown partial currents flowing through pins No. 1, 4 and 7 as a function of the total discharge current. It is seen that the distribution of currents among separate pins is, within a range of experimental error, uniform.

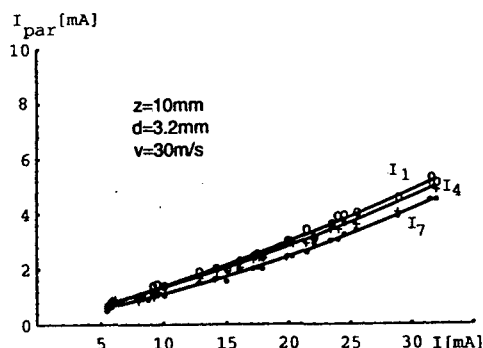


Fig.5. Current distribution

From the presented results it is obvious that V-A characteristics of the discharge are influenced not only by the distance  $d$  between the tips of pins and the plane anode but also by the distance  $z$  between the pins so that it could be possible to find a certain optimum ratio  $d/z$  for which the ratio of the power dissipated in the ballast resistors to that deposited into the bulk of plasma has an optimum value. When distance  $d$  is small with respect to  $z$  obviously discharge from the first pin does not influence significantly (for the range of velocities used) discharge from the second pin etc. This will be case of moreover separate discharges.

On the other side when  $d$  is comparable or greater than  $z$  there will be a strong influence among separate discharges. Obviously the ratio  $d/z$  also influences the volume of the channel occupied by plasma and thus the efficiency of the future possible plasmachemical reactor as a source of electrons and free radicals.

The complex nature of the studied phenomena requires further comprehensive experimental and theoretical work which may bring better insight into the physics of this type of discharge and consequently into its successful application.

#### References:

- [1] Jen-Shih Chang, Toshiaki Yamamoto, Corona Discharge Processes, IEEE Transactions on Plasma Science, Vol. 19, No.6, Dec. 1991.
- [2] A. Jaworek, A. Krupa, Electrical Characteristics of a Corona Discharge Reactor of Multipoint-to-plane Geometry, Czechoslovak Journal of Physics, Vol.45, No.12, Dec. 1995.
- [3] A.P. Napartovich et al, DC Glow Discharge with Fast Gas Flow for Flue Gas Processing, NATO ASI Series: Non-Thermal Plasma Techniques for Pollution Control, Series G, Vol. 34, Part B, (1993)
- [4] V. Kriha, F. Hanitz, S. Pekarek, J. Rosenkranz, Electric Discharge in Fast Flowing Medium for Ecological Applications, 9th Regional Central European Conference IUAPPA: Environmental Impact Assessment, Contr. Papers, Vol. 2, pages 335-338, Sept. 1996, Prague

# Development of a new reactor for the removing of the gaseous pollutants by cold plasmas

S. BRETHES, R. PEYROUS, B. HELD, C. COSTE\*

Laboratoire d'électronique, des gaz et des plasmas, Université de Pau, 64000 PAU, FRANCE

\* Société DEGREMONT 92508 RUEIL MALMAISON

## 1 Introduction

The evolution and the important progresses achieved these last years induced many unbalances in the physical and biologic mediums. In order to face serious problems of environment, new technologies of depollution (clean technologies, recycling, biotechnology, thermal and non thermal plasmas) are on the way of development especially as the environmental rules become stricter.

A new reactor using the technology of the high pressure cold plasmas and devoted to the destruction of the gaseous pollutants ( $H_2S$ ,  $CH_3SH$ ,  $NO_x$ , hydrocarbons, ...) is presently studied.

We tried in a first time to surround and understand the type of created discharges in this reactor, even if their quasiperiodic and non-stationary nature make the survey difficult. A theoretical description of such a discharge has been published quite recently [1] but the physical mechanism is not well understood.

## 2 Experimental setup

The reactor, the electric feeding and the gas system is represented in the figure 1.

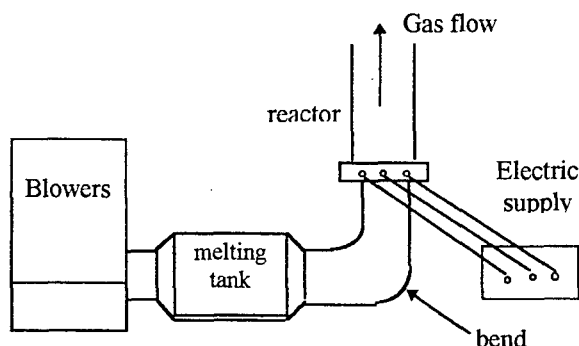


Fig. 1: Experimental setup

The reactor consists in a cylindrical surrounding wall in Pyrex of 35 cm high, 8 cm of inner diameter and 0.5 cm thick. It resists to strong temperatures and, being transparent, allows the observation of the electric discharges which take place all along the electrodes.

Inside the reactor, we have a wire-to-rods system with an axial symmetry made with a wire central electrode, constituted by one thread of Chromel 0.1 cm in diameter, and several stainless steel rods cylindrically

positioned around the axis of the cylinder on angles multiple of  $30^\circ$ . The ambient air, which constitutes our vector gas, is set in motion by two blowers placed in serie. A melting tank allows to inject the pollutants in the air and to homogenize the mixture passing through several grids each having numerous holes of different diameters.

The electric supply provides an AC high voltage (about 6 kV) which generates an initial discharge at the basis of the electrodes. Three power transformers permit the maintenance and development of the discharges all along the electrodes.

## 3 Achieved diagnosis

In order to characterize our discharge, several means of analysis were used.

A first survey of the fluidic (injection of fine threads of smoke) and visualisation of some profiles of speed informed us on the type of flow obtained inside the reactor.

Then we were interested in the electrical aspect by visualising the wave forms corresponding to the voltage and current. For it, we used resistive dividers, capacitive and current probes linked with a digital oscilloscope LeCroy MODEL 9400. A recording of the characteristic audible noise of the discharge was also performed. So as to obtain more indications on the type of discharge regime we also made some temperature measurements. A study of electric parameters has already been realized by SIMEK [2].

In order to determine the present gaseous species in the reactor before the injection of the pollutants, some measurements by emission spectroscopy were made. The obtained results will allow us to make some hypothesis on the reactions occurring during the discharge.

## 4 Results and discussion

### 4.1 Hydrodynamic aspect

The gas speed profiles, obtained for the various gas system configurations (one or two blowers running) have the same general shape. According to the entrance diameter used, the curve presents a more or less convex zone and another smooth one. We notice that the gas flowing is less turbulent for the smallest gas flows. Then, the most favourable gas flowing allowing a good treatment is obtained for a relatively small entrance diameter and a gas flow lower than 17 l/s.

#### 4.2 Electric aspect

The figure 2 shows voltage and current signals obtained on one electrode.

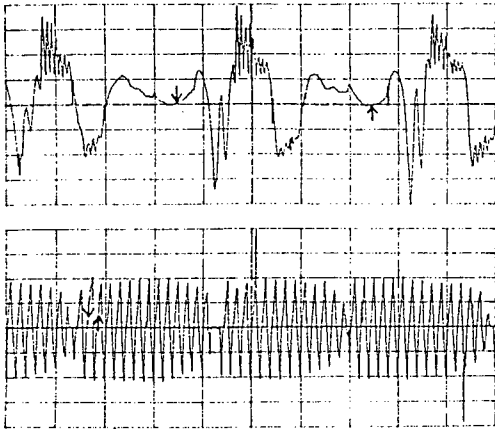


Fig. 2 : Voltage (above) and current ( below) of an electrode arrows indicating the same time.

Generally, we can observe that the current is modulated by a frequency of about 5 Hz. If we compare the signal recording voltage and current, we can notice that i) when we have modulated current, the voltage signal is rather simple ii) when we have a zero current, the signal is more complex with various impulses. The figure 3 shows the correlation between the recording of audible noise, modulated in the same way than the current, in relation with the gas flow increase. The end of the current modulation corresponds to the rupture of the arc. All the results, as temperature measurements, indicate that we are closer to the arc regime than to the corona discharge.

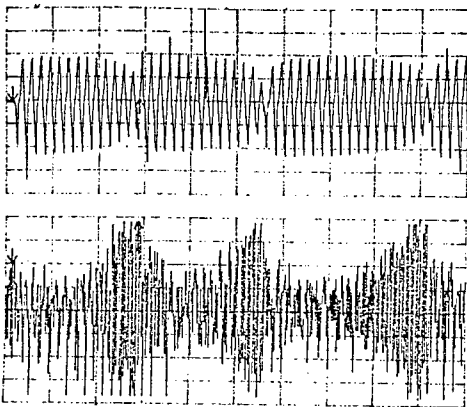


Fig. 3 : Current (above) and audible noise ( below) signals.

#### 4.3 Spectroscopic aspect

The spectroscopic measurements show the presence of numerous excited and ionized species of nitrogen and

oxygen, that demonstrates the high energy developed by the discharge. These species are essentially located at the level of the central electrode, starting point of the discharge taking place in the gas flow direction. It will be necessary to let the gaseous pollutant sufficiently in contact with the discharge in order to obtain a good treatment. During a cycle of spectral acquisition, we can obtain some spectra without signal, certainly in relation with the local extinction of the discharge.

#### 5 Conclusion

From these first studies, some of them reported in [3], we could conclude that, in the hydrodynamic point of view, we must work with a reduced gas flow passing through a small entrance diameter.

Among the electric parameters, we are more specially interested in the current and it will be necessary to limit it in order to avoid the transition to arc. Furthermore, assuming that the more energetic electrons are responsible of the pollutants removing, it will be necessary to avoid the lacks of current that we can observe at times.

As soon as the fluidic and electric parameters and their evolution are well defined, the optimization in the pollutants removing yield will start.

#### 6 References

- [1] A.A. Fridman, A. Petrousov, J. Chapelle, J.M. Cormier, A. Czernichowski, H. Lesueur, J. Stevefelt : J. Phys. III France 4 (1994) 1449-1465.
- [2] M. SIMEK, M. CLUPEK, J. DUSPIVA, P FILIP and F.MERXBAUER : IPPCZ - 344, Czech Republic, (1994) 1-22.
- [3] S.BRETHES : Rapport d'activité, Janv 1997 (1997).

# NO removal in a photo-triggered discharge reactor

M. Rozoy, M. P. Monin, C. Postel and V. Puech

Laboratoire de physique des Gaz et des Plasmas (associé au CNRS)  
Université Paris-Sud, 91405 Orsay Cedex, France

## 1- Introduction

In recent years, the removal of atmospheric pollutants by non thermal plasmas has been heavily investigated and the efficiency of pulsed discharges is now well established. Up to now, two kinds of discharges have been investigated: the pulsed corona discharges and the dielectric barrier discharges. These discharges are filamentary ones, and the resulting plasma is very inhomogeneous, such as only a small part of the gas is actually treated by the discharge.

On the other hand, in laser technology, different techniques have recently been developed to produce large volume of homogeneously excited plasmas in different gases at atmospheric pressures, even in presence of large amount of electro-negative components. Among these techniques, the so-called photo-triggered discharges [1-3] have been shown very efficient to dissociate many molecules and to produce the initial steps of a complex set of chemical reactions resulting in the production of new molecules and radicals. Thus, the physics of flue gas treatment appears somewhat similar to the physics involved in excimer or chemical lasers.

As a result, the goal of the present work is to assess the potentialities of these photo-triggered discharges for depollution applications.

## 2- Experimental set-up

As the basic operating mode of the photo-triggered discharges has been previously described in detail [1-3], only a brief description will be given here. The photo-triggered discharge reactor, figure 1, consists mainly of three sections: the energy storage unit, the discharge chamber and the preionisation circuit. The electrodes, 50 cm long, have a gap of 1 cm and a flat profile over 1 cm. As a result, a volume of 50 cm<sup>3</sup> can be homogeneously excited at each shot. The storage unit is pulsed charged up to 20 kV either directly from a power supply (rise time 15µs) or through a C-L-C circuit (rise time 200 ns). When this voltage is reached, the preionisation is fired and initial electrons are produced in the discharge gap by photo-ionization from the U.V. light produced by an auxiliary surface discharge located under one of the discharge electrodes. Several optical windows allow a spectroscopic investigation of the medium both in the longitudinal and transverse directions. N<sub>2</sub>, O<sub>2</sub> and NO are mixed at various concentrations in an auxiliary

tank of 1500 cm<sup>3</sup>. A gas compressor is used to produce, in a closed loop, a gas flow through the discharge gap.

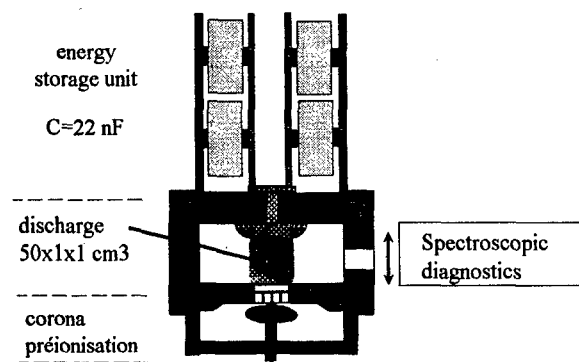


Figure 1: cross sectional view of the photo-triggered discharge reactor for gas treatment.

The evolution of the NO concentration has been monitored, mainly through spectroscopic techniques. Emission from the NO  $\gamma$ -bands is recorded to follow the NO(A) excited state concentration, while longitudinal absorption spectroscopy over the 50 cm discharge long, is used to study the evolution of the NO ground state concentration. Absorption spectroscopy has also been used to measure the ozone production in the discharge. These spectroscopic diagnostics allow a real time monitoring of the actual discharge volume (50 cm<sup>3</sup>) but with a limited sensitivity. Thus, we have also used a chemiluminescent detector giving a sensitivity of a about 1 ppm. However, this detector can only be used in a post-treatment mode: the NO concentration has to be checked in the total volume (1500 cm<sup>3</sup>) after a given number of shots.

## 3- Discharge modeling

A model has been developed to calculate the temporal evolution of the concentration of the different species produced by the discharge. The model self consistently couples the circuit equations, giving the input energy in the reactor, the solution of the Boltzmann equation for the electron distribution function, and the kinetic equations governing the evolution of the various heavy particles. The Boltzmann equation is solved using algorithms developed by Ségur and Bordage [4]. The collisions between electrons and nitrogen, oxygen and

NO molecules are described by detailed sets of collision cross-sections, whereas the physico-chemistry governing the temporal evolution of the various states of heavy particles is described by a set of 180 reactions compiled from the literature. The vibration-vibration and vibration-translation processes which are known to play an important role in non-equilibrium plasmas are included in the model.

#### 4- Results and discussion

Figure 2 shows emission spectra of a mixture of  $N_2/NO$  at 500 ppm of NO. The full line curve is the spectrum recorded on the first shot, while the dotted line curve is recorded after 185 shots. This figure clearly shows that the NO emission ( $\lambda < 290$  nm) completely disappears, while the intensity of the  $N_2$  lines ( $\lambda > 290$  nm) remains unchanged.

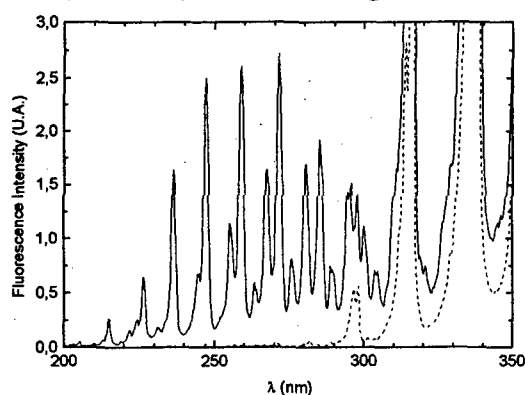


Figure 2: Emission spectra of a  $N_2/NO$  mixture at 500 ppm of NO. Full line: initial spectrum, dotted line: spectrum after 185 shots.

Absorption spectroscopy as well as chemiluminescent measurements confirm this result: NO molecules are completely removed from the photo-triggered discharge reactor after a given number of shots depending on the initial NO concentration. For each NO concentration, the NO removal efficiency is determined from the knowledge of the total input energy in the reactor. These efficiencies are shown in Figure 3, and the experimental results compared to the values predicted by the model. Except at very high NO concentration, the agreement between the model and the experiments is satisfactory.

In mixtures comprising more than 10% of  $O_2$ , the NO  $\gamma$ -bands can not be observed in emission, in such a way that only absorption spectroscopy can be used to follow in a real time the NO removal. Unfortunately the NO absorption bands are superposed to the large absorption continuum of ozone which is produced by the discharge. Thus, the determination of the NO removal in  $N_2/O_2/NO$  mixtures requires differential measurements which are currently performed.

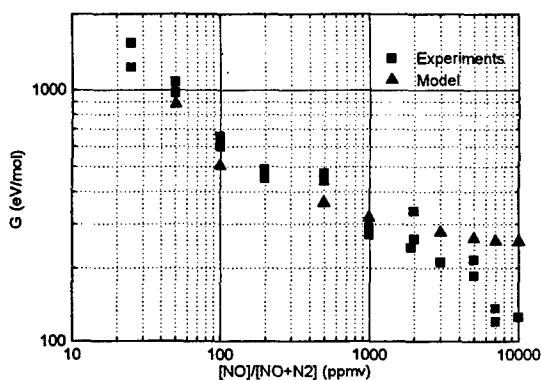


Figure 3: Comparison between experimental data and model predictions for the efficiency of NO removal.

For a 80/20 %  $N_2/O_2$  mixture, the predicted temporal evolution of various heavy particles are shown in figure 4, and the evolution of the predicted ozone population is compared to the experimental one. The agreement between model and experiment is within a factor of 2.

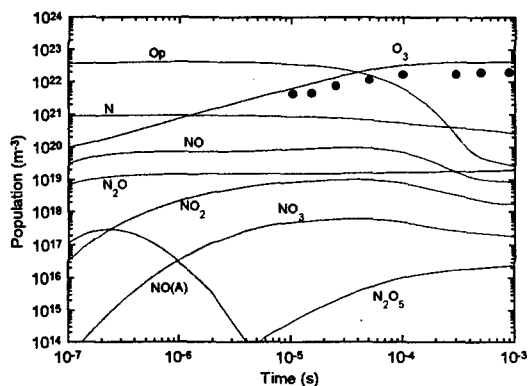


Figure 4: Temporal evolution of some species produced in  $N_2/O_2$ . Lines are the model predictions, and symbols the ozone concentration measurements.

#### 5- Conclusion

These preliminary results point out that the photo-triggered discharge reactors are very effective to homogeneously remove atmospheric pollutants from large volumes. Studies are in progress to optimize these new reactors. Moreover, as large amounts of ozone are produced in  $N_2/O_2$  mixtures, these reactors should also be investigated as ionizers.

#### 6- References

- [1] B. Lacour and C. Vannier: J. Appl. Phys. 62 (1987), 754
- [2] V. Puech, P. Prigent and H. Brunet: Appl. Phys. B55 (1992) 183
- [3] R. Riva, M. Legentil, S. Pasquiers and V. Puech: J. Phys. D: Appl. Phys. 28 (1996) 856
- [4] P. Ségur and M.C. Bordage: Proc. XIX ICPIG, ed. J. Labat (1989) pp 86-109 and references therein.

## The main channels of freon destruction in nanosecond corona discharge

R.A.Akhmedzhanov, A.L.Vikharev, A.M.Gorbachev, O.A.Ivanov, A.L.Kolisko.  
Institute of Applied Physics, Russian Academy of Science,  
46 Ulyanov st., Nizhny Novgorod 603600, Russia

A main reason for destruction of the ozone layer is high contents of freons (CFCs) in the Earth atmosphere. The characteristic lifetime of freons in the stratosphere is tens of years; therefore, destruction of the ozone layer will go on for a long time even after utilization of CFCs has stopped. At these conditions special importance is acquired by the search for efficient methods [1-2] of purification of gaseous wastes of the industries using CFC components (e.g. microelectronics), as well as the atmosphere proper.

This paper gives results of experimental studies of freon destruction in a pulse-periodic nanosecond corona discharge. The discharge chamber was a section of metal cylinder, 5 cm in diameters and 40 cm long, which was used as an external electrode. The chamber contained a quartz tube with optical windows at the ends. The second electrode, 0.7 mm in diameter, which was placed along the tube axis, was fed with pulses of negative polarization produced by a pulse generator. Pulse amplitude was 30-40 kV, duration  $\tau = 50$  ns, and repetition rate,  $F = 1$ -100 Hz. The experiment was performed under pressures  $p = 50$ -760 Torr in air for various percent content of  $C_2Cl_3F_3$  (freon-113) with no gas pumping.

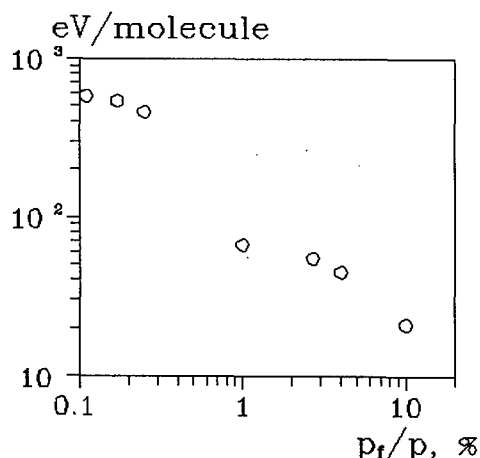


Fig.1

Freon concentration in the course of experiment was measured with a spectrograph basing on the data about absorption of IR radiation in the range of  $\lambda = 7.5 - 20 \mu m$ . Dependence of energy cost for destruction of one CFC-113 molecule on its percent content at the 80 % level of purification is shown in Fig.1 for the pulse repetition rate  $F = 25$  Hz un-

der the mixture pressure  $p = 100$  Torr. From these experiments it follows that the energy cost is higher when the share of freon content is lower.

Let us consider possible channels for CFC destruction in a discharge. There are a few such channels: CFC dissociation by an electron impact, CFC dissociation during collisions with molecules and atoms excited in a discharge, thermal dissociation, dissociative attachment of electrons and dissociative re-charging of negative ions. Gas heating in a nanosecond discharge is insignificant, hence one can neglect the thermal destruction of CFC. The process of dissociative attachment is characterized by its high selectivity. Efficiency of this channel is limited by the processes of death of electrons, which are not associated with attachment to CFC (in air it is attachment to  $O_2$  and recombination). However if CFC content in air is sufficiently high, such that

$$N_f > \nu_a/k_a \sim 7 \cdot 10^8 p^2 \quad (1)$$

where  $\nu_a = 140 p^2 s$  is frequency of three-body attachment of electrons to  $O_2$ , and  $k_a \approx 2 \cdot 10^{-7} cm^3/s$  is constant of dissociative attachment to CFC, then at the stage of plasma decay the main part of "cold" electrons will attach to freon molecules, and the number of destroyed molecules will be  $N_e$ .

The number of CFC molecules dissociated by an electron impact or by dissociative attachment during a pulse is determined by the following expression:

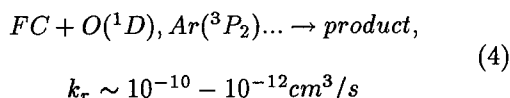
$$\Delta N_f = k_{d,a} \cdot N_e \cdot N_f \cdot \tau \quad (2)$$

where  $k_{d,a}$  is constant of CFC dissociation by an electron impact or constant of dissociative attachment of electrons in a discharge. From Eq.(1) and (2) one can determine the range of freon concentration, at which the processes of dissociative attachment in the decaying plasma play the main part in freon destruction:

$$\nu_a/k_a \leq N_f \leq 1/(\tau \cdot k_{d,a}) \quad (3)$$

For  $p = 100$  Torr and  $\tau = 5 \cdot 10^{-8} s$  it corresponds to the condition of  $10^{13} cm^{-3} \leq N_f \leq 3 \cdot 10^{15} cm^{-3}$ . At  $N_f > 1/(\tau \cdot k_{d,a})$  the main part of CFC will be destroyed during the pulse. Let us consider now the role of excited particle in the process of CFC destruction. Freons may be destroyed with sufficient efficiency by interaction with meta-stable atoms and

molecules of oxygen, nitrogen or inert gases in the processes of the following type:



The number of excited particles  $N^*$ , formed in the discharge during a pulse may be estimated basing on the following correlation:

$$N^* = k^* \cdot N_e \cdot N_0 \cdot \tau \quad (5)$$

where  $k^*$  is constant of excitation of active particles, and  $N_0$  is gas density. Efficiency of reactions (4) is limited by the processes of damping of excited particles by molecules of neutral gas. Having assumed that the characteristic lifetime of active particles equals  $\tau^* = 1/(k_n \cdot N_0)$  where  $k_n$  is constant of quenching  $N^*$  with neutral molecules, let us estimate the number of CFC molecules destroyed in time  $\tau^*$  in process (4):

$$N_f = k_r \cdot N^* \cdot N_f \cdot \tau^* =$$

$$k_r \cdot k^* / k_n \cdot N_e \cdot N_f \cdot \tau = \quad (6)$$

$$k_{\Phi\Phi} \cdot N_e \cdot N_f \cdot \tau$$

From comparing Eqs.(3) and (6) it is seen that the processes of CFC destruction with participation of excited particles are predominant over the processes of freon dissociation by electrons at  $k_{\Phi\Phi} = k_r \cdot k^* / k_n > k_{d,e}$ . In the experiment under air pressure  $p = 100$  Torr and  $N_f = 3.5 \cdot 10^{16} \text{ cm}^{-3}$ , over 80% of freon were destroyed after the mixture had been treated with a series of 3000 pulses. Estimations show that in this case about 1% of CFC may be destroyed in the process of dissociative attachment at the stage of plasma decay, and about 3%, in the process described by Eq. (2). From here one can conclude that an important channel for CFC destruction at its high content is reaction (4). Let us consider, for the sake of certainty, reactions with participation of an excited oxygen atom,  $O(^1D)$ . Having used the constants of the processes,  $k^* = 10^{-9} \text{ cm}^3/\text{s}$ ,  $k_n = 10^{-11} \text{ cm}^3/\text{s}$ ,  $k_r = 1.5 \cdot 10^{-10} \text{ cm}^3/\text{s}$ , we obtain  $k_{\Phi\Phi} = 1.5 \cdot 10^{-8} \text{ cm}^3/\text{s}$ . Then, in accord with (6), the number of freon molecules destroyed by one pulse will be  $\Delta N_f = 15 N_e$ . The experiments showed that a considerable part in freon destruction may be also played by  $O(^3P)$  atoms. By that, as freon concentration grows, efficiency of CFC destruction with participation of  $O(^3P)$  atoms also grows, and at  $N_f > k_{O_3} \cdot [O_2] \cdot [N_0] / k_r \sim 2 \cdot 10^{11} \cdot p^2$  (where  $k_r$  is constant of reaction (4) for  $O(^3P)$ ,  $k_{O_3}$  is constant of ozone formation), all the atoms of oxygen take part in process (5), and no ozone is produced.

Thus, the performed estimations show that under the experimental conditions at  $N_f \geq 2 \cdot 10^{15} \text{ cm}^{-3}$

an important item among the channels of freon destruction are collisions with excited particles and oxygen atoms. Energy cost of destroying one CFC molecule at these conditions decreases as freon content in the mixture grows (Fig. 1). At a lower level of CFC content, it is mainly destroyed in the process of dissociation attachment at the stage of plasma degeneration, and the energy cost does not depend on  $N_f$  and is determined by electron density achieved by the end of the pulse. At even lower concentrations one has to take into account the processes of  $N_e$  decay that are not associated with attachment to CFC.

## References

- [1] Yamamoto T. et al., IEEE Trans. Industr. Appl. **28**, 528-534 (1992)
- [2] Askaryan G.A. et al., Sov. J. Plasma Phys. **18**, 625-631 (1992)



## Energy cost of ozone production in nanosecond microwave discharges

R.A.Akhmedzhanov, A.L.Vikharev, A.M.Gorbachev, O.A.Ivanov, A.L.Kolisko  
Institute of Applied Physics, Russian Academy of Science,  
46 Ulyanov st., Nizhny Novgorod 603600, Russia

Recently the search for methods for ozone regeneration in the region of ozone "holes" by actively affecting the earth's atmosphere has become especially extensive. The proposed projects deal mainly with two different approaches: atmosphere purification from chlorofluorocarbons [1,2] and regeneration of ozone to the initial natural level [3,4]. Such projects are planned to be accomplished by means of an artificially ionized layer (AIL) produced in the atmosphere at different heights by nanosecond microwave pulses injected from ground-based antennas. This paper contains a discussion of the second research line. Here we report the results of laboratory experiments modeling production of the AIL in the atmosphere with a pulse-periodical nanosecond microwave discharge. An important parameter that makes the microwave discharge rather advantageous for generation of ozone in the atmosphere is amount of energy going into production of one ozone molecule.

In the first experiment the microwave generator (relativistic carsinotron) operating within the 8-mm wavelength band was used with power  $P = 20$  MW, pulse duration  $\tau = 5$  ns and pulse repetition frequency  $F = 1 - 10$  Hz. The second experiment was performed using a 3-cm wavelength-band magnetron with power  $P = 50$  kW at pulse duration  $\tau = 500$  ns. The magnetron could operate at a high pulse repetition rate, up to  $F = 10^3$  Hz. In the second case a cavity-based microwave pulse compressor was also used. This device transformed pulses of the magnetron into pulses with duration  $\tau = 6$  ns and  $P = 800$  kW. Figure 1 represents schemes of the experiments. The discharge was ignited in two basically different electrodynamic systems. In the first case microwave radiation was focused with a parabolic cylinder, so that the electromagnetic field in the breakdown region was close to a standing cylindrical TE-mode. The vector of electric field was parallel to the axis of the mirror. The discharge was shaped as a cylinder several millimeters in diameter and about 30 cm long. In the second case a quasi-planar standing electromagnetic wave was formed by means of a spherical mirror. Then the discharge was a set of plasmoids about 3 cm in diameter localized at the antinodes of the standing wave. The experiments were performed at the room temperature of the air in the pressure range  $p = 10 - 250$  Torr. The densi-

ties of ozone and nitrogen dioxide were measured by observing the absorption of the radiation of a hydrogen lamp at wavelengths  $\lambda \approx 260$  nm and  $\lambda \approx 360$  nm, respectively.

The following regularities of ozone production in the air were observed. In the nanosecond microwave discharge effective dissociation of molecules of  $O_2$  and  $N_2$  (effective production of  $O$  and  $N$  atoms) takes place. As the result, concentration of  $O_3$  increased linearly during the first pulses. The energy cost was determined basing on the total energy of the microwave pulse,  $W = P \cdot \tau$ , and using the following formula:

$$\delta = P \cdot \tau \cdot n_p / [O_3] \cdot V_k \quad (1)$$

where  $n_p$  is number of microwave pulses,  $[O_3]$  is ozone density after  $n_p$  pulses and  $V_k$  is the volume of the vacuum chamber. The results of measuring the energy cost of ozone production for two different types of the microwave discharge is shown in Fig.2. The energy cost was 2-3 times lower in a discharge created by standing waves than in a discharge formed by a converging cylindrical TE-mode. This shows that efficiency of ozone formation depends essentially on the electrodynamic system producing the discharge. For systems operating with standing waves or crossing wave beams efficiency turns out to be higher.

These experiments showed that the energy cost of production of one ozone molecule is lower in that type of the microwave discharge, in which the maximum of its energy goes into dissociation of oxygen molecules. Oxygen atoms are produced and then converted into ozone mainly in dissociation of  $O_2$  molecules by an electron impact (direct channel) and in collisions of  $O_2$  with metastable  $N_2$  molecules (indirect channel). The velocity constants for these processes are determined by the function of electron distribution over energies and depend on intensity of the electric field in plasma. The value of rate of  $O_2$  dissociation by an electron impact,  $k_d$ , is rather well known for a constant electric field. Using it we can evaluate the energy cost of production of one ozone molecule in the microwave discharge. We assume that all oxygen atoms are formed in the process of direct dissociation of oxygen, and then they enter the reaction of ozone synthesis. The ozone density produced in one microwave pulse is given by

$$[O_3] = [O] = 2 \cdot k_d(E_e/V) \cdot [O_2] \cdot N_e \cdot \tau. \quad (2)$$

The energy cost of one ozone molecule is found from the ratio of the microwave energy absorbed in plasma to ozone density:

$$\delta = \frac{\sigma E^2 \tau}{2k_d[O_2]N_e \tau} = \frac{5}{2} \cdot \frac{e^2}{m} \cdot \left(\frac{\nu}{N}\right)^{-1} \cdot \frac{(E_e/N)^2}{k_d} \quad (3)$$

where  $\sigma = e^2 N_e \nu / m(\nu^2 + \omega^2)$  is specific plasma conductivity,  $E_e = E \cdot \nu / (\omega^2 + \nu^2)^{1/2}$  is efficient electric field,  $\nu$  is rate of electron-molecule collisions, and  $\omega$  is the wave frequency. Using equation (3) it is easy to determine optimal conditions, when at the preset energy of the microwave pulse the number of oxygen atoms produced in the ionized region is maximal. The value of  $(E_e/N)^2/k_d$  is minimal when the value of reduced efficient electric field  $E_e/N$  is determined by

$$E_e/N = \frac{2 \cdot k_d}{dk_d/d(E_e/N)} \quad (4)$$

Figure 3 shows the dependence of  $\delta$  on the reduced electric field  $E_e/N$  determined by calculation (curve 1) using equation (3) and by experiment. The experimental value of efficient field  $E_e$  was determined from intensity of the electric field in the discharge region before the breakdown starts, and the rate of electron collisions in air was assumed equal to  $\nu = 5,3 \cdot 10^9 \cdot p(\text{cm}^{-1})$ .

As seen from Fig.3, experimental values of  $\delta$  are lower than the calculated ones. It witnesses that the channel of  $O_2$  dissociation associated with excitation of electronic levels of  $N_2$  molecules plays a significant part in the plasma of a nanosecond microwave discharge in air. We added curve 2 to Fig.3 to represent the results of calculating the energy cost of ozone formation with account for indirect channel of  $O_2$  dissociation.

Thus, there are optimal conditions for oxygen dissociation in air. The results of the performed modeling experiments make it possible to conclude that an efficient way to produce ozone in the atmosphere has been found. A nanosecond microwave discharge can efficiently generate ozone. The laboratory experiments demonstrated sufficiently low energy costs of producing one ozone molecule:  $\delta = 15 - 20 \text{ eV/molecule}$ , which corresponds to production of 100g of ozone per 1kW·h of consumed energy.

## References

- [1] Stix T.H., J. Appl. Phys. **66**, 5622-5626 (1989)
- [2] Askaryan G.A. et al., Sov. J. Plasma Phys. **18**, 625-631 (1992)
- [3] Vikharev A.L. et al., Proc. ICPIG -21, Bochum, **1**, 123-124 (1993)
- [4] Akhmedzhanov R.A. et al., Phys. Lett. **207A**, 209-213 (1995)

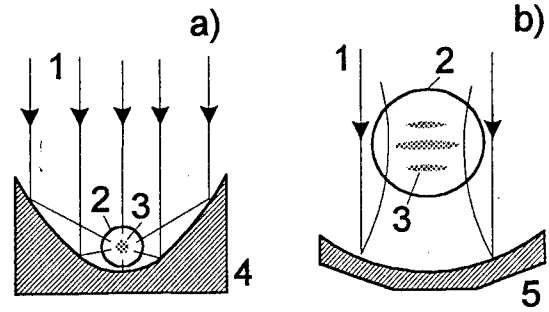


Fig.1. Different schemes for creation of microwave discharges: 1 – microwave radiation, 2 – quartz retort, 3 – discharge plasma, 4 – parabolic cylinder, 5 – spherical mirror.

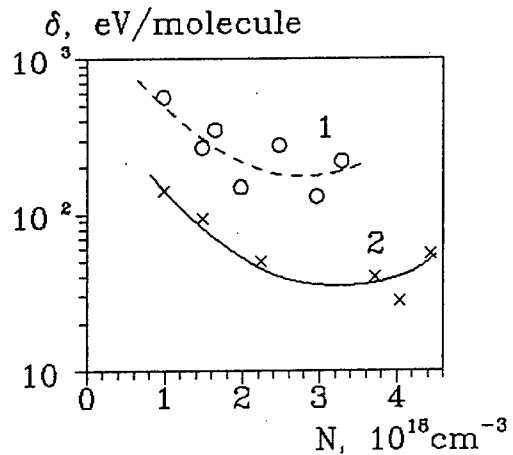


Fig.2. Dependence of energy cost of ozone production on air density for discharges created by a converging cylindrical TE-mode (1) and by standing wave (2).

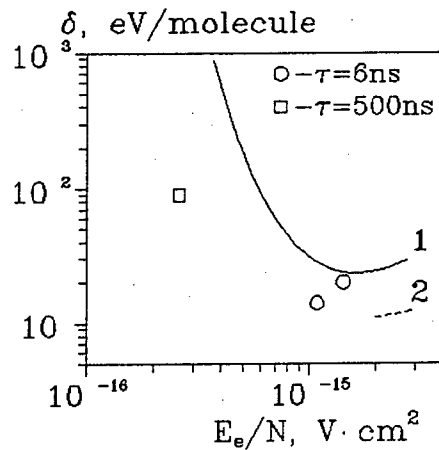


Fig.3. Dependence of energy cost of ozone production on the reduced electric field: 1, 2 – calculation, o, square – experiment.

## Authors Index

### A

Abbaoui M. I-4  
 Abdelli S. IV-264  
 Abdullin I.Sh. IV-72  
 Ablitzer D. IV-200  
 Abramzon N. I-62  
 Adachi K. I-246  
 Adler H.G. III-22  
 Afanas'ev V.P. III-104  
 Ahedo E. I-2  
     I-204  
 Akaishi K. IV-156  
 Akhmedzhanov R.A. I-272  
     I-274  
 Alcaide I. II-2  
 Aldea E. IV-254  
 Alekseeva L.M. I-206  
     II-156  
 Alexandrov A.F. I-44  
     I-108  
     III-88  
 Alexandrov L.S. I-208  
 Alexandrovich B. IV-76  
 Alexeff I. III-102  
 Al-Hussany A. II-216  
     II-218  
 Alkaa A. II-260  
 Allen J.E. I-116  
     I-132  
     I-192  
     I-194  
 Almi A. I-254  
 Alnot P. IV-244  
 Alvarez I. I-18  
 Alves L. I-120  
 Amakawa T. I-246  
 Amemiya H. I-110  
     IV-60  
     IV-62  
 Amirov A.H. IV-262  
 Ammelt E. II-182  
 Amorim J. IV-232  
 Andre P. I-4  
     III-104  
 Andreazza P. IV-252  
 Andreazza-Vignolles C. IV-252  
 Andrieux M. IV-192  
 Anikin N.B. IV-48  
 Annaratone B.M. I-116  
     I-132  
     I-192  
     I-194

Anschutz B. II-204  
 Anschutz F.B. II-202  
 Antoni V. II-262  
     IV-134  
 Antonova T.B. III-88  
 Arai T. IV-86  
     IV-88  
     IV-90  
 Arnal Y. IV-230  
 Arnas-Capeau C. I-202  
     II-164  
 Arriaga C. I-18  
 Asselman A. III-24  
 Atipo A. II-170  
 Aubes M. III-16  
     IV-64  
 Aubrecht V. II-78  
     II-80  
     II-82  
 Aubreton J. I-4  
     IV-102  
     IV-220  
 Auday G. I-58  
 Averyanov V.P. I-188  
 Awakowicz P. I-60  
     II-202  
     II-204

### B

Babaeva N.Yu. II-246  
 Babaritskiy A. IV-224  
 Babich I.L. II-154  
 Babich L.P. I-6  
     I-8  
     I-10  
     IV-2  
     I-10  
 Babich M.L. I-10  
 Babicky V. I-248  
     IV-14  
 Bacal M. I-12  
     III-78  
 Bachev K. I-160  
     I-162  
 Baclawski A. II-110  
 Badie J.M. IV-192  
 Bagatin M. II-262  
     IV-134  
 Bagautdinov A. IV-222  
 Baksht F.G. I-12  
     IV-138  
     IV-194  
 Baldwin M. IV-194  
 Baltog A. I-94

Bano G. III-96  
     IV-212  
 Baranov I.E. IV-224  
 Baravian G. IV-232  
 Barinov Yu.A. III-104  
 Barj M. IV-142  
 Bartlova M. II-80  
 Bashutin O.A. IV-112  
 Basner R. IV-196  
 Basurto E. I-18  
 Batanov G.M. I-138  
 Bauchire J.M. II-120  
     II-136  
     II-206  
 Baude S. III-86  
 Bayle P. I-252  
     II-220  
     IV-154  
 Becker K. I-62  
     I-64  
     IV-196  
 Behnke J. IV-226  
     II-4  
 Behnke J.F. II-4  
     II-6  
     II-8  
 Beilis I.I. I-14  
     II-84  
 Belenguer Ph. I-100  
 Belhaouari J.B. II-86  
 Belmonte T. IV-66  
     IV-198  
 Ben Gadri R. IV-44  
 Benabdessadok M.D. I-252  
 Bernard J.F. IV-130  
 Berreby R. III-92  
 Berthomieu D. I-148  
 Bezborodko P. IV-68  
 Bezemer J. II-224  
 Bhattacharjee S. I-110  
 Biborosh L. II-190  
 Biel W. II-226  
 Bilikmen S. I-172  
 Bindemann Th. II-6  
 Birau M. III-46  
 Bisch C. IV-192  
 Blaise G. III-86  
 Blanc E. III-10  
 Blois D. IV-142  
 Blundell R.E. II-150  
 Bobrov Yu.K. II-166  
     II-168

Bobrov Yu.K.	II-208 II-210 IV-4 IV-6	Busov B.	II-78	Choi W.K.	III-88
Bobrova L.N.	IV-6	Buzzi J.M.	III-46	Chorazy J.	I-82
Bockel S.	IV-200	Bykanov A.N.	IV-72	Christophorou L.G.	I-68
Boeuf J.P.	I-112 II-56 II-228 II-252 II-254 III-42 III-70	<b>C</b>		Chuaqui H.	II-12 III-28
Bogaerts A.	II-10	Cachoncinlle C.	III-30 III-32 III-44	Chumak G.M.	IV-206
Bonhomme G.	II-16 II-170	Cahoreau M.	IV-220	Cicconi G.	II-176
Bonifaci N.	IV-10 IV-12	Caillez Y.	III-46	Cicman P.	IV-250
Booth J.P.	IV-70 IV-202	Cajal D.	II-92 IV-74	Cinelli M.J.	IV-102 IV-220
Borcia C.	II-172	Calderon M.A.G.	II-112	Ciobanu S.S.	II-100 II-102 IV-150
Bordage M.C.	IV-44	Capitelli M.	I-24 I-26 I-66 II-116	Cisneros C.	I-18
Borisenko A.G.	I-38 IV-248	Cardinaud C.	III-90	Clavreul R.	III-94
Borodin V.	III-18	Carman R.J.	II-258	Clenet F.	II-212
Bouaziz M.	II-88	Cartry G.	II-70 II-72	Clupek M.	I-248 IV-14
Boubert P.	IV-152	Catherinot A.	IV-102 IV-220	Coitout H.	II-96 IV-78
Boucher I.	III-2	Cenian A.	I-16 III-18	Collins G.	IV-194
Bouchoule A.	I-200 III-66	Censor D.	I-234	Colombo V.	II-214
Boudjella A.	IV-16	Cercek M.	IV-162	Conde L.	I-70 II-2
Boufendi L.	IV-204	Cernak M.	I-248 IV-8	Coppa G.G.M.	II-214
Bougdira J.	IV-244	Cernogora G.	I-102 II-70 II-72	Cormier J.M.	II-122
Bougrov G.E.	III-88	Chabert P.	IV-202	Coste C.	I-268
Boxman R.L.	II-84	Chaker M.	I-166 I-168	Coulombe S.	II-98
Bozin J.V.	I-98	Champaign H.	IV-94	Courtois L.	II-42
Brablec A.	I-128 IV-226	Chapelle J.	II-122	Csambal C.	II-8
Bragin V.E.	IV-72	Chapput A.	IV-142	Cunge G.	IV-202
Braginskiy O.V.	III-76	Charles C.	IV-252	Czerwec T.	IV-66 IV-198
Brasile J.P.	II-42	Chatei H.	IV-244		
Bratescu M.A.	I-92	Chebotarev A.V.	IV-110	<b>D</b>	
Brault P.	IV-252	Chenevier M.	IV-70	D'yachkov L.	I-188 I-190
Bretagne J.	III-80 IV-184 IV-210	Cheredarchuk A.I.	II-154	Damelin court J.J.	III-16 III-24
Brethes S.	I-268	Chernukho A.	III-18	Darnon F.	III-66
Briaud Ph.	II-212 III-72	Chernyshev A.V.	I-176	Dauchot J.P.	IV-210
Bruhn B.	II-200	Cheron B.G.	II-90	David M.	II-226
Brunet H.	I-58 III-100	Chervy B.	II-104	Davies A.J.	II-216 II-218
Bruno D.	II-242	Chevolleau T.	III-90	De Benedictis S.	I-72 IV-14 IV-80
Bugrova A.I.	II-76 III-68	Chevrier P.	II-100 II-102	De Graaf A.	IV-254
Bultel A.	II-90	Chinnov V.F.	II-94	De Hoog F.J.	I-152 IV-246
Burke R.	IV-230	Chirkin M.V.	IV-262	De Souza A.R.	IV-46
Burm K.T.A.L.	II-108	Chizhik A.	I-208 II-174	De Urquijo J.	I-18
Bursikova V.	IV-260	Choi P.	III-110 II-12 III-28	Debal F.	IV-210
				Decomps Ph.	III-106
				Deegan C.M.	I-114
				Degond P.	III-64
				Deha I.	IV-116

Delaporte Ph.C.	I-48 III-26 IV-52	Dussoubs B.	II-158	Filippov A.A.	II-142
Delhaes P.	IV-236	Dyatko N.A.	I-24 I-66 II-116	Fitaire M.	IV-28
Denat A.	IV-10 IV-12	Dyomkin S.A.	IV-224	Fitzgerald T.J.	III-10
Derouard J.	I-150 IV-202	Dyson A.E.	I-116	Flamant G.	II-124
Deschamps N.	IV-46	Dzermanova N.	II-192	Flazi S.	IV-16
Desideri D.	II-262 IV-134	<b>E</b>		Fleddermann C.B.	IV-214
Desoppere E.	I-20 I-106 III-38	Eby S.D.	I-50	Fleurier C.	II-100 II-102 III-44 IV-150
Despax B.	IV-208	Egli W.	II-236	Flieser J.	IV-124
Dessaux O.	IV-142	Ehrich H.	II-118	Fliesser W.	IV-122 IV-126
Destombes V.	III-100	Eichwald O.	I-252 II-220 IV-154	Fodrek P.	IV-128
Deutsch H.	II-4 II-6 II-74 II-200 IV-188	El Bezzari M.	I-190	Foest R.	IV-196
Devyatov A.M.	I-44	El Shaer M.	I-118	Fontaine B.	III-26
Dewald E.	II-50 II-52	Elchinger M.F.	I-4	Fortov V.	I-212
Diamy A.M.	IV-218	Eldevik T.	I-32	Fortov V.E.	I-176 I-178
Dias F.M.	I-122	Elloumi H.	IV-64	Frank K.	II-52
Dilecce G.	I-72 IV-14 IV-80 IV-254	Entlicher M.	II-232	Franke St.	II-74
Dinescu G.	IV-254	Epifanie A.	II-160	Franklin R.N.	II-14
Dinklaga A.	II-200 IV-188	Ercilbengoa A.E.	III-84	Frost R.M.	I-60
Djakov A.F.	II-166 II-168 II-208 II-210 IV-4 IV-6 IV-94	Eremenko Yu.	IV-222	Fujioka H.	IV-88 IV-90
Djermoune D.	IV-94	Erraki A.	II-106	Fukuchi Y.	I-74
Dolgolenko D.A.	II-162	Ershov A.P.	II-60	Fukuda M.	IV-168
Domingo P.	II-238	Escarguel A.	I-174	Fulcheri L.	II-124
Dominguez I.	I-18	Essolbi R.	III-94	Funato Y.	IV-156
Donko Z.	II-64	Etievant C.	IV-224		
Dony M.F.	IV-210	Etoh A.	IV-104	<b>G</b>	
Doreswamy C.V.	II-146	Ezubchenko A.N.	II-162	Gajic D.Z.	I-222 I-224
Dorning J.	I-210	<b>F</b>		Galofaro J.T.	II-146
Dors M.	I-250	Fabry F.	II-124	Galy J.	I-58 III-100
Dorval N.	IV-216	Fanack C.	III-2		
Doveil F.	I-202	Fang M.T.C.	II-148 II-150	Ganciu M.	II-50 II-52 IV-158
Draghici-Lacoste A.	I-120	Fauchais P.	I-4 II-158	Garanin S.F.	IV-158
Drallos P.J.	I-30	Fauconneau J.	IV-68	Gardou J.	I-104
Druetta M.	III-92	Faure G.	III-104 IV-78	Garrigues L.	III-70
Ducarroir M.	IV-192	Favre M.	II-12 III-28	Gary F.	II-92 IV-74
Dudeck M.	III-78	Fedorovich O.A.	IV-240	Gasteiger S.	III-36
Dumitrescu-Zoita C.	III-28	Fergusson E.E.	I-84	Gavrilenko V.P.	IV-82
Dupont G.	IV-208	Ferguson D.C.	II-146	Gavrilov N.V.	II-32
Durand J.	I-148	Fernsler R.	II-30	Gavrilova T.	I-188
Dussart R.	III-44	Ferreira C.M.	I-120 I-122 I-124	Geroval E.	IV-120
		Fetisov I.K.	II-24	Gerteisen E.	II-238
		Fewell M.	IV-194	Gherman C.	II-172
		Fiala A.	III-86	Gicquel A.	IV-70
		Fiermans V.	I-20	Gigant L.	IV-114
		Fievet C.	II-102 IV-150	Gijbels R.	II-10
				Gillispie K.	III-102
				Giordano D.	I-26
				Girard A.	I-140 II-256
				Glanschnig M.	I-84

Gleizes A.	II-86	Gross B.	II-82	Henrion G.	II-16
	II-88	Grosswendt B.	I-78	Herben P.G.J.M.	III-63
	II-104	Grozev D.	I-156	Hertl M.	IV-216
	II-106		II-192	Heuraux S.	III-2
	II-126	Grozeva M.	II-130	Higaki H.	I-230
	II-136	Gryaznov V.	I-212	Hipp M.	IV-122
	II-140	Gubsch S.	II-200		IV-126
Glisic S.	IV-42	Guerra V.	IV-160	Hirech A.	II-230
Glosik J.	III-96	Guerrini G.	III-78		III-100
	IV-212	Guiberteau E.	II-16	Hirota A.	I-228
Godyak V.	IV-76	Guillot Ph.	I-58	Hitz D.	III-92
Goedheer W.J.	II-108		III-100	Hoang T.G	III-94
	II-222	Gyergyek T.	IV-162	Hoffmann D.H.H.	I-212
	II-224				II-52
Goldman A.	III-98	<b>H</b>		Hoffmann V.	I-146
Goldman M.	III-98	Hacquin S.	III-2	Holzinger R.	I-260
Goldsmith S.	II-84	Hadi H.	IV-16	Hong D.	III-44
Golly A.	II-110	Hadjadj A.	IV-204		IV-150
Golosnoy I.O.	IV-84	Hajek V.	IV-258	Hopkins M.B.	I-114
Golubev A.	I-212	Hallil A.	IV-62	Horikoshi K.	IV-88
Golubovskii Yu.B.	I-36	Hamada T.	IV-118		IV-90
Golubovskii Yu.B.	II-4	Hamers E.A.G.	II-224	Horvath M.	II-232
	II-6	Hanacek P.	II-78	Hosokawa T.	IV-16
	II-54	Hangai N.	I-144		IV-168
	II-62	Hanitz F.	I-266	Houska A.	II-82
Gombert M.M.	I-22	Hansel A.	I-84	Hrach R.	II-230
Gomes A.M.	I-254		I-260		II-232
	II-160	Harendt A.	I-126		IV-128
Gonzalez J.J.	II-86	Hartgers A.	III-108	Hrachova V.	IV-218
	II-120	Hartmann G.	IV-94		II-18
	II-136		IV-96		II-20
	II-140	Hartmann W.	IV-164		IV-218
	II-206	Hassouni K.	II-116	Hubicka Z.	I-130
Gonzalez-Aguilar J.A.	II-112		IV-70		IV-228
Gorbachev A.M.	I-272	Hatano Y.	I-74	Huet S.	IV-204
	I-274	Haug R.	III-98	Hugon R.	II-16
Gorbunov N.A.	I-80		IV-96	Hure L.	III-44
	I-82		IV-166		
Gordeev O.A.	IV-136	Hava O.	II-18	<b>I</b>	
Gordiets B.F.	I-124	Hayashi N.	I-216	Ieda Y.	II-22
Gorse C.	I-26		II-198	Ignatov A.M.	I-180
	II-116	Haydon S.	IV-194	Inagaki K.	IV-140
Gortchakov S.	III-58	Hbid T.	I-152	Inomata T.	IV-26
Goto M.	I-96		IV-246	Ion L.	IV-236
	IV-86	Hebner G.A.	IV-214		IV-238
	IV-88	Hecq M.	IV-210	Isakaev E.H.	II-94
	IV-90	Helbig V.	II-8	Iserov A.D.	II-94
Goudmand P.	IV-142	Held B.	I-268	Ishida A.	IV-118
Goulet J.C.	I-218		III-84	Ivanov M.S.	II-242
Gousset G.	I-120		IV-180	Ivanov O.A.	I-272
	III-80		IV-236		I-274
	IV-92		IV-238	Ivanov V.G.	I-12
	IV-184	Heldt J.	III-50	Ivanov V.V.	I-86
Grabowski D.	III-50	Hemmati M.	I-214		I-182
Graham W.G.	IV-151	Hemmers D.	II-226		II-28
Granier A.	III-72	Hempel F.	IV-196		II-234
	III-74	Henneberger K.	I-40		III-40
Gregor J.	II-30	Hennig A.	II-8		
Gresser L.	IV-180				

<b>J</b>					
Jacobsen L.M.	III-4	Kawakami R.	II-198	Korolev Yu.D.	IV-174
Jager H.	IV-122	Kawamura K.	IV-266	Korshunov O.V.	IV-262
	IV-124		IV-144	Kosbagarov A.	IV-222
	IV-126	Keidar M.	IV-186	Kosecek A.M.	IV-128
Janca J.	I-256	Kempkens H.	I-14	Kossyi I.A.	I-138
	IV-98	Kerdja T.	II-226		IV-110
	IV-100	Kettlitz M.	IV-264	Kouchi N.	I-74
	IV-260		II-114	Kovalev A.S.	III-76
Jang H.G.	III-88	Khacef A.	IV-108	Kozyrev A.V.	III-54
Jastrabik L.	IV-226		III-30		III-56
	IV-228	Khadka D.B.	III-32		IV-174
Jauberteau I.	IV-102	Kharchevnikov V.K.	I-74	Krajcar-Bronic I.	I-78
	IV-220	Khodachenko G.V.	II-76	Kralkina E.A.	III-88
Jauberteau J.L.	IV-102	Khodataev K.V.	II-24	Krasa J.	IV-272
	IV-220	Khodja H.	IV-24	Krasilnikov M.A.	III-46
Jelenkovic B.M.	I-98	Kidalov S.V.	I-140	Krcma F.	IV-100
Jivotov V.K.	IV-222		III-54	Krenek P.	II-104
	IV-224	Kimura T.	III-56	Kriha V.	I-266
Johnston C.	III-62		I-76	Kroesen G.M.W.	I-152
Jolly J.	IV-190	Kindel E.	II-22		IV-246
	IV-216		III-34	Ksiazek I.	II-110
Jones J.E.	IV-18	Kinoh Y.	IV-108	Kuba P.	IV-128
	IV-20	Kirillin A.	IV-104	Kubota Y.	IV-156
	IV-22	Kirnev G.S.	I-184	Kudelcik J.	IV-8
Jonkers J.	III-62	Kirov K.	II-26	Kudrle V.	IV-28
	III-63		I-156	Kudryavtsev A.Yu.	I-6
	III-108	Kiyooka C.	II-192		I-10
Jordan A.	I-260	Klima M.	IV-156		IV-2
Jugroot M.	II-220		I-128	Kudu K.	IV-34
	IV-154	Kling R.	IV-226	Kulikovskiy A.A.	I-258
Jung H.J.	III-88	Klopovskiy K.S.	III-36		IV-30
			I-86	Kulish M.	I-212
			I-88	Kumar S.	IV-194
			II-28	Kuraica M.M.	IV-146
			II-234	Kurilenkov Yu.K.	I-186
			III-40		I-188
<b>K</b>			I-164		I-190
Kalachov I.	IV-222	Kobayashi Y.	IV-144	Kurnaev V.A.	II-24
Kalinin A.V.	II-60		IV-54		II-26
Kameta K.	I-74	Koch A.W.	IV-56		IV-112
Kandah M.	IV-176		II-200	Kurunczi P.	I-64
Kando M.	IV-104	Koch B.P.	III-50	Kutsyk I.M.	I-6
Kaneda T.	IV-168	Kocik M.	IV-58		I-8
Kanka A.	II-18	Kof L.M.	I-216		IV-2
	II-20	Koga K.	I-244		II-198
Kapicka V.	I-128		II-236	Kuwae H.	III-46
	IV-226	Kogelschatz U.	IV-26	Kuzelev M.V.	I-154
	IV-228	Kogoma M.	III-88	Kuzovnikov A.A.	
Kaplan V.B.	III-104	Koh S.K.	IV-128		
Kapoun K.	I-130	Kolenic F.	I-272	<b>L</b>	
	IV-228	Kolisko A.L.	I-274	Laan M.	IV-32
Karchevsky A.I.	II-162		IV-170	Lagstad I.H.	IV-34
	IV-106	Kolosov V.Yu.	IV-172	Lamoureux M.	I-140
Karderinis S.N.	I-132		III-88	Lancellotti C.	I-210
Katkalo A.A.	IV-234	Kondranin S.G.	IV-146	Lange H.	IV-36
Kawaguchi M.	I-134	Konjevic N.	IV-222	Lapuerta V.	I-204
	II-34	Konstantinov E.	III-40	Laroussi M.	III-102
	IV-132	Kopytin A.A.	II-132	Lasgorceix P.	IV-102
Kawai Y.	I-136	Korbel A.	III-110	Laska L.	IV-272
	I-216	Korge H.			
	I-244				

Latocha V.	III-64	Lorthioir S.	III-86	Matsuoka M.	I-134
Latyshev Ph.E.	I-80	Louhibi D.	II-244		II-34
	I-82	Loureiro J.	I-90		IV-132
Laure C.	IV-252		I-102	Matveev A.A.	I-138
Laurent A.	II-92		IV-160	Maury J.	IV-114
	IV-74		IV-232	Maximov A.I.	I-256
Law D.A.	I-192	Louvet G.	I-186	Mayoux C.	III-106
	I-194	Loza O.T.	III-46	McFarland J.	IV-151
Laz'ko V.S.	II-162	Lozneau E.	II-184	Meger R.	II-30
Le Brizoual L.	III-72		II-186	Melin G.	I-140
Le Guen C.	I-188	Luca A.	IV-212	Melnig V.	II-172
Leborgne L.	I-218	Lungu C.P.	I-94	Melnikov A.S.	I-80
Leclert G.	III-2	Lyapin A.I.	IV-234	Mentel J.	II-130
Le Coeur F.	IV-230	Lyszyk M.	III-66		II-132
Lecot C.	II-256				III-48
Le Duc E.	IV-28				III-50
Lee Z.H.	IV-112				
Lefort A.	I-4			Merad A.	I-112
	III-104			Mercier M.	II-92
Legrand J.C.	IV-218	Machala Z.	I-262		IV-74
Lemaire P.	IV-114	Maftoul J.	IV-74		
Lemeur F.	II-90	Mage L.	III-74	Merel P.	I-168
Lemperiere G.	II-214	Magne L.	II-70	Mesyats G.A	II-32
Leon L.	I-70		II-72	Meunier J.L.	II-98
Leprince P.	I-120	Maheu B.	II-90		IV-176
	IV-92	Mahony C.M.O.	IV-151	Mezhiba A.	I-212
	II-238	Makasheva K.	I-156	Michaut C.	III-78
Leroux A.	IV-216	Malek S.	IV-264	Michel H.	IV-66
Leroy O.	I-174	Malinowsky G.Y.	I-48		IV-198
Lesage A.	II-118	Malovic G.N.	I-98		IV-200
Leu F.	II-188	Malykh N.I.	I-138	Michishita T.	I-230
	II-184	Mandache N.B.	II-50	Mikheev L.D.	I-48
Leu G.	II-186		II-52		IV-52
	II-240	Manheimer W.	II-30	Mikikian M.	I-202
Leys C.	III-38	Mankelevich Yu.A.	II-234	Milenin V.M.	III-54
Li Bo	I-52	Maouhoub E.	II-96		III-56
Li Y.M.	III-20	Marchal F.	I-104	Milic B.S.	I-28
Lindinger W.	I-84	Margot J.	I-166		I-222
	I-260	Mark T.D.	IV-250		I-224
	IV-212	Markovic V.Lj.	II-46		I-226
	IV-232		IV-178	Millet P.	I-104
Lino J.	I-178	Marliere C.	I-148	Mimura M.	IV-118
Lipaev A.M.	II-76	Marode E.	IV-46	Minami K.	I-144
Lipatov A.S.	III-22	Martines E.	IV-134		I-228
Lister G.G.	III-34	Martus K.	I-64	Minea T.M.	III-80
Loffhagen D.	III-58	Marty-Dessus D.	IV-236	Mintsev V.B.	I-212
	III-84		IV-238		
Loiseau J.F.	IV-262	Masek J.	II-78	Mitrofanov N.K.	II-134
Lomakin B.N.	II-144		II-82		IV-138
Londer J.I.	I-24	Masek K.	IV-272	Mizeraczyk J.	I-250
Longo S.	I-26	Mashino S.	IV-88		II-130
	II-116		IV-90		III-50
	II-242	Massines F.	III-106	Mobasher M.	I-118
Lopaev D.V.	I-86		IV-44	Modreanu G.	II-50
	I-88	Matejcik S.	IV-250	Mohri A.	I-230
	II-28	Matheron P.	IV-116	Moisan M.	I-168
	III-40	Mathew J.	II-30	Mokhtari A.E.	II-244
	III-76	Matsui T.	I-142	Molotkov V.I.	I-178
		Matsumoto M.	I-238	Mond M.	I-236
			II-58	Monin M.P.	I-270



Moreno J.	II-12	Neuilly F.	IV-202	Pauna O.	I-166
	III-28	Nichipor G.V.	I-250	Pavlenko V.N.	I-232
Mori A.	II-34	Nicolazo F.	III-74		II-178
Mori I.	IV-266	Nienhuis G.J.	II-224		II-180
Morimoto T.	IV-266	Niessen W.	I-264		IV-240
Morozov A.	IV-124	Nikulín S.P.	II-36		IV-248
Morozov A.I.	II-76	Nishioka T.	II-58	Pavlik J.	IV-128
	III-68	Nistor M.	II-50	Pavlik M.	IV-250
Morozov D.A.	I-208		II-52	Pavlov V.B.	III-88
Morrow R.	II-258	Nogaki M.	IV-40	Pawełec E.	II-122
	IV-38	Novak M.	IV-226	Pealat M.	IV-216
Morvova M.	I-262		IV-228	Pechacek R.	II-30
Mouadili A.	III-24	Novak S.	II-248	Pedoussat C.	II-252
Movtchan I.A.	I-80		IV-128	Pejovic M.M.	II-46
Mozgovoi A.L.	I-6	Novakovic N.V.	I-28		IV-178
Mozgrin D.V.	II-24	Nunomura S.	I-196	Pekarek S.	I-266
Muller H.J.	IV-54	Nur M.	IV-10	Pellerin S.	II-122
Muller I.	II-182		IV-12	Pelletier J.	IV-230
Muller S.	IV-120			Peres G.	II-254
Murata T.	III-82	<b>O</b>		Perret C.	II-256
Muromkin Yu. A.	II-162	Odagiri T.	I-74	Perrin J.	IV-190
Murphy D.	II-30	Ohe K.	I-76	Peska L.	II-78
Musa G.	I-92		II-22		II-82
	I-94		II-66	Petit L.	III-98
	II-118		IV-140	Petrov G.	II-266
	II-188		I-196	Petrov O.F.	I-176
Mushiaki M.	IV-156	Ohno N.	IV-86		I-178
Musikowski H.D.	II-128	Ohtani K.	I-32	Petrov T.	II-130
Musinov S.	IV-222	Oien A.H.	III-4	Petrovic Z.Lj.	I-34
Musiol K.	II-122		I-230		I-98
Mustata I.	II-118	Oishi H.	I-96		II-44
	II-188	Okada T.	IV-26		II-46
Myamoto K.	I-92	Okazaki S.	III-82		IV-42
		Okita Y.	I-68		IV-178
		Olthoff J.K.	IV-186	Peyrous R.	I-268
<b>N</b>		Ono M.	II-68		III-84
Nagahama T.	I-228	Onoda H.	I-144		IV-180
Naghizadeh-Kashani Y.	II-106	Onose H.	IV-110	Pfau S.	II-38
Nagorny V.P.	I-30	Otorbaev D.K.	II-38		II-40
Naidis G.V.	II-246	Otte M.	II-40	Phelps A.V.	II-48
Naito Y.	I-144		IV-222	Piejak R.	IV-76
Nakamura M.	I-76	Overchuk K.		Pierre Th.	II-164
	I-196				II-170
Nakamura Y.	I-242	<b>P</b>		Pierson J.F.	IV-198
	I-244	Pacheco J.	II-120	Pignolet P.	II-42
Nandelstädt D.	II-132	Paillol J.	II-42	Pinheiro M.J.	IV-232
Napartovich A.P.	I-24		II-250		I-124
	I-66	Panchenko V.G.	II-178	Pintassilgo C.D.	I-102
Nefedov A.P.	I-176		II-180	Pitchford L.C.	I-100
	I-178		IV-240		II-56
Neger T.	IV-122		IV-248		II-252
	IV-124	Pancheshnyi S.V.	IV-48		III-42
	IV-126	Panciatichi C.	II-214		III-70
Neiger M.	I-264	Pardo C.	II-112		III-86
	II-36	Paris P.	IV-32	Placinta G.	IV-242
Nekuchaev V.O.	I-36	Parizet M.J.	II-96	Pogora V.	II-138
	II-54	Parys P.	IV-272	Pointu A.M.	II-50
Nerushev O.A.	I-198	Pashkovsky V.G.	II-162		II-52
Ness K.F.	I-54	Passoth E.	II-8	Pokrzywka B.	II-122

Ponomarev N.S.	I-36 II-54	Revel I.	II-56	Sadeghi N.	I-150 I-152
Popa G.	II-66 IV-242	Riad H.	II-106		IV-202 IV-246
Popescu A.	II-118 II-188	Ricard A.	I-168 IV-66 IV-198 IV-200 IV-210	Saenko V.A.	I-38 IV-182 IV-248
Popescu I.I.	II-50 II-52	Richou J.	I-174 IV-116	Saidane K.	II-126
Popov A.M.	II-28	Rivaletto M.	II-42	Sakai T.	IV-16
Popov N.A.	I-88	Robert E.	III-30 III-32	Sakai Y.	I-92
Poppe F.	III-38	Robin L.	IV-152	Sakamoto S.	IV-186
Porokhova I.A.	II-4 II-6 II-62	Robson R.E.	I-52 I-54	Salabas A.	II-118
	III-60	Roca i Cabarrocas P.	IV-204	Salamero Y.	I-104
Porrás D.	I-270	Rodriguez-Yunta A.	II-112	Samarian A.	I-184
Postel C.	IV-106	Rohlena K.	IV-272	Sando K.	I-164
Potantin E.P.	IV-224	Rohmann J.	II-38 II-40	Sanduloviciu M.	II-172 II-184
Potapkin B.V.	II-126	Romeas P.	I-186		II-186 II-188 II-190
Pousse J.	III-30 III-32 III-44	Rosatelli C.	II-176	Sapozhnikov A.V.	I-138
Pouvesle J.M.	I-146	Rosenfeld W.	III-44	Sarrette J.P.	I-254 II-160
Praessler F.	I-260	Rosenkranz J.	I-266	Sarroukh H.	III-24
Prazeller P.	I-88	Rosum I.N.	II-178 II-180	Sarytchev D.V.	II-26
Proshina O.V.	II-234			Sasada T.	IV-132
Protuc I.	II-138	Roth M.	I-212	Sato K.	IV-118
Proulx P.	II-206	Rousseau A.	IV-92	Sato S.	I-242
Puech V.	I-270	Roussel J.	IV-130	Sato T.	I-164
Punset C.	III-42	Roussel-Dupre R.T.	III-6 III-8 III-10 III-12 III-52	Satoh H.	I-238 II-58
Purwins H.G.	II-182			Satoh K.	II-260
<b>R</b>				Saulle C.	III-46
Rabehi A.	IV-44	Rovtar J.	IV-162	Savinov V.P.	I-108
Rahal H.	I-22	Rozoy M.	I-270	Savjолоv A.S.	II-24 II-26 IV-112
Rahel J.	IV-250	Rozsa K.	II-64		
Rakhimov A.T.	I-86 I-88	Rudakowski S.	IV-148	Säyler G.S.	III-102
Rakhimov A.T.	II-28 II-234 III-40	Rudnitsky V.A.	I-38	Scheibe H.J.	II-128
		Rukhadze A.A.	I-172 III-46 III-88	Scheibner H.	IV-188
Rakhimova T.V.	I-86 I-88 I-182 II-28 II-234 III-40	Rulev G.B.	I-86	Schein J.	II-132
		Rusanov V.	IV-222	Scheiring Ch.	I-84
Ravary B.	II-124	Rusanov V.D.	IV-224	Scherbakov Yu.V.	II-210
Raynaud P.	I-148 III-74	Rusnak K.	IV-258	Schepe R.	I-40
		Rutkevich I.	I-234 I-236	Scheubert P.	II-202 II-204
Razafinimanana M.	II-88 II-120 II-126 II-136	Ryazantsev E.I.	IV-224	Schimke C.	III-34 IV-108
Redon R.	IV-116	Rybakov A.B.	IV-138	Schmidt E.	III-48
Reess T.	II-250	Rybakov V.V.	I-240	Schmidt M.	IV-196
Remscheid A.	IV-148			Schmoll R.	IV-164
Remy M.	IV-244	<b>S</b>		Schopp H.	II-114 IV-108
		Sa P.A.	I-90	Schram D.C.	II-108 III-62 III-63 III-108 IV-254
		Sabonnadiere M.P.	I-48		
		Sabotinov N.	II-130	Schrufft R.	I-264



Theroude C.	II-254	Van de Grift M.	I-152	<b>W</b>	
Thomann A.L.	IV-252		IV-246	Wachutka G.	II-204
Thomaz J.	IV-232	Van de Sanden M.C.M.	IV-254	Wakabayashi Y.	II-58
Tichonov M.G.	IV-262	Van der Mullen J.A.M.	II-108	Wang Yicheng	I-68
Tichy M.	IV-226		III-62	Watanabe T.	I-244
Tiirik A.	IV-32		III-63	Watanabe Y.	I-170
Timofeev N.A.	III-54		III-108	Wautelet M.	IV-210
	III-56	Van Dijk J.	III-63	Wendt R.	IV-36
Tioursi M.	IV-96	Van Egmond C.	III-38	Wetzig K.	I-146
	IV-166	Van Ootegem B.	I-218	White R.D.	I-52
Toader E.I.	IV-151	Vardelle A.	II-158		I-54
Toedter O.	IV-54	Vardelle M.	II-158	Wieme W.	I-20
	IV-56	Vaselli M.	I-44	Wiesemann K.	IV-148
Tokumasu H.	I-228		I-154	Wilke C.	II-74
Toma M.	II-190		II-60		II-200
Tominaga K.	IV-266	Vasenkov A.V.	I-56		IV-188
Tonegawa A.	IV-144		IV-256	Winkler R.	II-62
	IV-186	Vasilieva A.N.	III-76		II-266
Torchinskii V.M.	I-178	Vaulina O.	I-184		III-58
Tous M.	IV-226	Vayner B.V.	II-146	Wiolland R.	III-46
Touzeau M.	II-70	Veis P.	III-98	Wolf O.	I-264
	II-72	Veklich A.N.	II-154	Wolowski J.	IV-272
	IV-46	Velleaud G.	II-92	Woryna E.	IV-272
	IV-160		IV-74	Wujec T.	II-110
Tramontin L.	II-262	Verdes D.	IV-242	Wuttman M.	I-118
Trepanier J.Y.	I-50	Vereshchagin K.A.	I-42	Wyndham E.	II-12
Treshchalov A.	III-110		IV-136		III-28
Trinquecoste M.	IV-236	Vervisch P.	I-218		
Trusca A.	II-140		II-238	<b>Y</b>	
Tsuda N.	IV-268		IV-152	Yagi Y.	IV-134
Tsuda S.	I-142	Vervloet M.	III-74	Yamada J.	IV-268
Tsukabayashi I.	I-242	Vesselovzorov A.N.	III-78	Yamada K.	I-74
Tsvetkov T.S.	II-192	Vialle M.	II-70		I-142
Turban G.	II-212		II-72	Yamazawa Y.	I-230
	III-74	Videlot H.	IV-190	Yan J.D.	II-148
	III-90	Videnovic I.R.	IV-146		II-150
<b>U</b>		Viel V.	IV-130	Yasuda M.	I-170
Udrea M.	II-50	Vikharev A.L.	I-272	Yasui S.	I-246
Ueda Y.	I-136		I-274	Yatsu M.	II-68
Uhlenbusch J.	II-226	Viladrosa R.	III-30	Yilmaz A.	I-172
Uhrlandt D.	II-74		III-32	Yoshida M.	I-134
Ukai M.	I-74	Vill A.	III-44	Yoshimura S.	I-244
Ulyanov D.K.	III-46	Vitel Y.	III-110	Yousfi M.	I-252
Ulyanov K.N.	II-142		I-188		II-220
	II-144		I-190		IV-154
Uneyama T.	IV-118	Vivet F.	I-200	Yukhimuk V.	III-6
Ustalov V.V.	IV-240	Vizgalov I.V.	II-26		III-8
Ustinov A.L.	II-162	Vlcek J.	IV-258		III-12
Uteza O.	III-26	Vogel N.I.	III-14		III-52
			IV-270	Yumoto M.	IV-16
<b>V</b>		Voitik M.	III-26	Yurghelenas Yu.V.	II-208
Vacque S.	II-120	Vovchenko E.D.	IV-112		II-210
	II-126	Vrba P.	II-264	Yuyama T.	I-230
Valentini H.B.	II-202	Vrhovac S.B.	II-44		
Vallee C.	III-74	Vul A.Ya.	III-54	<b>Z</b>	
Vallone F.	IV-134		III-56	Zahoranova A.	IV-8
Van Bever T.	I-106			Zahraoui A.	II-260

Zajickova L.	IV-260
Zakouril P.	III-96
Zambra M.	II-12
	III-28
Zaretsky E	I-236
Zatsepin D.V.	IV-50
Zhelyazkov I.	I-160
	I-162
Zheng X.	I-228
Zhovtyansky V.A.	II-152
	II-154
Zicha J.	II-18
Zigman V.J.	I-226
Zissis G.	III-60
Zivkovic J.V.	IV-42
Zobnin A.V.	II-94
Zoller V.	IV-222
Zuev V.S.	IV-52
Zvonicek V.	IV-160